ULTRASOUND FOR PRECISION MEDICINE: DIAGNOSIS, DRUG DELIVERY AND IMAGE-GUIDED THERAPY

EDITED BY: Fei Yan, Jean Jose and Xiaobing Wang

PUBLISHED IN: Frontiers in Pharmacology

frontiers Research Topics

ISSN 1664-8714
ISBN 978-2-88963-735-5
DOI 10.3389/978-2-88963-735-5

About Frontiers

Frontiers is more than just an open-access publisher of scholarly articles: it is a pioneering approach to the world of academia, radically improving the way scholarly research is managed. The grand vision of Frontiers is a world where all people have an equal opportunity to seek, share and generate knowledge. Frontiers provides immediate and permanent online open access to all its publications, but this alone is not enough to realize our grand goals.

Frontiers Journal Series

The Frontiers Journal Series is a multi-tier and interdisciplinary set of open-access, online journals, promising a paradigm shift from the current review, selection and dissemination processes in academic publishing. All Frontiers journals are driven by researchers for researchers; therefore, they constitute a service to the scholarly community. At the same time, the Frontiers Journal Series operates on a revolutionary invention, the tiered publishing system, initially addressing specific communities of scholars, and gradually climbing up to broader public understanding, thus serving the interests of the lay society, too.

Dedication to Quality

Each Frontiers article is a landmark of the highest quality, thanks to genuinely collaborative interactions between authors and review editors, who include some of the world's best academicians. Research must be certified by peers before entering a stream of knowledge that may eventually reach the public - and shape society; therefore, Frontiers only applies the most rigorous and unbiased reviews.
Frontiers revolutionizes research publishing by freely delivering the most outstanding research, evaluated with no bias from both the academic and social point of view. By applying the most advanced information technologies, Frontiers is catapulting scholarly publishing into a new generation.

What are Frontiers Research Topics?

Frontiers Research Topics are very popular trademarks of the Frontiers Journals Series: they are collections of at least ten articles, all centered on a particular subject. With their unique mix of varied contributions from Original Research to Review Articles, Frontiers Research Topics unify the most influential researchers, the latest key findings and historical advances in a hot research area! Find out more on how to host your own Frontiers Research Topic or contribute to one as an author by contacting the Frontiers Editorial Office: researchtopics@frontiersin.org

ULTRASOUND FOR PRECISION MEDICINE: DIAGNOSIS, DRUG DELIVERY AND IMAGE-GUIDED THERAPY

Topic Editors:
Fei Yan, Chinese Academy of Sciences (CAS), China
Jean Jose, University of Miami, United States
Xiaobing Wang, Shaanxi Normal University, China

Precision medicine is an approach that proposes customized medical care based on the individual characteristics of each patient. The rapidly emerging field not only holds great promise for diagnosis of disease and prediction of risk of developing diseases, but also offers the possibility of remarkably fine-tuned remedies to improve patient health while minimizing the risk of harmful side effects.

Many technologies including genetics, informatics, and medical imaging, are rapidly expanding the scope of precision medicine. Among these technologies, imaging is poised to play a major role in the age of precision medicine. By characterizing anatomy, physiology and metabolism of the patient, medical imaging enables precise, personalized procedures and predictive, patient-specific therapy selection. In recent years, image-guided treatment procedures are becoming more and more common in hospitals, replacing conventional surgery or allowing faster recoveries with fewer post-procedure complications.

As the most widely used modality, ultrasound is playing an increasingly important role towards moving precision medicine into clinical practice. It is a safe, inexpensive diagnostic tool and capable of producing real-time and non-invasive images without significant biological effects. To date, lots of ultrasound imaging technology, such as gray-scale, color Doppler flow imaging (CDFI), contrast enhanced ultrasound (CEUS), elastography have been developed, which have greatly improved disease diagnosis, treatment and prognosis. Thanks to these progress, ultrasound imaging has also been used in fields that were not previously involved, such as the lungs and musculoskeletal tissues. With the rapid development of ultrasound contrast agents, ultrasound molecular imaging is moving from animal study into clinical practice. First-in-human results of ultrasound molecular imaging with BR55 (a kinase insert domain receptor [KDR]–targeted contrast microbubble) in patients with breast and ovarian lesions have been reported in 2017. Taking advantage of microbubble cavitation effect, ultrasound-assisted drug delivery technology also makes great progress. The clinical trial of blood-brain barrier disruption for chemotherapy delivery in the brain had been conducted and confirmed its safety and well toleration in patients with recurrent glioblastoma (GBM). Moreover, ultrasound provides an advantageous tool for image-guided therapy due to its capability of real-time imaging for deep tissues, contributing to greatly improved localization and targeting of diseased tissues. More interestingly, by imaging these drug-loaded contrast agents, ultrasound-mediated drug delivery can be visualized. All of the above examples help demonstrate the promising potential of ultrasound in precision medicine, not only for disease diagnosis, but also for treatment selection and prognosis evaluation.

The present Research Topic here in Frontiers in Pharmacology aims to bring a collection of research describing ultrasound used for precision medicine in diagnosis, drug delivery and image-guided therapy.

Citation: Yan, F., Jose, J., Wang, X., eds. (2020). Ultrasound for Precision Medicine: Diagnosis, Drug Delivery and Image-Guided Therapy. Lausanne: Frontiers Media SA. doi: 10.3389/978-2-88963-735-5

Table of Contents

06 ***Diagnostic Performance of Multiple Sound Touch Elastography for Differentiating Benign and Malignant Thyroid Nodules***
Lei Zhang, Zhimin Ding, Fajin Dong, Huaiyu Wu, Weiyu Liang, Hongtian Tian, Xiuqin Ye, Hui Luo and Jinfeng Xu

13 ***Value of Contrast-Enhanced Ultrasound and Acoustic Radiation Force Impulse Imaging for the Differential Diagnosis of Benign and Malignant Thyroid Nodules***
Yan He, Xiao Yan Wang, Qiao Hu, Xue Xue Chen, Bing Ling and Hai Ming Wei

21 ***Molecular Ultrasound Monitoring of Early Artery Injury After Carotid Balloon Angioplasty***
Xinhai Mo, Fei Yan and Bo Zhang

30 ***Atropine Premedication Facilitates Ultrasound-Guided Reduction by Saline Enema in Children With Intussusception***
Xiao Liu, Bei Xia, Hong-kui Yu, Lie-zhen Hu, Shu-min Fan, Dong Xiao, Li-xian Gu, Jia-kun Chen, Zhi-bo Wen and Xiao-peng Ma

37 ***Corrigendum: Atropine Premedication Facilitates Ultrasound-Guided Reduction by Saline Enema in Children With Intussusception***
Xiao Liu, Bei Xia, Hong-kui Yu, Lie-zhen Hu, Shu-min Fan, Dong Xiao, Li-xian Gu, Jia-kun Chen, Zhi-bo Wen and Xiao-peng Ma

38 ***Theranostic Strategy of Focused Ultrasound Induced Blood-Brain Barrier Opening for CNS Disease Treatment***
Ko-Ting Chen, Kuo-Chen Wei and Hao-Li Liu

52 ***Pelvic Ultrasound in Diagnosing and Evaluating the Efficacy of Gonadotropin-Releasing Hormone Agonist Therapy in Girls With Idiopathic Central Precocious Puberty***
Hong-kui Yu, Xiao Liu, Jia-kun Chen, Shan Wang and Xian-yue Quan

60 ***Ultrasound-Guided Percutaneous Release of A1 Pulley by Using a Needle Knife: A Prospective Study of 41 Cases***
Min Pan, Shuya Sheng, Zhiqi Fan, Hao Lu, Hong Yang, Fei Yan and Zhansen E

68 ***Ultrasound on Erect Penis Improves Plaque Identification in Patients With Peyronie's Disease***
Yu Liu, Dequan Zheng, Xiaolin Liu, Xiaohong Shi, Shengchun Shu and Jinbing Li

75 ***Evaluation of Uterosacral Ligament Involvement in Deep Endometriosis by Transvaginal Ultrasonography***
Yujuan Zhang, Xiaojun Xiao, Fanhua Xu, Qi Lin, Jinfeng Xu and Bo Du

81 ***Controlled* in vivo *Bone Formation and Vascularization Using Ultrasound-Triggered Release of Recombinant Vascular Endothelial Growth Factor From Poly(D,L-lactic-co-glycolicacid) Microbubbles***
Yong Gong, Songjian Li, Wei Zeng, Jianing Yu, Yan Chen and Bo Yu

89 ***Efficacy Assessment of Ultrasound Guided Lauromacrogol Injection for Ablation of Benign Cystic and Predominantly Cystic Thyroid Nodules***
Yijie Dong, Jianqiao Zhou, Zhenhua Liu, Ting Luo and Weiwei Zhan

95 ***Ultrasound Stimulation Modulates Voltage-Gated Potassium Currents Associated With Action Potential Shape in Hippocampal CA1 Pyramidal Neurons***
Zhengrong Lin, Xiaowei Huang, Wei Zhou, Wenjun Zhang, Yingzhe Liu, Tianyuan Bian, Lili Niu, Long Meng and Yanwu Guo

106 ***The Optimized Fabrication of a Novel Nanobubble for Tumor Imaging***
Jiaqi Zhang, Yihan Chen, Cheng Deng, Li Zhang, Zhenxing Sun, Jing Wang, Yali Yang, Qing Lv, Wei Han and Mingxing Xie

121 ***Evaluation of the Expression of Matrix Metalloproteinase-1 of Laryngeal Squamous Cell Carcinoma by Ultrasound Molecular Imaging***
Yi Zhou, Zhuqing Song, Qiao Hu, Xiaojuan Ji, Hongyu Zheng, Xiaoyan Wang and Zhenzhou Li

129 ***Prospective Study About the Relationship Between CEUS of Carotid Intraplaque Neovascularization and Ischemic Stroke in TIA Patients***
Zhenzhou Li, Xianfeng Xu, Lijie Ren, Yufeng Shao, Shuyu Luo, Shenghua Chen and Xiaoyun Guan

136 ***Effect of Ultrasound Combined With Microbubble Therapy on Interstitial Fluid Pressure and VX2 Tumor Structure in Rabbit***
Qianyun Zhang, Hai Jin, Liping Chen, Qiaoli Chen, Yan He, Yuwen Yang, Suihong Ma, Shuyi Xiao, Fen Xi, Qiong Luo and Jianhua Liu

146 ***The Role of Blood Flow in Corpus Luteum Measured by Transvaginal Two-Dimensional and Three-Dimensional Ultrasound in the Prediction of Early Intrauterine Pregnancy Outcomes***
Huijuan Han, Xinhai Mo, Yuqin Ma, Yuqing Zhou and Bo Zhang

153 ***Focused Ultrasound Improves NK-92MI Cells Infiltration Into Tumors***
Chaopin Yang, Meng Du, Fei Yan and Zhiyi Chen

164 ***Corrigendum: Focused Ultrasound Improves NK-92MI Cells Infiltration Into Tumors***
Chaopin Yang, Meng Du, Fei Yan and Zhiyi Chen

165 ***Ultrasound-Guided Biopsy of Pleural-Based Pulmonary Lesions by Injection of Contrast-Enhancing Drugs***
Ying Fu, Yuan-Yuan Zhang, Li-Gang Cui, Shi Tan and Yan Sun

173 ***The Application of DVDMS as a Sensitizing Agent for Sono-/Photo-Therapy***
Bingjie Mai, Xiaobing Wang, Quanhong Liu, Kun Zhang and Pan Wang

frontiers in Pharmacology

ORIGINAL RESEARCH
published: 26 November 2018
doi: 10.3389/fphar.2018.01359

Diagnostic Performance of Multiple Sound Touch Elastography for Differentiating Benign and Malignant Thyroid Nodules

Lei Zhang[1,2†], Zhimin Ding[1,2†], Fajin Dong[1,2,3], Huaiyu Wu[1,2], Weiyu Liang[1,2], Hongtian Tian[1,2], Xiuqin Ye[1,2], Hui Luo[1,2] and Jinfeng Xu[1,2*]*

[1] Department of Ultrasound, First Affiliated Hospital of Southern University of Science and Technology, Shenzhen Medical Ultrasound Engineering Center, Shenzhen People's Hospital, Shenzhen, China, [2] Department of Ultrasound, Second Clinical College of Jinan University, Shenzhen People's Hospital, Shenzhen, China, [3] The Key Laboratory of Cardiovascular Remodeling and Function Research, Chinese Ministry of Education, Chinese Ministry of Health, The State and Shandong Province Joint Key Laboratory of Translational Cardiovascular Medicine, Qilu Hospital of Shandong University, Jinan, China

OPEN ACCESS

Edited by:
Fei Yan,
Shenzhen Institutes of Advanced Technology (CAS), China

Reviewed by:
Cui Li Gang,
Peking University Third Hospital, China
JianQiao Zhou,
Ruijin Hospital, China

***Correspondence:**
Fajin Dong
dongfajin@szhospital.com
Jinfeng Xu
xujinfeng@yahooo.com

† These authors have contributed equally to this work as first authors

Specialty section:
This article was submitted to Translational Pharmacology, a section of the journal Frontiers in Pharmacology

Received: *11 September 2018*
Accepted: *05 November 2018*
Published: *26 November 2018*

Citation:
Zhang L, Ding Z, Dong F, Wu H, Liang W, Tian H, Ye X, Luo H and Xu J (2018) Diagnostic Performance of Multiple Sound Touch Elastography for Differentiating Benign and Malignant Thyroid Nodules. Front. Pharmacol. 9:1359. doi: 10.3389/fphar.2018.01359

This study evaluated the ability of Sound Touch Elastography (STE) to distinguish malignant from benign thyroid nodules by quantifying tumor stiffness using the elastic ratio (EI) and shear modulus (G). Eighty-six patients with 86 nodules were enrolled in this study. There were 24/86 (27.90%) thyroid papillary carcinomas (TPC) and 62/86 (72.10%) benign nodules. The mean EI was significantly lower in TPCs than in benign nodules. The EI area under the receiver operating characteristic curve (ROC) was 80%. The EI cutoff value for TPCs was 0.215%. The sensitivity (Sen), specificity (Spe), positive likelihood ratio (LR+), and negative likelihood ratio (LR−) were 71%, 73%, 2.58, and 0.40, respectively. G_{max}, G_{mean}, and G_{sd} were significantly higher in TPCs than in benign nodules. There were no significant differences in G_{min}. Compared with other G parameters, G_{max} with an optimal cutoff value of 15.82 kPa had the highest AUROC value (84%). The Sen, Spe, LR+, and LR− were 79.17%, 79.03%, 3.776, and 0.261, respectively. We pooled the EI, G_{max}, G_{mean}, and G_{sd} and the pooled-Sen, Spe, LR+, LR−, diagnostic odds ratio and odds ratio, and area under the summary ROC were 79%, 71%, 2.73, 0.29, 2.23, 9.29, and 82%, respectively. STE could be a new ultrasound diagnostic method for evaluating benign and malignant thyroid nodules.

Keywords: Sound Touch Elastography, thyroid cancer, shear modulus, summary receiver operating characteristic curve, diagnosis

INTRODUCTION

Thyroid cancer (TC) is the most well-known type of endocrine-related malignancy; TC has become threefold more common in the past 30 years (Cooper et al., 2006; Sebag et al., 2010; Saranac et al., 2011). Fine-needle aspiration (FNA) plays a critical role in differentiating thyroid nodules because of its high sensitivity and specificity (Paschke et al., 2011). However, it is invasive and involves high non-diagnostic (10–15%) or indeterminate (10–20%) outcomes (Rago et al., 2010).

Ultrasound elastography is a non-invasive tool, first introduced by Ophir et al. (1991), which has shown promise for the evaluation of tissue stiffness, providing additional and clinically relevant

information. Mapping the stiffness can either be estimated by analyzing the strain in tissue under stress (quasi-static method) or by imaging of shear waves, mechanical waves, whose propagation is governed by tissue stiffness rather than by its bulk modulus (Gennisson et al., 2013). Most malignant nodules are portrayed by the organization of their unusually firm stroma because of the features of collagen and myofibroblasts, which enable the identification of thyroid cancers with elastography imaging (Monpeyssen et al., 2013).

Nowadays, Sound Touch Elastography (STE) has emerged as a novel elastography technique, which can both provide maps of the strain and of the shear waves. STE allows for quantification of tissue stiffness with the elastic ratio (EI) and shear modulus (G) using the same ultrasound equipment. The main aim of our study was to evaluate the usefulness of STE in predicting malignant thyroid nodules using histopathological analysis as the reference standard.

MATERIALS AND METHODS

Study Population

This study was approved by the Ethics Committee of the Shenzhen people's Hospital. Between June 2016 and December 2017, 95 patients referred for ultrasound examinations were recruited for this study. All participants signed the informed consent form required by the human study committee before enrollment. Nine participants were lost to follow up. The inclusion criteria were as follows. (1) The nodules were stable when detected by ultrasound (US), (2) the size of the nodules ranged from 0.5 to 3.0 cm, (3) the nodules appeared solid or almost solid (<20% cystic) on US, (4) sufficient thyroid tissue surrounded the nodules at the same depth and US cross-section, (5) no intervention or surgery on the nodules had been performed before the US examination, and (6) thyroid surgery or fine needle aspiration biopsy (FNAB) was performed after the US examination within 1 week. Not every nodule could be included for the patients with multiple nodules in this study because of the size and component of nodule restrictions. For patients who had multiple nodules, only the nodule that best satisfied the inclusion criteria was included. Finally, 86 patients (mean age 46.43 ± 12.17 years, range 26–78 years) with 86 nodules (mean size 1.60 ± 0. 39 cm, range 1.01–2.98 cm) met the inclusion criteria and were enrolled in this study, including 24 thyroid papillary carcinomas (TPC) and 62 benign nodules. Thirty-eight patients underwent FNAB and 28 underwent surgery in our hospital.

Imaging Techniques

Both conventional US and STE examinations were performed with a Resona 7 ultrasound system (Mindray Medical Solutions, Shenzhen, China) equipped with a 11L3 linear array transducer (bandwidth frequency of 3–11 MHz) and STE software. When the patients met the inclusion criteria, an informed consent was obtained. Patients were in a supine position with a fully exposed neck. Following which, an STE examination of the lesion was performed. First, the examination probe was kept in contact with the skin. Next, the ROI size was adjusted, such that both the lesion and enough surrounding tissues were included in the ROI and the majority of the lesion's longitudinal section was included in the center of the ROI. When the left of the dual images was nearly green (area >95%) of ROI, the elastographic image of the lesion was acquired and saved. The nodule's morphology characteristics, size, boundary, echoes, and color Doppler features were observed by conventional US and stored. First, switching to EI of the STE model, the probe touched the skin lightly, adjusting the size of the region of interest (ROI), ensured that the nodule and sufficient surrounding gland tissue were included in the ROI. The maximum longitudinal section of the nodules was displayed at the center of the screen, and then the patients were instructed to hold their breath, when the green control bar at the bottom of the screen was stable, pressed the update button and the image was saved; then, the same method was used to obtain the short axis section. Second, switching to the shear wave model, the patient maintained the same position without breathing, when the left of the dual images is nearly green (area >95%) of the ROI, the update button was pressed to obtain the long and short axis section images.

Elastography images were produced, the nodules were circled, and the EI and G data (including G_{max}, G_{min}, G_{mean}, and G_{sd}) were obtained. The average of the long-axis and short-axis values were used for further statistical analysis.

All the examinations were conducted by a sonographer with more than 7 years of experience in US and 3 years of experience in elastography and who was blind to the histopathological results.

Pathological Diagnoses

All nodules were confirmed by histology in this study. All pathological diagnoses were performed by a pathologist with more than 8 years of experience in thyroid pathological examination.

Statistical Analysis

The STE data were recorded, including EI, G_{max}, G_{min}, G_{mean}, and G_{sd}. The true-positive (TP), true-negative (TN), false-positive (FP), and false-negative (FN) numbers per method were calculated. The Kruskal–Wallis non-parametric test was used to compare whether there were significant differences in the EI, G_{max}, G_{min}, G_{mean}, and G_{sd} between benign and malignant nodules. The abilities of EI, G_{max}, G_{min}, G_{mean}, and G_{sd} to differentiate malignant from benign nodules were evaluated by receiver-operating characteristic (ROC) curve analysis. The best cutoff values were obtained using the Youden index (sensitivity+specificity-1) from the ROC curve analysis. The sensitivity (Sen), specificity (Spe), positive likelihood ratio (LR+), and negative likelihood ratio (LR−) were calculated using the chi-squared test (χ^2-test). A P-value < 0.05 was considered to be statistically significant. The values were then combined to obtain an overall STE analysis. The area under the summary ROC (SROC) curve was used. The pooled Sen, Spe, LR+, and LR− were calculated. These data were analyzed with Stata 14.0 for Mac (Stata Corp, College Station, TX, United States) and GraphPad Prism 6.0 for Mac (GraphPad Software, Inc., San Diego, CA, United States).

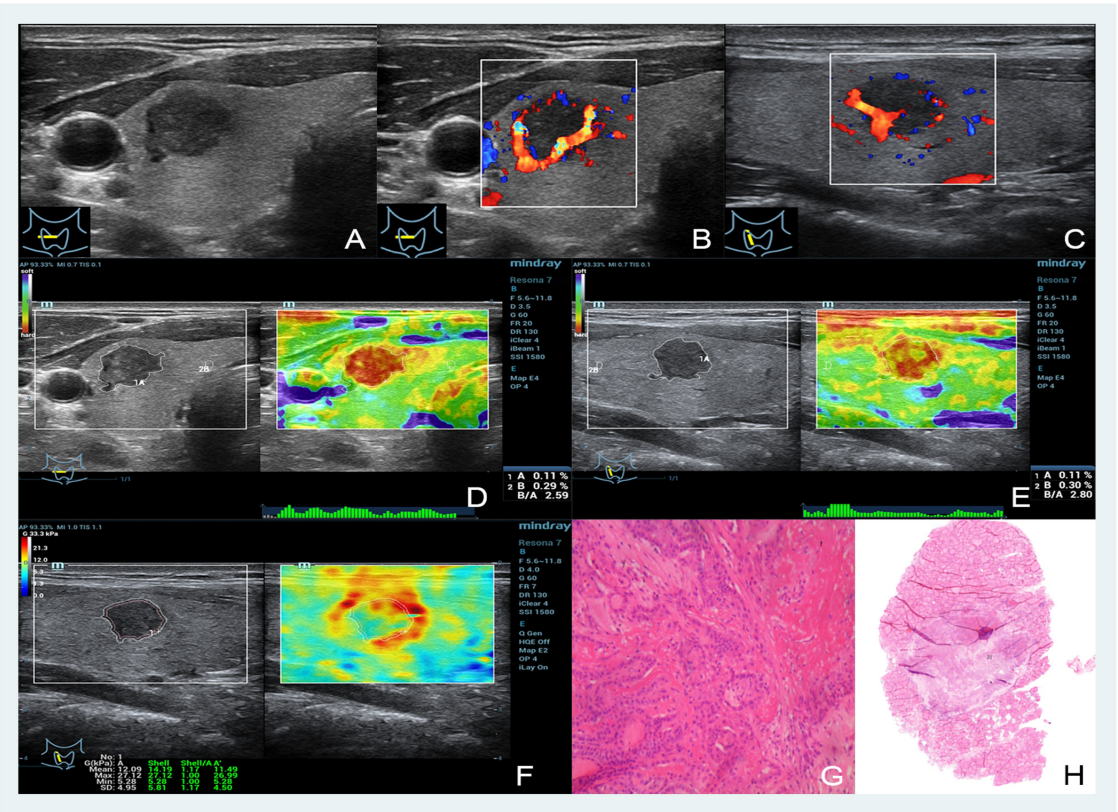

FIGURE 1 | Images showing a thyroid papillary carcinoma in a 48-year-old man. **(A–C)** The B- and color-mode images show a hypoechoic nodule by ultrasound, visible blood flow signal around; **(D,E)** short and long axis of the nodule evaluated by EI (the strain ratio both are 0.11%); **(F)** quantitative shear wave values (G_{mean}: 12.09 kPa, G_{max}: 27.12 kPa, G_{sd}: 4.95 kPa) were measured by drawing a ROI around the nodule to encompass the maximum area but not include the tissue outside the nodule displayed on the B-mode image; **(G,H)** the pathology results confirmed that the nodule was a thyroid papillary carcinoma.

RESULTS

Histology

The pathology results revealed that among the nodules (**Figures 1A–C,G,H**), there were 24/86 (27.90%) malignant papillary carcinomas and 62/86 (72.10%) benign nodules (46 goiter nodules and 16 adenomas) (**Figures 2A–C,H**).

EI of Benign and Malignant Nodules

The nodules' stiffness was indicated by different color changes. As shown in **Figures 1D,E** and **Figures 2D,E**, blue in the upper left indicates the softest and red indicates the hardest. In this study, 24 malignant nodules were red (20 nodules were bright red, which occupied the entire nodule, and the other 4 cases of red area more than 80%), and 62 benign nodules had similar color: green or yellow and white.

The EI measurements of benign and malignant nodules are shown in **Table 1**. The mean EI of malignant nodules was statistically lower than that of benign nodules ($0.19 \pm 0.02\%$ vs. $0.29 \pm 0.01\%$, $P < 0.001$). The area under the ROC curve (AUROC) for the EI of thyroid nodules for the diagnosis of malignant nodules was 0.8. The cutoff value of the EI for malignant nodules was 0.215%. Using this cut-off value, the TP, FP, FN, and TN were 17, 17, 7, and 45, respectively. The Sen, Spe, LR+, and LR− of the EI for diagnosing malignant nodules were 71%, 73%, 2.58, and 0.40, respectively (**Figure 3** and **Table 1**).

G of Benign and Malignant Nodules

The nodules' stiffness was indicated by different color changes like EI. As shown in **Figures 1F,G**, **2F,G**, blue in the upper left indicates the softest and red indicates the hardest. In this study, all 24 malignant nodules showed a reddish periphery (red rim-like) and a yellow or yellow-green in the middle, while the color of 62 benign nodules was similar to that of the surrounding tissues and was either green or yellow and had no red nodules with malignant nodules.

The G measurements of benign and malignant nodules are shown in **Table 1**. G_{max}, G_{mean}, and G_{sd} were significantly higher in malignant nodules than in benign nodules ($P < 0.005$) (**Table 1**). There were no significant differences in G_{min} ($P = 0.59$). The ROC curves of the three G parameters are shown in **Figure 3**. The optimal cut-off values with respective AUC are presented in **Table 1**. Compared with other G parameters, G_{max} with the optimal cutoff value set at 15.82 kPa had the highest AUC value,

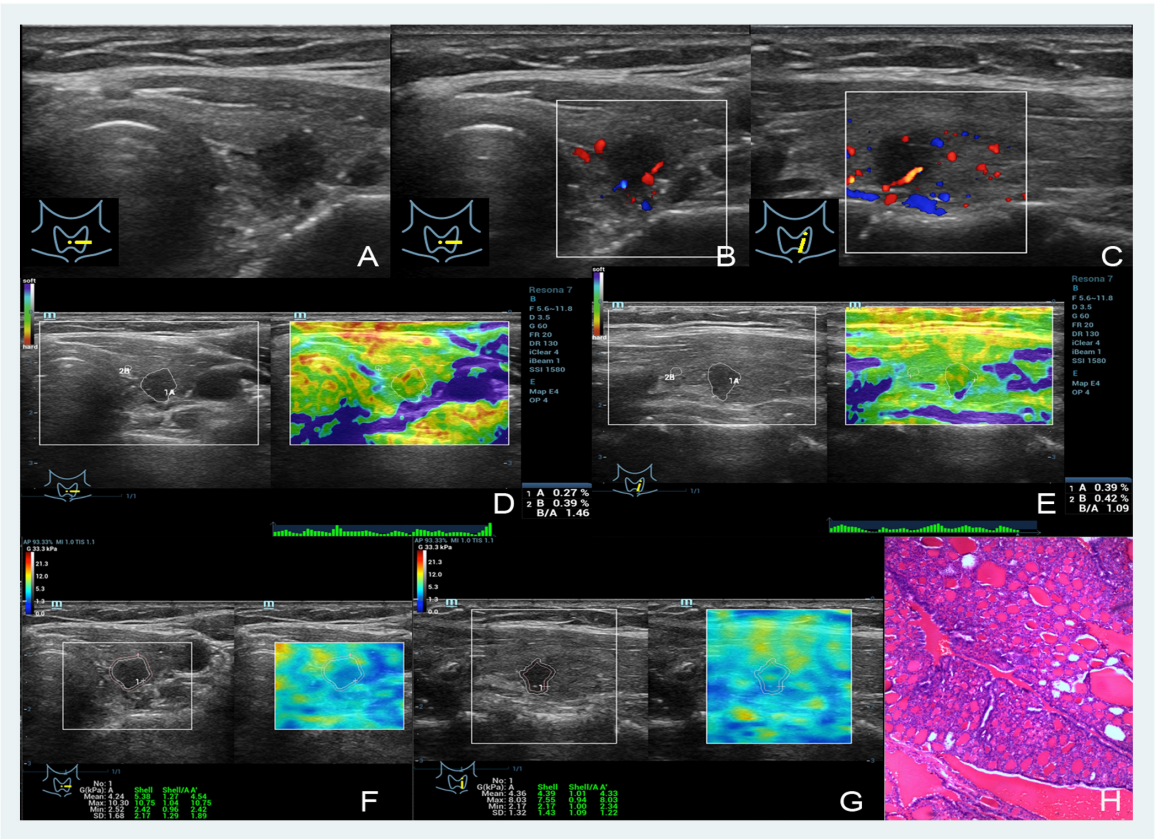

FIGURE 2 | Images showing a nodular goiter in a 46-year-old woman. **(A–C)** The B- and color-mode images show a hypoechoic nodule by ultrasound, minor visible blood flow signal around and inside; **(D,E)** short and long axis of the nodule evaluated by the EI (the strain ratios are 0.27 and 0.39%, respectively); **(F,G)** quantitative shear wave values (G_{mean}: 4.24 kPa, G_{max}: 10.30 kPa, G_{sd}: 1.68 kPa in the short axis; G_{mean}: 4.39 kPa, G_{max}: 8.03 kPa, G_{sd}: 1.32 kPa in the long axis) were measured by drawing a ROI around the nodule to encompass the maximum area but not include the tissue outside the nodule displayed on the B-mode image; **(H)** the pathology results confirmed that the nodule was a nodular goiter.

TABLE 1 | The EI and G measurements of benign and malignant nodules.

Lesion		MAX	MIN	Mean ± SD	*P*	Cut-off	AUROC	SEN	SPE	LR+	LR−	TP	FP	FN	TN
EI	Benign	0.78	0.13	0.29 ± 0.01	0.0001	0.215%	0.78	0.71	0.73	2.58	0.40	17	17	7	45
	Malignant	0.34	0.07	0.19 ± 0.02											
G_{mean}	Benign	0.51	0.13	5.82 ± 0.30	0.0006	6.715	0.78	0.86	0.68	2.71	0.19	21	20	3	42
	Malignant	0.34	0.07	8.22 ± 0.78											
G_{max}	Benign	49.36	4.48	12.12 ± 0.99	0.0001	15.82	0.84	0.79	0.79	3.78	0.26	19	13	5	49
	Malignant	41.97	8.03	21.62 ± 1.65											
G_{min}	Benign	5.61	0.14	2.64 ± 0.17	0.5905	–	–	–	–	–	–	–	–	–	–
	Malignant	8.48	0.45	2.83 ± 0.37											
G_{sd}	Benign	0.51	0.13	1.75 ± 0.15	0.0002	2.00	0.74	0.78	0.64	2.21	0.34	19	22	5	40
	Malignant	0.34	0.07	2.92 ± 0.30											

SEN, sensitivity; SPE, specificity; LR+, positive likelihood ratio; LR−, negative likelihood ratio; TP, true-positive; TN, true-negative; FP, false-positive; FN, false-negative.

the AUROC was 0.840 (95% CI: 0.759–0.928). Using this cutoff point, showing diagnostic Sen, Spe, LR+, and LR− were 79.17%, 79.03%, 3.776, and 0.261, respectively (**Table 1**). The other two G parameters, G_{mean} and G_{sd}, with the same cutoff value were 6.715 and 2.00 kPa, respectively. The details are shown in **Table 1** and **Figure 3**.

Pooled EI and G of Benign and Malignant Nodules

We pooled the EI, G_{max}, G_{mean}, and G_{sd} using the Midas module in Stata 14.0, which is equipped with the bivariate mixed-effects regression model developed by van Houwelingen et al. (1993, 2002), modified for the synthesis of diagnostic

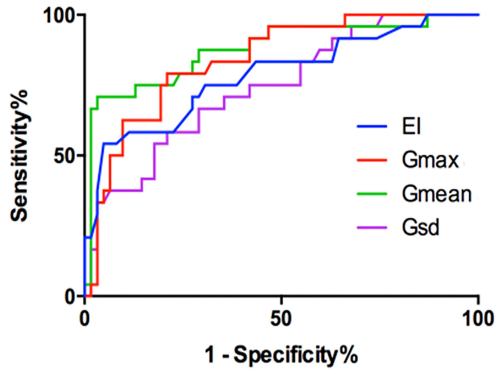

FIGURE 3 | The ROC of the EI (cutoff: 0.215%, Sen 71%, Spe 73%), G_{max} (cutoff: 15.82 kPa, Sen 79%, Spe 79%), G_{mean} (cutoff: 6.715 kPa, Sen 86%, Spe 68%), and G_{sd} (cutoff: 2.00 kPa, Sen 78%, Spe 64%).

test data, to pool the statistical indexes and draw the statistical graphs. The pooled sensitivity (P-Sen) and specificity (P-Spe), pooled positive likelihood ratio (PLR+), negative likelihood ratio (PLR−), diagnostic odds ratio (DOR), OR with corresponding 95% confidence intervals (CI), and area under the SROC curve were used to examine the diagnostic accuracy. As shown in **Figure 4**, significant heterogeneity in P-Sen (I^2 = 0%, Q = 2.02) and P-Spe (I^2 = 16.69%, Q = 3.60) were detected. The P-Sen, P-Spe, PLR+, PLR−, DOR, OR, and area under the SROC curve were 79% (95% CI: 70–86%), 71% (95% CI: 65–76%), 2.73 (95% CI: 2.19–3.40), 0.29 (95% CI: 0.20–0.44), 2.23 (95% CI: 1.67–2.79), 9.29 (95% CI: 5.29–16.32), and 82% (95% CI: 78–85%), respectively (**Figures 4**, **5**).

DISCUSSION

Approximately 60,000 people a year will be diagnosed with thyroid cancer in the United States. Statistics show that more women than men are diagnosed with thyroid cancer. It is the fourth most common type of cancer among women (National Comprehensive Cancer Network [NCCN], 2017). Tumor stiffness can reflect the nature of tumors to a certain extent (Mandel, 2004). The harder the tissue, the higher the risk of malignancy (Pacini et al., 2006). Overall, cancerous thyroid tumors tend to be harder than benign ones. Nodule stiffness is normally determined by palpation by a physician, but smaller nodules, particularly those that are deeply located, cannot be palpated.

Elastography is a non-invasive ultrasound method for assessing the mechanical qualities of the tissues, for example, elasticity and stiffness (Bamber et al., 2013). Since the thyroid is a superficial organ, it can undoubtedly be assessed by all elastography techniques. Elastography has been generally acknowledged and utilized for distinguishing the stiffness of thyroid nodules (Franchi-Abella et al., 2013). Different techniques, based on real-time two-dimensional image sequencing after applying a force that is either dynamic or slowly varying (and considered "quasi-static"), were developed. The principle of elastography is based on US measurement of tissue displacement (Gennisson et al., 2013). All elastographic techniques utilize signal processing to create an image and/or to evaluate the stiffness and elasticity of the investigated tissue (Golu et al., 2017). Two basic concepts are currently used for US elastography: to evaluate the strain or distortion of a tissue because of a power (static elastography, SE), the propagation speed of a shear wave (acoustic radiation force impulse imaging, ARFI), or the measurement of the Young's modulus of the tissue

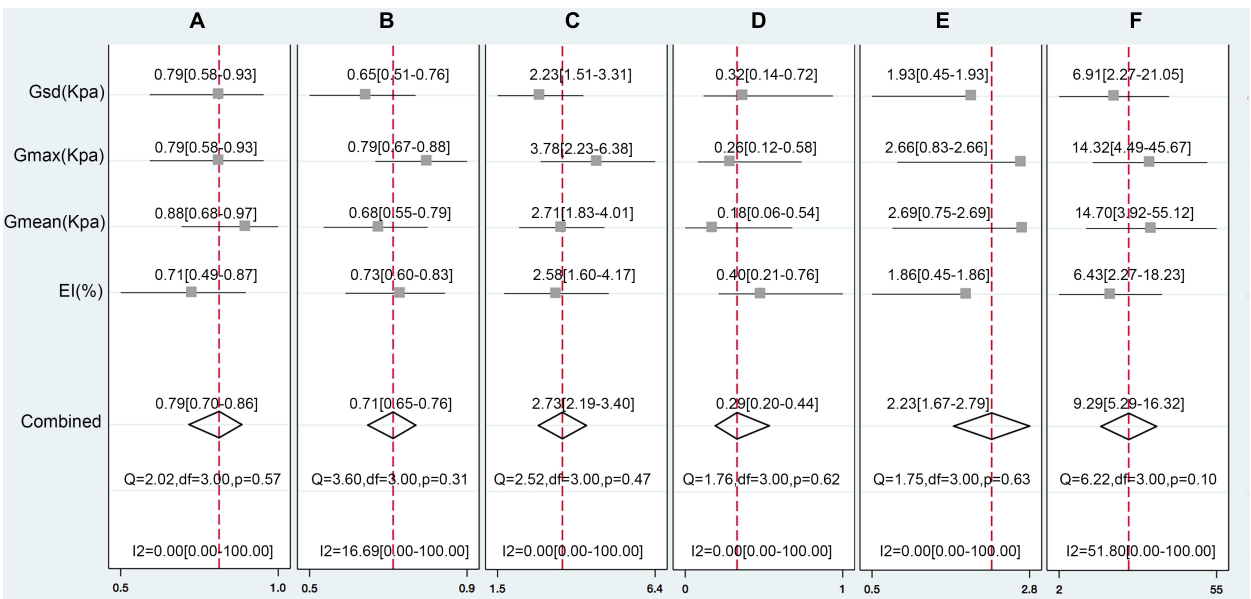

FIGURE 4 | The pooled Sen **(A)**, Spe **(B)**, LR+**(C)**, LR-**(D)**, DOR **(E)**, and OR **(F)** of the EI, G_{max}, G_{mean}, and G_{sd} with 95% CI.

(shear wave elastography, SWE). Manufacturers have built their elastography modules utilizing any of these principles and their own particular innovations.

All shear wave data in the entire ROI could be received at one time to achieve real time two-dimensional SWE imaging. STE can obtain the quantitative elastic parameters, EI and G, and non-invasively evaluate tissue stiffness. In this study, the diagnostic and clinical values of the EI and G of benign and malignant thyroid nodules were compared. The cut-off points of the EI, G_{max}, G_{mean}, and G_{sd} were 0.215% (Sen: 71%, Spe: 73%), 15.82 kPa (Sen: 79%, Spe: 79%), 6.715 kPa (Sen: 86%, Spe: 68%), and 2.00 kPa (Sen: 78%, Spe: 64%), respectively. A meta-analysis reported the diagnostic value of elastography in predicting malignant thyroid nodules. Tian et al. (2016) reported results indicating that real-time elastography (RTE) was more accurate than SWE as suggested by higher Sen, Spe, and AUROC. The P-Sen, P-Spe, and SROC of RTE and SWE were: 82.9% (95% CI: 79.9–85.5%), 82.8% (95% CI: 78.9–86.2%), and 88.9% and 78.4% (95% CI: 73.2–82.8%), 82.4% (95% CI: 76.6–87.1%), and 85.9%, respectively. We also performed a meta-analysis on ARFI for differentiating thyroid nodules (Dong et al., 2015). A total of 13 cohort studies involving 1617 thyroid nodules from 1451 patients were identified. Of 13 studies, one was retrospective and the others were prospective. The pooled Sen, Spe, LR+, LR−, and DOR of SWE in differentiating malignant from benign thyroid nodules were 86.3% (95% CI: 78.2–91.7), 89.5% (95% CI: 83.3–93.6), 7.04 (95% CI: 4.40–11.26), 0.17 (95% CI: 0.10–0.31), and 46.66 (95% CI: 19.47–111.81), respectively. The area under the SROC curve was 94% (95% CI: 92–96). In this study, we also pooled the data by systematic review and obtained P-Sen, P-Spe, and area under the SROC curve at 79% (95% CI: 70–86%), 71% (95% CI: 65–76%), and 82% (95% CI: 78–85%), respectively.

Regarding why on the STE elasticity image, the malignant nodules of EI showed a red nodule, the SWE images showed a red rim-like, and the inside were the same color as the benign nodules. We believe that this is attributable to the different principles of the two imaging methods. The EI is a stain-force imaging system. After an external force to the tissue which would cause deformation. Unlike other elastography modalities, STE does not need to be pressurized by the probe, which could monitor the third party's pulsating blood vessels and breathing. Regarding the nodule stiffness, for example, of shelled raw eggs (**Figures 6A,B**), when a force is applied, it will cause a slight deformation, but internal deformation would not be detected, and therefore, the machine would interpret that the nodules are all hard, in EI with pure red. In shear wave imaging, the probe emits shear waves into the nodule that are received by the probe, and can detect in-depth the hardness of different components inside the nodule and display, similar to detecting a peeled cooked egg (**Figures 6C,D**), which could display various internal. The details of stiffness were shown in different colors. During the invasive growth of malignant tumors, internal necrosis is often accompanied by shear wave elasticity. This is termed the "stiff-rim" sign, consistent with the relevant reports (Zhou et al., 2014). An increase in the stiffness of the surrounding tissue may signify that cancer cells have invaded the surrounding tissue of the tumor (Itoh et al., 2006). Studies have shown that tumor tissue infiltration around the tumor is an independent prognostic factor of tumor recurrence and patient death (De Mascarel et al., 1998).

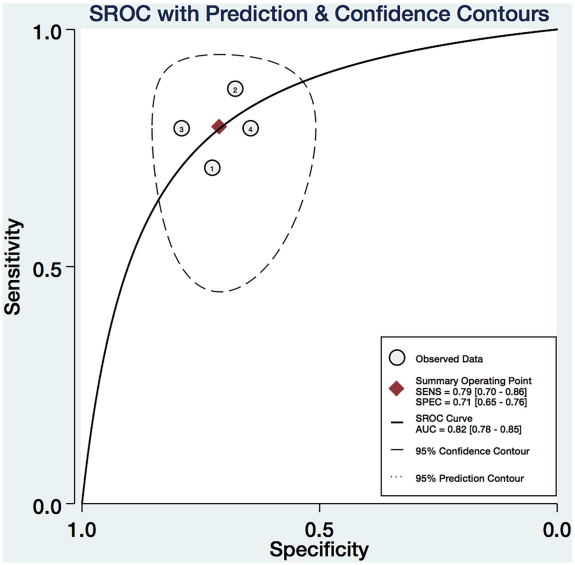

FIGURE 5 | The SROC of the EI, G_{max}, G_{mean}, and G_{sd} with 95% CI.

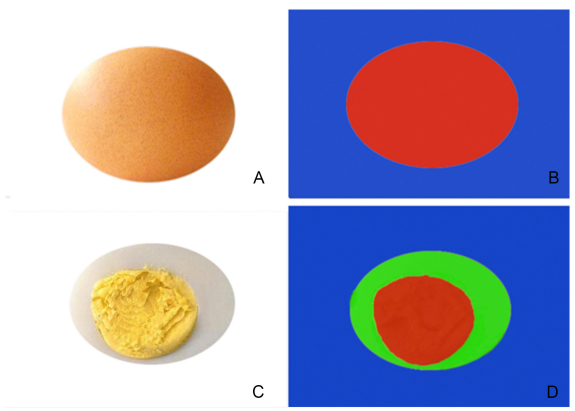

FIGURE 6 | Simple schematic diagram of EI **(A,B)** and shear wave imaging **(C,D)**, **(A,B)** show the shelled raw eggs, when a force is applied, it will cause a slight deformation, but internal deformation would not be detected, and therefore, the machine would interpret that the nodules are all hard, in EI with pure red. **(C,D)** Show in shear wave imaging, the probe emits shear waves into the nodule that are received by the probe, and can detect in-depth the hardness of different components inside the nodule and display, similar to detecting a peeled cooked egg which could display various internal.

These results suggested that tissue stiffness detected by STE can excellently reflect the nature of the nodules. Moreover, STE has some advantages. First, the EI and G can be obtained with the same ultrasound equipment with the same probe; second, the elastography images can be stored in the equipment and analyzed later, which reduces the examination time and the patient's discomfort. However, the study still had limitations. First, the number of cases was small, further study is needed with a larger sample size. Second, only the EI and G were evaluated by

ROC curve analysis in this study, and in the further research, E and V and edge infiltration should be also evaluated.

CONCLUSION

The present study showed comparable results for the novel quantitative STE for the differentiation of thyroid nodules. With high Sen and Spe, STE could be recognized as a new ultrasound diagnostic method in evaluating benign and malignant thyroid nodules. However, the sample of this preliminary study may not be representative of a screening population. Multicenter prospective studies with non-surgical populations and larger samples and more noteworthy difference of pathology are warranted.

AUTHOR CONTRIBUTIONS

FD guarantees the integrity of the entire study and contributed to the experimental studies. JX and ZD contributed to the study concepts. FD and ZD designed the study. LZ contributed to the literature research. FD and HW contributed to the clinical studies. HW acquired the data. FD and LZ contributed to the data analysis and interpreted the data. FD and HT contributed to the statistical analysis. XY prepared the manuscript. WL and ZD contributed to the intellectual content of the manuscript. FD and XY edited, revised, and reviewed the manuscript.

FUNDING

This project was supported by the Clinical Research Project of Shenzhen People's Hospital (No. SYLY201702) and The Key Laboratory of Cardiovascular Remodeling and Function Research, Chinese Ministry of Education, Chinese Ministry of Health, The State and Shandong Province Joint Key Laboratory of Translational Cardiovascular Medicine, Qilu Hospital of Shandong University, Jinan, China.

REFERENCES

Bamber, J., Cosgrove, D., Dietrich, C. F., Fromageau, J., Bojunga, J., Calliada, F., et al. (2013). EFSUMB guidelines and recommendations on the clinical use of ultrasound elastography. Part 1: basic principles and technology. *Ultraschall Med.* 34, 169–184. doi: 10.1055/s-0033-1335205

Cooper, D. S., Doherty, G. M., Haugen, B. R., Kloos, R. T., Lee, S. L., Mandel, S. J., et al. (2006). Management guidelines for patients with thyroid nodules and differentiated thyroid cancer: the american thyroid association guidelines taskforce. *Thyroid* 16, 109–142. doi: 10.1089/thy.2006.16.109

De Mascarel, I., Bonichon, F., Durand, M., Mauriac, L., MacGrogan, G., Soubeyran, I., et al. (1998). Obvious peritumoral emboli: an elusive prognostic factor reappraised. Multivariate analysis of 1320 node-negative breast cancers. *Eur. J. Cancer* 34, 58–65. doi: 10.1016/S0959-8049(97)00344-4

Dong, F. J., Li, M., Jiao, Y., Xu, J. F., Xiong, Y., Zhang, L., et al. (2015). Acoustic Radiation Force Impulse imaging for detecting thyroid nodules: a systematic review and pooled meta-analysis. *Med. Ultrason.* 17, 192–199. doi: 10.11152/mu.2013.2066.172.hyr

Franchi-Abella, S., Elie, C., and Correas, J. M. (2013). Ultrasound elastography: advantages, limitations and artefacts of the different techniques from a study on a phantom. *Diagn. Interv. Imaging* 94, 497–501. doi: 10.1016/j.diii.2013.01.024

Gennisson, J. L., Deffieux, T., Fink, M., and Tanter, M. (2013). Ultrasound elastography: principles and techniques. *Diagn. Interv. Imaging* 94, 487–495. doi: 10.1016/j.diii.2013.01.022

Golu, I., Sporea, I., Moleriu, L., Tudor, A., Cornianu, M., Vlad, A., et al. (2017). 2D-shear wave elastography in the evaluation of parathyroid lesions in patients with hyperparathyroidism. *Int. J. Endocrinol.* 2017:9092120. doi: 10.1155/2017/9092120

Itoh, A., Ueno, E., Tohno, E., Kamma, H., Takahashi, H., Shiina, T., et al. (2006). Breast disease: clinical application of US elastography for diagnosis. *Radiology* 239, 341–350. doi: 10.1148/radiol.2391041676

Mandel, S. J. (2004). Diagnostic use of ultrasonography in patients with nodular thyroid disease. *Endocr. Pract.* 10, 246–252. doi: 10.4158/EP.10.3.246

Monpeyssen, H., Tramalloni, J., Poirée, S., Hélénon, O., and Correas, J. M. (2013). Elastography of the thyroid. *Diagn. Interv. Imaging* 94, 535–544. doi: 10.1016/j.diii.2013.01.023

National Comprehensive Cancer Network [NCCN] (2017). *Guidelines for Patients®: Thyroid Cancer. Version 1.*

Ophir, J., Cespedes, I., Ponnekanti, H., Yazdi, Y., and Li, X. (1991). Elastography: a quantitative method for imaging the elasticity of biological tissues. *Ultrasonic Imaging* 13, 111–134. doi: 10.1177/016173469101300201

Pacini, F., Schlumberger, M., Dralle, H., Elisei, R., Smit, J. W., and Wiersinga, W. (2006). European consensus for the management of patients with differentiated thyroid carcinoma of the follicular epithelium. *Eur. J. Endocrinol.* 154, 787–803. doi: 10.1530/eje.1.02158

Paschke, R., Hegedüs, L., Alexander, E., Valcavi, R., Papini, E., and Gharib, H. (2011). Thyroid nodule guidelines: agreement, disagreement and need for future research. *Nat. Rev. Endocrinol.* 7, 354–361. doi: 10.1038/nrendo.2011.1

Rago, T., Scutari, M., Santini, F., Loiacono, V., Piaggi, P., Di Coscio, G., et al. (2010). Real-time elastosonography: useful tool for refining the presurgical diagnosis in thyroid nodules with indeterminate or nondiagnostic cytology. *J. Clin. Endocrinol. Metab.* 95, 5274–5280. doi: 10.1210/jc.2010-0901

Saranac, L., Zivanovic, S., Bjelakovic, B., Stamenkovic, H., Novak, M., and Kamenov, B. (2011). Why is the thyroid so prone to autoimmune disease? *Horm. Res. Paediatr.* 75, 157–165. doi: 10.1159/000324442

Sebag, F., Vaillant-Lombard, J., Berbis, J., Griset, V., Henry, J. F., Petit, P., et al. (2010). Shear wave elastography: a new ultrasound imaging mode for the differential diagnosis of benign and malignant thyroid nodules. *J. Clin. Endocrinol. Metab.* 95, 5281–5288. doi: 10.1210/jc.2010-0766

Tian, W., Hao, S., Gao, B., Jiang, Y., Zhang, X., Zhang, S., et al. (2016). Comparing the diagnostic accuracy of RTE and SWE in differentiating malignant thyroid nodules from benign ones: a meta-analysis. *Cell Physiol. Biochem.* 39, 2451–2463. doi: 10.1159/000452513

van Houwelingen, H. C., Arends, L. R., and Stijnen, T. (2002). Advanced methods in meta-analysis: multivariate approach and meta-regression. *Stat. Med.* 21, 589–624. doi: 10.1002/sim.1040

van Houwelingen, H. C., Zwinderman, K. H., and Stijnen, T. (1993). A bivariate approach to meta-analysis. *Stat. Med.* 12, 2273–2284. doi: 10.1002/sim.4780122405

Zhou, J., Zhan, W., Chang, C., Zhang, X., Jia, Y., Dong, Y., et al. (2014). Breast lesions: evaluation with shear wave elastography, with special emphasis on the "stiff rim" sign. *Radiology* 272, 63–72. doi: 10.1148/radiol.14130818

Conflict of Interest Statement: The authors declare that the research was conducted in the absence of any commercial or financial relationships that could be construed as a potential conflict of interest.

frontiers in Pharmacology

ORIGINAL RESEARCH
published: 27 November 2018
doi: 10.3389/fphar.2018.01363

Value of Contrast-Enhanced Ultrasound and Acoustic Radiation Force Impulse Imaging for the Differential Diagnosis of Benign and Malignant Thyroid Nodules

Yan He[1], Xiao Yan Wang[1†], Qiao Hu[1*†], Xue Xue Chen[1], Bing Ling[1] and Hai Ming Wei[2]*

[1] Department of Ultrasound, The People's Hospital of Guangxi Zhuang Autonomous Region, Nanning, China, [2] Department of Pathology, The People's Hospital of Guangxi Zhuang Autonomous Region, Nanning, China

Objectives: To assess the value of contrast-enhanced ultrasound (CEUS) and acoustic radiation force impulse (ARFI) imaging for the differential diagnosis of benign and malignant thyroid nodules.

Methods: CEUS was performed in eighty-eight thyroid nodules. The patterns of CEUS were analyzed, and ARFI was then performed. The shear wave velocities (SWVs) of the nodules and the surrounding normal thyroid tissue were obtained. The areas under the curve (AUCs) and cut-off value were obtained by a receiver operating characteristic (ROC) curve analysis. The sensitivity, specificity, positive predictive value (PPV), negative predictive value (NPV) and diagnostic rate of each modality were assessed and compared using pathological diagnosis.

Results: Among 88 nodules, 29 nodules were malignant and 59 were benign. The sensitivity, specificity, PPV, NPV, and diagnostic rate of CEUS were 79.3, 91.5, 82.1, 90, and 87.5%, respectively. Using a cut-off value of 2.565 m/s for SWV, the sensitivity, specificity, PPV, NPV and diagnostic rate for malignancy were 75.9, 94.9, 88.0, 88.9, and 88.6%, respectively. The AUC was 0.878. The sensitivity, specificity, PPV, NPV and diagnostic rate of CEUS in combination with ARFI were 93.1, 89.8, 81.8, 96.3, and 90.9%, respectively.

Conclusion: Both CEUS and ARFI are valuable for the differential diagnosis of benign and malignant thyroid nodules. Combining these two methods can improve the diagnostic rate.

Keywords: thyroid nodule, contrast-enhanced ultrasound, acoustic radiation force impulse-imaging, shear wave velocity, receiver operating characteristic curve

OPEN ACCESS

Edited by:
Fei Yan,
Shenzhen Institutes of Advanced Technology (CAS), China

Reviewed by:
Fajin Dong,
Shenzhen People's Hospital, China
Dirong Zhang,
Peking University Shenzhen Hospital, China

***Correspondence:**
Xiao Yan Wang
ultrasoundwang@sina.com
Qiao Hu
xyyxyhq@163.com

† These authors have contributed equally to this work

Specialty section:
This article was submitted to Translational Pharmacology, a section of the journal Frontiers in Pharmacology

Received: *05 September 2018*
Accepted: *05 November 2018*
Published: *27 November 2018*

Citation:
He Y, Wang XY, Hu Q, Chen XX, Ling B and Wei HM (2018) Value of Contrast-Enhanced Ultrasound and Acoustic Radiation Force Impulse Imaging for the Differential Diagnosis of Benign and Malignant Thyroid Nodules. Front. Pharmacol. 9:1363. doi: 10.3389/fphar.2018.01363

INTRODUCTION

Thyroid nodules are not specific to a particular disease but are a common clinical manifestation of various thyroid diseases. Only 4∼7% of adult cases can be found by palpation of the thyroid nodules (Vander et al., 1968), but up to 50∼ 67% can be found by conventional ultrasound examination (Mehanna et al., 2009). Most thyroid nodules are benign, and approximately 5% are malignant (Gharib, 1997). The incidence of thyroid cancer has increased in recent years (Paes et al., 2010). The degree of malignancy is low and the prognosis is good for most differentiated thyroid cancers,

however, some thyroid cancers are invasive (Gilliland et al., 1997). Therefore, early detection, early diagnosis and early treatment are key in the prevention and treatment of thyroid malignant nodules.

Conventional ultrasound has become the preferred imaging examination method, but two-dimensional ultrasound overlaps to some degree between benign and malignant nodules. Therefore, the diagnosis of thyroid nodules by conventional ultrasound alone has some limitations (Hoang et al., 2007; Azar et al., 2013).

The development of contrast-enhanced ultrasound (CEUS) can be traced back to 1969. Gramiak et al. (1969) found using an aortic root injection of indocyanine blue that M echocardiography can present an echo enhancement phenomenon. Researchers later discovered that the phenomenon was due to the injection of liquid-containing microbubbles and began to search for a more ideal ultrasound contrast agent, leading to new prospects for the use of CEUS. The value of CEUS for evaluating liver lesions has been widely recognized (Chen et al., 2005; Seitz et al., 2010), and its applications in assessments of breast, thyroid, prostate and other organs have become a focus of research (Mitterberger et al., 2007; Friedrich-Rust et al., 2010). CEUS can dynamically respond to tissue perfusion in real time and has important clinical value for the diagnosis of thyroid nodules.

The concept of elastic imaging was proposed by Ophir et al. (1991). Traditional compression elastic imaging is applied by the operator according to the degree of tissue deformation after pressure to obtain the relative stiffness of the organization. However, traditional compression elastic imaging can easily be affected by the operating frequency, the intensity of the pressure, the size of the area of interest and the size of the lesion, among other factors. The technique has some shortcomings, including poor reproducibility and subjectivity (Luo et al., 2008). Acoustic radiation force impulse imaging (ARFI) includes virtual touch tissue imaging (VTI), and virtual touch tissue quantification (VTQ) (Nightingale et al., 2001, 2002, 2003). The parenchyma is characterized by a greater degree of microstructure, greater stiffness, less deformation and faster shear wave speed. The stiffness of thyroid nodules is related to their pathological structure. ARFI can directly reflect the stiffness of thyroid nodules and can provide information that can be used in the differential diagnosis of benign and malignant thyroid nodules. Many studies have reported differential diagnoses of benign and malignant thyroid nodules by CEUS or ARFI (Nemec et al., 2012; Calvete et al., 2014), but few reports have described the difference between these two tests in the diagnosis of thyroid nodules. This study aimed to study the characteristics of micro-blood flow perfusion and shear wave velocity (SWV) in benign and malignant thyroid nodules by CEUS and ARFI.

MATERIALS AND METHODS

Patients

The study was approved by the Ethical Committee of the People's Hospital of Guangxi Zhuang Autonomous Region, and written informed consent was obtained from all patients. Eighty-three patients were recruited from November 2013 to March 2017 (a total of 88 thyroid nodules); the patients were aged from 15 to 87 years with a mean age of (46.0 $\pm$ 15.2) years. The size of the nodules ranged from 7 to 66 mm, with an average of (28.7 $\pm$ 13.9) mm. All cases were confirmed by pathology.

Selection criteria: (1) Solid or cystic nodules with a solid fraction $>$ 50%. Shear waves cannot spread the liquid. (2) A nodule diameter $>$ 6 mm was required because the sampling frame size of ARFI is 5*6 mm. The nodule size was set to be smaller than the sampling frame such that the sampling frame would include normal tissue surrounding the nodules. The results obtained for the sampling frame did not reflect the results for the nodule. (3) Normal thyroid tissue was present around the nodule for comparison. (4) No surgery, drug or chemotherapy was performed/administered before the operation. The pathological results were confirmed postoperatively.

Instruments and Inspection Methods

CEUS was performed by using a GE E9 color Doppler ultrasound instrument equipped with a 15.0 MHz linear array transducer and a 9.0 MHz contrast transducer with a mechanical index of 0.08.

ARFI was performed by a Siemens ACUSON S2000 system equipped with a 9L4 line array probe, built-in ARFI imaging technology and the related software. The region of interest (ROI) was defined 3–40 mm from the probe surface, and the ROI was a fixed size of 5 $\times$ 6 mm.

The patient was placed in a supine position and told to breathe calmly; full exposure of the thyroid was obtained. The thyroid and bilateral neck were scanned using routine ultrasound. The position, number, size, shape, aspect ratio, boundary, internal echo, calcification type, and sound halo of the lesion and the presence or absence of neck lymph node enlargement were observed.

The patient was asked to breath calmly and avoid swallowing during the CEUS examination. The contrast agent used was Bracco SonoVue (Italy). Saline (5 mL) was added to the dry powder and mixed in an oscillating shaker. Six sulfur hexafluoride microbubble suspensions were configured. An appropriate section showing both the complete lesion and the surrounding normal tissue was selected. The channel was established in patients using the superficial elbow vein. Five milliliters of physiological saline was injected after a rapid bolus injection of 1.8 mL of the mixed contrast agent. The timer was then started, and the observation section remained unchanged. The image was dynamically observed after administration for 3 min. The imaging data were then stored. Contrast performance was observed, including the time required for contrast wash-in (earlier wash-in, wash-in at the same time, later wash-in), the pattern of contrast wash-in (concentric or non-concentric), ring enhancement or lack thereof, contrast intensity at the peak time (low enhancement, equal enhancement, or high enhancement), contrast-enhanced distribution (homogeneous enhancement or inhomogeneous enhancement) and contrast wash-out (earlier or not earlier).

The probe was vertically touched to the surface of the skin at the location of the target thyroid lesion, avoiding the pulsation of the carotid artery. The patient was asked to continue breathing calmly and avoid swallowing. VTQ imaging mode was then begun. The "Update" key was pressed to capture the image after it became stable. The SWV value was then recorded. Gross calcification, necrosis and cystic regions were avoided. Five VTQ results were obtained for the internal and peripheral normal tissues of each nodule. If the ROI was confirmed by CEUS to be a solid lesion ("X.XX m/s"), the ROI was considered too hard and beyond the scope of measurement (Tozaki et al., 2011b). This value was replaced by "9.00 m/s." The average SWV value was recorded.

Statistics Analysis

Statistical analyses were performed using SPSS software version 16.0. Quantitative data are expressed as the means ± SD or as a minimum–maximum range. The distribution of variables was analyzed using the K-S test. Groups were compared using the *t*-test. The effect of SWV on the diagnosis of thyroid cancer was evaluated based on the ROC curve, which was used to select the best critical value. The accuracy of the diagnostic test was evaluated based on the AUC and the diagnostic test evaluation method. Categorical data were compared using Fisher's exact test or the χ^2-test. *P*-values < 0.05 were considered to indicate significant differences.

RESULTS

Pathological Results

In total, 88 thyroid nodules were confirmed by pathology, including 29 malignant and 59 benign nodules. Malignant nodules included 27 thyroid papillary carcinomas, 1 thyroid follicular carcinoma, and 1 thyroid metastasis from a nasopharyngeal carcinoma. Benign nodules included 35 nodular goiters, 15 nodular goiters with nodular hyperplasia, and 9 thyroid adenomas.

CEUS Results

Eighty-eight contrast-enhanced ultrasound modes of thyroid nodules are shown in **Table 1**. Malignant nodules showed concentric and inhomogeneous low or equal enhancement, and earlier contrast wash-out. Benign nodules showed diffuse and ring enhancement. Inhomogeneous, low or equal enhancement has been used as an index for the diagnosis of malignant nodules based on contrast-enhanced ultrasound (Zhang B. et al., 2010).

ARFI Results

The SWV values of the internal and peripheral tissues of 88 thyroid nodules and the SWV ratios of the internal and peripheral normal tissues of the lesions are presented in **Table 2**.

There were significant differences in SWV values between the malignant nodules and the surrounding tissue ($P < 0.05$). There were also significant differences in SWV values between benign and malignant nodules ($P < 0.05$). There was no significant difference in SWV value between benign nodules and the surrounding tissue ($P > 0.05$), although there were significant differences in the SWV ratios between benign and malignant nodules ($P < 0.05$).

Using cut-off values of 2.565 m/s for SWV and 1.565 for the SWV ratio, the areas under the ROC curves were 0.878 and 0.875, respectively, for the diagnosis of malignant thyroid nodules (**Table 3** and **Figure 1**).

Value of CEUS, ARFI and Their Combination for the Diagnosis of Benign and Malignant Thyroid Nodules

The diagnostic values of CEUS, ARFI and their combination in the diagnosis of thyroid nodules are shown in **Table 4**. There was no significant difference between CEUS and ARFI in terms of their diagnostic value regarding thyroid nodules ($P > 0.05$). However, there were significant differences in the diagnostic values of CEUS, ARFI and the combination of CEUS and ARFI ($P < 0.05$).

TABLE 1 | Contrast-enhanced ultrasound modes of thyroid nodules.

Pathology	Entry pattern			Regression pattern			Contrast pattern	
	Wash-in earlier	Wash-in at the same time	Wash-in later	Wash-out earlier	Wash-out at the same time	Wash-out later	Concentric	Non-concentric
Benign	23	29	7	9	40	10	6	53
Nodular goiter	12	16	7	7	25	3	6	29
Nodular goiter with nodular hyperplasia	4	11	–	2	11	2	–	15
Adenoma	7	2	–	–	4	5	–	9
Malignant	9	7	13	17	11	1	22	7
Papillary carcinoma	8	7	12	16	11	–	21	6
Follicular carcinoma	1	–	–	–	–	1	–	1
Metastasis carcinoma	–	–	1	1	–	–	1	–
χ^2-value		12.607			17.101		38.677	
P-value		0.002			<0.001		<0.001	

TABLE 2 | ARFI results for thyroid nodules.

	Internal SWV value (m/s)	Surrounding SWV value (m/s)	SWV ratio
Malignant	5.81 ± 3.21 (range: 0.97∼9.00)	2.11 ± 0.45 (range: 1.24∼3.44)	2.74 ± 1.40 (range: 0.56∼5.57)
Papillary carcinoma	5.86 ± 3.15 (range: 1.24∼9.00)	2.10 ± 0.42 (range: 1.31∼3.44)	2.79 ± 1.41 (range: 0.56∼5.57)
Follicular carcinoma	1.65 ± 0.41 (range: 0.97∼2.00)	1.48 ± 0.21 (range: 1.24∼1.70)	1.12
Metastasis carcinoma	9.00	2.91 ± 0.23 (range: 2.55∼3.00)	3.09
Benign	2.00 ± 1.17 (range: 0.51∼9.00)	2.02 ± 0.40 (range: 1.16∼3.82)	1.02 ± 0.62 (range: 0.20∼4.78)
Nodular goiter	2.02 ± 1.38 (range: 0.51∼9.00)	2.01 ± 0.41 (range: 1.16∼3.32)	1.03 ± 0.73 (range: 0.20∼4.78)
Nodular goiter with nodular hyperplasia	2.13 ± 0.92 (range: 1.56∼8.40)	1.99 ± 0.31 (range: 1.50∼3.82)	1.08 ± 0.44 (range: 0.46∼2.41)
Adenoma	1.74 ± 0.51 (range: 1.05∼3.80)	2.12 ± 0.47 (range: 1.31∼3.23)	0.87 ± 0.35 (range: 0.40∼1.48)

TABLE 3 | Area under the ROC curve for the SWV value and the SWV ratio of thyroid nodules.

	Under curve area	*P*-value	95% confidential interval	
			Lower limit	Upper limit
SWV value	0.878	<0.001	0.791	0.964
SWV ratio	0.875	<0.001	0.785	0.964

DISCUSSION

Differences in benign and malignant thyroid nodules can be found in the boundary, internal echo, aspect ratio, calcification type, blood supply distribution characteristics and blood flow resistance index in conventional ultrasound. However, two-dimensional ultrasound images of benign and malignant nodules overlap to some extent. It is difficult to differentiate benign and malignant thyroid nodules using only conventional ultrasound, whereas CEUS can show microvascular perfusion in the nodules. Benign and malignant nodules can show different patterns of contrast. During ARFI, no external force is applied, potentially avoiding the influence of subjective factors. ARFI can be used to quantitatively evaluate tissue stiffness, yielding a specific numerical value. Tissue stiffness is often closely related to the underlying pathological structure, and malignant nodules often have greater tissue stiffness than benign nodules (Mandel, 2004).

CEUS Modes Relating to Thyroid Nodules and Their Pathology

Zhang B. et al. (2010) prospectively observed CEUS modes for thyroid nodules and proposed that inhomogeneous

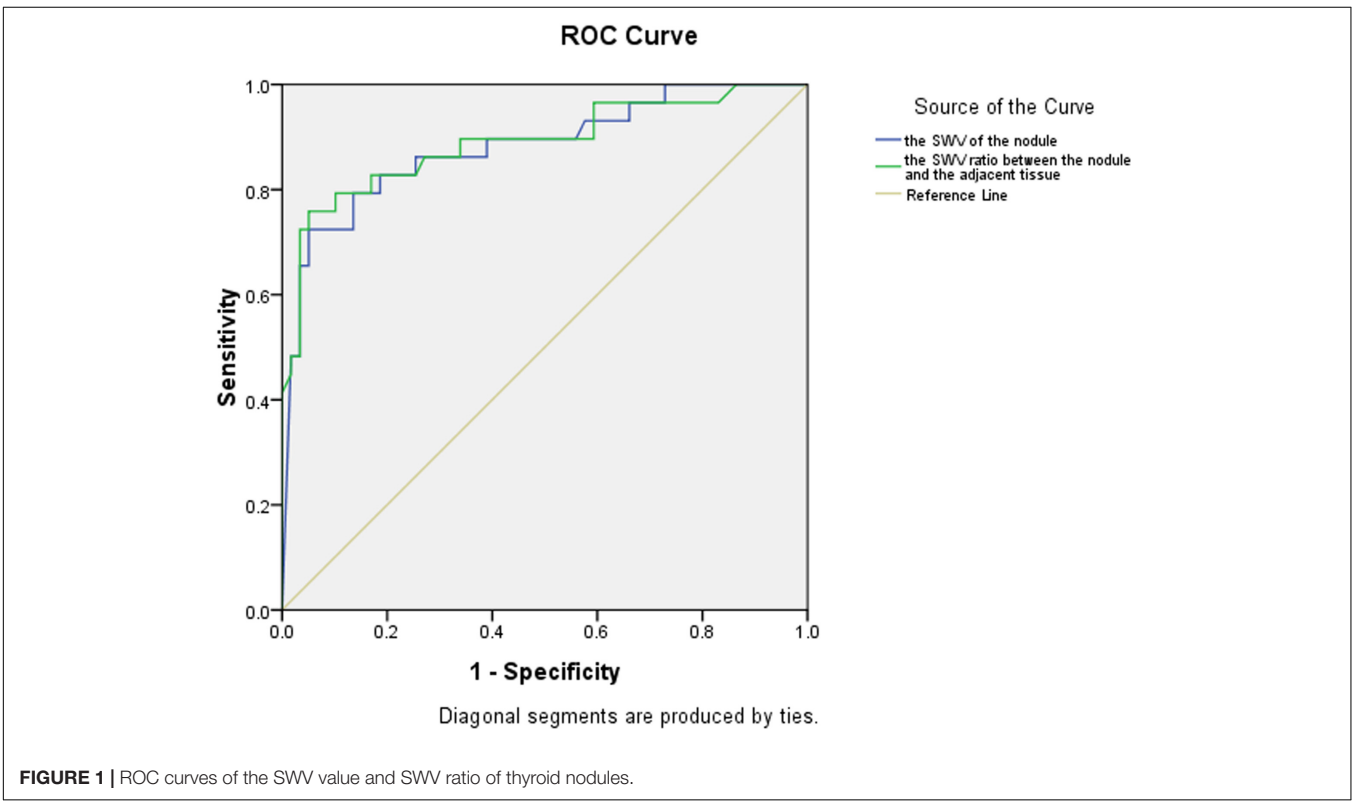

FIGURE 1 | ROC curves of the SWV value and SWV ratio of thyroid nodules.

TABLE 4 | Comparison of various CEUS and ARFI indices for the diagnosis of thyroid nodules.

		Pathology		Sensitivity	Specificity	Positive predictive value	Negative predictive value	Accuracy rate	Youden index
		Malignant	Benign						
CEUS	Malignant	23	5	79.3%	91.5%	82.1%	90%	87.5%	0.708
	Benign	6	54						
ARFI (SWV)	Malignant	22	3	75.9%	94.9%	88.0%	88.9%	88.6%	0.708
	Benign	7	56						
Both	Both negative or one positive	27	6	93.1%	89.8%	81.8%	96.3%	90.9%	0.829
	Both negative	2	53						

enhancement is an important indicator that can be used in the diagnosis of malignant nodules. In the malignant group of this study, most thyroid papillary carcinomas showed concentric and inhomogeneous enhancement (**Figure 2**). The reasons for this may be as follows: (1) Malignant nodules secrete vascular endothelial growth factor (VEGF), which stimulates the growth of new blood vessels within the nodule and adjacent tissues. Neovascularization comprises tortuous and complicated vessels with uneven diameters, eccentric distributions and irregular vascular branches (Zhang Y. et al., 2010). (2) Microcalcification exists in thyroid papillary carcinoma, which influences neovascularization. This further aggravates the uneven distribution of blood vessels. The vascular space distribution of malignant nodules is complex. Angiogenesis can be divided into forms that are present in marginal and central areas. Blood vessels are relatively dense in marginal areas but are sparse in central areas. Differences in vascular density between marginal and central areas may cause concentric enhancement, in accordance with the results reported by Hornung et al. (2012) that the AUC of the TIC of the contrast agent in the marginal zone of the nodules was higher than that in the central area. Because of the arteriovenous fistula in malignant nodules, the contrast agent washed out earlier. Thyroid papillary carcinoma showed low enhancement, equal enhancement, and high enhancement in the malignant group, which may be related to the size and vascular density of the nodules. Molinari et al. (2010) proposed that the vascular density of thyroid malignant nodules is higher than that of benign nodules, while Moon et al. (2010) found that internal flow is more likely to occur in benign nodules, and the lack of blood supply in the nodules may be related to malignancy. These findings reflect the complexity of the blood supply of malignant thyroid nodules. Thyroid papillary carcinoma may exhibit a lack of blood supply or a rich blood supply (**Figure 3**).

There was 1 case of follicular carcinoma in the malignant group (**Figure 4**). CEUS showed a fast wash-in, a slow wash-out, and homogeneous and high enhancement, which was similar to the CEUS results for adenoma, without ring enhancement. However, CEUS cannot distinguish between thyroid follicular carcinoma and follicular adenoma based on the mode of growth, envelope thickness or cytological features. The only pathological diagnostic criterion of follicular carcinoma was tumor invasion of the envelope or blood vessels. Due to infiltration of the surrounding tissue by the tumor in follicular carcinoma, CEUS showed no ring enhancement, which is caused by the expansive growth of the adenoma, leading to extrusion of the peripheral blood vessels.

The main manifestation of benign nodules was ring enhancement (**Figure 5**). Thyroid adenoma is derived from follicular epithelial cells. Benign tumors show expansive growth with complete capsules. Blood vessels are gradually extruded to the surroundings of the tumor during the growth process, forming rich encircled blood vessels. During the process of repeated hyperplasia and nodular goiter repair, the nodule extrudes to the surrounding thyroid tissue and forms a peripheral vascular ring. Therefore, CEUS examination of most benign nodules showed ring enhancement. Various contrast patterns of nodular goiter were observed, and most showed wash-in and wash-out at the same time as the surrounding thyroid tissue.

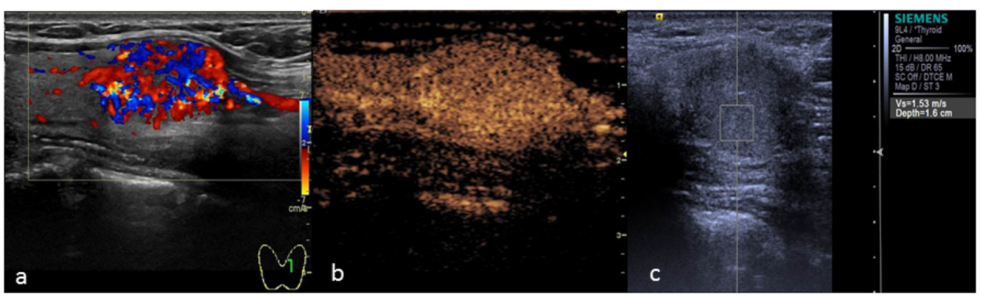

FIGURE 2 | Papillary thyroid carcinoma. **(a)** Two-dimensional ultrasound showing a hypo-echoic nodule with calcification. **(b)** CEUS showing heterogeneous low enhancement. **(c)** The SWV value was X.XX m/s.

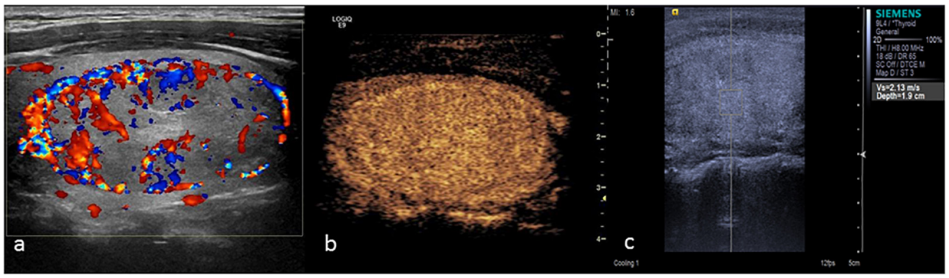

FIGURE 3 | Papillary thyroid carcinoma. **(a)** Color Doppler ultrasound showing rich blood flow in the nodule. **(b)** CEUS showing heterogeneous homogeneous equal enhancement. **(c)** The SWV value was 1.53 m/s.

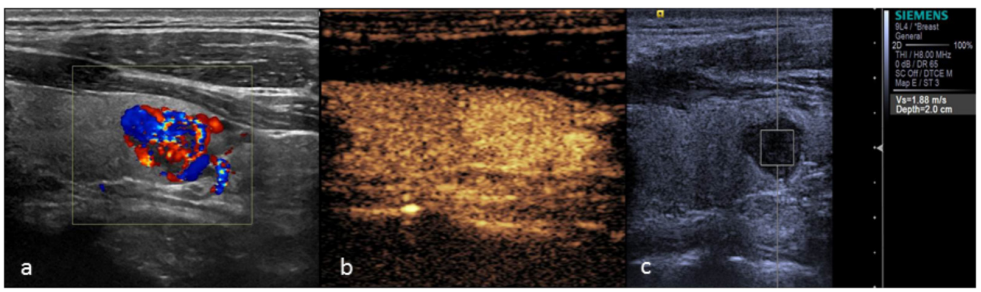

FIGURE 4 | Thyroid follicular carcinoma. **(a)** Color Doppler ultrasound showing rich blood flow in the nodule. **(b)** CEUS showing heterogeneous homogeneous high enhancement. **(c)** The SWV value was 1.88 m/s.

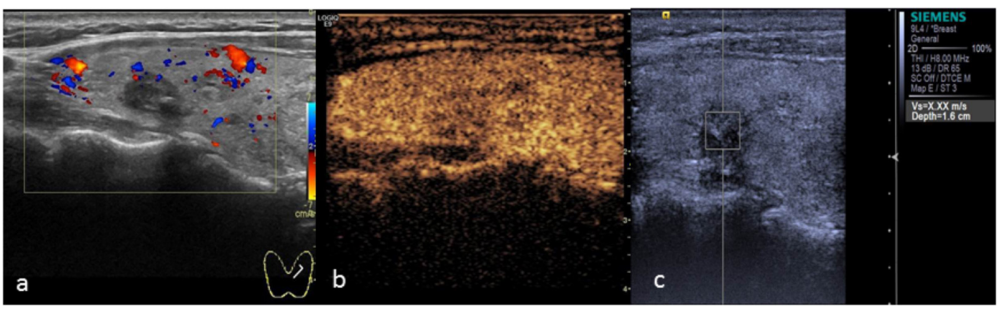

FIGURE 5 | Thyroid adenoma. **(a)** Color Doppler ultrasound showing circumferential blood flow around the nodule. **(b)** CEUS showing ring enhancement. **(c)** The SWV value was 2.13 m/s.

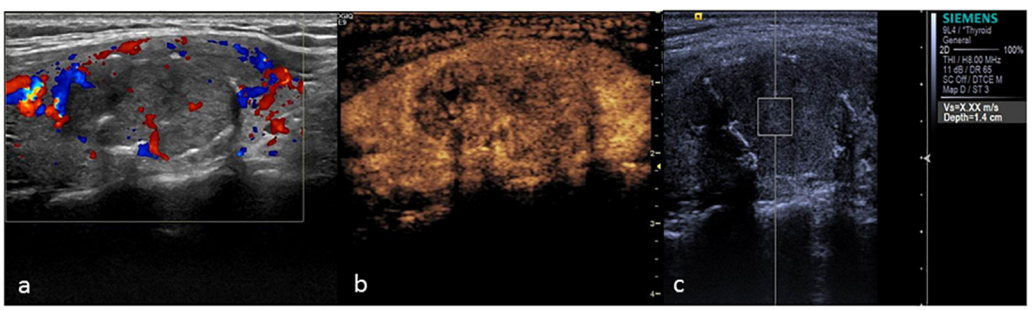

FIGURE 6 | Nodular goiter. **(a)** Color Doppler ultrasound showing a hypo-echoic nodule with coarse calcification. **(b)** CEUS showing heterogeneous low enhancement. **(c)** The SWV value was X.XX m/s.

Zhang H.L. et al. (2013) showed that nodular goiters underwent different stages of hyperplasia and repair. The distribution of blood vessels within the nodules was different at different stages of the disease, ultimately yielding a range of CEUS performance levels. In this study, 5 cases of nodular goiter were misdiagnosed as thyroid carcinoma because of inhomogeneous low enhancement (**Figure 6**).

ARFI Results for Thyroid Nodules and Their Pathology

The VTQ technique quantitatively measures tissue stiffness by calculating the SWV during tissue deformation; the greater the SWV value is, the harder the tissue. Benign thyroid lesions, such as thyroid adenoma or nodular goiter, are mainly composed of follicular cells of different sizes containing a large amount of colloidal components. The texture of the tissue is soft, whereas malignant thyroid lesions are harder. For example, nipple branches and fibrovascular stroma are found in thyroid papillary cancer, with psammoma bodies concentrically arranged in the stroma and greater hardness.

The results of this study showed that the SWV value of benign nodules was close to that of the surrounding normal tissue. Malignant thyroid nodules were harder than benign nodules, which were in turn harder than the surrounding normal tissues. The average SWV value was 5.81 m/s. To account for individual differences, we measured the ratio between the SWV value of the lesion and the surrounding normal tissue. The SWV ratio of malignant nodules was 2.74 ± 1.40, which was significantly higher ($P < 0.05$) than that of benign nodules (1.02 ± 0.62). This finding suggests that the texture of malignant nodules was harder than that of benign nodules. Using a cut-off SWV value of 2.565 m/s for the diagnosis of thyroid malignant nodules, the area under the ROC curve was 0.878, similar to the result reported by Hamidi et al. (2015). We concluded that 2.66 m/s was the optimum cut-off point. In the malignant group, the SWV values of 13 thyroid cancers were found to be "X.XX m/s" in repeated tests (**Figure 2**). CEUS confirmed the nodule to be a solid lesion, whose stiffness exceeded the scope of detection using this instrument. The output of "X.XX m/s" when measuring SWV for a solid nodule was highly suggestive of malignancy. This finding is similar to the results of Tozaki et al. (2011a) and Fukuhara et al. (2014). However, not all nodules yielding "X.XX m/s" were malignant. "X.XX M/s" appeared in the SWV measurement of 1 nodular goiter (**Figure 6**), possibly indicating that the nodule was found during the late stage of the disease. The occurrence of fibrosis, degenerative changes or a large number of calcium salt deposits hardened the nodule, causing the appearance of "X.XX M/s." The mean SWV value of 1 thyroid follicular carcinoma was 1.65 m/s. The SWV ratio of the nodule to the peripheral normal tissue was 1.12, suggesting that the texture of the nodule was soft. This finding may be related to the pathological characteristics of thyroid follicular carcinoma. Except in cases of infiltration of the envelope or the blood vessels, thyroid follicular carcinoma is composed of follicles of different sizes, and the texture is no different from that of thyroid follicular adenoma. Therefore, the SWV value for thyroid follicular carcinoma may not be higher than that for benign nodules or the surrounding normal tissue.

Value of CEUS and ARFI for the Diagnosis of Thyroid Nodules

In this study, the sensitivities of CEUS and ARFI for the diagnosis of thyroid malignant nodules were 79.3 and 75.9%, respectively. To reduce the rate of misdiagnosis, CEUS and ARFI can be combined for the diagnosis of thyroid malignant nodules, increasing the sensitivity to 93.1%. This difference was statistically significant ($P < 0.05$). Although the specificity of the combination of CEUS and ARFI for the diagnosis of thyroid malignant nodules was lower, the Youden index was increased to 0.829. The Youden index combines information regarding sensitivity and specificity and is used to evaluate the authenticity of a test. Larger values of the index indicate a better effectiveness of the test and a higher authenticity. Combining the CEUS and ARFI tests yielded a higher diagnostic value for the diagnosis of thyroid nodules than either of the tests alone.

This study has several limitations. First, the sample size of this study was small. Nodules with a diameter of less than 6 mm were excluded from this study. Thus, the study cannot provide information about thyroid microcarcinoma. Second, only one pathological type was observed in the malignant group. Most of the nodules were papillary thyroid cancers; only 1 follicular carcinoma and 1 metastatic cancer were included. Finally, "X.XX m/s" was output for several cases for the measurement of papillary thyroid cancer, and this value was replaced by "9 m/s." The actual SWV value of these papillary thyroid cancer was likely much larger than "9 m/s." Thus, the SWV value of papillary thyroid cancercould have been underestimated. It is necessary to expand on this research in the future by increasing the sample size, increasing the number of pathological types and using real-time shear wave elastic imaging.

CONCLUSION

To conclude, CEUS and ARFI were of value for the differential diagnosis of benign and malignant thyroid nodules. The combination of these techniques can improve the accuracy of the diagnosis.

AUTHOR CONTRIBUTIONS

XW and QH conceived and designed the experiments. YH and QH performed the experiments. YH analyzed the data. BL, XC, and HW contributed reagents, materials, and analysis tools. QH and YH wrote the paper.

FUNDING

The present study was supported by The National Natural Science Foundation of China (81660292 and 81260223) and Guangxi Scientific Research and Technology Development Project (No. GKG 14279012).

REFERENCES

Azar, N., Lance, C., Nakamoto, D., Michael, C., and Wasman, J. (2013). Ultrasonographic thyroid findings suspicious for malignancy. *Diagn. Cytopathol.* 41, 1107–1114. doi: 10.1002/dc.23058

Calvete, A. C., Mestre, J. D., Gonzalez, J. M., Martinez, E. S., Sala, B. T., and Zambudio, A. R. (2014). Acoustic radiation force impulse imaging for evaluation of the thyroid gland. *J. Ultrasound Med.* 33, 1031–1040. doi: 10.7863/ultra.33.6.1031

Chen, M. H., Dai, Y., Yan, K., Yang, W., Wu, W., Li, J. Y., et al. (2005). Early diagnosis of small hepatocellular carcinoma in patients with cirrhosis using contrast-enhanced ultrasound. *Chin. J. Ultrasound* 14, 116–120.

Friedrich-Rust, M., Sperber, A., Holzer, K., Diener, J., Grünwald, F., Badenhoop, K., et al. (2010). Real-time elastography and contrast-enhanced ultrasound for the assessment of thyroid nodules. *Exp. Clin. Endocrinol. Diabetes* 118, 602–609. doi: 10.1055/s-0029-1237701

Fukuhara, T., Matsuda, E., Fujiwara, K., Tanimura, C., Izawa, S., Kataoka, H., et al. (2014). Phantom experiment and clinical utility of quantitative shear wave elastography for differentiating thyroid nodules. *Endocr J.* 61, 615–621. doi: 10.1507/endocrj.EJ14-0061

Gharib, H. (1997). Changing concepts in the diagnosis and management of thyroid nodules. *Endocrinol. Metab. Clin. North Am.* 26, 777–800. doi: 10.1016/S0889-8529(05)70282-6

Gilliland, F. D., Hunt, W. C., Morris, D. M., and Key, C. R. (1997). Prognostic factors for thyroid carcinoma. A population-based study of 15,698 cases from the Surveillance, Epidemiology and End Results (SEER) program 1973-1991. *Cancer* 79, 564–573. doi: 10.1002/(SICI)1097-0142(19970201)79:3<564::AID-CNCR20>3.0.CO;2-0

Gramiak, R., Shah, P. M., and Kramer, D. H. (1969). Ultrasound cardiography: contrast studies in anatomy and function. *Radiology* 92, 939–948. doi: 10.1148/92.5.939

Hamidi, C., Göya, C., Hattapoğlu, S., Uslukaya, Ö, Teke, M., Durmaz, M. S., et al. (2015). Acoustic Radiation Force Impulse (ARFI) imaging for the distinction between benign and malignant thyroid nodules. *Radiol. Med.* 120, 579–583. doi: 10.1007/s11547-014-0495-8

Hoang, J. K., Lee, W. K., Lee, M., Johnson, D., and Farrell, S. (2007). US Features of thyroid malignancy: pearls and pitfalls. *Radiographics* 27, 847–860. doi: 10.1148/rg.273065038

Hornung, M., Jung, E. M., Georgieva, M., Schlitt, H. J., Stroszczynski, C., and Agha, A. (2012). Detection of microvascularization of thyroid carcinomas using linear high resolution contrast-enhanced ultrasonography (CEUS). *Clin. Hemorheol. Microcirc.* 52, 197–203. doi: 10.3233/CH-2012-1597

Luo, B. M., Ou, B., and Zhi, H. (2008). Factors affecting the performance of ultrasonic elastography in breast tumors and its solutions. *Zhong guo Yi Xue Ke Xue Yuan Xue Bao.* 30, 112–115.

Mandel, S. J. (2004). Diagnostic use of ultrasonography in patients with nodular thyroid disease. *Endocr. Pract.* 10, 246–252. doi: 10.4158/EP.10.3.246

Mehanna, H. M., Jain, A., Morton, R. P., Watkinson, J., and Shaha, A. (2009). Investigating the thyroid nodule. *BMJ* 338:b733. doi: 10.1136/bmj.b733

Mitterberger, M., Pelzer, A., Colleselli, D., Bartsch, G., Strasser, H., Pallwein, L., et al. (2007). Contrast-enhanced ultrasound for diagnosis of prostate cancer and kidney lesions. *Eur. J. Radiol.* 64, 231–238. doi: 10.1016/j.ejrad.2007.07.027

Molinari, F., Mantovani, A., Deandrea, M., Limone, P., Garberoglio, R., and Suri, J. S. (2010). Characterization of single thyroid nodules by contrast-enhanced 3-D ultrasound. *Ultrasound Med. Biol.* 36, 1616–1625. doi: 10.1016/j.ultrasmedbio.2010.07.011

Moon, H. J., Kwak, J. Y., Kim, M. J., Son, E. J., and Kim, E. K. (2010). Can vascularity at power Doppler US help predict thyroid malignancy? *Radiology* 255, 260–269. doi: 10.1148/radiol.09091284

Nemec, U., Nemec, S. F., Novotny, C., Weber, M., Czerny, C., and Krestan, C. R. (2012). Quantitative evaluation of contrast-enhanced ultrasound after intravenous administration of a microbubble contrast agent for differentiation of benign and malignant thyroid nodules: assessment of diagnostic accuracy. *Eur. Radiol.* 22, 1357–1365. doi: 10.1007/s00330-012-2385-6

Nightingale, K., McAleavey, S., and Trahey, G. (2003). Shear-wave generation using acoustic radiation force: in vivo and ex vivo results. *Ultrasound Med. Biol.* 29, 1715–1723. doi: 10.1016/j.ultrasmedbio.2003.08.008

Nightingale, K., Soo, M. S., Nightingale, R., and Trahey, G. (2002). Acoustic radiation force impulse imaging: in vivo demonstration of clinical feasibility. *Ultrasound Med. Biol.* 28, 227–235. doi: 10.1016/S0301-5629(01)00499-9

Nightingale, K. R., Palmeri, M. L., Nightingale, R. W., and Trahey, G. E. (2001). On the feasibility of remote palpation using acoustic radiation force. *J. Acoust. Soc. Am.* 110, 625–634. doi: 10.1121/1.1378344

Ophir, J., Céspedes, I., Ponnekanti, H., Yazdi, Y., and Li, X. (1991). Elastography: a quantitative method for imaging the elasticity of biological tissues. *Ultrason. Imaging* 13, 111–134. doi: 10.1177/016173469101300201

Paes, J. E., Hua, K., Nagy, R., Kloos, R. T., Jarjoura, D., and Ringel, M. D. (2010). The relationship between body mass index and thyroid cancer pathology features and outcomes: a clinicopathological cohort study. *J. Clin. Endocrinol. Metab.* 95, 4244–4250. doi: 10.1210/jc.2010-0440

Seitz, K., Bernatik, T., Strobel, D., Blank, W., Friedrich-Rust, M., Strunk, H., et al. (2010). Contrast-enhanced ultrasound (CEUS) for the characterization of focal liver lesions in clinical practice (DEGUM Multicenter Trial): CEUS vs. MRI–a prospective comparison in 269 patients. *Ultraschall. Med.* 31, 492–499. doi: 10.1055/s-0029-1245591

Tozaki, M., Isobe, S., and Fukuma, E. (2011a). Preliminary study of ultrasonographic tissue quantification of the breast using the acoustic radiation force impulse (ARFI) technology. *Eur. J. Radiol.* 80, e182–e187. doi: 10.1016/j.ejrad.2011.05.020

Tozaki, M., Saito, M., Joo, C., Yamaguchi, M., Isobe, S., Ogawa, Y., et al. (2011b). Ultrasonographic tissue quantification of the breast using acoustic radiation force impulse technology: phantom study and clinical application. *Jpn. J. Radiol.* 29, 598–603. doi: 10.1007/s11604-011-0591-9

Vander, J. B., Gaston, E. A., and Dawber, T. R. (1968). The significance of nontoxic thyroid nodules. Final report of a 15-year study of the incidence of thyroid malignancy. *Ann. Intern. Med.* 69, 537–540. doi: 10.7326/0003-4819-69-3-537

Zhang, B., Jiang, Y. X., Liu, J. B., Yang, M., Dai, Q., Zhu, Q. L., et al. (2010). Utility of contrast-enhanced ultrasound for evaluation of thyroid nodules. *Thyroid* 20, 51–57. doi: 10.1089/thy.2009.0045

Zhang, H. L., Wang, H., and Jiang, J. (2013). Contrast-enhanced ultrasound in nodular goiter. *Chin. J. Ultrasound Med.* 29, 481–484.

Zhang, Y., Jiang, Q., Chen, J., Gu, X. M., and Zhang, J. Q. (2010). The diagnostic value of three-dimensional ultrasonography in single thyroid nodule and the analysis of ROC curve. *J. Chin. Clin. Med. Imaging* 21, 13–16.

Conflict of Interest Statement: The authors declare that the research was conducted in the absence of any commercial or financial relationships that could be construed as a potential conflict of interest.

frontiers in Pharmacology

ORIGINAL RESEARCH
published: 25 January 2019
doi: 10.3389/fphar.2018.01569

Molecular Ultrasound Monitoring of Early Artery Injury After Carotid Balloon Angioplasty

Xinhai Mo[1], *Fei Yan*[2]* *and Bo Zhang*[1]*

[1] Department of Ultrasound in Medicine, Shanghai East Hospital, Tongji University School of Medicine, Shanghai, China,
[2] Paul C. Lauterbur Research Center for Biomedical Imaging, Institute of Biomedical and Health Engineering, Shenzhen Institutes of Advanced Technology, Chinese Academy of Sciences, Shenzhen, China

Cardiovascular intervention is a common treatment procedure for many cardiovascular diseases. But restenosis often occurs after these procedures, greatly discounting their long-term therapeutic effects. Early detection of endothelial denudation is helpful for the diagnosis and prevention of restenosis. Here, we fabricated targeted microbubbles by conjugating anti-collagen IV antibodies to the surface of biotinylated microbubbles ($MB_{Col\,IV}$) and applied them for ultrasound molecular imaging of endothelial injury at early stage. Our results showed that the MB_{ColIV}, with a typical multi-peak particle distribution, was successfully constructed, which was confirmed by Alexa Fluor® 555-labeled secondary antibody. *Ex vivo* adhesion of microbubbles revealed that MB_{ColIV} can effectively and specially bind to the surface of balloon-injured carotid artery. The *in vivo* animal experiments showed ultrasound molecular imaging signals from carotid artery-injured rats administrated with $MB_{Col\,IV}$ were significantly higher than those administrated with isotype control microbubbles. Histological staining of the left carotid common artery revealed that collagen IV was obviously exposed after endothelium denudation in balloon-injured artery. In conclusion, our current study provides an effective approach to detect vascular injury at the early stage and a potential platform for image-guided therapy to vascular injury.

Keywords: ultrasound molecular imaging, collagen IV, artery injury, restenosis, targeted microbubbles

OPEN ACCESS

Edited by:
Ali H. Eid,
American University of Beirut, Lebanon

Reviewed by:
Antonio Curcio,
Università Degli Studi Magna Græcia di Catanzaro, Italy
Christoph Eugen Hagemeyer,
Monash University, Australia

***Correspondence:**
Bo Zhang
zhangbodongfang@qq.com
Fei Yan
fei.yan@siat.ac.cn

Specialty section:
This article was submitted to Translational Pharmacology, a section of the journal Frontiers in Pharmacology

Received: *01 November 2018*
Accepted: *24 December 2018*
Published: *25 January 2019*

Citation:
Mo X, Yan F and Zhang B (2019) Molecular Ultrasound Monitoring of Early Artery Injury After Carotid Balloon Angioplasty. Front. Pharmacol. 9:1569. doi: 10.3389/fphar.2018.01569

INTRODUCTION

Cardiovascular diseases from atherosclerosis are responsible for the major cause of mortality worldwide (Murray et al., 2012). Pathologically, atherosclerosis is a chronic and progressive disease featured with retention of lipids, accumulation of extracellular matrix and infiltration of smooth muscle cells (SMCs) with or without macrophages (Otsuka et al., 2016). Due to atherosclerotic lesions, cardiovascular events often occur in a complex and unpredictable manner, resulting in a series of complications. Among these, stenosis and thrombosis are the two major complications. Stenosis may cause distal organ ischemia and thrombosis, and trigger thrombotic occlusion of artery to organs, ultimately resulting in life-threatening cardiovascular events.

Early invasive therapies, such as percutaneous coronary intervention (PCI), could improve long-term survival and reduce late myocardial infarction and recurrent unstable angina requiring rehospitalization for patients with non-ST-elevation myocardial infarction (Bavry et al., 2006; Amsterdam et al., 2014). Although the narrowed or obstructed arteries are recovered through

endovascular procedures, post-operational restenosis is generally inevitable. The main reason is that mechanical endovascular procedures often cause endothelial damage by activating a series of inflammatory pathways. Due to these inflammatory effects, excessive migration, and proliferation of SMCs, and plentiful synthesis and deposition of extracellular matrix lead to intimal hyperplasia. The serious intimal hyperplasia will result in restenosis which may represent a fatal threat for patients. Evidence demonstrated that restenosis occurs in up to 60% post-angioplasty patients within the first year because of mechanical vascular injury (Petrasheskaya et al., 2016). Therefore, early detection at the stage of endothelial denudation is desirable for the diagnosis and prevention of restenosis.

During vascular injury, many cell adhesion molecules are overexpressed or upregulated. Selectins, integrins, and the immunoglobulin superfamily of cell adhesion molecules are the three major classes of leukocyte cell adhesion molecules (Davis et al., 2003). Numerous studies have shown that intracellular adhesion molecules-1 (ICAM-1), vascular cell adhesion molecules-1 (VCAM-1) or P-selectin can serve as the targets for various imaging probes (Wu et al., 2011; Yan et al., 2018). However, these cell adhesion molecules are not expressed promptly during vascular injury. Generally, it takes 1 day, or even longer, to increase their expression on the surface of vascular endothelial cells (Tanaka et al., 1993; Kennedy et al., 2000).

Collagen IV, representing 50% of the vascular basement membrane, could be exposed immediately when the intact endothelial monolayer is denuded by mechanical injury of vascular intervention (Kalluri, 2003). That is, the expression of collagen IV is time-independent and related to endothelial denudation and damage. Therefore, collagen IV can be used as targeting receptor for detection, and even treatment at the site of vascular injury (Chan et al., 2011; Meyers et al., 2017).

Ultrasonography, a non-invasive and real-time imaging method, is widely used to examine cardiovascular diseases (Yan et al., 2018). With the help of targeted microbubbles (MBs), ultrasound molecular imaging allows to detect specific lesions at molecular level. Generally, the applications of ultrasound molecular imaging require the effective binding of ultrasonic probes to the receptors in the physiologic flow conditions after their intravenous administration. Antibodies, antibody fragments, peptides, and carbohydrates have been conjugated to the surface of MBs. By detecting the signals derived from retained MBs in the target regions, ultrasound molecular imaging can visualize molecular dynamics *in situ*. Currently, several stuieds have been published to demonstrate the diagnostic utility of ultrasound molecular imaging for the detection of inflammation, atherosclerosis and tumor angiogenesis (Villanueva and Wagner, 2008; Willmann et al., 2008; Leong-Poi, 2009; Lindner, 2009; Deshpande et al., 2010). In this study, we fabricated a novel targeted MBs by conjugating anti-collagen IV antibodies to the surface of biotinylated MBs ($MB_{Col\,IV}$) and applied them for ultrasound molecular imaging of endothelial injury at early stage (**Figure 1**).

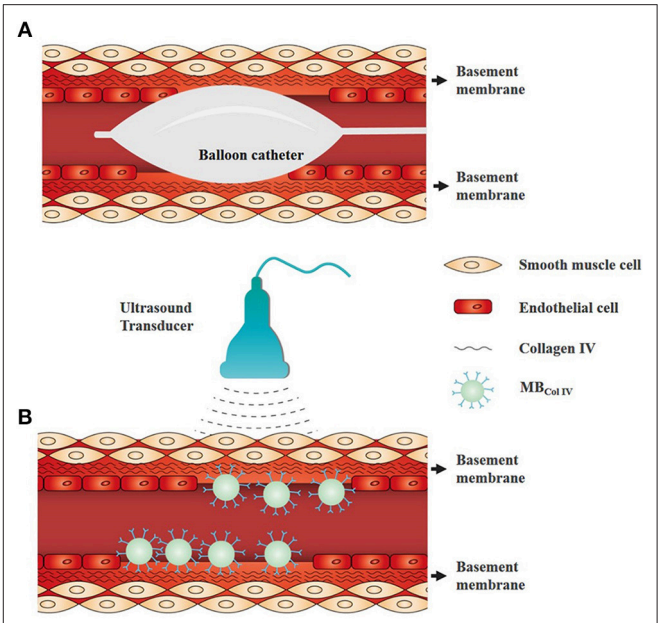

FIGURE 1 | Schematic representation of ultrasound molecular imaging for detecting the vascular injury of endothelium denudation. **(A)** Schematic diagram of balloon angioplasty for endothelial denudation to the carotid artery. **(B)** Schematic of ultrasound molecular imaging for detecting the site of endothelium denudation. Collagen IV is a major component of vascular basement membrane and exposed after endothelium denudation. Collagen IV-targeted microbubbles ($MB_{Col\,IV}$) were adhered to the vascular injury site without endothelium coverage.

MATERIALS AND METHODS

Preparation of MBs

Biotinylated, lipid-shelled MBs were prepared as previously described (Yan et al., 2013). Briefly, DSPC, DSPE–PEG2000 and DSPE–PEG2000-Biotin (Avanti Polar Lipids, Alabaster, AL, USA) (molar ratios = 9:0.5:0.5) were blended in chloroform. The solvent was evaporated under nitrogen flow at room temperature, forming a thin film on the wall of the test tube. Residual chloroform was further removed by vacuum treatment for at least 2 h. The completely dried phospholipid membrane was hydrated at 60°C with a given buffer consisting of 0.1 M Tris (pH 7.4):glycerol:propylene glycol (80:10:10 by volume), and then transferred into vials. After sealing the vials, the air in the vials was replaced with perfluoropropane (C_3F_8). Biotinylated MBs (MB_{biotin}) were obtained by mechanically vibrating for 30 s. The resulting MB_{biotin} were washed with phosphate buffered saline (PBS) solution twice to eliminate excess unincorporated lipids by centrifuge at 400 g for 3 min. Three microgram of avidin per 10^7 MBs was then incubated with the MB_{biotin} dispersion for 30 min at room temperature, followed by rinsing three times to remove unreacted avidin (Aladdin, Pudong, Shanghai, China). Then either 2.5 μg of biotinylated goat anti-rat Type IV Collagen antibody or biotinylated goat IgG isotype control antibody (SouthernBiotech, Birmingham, AL, USA) was added to per 10^8 MBs. After incubation for 30 min at room temperature, $MB_{Col\,IV}$ or isotype control MBs (MB_{Ctrl}) were collected by centrifugation.

Non-targeted MBs (MB_N) without conjugated primary antibody were also prepared.

Characterization of MBs

To confirm the conjugation of Type IV Collagen antibody to the surface of MBs, Alexa Fluor® 555-labeled anti-goat secondary antibody (Invitrogen, Carlsbad, CA, USA) was added to $MB_{Col\,IV}$ and mixed for 30 min at room temperature. The mixture was separated by centrifugation and the upper layer was washed twice with PBS to eliminate the free secondary antibody. The fluorescence-labeled $MB_{Col\,IV}$ were examined by a fluorescence inversion microscopy (Olympus Corporation, Tokyo, Japan).

To analyze the characteristics of the $MB_{Col\,IV}$, MB_N were used as the blank control. The morphology of the MBs were examined by using bright-field and fluorescence inversion microscopy (Olympus Corporation, Tokyo, Japan). Particle size, size distribution and concentration of MBs were determined by using the Accusizer 780 Optical Particle Sizer (Particle Sizing Systems, Santa Barbara, CA, USA) with a 0.5 μm diameter detection limit.

Carotid Artery Injury Model

All animal procedures were performed in accordance with the principles outlined in the Guide for the Care and Use of Laboratory Animals and approved by Animal Care and Use Committee. Adult male Sprague–Dawley rats (Vital River Laboratory, Beijing, China), weighing 400–500 g, underwent the rat carotid artery balloon injury as previously described (Chan et al., 2011; Petrasheskaya et al., 2016). Rats were given aspirin by oral gavage before surgery and kept anesthetized by isoflurane at 2% at 2 L/min oxygen. Following a midline neck incision, the left common carotid artery (LCCA), left external carotid artery (LECA), and left internal carotid artery (LICA) were exposed. After distal ligation of the LECA, the proximal end of LCCA and the distal end of LICA were then temporarily clipped by arterial clamps and a 2-French arterial embolectomy catheter (Edwards Lifesciences, Irvine, CA, USA) was advanced proximally into LCCA through the incision of LECA. The balloon was inflated and withdrawn with a rotating action to the arteriotomy in LECA and then reintroduced and retracted twice again. The balloon catheter was removed and the LECA was ligated. Finally, arterial clamps were removed to restore the blood flow, and then the neck incision was closed. Thereafter, rat carotid artery injury model was performed and used for the following experiments.

Histological Analysis

Bilateral carotid arteries were harvested following *in situ* perfusion fixation with PBS and 4% paraformaldehyde. Tissues were placed in paraformaldehyde for 1 h at 4°C, then overnight in 30% sucrose in PBS at 4°C for cryo-protection. Vessels were coated with Optimum Cutting Temperature O.C.T.™ compound (Tissue Tek, Hatfield, PA) and transferred to liquid nitrogen for flash-freeze. Vessels were sectioned to obtain arterial cross-sections across the length of the artery by cryostat microtome (CM1950; Leica, Heidelberg, Germany) and were examined histologically using routine hematoxylin-eosin (H&E) staining for morphometric analysis. Digital images were collected with bright-field by inversion microscopy (Olympus Corporation, Tokyo, Japan).

Ex vivo Adhesion of MBs

Attachment ability of MBs to collagen IV was evaluated by counting the number of adhering MBs. Briefly, after the rat carotid artery injury model and the *in situ* perfusion fixation were completed, the LCCA was harvested and then opened longitudinally. The side of adventitia was adhered to a coverslip. Then MBs were added into a 6-well plate (2×10^7 MBs per well) and filled with PBS. Due to the static flotation nature of MBs, the coverslip with the artery coated faced downward to maximize interaction between the tissue and MBs for 5 min at room temperature. After that, the free MBs were removed by rinsing five times with PBS. To further determine the specificity of MBs adhesion, vessel tissues were pretreated with 25 μg/mL goat anti-rat Type IV Collagen antibody to block available receptors prior to $MB_{Col\,IV}$ incubation. Digital images were obtained with bright-field by inversion microscopy (Olympus Corporation, Tokyo, Japan) to count the number of attached MBs in five random fields of view.

In vivo Ultrasound Molecular Imaging

After rat carotid artery injury model was developed as described above, rats were kept anesthetized on a heated stage throughout the imaging session. Ultrasound molecular imaging was performed with a commercial ultrasound system Resona 7 (Mindray Medical Systems, Shenzhen, China) using a L11-3 linear array transducer. Contrast imaging mode was applied in the ultrasound molecular imaging experiments. All imaging parameters were kept constant throughout the whole procedure as follows: frequency 5.6 MHz, depth 2 cm, gain 45 dB, frame rate 10 Hz, dynamic range 115 dB, and mechanical index 0.085. In order to reduce motion interference, both the transducer and the rats were fixed to maintain the same long axis cross section of carotid artery. The concentration of MBs suspension was adjusted to 2×10^8 MBs/ml. Then 200 μl MBs suspension was injected intravenously through tail vein following by flushing with 50 μl PBS. Four minutes after MBs injection, 100 frames of images were captured to obtain a signal from adherent and freely circulating MBs. A continuous high-power destructive pulse (mechanical index: 0.553) was then applied for 2 s to destroy these MBs. After 2 s, to allow the freely circulating MBs to replenish, another 100 frames of images were acquired, in which the ultrasonic signals were from any residual freely circulating MBs and tissue. To minimize the bias and test the specificity of these molecular imaging signals only resulting from adherent targeted MBs, $MB_{ColIV,}$ and MB_{Ctrl} were administered in random order to all rats. Another 30-min delay was allowed to clear MBs from the preceding imaging session. As a control, ultrasound molecular imaging was also performed in normal rats to further assess the specificity of MBs adhesion. The acoustic imaging signals were analyzed by using commercially available analysis software (Mindray Medical Systems, Shenzhen, China). As previously described (Wu et al., 2011), the difference in signal intensity from adherent MBs was calculated by subtracting the post-destruction signal from the pre-destruction signal.

Immunohistochemistry

Immunostaining analysis for collagen IV was performed to confirm that collagen IV was exposed through endothelium denudation. Briefly, LCCAs from normal artery group and balloon-injured artery group were excised, followed by *in situ* perfusion fixation with PBS and 4% paraformaldehyde. Then artery samples were transferred to paraformaldehyde overnight, followed by ethanol dehydration and paraffin

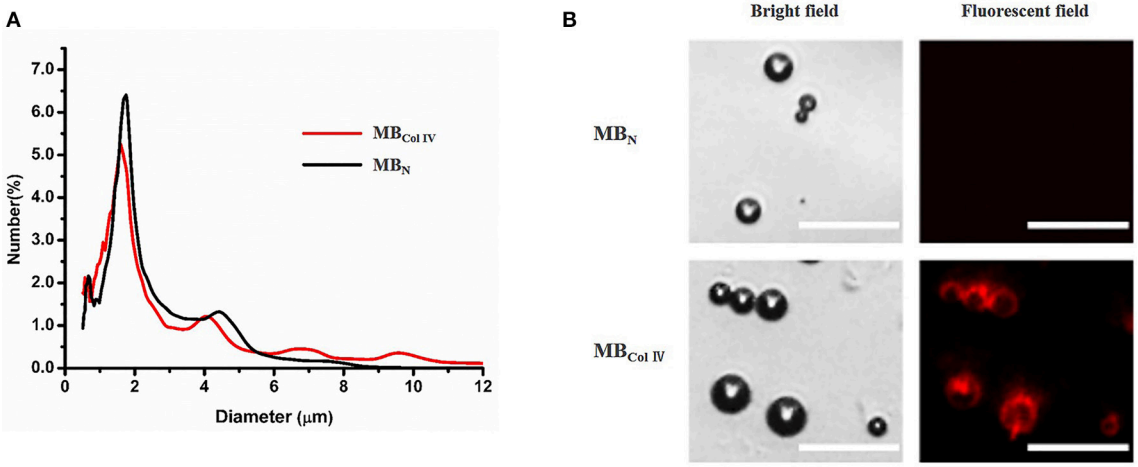

FIGURE 2 | Characterization of ultrasound contrast agents. **(A)** Size distribution of non-targeted microbubbles (MB_N) and Collagen IV-targeted microbubbles ($MB_{Col IV}$). The size distribution curves of MB_N and $MB_{Col IV}$ were similar. **(B)** MB_N and $MB_{Col IV}$ under bright–field and fluorescence microscopy. The red fluorescence indicated the conjugation of Alexa Fluor 555-labeled secondary antibody with the Type IV Collagen antibody (Scale bar = 15 μm).

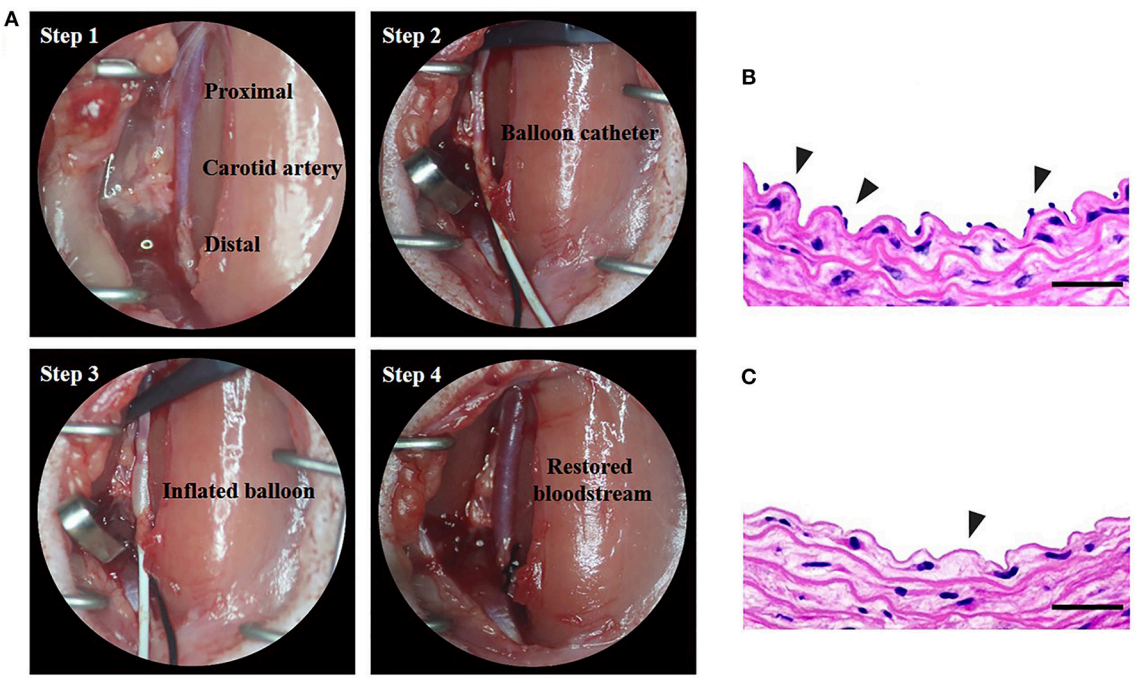

FIGURE 3 | Construction of rat carotid artery injury model. [**(A)** Step 1] The left carotid common artery (LCCA) has been exposed. [**(A)** Step 2] the proximal LCCA and the distal left internal carotid artery (LICA) have been temporarily clipped by arterial clamps. 2-French uninflated balloon catheter has been inserted into the LCCA through the incision of the left external carotid artery (LECA). [**(A)** Step 3] The balloon has been inflated and will be withdrawn with a rotating action to the incision of LECA. The procedure of reintroduction and retraction will be repeated thrice. [**(A)** Step 4] Remove the catheter and ligate LECA, and then remove arterial clamps to restore the blood flow. **(B,C)** The H&E staining of normal and balloon-injured carotid artery. **(B)** Normal right carotid artery. Note the endothelial monolayer (arrowheads) lines the lumen of artery underlying the media. **(C)** Balloon-injured left carotid artery. The left carotid artery which was harvested immediately after balloon injury procedure exhibits endothelial denudation in the intima (arrowheads) (Scale bar = 150 μm).

embedment. Artery samples were sectioned to obtain arterial cross-sections. After the process of deparaffinage and rehydration, slides were blocked and then incubated with the primary antibody goat anti-rat Type IV Collagen (SouthernBiotech, Birmingham, AL, USA), followed by being rinsed with PBS thrice and then incubated with horseradish peroxidase-conjugated secondary antibodies. Finally, slides were incubated with diaminobenzidine for horseradish peroxidase reaction. In order to exhibit the tissue morphology of vascular wall, slides were counterstained with hematoxylin. Immunohistochemical images were acquired by using inversion microscopy (Olympus Corporation, Tokyo, Japan) under bright field.

Statistical Analysis

Data were analyzed by the statistic software SPSS 20.0 (IBM Corp, Armonk, New York, USA). As values were normally distributed, statistic difference between two groups was determined by Student's *t*-test, and one-way ANOVA were used to compare among more than two groups. If the differences among these groups were significant for one-way ANOVA, the difference between the two groups was conducted by Student-Newman-Keuls test. The $P < 0.05$ indicated statistically significant difference.

RESULTS

Characteristics of MBs

The fabricated $MB_{Col\,IV}$ appeared a typical multi-peak particle distribution. There was no significant difference between $MB_{Col\,IV}$ and MB_N for the particle size and distribution (all $P > 0.05$). The mean diameter of $MB_{Col\,IV}$ and MB_N were 1.92 and 1.89 μm, respectively. The results demonstrated that the conjunction of avidin and biotinylated antibody to MBs surface did not change the particle size and distribution of MBs (**Figure 2A**). **Figure 2B** showed that both $MB_{Col\,IV}$ and MB_N had smooth and spherical morphology for microscopic observation. The surface of $MB_{Col\,IV}$ emitted a bright red fluorescence, indicating the anti-rat Type IV Collagen antibodies were successfully conjugated onto the surface of these MBs (**Figure 2B**).

Confirmation of Rat Carotid Artery Injury

Vascular balloon injury is a standardized protocol for endothelial denudation and intimal damage through repeated insertion and retreat of the balloon catheter (**Figure 3A**). In order to confirm the successful development of carotid artery injury model, cross-sections were stained with H&E. From the **Figures 3B,C** we can see that LCCA lost an endothelial monolayer after vascular

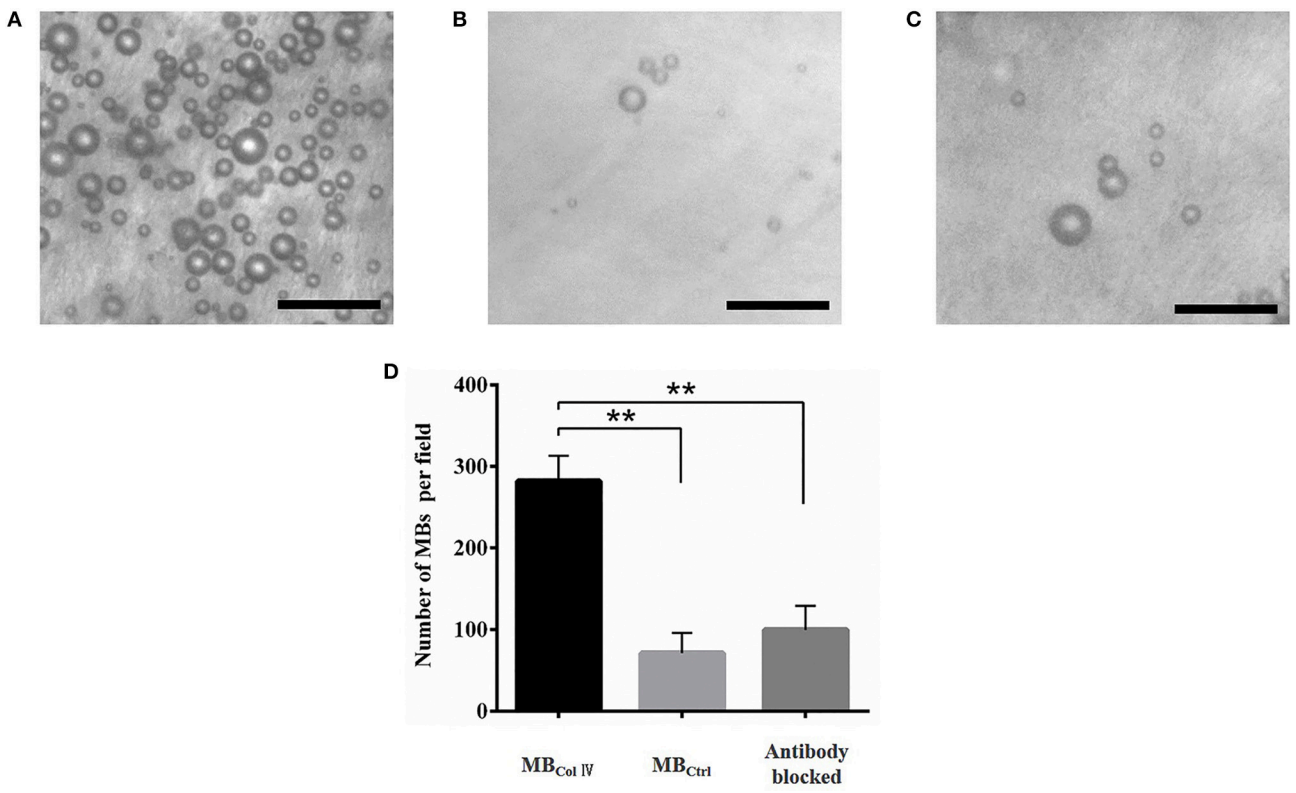

FIGURE 4 | *Ex vivo* adhesion of MBs to the balloon-injured carotid artery. Representative bright-field micrographs show the balloon-injured carotid artery after incubation with $MB_{Col\,IV}$ **(A)**, MB_{Ctrl} **(B)**, or $MB_{Col\,IV}$ with antibody blocking **(C)**. $MB_{Col\,IV}$ adhesion is significantly higher than MB_{Ctrl}. But there is significantly lower adhesion of $MB_{Col\,IV}$ after blocking the receptors with the Type IV Collagen antibody. (Scale bar = 20 μm). **(D)** Quantitative assay for MBs adhesion to the balloon-injured carotid artery $^{**}P < 0.01$ ($n = 3$).

balloon injury, compared with the normal right common carotid artery (RCCA). The results showed that we successfully constructed the carotid injury model.

Binding Specificity of MBs *ex vivo*

To determine the binding specificity of $MB_{Col\,IV}$, we performed the binding specificity experiments *ex vivo* through incubating the $MB_{Col\,IV}$ or MB_{Ctrl} with the injured LCCA. After a static exposure of the injured LCCA to MBs, we could see that a large number of $MB_{Col\,IV}$ were adhered to the injured vessel (**Figure 4A**), which was significantly higher than MB_{Ctrl} (**Figure 4B**). Meanwhile, pre-blocking receptors in injured LCCA by anti-rat Type IV Collagen antibodies greatly reduced the attachment of $MB_{Col\,IV}$ (**Figure 4C**). Quantitative analysis indicated that the binding efficiency of $MB_{Col\,IV}$ was about four times higher compared with MB_{Ctrl} (282.1 ± 77.2 MBs per field vs. 71.07 ± 62.07 per field, $P < 0.01$) (**Figure 4D**).

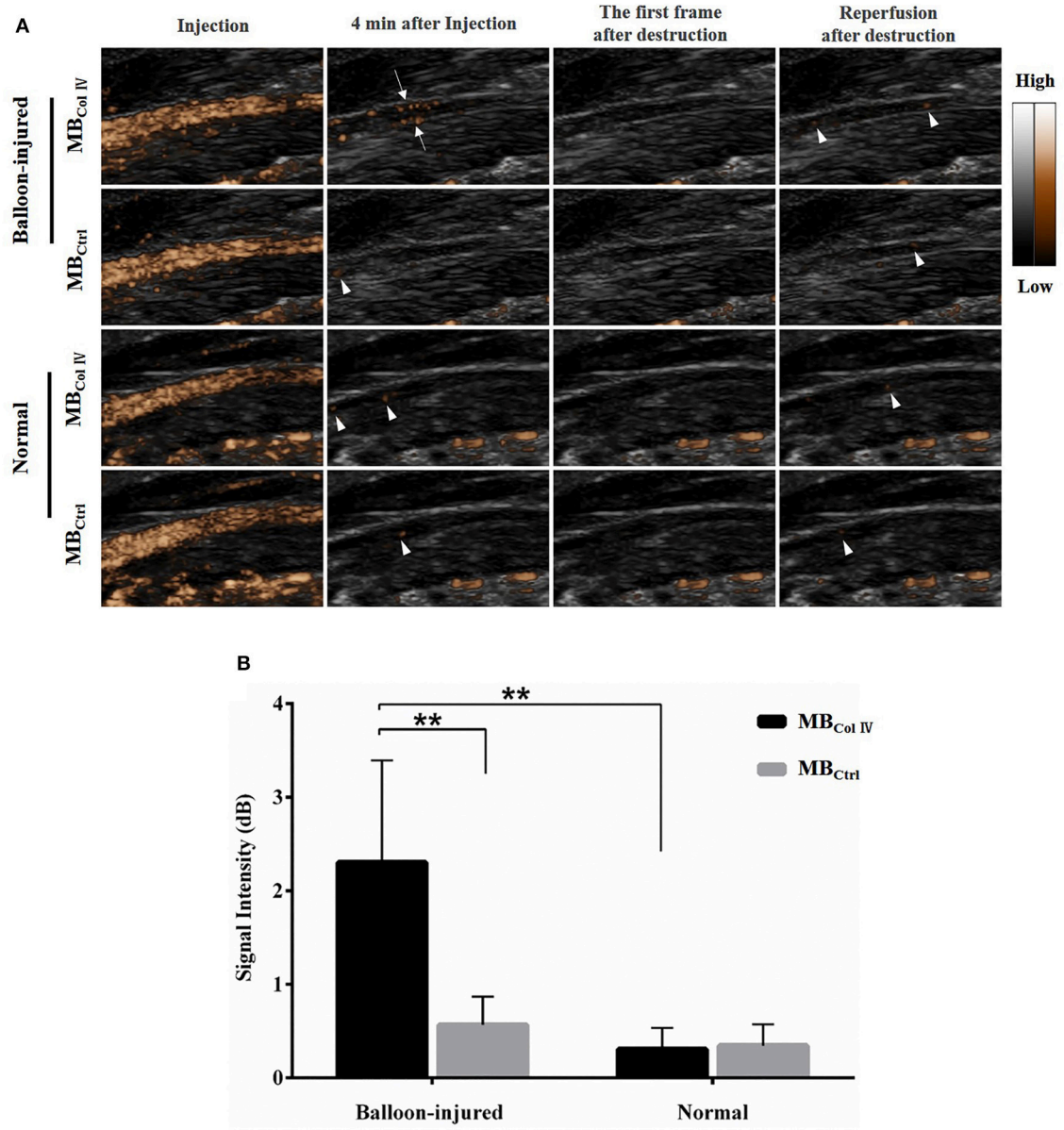

FIGURE 5 | Ultrasound molecular imaging of balloon-injured ($n = 8$) and normal ($n = 7$) carotid arteries and the quantitative analysis of signal intensity. **(A)** Representative results of ultrasound molecular imaging show the long-axis images of rat carotid arteries. $MB_{Col\,IV}$ are obviously bound to the wall of balloon-injured vascular (arrows) but hardly to normal vascular. And ultrasound imaging also exhibits MB_{Ctrl} freely circulate in either balloon-injured vascular or normal vascular (arrowheads). **(B)** The quantitative analysis of signal intensity in balloon-injured ($n = 8$) and normal ($n = 7$) carotid artery after bolus injection of $MB_{Col\,IV}$ or MB_{Ctrl}. $^{**}P < 0.01$ for $MB_{Col\,IV}$ vs. MB_{Ctrl} in balloon-injured group, and for $MB_{Col\,IV}$ in balloon-injured group vs. normal group.

Ultrasound Molecular Imaging

To further evaluate the special adherence of MBs and their ultrasound imaging effect *in vivo*, ultrasound molecular imaging was performed in the balloon-injured carotid artery group ($n = 8$) and the normal carotid artery group ($n = 7$). As shown in **Figure 5A**, 4 min after MBs injection, almost all of MBs had been washed out. Meanwhile, $MB_{Col\,IV}$ were hardly attached to the normal artery wall (**Figure 5A**). By contrast, $MB_{Col\,IV}$ were obviously adhered to the inner wall of balloon-injured artery (**Figure 5A** and Supplementary Video 1). After the trigger of the destruction pulse, no echo signal of MBs was found in balloon-injured the carotid artery group and the normal carotid artery group (**Figure 5A**). This procedure further confirmed that $MB_{Col\,IV}$ were attached to the inner vessel wall. Quantitative analysis revealed that the signal intensity of $MB_{Col\,IV}$ (2.30 ± 0.91 dB) was higher than MB_{Ctrl} (0.57 ± 0.26 dB) in balloon-injured carotid artery group ($P < 0.01$) (**Figure 5B**). Moreover, the signal intensity of $MB_{Col\,IV}$ in the balloon-injured carotid artery group was also significantly higher than normal carotid artery group (2.30 ± 0.91 dB vs. 0.31 ± 0.21 dB, $P < 0.01$) (**Figure 5B**).

Immunohistochemistry

To confirm the results of ultrasound molecular imaging, LCCAs of the normal group and balloon-injured group were harvested and analyzed for the exposure of collagen IV after endothelium denudation. The results of immunohistochemical staining examination were presented in **Figure 6**. We could see that both balloon-injured artery and normal artery were stained dark brown for collagen IV in basement membrane, indicating collagen IV was a major constituent of the basement membrane. It was consistent with the previous studies (Kalluri, 2003; Abreu-Velez and Howard, 2012; Manon-Jensen et al., 2016). In normal artery intima, collagen IV presenting in basement membrane, was covered by a monolayer endothelium (**Figure 6A**). However, without endothelium coverage, collagen IV was directly exposed in balloon-injured artery (**Figure 6B**). The exposure of collagen IV greatly enhanced the interaction opportunity with $MB_{Col\,IV}$. In addition, collagen IV was also a component of the basement membrane for SMCs in tunica media, which had been reported in previous studies (Shekhonin et al., 1985; Howard and Macarak, 1989).

DISCUSSION

Microbubble-based ultrasound molecular imaging is a promising approach in the disease diagnosis at the early stage. This is especially the case for vascular disorders since the microscale-targeted bubbles only exist in the blood and are not extravasate from the circulation. This feature makes it greatly standing out from other nanoparticle-based molecular imaging modalities, such as quantum dot-based optical molecular imaging and iron nanoparticle-based magnetic imaging resonance (Lobatto et al., 2011). Moreover, ultrasound is a safe, affordable and real-time imaging modality and can detect deep-seated diseased tissues. All of these features of ultrasound prompted us to explore the diagnosis feasibility of injured artery by using ultrasound molecular imaging.

In our study, we fabricated the targeted $MB_{Col\,IV}$ by biotin-avidin bridging method. As shown in **Figure 2B**, collagen IV antibodies were successfully conjugated to the surface of MBs. It has to be pointed out that we did not use the *in vitro* tool in our static binding experiments such as culture plates, pre-coated with Matrigel, which has been taken to examine the binding of targeted particles to collagen IV (Dong et al., 2016). In fact, they are not suitable in our experiments. Due to the Matrigel's water solubility, Matrigel dissolves in PBS during rinsing, and almost all MBs would be washed away (data not shown). Therefore, we used the harvested tissue of injured carotid artery to examine the affinity effect of MBs. Effective and special targeting affinity was achieved in our *ex vivo* binding experiments (**Figure 4**). The number of $MB_{Col\,IV}$ binding to the tissue of injured artery was nearly four times higher than MB_{Ctrl}, indicating $MB_{Col\,IV}$ we obtained can be used as a potential ultrasound molecular imaging probe.

In our present study, we used intravenously injection for ultrasound molecular imaging *in vivo* in order to determine whether $MB_{Col\,IV}$ could adhere to the site of endothelial denudation and be visually detected by a clinical ultrasound scanner or not. Surprisingly, we found stronger ultrasound molecular imaging signals from injured vascular wall after $MB_{Col\,IV}$ injection but not MB_{Ctrl}, the former being nearly five times higher than MB_{Ctrl}. Interestingly, no obvious ultrasound molecular imaging signals were detected from the normal

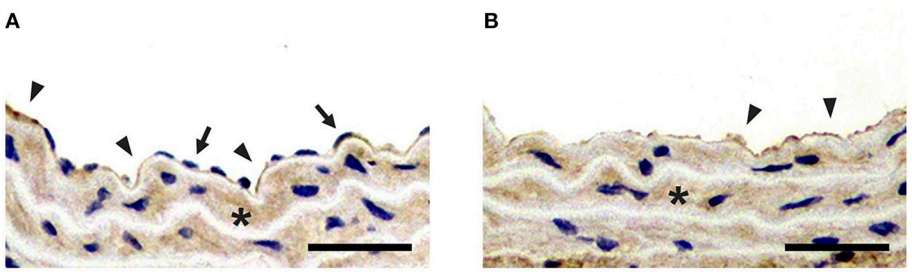

FIGURE 6 | Immunohistochemical staining for collagen IV. **(A)** Immunohistochemical staining of the left carotid common artery (LCCA) from normal group. **(B)** Immunohistochemical staining of LCCA from balloon-injured group. Positive staining for collagen IV is presented in both normal and balloon-injured artery (brown stain; arrowheads). Compared with the endothelium (arrows) coverage for collagen IV (arrowheads) in normal artery, collagen IV is exposed after endothelium denudation in balloon-injured artery (arrowheads). Besides, Collagen IV is also localized to tunica media (asterisk) (Scale bar = 150 μm).

arterial wall after $MB_{Col\,IV}$ or MB_{Ctrl} injection. These results suggested that $MB_{Col\,IV}$ had a highly specific binding ability to these collagen IV targets and could function as an ultrasound molecular imaging probe to detect vascular injury. To take the drug-loaded advantages of MBs into consideration, it is easy to design the $MB_{Col\,IV}$ into drug-loaded targeted MBs through carrying drugs (Lammertink et al., 2015), gene (Zhao et al., 2018) and/or especially therapeutic gas, such as nitric oxide, hydrogen sulfide, carbon monoxide, and so on (Fix et al., 2015). If that is the case, we have reasons to believe that $MB_{Col\,IV}$ could be further functionalized as theranostics agent and would play a great role for ultrasound imaging-guided treatment of vascular injury.

There are several limitations in our study. The rat carotid artery balloon injury model described in our study imitate vascular injury by angioplasty. However, in clinical practice, restenosis occurs in patients who have occlusive atherosclerotic lesions after dilating the narrow lumen through angioplasty. Besides, to evaluate non-culprit stenosis severity, the instantaneous wave-free ratio, which is helpful for guiding PCI strategy, has been regarded as the promising method and used in patients with acute coronary syndrome and multivessel disease (Indolfi et al., 2015). In order to reduce complications, coronary balloon angioplasty is usually combined with stent implantation during PCI (Byrne et al., 2017). Compared with human angioplasty, the rat carotid artery balloon injury model is lacking atherosclerotic lesions and stent implantation. Whereas, the above artery injury model is widely perceived as a well-defined model for researching vascular remodeling and vascular cell proliferation, and it is only suitable for the proof-of-concept study. Another limitation is that once the collagen underlying the basement membrane is exposed, it may cause thrombogenesis, producing an obstruction for targeted MBs. To prevent thrombogenesis, an anticoagulant drug is used before balloon manipulation, but this procedure does not affect the prognosis of restenosis model (Chan et al., 2011; Riegler et al., 2013). Furthermore, the method of avidin-biotin linkage is unlikely to be applied in human clinical practice because of the potential immune response. Therefore, a covalent linkage method is expected to be used to develop targeted contrast agents in the future. For instance, small molecules such as biotin and peptides can be attached to the shell-forming material (protein or lipid) before bubble generation (Weinkauf et al., 2018).

In summary, we have successfully fabricated $MB_{Col\,IV}$ by conjugating anti-collagen IV antibodies to the surface of MBs and confirmed the feasibility to apply them for ultrasound molecular imaging of endothelial injury at early stage. Our study provides an early diagnosis tool for restenosis due to endothelial damage and a potential platform for image-guided therapy for vascular injury.

AUTHOR CONTRIBUTIONS

XM and BZ initialed the project. XM and FY conducted the experiment and data analysis. BZ and FY provided equipment, materials, and experimental methods. XM wrote the manuscript. FY proofread the manuscript. All authors agreed with the final version of the manuscript.

FUNDING

The study was financially supported by National Natural Science Foundation of China (Grant No. 81571693, 81871361, 81530056, 81727805, 81571701). The Pudong Health Bureau of Shanghai (Grant No. PWZbr2017-09). Natural Science Foundation of Guangdong Province (Grant No. 2014A030312006), and Shenzhen Science and Technology Innovation Committee (Grant No. JCYJ20170413100222613, JCYJ20170307165254568).

ACKNOWLEDGMENTS

We thank all staffs at Paul C. Lauterbur Research Center for Biomedical Imaging for their sincere help, especially Fei Yu and Yu Xie, for their guidance of the construction of rat carotid artery injury model.

REFERENCES

Abreu-Velez, A., and Howard, M. (2012). Collagen IV in normal skin and in pathological processes. *N. Am. J. Med. Sci.* 4, 1–8. doi: 10.4103/1947-2714.92892

Amsterdam, E. A., Wenger, N. K., Brindis, R. G., Casey, D. E. Jr., Ganiats, T. G., Holmes, D. R. Jr., et al. (2014). 2014 AHA/ACC guideline for the management of patients with non-ST-elevation acute coronary syndromes: a report of the american college of cardiology/american heart association task force on practice guidelines. *J. Am. Coll. Cardiol.* 64, e139–e228. doi: 10.1016/j.jacc.2014.09.017

Bavry, A. A., Kumbhani, D. J., Rassi, A. N., Bhatt, D. L., and Askari, A. T. (2006). Benefit of early invasive therapy in acute coronary syndromes: a meta-analysis of contemporary randomized clinical trials. *J. Am. Coll. Cardiol.* 48, 1319–1325. doi: 10.1016/j.jacc.2006.06.050

Byrne, R. A., Stone, G. W., Ormiston, J., and Kastrati, A. (2017). Coronary balloon angioplasty, stents, and scaffolds. *Lancet* 390, 781–92. doi: 10.1016/S0140-6736(17)31927-X

Chan, J. M., Rhee, J. W., Drum, C. L., Bronson, R. T., and Golomb, G. (2011). *In vivo* prevention of arterial restenosis with paclitaxel-encapsulated targeted lipid–polymeric nanoparticles. *Proc. Natl. Acad. Sci. U.S.A.* 108, 19347–52. doi: 10.1073/pnas.1115945108

Davis, C., Fischer, J., Ley, K., and Sarembock, I. J. (2003). The role of inflammation in vascular injury and repair. *J. Thromb. Haemost.* 1, 1699–709. doi: 10.1046/j.1538-7836.2003.00292.x

Deshpande, N., Pysz, M. A., and Willmann, J. K. (2010). Molecular ultrasound assessment of tumor angiogenesis. *Angiogenesis* 13, 175–188. doi: 10.1007/s10456-010-9175-z

Dong, Y., Chen, H., Chen, C., Zhang, X., Tian, X., Zhang, Y., et al. (2016). Polymer-lipid hybrid theranostic nanoparticles co-delivering ultrasmall superparamagnetic iron oxide and paclitaxel for targeted magnetic resonance imaging and therapy in atherosclerotic plaque. *J. Biomed. Nanotechnol.* 12, 1245–1257. doi: 10.1166/jbn.2016.2239

Fix, S. M., Borden, M. A., and Dayton, P. A. (2015). Therapeutic gas delivery via microbubbles and liposomes. *J. Control. Release* 209, 139–149. doi: 10.1016/j.jconrel.2015.04.027

Howard, P. S., and Macarak, E. J. (1989). Localization of collagen types in regional segments of the fetal bovine aorta. *Lab. Invest.* 61, 548–555.

Indolfi, C., Mongiardo, A., Spaccarotella, C., Torella, D., Caiazzo, G., Polimeni, A., et al. (2015). The instantaneous wave-free ratio (iFR) for evaluation of

non-culprit lesions in patients with acute coronary syndrome and multivessel disease. *Int. J. Cardiol.* 178, 46–54. doi: 10.1016/j.ijcard.2014.03.210

Kalluri, R. (2003). Basement membranes: structure, assembly and role in tumour angiogenesis. *Nat. Rev. Cancer* 3, 422–433. doi: 10.1038/nrc1094

Kennedy, S., McPhaden, A. R., Wadsworth, R. M., and Wainwright, C. L. (2000). Correlation of leukocyte adhesiveness, adhesion molecule expression and leukocyte-induced contraction following balloon angioplasty. *Br. J. Pharmacol.* 130, 95–103. doi: 10.1038/sj.bjp.0703282

Lammertink, B. H., Bos, C., Deckers, R., Storm, G., Moonen, C. T. W., and Escoffre, J.-M. (2015). Sonochemotherapy: from bench to bedside. *Front. Pharmacol.* 6:138. doi: 10.3389/fphar.2015.00138

Leong-Poi, H. (2009). Molecular imaging using contrast-enhanced ultrasound: evaluation of angiogenesis and cell therapy. *Cardiovasc. Res.* 84, 190–200. doi: 10.1093/cvr/cvp248

Lindner, J. R. (2009). Contrast ultrasound molecular imaging of inflammation in cardiovascular disease. *Cardiovasc. Res.* 84, 182–189. doi: 10.1093/cvr/cvp302

Lobatto, M. E., Fuster, V., Fayad, Z. A., and Mulder, W. J. (2011). Perspectives and opportunities for nanomedicine in the management of atherosclerosis. *Nat. Rev. Drug Discov.* 10, 835–852. doi: 10.1038/nrd3578

Manon-Jensen, T., Kjeld, N. G., and Karsdal, M. A. (2016). Collagen-mediated hemostasis. *J. Thromb. Haemost.* 14, 438–448. doi: 10.1111/jth.13249

Meyers, M. W., Rink, J. S., Jiang, Q., Kelly, M. E., Vercammen, J. M., Thaxton, C. S., et al. (2017). Systemically administered collagen-targeted gold nanoparticles bind to arterial injury following vascular interventions. *Physiol. Rep.* 5:e13128. doi: 10.14814/phy2

Murray, C. J., Vos, T., Lozano, R., Naghavi, M., Flaxman, A. D., Michaud, C., et al. (2012). Disability-adjusted life years (DALYs) for 291 diseases and injuries in 21 regions, 1990-2010: a systematic analysis for the Global Burden of Disease Study 2010. *Lancet* 380, 2197–2223. doi: 10.1016/S0140-6736(12)61689-4

Otsuka, F., Yasuda, S., Noguchi, T., and Ishibashi-Ueda, H. (2016). Pathology of coronary atherosclerosis and thrombosis. *Cardiovasc. Diagn. Ther.* 6, 396–408. doi: 10.21037/cdt.2016.06.01

Petrasheskaya, N., Tae, H.-J., Ahmet, I., Talan, M. I., Lakatta, E. G., and Lin, L. (2016). A rat carotid balloon injury model to test anti-vascular remodeling therapeutics. *J. Vis. Exp.* 2016:e53777. doi: 10.3791/53777

Riegler, J., Liew, A., Hynes, S. O., Ortega, D, o'Brien, T., Day, R. M., et al. (2013). Superparamagnetic iron oxide nanoparticle targeting of MSCs in vascular injury. *Biomaterials* 34, 1987–1994. doi: 10.1016/j.biomaterials.2012.11.040

Shekhonin, B. V., Domogatsky, S. P., Muzykantov, V. R., Idelson, G. L., and Rukosuev, V. S. (1985). Distribution of type I, III, IV and V collagen in normal and atherosclerotic human arterial wall: immunomorphological characteristics. *Coll. Relat. Res.* 5, 355–368.

Tanaka, H., Sukhova, G. K., Swanson, S. J., Clinton, S. K., Ganz, P., Cybulsky, M. I., et al. (1993). Sustained activation of vascular cells and leukocytes in the rabbit aorta after balloon injury. *Circulation* 88, 1788–1803.

Villanueva, F. S., and Wagner, W. R. (2008). Ultrasound molecular imaging of cardiovascular disease. *Nat. Clin. Pract. Cardiovasc. Med.* 5(Suppl. 2), S26–S32. doi: 10.1038/ncpcardio1246

Weinkauf, C. C., Concha-Moore, K., Lindner, J. R., Marinelli, E. R., Hadinger, K. P., Bhattacharjee, S., et al. (2018). Endothelial vascular cell adhesion molecule 1 is a marker for high-risk carotid plaques and target for ultrasound molecular imaging. *J. Vasc. Surg.* 68, 105S−113S. doi: 10.1016/j.jvs.2017.10.088

Willmann, J. K., Paulmurugan, R., Chen, K., Gheysens, O., Rodriguez-Porcel, M., Lutz, A. M., et al. (2008). US imaging of tumor angiogenesis with microbubbles targeted to vascular endothelial growth factor receptor type 2 in mice. *Radiology* 246, 508–518. doi: 10.1148/radiol.2462070536

Wu, J., Leong-Poi, H., Bin, J., Yang, L., Liao, Y., Liu, Y., et al. (2011). Efficacy of contrast-enhanced US and magnetic microbubbles targeted to vascular cell adhesion molecule-1 for molecular imaging of atherosclerosis. *Radiology* 260, 463–471. doi: 10.1148/radiol.11102251

Yan, F., Li, L., Deng, Z., Jin, Q., Chen, J., Yang, W., et al. (2013). Paclitaxel-liposome-microbubble complexes as ultrasound-triggered therapeutic drug delivery carriers. *J. Control. Release* 166, 246–255. doi: 10.1016/j.jconrel.2012.12.025

Yan, F., Sun, Y., Mao, Y., Wu, M., Deng, Z., Li, S., et al. (2018). Ultrasound molecular imaging of atherosclerosis for early diagnosis and therapeutic evaluation through leucocyte-like multiple targeted microbubbles. *Theranostics* 8, 1879–1891. doi: 10.7150/thno.22070

Zhao, R., Liang, X., Zhao, B., Chen, M., Liu, R., Sun, S., et al. (2018). Ultrasound assisted gene and photodynamic synergistic therapy with multifunctional FOXA1-siRNA loaded porphyrin microbubbles for enhancing therapeutic efficacy for breast cancer. *Biomaterials* 173, 58–70. doi: 10.1016/j.biomaterials.2018.04.054

Conflict of Interest Statement: The authors declare that the research was conducted in the absence of any commercial or financial relationships that could be construed as a potential conflict of interest.

frontiers in Pharmacology

ORIGINAL RESEARCH
published: 31 January 2019
doi: 10.3389/fphar.2019.00043

Atropine Premedication Facilitates Ultrasound-Guided Reduction by Saline Enema in Children With Intussusception

Xiao Liu[1,2], Bei Xia[1], Hong-kui Yu[1], Lie-zhen Hu[1], Shu-min Fan[1], Dong Xiao[1], Li-xian Gu[1], Jia-kun Chen[1], Zhi-bo Wen[2] and Xiao-peng Ma[1]**

[1] Shenzhen Children's Hospital, Shenzhen, China, [2] Zhujiang Hospital, Southern Medical University, Guangzhou, China

Background and Objective: Intussusception is the most frequent pediatric abdominal emergency. Intestinal spasm, ischemia, necrosis and even death may occur without prompt diagnosis and treatment. The ultrasound-guided reduction by saline enema is a preferred non-surgical procedure for intussusception. Muscular relaxants can relieve the intestinal spasm and edema by relaxing the intestinal smooth muscle, which may facilitate the treatment of intussusception. However, controversy persists on whether muscular relaxants are effective in the procedure. Therefore, the purpose of our study was to assess the efficacy of atropine known as a muscular relaxant in ultrasound-guided reduction by saline enema in children with intussusception.

Methods: All patients with intussusception diagnosed and treated in our department from July 2016 to February 2018 were included. Four hundred and thirty-seven children were enrolled and randomly divided into two groups: an atropine group and a control group. Intramuscular atropine at a dose of 0.02 mg per kilogram of body weight was administrated 15 min before ultrasound-guided reduction by saline enema in the atropine group. In the control group, the ultrasound-guided reduction was performed without using any muscular relaxants. The success rate, duration of the reduction, volume of saline, maximum intra-rectal pressure and complications were recorded and compared between the two groups.

Results: The success rate was 95.9% (212 out of 221) and 94.9% (205 out of 216) in the atropine group and the control group, respectively. No significant difference was observed in the success rate between the two groups ($P > 0.05$). The duration of reduction was significantly lower in the atropine group than in the control group ($P < 0.01$). The volume of saline was also significantly lower in the atropine group than in the control group ($P < 0.05$). The maximum intra-rectal pressure showed no difference between the two groups ($P > 0.05$).

Conclusion: Atropine premedication can facilitate ultrasound-guided reduction by saline enema in children with intussusception, by reducing the duration of reduction and the volume of saline in the procedure.

Keywords: intussusception, atropine, enema, ultrasound, children

OPEN ACCESS

Edited by:
Fei Yan,
Shenzhen Institutes of Advanced Technology (CAS), China

Reviewed by:
Erjiao Xu,
Third Affiliated Hospital of Sun Yat-sen University, China
Sheng Zhao,
Hubei Maternal and Child Health Hospital, China

****Correspondence:***
Xiao-peng Ma
maxiaopeng@126.com
Zhi-bo Wen
zhibowen@163.com

Specialty section:
This article was submitted to Translational Pharmacology, a section of the journal Frontiers in Pharmacology

Received: *23 November 2018*
Accepted: *14 January 2019*
Published: *31 January 2019*

Citation:
Liu X, Xia B, Yu H-k, Hu L-z, Fan S-m, Xiao D, Gu L-x, Chen J-k, Wen Z-b and Ma X-p (2019) Atropine Premedication Facilitates Ultrasound-Guided Reduction by Saline Enema in Children With Intussusception. Front. Pharmacol. 10:43. doi: 10.3389/fphar.2019.00043

INTRODUCTION

Intussusception is the most common cause of acute abdomen in children. The mean annual incidence worldwide varies from 0.24 to 2.4 per 1000 live births (Blanch et al., 2007; Gluckman et al., 2017). There is a high incidence in boys, and the male-to-female ratio is approximately 2:1 (Ko et al., 2007). The classic symptoms and signs include paroxysmal abdominal pain, vomiting, red jelly stool and a palpable abdominal mass (Lehnert et al., 2009; Territo et al., 2014). Accurate and timely diagnosis is imperative as a delay with longer duration of symptoms may result in intestinal ischemia, necrosis, perforation with peritonitis, higher rates of surgical intervention and rarely, death (Ito et al., 2012). Diagnosis based on clinical manifestations can be difficult sometimes due to the variability of its clinical manifestations. Ultrasound is currently the initial imaging modality in the diagnosis of pediatric intussusceptions with high sensitivity and specificity, 97.9 and 97.8%, respectively (Hryhorczuk and Strouse, 2009).

Intussusception can cause strangulated intestinal obstruction (Ito et al., 2012). It describes the process whereby a segment of bowel (the intussusceptum) telescopes into the lumen of the immediate distal segment (the intussuscipiens). The attached mesentery gets pulled along with the loop of bowel, resulting in constriction of venous outflow and impaired arterial perfusion. Intestinal spasm and ischemia remain continuously due to intestinal obstruction and impaired blood supply, eventually lead to intestinal necrosis and perforation.

Once the diagnosis of intussusception is established, the ultrasound-guided reduction by saline enema is a preferred non-surgical procedure with the advantages of lesser trauma, low cost and short hospital stay (Daneman and Navarro, 2004). The procedure involves introducing saline into the bowel, via the rectum, with a particular pressure that induces the bowel into its normal position. Most of the patients can be cured by saline enema reduction. But long duration of reduction and high hydrostatic pressure may cause further damage to the impaired intestine during the procedure, subsequently lead to intestinal perforation and other complications (Shehata et al., 2000; Bai et al., 2006).

The use of muscular relaxants might make the enema procedure faster and safer. Muscular relaxants can relieve the intestinal spasm and edema by relaxing the intestinal smooth muscle, which is beneficial to restore the blood supply. Recent animal studies have shown that scopolamine has a certain preventive effect on intussusceptions (Wetherell et al., 2007). However, there have been only a few reports on the use of atropine-assisted enema to improve the success rate (Grahl, 1983). At present, the efficacy of muscular relaxants is still controversial around the world, so it is seldom used in clinical practice (Ito et al., 2012). Therefore, the purpose of our study was to assess the efficacy of atropine known as a muscular relaxant in ultrasound-guided reduction by saline enema in children with intussusception.

PATIENTS AND METHODS

Patients

Patients with intussusception diagnosed in our department from July 2016 to February 2018 were included. Intussusception was diagnosed according to the typical characteristic sonographic appearance of "target sign" in transverse view and "sleeve sign" in longitudinal view (Edwards et al., 2017). Inclusion criteria were: patients diagnosed with intussusceptions and treated by ultrasound-guided saline enema in our department. Exclusion criteria were: patients presented with clinical evidence of dehydration, shock, peritonitis or intestinal perforation, and suspected glaucoma patients. The ethics committee of Shenzhen children's hospital approved the study and all parents of the patients gave written informed consent.

All patients were randomly divided into two groups: an atropine group and a control group. Fifteen minutes before reduction, an intramuscular atropine at the dose of 0.02 mg per kilogram of body weight was administrated and then ultrasound-guided reduction by saline enema was performed in the atropine group. In the control group, the ultrasound-guided reduction by saline enema was performed without using any muscular relaxants.

The Protocol of Ultrasound-Guided Reduction by Saline Enema

The procedure including its necessity and risks was explained in detail to the parents. The materials for saline enema were prepared such as sufficient saline, a manometer, a tee pipe, an infusion rack, a Foleys catheter [16F] and a 50 ml syringe. The treatment room was equipped with an ECG monitor, central oxygen supply, a sphygmomanometer, etc., in case of emergency.

A well-lubricated Foleys catheter [16F] was introduced per rectally for 7–10 cm. The bulb of the Foleys catheter was inflated with 30–50 ml of air and its position was confirmed by ultrasound. The catheter was connected to the tee pipe, another end of the tee pipe was connected to the manometer to measure the intra-rectal pressure, and the third end of the tee pipe was connected to the infusion bag containing warm saline (37–40°C). The infusion bag was kept at an extra height of 120 cm above the level of the bed. The parents kept company and held the child tightly on the thigh to seal the anus against leakage. The child was awake in a supine position whose condition was observed during the whole procedure (**Figure 1**).

When the patient was well prepared, the switch of the infusion device was turned on. Saline full filled the sigmoid colon, descending colon, transverse colon and ascending colon in sequence and arrived at the intussuscipiens (**Figure 2A**) under ultrasound monitoring (GE LogiQ E9, GE Co., Ltd., United States). Then *trans*-abdominal manual manipulation was performed to assist reduction by gently pressing abdomen counterclockwise to drive the liquid from left to right abdomen toward the intussuscipiens. In the meantime, the patients were instructed to mount a Valsalva maneuver.

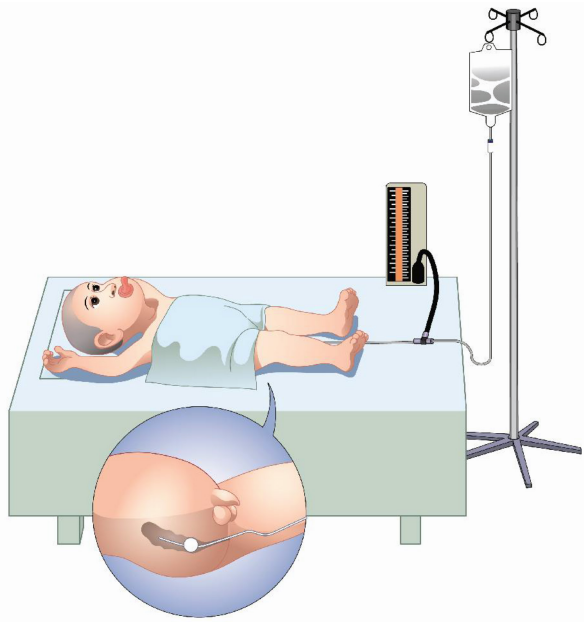

FIGURE 1 | Illustration of the ultrasound-guided reduction by saline enema in children with intussusception.

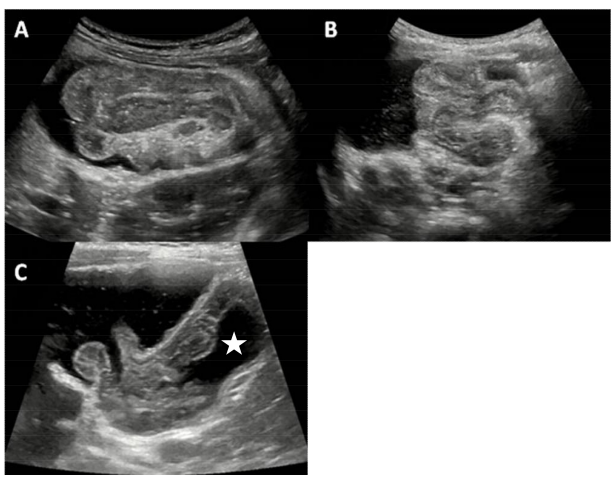

FIGURE 2 | The ultrasonic manifestations during the ultrasound-guided reduction by saline enema. **(A)** Saline arrived at the intussuscipiens. **(B)** Intussusception gradually shortened. **(C)** Intussusception disappeared, saline passed through the ileocecal valve and fulfilled the terminal ileum (star).

The above actions could be repeated for several times until the intussusception gradually shortened (**Figure 2B**) and disappeared (**Figure 2C**). During continuous ultrasound monitoring, underlying pathologic factors (lead points) in the intestinal wall and lumen were observed. If the intussusception could not be reduced in 30 min, the procedure was suspended. A repeated enema was performed after the patient took a rest for 30 min. The procedure could be repeated up to 3 times.

Criteria for successful reduction were disappearance of the intussusception and passage of fluid through the ileocecal valve (**Figure 2C**). Generally, the abdominal pain relieved and the child felt comfortable and became quiet at the same time.

During the procedure, the patients were monitored by ultrasound to observe whether there was presence of free peritoneal air or increased peritoneal fluid to exclude intestinal perforation. Once intestinal perforation occurred, the procedure should be stopped immediately, the fluid in the intestinal canal should be drained as far as possible, and the vital signs should be monitored. The patient was transferred to the operating room as soon as possible.

After successful reduction, all patients were admitted under observation and discharged when oral feeding and bowel movements were normal. All patients underwent unsuccessfully reduced intussusception were managed surgically.

Success or failure, duration of the reduction, volume of saline, maximum intra-rectal pressure and complications were recorded in each patient. The duration of the reduction included the time of saline infusion throughout the procedure. When the saline enema was repeated, the accumulated time is calculated as the duration of the reduction.

Statistics Analysis

Measurement data were expressed as mean ± SD. Differences in duration of reduction, volume of saline and maximum intra-rectal pressure between the two groups were compared using unpaired Student's *t*-test. The success rates and recurrent rates between the two groups were compared through χ^2 test. The ultrasonic characteristics of intussusceptions, pathological lead points of secondary intussusceptions and unsuccessful factors of reduction between the two groups were also compared through χ^2 test. Two-tailed *p*-values < 0.05 were considered statistically significant. All statistical analyses were performed using SPSS version 19.0 (SPSS, Inc., Chicago, IL, United States).

RESULTS

Generally, 437 patients were enrolled, of which 294 were male and 143 were female. The male-to-female ratio was approximately 2.06: 1. The median age of patients was 16 months (the youngest patient aged 2 months and the oldest aged 9 years). In our study, 92.2% (403 out of 437) of intussusceptions were ileocolic, 5.3% (23 out of 437) were colocolic, and the remaining 2.5% cases (11 out of 437) were ileoileocolic. Two hundred and twenty-one patients received atropine premedication before ultrasound-guided reduction by saline enema and 216 patients received the procedure without any muscular relaxants. There was no significant difference in age between the two groups ($P > 0.05$). The duration of symptoms was 3–72 h, with no significant difference between the two groups ($P > 0.05$). The size of the intussusceptions, including the length and the maximum external diameter, was not found to differ between the two groups ($P > 0.05$). There was also no significant difference in ultrasonic characteristics and specific

classification of secondary intussusceptions between the two groups ($P > 0.05$). Main complaints and symptoms included 212 cases (48.5%) of paroxysmal abdominal pain, 207 cases (47.4%) of vomiting, 133 cases (30.4%) of excessive crying, 62 cases (14.2%) of bloody stool, 22 cases (5.0%) of abdominal mass, 15 cases (3.4%) of diarrhea, and 12 cases (2.7%) of fever. Background characteristics of patients are listed in **Table 1**.

The success rate was 95.9% (212 out of 221) and 94.9% (205 out of 216) in the atropine group and the control group, respectively. No significant difference was observed in the success rate between the two groups ($P > 0.05$). The duration of reduction was significantly lower in the atropine group than in the control group ($P < 0.01$) (**Figure 3A**). Volume of saline was also significantly lower in the atropine group than in the control group ($P < 0.05$) (**Figure 3B**). The maximum intra-rectal pressure showed no difference between the two groups ($P > 0.05$) (**Figure 3C**). In the control group, intestinal perforation occurred in one patient, presenting increased peritoneal effusion during the procedure. There was no significant difference in recurrence rates between the atropine group and the control group, which were 4.07 and 4.17%, respectively. Parameters of enema reduction and unsuccessful factors are listed in **Table 2**.

All 20 patients in whom enema reduction was unsuccessful underwent surgical reduction. Bowel resection was performed in six patients due to intestinal necrosis without lead points.

TABLE 1 | Background characteristics of patients in the two groups.

	The atropine group (*n* = 221)	The control group (*n* = 216)	*P*-value
Age (y)	1.83 ± 1.52	2.01 ± 1.62	0.256
Sex (Male/Female)	150/71	144/72	0.788
Duration of symptoms (hours)	22.19 ± 17.14	21.92 ± 15.81	0.867
Size of the intussusception			
Length (cm)	7.16 ± 2.10	7.18 ± 1.68	0.941
Maximum external diameterh (cm)	3.02 ± 0.37	3.03 ± 0.42	0.750
Ultrasonic characteristics			
Lymph node within the intussusception	45	48	0.636
Effusion inside the intussusception	15	13	0.743
Peritoneal fluid	36	43	0.326
Intestinal obstruction	3	5	0.455
Thicken intestinal wall of intussuscipiens	14	16	0.658
Lack of blood flow by color Doppler	4	3	0.726
Secondary intussusception			
Polyps	1	2	0.549
Meckel's diverticulum	3	3	0.977
Intestinal duplication cyst	2	1	0.576
Lymphoma	1	1	0.987

DISCUSSION

In the present study, our findings showed atropine premedication could significantly reduce the duration of reduction and the volume of saline in the ultrasound-guided reduction by saline enema in children with intussusceptions, and the success rate had no difference between the atropine group and the control group. To the authors' knowledge, this is the first comparative study with large samples on the application of atropine known as a muscular relaxant for ultrasound-guided reduction by saline enema in children with intussusception.

The ultrasound-guided reduction of intussusception by saline enema has gradually become a worldwide-preferred non-surgical procedure for pediatric intussusception (Bai et al., 2006) since first described by Kim et al. (1982). Compared with air enema monitored by X-ray, the ultrasound-guided reduction by saline enema is visualized and more intuitive. It can visualize the various parts of the intussusception, showing possible pathological lead points such as polyps, Meckel's diverticulum, lymphoma, etc. (Navarro et al., 2000). It's radiation-free, avoiding the gonads' exposure of children with long-term risk. Successful reduction can quickly relieve the child's symptoms, avoiding surgery and complications such as surgery-related intestinal adhesion and infection. It is reported that the reduction rate of saline enema was similar to air enema, and complications such as perforation were rare, generally less than 1% (Daneman and Navarro, 2004). However, liquid reduction might associate with higher risk of peritoneal contamination compared with air enemas in the event of perforation (Carroll et al., 2017). All patients in our study were treated with saline enema reduction rather than air enema. From the results of our study, the success rate in the atropine group and the control group were 95.9 and 94.9%, respectively, both superior to the success rate of the previous literatures (Crystal et al., 2002; Flaum et al., 2016; Kanglie et al., 2018).

Reviewing the ultrasound characteristics, the unfavorable factors of unsuccessful reduction mainly included ultrasound findings of intestinal obstruction, peritoneal fluid, thicken intestinal wall of intussuscipiens, effusion inside the intussusception, and lack of blood flow by color Doppler in the intestinal wall of intussuscipiens (He et al., 2014; Gondek et al., 2018). The above ultrasound characteristics mainly caused by ileoileocolic intussusception, secondary intussusception, edema, necrosis and perforation of the intestinal wall according to surgery and pathologic findings, which were consistent with the literatures (Bramson and Blickman, 1992; Applegate, 2009). Therefore, it is necessary to consider the possibility of unsuccessful reduction and prepare for surgery in advance in the presence of the above findings by ultrasound. In our study, intestinal perforation occurred in one patient in the control group, presenting increased peritoneal fluid during the enema procedure.

Intussusception can cause strangulated intestinal obstruction (Ito et al., 2012). It describes the process whereby a segment of bowel telescopes into the lumen of the immediate distal segment. The attached mesentery gets pulled along with the loop of bowel, resulting in constriction of venous outflow and impaired arterial perfusion. With the persistent intestinal

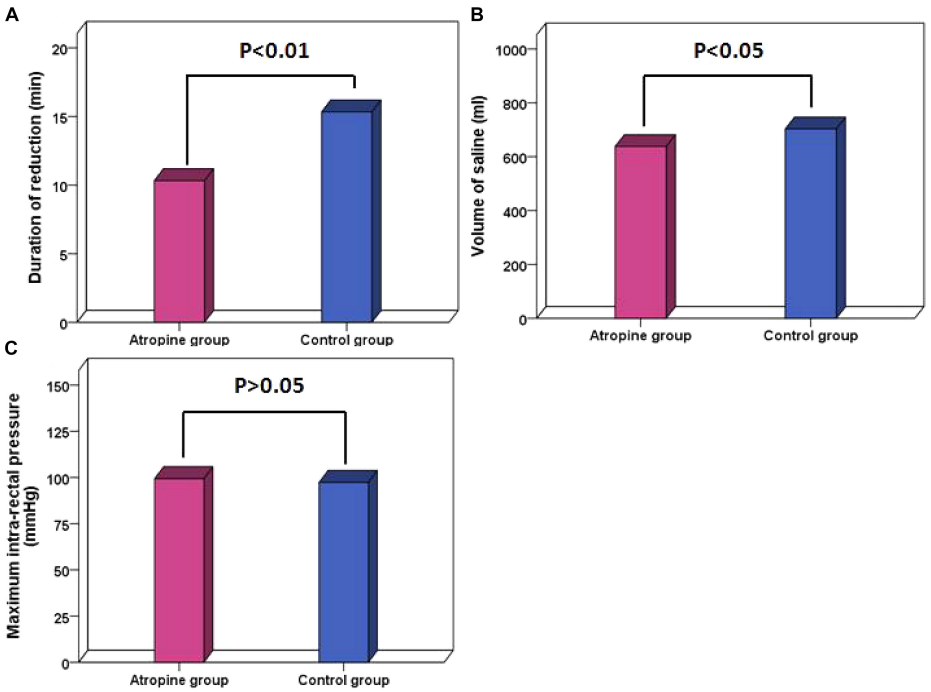

FIGURE 3 | Parameters compared between the atropine group and the control group. **(A)** Duration of reduction. **(B)** Volume of saline. **(C)** Maximum intra-rectal pressure. $P < 0.05$ shows statistical significance.

TABLE 2 | Parameters of enema reduction and unsuccessful factors in both groups.

	Atropine group (n = 221)	Control group (n = 216)	P-value
Success rate	95.9% (212/221)	94.9% (205/216)	0.610
Time of reduction (min)	10.32 ± 8.89	15.34 ± 9.50	0.000
Volume of saline (ml)	637.96 ± 259.35	702.92 ± 342.73	0.026
Maximum intra-rectal pressure (mmHg)	99.30 ± 20.58	97.31 ± 17.04	0.273
Recurrence rate	4.07% (9/221)	4.17% (9/216)	0.960
Unsuccessful factors			
Ileoileocolic intussusception	4	4	0.974
Intestinal necrosis	3	3	0.977
Secondary intussusception	1	4	0.169
Deteriorated general condition	1	0	0.322

peristalsis, the intussusceptum continues to advance and cannot be reduced automatically. Intestinal spasm and ischemia remain continuously due to intestinal obstruction and impaired blood supply, eventually lead to intestinal necrosis, perforation and rarely, death. Prolonged enema procedure and excess pressure may increase the risk of perforation of the impaired intestine (Daneman et al., 1995).

The muscular relaxants can relieve the intestinal spasm and edema by relaxing intestinal smooth muscle, which may loosen the intussuscipiens, so that the intussusception reduction may be easier to achieve (Ito et al., 2012). So far, there are a few reports on the application of muscular relaxants in the reduction of intussusceptions. Three decades ago, Grahl (1983) summarized the experience of using scopolamine before enema, which is considered to improve the effect of enema. But this conclusion did not attract extensive attention. There is no consensus on the role of pharmacological adjuvants on enema reduction of intussusception (Gluckman et al., 2017). Therefore, they are not routinely used in clinical practice.

Atropine is a typical muscarinic cholinergic antagonist which can relieve spasms or cramps in the gastrointestinal smooth muscle, inhibit glandular secretion, expanding pupil, increasing intraocular pressure and regulating vision. It is clinically used to relieve visceral pain, including pain caused by gastrointestinal spasm, renal colic, biliary colic, gastric and duodenal ulcer. The blood concentration of atropine peaks 15–20 min after intramuscular injection. The effect lasts for 4–6 h with a half-life of 3.7–4.3 h. The metabolism of atropine is mainly through the hydrolysis of hepatocyte enzymes, and about 13–50% are discharged in the original form with urine within 12 h. In our study, the route of administration was intramuscular injection with a dose of 0.02 mg per kilogram of body weight. After intramuscular injection, atropine takes effect in 15–20 min. Therefore, the patient may show symptoms such as dry mouth and flushed face when the enema reduction gets started, indicating that the drug is effective. Small dose (less than 1 mg) of atropine has few side effects. Occasionally it may cause slow heart rate, slightly dry mouth and less sweat. Infants are more sensitive,

so we need to focus on the heart rate especially for patients with brain injury. Atropine is banned for patients with glaucoma.

In this study, the duration of reduction and the volume of saline were significantly decreased and no complication of intestinal perforation occurred in the atropine group. We considered that atropine might play an important role since it can relax the intestinal smooth muscle and alleviate intestinal spasm and edema. It can also restore blood supply by loosening the intussuscipiens. Through the above mechanism, intussusception was easier and safer to be reduced. During the study period, we also found automatic reduction of intussusception occurred in three patients when we tried to perform the enema procedure after atropine administration, which might also benefit from the effect of atropine. The maximum intra-rectal pressure had no significant difference between the two groups, because it was determined by the height of the infusion bag, the pressure induced by *trans*-abdominal manual manipulation, and the pressure caused by children crying or mounting a Valsalva maneuver. Our results also indicated that the atropine group was easier and faster to achieve reduction under the same pressure compared with the control group. The recurrence rates in our study were 4.07% in the atropine group and 4.17% in the control group, which were consistent with previous study (Koh et al., 2006). Although atropine was seldom used in water enema, the application of atropine in barium enema could reduce the tension of colon, and aid comfort and reduce the duration of the enema procedure according to a previous study (Skucas, 1994).

Glucagon is another pharmacological adjuvant that can be used in intussusception according to previous studies. Glucagon is a hormone secreted by pancreatic islet α-cells and has a muscle relaxing effect. Early studies suggested that glucagon could improve the success rate of enema reduction (Ito et al., 2012), but a multicenter comparative study showed no significant effect on intussusception (Franken et al., 1983).

Sedatives are also applied in reduction of intussusception. Many sedatives have been reported in the literature, including diazepam, chloral hydrate, metazosing and morphine sulfate (Ito et al., 2012; van de Bunt et al., 2017). The use of sedatives or anesthesia during enema procedure can alleviate fear and pain. Children can calm down and be more cooperative. A study suggested that the success rate of reduction increased from 68.8 to 93.8% after the application of Midazolam with limited cases, only 16 cases in the atropine group and 16 cases in the control group (Eisapour et al., 2015). So far, there are few clinical studies support or oppose the use of sedatives. In a survey of European pediatric radiologists, only 34.9% of respondents routinely used sedatives for intussusception (Schmit et al., 1999). No sedatives were used in our study. We considered that children could be more initiative and cooperate with the parents' company during the procedure. When the children were awake, the manometer showed increased intra-rectal pressure while they were crying or mounting a Valsalva maneuver which was conducive to reduction. There are also disadvantages to the use of sedatives including unpredictable complications, additional medical staff, inconvenience to observation of reaction and vital signs of children, and possible risks of allergic reaction such as shortness of breath (Mc and Rosenfeld, 2000).

The application of proper abdominal massage during the saline enema can promote reduction of intussusception. Grasso et al. (1994) reported that the success rate increased from 58 to 76% with the aid of transabdominal massage in air enema reduction. Real-time ultrasound monitoring revealed that *trans*-abdominal massage counterclockwise with the major thenar could promote the reduction. However, multiple repetitions are not recommended to avoid further damage to the intestinal wall of intussusception. If the enema procedure takes too long, the infusion should be suspended and the saline should be drained out if only a part of intussusception is retracted. Through the above operation, the intra-abdominal pressure reduced and the blood supply of intestinal wall may be restored. After an interval of 30 min, the saline enema could be performed again, which can increase the success rate of reduction and lower the risk of intestinal perforation. In this study, six patients underwent 2 or 3 enema procedures.

This article analyzed the role of atropine premedication in the ultrasound-guided reduction by saline enema through a comparative study of larger samples. However, there are certain limitations by ignoring other variables involved in the study, such as the skills of all the care team responsible for the reduction and characteristics of the patients can also be partly add to the duration of reduction and volume of saline.

CONCLUSION

Atropine premedication can facilitate ultrasound-guided reduction by saline enema in children with intussusception by reducing the duration of reduction and the volume of saline in the procedure, which is beneficial to ease the suffering of children and lower the risk of complications. Therefore, we recommend the use of atropine prior to the reduction procedure.

AUTHOR CONTRIBUTIONS

XL wrote the paper and conceived and conducted the study. BX designed and improved the procedure of the technique and ensured its quality and safety as the ultrasonography department lead. H-kY wrote the paper and carried out the analysis. L-zH and S-mF implemented quality control of the procedure. DX provided valuable support in the therapeutic process. L-xG and J-kC contributed to data collection and management. Z-bW contributed to the discussion, supervised, and reviewed the text. X-pM promoted the clinical application of the technique. All authors read and approved the manuscript.

ACKNOWLEDGMENTS

The authors would like to thank Dr. Xue-bing Liang (Emergency department, Eastern Health & Intensive Care Unit, Epworth Richmond, Melbourne) for her contribution to the English grammar of this article.

REFERENCES

Applegate, K. E. (2009). Intussusception in children: evidence-based diagnosis and treatment. *Pediatr. Radiol.* 39(Suppl. 2), S140–S143. doi: 10.1007/s00247-009-1178-9

Bai, Y. Z., Qu, R. B., Wang, G. D., Zhang, K. R., Li, Y., Huang, Y., et al. (2006). Ultrasound-guided hydrostatic reduction of intussusceptions by saline enema: a review of 5218 cases in 17 years. *Am. J. Surg.* 192, 273–275. doi: 10.1016/j.amjsurg.2006.04.013

Blanch, A. J., Perel, S. B., and Acworth, J. P. (2007). Paediatric intussusception: epidemiology and outcome. *Emerg. Med. Australas.* 19, 45–50. doi: 10.1111/j.1742-6723.2007.00923.x

Bramson, R. T., and Blickman, J. G. (1992). Perforation during hydrostatic reduction of intussusception: proposed mechanism and review of the literature. *J. Pediatr. Surg.* 27, 589–591. doi: 10.1016/0022-3468(92)90454-F

Carroll, A. G., Kavanagh, R. G., Ni Leidhin, C., Cullinan, N. M., Lavelle, L. P., and Malone, D. E. (2017). Comparative effectiveness of imaging modalities for the diagnosis and treatment of intussusception: a critically appraised topic. *Acad. Radiol.* 24, 521–529. doi: 10.1016/j.acra.2017.01.002

Crystal, P., Hertzanu, Y., Farber, B., Shabshin, N., and Barki, Y. (2002). Sonographically guided hydrostatic reduction of intussusception in children. *J. Clin. Ultrasound* 30, 343–348. doi: 10.1002/jcu.10085

Daneman, A., Alton, D. J., Ein, S., Wesson, D., Superina, R., and Thorner, P. (1995). Perforation during attempted intussusception reduction in children–a comparison of perforation with barium and air. *Pediatr. Radiol.* 25, 81–88. doi: 10.1007/bf02010311

Daneman, A., and Navarro, O. (2004). Intussusception. Part 2: an update on the evolution of management. *Pediatr. Radiol.* 34, 97–108; quiz 187. doi: 10.1007/s00247-003-1082-7

Edwards, E. A., Pigg, N., Courtier, J., Zapala, M. A., MacKenzie, J. D., and Phelps, A. (2017). Intussusception: past, present and future. *Pediatr. Radiol.* 47, 1101–1108. doi: 10.1007/s00247-017-3878-x

Eisapour, A., Mehrayin, R., and Esmaeili-Dooki, M. (2015). The effect of midazolam on decreasing the duration of intussusception hydrostatic reduction in children. *Med. Arch.* 69, 289–292. doi: 10.5455/medarh.2015.69.289-292

Flaum, V., Schneider, A., Gomes Ferreira, C., Philippe, P., Sebastia Sancho, C., Becmeur, F., et al. (2016). Twenty years' experience for reduction of ileocolic intussusceptions by saline enema under sonography control. *J. Pediatr. Surg.* 51, 179–182. doi: 10.1016/j.jpedsurg.2015.09.022

Franken, E. A., Smith, W. L., Chernish, S. M., Campbell, J. B., Fletcher, B. D., and Goldman, H. S. (1983). The use of glucagon in hydrostatic reduction of intussusception: a double-blind study of 30 patients. *Radiology* 146, 687–689. doi: 10.1148/radiology.146.3.6828682

Gluckman, S., Karpelowsky, J., Webster, A. C., and McGee, R. G. (2017). Management for intussusception in children. *Cochrane Database Syst. Rev.* 6:CD006476. doi: 10.1002/14651858.CD006476.pub3

Gondek, A. S., Riaza, L., Cuadras, D., Castellarnau, X. T., and Krauel, L. (2018). Ileocolic intussusception: predicting the probability of success of ultrasound guided saline enema from clinical and sonographic data. *J. Pediatr. Surg.* 53, 599–604. doi: 10.1016/j.jpedsurg.2017.10.050

Grahl, K. O. (1983). Experiences with hydrostatic reposition of juvenile intestinal invagination–improvement of results with atropine premedication. *Radiol. Diagn.* 24, 619–626.

Grasso, S. N., Katz, M. E., Presberg, H. J., and Croitoru, D. P. (1994). Transabdominal manually assisted reduction of pediatric intussusception: reappraisal of this historical technique. *Radiology* 191, 777–779. doi: 10.1148/radiology.191.3.8184063

He, N., Zhang, S., Ye, X., Zhu, X., Zhao, Z., and Sui, X. (2014). Risk factors associated with failed sonographically guided saline hydrostatic intussusception reduction in children. *J. Ultrasound Med.* 33, 1669–1675. doi: 10.7863/ultra.33.9.1669

Hryhorczuk, A. L., and Strouse, P. J. (2009). Validation of US as a first-line diagnostic test for assessment of pediatric ileocolic intussusception. *Pediatr. Radiol.* 39, 1075–1079. doi: 10.1007/s00247-009-1353-z

Ito, Y., Kusakawa, I., Murata, Y., Ukiyama, E., Kawase, H., Kamagata, S., et al. (2012). Japanese guidelines for the management of intussusception in children, 2011. *Pediatr. Int.* 54, 948–958. doi: 10.1111/j.1442-200X.2012.03622-1.x

Kanglie, M. M. N. P., de, Graaf N, Beije, F., Brouwers, E. M. J., Theuns-Valks, S. D. M., Jansen, F. H., et al. (2018). The incidence of negative intraoperative findings after unsuccessful hydrostatic reduction of ileocolic intussusception in children: a retrospective analysis. *J. Pediatr. Surg.* doi: 10.1016/j.jpedsurg.2018.05.006 [Epub ahead of print].

Kim, Y. G., Choi, B. I., Yeon, K. M., and Kim, C. W. (1982). Diagnosis and treatment of childhood intussusception using real-time ultrasonography and saline enema: preliminary report. *J. Korean Soc. Med. Ultrasound* 1, 66–70.

Ko, H. S., Schenk, J. P., Tröger, J., and Rohrschneider, W. K. (2007). Current radiological management of intussusception in children. *Eur. Radiol.* 17, 2411–2421. doi: 10.1007/s00330-007-0589-y

Koh, C. C., Sheu, J. C., Wang, N. L., Lee, H. C., Chang, P. Y., and Yeh, M. L. (2006). Recurrent ileocolic intussusception after different surgical procedures in children. *Pediatr. Surg. Int.* 22, 725–728. doi: 10.1007/s00383-006-1748-y

Lehnert, T., Sorge, I., Till, H., and Rolle, U. (2009). Intussusception in children-clinical presentation, diagnosis and management. *Int. J. Colorectal. Dis.* 24, 1187–1192. doi: 10.1007/s00384-009-0730-2

Mc, D. K., and Rosenfeld, D. K. (2000). A reply. *Clin. Radiol.* 55:895. doi: 10.1053/crad.2000.0424

Navarro, O., Dugougeat, F., Kornecki, A., Shuckett, B., Alton, D. J., and Daneman, A. (2000). The impact of imaging in the management of intussusception owing to pathologic lead points in children. A review of 43 cases. *Pediatr. Radiol.* 30, 594–603. doi: 10.1007/s002470000261

Schmit, P., Rohrschneider, W. K., and Christmann, D. (1999). Intestinal intussusception survey about diagnostic and nonsurgical therapeutic procedures. *Pediatr. Radiol.* 29, 752–761. doi: 10.1007/s002470050689

Shehata, S., Ei Kholi, N., Sultan, A., and El Sahwi, E. (2000). Hydrostatic reduction of intussusception: barium, air, or saline? *Pediatr. Surg. Int.* 16, 380–382. doi: 10.1007/s003830000388

Skucas, J. (1994). The use of antispasmodic drugs during barium enemas. *Am. J. Roentgenol.* 162, 1323–1325. doi: 10.2214/ajr.162.6.8191992

Territo, H. M., Wrotniak, B. H., Qiao, H., and Lillis, K. (2014). Clinical signs and symptoms associated with intussusception in young children undergoing ultrasound in the emergency room. *Pediatr. Emerg. Care* 30, 718–722. doi: 10.1097/PEC.0000000000000246

van de Bunt, J. A., Veldhoen, E. S., Nievelstein, R. A. J., Hulsker, C. C. C., Schouten, A. N. J., and van Herwaarden, M. Y. A. (2017). Effects of esketamine sedation compared to morphine analgesia on hydrostatic reduction of intussusception: a case-cohort comparison study. *Paediatr. Anaesth.* 27, 1091–1097. doi: 10.1111/pan.13226

Wetherell, J., Price, M., Mumford, H., Armstrong, S., and Scott, L. (2007). Development of next generation medical countermeasures to nerve agent poisoning. *Toxicology* 233, 120–127. doi: 10.1016/j.tox.2006.07.028

Conflict of Interest Statement: The authors declare that the research was conducted in the absence of any commercial or financial relationships that could be construed as a potential conflict of interest.

frontiers in Pharmacology

CORRECTION
published: 02 August 2019
doi: 10.3389/fphar.2019.00862

Corrigendum: Atropine Premedication Facilitates Ultrasound-Guided Reduction by Saline Enema in Children With Intussusception

Xiao Liu[1,2], Bei Xia[1], Hong-kui Yu[1], Lie-zhen Hu[1], Shu-min Fan[1], Dong Xiao[1], Li-xian Gu[1], Jia-kun Chen[1], Zhi-bo Wen[2] and Xiao-peng Ma[1]**

[1] Shenzhen Children's Hospital, Shenzhen, China, [2] Zhujiang Hospital, Southern Medical University, Guangzhou, China

Keywords: intussusception, atropine, enema, ultrasound, children

A Corrigendum on

Atropine Premedication Facilitates Ultrasound-Guided Reduction by Saline Enema in Children With Intussusception

By Liu X, Xia B, Yu H-k, Hu L-z, Fan S-m, Xiao D, Gu L-x, Chen J-k, Wen Z-b, and Ma X-p (2019). Front. Pharmacol. 10:43. doi: 10.3389/fphar.2019.00043

Xiao-peng Ma, Bei Xia, Lie-zhen Hu, Shu-min Fan and Dong Xiao were not included as authors in the published article. The corrected Author Contributions statement and Acknowledgments appear below. The authors apologize for this error and state that this does not change the scientific conclusions of the article in any way. The original article has been updated.

AUTHOR CONTRIBUTIONS

XL wrote the paper and conceived and conducted the study. BX designed and improved the procedure of the technique and ensured its quality and safety as the ultrasonography department lead. H-kY wrote the paper and carried out the analysis. L-zH and S-mF implemented quality control of the procedure. DX provided valuable support in the therapeutic process. L-xG and J-kC contributed to data collection and management. Z-bW contributed to the discussion, supervised, and reviewed the text. X-pM promoted the clinical application of the technique. All authors read and approved the manuscript.

ACKNOWLEDGMENTS

The authors would like to thank Dr Xue-bing Liang (Emergency department, Eastern Health & Intensive Care Unit, Epworth Richmond, Melbourne) for her contribution to the English grammar of this article.

OPEN ACCESS

Approved by:
Frontiers Editorial Office, Frontiers Media SA, Switzerland

***Correspondence:**
Xiao-peng Ma
maxiaopeng@126.com
Zhi-bo Wen
zhibowen@163.com

Specialty section:
This article was submitted to Translational Pharmacology, a section of the journal Frontiers in Pharmacology

Received: *20 June 2019*
Accepted: *08 July 2019*
Published: *02 August 2019*

Citation:
Liu X, Xia B, Yu H-k, Hu L-z, Fan S-m, Xiao D, Gu L-x, Chen J-k, Wen Z-b, and Ma X-p (2019) Corrigendum: Atropine Premedication Facilitates Ultrasound-Guided Reduction by Saline Enema in Children With Intussusception. Front. Pharmacol. 10:862. doi: 10.3389/fphar.2019.00862

frontiers in Pharmacology

REVIEW
published: 07 February 2019
doi: 10.3389/fphar.2019.00086

Theranostic Strategy of Focused Ultrasound Induced Blood-Brain Barrier Opening for CNS Disease Treatment

Ko-Ting Chen[1,2], *Kuo-Chen Wei*[2] *and Hao-Li Liu*[1,2,3]*

[1] *Ph.D. Program in Biomedical Engineering, Chang Gung University, Taoyuan, Taiwan,* [2] *Department of Neurosurgery, Chang Gung Memorial Hospital at Linkou, Taoyuan, Taiwan,* [3] *Department of Electrical Engineering, Chang-Gung University, Taoyuan, Taiwan*

Focused Ultrasound (FUS) in combination with gaseous microbubbles has emerged as a potential new means of effective drug delivery to the brain. Recent research has shown that, under burst-type energy exposure with the presence of microbubbles, this modality can transiently permeate the blood-brain barrier (BBB). The bioavailability of therapeutic agents is site-specifically augmented only in the zone where the FUS energy is targeted. The non-invasiveness of this approach makes FUS-induced BBB opening a novel and attractive means to perform localized CNS therapeutic agent delivery. Over the past decade, FUS-BBB opening has been preclinically confirmed to successfully enhance CNS penetration of therapeutic agents including chemotherapeutic agents, therapeutic peptides, monoclonal antibodies, and nanoparticles. Recently, a number of clinical human trials have begun to explore clinical utility. This review article, explores this technology through its physical mechanisms, summarizes the existing preclinical findings (including current medical device designs and technical approaches), and summarizes current ongoing clinical trials.

Keywords: focused ultrasound, blood-brain barrier, brain drug delivery, brain tumor, Alzheimer's disease

OPEN ACCESS

Edited by:
Fei Yan,
Shenzhen Institutes of Advanced Technology (CAS), China

Reviewed by:
Ai-Ho Liao,
National Taiwan University of Science and Technology, Taiwan
Feng Wang,
Xinxiang Medical University, China

***Correspondence:**
Hao-Li Liu
haoliliu@mail.cgu.edu.tw

Specialty section:
This article was submitted to Translational Pharmacology, a section of the journal Frontiers in Pharmacology

Received: *09 December 2018*
Accepted: *21 January 2019*
Published: *07 February 2019*

Citation:
Chen K-T, Wei K-C and Liu H-L (2019) Theranostic Strategy of Focused Ultrasound Induced Blood-Brain Barrier Opening for CNS Disease Treatment. Front. Pharmacol. 10:86. doi: 10.3389/fphar.2019.00086

MECHANISM

The Blood-Brain Barrier (BBB)

The blood-brain barrier (BBB) is the major part of the brain's neurovascular unit (NVU) and serves as a key homeostatic site for the central nervous system (CNS), maintaining both structural, and functional brain connectivity (Zhao et al., 2015). The BBB is composed of specialized highly polarized endothelial cells, pericytes, and astrocytic processes and develops through a multi-step process starting in the neuro-ectoderm with angiogenesis followed by endothelium growth (Zhao et al., 2015; Maiuolo et al., 2018; Warren, 2018). The capillary endothelium composes of the majority of the BBB surface area (>85%) and numerous transport systems facilitate or actively shuttle molecules across the BBB (Sweeney et al., 2018). Dysfunction of BBB permeability and transporters lead to various kinds of neurological disorders, including stroke, Alzheimer's, Huntington's, Parkinson's, amyotrophic lateral sclerosis, multiple sclerosis, various types of infectious disease and even neoplasms, which may alter the regional or even global cerebral microenvironment (Schoknecht et al., 2015; Nelson et al., 2016; Maiuolo et al., 2018; Sweeney et al., 2018). Therapeutic targets have been proposed to treat a broad spectrum of disease, but must first cross the BBB for effective drug delivery or to increase waste elimination (e.g., amyloid β) (Nelson et al., 2016; Sweeney et al., 2018).

Various Approach to Overcome BBB

Many drug molecules and therapeutics cannot naturally permeate the BBB into the brain parenchyma, presenting a serious challenge to treating brain disorders. Several methods of penetrating the BBB can be categorized as physical or non-physical. In physical delivery methods, an opening of tight junctions between endothelial cell barriers provides paths by which molecules can diffuse passively into the brain parenchyma. Osmotic agents, offering globally transient disruption of the BBB via osmotic shrinkage of endothelial cells and through creating an osmotic pressure gradient across the BBB, are widely used for drug delivery for brain tumor patients (Rodriguez et al., 2015). Concurrent intra-arterial administration of osmotic and chemotherapeutic agents has raised patient survival from 11.4 to 17.5 months (Gumerlock et al., 1992). Nevertheless, due to its systemic effect rather than localized BBB alterations, complications such as neurological deficits, seizures and potential tumor migration have been reported (Gumerlock et al., 1992). On the other hand, invasive procedures such as direct injection can specifically target the brain compartment and cells of interest, removing the loss of first pass clearance and off-target toxicity (Duskey et al., 2017). Chemotherapeutic agents can be delivered interstitially by local injection or drug-carrying biodegradable matrices can be directly implanted into the debulked tumor cavity (Westphal et al., 2003). Convection-enhanced delivery (CED) interstitially infuses drugs under a constant pressure gradient, producing bulk interstitial fluid flow through the brain following the opening of the skull (Ferguson et al., 2007). Animal models show CED achieves greater localized penetration of chemotherapy drugs than intravenous administration, but the local distribution is dependent on the volume and rate of the gradient of infusion, along with the drug's concentration, polarity and molecular weight. Low infusion rates and volumes can result in highly inconsistent distribution and tumor interstitial fluid pressure, resulting in rapid efflux of drugs from the injection site. In addition, the insertion of objects into the brain is inherently invasive, and can increase the likelihood of infection or damage.

In non-physical delivery, drug molecules and therapeutics are systemically delivered to the luminal side of the BBB. The design of such approaches must consider several hurdles including first pass clearance, blood instability, immune response, and off-target effects (Chen et al., 2010; Upadhyay, 2014; Duskey et al., 2017). Viral- or nanopartical-based modification of therapeutics seek to penetrate the BBB through active or passive crossing non-specific or receptor-mediated uptake (Duskey et al., 2017). A more effective solution may involve combining both physical and non-physical methods, such as combining physical methods with nanoparticles or advanced bioconjugate technologies to enhance the delivery while simultaneously stabilizing proteins or enzymes as necessary (Duskey et al., 2017).

FUS-Induced BBB Opening Concepts

The BBB blocks nearly 98% of drug compounds from accessing the CNS, and the use of focused ultrasound raises the potential for developing a drug delivery platform (Pardridge, 2005). The permeability of the BBB can be transiently increased using low-energy burst-tone focused ultrasound following an administration of intravenous microbubbles (Hynynen et al., 2001, 2003; Park et al., 2012; Chai et al., 2014). A physical cavitation effect is created from circulating microbubbles, significantly reducing the ultrasound pressure to produce an equivalent acoustic cavitation effect (concepts see **Figure 1**). The subsequent application of ultrasonic energy can achieve a local detachment of tightly sealed junctions on the capillary wall without inducing neuronal damage (Hynynen et al., 2005). Due to its spherically concaved transducer design, ultrasonic energy focused at the geometrical center can be sharply cascaded, allowing ultrasonic energy to be tightly deposited deeply within the brain tissue while minimizing skull energy absorption (Clement et al., 2000). Since the BBB blocks nearly 98% of drugs from accessing the CNS, the use of focused ultrasound raises a potential therapeutic delivery platform to the CNS (Pardridge, 2005).

Focused ultrasound could focally and transiently open the BBB to introduce drugs via a physical delivery, which has several advantages. Compared with alternative routes, such as using osmotic agents or modified lipophilic chemicals via intravascular infusion, FUS can locally increase BBB permeability (Doolittle et al., 2000; Pardridge, 2002). Compared with other physical approach like CED, FUS is a less invasive method. While non-physical delivery methods use a different mechanism, which depends on cellular non-specific or receptor uptake, to overcome BBB, FUS holds abovementioned advantages and provides high flexibility in combing with various CNS treatment modalities (Hsu et al., 2013; Fan et al., 2016).

PRECLINICAL TECHNICAL VALIDATION

Biophysical Observation Caused by FUS-BBB Opening

Several tight junction integrated adhesion molecules, including claudin-1, claudin-5, and ZO-1, can be transiently regulated by FUS (Sheikov et al., 2006, 2008). Glial fibrillary acidic protein staining confirms that FUS-BBB opening triggers the activation of microglia and astrocytes (Alonso et al., 2011). It has been reported that ultrasound can temporarily suppress P-glycoprotein expression, the most dominant multi-drug resistant protein found in the BBB, for days even after BBB closure (Cho et al., 2016). FUS-BBB opening may trigger acute transcriptional changes, particularly a transient inflammatory response in microvessels, but the increased transcription of proinflammatory cytokine genes appears to quickly return to the baseline (Kovacs et al., 2017; McMahon et al., 2017).

Modality to Identify BBB Opening

Numerous tools have been developed to identify BBB opening (see **Figure 2**). Direct microscopic observations of BBB-opened phenomena have been made at the cellular scale. An *in-vivo* imaging approach was designed to monitor the pharmacodynamic behavior of BBB-opening. By providing an indicator of diethylenetriamine penta-acetic acid (Gd-DTPA; molecular size about 1 kDa), dynamic contrast enhanced magnetic resonance imaging (DCE-MRI) can be used to monitor the kinetic behavior of the T1-weithed MRI contrast agent, thus

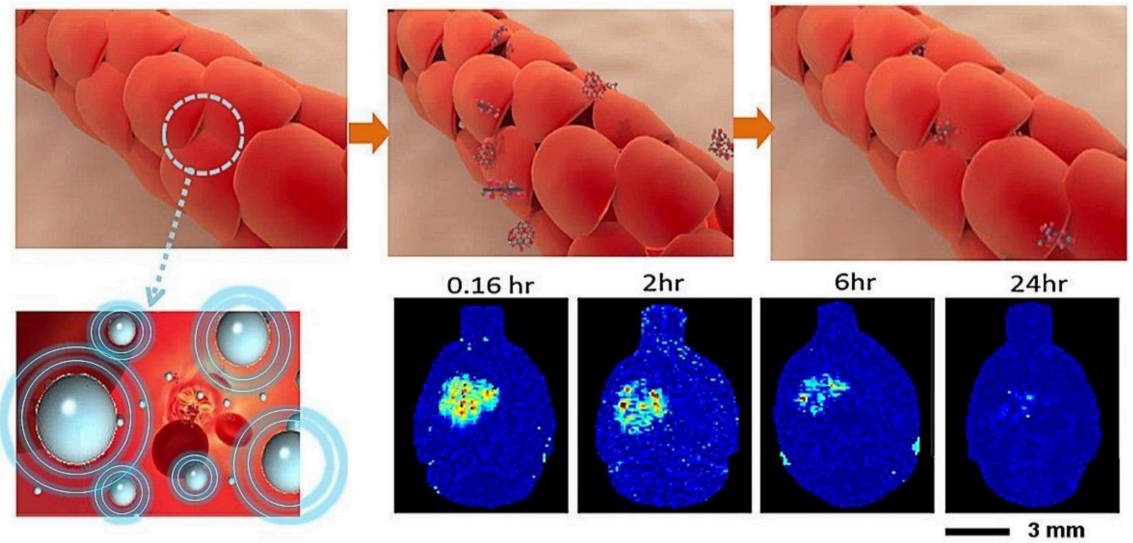

FIGURE 1 | BBB opening concepts: interaction of microbubbles and focused ultrasound transiently disrupts the tight junction of the capillary lumen to allow therapeutic agents to penetrate into the brain. The BBB return to normal a few hours following focused ultrasound exposure (Chai et al., 2014).

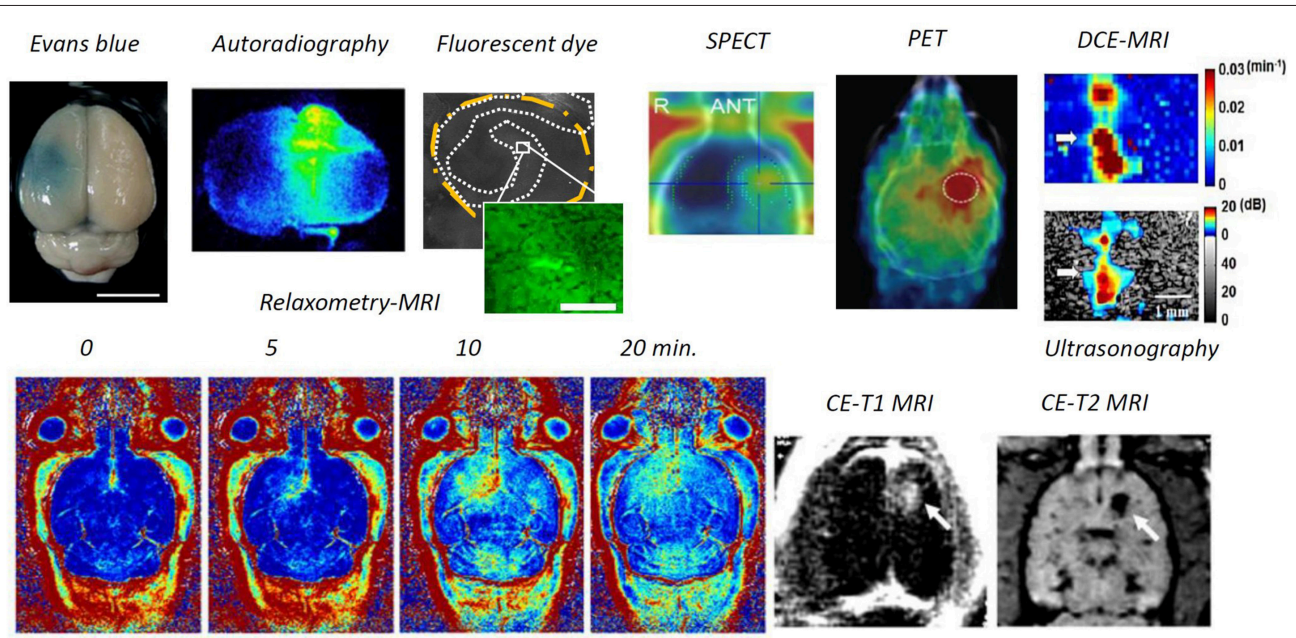

FIGURE 2 | Modalities to identify BBB opening. Through *ex-vivo* examination, Evans blue dye can directly depict the BBB-opened region from gross section, or fluorescent dextran or the radioactivity readout through autoradiography from the brain gross section can be used to identify the BBB-opened region. Previous attempts have included *in-vivo* examination, ultrasonography via microbubble dynamic characterization, SPECT/ PET via radiotracer, contrast-enhanced MRI either via Gd-DTPA or MNPs), and dynamic contrast-enhanced MRI via Gd-DTPA (Lin et al., 2009; Liu et al., 2009, 2010a, 2016; Chai et al., 2014; Fan et al., 2014; Xia et al., 2016; Wu et al., 2017).

the transient BBB opening is estimated to have a half-life of 2–5 h based on the acoustic pressure level (Park et al., 2012; Chai et al., 2014). Compare with quantification through a surrogate molecule (Evans blue), a strong association was found between kinetic behavior and the 70-kDa surrogate, thus imaging contrast agents could be used as a molecule-delivered surrogate (Chai et al., 2014).

In addition to contrast-enhanced T1-weighted MRI, various other imaging tracers have been delivered across the BBB, including horseradish peroxidase (Hynynen et al., 2005),

lanthanum chloride (Sheikov et al., 2008), and ionic manganese (Howles et al., 2010) from immunohistochemistry based microscopy; Alexa Fluor 488 (Raymond et al., 2007), Texas-Red-tagged dextran (Choi et al., 2010) and GFP-tagged dextran (Liu et al., 2016) from fluorescent microscopy; 99 mTc diethylenetriamine pentaacetate and 68-Ga-surrogate compound through nuclear imaging SPECT/ PET (Lin et al., 2009; Liu et al., 2016); superparamagnetic iron oxide (SPIO, 60 nm) through T2-weighted MRI (Liu et al., 2009); and gold nanorods through photoacoustic imaging (Wang et al., 2012).

Physical Characterization

BBB Opening Associated With Acoustic Cavitation

Inertial and stable microbubble-present acoustic cavitation can be characterized from distinct backscattered acoustic emissions (McDannold et al., 2006). Acoustic cavitation is a physical effect produced by gas-filled bubbles after exposure to certain ultrasound frequencies, causing harmonic microbubble compression and expansion (Crum et al., 1992; Stride and Saffari, 2003). Acoustic cavitation contributes to BBB-opening through stable or inertial cavitation. Stable cavitation directly contributes to tight junctional disruption (McDannold et al., 2006), while inertial caviation can result in additional erythrocyte extravasations (Liu et al., 2008).

In stable cavitation, ultrasound stimulation causes repetitive microbubble volumetric oscillation. The expansion of the microbubbles separates the endothelial cell lining, and contraction causes invagination of the vascular lining. This push-pull action broadens tight junctions in the BBB (Caskey et al., 2007). Rapid oscillation of microbubbles also results in consistent microstreaming, which can stimulate the capillary endothelium, thus increasing shear stress on cells, damaging the endothelial lining and enhancing internal cell permeability (Sboros, 2008). Excessive ultrasound energy results in the sudden collapse of microbubbles (i.e., inertial cavitation), producing strong mechanical stress, microstreaming, and micro-jets in the surrounding media (Husseini et al., 2005), inducing cellular membrane perforation and large-scale blood-tissue permeation (Mitragotri, 2005), along with erythrocyte extravasations or micro-hemorrhages (Hynynen et al., 2005; Liu et al., 2008). Inertial cavitation is characterized by a wideband emission causing microbubble collapse and disruption, and a stable cavitation is characterized by subharmonic/ultraharmonic emissions which produce a stable contraction and expansion of microbubbles (Bader and Holland, 2013; Jin et al., 2016).

Clinical applications of FUS-BBB opening require the development of indices to assess the likelihood of such opening occurring, to allow for the assessment and estiation of CNS therapeutic molecule delivery. Passive cavitation dose (PCD) analysis is applied to microbubble activity to detect and characterize backscattered acoustic emissions. FUS-induced BBB opening is both associated with inertial cavitation and likely caused by stable cavitation (O'Reilly and Hynynen, 2012; Chen and Konofagou, 2014; Marquet et al., 2014; Sun et al., 2015). A mechanical index (MI) is defined as the peak negative acoustic pressure over the square root of the frequency (i.e., $MI = P/\sqrt{f}$, P in MPa, f in MHz) and is used to assess ultrasound-induced mechanical bio-effects (Apfel and Holland, 1991). McDannold et al. identified a strong association between the degree of FUS-induced BBB opening and MI using signal intensity (SI) change to contrast-enhanced magnetic resonance imaging (CE-MRI), identifying a threshold which serves as an indicator for BBB opening (McDannold et al., 2006). Despite reports of this correlation, the level of MI is usually seen as a reflection of the extent of inertial cavitation (Apfel and Holland, 1991). The cavitation index (CI) also serves as an indicator of stable microbubble-ultrasound cavitation. Bader et al. used the CI, defined as peak negative acoustic pressure (in MPa) over frequency (in MHz); i.e., $CI = P/f$, to assess the chance of subharmonic emissions being caused by stable microbubble-presented cavitation activity (Bader and Holland, 2013), which is highly associated with the extent of BBB opening (McDannold et al., 2007). We recently used dynamic contrast-enhanced (DCE)-MRI and PCD analysis to assess the feasibility of gauging the extent of FUS-induced BBB opening using MI and CI,. DCE-MRI was found to evaluate pharmacodynamics/pharmacokinetic BBB-opening dynamics, and was strongly associated with both with MI and CI, implying the feasibility in using these two indices to gauge the scale of FUS-induced BBB opening (Chu et al., 2016).

Inference of Ultrasound Exposure on BBB Opening

Several preclinical studies have used a range of FUS parameters for FUS-induced BBB opening, including exposure frequency, acoustic pressure, burst length, pulse-repetition frequency, and duration (Hynynen et al., 2005; McDannold et al., 2008; O'Reilly et al., 2011). The acoustic pressure of sonication (i.e., different types of cavitation) can modulate the leakage kinetics of fluorescent dye in the cerebral vasculature, and can be used to characterize leakage as fast or slow (Cho et al., 2011; Nhan et al., 2013). During high-pressure exposure, the oscillating microbubbles cause a direct and immediate broadening of tight junctions and pores on the cell membrane, but low-pressure exposure causes microbubble oscillation to activate endothelial cell receptors, thus promoting the trans-cellular transport of molecules from the lumen side to the abluminal space (Deng et al., 2012).

Microbubble

Microbubbles (MB) assume an important part in the FUS-induced BBB opening effect. Currently, commercialized MBs include Optison (GE Healthcare, WI, USA), Definity® (Lantheus Medical Imaging, MA, USA), and SonoVue® (Bracco, Milano, Italy). All have received FDA approval for diagnostic use and have been used for FUS-induced BBB opening. Commercial MBs generally exceed 2 μm in diameter and have an application window of 5–10 min. Each, however have different compositions, concentrations, half-lives, and hydrodynamic sizes, which must be considered in terms of impact on interaction between ultrasound-MBs and capillary permeability. McDannold et al. achieved BBB-opening using similar acoustic pressure thresholds for Optison™ (human serum albumin) and Definity® (lipid) MBs (McDannold et al., 2007), though Optison™ produced a more serious bio-effect, possibly because the lipid shell in Definity® is stronger than the albumin shell in Optison™. We

assessed the impact of BBB opening using three different MBs–SonoVue®, Definity®, and USphere® in combination with FUS. Under identical MB concentrations, all induced similar and equivalent BBB-opening effects (Wu et al., 2017).

In addition to MB type, the concentration of injected MBs produces various numbers of nuclei for cavitation within the vasculature, which can also significantly affect the distribution and degree of BBB opening (McDannold et al., 2008; Yang et al., 2008). An increase of MB volume would increase the mechanical force acting on nearby cells, thus expanding to a size sufficient to stimulate the vessel walls. Previous studies have found that, compared with larger Mbs (4–5 μm and 6–8 μm), MBs with a diameter of 1–2 μm offer significantly less permeability enhancement (Vlachos et al., 2011). Meanwhile, smaller (1–2 μm) MBs have been reported to reduce recovery time following transient BBB opening (Samiotaki et al., 2012). Considering the effect of total MB volume on BBB opening, Song et al. have demonstrated that, to optimize BBB-opening efficiency, size and concentration can be merged into one single parameter, microbubbles gas volume dose (Song et al., 2017). The duration of the BBB-opening effect has been found to depend on the degradation dynamics of each MB type. Wu et al. delivered a large treatment volume through multiple exposures, thus compensating for MB degradation and producing a more durable BBB-opening effect (Wu et al., 2017).

Intraoperative Monitoring and Guidance

Although FUS-BBB opening appears promising, FUS energy must be precisely controlled to avoid adverse effects including massive erythrocyte extravasation (Hynynen et al., 2005; Liu et al., 2008). Indeed, DCE-MRI can indicate BBB-opening by postoperatively detecting contrast medium leakage into the brain parenchyma, a real-time monitoring scheme is required to provide instant intraoperative feedback to assure the safety and effectiveness of FUS energy exposure (Hynynen et al., 2005). To integrate diagnostic ultrasound into the therapeutic transducer to passively receive the backscattered emission waves provides a potential approach for intraoperative beam mapping and monitoring. Passive cavitation detection (PCD), therefore, served as a tool for real-time transcranial monitoring during FUS, and served as an online treatment evaluation complement to the postoperative MRI-based methods (see **Figure 3**) (Wu et al., 2016). The passive image is reconstructed using passive beam formation theory originally developed for seismic source identification (Jensen et al., 2012; Arvanitis et al., 2013). Ultrasound research has recently focused on passive imaging as a way to monitor bubble activity during cavitation-enhanced therapy, thus improving safety and outcome assessments (Lin et al., 2009; Liu et al., 2009, 2016; Choi et al., 2010; Howles et al., 2010). Good synchronization between therapeutic exposure and diagnostic backscattered reception allows for focal beam reconstruction at the sub-MPa level without the use of MBs (Xia et al., 2016; Liu et al., 2018). To improve transcranial detectability, an alternative to a separate transmission/receiving transducer is to match the backscatter reception with the transmission ultrasound frequency. O'Reilly et al. proposed a lateral-mode vibration large-scale hemispherical phased array structure, with a low-density PVDF membrane covering the hemisphere to locate the microbubble activation source (O'Reilly et al., 2014), producing a high-resolution tracking of the MB distribution that can be used for real-time monitoring of the BBB-opening process.

Other researchers have sought to use passive acoustic detection to detect cavitation activity and successfully predict FUS-BBB opening. McDannold et al. used multiple piezoelectric

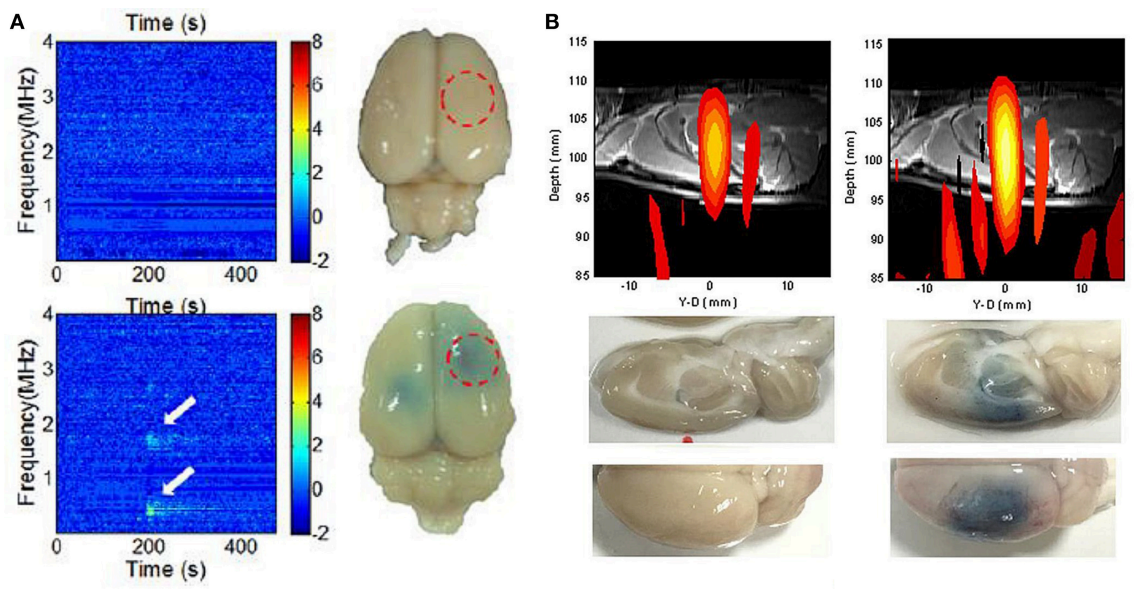

FIGURE 3 | Intraoperative monitoring and guidance of focused ultrasound-induced BBB opening. **(A)** Detection of subharmonic/ ultraharmonic of backscattered spectrum for real-time BBB opening monitoring (Tsai et al., 2016). **(B)** Dual transmit/receive mode ultrasound phase array to intraoperatively reconstruct focal beam for ultrasound energy guidance (Liu et al., 2018).

elements to receive emissions during FUS exposure, and confirmed that FUS-BBB opening can occur without wideband emission (McDannold et al., 2006). They also found good correlation with receiving passive signals, with BBB-opened sites providing increased second and third harmonic signal levels (McDannold et al., 2012). Tung et al. achieved FUS-BBB opening without inertial cavitation, and proposed that a higher order (i.e., fourth or fifth) harmonic level change is associated with FUS-BBB opening (Deng et al., 2012; Nhan et al., 2013). Vykhodtseva et al. detected subharmonic emissions during FUS exposure (Vykhodtseva et al., 1995). O'Reilly and Hynynen detected ultraharmonic components using a wideband polyvinylidene-difluoride (PVDF) receiver as an indicator of BBB-opening detection, and showed high detectability and success rate for BBB-opening (O'Reilly and Hynynen, 2010). Subsequently, more recent attempts have sought to use acoustic emission detection technologies (particularly harmonic and ultraharmonic) for real-time tracking of FUS-BBB opening. Arvanitis et al used a PVDF hydrophone to track changes in the magnitude of an integrated component set (2×, 3×, and 4× harmonics and 1.5× and 2.5× ultraharmonics) to detect FUS-BBB opening (Arvanitis et al., 2012). Sun et al. used passive cavitation activity detection to monitor BBB-opening (Sun et al., 2015). Other research also indicates that subharmonics or ultraharmonics correlate better with BBB opening (O'Reilly and Hynynen, 2010, 2012; Arvanitis et al., 2012). A dual-confocal transducer was also used to improve subharmonic PCD for highly accurate prediction of BBB-opening, raising the potential for application in real-time ultrasound BBB opening control (Tsai et al., 2016).

Brain Tumor Treatment

Clinically Approved Therapeutic Agent Delivery

The BBB shows heterogeneous integrity within tumor tissues, meaning the degree of permeability can vary within a single tumor. The core region of a tumor is usually more permeable than the periphery (Ewing et al., 2006). In gliomas, the integrity of the BBB in peripheral areas has been shown to remain highly functional (Groothuis et al., 1982; Neuwelt et al., 1982). In treating an intrinsic brain tumor, such as a glioma, the intact BBB of the tumor periphery limits drug penetration and treatment success. Effectively enhancing BBB permeability of the tumor periphery represents a potential strategy for improving treatment efficacy and ultimately patient survival.

Enhanced drug delivery via MB-assisted FUS-BBB opening is widely established. Herceptin (150 kDa) and D4 receptor antibodies (150 kDa) have been successfully delivered into mouse brain (Kinoshita et al., 2006). Methotrexate (545 Da) has also been delivered into normal rat brains in the FUS-assisted model at significantly higher concentrations than in control rats (Mei et al., 2009). The earliest attempt for FUS-enhanced drug delivery for glioma treatment used doxorubicin as Doxil® (Ben Venue Laboratories, OH, USA) encapsulated in the form of long-circulating pegylated liposomes (Treat et al., 2007, 2012). Enhanced delivery of boronophenylalanine, with a high thermal neutron capture cross-section for boron neutron-capture therapy (BNCT), has been achieved via MB-FUS BBB opening, indicating that this technique has potential for increasing the treatment efficiency of BNCT (Yang et al., 2012; Alkins et al., 2013). Another drug called BCNU, which has been used for many years as a chemotherapeutic agent for treating glioma patients, was also tested in an MB-FUS-enhanced model. Although BCNU is lipophilic, meaning it has potential to penetrate BBB, its substantial toxicity limits the overall dosage and thus concentrations in tumors (Liu et al., 2010a). We also demonstrated enhanced TMZ delivery by MB-FUS BBB opening. A liquid chromatography–tandem mass spectrometer was used to measure the TMZ levels in both CSF and plasma (Wei et al., 2013a; Liu et al., 2014). Finally, the enhanced delivery of an antiangiogenic monoclonal antibody, bevacizumab, has been shown to significantly retard glioma progression, leading to a markedly increased median survival in animal models (Liu et al., 2016).

Novel Multi-functioned Therapeutic Agent Design for Glioma Treatment

Besides using microbubbles as a catalyst to induce BBB opening, the MB itself has been designed as a carrier of therapeutic drugs. Encapsulating therapeutic agents in or conjugating them with MBs is a more recent approach. Therapeutic agents have been incorporated into in MB carriers by attachment to the outer shell surface, embedding in the shell, dissolving hydrophobic drugs in the oily layer between the gas core and shell, and by linking them to the shell (Unger et al., 2004; Hernot and Klibanov, 2008). Drugs can also be pre-incorporated into carriers such as liposomes, micelles, or microspheres which can be easily attached to lipid MBs, usually via avidin–biotin interactions (Lum et al., 2006). A lipid-shell-based and BCNU-loaded MB could carry drugs, thus protecting the BCNU from rapid degradation, and could also be activated by FUS to simultaneously achieve BBB opening and trigger the local release of BCNU (Ting et al., 2012).

Progress has also been made in the manufacturing of smart MBs equipped with multi-functions. An example is VEGF-ligand conjugated and BCNU encapsulated MBs which was designed to ensure targeted delivery to areas where the tumor vasculature shows signs of angiogenesis, characterized by overexpression of the VEGF-R2 receptor (Fan et al., 2013b). A DOX-loaded and SPIO-nanoparticle conjugated phospholipid-based MB structure (DOX-SPIO-MB) simultaneously produced BBB opening and drug delivery, while also serving as a dual contrast agent in both ultrasound and MR imaging to confirm drug quantification and deposition (Fan et al., 2013a). In addition, applying an external magnetic force to magnetic nanoparticles offers the possibility of active magnetic targeting (MT) of particular brain regions. We had previously used FUS-BBB disruption to improve the delivery of magnetic nanoparticles (MNPs) into the brains of small animals (Chen et al., 2010; Liu et al., 2010b). Using external magnetic targeting, highly magnetized MNPs followed a time-dependent deposition pattern in the sonicated brain, with concentrations increased up to 20-fold compared with the contralateral brain.

CNS Gene Delivery

Gene Delivery Into CNS Using FUS-BBB Opening

Gene therapy has the benefit of long-term expression of a therapeutic protein with limited distribution and may potentially provide a better solution for neurodegenerative diseases.

Attempts have been recently made to use focused ultrasound for gene delivery either through viral- or non-viral-type vectors for gene transport.

Viral-Vector Gene Delivery

Adeno-associated virus (AAV) is widely used to express and secrete encoded human genes through genetically engineered modification. AAV vectors for the treatment of CNS diseases rely on localized, direct injection into the brain (Ridet et al., 2000; Miranpuri et al., 2012), but the region of recombinant gene expression is highly restricted by the blood-brain barrier (BBB).

Thevenot et al. applied focused-ultrasound exposure with a self-complementary adeno-associated virus serotypes 9 (scAAV-9) carrying a green fluorescent protein (GFP) gene in mice brains (Thevenot et al., 2012). Hsu et al. used GFP-encoded recombinant adeno-associated virus serotype 2 (rAAV-2) as the viral vector; fluorescent microscopic quantitative analysis indicated a high degree of GFP expression in the ultrasound exposure areas (Hsu et al., 2013). Additional comparison with a direct local virus injection showed the expression level of GFP fluorescence via focused ultrasound was almost equivalent to that of direct gene injection (Hsu et al., 2013). Wang et al. also compared transfection efficiency with reporter genes encoded in rAAV-1 and rAAV-2 and combined with ultrasound facilitated BBB opening (Wang et al., 2015).

Non-viral-vector Gene Delivery for PD Treatment

Viral-vector based ultrasound-facilitated CNS gene delivery has shown potential for promoting long-term endogenous expression of neurotrophic factors in the brain. It can also significantly enhance the length of the effective therapeutic periodic window. However, viral-vectors change the administration route from local injection to intravenous systemic circulation, which could result in systemic immunogenicity (Yoon et al., 2014).

Naked plasmid DNA delivery without using viral vectors has been attempted. Rather than microbubbles, Negishi et al. developed a nanobubble system (using nanobubbles about 200 nanometers (nm) in diameter) that successfully induced BBB-opening (Negishi et al., 2015). We offered a similar strategy to evaluate naked plasmid DNA delivery and gene expression via ultrasound-facilitated BBB opening (Fan et al., 2016). The results suggest successful plasmid delivery and gene expression, but the expression level did not outperform the traditional direct viral-gene vector injection approach. On the other hand, liposome as a vector can be used to encapsulate plasmid DNA to protect the plasmid from being degraded and neutralized during circulation. Unlike a viral-vector which delays expression by at least 7 days post sonication, a non-viral gene approach showed a delay expression about 48 h after sonication (Fan et al., 2016).

Parkinson's disease (PD) is a progressive neurodegenerative disease result from loss of dopaminergic neurons in the substantia nigra pars compacta. Currently, the most commonly used therapeutic strategy for PD, a systemic dopamine replacement therapy, can only improve the clinical motor symptoms for various period of time (Shao and Le, 2019). We previously demonstrated the feasibility of synthesizing liposome-based gene vectors for CNS gene delivery to treat neurodegenerative disease on PD animal models (Lin et al., 2015, 2016). A recovery of dopamine and their key metabolite levels as well as a recovery of motor symptoms in PD animals indicated the promise of the liposome-MB system as a vector to facilitate gene delivery in the CNS. We also developed a novel cationic MB system for plasmid DNA loading. Due to the positive charge of the cationic MB surface, the negatively-charged plasmid can easily be conjugated on the lipid surface with high DNA payload yields via charge interaction (Fan et al., 2016).

BBB Opening for AD Treatment

Focal CNS diseases with unsatisfied treatment results exhibit apparent therapeutic targets to be aimed at, such as malignant glioma and PD. However, the scenario is different in treating a diffuse CNS disease. Alzheimer's disease (AD) is a diffuse neurodegenerative disease result from the abnormal accumulation of amyloid beta (Aβ) plaques and is the most common cause of age-related dementia (Madav et al., 2019). Several therapeutic agents including monoclonal antibodies (mAbs), stem cells and genes are under development and in clinical trials, but a BBB-penetrating issue has limited the therapeutic effect of these large molecular agents. In contrast to focally enhanced drug or gene delivery by FUS system, two hurdles including a diffuse deposition of Aβ plaques and currently no effective drugs targeting on the root cause of AD limit the therapeutic potential on AD using FUS-BBB system. However, FUS-BBB opening has not only physical effects of loosening the cellular tight junctions but also of inducing neuromodulation and immunogenic responses (see section BBB opening for CNS immune-modulation). The multidirectional responses from different components (i.e., microglial activation) of the therapeutic area offer an opportunity to change the microenvironment and immunogenicity, which might be beneficial for disease control (Leinenga and Gotz, 2015).

Burgess et al. attempted to open the BBB at the bilateral hippocampus (with a total of 3 exposures at 7 day intervals) (Burgess et al., 2014). Aβ plaques were observed by 3 months in the animal model (TgCRND8) and a near 20% plaque reduction was observed. Behavioral tests also showed that memory function and cognitive performance can be significantly restored in AD animal models (Burgess et al., 2014). Leinenga et al. conducted a more frequent exposure in the whole animal brain (with a total of 7 daily exposures). In their results, the amyloid plaque was reduced by up to 75% with a clear improvement in behavioral tests (Leinenga and Gotz, 2015). Two potential mechanisms have been proposed for FUS-mediated plaque reduction in the AD model. First, FUS-induced BBB opening delivered the endogenous IgG and IgM from the periphery into the brain, contributing to plaque clearance. Second, mild immune responses are induced by FUS and microglia was activated to internalize amyloid, contributing to plaque reduction (Jordao et al., 2013; Leinenga and Gotz, 2015).

We sought to determine if the use of FUS exposure to enhance GSK-3 inhibitor (AR-A014418) delivery can trigger

the down regulation of Aβ synthesis and overexpression (Hsu et al., 2018). Microglia/immunogenic activation caused by FUS-BBB opening alone has been shown to be useful in removing existing plaque, thus adding GSK-3 inhibitor to decrease plaque synthesis presents a supplementary strategy to further reduce plaque deposition. An IHC examination showed GSK-3 inhibitor effectively reduced GSK-3 activity by up to 61.3%. FUS-induced BBB opening combined with GSK-3 inhibitor delivery had an additive effect on plaque reduction efficiency (39.6%, compared to 15.1% with FUS-BBB opening alone and 22.6% with GSK-3 inhibitor administration alone) (Hsu et al., 2018).

BBB Opening for CNS Immune-Modulation

Focused ultrasound pulsation with microbubbles has been shown to trigger local immune response for tumor suppression (Liu et al., 2012). The discovery of the meningeal lymphatic system within the CNS helps explain the therapeutic role of systemic immune cells in various brain disorders. FUS-BBB opening could enhance delivery of immune-stimulating agents such as interleukin-12 (IL-12) (Chen et al., 2015a) or immune check point inhibitors such as anti-cytotoxic T-lymphocyte-associated antigen 4 (CTLA-4) monoclonal antibodies (mAb) to affect the tumor immunosuppressive microenvironment (Curley et al., 2017). Aside from delivering therapeutic agents to the brain, the procedure itself may exert some immune-related effects. For innate immune response, concentrations of several proinflammatory cytokines and heat shock proteins have been found to be transiently increased within 24 h following FUS exposure. FUS was also found to activate microglia, astrocytes, macrophages, and NK cells, and to enhance the infiltration capabilities of dendritic cells (DCs) as well as other antigen presenting cells in the treated tumor (Cohen-Inbar et al., 2016). For adaptive immunity, MB-assisted pulsed FUS stimulation was found to enrich cytotoxic T lymphocyte (CTL) infiltration, increase the CTL-to-regulatory T cell ratio and retard tumor growth in a murine model (Chen et al., 2015b). FUS-induced BBB opening results in CNS immune modulation in the following ways. First, it increases local BBB permeability to allow penetration of circulating mAbs or cytokines for immune-regulation. It also recruits or adjusts desirable immune cells to infiltrate and target the lesion. Finally, it activates neuroglial cells and other innate cells to create microenvironment conditions unfavorable to the disease. These three mechanisms suggest future applications for FUS-induced BBB opening for neuro-immune modulation and immunotherapy.

CLINICAL PROOF-OF-CONCEPT TESTING

Focused Ultrasound Device Design for Clinical Use

Recent advances in ultrasound-induced BBB opening techniques have led to the development of translational work on human patients. A recent study demonstrated the safety of an MRI-guided FUS platform for BBB opening in patients with brain tumors and AD (Dasgupta et al., 2016; Lipsman et al., 2018). Once the target has been confirmed to preoperatively assist procedure guidance, the focal energy deposition can be identified through a slight temperature rise due to weak FUS energy exposure, but exact occurrence of BBB opening can only be confirmed postoperatively via contrast-enhanced MRI via Gd-DTPA.

In addition, a planar implantable ultrasound device has also been developed using a surgical burr hole as an insertion point for an ultrasound disk to sonicate brain regions without the need for additional guidance procedures (SonoCloud®, CarThera) (Carpentier et al., 2016).

Neuronavigation systems have also been designed to guide FUS for precise BBB opening (Wei et al., 2013b; Wu et al., 2018). Preoperative diagnostic scans (CT or MRI) are first analyzed, followed by a registration process that allows for the 3D localization of the surgical tools to assist neurosurgeons in mapping the safest, least invasive path to the target site. Neuronavigation-guided FUS brain drug delivery has been shown to be feasible, with precision comparable to neurosurgical stereotactic procedures (Wei et al., 2013a; Wu et al., 2018).

Brain Tumor Trial

The major hurdle to treating brain tumors is the delivery of drugs including chemotherapeutic and targeted therapy agents. One currently emerging concept focuses on turning the immune-suppressive environment, or "cold tumor," into an immune-activated "hot" tumor. This approach has been shown to be effective in terms of improving therapeutic agent delivery and immune-modulation effect using the FUS-BBB opening technique. Based on significant preclinical evidence, clinical trials of FUS-BBB opening via various devices have been conducted since 2014 (**Table 1**). A total of six trials have been conducted on glioblastoma patients using a variety of devices including SonoCloud® (CarThera), ExAblate® (InSightec), and NaviFUS® (NaviFUS cooperation), both with and without chemotherapy regimens, such as carboplatin, doxorubicin and temozolomide. One trial in Spain focuses on patients with breast cancer brain metastases. All announced trials are still recruiting participants, with the exception of one trial using SonoCloud® in treating recurrent glioblastoma patients. A repeated opening of the BBB using implanted pulsed ultrasound device (SonoCloud®), in combination with Sonovue® (dose: 0.1 ml/kg) at an acoustic pressure ranged from 0.5 to 1.1 MPa, has been shown to be safe and well tolerated in treating recurrent GBM patients (Carpentier et al., 2016).

AD Trial

For Alzheimer disease, exciting results from animal experiments have shown a possibility for decreasing Aβ deposits via scanning ultrasound with BBB opening parameters (Burgess et al., 2014; Leinenga and Gotz, 2015). Since 2016, four clinical trials including SonoCloud® (CarThera) and ExAblate® (InSightec) have been applied on early AD patients to evaluate safety and feasibility. Lipsman et al. conducted a phase I trial on 5 AD patients using an PCD-feedback power regulation approach but with an average exposure level of 4.6W with Definity® (dose: 4 μl/kg), demonstrating a safe, reversible and repeated

TABLE 1 | Summary of the FUS-BBB opening Clinical Trials.

	Trial no.	Study start day	Study title	Indication	Intervention and parameters	Location	Status
BRAIN TUMOR							
1	NCT02253212	2014/7	Safety of BBB Opening with the SonoCloud (SONOCLOUD)[a]	Recurrent glioblastoma	SonoCloud; $n = 27$ 0.5–1.1MPa Microbubble: Sonovue® (0.1 ml/kg) Drug: Carboplatin	France	Completed
2	NCT02343991	2014/10	BBB Disruption Using Transcranial MRI-Guided Focused Ultrasound[b]	Brain Tumor	Exablate; $n = 10$ PCD-based power regulation Microbubble: Definity® (4 μ/kg) Drug: Doxorubicin	Canada	Active, not recruiting
3	NCT03626896	2018/8/17	Safety of BBB disruption using NaviFUS system in recurrent glioblastoma multiforme (GBM) patients[c]	Recurrent glioblastoma	NaviFUS; $n = 6$ Escalated exposure average 10–16W; Microbubble: Sonovue® (0.1 ml/kg)	Taiwan	Recruiting
4	NCT03712293	2018/8/28	ExAblate Blood-Brain Barrier Disruption for Glioblastoma in Patients Undergoing Standard Chemotherapy[d]	Glioblastoma patients undergo adjuvant Temozolomide	Exablate; $n = 10$ PCD-based power regulation Microbubble: Definity® (4 μl/kg) Drug: Temozolomide	Korea	Recruiting
5	NCT03616860	2018/10	Assessment of Safety and Feasibility of ExAblate Blood-Brain Barrier (BBB) Disruption for Treatment of Glioma[e]	Glioblastoma	Exablate; $n = 20$ PCD-based power regulation Microbubble: Definity® (4 μl/kg) Drug: Lipodox, Temozolomide	Canada	Recruiting
6	NCT03551249	2018/11	Assessment of Safety and Feasibility of ExAblate Blood-Brain Barrier (BBB) Disruption[f]	Glioblastoma	Exablate; $n = 20$ Power level: PCD-based power regulation Microbubble: Definity® (4 μl/kg) Drug: Temozolomide	USA	Not yet recruiting
7	NCT03714243	2018/12	Blood Brain Barrier Disruption (BBBD) Using MRgFUS in the Treatment of Her2-positive Breast Cancer Brain Metastases[g]	Breast cancer with brain metastases	Exablate; $n = 10$ Power level: PCD-based power regulation Microbubble: Definity® (4 μl/kg)	N/A	Not yet recruiting
ALZHEIMER'S DISEASE							
8	NCT02986932	2016/12	BBB Opening Using Focused Ultrasound with IV Contrast Agents in Patients with Early Alzheimer's Disease[h]	Alzheimer's Disease	Exablate; $n = 6$ Power level: PCD-based exposure level regulation (average 4.6W) Microbubble: Definity® MB (4μl/kg)	Canada	Completed
9	NCT03119961	2017/6/26	Blood Brain Barrier Opening in Alzheimer's Disease (BOREAL1)[i]	Alzheimer's Disease	Sonocloud; $n = 10$ Power level: 0.5–1.1MPa, Microbubble: Sonovue® MB (0.1 ml/kg)	France	Recruiting
10	NCT03671889	2018/9/28	ExAblate Blood-Brain Barrier (BBB) Disruption for the Treatment of Alzheimer's Disease[j]	Alzheimer's Disease	Exablate; $n = 10$ Power level: PCD-based exposure level regulation Definity® MB (4μl/kg)	USA	Recruiting
11	NCT03739905	2018/12	ExAblate Blood-Brain Barrier Opening for Treatment of Alzheimer's Disease[k]	Alzheimer's Disease	Exablate; $n = 30$ PCD-based exposure level regulation Microbubble: Definity® MB (4μl/kg)	Canada	Not yet recruiting
OTHERS							
12	NCT03321487	2018/4/13	BBB Opening Using MR-Guided Focused Ultrasound in Patients with Amyotrophic Lateral Sclerosis[l]	Amyotrophic Lateral Sclerosis	Exablate; $n = 8$ PCD-based exposure level regulation Microbubble: Definity® (4μl/kg)	Canada	Recruiting

(Continued)

TABLE 1 | Continued

	Trial no.	Study start day	Study title	Indication	Intervention and parameters	Location	Status
13	NCT03608553	2018/12	Evaluate Temporary Blood Brain Barrier Disruption in Patients with Parkinson's Disease Dementia[m]	Parkinson's Disease Dementia	Exablate; $n = 10$ PCD-based exposure level regulation Microbubble: Definity® (4μl/kg)	Spain	Recruiting

[a] *ClinicalTrials.gov. Ahmed Idbaih (MD): Groupe Hospitalier Pitié Salpetriere (France) (2014). Identifier NCT02253212, Safety of BBB Opening With the SonoCloud (SONOCLOUD). Available online at: http://clinicaltrials.gov/ct/show/NCT02253212 (Accessed January 15, 2019).*

[b] *ClinicalTrials.gov. InSightec: Sunnybrook Health Science Center (Canada) (2014). Identifier NCT02343991, BBB Disruption Using Transcranial MRI-Guided Focused Ultrasound. Available online at: http://clinicaltrials.gov/ct/show/NCT02343991 (Accessed January 15, 2019).*

[c] *ClinicalTrials.gov. Kuo-Chen Wei (MD): Linkou Chang Gung Memorial Hospital (Taiwan). (2018). Identifier NCT03626896, Safety of BBB disruption using NaviFUS system in recurrent glioblastoma multiforme (GBM) patients. Available online at: http://clinicaltrials.gov/ct/show/NCT03626896 (Accessed January 15, 2019).*

[d] *ClinicalTrials.gov. Martine Bernstein: Severance Hospital, Yonsei University Health System (Korea). (2018). Identifier NCT03712293, ExAblate Blood-Brain Barrier Disruption for Glioblastoma in Patients Undergoing Standard Chemotherapy. Available online at: http://clinicaltrials.gov/ct/show/NCT03712293 (Accessed January 15, 2019).*

[e] *ClinicalTrials.gov. Nir Lipsman (MD): Sunnybrook Health Science Center (Canada). (2018). Identifier NCT03616860, Assessment of Safety and Feasibility of ExAblate Blood-Brain Barrier (BBB) Disruption for Treatment of Glioma. Available online at: http://clinicaltrials.gov/ct/show/NCT03616860 (Accessed January 15, 2019).* [f] *ClinicalTrials.gov. InSightec. (2019). Identifier NCT03551249, Assessment of Safety and Feasibility of ExAblate Blood-Brain Barrier (BBB) Disruption. Available from: http://clinicaltrials.gov/ct/show/NCT03551249 (Accessed January 15, 2019).*

[g] *ClinicalTrials.gov. Nir Lipsman (MD): Sunnybrook Health Science Center (Canada). (2018). Identifier NCT03714243, Blood Brain Barrier Disruption (BBBD) Using MRgFUS in the Treatment of Her2-positive Breast Cancer Brain Metastases. Available online at: http://clinicaltrials.gov/ct/show/NCT03714243 (Accessed January 15, 2019).*

[h] *ClinicalTrials.gov. Nir Lipsman (MD): Sunnybrook Health Science Center (Canada). (2016). Identifier NCT02986932, BBB Opening Using Focused Ultrasound with IV Contrast Agents in Patients with Early Alzheimer's Disease. Available online at: http://clinicaltrials.gov/ct/show/NCT02986932 (Accessed January 15, 2019).*

[i] *ClinicalTrials.gov. Stephane Epelbaum(MD): APHP - Pitié-Salpêtrière Hospital (France). (2017). Identifier NCT03119961, Blood Brain Barrier Opening in Alzheimer's Disease (BOREAL1). Available online at: http://clinicaltrials.gov/ct/show/NCT03119961 (Accessed January 15, 2019).*

[j] *ClinicalTrials.gov. InSightec: Weill Corneal Medicine (US); Weill Corneal Medicine, The Ohio State University-Wexner Medical Center, West Virginia University Rockefeller Neuroscience Center (US). (2018). Identifier NCT03671889, ExAblate Blood-Brain Barrier (BBB) Disruption for the Treatment of Alzheimer's Disease. Available online at: http://clinicaltrials.gov/ct/show/NCT03671889 (Accessed January 15, 2019).*

[k] *ClinicalTrials.gov. InSightec: Sunnybrook Health Science Center (Canada). (2018). Identifier NCT03739905, ExAblate Blood-Brain Barrier Opening for Treatment of Alzheimer's Disease. Available online at: http://clinicaltrials.gov/ct/show/NCT03739905 (Accessed January 15, 2019).*

[l] *ClinicalTrials.gov. InSightec: Sunnybrook Health Science Center (Canada). (2018). Identifier NCT03321487, BBB Opening Using MR-Guided Focused Ultrasound in Patients with Amyotrophic Lateral Sclerosis. Available online at: http://clinicaltrials.gov/ct/show/NCT03321487 (Accessed January 15, 2019).*

[m] *ClinicalTrials.gov. Jose Obeso: HM Hospitales Puerta del Sur – CINAC (Spain). (2018). Identifier NCT03608553, Evaluate Temporary Blood Brain Barrier Disruption in Patients with Parkinson's Disease Dementia. Available online at: http://clinicaltrials.gov/ct/show/NCT03608553 (Accessed January 15, 2019).*

BBB, blood brain barrier; FUS, focused ultrasound; MB, microbubble; PCD, passive cavitation detection.

opening of BBB by MRgFUS device (ExAblate®) (Lipsman et al., 2018). Recently, a single-arm, non-randomized phase IIa trial has been announced in Canada to evaluate the efficacy of FUS-BBB opening on treating AD patients (trial number: NCT03739905, **Table 1**).

ALS and PD Dementia Trial

Phase I trials are currently ongoing for amyotrophic lateral sclerosis (ALS) and Parkinson's disease dementia using an MRgFUS device (ExAblate®) for BBB opening (Trial numbers NCT03321487 and NCT03608553; **Table 1**).

Technical Gap of Translational Application From Preclinical to Clinical

Although substantially accumulative proof-of-concept preclinical studies have concluded and demonstrated the potential benefit of utilizing FUS-BBB opening technique for CNS disease treatments, a number of technical gaps need to be filled prior to its wide clinical translation. First, the heterogeneity of intracranial structures such as gray and white matter and dense vasculature, as well as the thick and uneven skull, may cause substantial FUS beam distortion and transcranial pressure attenuation when ultrasound passes through the skull. Moreover, concerns about physical parameters and individual BBB-opened threshold level variation due to different treatment portion containing various vascular density or personalized variation are critical issues that need to addressed. In addition, current ongoing clinical trials employed various medical devices combined with various types of microbubbles bring extra difficulty to unify the ultrasound dose to be delivered into patient brain. Last but not least, the current standard to verify the occurrence of BBB opening can only be confirmed via post-operative MRI contrast agent administration and the process so far lacks tools for intraoperative BBB-opened monitoring.

For filling the above technical gaps, a promising scheme is to utilize the PCD as an tool to (1) provide correlations between delivery efficiency and BBB opening volume in steering the treatment as real-time monitoring, and (2) to provide real-time means to control the occurrence of BBB opening to avoid adverse effect (Wu et al., 2016, 2018; Xia et al., 2016; Liu et al., 2018). In addition, a personalized treatment planning tools need to be developed to individually determining FUS physical parameters with dedicated consideration of transcranial focal beam distortion and compensation prior to the treatment.

For now, three different types of therapeutic ultrasound devices, including the implanted ultrasound device (SonoCloud®), the extracorporeal fixed stereotactic frame-based MRI-guided device (Exablate®) to the frameless neuronavigation-guided device (NaviFUS®) are available on the market to treat and to explore the efficacy in human

clinical trials. A trend toward a less invasive FUS modality with patient-centered protocol design, in a meanwhile, maintaining the treatment efficacy with proper parameters under on-line feedback would be the paramount goal in FUS-BBB development.

CONCLUSION

The use of focused ultrasound for blood-brain barrier opening is an innovative and non-invasive means to achieve drug delivery deep within the CNS along with other therapy modalities. Compared to other drug delivery approaches, focused ultrasound BBB opening provides significant advantages in terms of locality, non-invasiveness, and effect reversibility. Over the past decade, significant advances have been made in technological development and preclinical validation, and this technique is now entering clinical trials for patients suffering from brain tumors, Alzheimer's disease, ALS, and Parkinson's disease dementia. Preliminary results have confirmed safety and efficacy for brain tumor treatment, and show significant promise for additional indications, raising the potential for focused ultrasound blood-brain barrier opening to emerge as an important tool for CNS disease treatment.

AUTHOR CONTRIBUTIONS

K-TC, K-CW, and H-LL together drafted, organized, and finalized the manuscript

FUNDING

This study was supported by the Ministry of Science and Technology, Taiwan, under grants 105-2221-E-182-022 and 106-2221-E-182-02, and by Chang Gung Memorial Hospital, Taiwan, under grants CIRPD2E0051-53 and CMRPD2D0111-13. We also thanks for the facility support from Center for Advanced Molecular Imaging and Translation, Chang Gung Memorial Hospital, Taiwan.

REFERENCES

Alkins, R. D., Brodersen, P. M., Sodhi, R. N., and Hynynen, K. (2013). Enhancing drug delivery for boron neutron capture therapy of brain tumors with focused ultrasound. *NeuroOncology* 15, 1225–1235. doi: 10.1093/neuonc/not052

Alonso, A., Reinz, E., Fatar, M., Hennerici, M. G., and Meairs, S. (2011). Clearance of albumin following ultrasound-induced blood-brain barrier opening is mediated by glial but not neuronal cells. *Brain Res.* 1411, 9–16. doi: 10.1016/j.brainres.2011.07.006

Apfel, R. E., and Holland, C. K. (1991). Gauging the likelihood of cavitation from short-pulse, low-duty cycle diagnostic ultrasound. *Ultrasound Med. Biol.* 17, 179–185. doi: 10.1016/0301-5629(91)90125-G

Arvanitis, C. D., Livingstone, M. S., and McDannold, N. (2013). Combined ultrasound and MR imaging to guide focused ultrasound therapies in the brain. *Phys. Med. Biol.* 58, 4749–4761. doi: 10.1088/0031-9155/58/14/4749

Arvanitis, C. D., Livingstone, M. S., Vykhodtseva, N., and McDannold, N. (2012). Controlled ultrasound-induced blood-brain barrier disruption using passive acoustic emissions monitoring. *PLoS ONE* 7:e45783. doi: 10.1371/journal.pone.0045783

Bader, K. B., and Holland, C. K. (2013). Gauging the likelihood of stable cavitation from ultrasound contrast agents. *Phys. Med. Biol.* 58, 127–144. doi: 10.1088/0031-9155/58/1/127

Burgess, A., Dubey, S., Yeung, S., Hough, O., Eterman, N., Aubert, I., et al. (2014). Alzheimer disease in a mouse model: MR imaging-guided focused ultrasound targeted to the hippocampus opens the blood-brain barrier and improves pathologic abnormalities and behavior. *Radiology* 273, 736–745. doi: 10.1148/radiol.14140245

Carpentier, A., Canney, M., Vignot, A., Reina, V., Beccaria, K., Horodyckid, C., et al. (2016). Clinical trial of blood-brain barrier disruption by pulsed ultrasound. *Sci. Transl. Med.* 8:343re2. doi: 10.1126/scitranslmed.aaf6086

Caskey, C. F., Stieger, S. M., Qin, S., Dayton, P. A., and Ferrara, K. W. (2007). Direct observations of ultrasound microbubble contrast agent interaction with the microvessel wall. *J. Acoust. Soc. Am.* 122, 1191–1200. doi: 10.1121/1.2747204

Chai, W. Y., Chu, P. C., Tsai, M. Y., Lin, Y. C., Wang, J. J., Wei, K. C., et al. (2014). Magnetic-resonance imaging for kinetic analysis of permeability changes during focused ultrasound-induced blood-brain barrier opening and brain drug delivery. *J. Control. Release* 192, 1–9. doi: 10.1016/j.jconrel.2014.06.023

Chen, H., and Konofagou, E. E. (2014). The size of blood-brain barrier opening induced by focused ultrasound is dictated by the acoustic pressure. *J. Cereb. Blood Flow Metab.* 34, 1197–1204. doi: 10.1038/jcbfm.2014.71

Chen, P. Y., Hsieh, H. Y., Huang, C. Y., Lin, C. Y., Wei, K. C., and Liu, H. L. (2015a). Focused ultrasound-induced blood-brain barrier opening to enhance interleukin-12 delivery for brain tumor immunotherapy: a preclinical feasibility study. *J. Transl. Med.* 13:93. doi: 10.1186/s12967-015-0451-y

Chen, P. Y., Liu, H. L., Hua, M. Y., Yang, H. W., Huang, C. Y., Chu, P. C., et al. (2010). Novel magnetic/ultrasound focusing system enhances nanoparticle drug delivery for glioma treatment. *NeuroOncology* 12, 1050–1060. doi: 10.1093/neuonc/noq054

Chen, P. Y., Wei, K. C., and Liu, H. L. (2015b). Neural immune modulation and immunotherapy assisted by focused ultrasound induced blood-brain barrier opening. *Hum. Vaccin. Immunother.* 11, 2682–2687. doi: 10.1080/21645515.2015.1071749

Cho, E. E., Drazic, J., Ganguly, M., Stefanovic, B., and Hynynen, K. (2011). Two-photon fluorescence microscopy study of cerebrovascular dynamics in ultrasound-induced blood-brain barrier opening. *J. Cereb. Blood Flow Metab.* 31, 1852–1862. doi: 10.1038/jcbfm.2011.59

Cho, H., Lee, H. Y., Han, M., Choi, J. R., Ahn, S., Lee, T., et al. (2016). Localized down-regulation of P-glycoprotein by focused ultrasound and microbubbles induced blood-brain barrier disruption in rat brain. *Sci. Rep.* 6:31201. doi: 10.1038/srep31201

Choi, J. J., Feshitan, J. A., Baseri, B., Wang, S., Tung, Y. S., Borden, M. A., et al. (2010). Microbubble-size dependence of focused ultrasound-induced blood-brain barrier opening in mice *in vivo*. *IEEE Trans. Biomed. Eng.* 57, 145–154. doi: 10.1109/TBME.2009.2034533

Chu, P. C., Chai, W. Y., Tsai, C. H., Kang, S. T., Yeh, C. K., and Liu, H. L. (2016). Focused ultrasound-induced blood-brain barrier opening: association with mechanical index and cavitation index analyzed by dynamic contrast-enhanced magnetic-resonance imaging. *Sci. Rep.* 6:33264. doi: 10.1038/srep33264

Clement, G. T., White, J., and Hynynen, K. (2000). Investigation of a large-area phased array for focused ultrasound surgery through the skull. *Phys. Med. Biol.* 45, 1071–1083. doi: 10.1088/0031-9155/45/4/319

Cohen-Inbar, O., Xu, Z., and Sheehan, J. P. (2016). Focused ultrasound-aided immunomodulation in glioblastoma multiforme: a therapeutic concept. *J. Ther. Ultrasound* 4:2. doi: 10.1186/s40349-016-0046-y

Crum, L. A., Roy, R. A., Dinno, M. A., Church, C. C., Apfel, R. E., Holland, C. K., et al. (1992). Acoustic cavitation produced by microsecond pulses of ultrasound: a discussion of some selected results. *J. Acoust. Soc. Am.* 91, 1113–1119. doi: 10.1121/1.402638

Curley, C. T., Sheybani, N. D., Bullock, T. N., and Price, R. J. (2017). Focused ultrasound immunotherapy for central nervous system pathologies: challenges and opportunities. *Theranostics* 7, 3608–3623. doi: 10.7150/thno.21225

Dasgupta, A., Liu, M., Ojha, T., Storm, G., Kiessling, F., and Lammers, T. (2016). Ultrasound-mediated drug delivery to the brain: principles,

progress and prospects. *Drug Discov. Today Technol.* 20, 41–48. doi: 10.1016/j.ddtec.2016.07.007

Deng, J., Huang, Q., Wang, F., Liu, Y., Wang, Z., Wang, Z., et al. (2012). The role of caveolin-1 in blood-brain barrier disruption induced by focused ultrasound combined with microbubbles. *J. Mol. Neurosci.* 46, 677–687. doi: 10.1007/s12031-011-9629-9

Doolittle, N. D., Miner, M. E., Hall, W. A., Siegal, T., Jerome, E., Osztie, E., et al. (2000). Safety and efficacy of a multicenter study using intraarterial chemotherapy in conjunction with osmotic opening of the blood-brain barrier for the treatment of patients with malignant brain tumors. *Cancer* 88, 637–47. doi: 10.1002/(SICI)1097-0142(20000201)88:3<637::AID-CNCR22>3.0.CO;2-Y

Duskey, J. T., Belletti, D., Pederzoli, F., Vandelli, M. A., Forni, F., Ruozi, B., et al. (2017). Current strategies for the delivery of therapeutic proteins and enzymes to treat brain disorders. *Int. Rev. Neurobiol.* 137, 1–28. doi: 10.1016/bs.irn.2017.08.006

Ewing, J. R., Brown, S. L., Lu, M., Panda, S., Ding, G., Knight, R. A., et al. (2006). Model selection in magnetic resonance imaging measurements of vascular permeability: gadomer in a 9L model of rat cerebral tumor. *J. Cereb. Blood Flow Metab.* 26, 310–320. doi: 10.1038/sj.jcbfm.9600189

Fan, C. H., Lin, W. H., Ting, C. Y., Chai, W. Y., Yen, T. C., Liu, H. L., et al. (2014). Contrast-enhanced ultrasound imaging for the detection of focused ultrasound-induced blood-brain barrier opening. *Theranostics* 4, 1014–1025. doi: 10.7150/thno.9575

Fan, C. H., Ting, C. Y., Lin, C. Y., Chan, H. L., Chang, Y. C., Chen, Y. Y., et al. (2016). Noninvasive, targeted, and non-viral ultrasound-mediated GDNF-plasmid delivery for treatment of Parkinson's disease. *Sci. Rep.* 6:19579. doi: 10.1038/srep19579

Fan, C. H., Ting, C. Y., Lin, H. J., Wang, C. H., Liu, H. L., Yen, T. C., et al. (2013a). SPIO-conjugated, doxorubicin-loaded microbubbles for concurrent MRI and focused-ultrasound enhanced brain-tumor drug delivery. *Biomaterials* 34, 3706–3715. doi: 10.1016/j.biomaterials.2013.01.099

Fan, C. H., Ting, C. Y., Liu, H. L., Huang, C. Y., Hsieh, H. Y., Yen, T. C., et al. (2013b). Antiangiogenic-targeting drug-loaded microbubbles combined with focused ultrasound for glioma treatment. *Biomaterials* 34, 2142–2155. doi: 10.1016/j.biomaterials.2012.11.048

Ferguson, S. D., Foster, K., and Yamini, B. (2007). Convection-enhanced delivery for treatment of brain tumors. *Expert Rev. Anticancer Ther.* 7, S79–85. doi: 10.1586/14737140.7.12s.S79

Groothuis, D. R., Fischer, J. M., Lapin, G., Bigner, D. D., and Vick, N. A. (1982). Permeability of different experimental brain tumor models to horseradish peroxidase. *J. Neuropathol. Exp. Neurol.* 41, 164–185. doi: 10.1097/00005072-198203000-00006

Gumerlock, M. K., Belshe, B. D., Madsen, R., and Watts, C. (1992). Osmotic blood-brain barrier disruption and chemotherapy in the treatment of high grade malignant glioma: patient series and literature review. *J. Neurooncol.* 12, 33–46. doi: 10.1007/BF00172455

Hernot, S., and Klibanov, A. L. (2008). Microbubbles in ultrasound-triggered drug and gene delivery. *Adv. Drug Deliv. Rev.* 60, 1153–1166. doi: 10.1016/j.addr.2008.03.005

Howles, G. P., Bing, K. F., Qi, Y., Rosenzweig, S. J., Nightingale, K. R., and Johnson, G. A. (2010). Contrast-enhanced *in vivo* magnetic resonance microscopy of the mouse brain enabled by noninvasive opening of the blood-brain barrier with ultrasound. *Magn. Reson. Med.* 64, 995–1004. doi: 10.1002/mrm.22411

Hsu, P. H., Lin, Y. T., Chung, Y. H., Lin, K. J., Yang, L. Y., Yen, T. C., et al. (2018). Focused ultrasound-induced blood-brain barrier opening enhances GSK-3 inhibitor delivery for amyloid-beta plaque reduction. *Sci. Rep.* 8:12882. doi: 10.1038/s41598-018-31071-8

Hsu, P. H., Wei, K. C., Huang, C. Y., Wen, C. J., Yen, T. C., Liu, C. L., et al. (2013). Noninvasive and targeted gene delivery into the brain using microbubble-facilitated focused ultrasound. *PLoS ONE* 8:e57682. doi: 10.1371/journal.pone.0057682

Husseini, G. A., M. A., Diaz de la Rosa, Richardson, E. S., Christensen, D. A., and Pitt, W. G. (2005). The role of cavitation in acoustically activated drug delivery. *J. Control. Release* 107, 253–261. doi: 10.1016/j.jconrel.2005.06.015

Hynynen, K., McDannold, N., Sheikov, N. A., Jolesz, F. A., and Vykhodtseva, N. (2005). Local and reversible blood-brain barrier disruption by noninvasive focused ultrasound at frequencies suitable for trans-skull sonications. *Neuroimage* 24, 12–20. doi: 10.1016/j.neuroimage.2004.06.046

Hynynen, K., McDannold, N., Vykhodtseva, N., and Jolesz, F. A. (2001). Noninvasive MR imaging-guided focal opening of the blood-brain barrier in rabbits. *Radiology* 220, 640–646. doi: 10.1148/radiol.2202001804

Hynynen, K., McDannold, N., Vykhodtseva, N., and Jolesz, F. A. (2003). Non-invasive opening of BBB by focused ultrasound. *Acta Neurochir. Suppl.* 86, 555–558. doi: 10.1007/978-3-7091-0651-8_113

Jensen, C. R., Ritchie, R. W., Gyongy, M., Collin, J. R., Leslie, T., and Coussios, C. C. (2012). Spatiotemporal monitoring of high-intensity focused ultrasound therapy with passive acoustic mapping. *Radiology* 262, 252–261. doi: 10.1148/radiol.11110670

Jin, Q., Kang, S. T., Chang, Y. C., Zheng, H., and Yeh, C. K. (2016). Inertial cavitation initiated by polytetrafluoroethylene nanoparticles under pulsed ultrasound stimulation. *Ultrason. Sonochem.* 32, 1–7. doi: 10.1016/j.ultsonch.2016.02.009

Jordao, J. F., Thevenot, E., Markham-Coultes, K., Scarcelli, T., Weng, Y. Q., Xhima, K., et al. (2013). Amyloid-beta plaque reduction, endogenous antibody delivery and glial activation by brain-targeted, transcranial focused ultrasound. *Exp. Neurol.* 248, 16–29. doi: 10.1016/j.expneurol.2013.05.008

Kinoshita, M., McDannold, N., Jolesz, F. A., and Hynynen, K. (2006). Targeted delivery of antibodies through the blood-brain barrier by MRI-guided focused ultrasound. *Biochem. Biophys. Res. Commun.* 340, 1085–1090. doi: 10.1016/j.bbrc.2005.12.112

Kovacs, Z. I., Kim, S., Jikaria, N., Qureshi, F., Milo, B., Lewis, B. K., et al. (2017). Disrupting the blood-brain barrier by focused ultrasound induces sterile inflammation. *Proc. Natl. Acad. Sci. U.S.A.* 114, E75–E84. doi: 10.1073/pnas.1614777114

Leinenga, G., and Gotz, J. (2015). Scanning ultrasound removes amyloid-beta and restores memory in an Alzheimer's disease mouse model. *Sci. Transl. Med.* 7:278ra33. doi: 10.1126/scitranslmed.aaa2512

Lin, C. Y., Hsieh, H. Y., Chen, C. M., Wu, S. R., Tsai, C. H., Huang, C. Y., et al. (2016). Non-invasive, neuron-specific gene therapy by focused ultrasound-induced blood-brain barrier opening in Parkinson's disease mouse model. *J. Control. Release* 235, 72–81. doi: 10.1016/j.jconrel.2016.05.052

Lin, C. Y., Hsieh, H. Y., Pitt, W. G., Huang, C. Y., Tseng, I. C., Yeh, C. K., et al. (2015). Focused ultrasound-induced blood-brain barrier opening for non-viral, non-invasive, and targeted gene delivery. *J. Control. Release* 212, 1–9. doi: 10.1016/j.jconrel.2015.06.010

Lin, K. J., Liu, H. L., Hsu, P. H., Chung, Y. H., Huang, W. C., Chen, J. C., et al. (2009). Quantitative micro-SPECT/CT for detecting focused ultrasound-induced blood-brain barrier opening in the rat. *Nucl. Med. Biol.* 36, 853–861. doi: 10.1016/j.nucmedbio.2009.04.011

Lipsman, N., Meng, Y., Bethune, A. J., Huang, Y., Lam, B., Masellis, M., et al. (2018). Blood-brain barrier opening in Alzheimer's disease using MR-guided focused ultrasound. *Nat. Commun.* 9:2336. doi: 10.1038/s41467-018-04529-6

Liu, H. L., Hsieh, H. Y., Lu, L. A., Kang, C. W., Wu, M. F., and Lin, C. Y. (2012). Low-pressure pulsed focused ultrasound with microbubbles promotes an anticancer immunological response. *J. Transl. Med.* 10:221. doi: 10.1186/1479-5876-10-221

Liu, H. L., Hsu, P. H., Chu, P. C., Wai, Y. Y., Chen, J. C., Shen, C. R., et al. (2009). Magnetic resonance imaging enhanced by superparamagnetic iron oxide particles: usefulness for distinguishing between focused ultrasound-induced blood-brain barrier disruption and brain hemorrhage. *J. Magn. Reson. Imaging* 29, 31–38. doi: 10.1002/jmri.21599

Liu, H. L., Hsu, P. H., Lin, C. Y., Huang, C. W., Chai, W. Y., Chu, P. C., et al. (2016). Focused ultrasound enhances central nervous system delivery of bevacizumab for malignant glioma treatment. *Radiology* 281, 99–108. doi: 10.1148/radiol.2016152444

Liu, H. L., Hua, M. Y., Chen, P. Y., Chu, P. C., Pan, C. H., Yang, H. W., et al. (2010a). Blood-brain barrier disruption with focused ultrasound enhances delivery of chemotherapeutic drugs for glioblastoma treatment. *Radiology* 255, 415–425. doi: 10.1148/radiol.10090699

Liu, H. L., Hua, M. Y., Yang, H. W., Huang, C. Y., Chu, P. C., Wu, J. S., et al. (2010b). Magnetic resonance monitoring of focused ultrasound/magnetic nanoparticle targeting delivery of therapeutic agents to the brain. *Proc. Natl. Acad. Sci. U.S.A.* 107, 15205–15210. doi: 10.1073/pnas.1003388107

Liu, H. L., Huang, C. Y., Chen, J. Y., Wang, H. Y., Chen, P. Y., and Wei, K. C. (2014). Pharmacodynamic and therapeutic investigation of focused ultrasound-induced blood-brain barrier opening for enhanced temozolomide delivery in glioma treatment. *PLoS ONE* 9:e114311. doi: 10.1371/journal.pone.0114311

Liu, H. L., Tsai, C. H., Jan, C. K., Chang, H. Y., Huang, S. M., Li, M. L., et al. (2018). Design and Implementation of a transmit/receive ultrasound phased array for brain applications. *IEEE Trans. Ultrason. Ferroelectr. Freq. Control.* 65, 1756–1767. doi: 10.1109/TUFFC.2018.2855181

Liu, H. L., Wai, Y. Y., Chen, W. S., Chen, J. C., Hsu, P. H., Wu, X. Y., et al. (2008). Hemorrhage detection during focused-ultrasound induced blood-brain-barrier opening by using susceptibility-weighted magnetic resonance imaging. *Ultrasound Med. Biol.* 34, 598–606. doi: 10.1016/j.ultrasmedbio.2008.01.011

Lum, A. F., Borden, M. A., Dayton, P. A., Kruse, D. E., Simon, S. I., and Ferrara, K. W. (2006). Ultrasound radiation force enables targeted deposition of model drug carriers loaded on microbubbles. *J. Control. Release* 111, 128–134. doi: 10.1016/j.jconrel.2005.11.006

Madav, Y., Wairkar, S., and Prabhakar, B. (2019). Recent therapeutic strategies targeting beta amyloid and tauopathies in Alzheimer's disease. *Brain Res. Bull.* 146, 171–184. doi: 10.1016/j.brainresbull.2019.01.004

Maiuolo, J., Gliozzi, M., Musolino, V., Scicchitano, M., Carresi, C., Scarano, F., et al. (2018). The "Frail" brain blood barrier in neurodegenerative diseases: role of early disruption of endothelial cell-to-cell connections. *Int. J. Mol. Sci.* 19:2693. doi: 10.3390/ijms19092693

Marquet, F., Teichert, T., Wu, S. Y., Tung, Y. S., Downs, M., Wang, S., et al. (2014). Real-time, transcranial monitoring of safe blood-brain barrier opening in non-human primates. *PLoS ONE* 9:e84310. doi: 10.1371/journal.pone.0084310

McDannold, N., Arvanitis, C. D., Vykhodtseva, N., and Livingstone, M. S. (2012). Temporary disruption of the blood-brain barrier by use of ultrasound and microbubbles: safety and efficacy evaluation in rhesus macaques. *Cancer Res.* 72, 3652–3663. doi: 10.1158/0008-5472.CAN-12-0128

McDannold, N., Vykhodtseva, N., and Hynynen, K. (2006). Targeted disruption of the blood-brain barrier with focused ultrasound: association with cavitation activity. *Phys. Med. Biol.* 51, 793–807. doi: 10.1088/0031-9155/51/4/003

McDannold, N., Vykhodtseva, N., and Hynynen, K. (2007). Use of ultrasound pulses combined with Definity for targeted blood-brain barrier disruption: a feasibility study. *Ultrasound Med. Biol.* 33, 584–590. doi: 10.1016/j.ultrasmedbio.2006.10.004

McDannold, N., Vykhodtseva, N., and Hynynen, K. (2008). Effects of acoustic parameters and ultrasound contrast agent dose on focused-ultrasound induced blood-brain barrier disruption. *Ultrasound Med. Biol.* 34, 930–937. doi: 10.1016/j.ultrasmedbio.2007.11.009

McMahon, D., Bendayan, R., and Hynynen, K. (2017). Acute effects of focused ultrasound-induced increases in blood-brain barrier permeability on rat microvascular transcriptome. *Sci. Rep.* 7:45657. doi: 10.1038/srep45657

Mei, J., Cheng, Y., Song, Y., Yang, Y., Wang, F., Liu, Y., et al. (2009). Experimental study on targeted methotrexate delivery to the rabbit brain via magnetic resonance imaging-guided focused ultrasound. *J. Ultrasound Med.* 28, 871–880. doi: 10.7863/jum.2009.28.7.871

Miranpuri, G. S., Kumbier, L., Hinchman, A., Schomberg, D., Wang, A., Marshall, H., et al. (2012). Gene-based therapy of Parkinson's Disease: translation from animal model to human clinical trial employing convection enhanced delivery. *Ann. Neurosci.* 19, 133–146. doi: 10.5214/ans.0972.7531.190310

Mitragotri, S. (2005). Healing sound: the use of ultrasound in drug delivery and other therapeutic applications. *Nat. Rev. Drug Discov.* 4, 255–260. doi: 10.1038/nrd1662

Negishi, Y., Yamane, M., Kurihara, N., Endo-Takahashi, Y., Sashida, S., Takagi, N., et al. (2015). Enhancement of blood-brain barrier permeability and delivery of antisense oligonucleotides or plasmid DNA to the brain by the combination of bubble liposomes and high-intensity focused ultrasound. *Pharmaceutics* 7, 344–362. doi: 10.3390/pharmaceutics7030344

Nelson, A. R., Sweeney, M. D., Sagare, A. P., and Zlokovic, B. V. (2016). Neurovascular dysfunction and neurodegeneration in dementia and Alzheimer's disease. *Biochim. Biophys. Acta* 1862, 887–900. doi: 10.1016/j.bbadis.2015.12.016

Neuwelt, E. A., Barnett, P. A., Bigner, D. D., and Frenkel, E. P. (1982). Effects of adrenal cortical steroids and osmotic blood-brain barrier opening on methotrexate delivery to gliomas in the rodent: the factor of the blood-brain barrier. *Proc. Natl. Acad. Sci. U.S.A.* 79, 4420–4423. doi: 10.1073/pnas.79.14.4420

Nhan, T., Burgess, A., Cho, E. E., Stefanovic, B., Lilge, L., and Hynynen, K. (2013). Drug delivery to the brain by focused ultrasound induced blood-brain barrier disruption: quantitative evaluation of enhanced permeability of cerebral vasculature using two-photon microscopy. *J. Control. Release* 172, 274–280. doi: 10.1016/j.jconrel.2013.08.029

O'Reilly, M. A., and Hynynen, K. (2010). A PVDF receiver for ultrasound monitoring of transcranial focused ultrasound therapy. *IEEE Trans. Biomed. Eng.* 57, 2286–2294. doi: 10.1109/TBME.2010.2050483

O'Reilly, M. A., and Hynynen, K. (2012). Blood-brain barrier: real-time feedback-controlled focused ultrasound disruption by using an acoustic emissions-based controller. *Radiology* 263, 96–106. doi: 10.1148/radiol.11111417

O'Reilly, M. A., Jones, R. M., and Hynynen, K. (2014). Three-dimensional transcranial ultrasound imaging of microbubble clouds using a sparse hemispherical array. *IEEE Trans. Biomed. Eng.* 61, 1285–1294. doi: 10.1109/TBME.2014.2300838

O'Reilly, M. A., Waspe, A. C., Ganguly, M., and Hynynen, K. (2011). Focused-ultrasound disruption of the blood-brain barrier using closely-timed short pulses: influence of sonication parameters and injection rate. *Ultrasound Med. Biol.* 37, 587–594. doi: 10.1016/j.ultrasmedbio.2011.01.008

Pardridge, W. M. (2002). Blood-brain barrier drug targeting enables neuroprotection in brain ischemia following delayed intravenous administration of neurotrophins. *Adv. Exp. Med. Biol.* 513, 397–430. doi: 10.1007/978-1-4615-0123-7_15

Pardridge, W. M. (2005). The blood-brain barrier and neurotherapeutics. *NeuroRx* 2, 1–2. doi: 10.1602/neurorx.2.1.1

Park, J., Zhang, Y., Vykhodtseva, N., Jolesz, F. A., and McDannold, N. J. (2012). The kinetics of blood brain barrier permeability and targeted doxorubicin delivery into brain induced by focused ultrasound. *J. Control. Release* 162, 134–142. doi: 10.1016/j.jconrel.2012.06.012

Raymond, S. B., Skoch, J., Hynynen, K., and Bacskai, B. J. (2007). Multiphoton imaging of ultrasound/Optison mediated cerebrovascular effects *in vivo*. *J. Cereb. Blood Flow Metab.* 27, 393–403. doi: 10.1038/sj.jcbfm.9600336

Ridet, J. L., Deglon, N., and Aebischer, P. (2000). Gene transfer techniques for the delivery of GDNF in Parkinson's disease. *Novartis Found Symp.* 231, 202–15; discussion 215–9, 302–306. doi: 10.1002/0470870834.ch13

Rodriguez, A., Tatter, S. B., and Debinski, W. (2015). Neurosurgical techniques for disruption of the blood-brain barrier for glioblastoma treatment. *Pharmaceutics* 7, 175–187. doi: 10.3390/pharmaceutics7030175

Samiotaki, G., Vlachos, F., Tung, Y. S., and Konofagou, E. E. (2012). A quantitative pressure and microbubble-size dependence study of focused ultrasound-induced blood-brain barrier opening reversibility *in vivo* using MRI. *Magn. Reson. Med.* 67, 769–777. doi: 10.1002/mrm.23063

Sboros, V. (2008). Response of contrast agents to ultrasound. *Adv. Drug Deliv. Rev.* 60, 1117–1136. doi: 10.1016/j.addr.2008.03.011

Schoknecht, K., David, Y., and Heinemann, U. (2015). The blood-brain barrier-gatekeeper to neuronal homeostasis: clinical implications in the setting of stroke. *Semin. Cell Dev. Biol.* 38, 35–42. doi: 10.1016/j.semcdb.2014.10.004

Shao, Y., and Le, W. (2019). Recent advances and perspectives of metabolomics-based investigations in Parkinson's disease. *Mol. Neurodegener.* 14:3. doi: 10.1186/s13024-018-0304-2

Sheikov, N., McDannold, N., Jolesz, F., Zhang, Y. Z., Tam, K., and Hynynen, K. (2006). Brain arterioles show more active vesicular transport of blood-borne tracer molecules than capillaries and venules after focused ultrasound-evoked opening of the blood-brain barrier. *Ultrasound Med. Biol.* 32, 1399–1409. doi: 10.1016/j.ultrasmedbio.2006.05.015

Sheikov, N., McDannold, N., Sharma, S., and Hynynen, K. (2008). Effect of focused ultrasound applied with an ultrasound contrast agent on the tight junctional integrity of the brain microvascular endothelium. *Ultrasound Med. Biol.* 34, 1093–1104. doi: 10.1016/j.ultrasmedbio.2007.12.015

Song, K. H., Fan, A. C., Hinkle, J. J., Newman, J., Borden, M. A., and Harvey, B. K. (2017). Microbubble gas volume: a unifying dose parameter in blood-brain barrier opening by focused ultrasound. *Theranostics* 7, 144–152. doi: 10.7150/thno.15987

Stride, E., and Saffari, N. (2003). Microbubble ultrasound contrast agents: a review. *Proc. Inst. Mech. Eng. H* 217, 429–447. doi: 10.1243/09544110360729072

Sun, T., Samiotaki, G., Wang, S., Acosta, C., Chen, C. C., and Konofagou, E. E. (2015). Acoustic cavitation-based monitoring of the reversibility and permeability of ultrasound-induced blood-brain barrier opening. *Phys. Med. Biol.* 60, 9079–9094. doi: 10.1088/0031-9155/60/23/9079

Sweeney, M. D., Kisler, K., Montagne, A., Toga, A. W., and Zlokovic, B. V. (2018). The role of brain vasculature in neurodegenerative disorders. *Nat. Neurosci.* 21, 1318–1331. doi: 10.1038/s41593-018-0234-x

Thevenot, E., Jordao, J. F., O'Reilly, M. A., Markham, K., Weng, Y. Q., Foust, K. D., et al. (2012). Targeted delivery of self-complementary adeno-associated virus serotype 9 to the brain, using magnetic resonance imaging-guided focused ultrasound. *Hum. Gene Ther.* 23, 1144–1155. doi: 10.1089/hum.2012.013

Ting, C. Y., Fan, C. H., Liu, H. L., Huang, C. Y., Hsieh, H. Y., Yen, T. C., et al. (2012). Concurrent blood-brain barrier opening and local drug delivery using drug-carrying microbubbles and focused ultrasound for brain glioma treatment. *Biomaterials* 33, 704–712. doi: 10.1016/j.biomaterials.2011.09.096

Treat, L. H., McDannold, N., Vykhodtseva, N., Zhang, Y., Tam, K., and Hynynen, K. (2007). Targeted delivery of doxorubicin to the rat brain at therapeutic levels using MRI-guided focused ultrasound. *Int. J. Cancer* 121, 901–907. doi: 10.1002/ijc.22732

Treat, L. H., McDannold, N., Zhang, Y., Vykhodtseva, N., and Hynynen, K. (2012). Improved anti-tumor effect of liposomal doxorubicin after targeted blood-brain barrier disruption by MRI-guided focused ultrasound in rat glioma. *Ultrasound Med. Biol.* 38, 1716–1725. doi: 10.1016/j.ultrasmedbio.2012.04.015

Tsai, C. H., Zhang, J. W., Liao, Y. Y., and Liu, H. L. (2016). Real-time monitoring of focused ultrasound blood-brain barrier opening via subharmonic acoustic emission detection: implementation of confocal dual-frequency piezoelectric transducers. *Phys. Med. Biol.* 61, 2926–2946. doi: 10.1088/0031-9155/61/7/2926

Unger, E. C., Porter, T., Culp, W., Labell, R., Matsunaga, T., and Zutshi, R. (2004). Therapeutic applications of lipid-coated microbubbles. *Adv. Drug Deliv. Rev.* 56, 1291–1314. doi: 10.1016/j.addr.2003.12.006

Upadhyay, R. K. (2014). Drug delivery systems, CNS protection, and the blood brain barrier. *Biomed Res. Int.* 2014:869269. doi: 10.1155/2014/869269

Vlachos, F., Tung, Y. S., and Konofagou, E. (2011). Permeability dependence study of the focused ultrasound-induced blood-brain barrier opening at distinct pressures and microbubble diameters using DCE-MRI. *Magn. Reson. Med.* 66, 821–830. doi: 10.1002/mrm.22848

Vykhodtseva, N. I., Hynynen, K., and Damianou, C. (1995). Histologic effects of high intensity pulsed ultrasound exposure with subharmonic emission in rabbit brain *in vivo*. *Ultrasound Med. Biol.* 21, 969–979. doi: 10.1016/0301-5629(95)00038-S

Wang, P. H., Liu, H. L., Hsu, P. H., Lin, C. Y., Wang, C. R., Chen, P. Y., et al. (2012). Gold-nanorod contrast-enhanced photoacoustic micro-imaging of focused-ultrasound induced blood-brain-barrier opening in a rat model. *J. Biomed. Opt.* 17:061222. doi: 10.1117/1.JBO.17.6.061222

Wang, S., Olumolade, O. O., Sun, T., Samiotaki, G., and Konofagou, E. E. (2015). Noninvasive, neuron-specific gene therapy can be facilitated by focused ultrasound and recombinant adeno-associated virus. *Gene Ther.* 22, 104–110. doi: 10.1038/gt.2014.91

Warren, K. E. (2018). Beyond the blood:brain barrier: the importance of Central Nervous System (CNS) pharmacokinetics for the treatment of CNS tumors, including diffuse intrinsic pontine glioma. *Front. Oncol.* 8:239. doi: 10.3389/fonc.2018.00239

Wei, K. C., Chu, P. C., Wang, H. Y., Huang, C. Y., Chen, P. Y., Tsai, H. C., et al. (2013a). Focused ultrasound-induced blood-brain barrier opening to enhance temozolomide delivery for glioblastoma treatment: a preclinical study. *PLoS ONE* 8:e58995. doi: 10.1371/journal.pone.0058995

Wei, K. C., Tsai, H. C., Lu, Y. J., Yang, H. W., Hua, M. Y., Wu, M. F., et al. (2013b). Neuronavigation-guided focused ultrasound-induced blood-brain barrier opening: a preliminary study in swine. *AJNR Am. J. Neuroradiol.* 34, 115–120. doi: 10.3174/ajnr.A3150

Westphal, M., Hilt, D. C., Bortey, E., Delavault, P., Olivares, R., Warnke, P. C., et al. (2003). A phase 3 trial of local chemotherapy with biodegradable carmustine (BCNU) wafers (Gliadel wafers) in patients with primary malignant glioma. *Neuro-oncology* 5, 79–88. doi: 10.1093/neuonc/5.2.79

Wu, S. K., Chu, P. C., Chai, W. Y., Kang, S. T., Tsai, C. H., Fan, C. H., et al. (2017). Characterization of different microbubbles in assisting focused ultrasound-induced blood-brain barrier opening. *Sci. Rep.* 7:46689. doi: 10.1038/srep 46689

Wu, S. Y., Aurup, C., Sanchez, C. S., Grondin, J., Zheng, W., Kamimura, H., et al. (2018). Efficient blood-brain barrier opening in primates with neuronavigation-guided ultrasound and real-time acoustic mapping. *Sci. Rep.* 8:978. doi: 10.1038/s41598-018-25904-9

Wu, S. Y., Sanchez, C. S., Samiotaki, G., Buch, A., Ferrera, V. P., and Konofagou, E. E. (2016). Characterizing focused-ultrasound mediated drug delivery to the heterogeneous primate brain *in vivo* with acoustic monitoring. *Sci. Rep.* 6, 37094. doi: 10.1038/srep37094

Xia, J., Tsui, P. H., and Liu, H. L. (2016). Low-pressure burst-mode focused ultrasound wave reconstruction and mapping for blood-brain barrier opening: a preclinical examination. *Sci. Rep.* 6:27939. doi: 10.1038/srep 27939

Yang, F. Y., Chen, Y. W., Chou, F. I., Yen, S. H., Lin, Y. L., and Wong, T. T. (2012). Boron neutron capture therapy for glioblastoma multiforme: enhanced drug delivery and antitumor effect following blood-brain barrier disruption induced by focused ultrasound. *Future Oncol.* 8, 1361–1369. doi: 10.2217/fon.12.118

Yang, F. Y., Fu, W. M., Chen, W. S., Yeh, W. L., and Lin, W. L. (2008). Quantitative evaluation of the use of microbubbles with transcranial focused ultrasound on blood-brain-barrier disruption. *Ultrason. Sonochem.* 15, 636–643. doi: 10.1016/j.ultsonch.2007.08.003

Yoon, Y. I., Kwon, Y. S., Cho, H. S., Heo, S. H., Park, K. S., Park, S. G., et al. (2014). Ultrasound-mediated gene and drug delivery using a microbubble-liposome particle system. *Theranostics* 4, 1133–1144. doi: 10.7150/thno.9945

Zhao, Z., Nelson, A. R., Betsholtz, C., and Zlokovic, B. V. (2015). Establishment and dysfunction of the blood-brain barrier. *Cell* 163, 1064–1078. doi: 10.1016/j.cell.2015.10.067

Conflict of Interest Statement: H-LL serves as the technical consultant of NaviFUS Inc. Taiwan.

The remaining authors declare that the research was conducted in the absence of any commercial or financial relationships that could be construed as a potential conflict of interest.

frontiers in Pharmacology

ORIGINAL RESEARCH
published: 11 February 2019
doi: 10.3389/fphar.2019.00104

Pelvic Ultrasound in Diagnosing and Evaluating the Efficacy of Gonadotropin-Releasing Hormone Agonist Therapy in Girls With Idiopathic Central Precocious Puberty

*Hong-kui Yu[1,2], Xiao Liu[2], Jia-kun Chen[2], Shan Wang[2] and Xian-yue Quan[1]**

[1] Department of Radiology, Zhujiang Hospital, Southern Medical University, Guangzhou, China, [2] Department of Ultrasonography, Shenzhen Children's Hospital, Shenzhen, China

OPEN ACCESS

Edited by:
Xiaobing Wang,
Shaanxi Normal University, China

Reviewed by:
Fajin Dong,
Shenzhen People's Hospital, China
Chin Moi Chow,
University of Sydney, Australia

***Correspondence:**
Xian-yue Quan
quanxianyue2014@163.com

Specialty section:
This article was submitted to Translational Pharmacology, a section of the journal Frontiers in Pharmacology

Received: *25 November 2018*
Accepted: *25 January 2019*
Published: *11 February 2019*

Citation:
Yu H-k, Liu X, Chen J-k, Wang S and Quan X-y (2019) Pelvic Ultrasound in Diagnosing and Evaluating the Efficacy of Gonadotropin-Releasing Hormone Agonist Therapy in Girls With Idiopathic Central Precocious Puberty. Front. Pharmacol. 10:104. doi: 10.3389/fphar.2019.00104

Background and Objective: Idiopathic central precocious puberty (ICPP) is characterized by early pubertal changes, the acceleration of growth velocity, and rapid bone maturation that often results in reduced adult height. Gonadotrophin-releasing hormone agonist (GnRHa) is currently considered to be an effective therapeutic agent. At present, GnRH stimulation test is adopted as a gold standard for the diagnosis of ICPP and the efficacy evaluation of GnRHa therapy. However, it is difficult to operate in practice due to the cumbersome procedures and multiple blood samples required. This study was conducted to establish the value of pelvic ultrasound in diagnosing ICPP and evaluating the efficacy of GnRHa therapy.

Materials and Methods: One hundred and twenty-two girls with ICPP (ICPP group) were enrolled in the study. Pelvic ultrasound and levels of luteinizing hormone (LH) and follicle-stimulating hormone (FSH) were examined before and after GnRHa therapy for 3 months. Eighty normal prepubertal girls were enrolled as the control group. The difference in pelvic ultrasound parameters between the ICPP group before GnRHa therapy and the control group was compared by independent-sample *t*-test, while paired *t*-test for ICPP group before and after GnRHa therapy. Receiver operating characteristic (ROC) curve was used to explore the optimal pelvic ultrasound parameters for diagnosing ICPP. Pearson correlation analysis was performed between the pelvic ultrasound parameters and serum sexual hormone level.

Results: The pelvic ultrasound parameters (length of the uterine body, anteroposterior diameter of the uterine body, transverse diameter of the uterine body, volume of the uterine body, uterine body-cervix ratio, length of the ovary, transverse diameter of the ovary, anteroposterior diameter of the ovary, volume of the ovary, number of increased follicles and maximum diameter of the follicle) in the ICPP group before GnRHa therapy were significantly larger than those of the control group ($P < 0.05$). All the above pelvic ultrasound parameters in the ICPP group were significantly decreased after GnRHa

therapy compared with those before treatment ($P < 0.05$). The volume of the uterine body had the largest area under the ROC curve in differentiating between patients with ICCP and the control group. Pelvic ultrasound parameters were significantly correlated with serum sexual hormone levels ($P < 0.05$).

Conclusion: This study indicates pelvic ultrasound is a simple and reliable tool to diagnose ICPP and evaluates the efficacy of GnRHa therapy by dynamically observing the morphology of internal genitalia. The volume of uterine body was the best ultrasound parameter to distinguish patients with ICPP from normal girls.

Keywords: ultrasonography, uterus, ovary, isosexual precocity, sexual characteristics

INTRODUCTION

Central precocious puberty is a condition characterized by early pubertal changes, the acceleration of growth velocity, and rapid bone maturation (Kaplowitz and Oberfield, 1999). The incidence of precocious puberty in children is on the rise year by year due to the influence of environment, food and social factors (Muir, 2006). Precocious puberty can be divided into central precocious puberty and peripheral precocious puberty according to pathogenesis. The most common type is idiopathic central precocious puberty (ICPP) (Chemaitilly et al., 2001). In girls, ICPP is caused by an increase in gonadotropin-releasing hormone (GnRH), due to early activation of the hypothalamic-pituitary-gonadal axis before the age of 8, which results in the development of the sexual organs and secondary sexual characteristics (Merke and Cutler, 1996). Without physical and mental maturity, the early onset of second sexual characteristics often cause fear, inferiority, anxiety and other adverse psychological problems, and can even lead to social problems and mental burdens to the parents. Additionally, due to accelerated skeletal growth and premature closure of the epiphysis, patients tend to be taller at the beginning, but shorter than normal adults when they grow up (Franceschi et al., 2010). Therefore, early diagnosis and treatment are essential (Rodriguez-Macias et al., 1999). Gonadotrophin-releasing hormone agonist (GnRHa) is currently considered to be an effective therapeutic agent (Latronico et al., 2016). Monitoring is required during GnRHa therapy to prevent ineffective administration caused by various factors. It is not convincing just to monitor blood levels of hormones such as luteinizing hormone (LH) and follicle-stimulating hormone (FSH) or physically examine the secondary sexual characteristics (Antoniazzi and Zamboni, 2004). The diagnosis of CPP and the efficacy of GnRHa therapy are both evaluated by GnRH stimulation tests as a gold standard so far (Lee, 1994; Choi et al., 2007). However, GnRH stimulation test is a cumbersome procedure with multiple invasive blood samplings, which are painful and expensive (Calcaterra et al., 2009).

Pelvic ultrasound can observe the size and structure of internal genitalia in girls, and can be used for the diagnosis and differential diagnosis of CPP, especially when the results of the GnRH stimulation test are ambiguous (de Vries et al., 2006; Badouraki et al., 2008; de Vries and Phillip, 2011a; Wen et al., 2018), and the operation is simple, non-invasive and easy to be accepted by children and their parents (Ziereisen et al., 2005). Up to now, a few literatures have reported the value of pelvic ultrasound in monitoring GnRHa therapy in girls with ICPP (Hall et al., 1986; Ambrosino et al., 1994; Jensen et al., 1998; de Vries and Phillip, 2011b), with limited cases (less than 30), and most of the literatures were published about a decade ago. There is also limited research data from China. Moreover, there is some controversy regarding which is the best parameter of pelvic ultrasound in evaluating the suppression of the hypothalamic-pituitary-gonadal axis. Ambrosino et al. suggested that ovarian volume changes can best reflect the efficacy of treatment (Ambrosino et al., 1994). However, de Vries and Phillip found that uterine parameters and absence of endometrial echo were better indicators of adequate suppression than ovarian parameters (de Vries and Phillip, 2011b). Therefore, this study was conducted to establish the value of pelvic ultrasound in diagnosing ICPP and evaluating the efficacy of GnRHa therapy.

MATERIALS AND METHODS

Patients

All the girls enrolled in the ICPP group in this study had been clinically diagnosed as ICPP and received GnRHa treatment in our hospital from August 2013 to August 2018. The average age was (8.27 ± 0.72) years. ICPP was diagnosed according to the following criteria: (1) objective breast enlargement before 8 years of age, accompanied by the presence of one or more of the following findings: menses, pubic hair, accelerated growth velocity, (2) bone age that exceeds chronological age by at least 1 year, and (3) increased pubertal LH response (cutoff value $\geq$ 5 IU/L) on an immunoradiometric assay (IRMA) and LH-FSH ratio $>$ 0.66 during GnRH stimulation test (Carel et al., 2009). The inclusion criteria included: patients diagnosed as ICPP, received GnRHa treatment, followed-up for at least 3 months, with intact clinical data. Patients with precocious puberty caused by tumor, organic disease, endocrine disease, simple premature breast development, a rare syndrome, misuse of contraceptives or other exogenous hormones were all excluded. Patients with poor ultrasound image quality or incomplete clinical data were also excluded. Pelvic ultrasound, GnRH stimulation test and sexual hormone levels were performed before GnRHa treatment and again 3 months after treatment.

Eighty normal prepubertal girls were enrolled in the control group. The controls were invited to participate in the study by the research staff. They were screened through studying their clinical history and through physical examination. All girls in the control group underwent pelvic ultrasound.

The body weights and heights of all subjects were measured, and the body mass indices (BMI) were calculated accordingly.

The ethics committee of our hospital approved the study and all parents of the patients gave informed written consent.

Pelvic Ultrasound

Transabdominal pelvic ultrasound was performed using a GE LogiQ E9 ultrasound set (GE Medical Systems Inc., Ltd, United States), equipped with a 3–5 MHz convex-array broad-band transducer and a 9 MHz linear-array small parts transducer. Pelvic ultrasound was performed by experienced physicians with more than 3 years experience, who were blinded to the condition of the subjects. Oral intake of fluids was prescribed to all girls to obtain a moderately filled bladder, which serves as an acoustic window to view the pelvic organs and pushes the air-filled bowels aside. Scans of the ovaries and uterus were obtained carefully in both sagittal and transverse planes. The transducer was angled obliquely from multiple directions to improve visualization of the uterus and ovaries until optimal images were achieved.

After obtaining satisfactory ultrasound images of the uterus, the length, anteroposterior diameter and transverse diameter of uterus body, as well as the length of the cervix and the endometrial bilaminar thickness was measured. The uterus body-cervix ratio was calculated. The length, anteroposterior diameter and transverse diameter of ovaries were measured based on the optimal images of the ovaries. Increased follicle was defined as the diameter greater than 4 mm. The maximum diameter of the follicle and number of increased follicles were also recorded. Each data was measured three times and the average value was taken as the final measurement value. The uterine and ovarian volume was calculated by the formula: Volume = length × anteroposterior diameter × transverse diameter × 0.5233. There was no significant difference in the size of the bilateral ovaries (Wen et al., 2018). Therefore, the average of the bilateral ovaries was calculated for statistical analysis.

Ten randomly selected subjects underwent ultrasound examinations on the same occasion by two experienced operators who were unaware of the other's results for reproducibility analysis.

Measurement of Serum Sexual Hormones During the GnRHa Stimulation Test

The peak concentration of serum LH and FSH were measured before and after the GnRHa therapy. On an empty stomach in the morning, the patients were subcutaneously injected with Gonadorelin at a dose of 2.5∼3.0 μg/kg at the beginning of the GnRHa stimulation test. Blood samples (3 ml each time) were taken before (0 min) and after the test (30, 60, 90 min), and the levels of sexual hormones were determined by immunochemiluminescence (DX800; Beckman Coulter, Inc., CA, United States).

The GnRHa Therapy

All children diagnosed as ICPP were treated with Triptorelin (produced by France's Beaufort-Ipson Pharmaceutical Co., Ltd.), which was injected intramuscularly once every 4 weeks, 100 μg /kg each time. The maximum dosage was 3.75 mg. The dosage was adjusted according to the clinical symptoms of the children (Cirpan et al., 2013).

Statistical Analysis

All statistical analyses were performed using SPSS version 19.0 (SPSS, Inc., Chicago, IL, United States). Measurement data were expressed as mean ± SD (standard deviation). The normal distribution test was conducted in the all pelvic ultrasound parameters. Independent-sample *t*-test was used to compare the difference of pelvic ultrasound parameters between the ICPP group before GnRHa therapy and the control group. Paired *t*-test was used to compare the difference in pelvic ultrasound parameters between ICPP group before and after GnRHa therapy. Receiver operating characteristic (ROC) curve was used to explore the optimal pelvic ultrasound parameters for distinguishing patients with ICPP from the normal population. Pearson correlation analysis was used to analyze the correlation between uterine and ovarian structural parameters and serum sex hormone levels before and after treatment. Two-tailed p values < 0.05 were considered statistically significant.

RESULTS

General Information

A total of 122 girls were initially enrolled as ICPP group, and 3 cases of them were excluded due to poor ultrasound image quality, then 119 patients were eventually studied. There was no difference in age, height, weight and BMI between the ICPP group and the control group ($p > 0.05$) (**Table 1**). Compared with before GnRHa therapy, there was no significant difference in height and BMI after treatment ($p > 0.05$). Five patients had menstruation before treatment, and no menstruation existed in girls within the ICPP group after treatment. Before treatment, the Tanner stages of the breast in girls of the ICPP group were stage 2($n = 59$), stage 3($n = 54$) and stage 4($n = 6$). After treatment, the breast development was inhibited to varying degrees, with Tanner stage 1($n = 14$), stage 2($n = 77$), and stage 3($n = 28$).

LH Hormones and LH/FSH Ratio Before and After GnRHa Therapy

The LH level was significantly decreased after GnRHa therapy compared to before the therapy (22.48 ± 14.27 mIU/ml, vs. 1.06 ± 0.76 mIU/ml, $p < 0.001$). The LH/FSH was also significantly decreased after GnRHa therapy compared to before the therapy (1.45 ± 0.69, vs. 0.49 ± 0.27, $p < 0.001$).

TABLE 1 | Comparisons of demographic data among ICPP patients before GnRHa therapy, ICPP patients after GnRHa therapy and normal controls.

Variables	Control subjects (n = 80)	ICPP before GnRHa therapy (n = 119)	ICPP after GnRHa therapy (n = 119)
Age (year)	8.41 ± 0.98	8.27 ± 0.72	8.52 ± 0.72[a]
Height (cm)	135.27 ± 4.43	135.02 ± 6.05	135.20 ± 6.04
Weight (kg)	33.41 ± 4.66	32.18 ± 6.11	33.10 ± 5.99
BMI (kg/m^2)	19.18 ± 3.23	18.60 ± 5.79	18.52 ± 2.36

Values are given as mean ± SD.
[a]*Statistically significant compared with ICPP before GnRHa therapy.*

Pelvic Ultrasound

The pelvic ultrasound parameters, including length of the uterine body, anteroposterior diameter of the uterine body, transverse diameter of the uterine body, volume of the uterine body, uterine body-cervix ratio, length of the ovary, transverse diameter of the ovary, anteroposterior diameter of the ovary, volume of the ovary, number of increased follicles and maximum diameter of the follicle, in the ICPP group before GnRHa therapy were significantly larger than those of control group ($P < 0.05$). All the above pelvic ultrasound parameters in the ICPP group were significantly decreased after GnRHa therapy compared with parameters before treatment ($P < 0.05$) (**Table 2**). Endometrial bilaminar thickening was observed in 6 ICPP patients. The thickness of endometrium was between 3 and 6 mm, and the thickened endometrium was not detected in any of the patients after GnRHa therapy. The typical sonograms of the uterus and ovaries of patients before and after GnRHa therapy are shown in **Figure 1**. The intraclass correlation coefficients between two observers of all of the above pelvic ultrasound parameters were 0.93–0.98 ($p < 0.001$ for all).

ROC Analysis

The area under the ROC curve of pelvic ultrasound parameters are shown in **Table 3** and **Figure 2**. The volume of the uterine body had the largest area under the curve in differentiating between patients with ICPP and normal girls. With the cutoff value of 1.01 cm^3, the sensitivity and specificity in the diagnosis of ICPP were 91.6 and 68.7%, respectively.

Correlation Between Sexual Hormone Levels and Ultrasound Parameters

Pearson correlation analysis showed that the pelvic ultrasound parameters were significantly correlated with serum sexual hormone levels ($P < 0.05$) (**Table 4**).

DISCUSSION

In the present study, our findings showed that the level of serum sexual hormones decreased, which confirmed that GnRHa therapy was effective in girls with ICPP. A significant reduction in uterine and ovarian dimensions derived from pelvic ultrasound after GnRHa therapy was also discovered. The volume of uterine body had the highest discriminative ability to separate patients with ICPP from normal girls. The sensitivity and specificity in the diagnosis of ICPP were 91.6 and 68.7%, respectively, with the cutoff value of 1.01 cm^3. The pelvic ultrasound parameters were significantly correlated with serum sexual hormone levels in the ICPP group before and after GnRHa therapy.

In this study, we found that the uterus, ovaries and the follicles were enlarged in the ICPP group before GnRHa therapy, which

TABLE 2 | Comparisons of uterine and ovarian parameters among ICPP patients before GnRHa therapy, ICPP patients after GnRHa therapy and normal controls.

Variables	Control subjects (n = 80)	ICPP before GnRHa therapy (n = 119)	ICPP after GnRHa therapy (n = 119)
Length of the Uterine body (cm)	2.02 ± 0.25	2.57 ± 0.47[a]	2.21 ± 0.28[b,c]
Anteroposterior diameter of the uterine body (cm)	1.10 ± 0.19	1.58 ± 0.42[a]	1.27 ± 0.25[b,c]
Length of the uterine body (cm)	2.02 ± 0.25	2.57 ± 0.47[a]	2.21 ± 0.28[b,c]
Anteroposterior diameter of the uterine body (cm)	1.10 ± 0.19	1.58 ± 0.42[a]	1.27 ± 0.25[b,c]
Transverse diameter of the uterine body (cm)	0.79 ± 0.18	1.21 ± 0.38[a]	0.91 ± 0.23[b,c]
Volume of the uterine body (cm^3)	0.96 ± 0.49	2.94 ± 2.28[a]	1.43 ± 0.90[b,c]
Uterine body-cervix ratio	1.19 ± 0.08	1.37 ± 0.14[a]	1.25 ± 0.09[b,c]
Length of the ovary (cm)	2.26 ± 0.31	2.67 ± 0.37[a]	2.32 ± 0.29[b]
Transverse diameter of the ovary (cm)	1.06 ± 0.17	1.35 ± 0.26[a]	1.09 ± 0.16[b]
Anteroposterior diameter of the ovary (cm)	0.91 ± 0.17	1.15 ± 0.17[a]	0.93 ± 0.13[b]
Volume of the ovary (cm^3)	1.19 ± 0.51	2.25 ± 0.88[a]	1.26 ± 0.41[b,c]
Number of increased follicles	1.19 ± 1.09	2.96 ± 0.84[a]	1.18 ± 1.16[b]
Maximum diameter of the follicle (mm)	3.45 ± 2.85	6.10 ± 1.18[a]	5.33 ± 0.89[b,c]

Values are given as mean ± SD.
[a,c]*Statistically significant compared with controls.*
[b]*Statistically significant compared with ICPP before GnRHa therapy.*

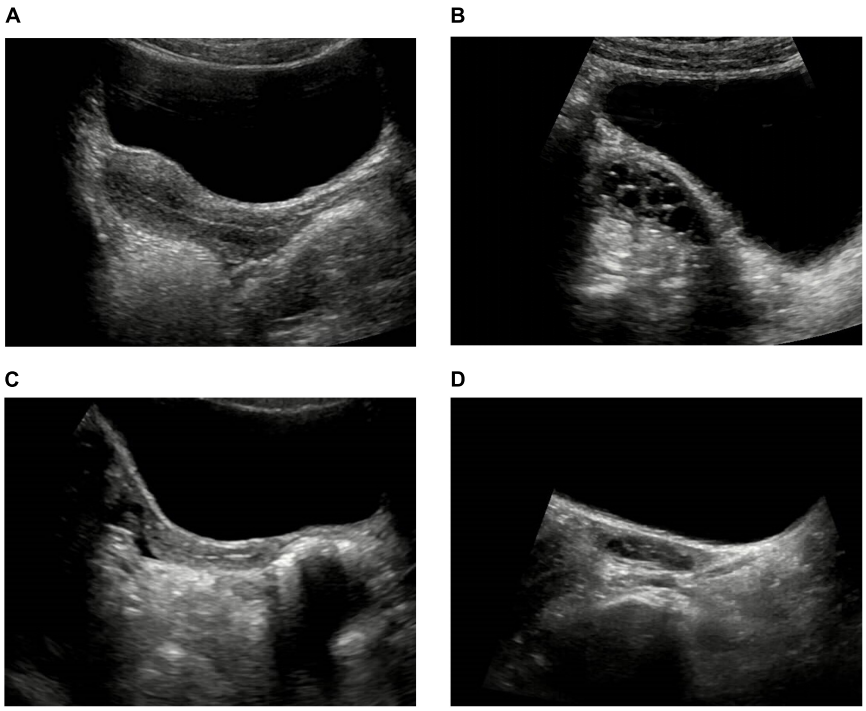

FIGURE 1 | Typical sonograms of the uterus and ovaries of a ICPP patient before and after GnRHa therapy. **(A,B)** Before GnRHa therapy: the length, anteroposterior diameter, transverse diameter, volume of the uterine body and the ovary, uterine body-cervix ratio were all increased. There were three increased follicles in the ovary, and the maximum diameter of follicle was 8 mm. **(C,D)** After GnRHa therapy: the length, anteroposterior diameter, transverse diameter, volume of the uterine body and the ovary, uterine body-cervix ratio were all decreased. There was no increased follicle in the ovary.

TABLE 3 | Receiver operative characteristic analyses of pelvic ultrasound parameters.

Parameter	Area under the curve	95% CI	Cutoff value	Sensitivity	Specificity
Length of the uterine body (cm)	0.871	0.822—0.920	2.15	82.4%	76.2%
Anteroposterior diameter of the uterine body (cm)	0.880	0.834—0.926	1.15	89.1%	65.0%
Transverse diameter of the uterine body (cm)	0.860	0.809—0.911	0.85	83.2%	71.2%
Volume of the uterine body (cm^3)	0.904	0.863—0.945	1.01	91.6%	68.7%
Uterine body-cervix ratio	0.876	0.829—0.923	1.25	79.0%	85.0%
Length of the ovary (cm)	0.812	0.749—0.875	2.38	81.5%	68.7%
Transverse diameter of the ovary (cm)	0.871	0.821—0.921	1.18	82.4%	68.7%
Anteroposterior diameter of the ovary (cm)	0.825	0.766—0.884	1.03	79.8%	72.5%
Volume of the ovary (cm^3)	0.871	0.822—0.921	1.43	89.1%	71.2%
Number of increased follicles	0.882	0.835—0.928	2.5	72.3%	87.5%
Maximum diameter of the follicle (mm)	0.622	0.533—0.712	5.5	63.9%	55.1%

was consistent with the previous study (Bridges et al., 1995). Another earlier study determined that ovarian enlargement was an important piece of evidence for the diagnosis of central precocious puberty (King et al., 1993), but the sample size of the study was limited. The results of this study showed that the ovarian volume of the girls with ICPP was significantly larger than that of the control group, and the number of follicles and maximum follicle diameter both increased, demonstrating the characteristics of ovarian maturation. The ovarian maturation was promoted by the increased secretion of FSH, therefore, the increase in bilateral ovarian volume is an important indicator of ICPP and will be useful for its diagnosis. However, the results of our study showed that the volume of the uterine body was the best indicator for the diagnosis of ICPP. We consider that our findings were consistent with the general rule of uterine and ovary development. As the development of the uterus is influenced by the sexual hormones secreted by the ovary, the increase in the uterine volume indicates that the ovary has developed. Therefore uterine enlargement provides a better diagnostic index than ovarian enlargement. According to our study, with a cutoff value of 1.01 cm^3 in the volume of uterine body to diagnose ICPP, the sensitivity and specificity are 91.6 and 68.7%, respectively. Wen et al. reported endometrial thickness was the best parameter for distinguishing CPP from normal girls in the 8–10 year interval,

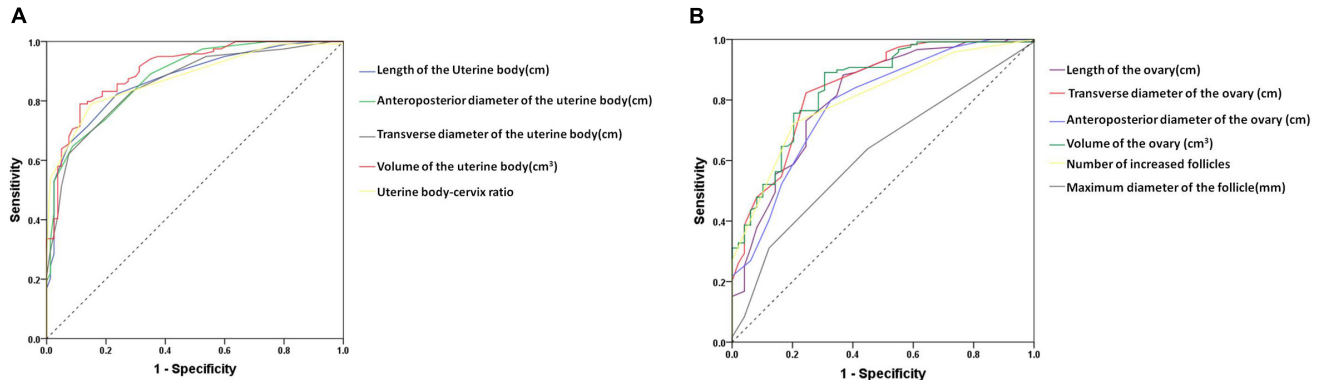

FIGURE 2 | The receiver-operating characteristic curve for the pelvic ultrasound parameters to distinguish between patients with ICPP and controls. **(A)** uterine parameters, **(B)** ovary parameters.

TABLE 4 | Correlation of the pelvic ultrasound parameters with serum sexual hormone levels in ICPP group before and after GnRHa therapy.

Variables	LH (mIU/ml)		*LH/FSH*	
	r	*P*	*r*	*P*
Length of the uterine body (cm)	0.411	<0.001*	0.380	<0.001*
Anteroposterior diameter of the uterine body (cm)	0.354	<0.001*	0.351	<0.001*
Transverse diameter of the uterine body (cm)	0.378	<0.001*	0.333	<0.001*
Volume of the uterine body (cm^3)	0.327	<0.001*	0.311	<0.001*
Uterine body-cervix ratio	0.327	<0.001*	0.395	<0.001*
Length of the ovary (cm)	0.324	<0.001*	0.420	<0.001*
Transverse diameter of the ovary (cm)	0.397	<0.001*	0.373	<0.001*
Anteroposterior diameter of the ovary (cm)	0.452	<0.001*	0.448	<0.001*
Volume of the ovary (cm^3)	0.452	<0.001*	0.486	<0.001*
Number of increased follicles	0.547	<0.001*	0.492	<0.001*
Maximum diameter of the follicle (mm)	0.431	<0.001*	0.337	<0.001*

**Statistically significant.*
LH, luteinizing hormone; FSH, follicle-stimulating hormone; r, Pearson correlation coefficient.

where a cutoff of 0.26 cm had a sensitivity of 76.92% and specificity of 100% (Wen et al., 2018). The cutoff values have a certain reference value for the diagnosis of CPP. However, as mentioned in previous studies (Eksioglu et al., 2013), there was a partial overlap between normally developed girls and CPP girls, and it could only be applied to girls of the age group involved in this study. Therefore, it is necessary to combine multiple ultrasound parameters with clinical manifestations and sexual hormone levels for the diagnosis of CPP.

GnRHa Is Currently the Top Choice for the Treatment of ICPP

Gonadotropin-releasing hormone (GnRH), also known as luteinizing hormone-releasing hormone (LHRH), is a decapeptide hormone secreted by the hypothalamus (Latronico et al., 2016). GnRH is secreted by pulses from the hypothalamus into the pituitary portal system, stimulating the synthesis and secretion of pituitary LH and FSH, thereby regulating the secretion of sex hormones. GnRHa is a structural analog synthesized through modifying the molecular structure of GnRH. It can help the children achieve their expected height in adulthood, by eliminating the symptoms of precocious puberty and slowing down the maturity process of bone. GnRHa can block the receptors of GnRH as an extrinsic GnRH analog, then the pituitary gland no longer responds to normal GnRH and the hypothalamic-pituitary-ovarian axis is blocked, resulting in reduced secretion of the sex hormones. After intramuscular administration of the slow-released dosage form, the medicine was steadily released for 28 days after an initial release phase. The most widely used drugs are Triptorelin and Leuprorelin in long-acting depot preparations, which are considered to be more effective than daily doses (Tatò et al., 2001). Depot preparations have fewer compliance problems compared with daily subcutaneous and nasal spray preparations (Tuvemo et al., 2002). The drug used in this study was Triptorelin.

We can infer whether the hypothalamic-pituitary-gonad axis is activated or not through the changes of the ultrasound parameters, which can indirectly reflect the serum sexual hormone levels (Jensen et al., 1998). To the authors' knowledge, this is the first comparative study, using large samples, studying

the application of pelvic ultrasound and assessing the efficacy of GnRHa in the treatment of girls with ICPP. In our study, 122 girls with ICPP were enrolled, and 119 girls with complete data were eventually analyzed. Previous investigators suggested that the uterine and ovarian structural parameters decreased rapidly after GnRHa treatment in 3 months but decreased slightly with the prolonged treatment (de Vries and Phillip, 2011b). Therefore, our study focused on the evaluation of the parameters of uterus and ovaries and the serum sexual hormone levels before and after treatment in 3 months, then compared the changes accordingly.

Our results indicated that the pelvic ultrasound parameters in the ICPP group were significantly decreased after GnRHa therapy for 3 months compared with that before treatment, indicating that the stimulation effect on the uterus and ovaries induced by excessive sex hormones was well controlled. The morphology of uterus and ovaries was restored to different degrees through the therapy. The results indicated that the ovarian and uterine morphological changes measured by pelvic ultrasound in ICPP patients before and after GnRHa therapy can indirectly reflect the changes in hypothalamic-pituitary-gonadal axis function. However, the uterus parameters after GnRHa therapy were still significantly increased compared with those in the control group, while most ovarian parameters, except for the volume of the ovary and maximum diameter of the follicle, had no significant difference. In other words, after 3 months' treatment, the ovaries shrink to normal size, while the uterus remains larger than normal. This might be attributable to the development of uterus being affected by ovarian hormones, therefore, the change in the uterus lags behind that of the ovaries. The pelvic ultrasound parameters were also consistent with the serum sexual hormone levels, demonstrating a good correlation. The LH peak level and the LH/FSH ratio in ICPP group were significantly increased under basic conditions. LH peak value and LH/FSH ratio were decreased after treatment compared to before treatment. After treatment, menstruation disappeared and the development of breast decreased in different degrees, however, there is no statistically significant change in height and BMI, which is consistent with a previous study (de Vries and Phillip, 2011b). This could be due to the fact that patients with ICPP tend to be taller at the beginning and shorter during the late phase, and patients in our study were at different stages of precocious puberty.

There were only six cases of endometrium thickening before treatment in the ICPP group in our study, and endometrium all disappeared after treatment. Some authors (de Vries and Phillip, 2011b) considered that the most significant response of treatment is the disappearance or reduction of endometrium. There were fewer cases with endometrial thickening in this study than in their study. The probable reason might be that patients in our study were in the primary stage of the disease with a relatively mild degree of development.

Ultrasound parameters were significantly correlated with serum sexual hormone levels before and after GnRHa therapy. The number of increased follicles had the best correlation with sexual hormone levels. This may indicate that the number of enlarged follicles is the most valuable parameter to reflect the changes after treatment. A few studies suggested that follicular development is not a good indicator of ovarian development (King et al., 1993). However, absence of visible cysts is a significant indicator of suppression (Ambrosino et al., 1994), and the number and size of stimulated follicles progressively approach those of the infantile ovary with suppression.

In brief, consistent with previous studies (Lekaemiri et al., 2014; Iannetta et al., 2015), our results indicated that pelvic ultrasound could dynamically monitor the therapeutic efficacy of GnRHa and provide reference for the clinical adjustment of follow-up treatment of ICPP. Pelvic ultrasonography provides a convenient and objective modality for monitoring pituitary-gonadal axis inhibition during ICPP therapy, which can lower the need for repetitive GnRH stimulation tests. It is helpful to confirm the efficiency of treatment. It could be a supplement of the GnRH stimulation test and more acceptable by ICPP girls and their parents. The advantages of pelvic ultrasound also include the ability to non-invasively and quickly evaluate the efficacy of the GnRHa therapy.

There were several limitations in our study, firstly that this was not a randomized controlled trial as the development stages of each patient were different. Secondly, although the sample size of this study was larger than most of previous studies, the age of patients in our study was concentrated between 6 and 10 years old. Normal reference values of uterus and ovary parameters for girls of all ages of puberty still need to be further explored. Thirdly, the follow-up time of girls with precocious puberty was short, and some were not followed up until drug withdrawal. The long-term application value of pelvic ultrasound in GnRHa therapy still needs to be further explored through prolonged follow-up time.

CONCLUSION

In conclusion, pelvic ultrasound is a simple, non-invasive and reproducible method for the diagnosis of ICPP. Pelvic ultrasound is also a reliable method for the evaluation of the efficacy of GnRHa treatment. Pelvic ultrasound could serve as a promising tool for the clinical diagnosis and treatment in girls with ICPP.

AUTHOR CONTRIBUTIONS

H-kY and XL carried out analysis and calculations of data, and contributed to the writing of the manuscript. SW and J-kC contributed to data collection and management. X-yQ designed and coordinated the project, contributed to the discussion, supervised and reviewed the writing of the manuscript. All authors read and approved the final manuscript.

ACKNOWLEDGMENTS

We thank to colleagues from department of endocrinology for their valuable support and comments.

REFERENCES

Ambrosino, M. M., Hernanz-Schulman, M., Genieser, N. B., Sklar, C. A., Fefferman, N. R., and David, R. (1994). Monitoring of girls undergoing medical therapy for isosexual precocious puberty. *J. Ultrasound Med.* 13, 501–508. doi: 10.7863/jum.1994.13.7.501

Antoniazzi, F., and Zamboni, G. (2004). Central precocious puberty: current treatment options. *Paediatr. Drugs* 6, 211–231. doi: 10.2165/00148581-200406040-00002

Badouraki, M., Christoforidis, A., Economou, I., Dimitriadis, A. S., and Katzos, G. (2008). Evaluation of pelvic ultrasonography in the diagnosis and differentiation of various forms of sexual precocity in girls. *Ultrasound Obstet. Gynecol.* 32, 819–827. doi: 10.1002/uog.6148

Bridges, N. A., Cooke, A., Healy, M. J., Hindmarsh, P. C., and Brook, C. G. (1995). Ovaries in sexual precocity. *Clin. Endocrinol.* 42, 135–140. doi: 10.1111/j.1365-2265.1995.tb01853.x

Calcaterra, V., Sampaolo, P., Klersy, C., Larizza, D., Alfei, A., Brizzi, V., et al. (2009). Utility of breast ultrasonography in the diagnostic work-up of precocious puberty and proposal of a prognostic index for identifying girls with rapidly progressive central precocious puberty. *Ultrasound Obstet. Gynecol.* 33, 85–91. doi: 10.1002/uog.6271

Carel, J. C., Eugster, E. A., Rogol, A., Ghizzoni, L., Palmert, M. R., Espe-Lwpes GnRH Analogs Consensus Conference Group, et al. (2009). Consensus statement on the use of gonadotropin-releasing hormone analogs in children. *Pediatrics* 123, e752–e762. doi: 10.1542/peds.2008-1783

Chemaitilly, W., Trivin, C., Adan, L., Gall, V., Sainte-Rose, C., and Brauner, R. (2001). Central precocious puberty: clinical and laboratory features. *Clin. Endocrinol.* 54, 289–294. doi: 10.1046/j.1365-2265.2001.01229.x

Choi, J. H., Shin, Y. L., and Yoo, H. W. (2007). Predictive factors for organic central precocious puberty and utility of simplified gonadotropin-releasing hormone tests. *Pediatr. Int.* 49, 806–810. doi: 10.1111/j.1442-200X.2007.02475.x

Cirpan, T., Akman, L., Yucebilgin, M. S., Terek, M. C., and Kazandi, M. (2013). Reproductive outcome after surgical treatment of endometriosis-retrospective analytical study. *Ginekol. Pol.* 84, 1041–1044. doi: 10.17772/gp/1677

de Vries, L., Horev, G., Schwartz, M., and Phillip, M. (2006). Ultrasonographic and clinical parameters for early differentiation between precocious puberty and premature thelarche. *Eur. J. Endocrinol.* 154, 891–898. doi: 10.1530/eje.1.02151

de Vries, L., and Phillip, M. (2011b). Pelvic ultrasound examination in girls with precocious puberty is a useful adjunct in gonadotrophin-releasing hormone analogue therapy monitoring. *Clin. Endocrinol.* 75, 372–377. doi: 10.1111/j.1365-2265.2011.04086.x

de Vries, L., and Phillip, M. (2011a). Role of pelvic ultrasound in girls with precocious puberty. *Horm. Res. Paediatr.* 75, 148–152. doi: 10.1159/000323361

Eksioglu, A. S., Yilmaz, S., Cetinkaya, S., Cinar, G., Yildiz, Y. T., and Aycan, Z. (2013). Value of pelvic sonography in the diagnosis of various forms of precocious puberty in girls. *J. Clin. Ultrasound* 41, 84–93. doi: 10.1002/jcu.22004

Franceschi, R., Gaudino, R., Marcolongo, A., Gallo, M. C., Rossi, L., Antoniazzi, F., et al. (2010). Prevalence of polycystic ovary syndrome in young women who had idiopathic central precocious puberty. *Fertil. Steril.* 93, 1185–1191. doi: 10.1016/j.fertnstert.2008.11.016

Hall, D. A., Crowley, W. F., Wierman, M. E., Simeone, J. F., and McCarthy, K. A. (1986). Sonographic monitoring of LHRH analogue therapy in idiopathic precocious puberty in young girls. *J. Clin. Ultrasound* 14, 331–338. doi: 10.1002/jcu.1870140503

Iannetta, R., Melo, A. S., Lannetta, O., Marchini, J. S., Paula, F. J., Martinelli, C. E., et al. (2015). Use of a Gonadotropin-releasing hormone analog to treat idiopathic central precocious puberty is not associated with changes in bone structure in postmenarchal adolescents. *J. Pediatr. Adolesc. Gynecol.* 28, 304–308. doi: 10.1016/j.jpag.2014.09.002

Jensen, A. M., Brocks, V., Holm, K., Laursen, E. M., and Müller, J. (1998). Central precocious puberty in girls: internal genitalia before, during, and after treatment with long-acting gonadotropin-releasing hormone analogues. *J. Pediatr.* 132, 105–108. doi: 10.1016/S0022-3476(98)70493-7

Kaplowitz, P. B., and Oberfield, S. E. (1999). Reexamination of the age limit for defining when puberty is precocious in girls in the United States: implications for evaluation and treatment. drug and therapeutics and executive committees of the lawson wilkins pediatric endocrine society. *Pediatrics* 104(4 Pt 1), 936–941. doi: 10.1542/peds.104.4.936

King, L. R., Siegel, M. J., and Solomon, A. L. (1993). Usefulness of ovarian volume and cysts in female isosexual precocious puberty. *J. Ultrasound Med.* 12, 577–581. doi: 10.7863/jum.1993.12.10.577

Latronico, A. C., Brito, V. N., and Carel, J. C. (2016). Causes, diagnosis, and treatment of central precocious puberty. *Lancet Diabetes Endocrinol.* 4, 265–274. doi: 10.1016/S2213-8587(15)00380-0

Lee, P. A. (1994). Laboratory monitoring of children with precocious puberty. *Arch. Pediatr. Adolesc. Med.* 148, 369–376. doi: 10.1001/archpedi.1994.02170040035006

Lekaemiri, S., Louizou, E., Kambouris, M., Chrousos, G., De Roux, N., and Kanaka-Gantenbein, C. (2014). Absence of GPR54 and TACR3 mutations in sporadic cases of idiopathic central precocious puberty. *Horm. Res. Paediatr.* 81, 177–181. doi: 10.1159/000356913

Merke, D. P., and Cutler, G. B. (1996). Evaluation and management of precocious puberty. *Arch. Dis. Child* 75, 269–271. doi: 10.1136/adc.75.4.269

Muir, A. (2006). Precocious puberty. *Pediatr. Rev.* 27, 373–381. doi: 10.1542/pir.27-10-373

Rodriguez-Macias, K. A., Thibaud, E., Houang, M., Duflos, C., Beldjord, C., and Rappaport, R. (1999). Follow up of precocious pseudopuberty associated with isolated ovarian follicular cysts. *Arch. Dis. Child.* 81, 53–56. doi: 10.1136/adc.81.1.53

Tatò, L., Savage, M. O., Antoniazzi, F., Buzi, F., Di, Maio S, Oostdijk, W., et al. (2001). Optimal therapy of pubertal disorders in precocious/early puberty. *J. Pediatr. Endocrinol. Metab.* 14(Suppl. 2), 985–995. doi: 10.1515/jpem-2001-s211

Tuvemo, T., Gustafsson, J., Proos, L. A., and Swedish Growth Hormone Group. (2002). Suppression of puberty in girls with short- acting intranasal versus subcutaneous depot GnRH agonist. *Horm. Res.* 57, 27–31. doi: 10.1159/000057943

Wen, X. D., Wen, D. G., Zhang, H., Zhang, H. F., and Yang, Y. (2018). Observational study pelvic ultrasound a useful tool in the diagnosis and differentiation of precocious puberty in Chinese girls. *Medicine* 97:e0092. doi: 10.1097/MD.0000000000010092

Ziereisen, F., Guissard, G., Damry, N., and Avni, E. F. (2005). Sonographic imaging of the paediatric female pelvis. *Eur. Radiol.* 15, 1296–1309. doi: 10.1007/s00330-005-2648-6

Conflict of Interest Statement: The authors declare that the research was conducted in the absence of any commercial or financial relationships that could be construed as a potential conflict of interest.

frontiers in Pharmacology

ORIGINAL RESEARCH
published: 26 March 2019
doi: 10.3389/fphar.2019.00267

Ultrasound-Guided Percutaneous Release of A1 Pulley by Using a Needle Knife: A Prospective Study of 41 Cases

Min Pan[1], *Shuya Sheng*[2], *Zhiqi Fan*[3], *Hao Lu*[1], *Hong Yang*[1], *Fei Yan*[4]* *and Zhansen E*[5]*

[1] *Shenzhen Hospital of Guangzhou University of Chinese Medicine, Shenzhen, China,* [2] *Shenzhen Middle School, Paul C. Lauterbur Research Center for Biomedical Imaging, Shenzhen, China,* [3] *College of Optoelectronic Engineering of Shenzhen University, SPACEnter Space Science and Technology Institute, Shenzhen, China,* [4] *Paul C. Lauterbur Research Center for Biomedical Imaging, Shenzhen Institutes of Advanced Technology (CAS), Shenzhen, China,* [5] *Longgang Central Hospital, Shenzhen, China*

Objective: The purpose of this study was to evaluate the efficacy of ultrasonography-guided percutaneous A1 pulley release with the needle knife for trigger finger.

Methods: The prospective study included 21 patients (21 fingers) who underwent blind release with the needle knife and 20 patients (20 fingers) who underwent ultrasonography-guided release with the needle knife. The thickness and width of A1 pulley, clinical grade before and after release, complications, and operation time were compared between the groups.

Results: The results showed that the ultrasonography-guided group had significantly better grade postoperatively and reached to 100% complete release in one time compared to the blind group ($p < 0.05$). Moreover, no any complications had been happened in the ultrasonography-guided group. A relatively longer operation time of the ultrasonography-guided group was observed compared to the time of the blind group.

Conclusions: The needle knife is a very good tool for release of triggering fingers. Ultrasound provides a direct and precise visualization of the thickness, width and location of A1 pulley lesion. The combined use of ultrasound and the needle knife can achieve the best result for trigger finger. Moreover, the combination changes the traditional opinion and operator-dependent mode that were once widely adopted in the hospital of Chinese Medicine.

Keywords: ultrasonography-guided, release, A1 pulley, needle knife, trigger finger

OPEN ACCESS

Edited by:
Ke-Vin Chang,
National Taiwan University Hospital, Taiwan

Reviewed by:
Wei-Ting Wu,
National Taiwan University Hospital Bei-Hu branch, Taiwan
Vincenzo Ricci,
University of Bologna, Italy

***Correspondence:**
Fei Yan
fei.yan@siat.ac.cn
Zhansen E
951436027@qq.com

Specialty section:
This article was submitted to Translational Pharmacology, a section of the journal Frontiers in Pharmacology

Received: *28 October 2018*
Accepted: *04 March 2019*
Published: *26 March 2019*

Citation:
Pan M, Sheng S, Fan Z, Lu H, Yang H, Yan F and E Z (2019) Ultrasound-Guided Percutaneous Release of A1 Pulley by Using a Needle Knife: A Prospective Study of 41 Cases. Front. Pharmacol. 10:267. doi: 10.3389/fphar.2019.00267

INTRODUCTION

Stenosing tenosynovitis, also called trigger finger (TF), is the snapping and locking of the finger, related mainly to an imbalance between the size of the flexor tendons and that of the tendon sheath (Yin and Guo, 2016; Nikolaou et al., 2017). The cause for TF is thickening of the A1 pulley due to excessive flexion and extension of digits, repeated friction between flexor tendon and tendon sheath, or failure in prompt treatment of palm skin injury. Patients with TF are often diagnosed clinically according to their medical histories, symptoms, and signs. Generally, mild cases are first treated conservatively, with oral anti-inflammatory drugs, physical therapy, or corticosteroid injections; while severe cases are often treated with an open surgical release, which is successful in 83∼98% of cases (Paulius and Maguina, 2009).

Blind percutaneous A1 pulley release was first described by Lorthior in 1958 (Paulius and Maguina, 2009). This operation can be done without any special preparation and can obtain the effect equal to that of an open procedure. Besides, this procedure has many advantages, including shorter recovery time, avoidance of scar tenderness, and application in the outpatient setting (Rajeswaran et al., 2009; Rojo-Manaute et al., 2010, 2012a,b; Smith et al., 2010). However, there is still a potential risk of damage to the tendon and neurovascular structures. Also, it is difficult to confirm whether the release is complete or not during operation because of invisualization directly (Lee et al., 2018).

Ultrasound has become widely accepted as an imaging modality in assessment of the musculoskeletal system, as it is quick, cheap, and readily available. Also, it has real-time, non-invasive and non-radiative advantages for musculoskeletal diseases by ultrasonography-guided treatment (Chang et al., 2017, 2018; Wu et al., 2018). To date, ultrasonography-guided percutaneous A1 pulley release has been introduced in this procedure, providing direct visualization of the vascular and nerve structures during the procedure (Hopkins and Sampson, 2014; Hoang et al., 2016; Lapègue et al., 2016; Rajeswaran et al., 2016; Guo et al., 2017). With the application of high-frequency ultrasonographic instrument, the flexor digitorum tendons, pulley systems, volar plate, metacarpophalangeal and interphalangeal joints can be clearly seen. Moreover, the TF pathologic anatomic structures identified by ultrasound are even far superior by MRI, especially in the dynamic evaluation. The ultrasonographic characteristics of TF are hypoechonic thickening of the A1 pulley, or increased Doppler flow and the fluid of surrounding tissues.

To facilitate surgeon manipulation, some simple clinical tools are developed for the A1 pulley surgical release, such as a 19 gauge needle or 21 gauge needle (Hoang et al., 2016; Lapègue et al., 2016; Rajeswaran et al., 2016; Guo et al., 2017). Lapègue et al. (2016) reported US-guided percutaneous release of the TF by using a 21-gauge needle, achieving an 81.7% complete resolved cases immediately after the procedure with minimal complications. However, it was reported that the gauge needles can be twisted easily and the sharp tip might increase the possibility of hurting the surrounding tissues. Specially designed knives have been used for percutaneous release, including the knife with a hook shape or with long body (Nikolaou et al., 2017; Lee et al., 2018). A success rate of 100% using this knife was achieved in ultrasonography-guided percutaneous release. However, the long body makes it difficult to control and the hook shape might hurt the tendon during operation. Moreover, the designed knife is not common everywhere.

The needle knife is a traditional tool of Chinese medicine which has been used widely by the rehabilitation doctors of China since thousands of years ago. TF is the preferred alternative for the needle knife (Ma and Wu, 2016). However, blind percutaneous release has several native problems. For example, inexperience of the operator and anatomical variation of the patient can lead to accidental injury to the flexor tendon or adjacent neurovascular bundles, as well as difficulty in determining the completeness of release. In addition, a vertical insertion from above the skin surface may increase the risk of nerve and the flexor tendon damage (Ma and Wu, 2016; Lee et al., 2018).

In this study, we attempted to evaluate the efficacy of ultrasonography-guided percutaneous A1 pulley release with the needle knife.

MATERIALS AND METHODS

Our clinical study was approved by the Research Ethics Committee of Shenzhen Hospital (Futian) of Guangzhou University of Chinese Medicine. All patients were conducted by a rehabilitation doctor (Shaoyang Cui, 10 years of experience)

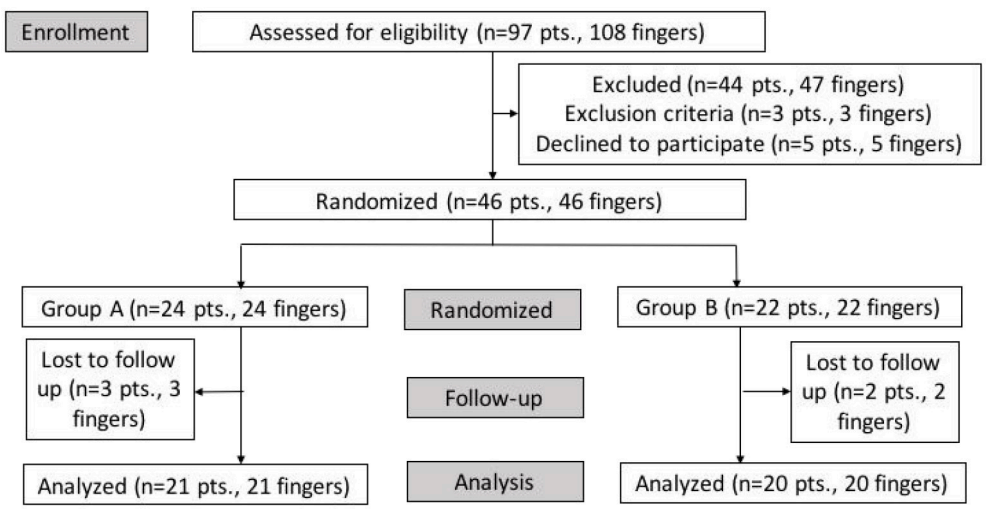

FIGURE 1 | Patients' flowchart.

and an interventional radiologist specializing in musculoskeletal ultrasound (Min Pan, 15 years of experience).

Study Population (Figure 1)

During a 12-month period starting in March 2017, 97 patients were enrolled in our prospective study. The range of age was from 45 to 72 years (average age 57 ± 8 years), with trigger finger, Grade II-IV.

The inclusion criterion was idiopathic trigger finger present for at least 3 months. The exclusion criteria were a previous history of open release for trigger finger, rheumatoid arthritis, a concomitant pathologic condition in hand at the first visit to the rehabilitation doctor, and A1 pulley thickness more than one finger.

After being diagnosed and graded by the Department of Rehabilitation, the patients were required to write informed consent at the first visit. Of 97 patients (108 fingers), 44 patients (47 fingers) were excluded due to an improvement in symptoms after conservative treatments or triggering more than one finger. And five patients (5 fingers) refused to participate in the clinical research. Three patients (3 fingers) were excluded due to rheumatic arthritis. Finally, a total of 46 patients (46 fingers) were included in this study. Patients were divided into two groups randomly. Twenty-four patients (24 fingers) included in group A underwent blind percutaneous A1 pulley release, while 22 patients (22 fingers) included in group B underwent ultrasonography-guided percutaneous A1 pulley release. A total of five patients were lost in the last follow-up. Thus, 21 patients (21 fingers) in group A and 20 patients (20 fingers) in group B were analyzed (**Table 1**).

The Clinical Diagnostic Criteria of TF

(1) The history of finger microtrauma or overuse; (2) Pain, tenderness, or palpable nodules at the proximal palmar crease; (3) Limited finger flexion and extension; (4) Positive value of flexor resistance test.

According to the degree of entrapment between the flexor digitorum tendon and tendon sheath, TF are divided into five grades (Lapègue et al., 2016; Lee et al., 2018) (clinical semi-quantitative evaluation criteria): (1) Grade 0: no triggering; (2) Grade 1: intermittent, moderate triggering; (3) Grade 2: continuous triggering that is eliminated with active extension; (4) Grade 3: triggering with flexion contracture that requires the patient to use the other hand to unlock the involved finger; (5) Grade 4: active flexion of finger is impossible.

Ultrasonic Examination

Aplio 500 (Toshiba company, linear array probe PLT-1005BT, frequency 5∼14 MHz) and Resona 7 (Mindray company, linear array probe L14-5WU, frequency 6.6∼14 MHz) ultrasound imaging machines were used.

The patients received ultrasound examine before release, day 0 and day 7 after release. Patients sat on the chair with palm up on the bed. The probe was placed on the metacarpophalangeal joints. The short and longitudinal axes were observed along the tender point and/or painful nodules. The dynamic examine was carried out as the flexion and extension of finger (see **Videos 3**, **4**). The thickened A1 pulley was measured and marked by ultrasound: (a) The thickness of A1 pulley in short axis. (b) The length of the thickened A1 pulley in longitudinal axis.

The Procedure of Release

Hanzhang needle knife (**Figure 2**, Beijing Huaxia Needle Knife Medical Equipment Factory) was used. All patients were treated with only needle knife, and no any other treatment such as local injection was used. The dynamic flexion and extension of fingers before and after release were recorded immediately (see **Video 2**). All patients were graded again by the semi-quantitative evaluation in day 0 and day 7 after release.

The group A followed three steps: (1) Fix point (**Figure 3**): The point was set proximally to avoid the painful nodule according to the anatomical landmarks and the marking entry point. (2) Fix orientation (**Figure 4**): The body of the needle knife was

TABLE 1 | Demographics of patients*.

	Group A (Blind release)	Group B (Ultrasonography-guided release)
Number of patients	21	20
Mean age (years)	56 ± 6 (47–67)	58 ± 10 (45–72)
Sex	F	F
Mean follow-up (weeks)	15.7 (15–18)	12.2 (12–13)
Digit involved Thumb/index/middle /ring/small	6/3/9/3/0	7/2/8/3/0
Thickness of A1 pulley by US (mm)	1.80 ± 0.44 (1.20–2.40)	1.49 ± 0.23 (1.10–1.80)
Width of A1 pulley by US (mm)	5.59 ± 0.76 (4.40–7.10)	5.29 ± 1.16 (5.00–6.30)

No significant differences between two groups.

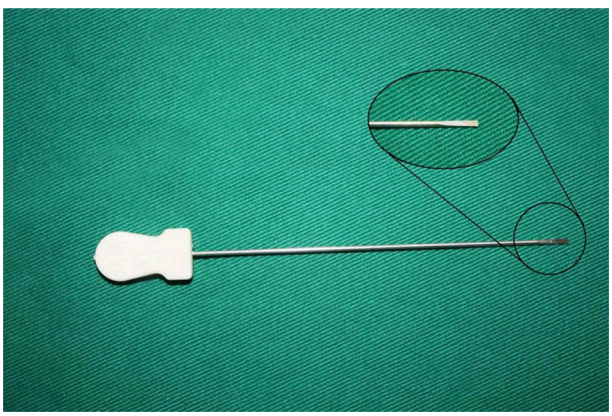

FIGURE 2 | The scheme of Hanzhang needle knife. The needle knife consists of three parts: tip, body and handle, with a 0.8 mm blade on the tip, and 40 mm length of the body. The tip can serve as a scalpel during release.

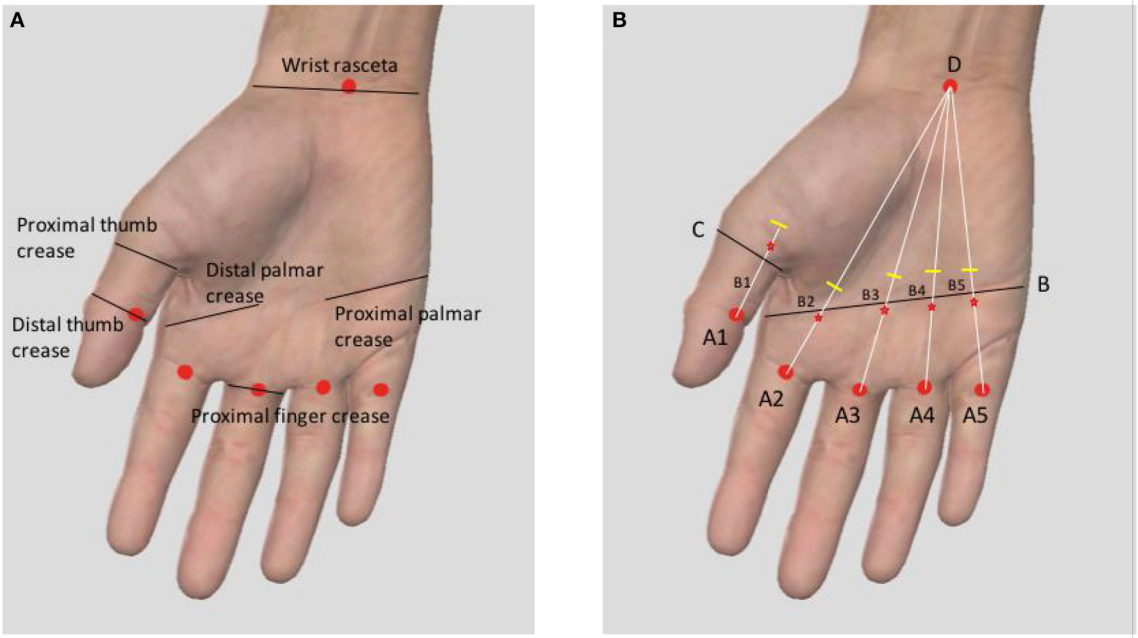

FIGURE 3 | (A) The anatomical landmark of entry point. **(B)** The marking method of the entry point (Triggering thumb: A straight line paralleling to the thumb from the midpoint A1 of the distal thumb crease is drawn. The line C is the transverse line of proximal thumb crease. B1 is the intersection point of A1 parallel line and C line. The entry point is +0.5 mm of B1 proximally. Triggering finger: A connection line is drawn between the midpoint of the proximal finger crease (A2∼A5) and D (the midpoint of wrist rasceta). Line B is drawn between the distal and proximal palmar creases. B2∼B5 are the intersection points of lines B and line AD. The entry point is −0.5 mm of B2∼B5 distally).

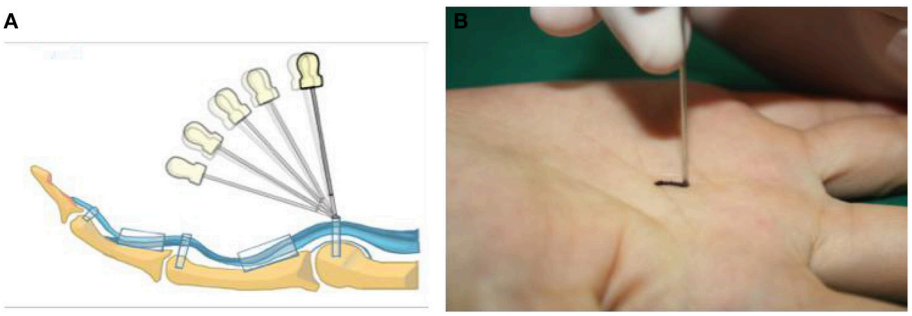

FIGURE 4 | The scheme **(A)** and spot **(B)** of the blind release.

perpendicular to the skin surface. The blade-edge line is parallel to the imaginary line of flexor tendon sheath; (3) Stab: The tip of the needle knife was stabbed into the skin quickly, and then entered into sheath slowly and carefully. For an operator, if a break is felt, he should stop piercing further, and start to cut 1.0∼1.5 mm proximally. Meanwhile, the handle of the needle knife is slightly tilted distally, shifting from an angle of 90° to 60° to 30° on the skin surface (**Figure 4A**). The total forward cutting number is five to six. In backward direction, five to six cuts are performed again along the marking orientation (A1 parallel line of thumb or a connection line AD of finger).

The group B were monitored by ultrasound during the whole procedure. The tip and body of the needle knife were parallel to the tendon (see **Video 1**) and (**Figures 6A,B**).

Statistical Analysis

The descriptive data were tested for normal distribution. Differences in clinical outcome were analyzed using the Student's *t*-test. A $p < 0.05$ was considered statistically significant. Data were expressed as mean ± standard deviation.

RESULTS

Age, mean follow-up, involvement of digit, and the thickness and width of A1 pulley were evaluated as demographic factors. No significant differences were found in demographic characteristics between two groups (**Table 1**).

No significant difference was found in the clinical grade of two groups before release (**Table 2**). Almost all patients showed

TABLE 2 | Type of Trigger Finger before Release, Day 0 and Day 7 after Release ($n = 41$).

Grade and type of trigger finger	Group A ($n = 21$)			Group B ($n = 20$)		
	Before release	Day 0 after release	Day 7 after release	Before release	Day 0 after release	Day 7 after release
Grade 0	0 (0)	0 (0)	4 (19.0)	0 (0)	11 (52.4)	20 (100.0)
Grade 1	0 (0)	16 (76.1)	15 (71.4)	0 (0)	8 (40.0)	0 (0)
Grade 2	2 (9.5)	3 (14.2)	0 (0)	2 (10.0)	1 (5.0)	0 (0)
Grade 3	8 (38.0)	1 (4.8)	1 (4.8)	10 (50.0)	0 (0)	0 (0)
Grade 4	11 (52.4)	1 (4.8)	1 (4.8)	8 (40.0)	0 (0)	0 (0)

Data in parentheses are percentages.

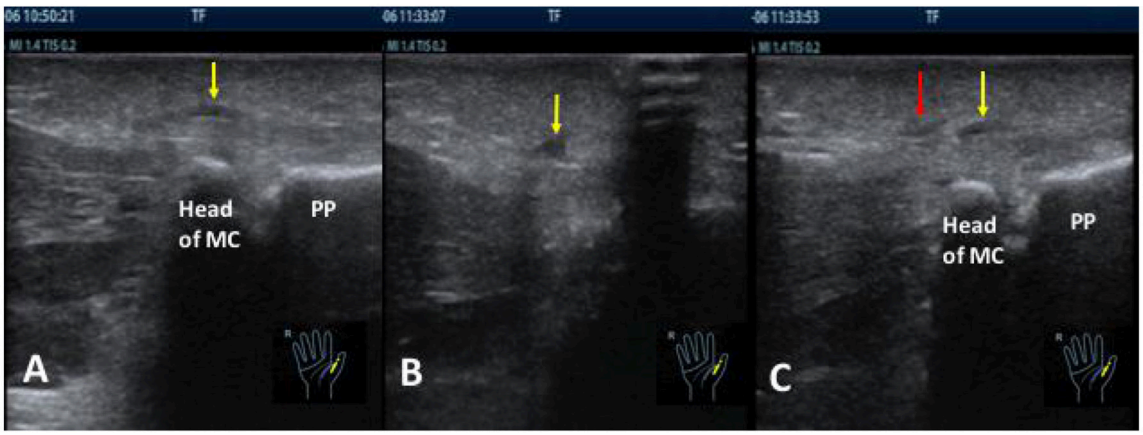

FIGURE 5 | The ultrasound images before **(A)** and after **(B,C)** release in the blind group. **(A)** The yellow arrow showed the thickness of A1 pulley in the right thumb before release. **(B)** The yellow arrow showed the fluid of the surrounding tissue immediately after release. **(C)** The red arrow was the wrong cutting direction after piercing into the skin from the marked entry point. The yellow arrow was the thickening location of A1 pulley. They were not at the same point. PP, proximal phalange, MC, metacarpal bone.

significant improvement in clinical grade after release ($p < 0.05$). In addition, the group B (the ultrasonography-guided group; **Figures 7A–C**). showed significantly better grade at day 0 and day 7 postoperatively compared with the group A (the blind group, $p < 0.05$).

Triggering disappeared in all patients who underwent ultrasonography-guided release, whereas mild triggering continued in 15 patients who underwent blind release at day 7. In 1 case of group A, no significant improvement was found in clinical grade before release, day 0 and day 7 after release. In one case of group A, the blade of the needle knife was deviated from the A1 pulley after incision, and the fluid of surrounding tissue was found immediately after release (**Figures 5A–C**). Ultrasonography-guided release was performed in these two patient at 4 weeks postoperatively.

A relatively longer operation time of the ultrasonography-guided group (15.21 ± 0.87 min) was observed compared to the time of the blind group (5.23 ± 0.55 min, $p < 0.05$).

DISCUSSION

Flexor digitorum tendon sheath extends distally from the metacarpal neck to the distal interphalangeal joint. The tendon fiber sheath thickens in different areas to form a series of dense connective tissue bundles with different widths, thicknesses, and morphologies. This structure is called the flexor tendon sheath pulley system, which consists of five annular pulleys (A1∼A5), four cruciform pulleys (C1∼C4), and one palmar aponeurosis pulley. The A1 pulley is attached to the volar plate of the metacarpophalangeal joint, with an average width of 7.1 mm, and an average thickness of <1 mm.

It has not been very clear which is earlier predominant factor of triggering finger considering the injured pulley or tendinopathy, but both are involved when clinical symptom appears. During the early stage, aseptic inflammations such as hemorrhage, edema occur around the tendon sheath. At a later stage, the chronic pathologies of pulley and tendon such as hypertrophy, adhesion occur. The thickness of pulley can increase up to 2∼3 mm from the normal value, which is

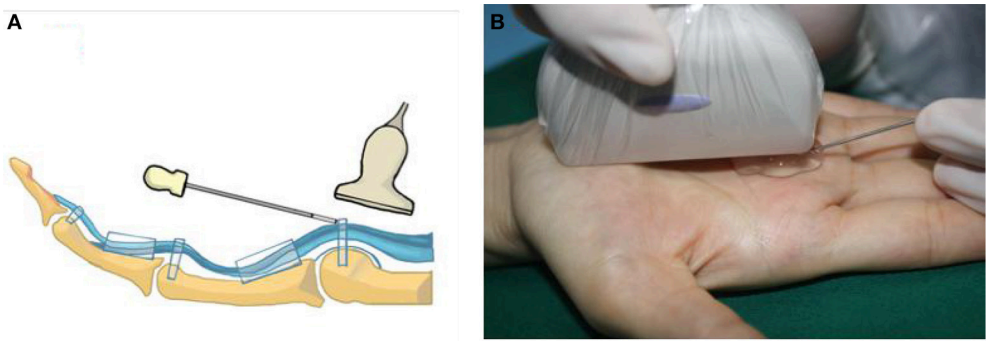

FIGURE 6 | The scheme **(A)** and spot **(B)** of the ultrasonography-guided release. The body of the needle knife paralleled to the tendon. With the help of ultrasound, it was easy and safe to complete the whole procedure.

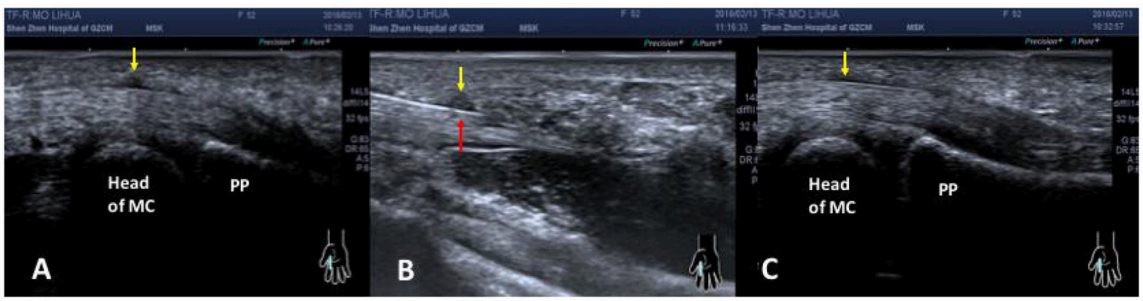

FIGURE 7 | The ultrasound images before **(A)**, during **(B)** and after **(C)** release with ultrasonography-guided. **(A)** The yellow arrow showed the thickening of A1 pulley in the right index finger before operation. **(B)** The red arrow showed the needle knife was cutting the A1 pulley (yellow arrow). **(C)** The A1 pulley (the yellow arrow) became normal thickness immediately after ultrasonography-guided release. PP, proximal phalange; MC, metacarpal bone.

<1 mm. The annular stenosis forms as the pulley system at the lesion thickens. Patients suffer from dysfunction of flexion and extension of fingers, and this situation is particularly obvious when waking up early in the morning. A feeling of bounce occurs at the nodule when fingers are flexed and extended, and the subcutaneous nodular-like lump is palpable. In the early stage, the flexor tendon slides over the stenosis of the pulley with difficulty, resulting in a trigger-like movement. In the later stage, patients cannot flex or extend actively, keeping in a stiff position. This condition is called "locking and snapping."

The needle knife is a traditional tool of Chinese medicine based on the therapy of "damage first, recover later." It consists of three parts: tip, body and handle. It has a 0.8 mm blade on the tip, and its length is 40 mm. It does not need to cut the skin to enter the body and reach the lesion. The main role of a needle knife is to loosen adhesion that improves blood circulation, increases the metabolism of local pain-causing substances, and relieves tension.

Blind needle knife release by using palm anatomical landmarks has been well-known as the rehabilitation doctors of China since thousands of years ago (Paulius and Maguina, 2009; Yin and Guo, 2016). The effectiveness has been accepted by clinical doctors and patients. TF is the preferred alternative for the needle knife. Other illnesses, such as radial styloid stenosing tenosynovitis, carpal tunnel syndrome, ankle tunnel syndrome, ganglion cyst, chronic fasciitis, and trigger point release are often treated by the needle knife. The operator's experience during the operation of the needle knife is the key to determine if release is completed, flexion and extension is recovered, and the surrounding tissue is damaged. Thus, the complications such as damage to interdigital nerves, vessels, or flexor tendon have been existed. On the other hand, it is common of the recurrence and incomplete release, or rare tendon rupture due to the repeated steroidal injection inaccurately.

The result showed that almost all patients had significant improvement after release. However, comparing to the ultrasonography-guided group in which the completion of release was 100% in all patients at day 7 postoperatively, that of the blind group was 19.0%, and mild triggering of the blind group was 71.4% postoperatively. In the blind group, one case had such complications as the fluid of surrounding tissue and cutting in the wrong place, and one case had no improvement. Both were received ultrasonography-guided release 4 weeks later after their first blind releases. The causes for limited efficiency in the blind group were: (1) The process of the cutting diverged from the lesion. **Figure 5C** showed that the cutting position after piercing into the skin from the marked point was not the same as the location of thickening pulley. (2) The cutting depth was difficult to control. If cutting is too superficial, the snapping cannot be released. Likewise, if it is

too deep, it is possible to injure the tendon or surrounding tissue. **Figure 5B** showed the fluid of surrounding tissue. (3) The cutting width was difficult to control: The tip of the needle knife has a blade of 0.8 mm. Generally, five to six cuts proximally and distally were performed along the imaginary line of flexor tendon sheath with a cutting width of 4∼4.8 mm. The range of thickening width of A1 pulley measured by ultrasound before release in the blind group was 4.40∼7.10 mm. It meant that there was an incomplete cut existed partly in the blind group.

CONCLUSION

The needle knife is a very good tool for release of triggering fingers. The combined use of ultrasound and the needle knife can achieve the best result for trigger finger.

Ultrasonography-guided release of trigger finger with the needle knife is feasible and safe in current clinical practice. With the help of ultrasound, it will be independent of operator's experience, easy to solve the problems of depth and width in the cutting process, or the injury of surrounding tissue.

Complete one-time release of trigger finger was achieved in all ultrasonography-guided release in 1 week.

Our microinvasive procedure is nearly painless and requires less than half a day off work for all of our subjects.

LIMITATION

There were several limitations in our study, firstly that this was not a randomized controlled trial as the development stage of each patient was different. Secondly, the age of patients in our study was concentrated among middle aged and elderly people, and the gender of that was female, no male. Thirdly, the follow-up time of patients postoperatively was short. The long-term recovery value of ultrasound-guided release in the patients of trigger finger still needs to be further explored through prolonged follow-up time. Finally, there was a relatively longer operation time of the ultrasonography-guided group compared to the time of the blind group. Time will decrease if more practice and collaboration are maintained between the rehabilitation doctor and ultrasound doctor.

DATA AVAILABILITY

All datasets generated for this study are included in the manuscript and/or the **Supplementary Files**.

AUTHOR CONTRIBUTIONS

MP and SS carried out analysis and calculations of data, drawings, and contributed to the writing of the manuscript. HL and HY contributed to data collection and management. ZF contributed to the release by needle knife. FY and EZ designed and coordinated the project, contributed to the discussion, supervised and reviewed the writing of the manuscript. All authors read and approved the final manuscript.

FUNDING

Public Health Project of Futian District (FTWS2018049).

SUPPLEMENTARY MATERIAL

The Supplementary Material for this article can be found online at: https://www.frontiersin.org/articles/10.3389/fphar.2019.00267/full#supplementary-material

REFERENCES

Chang, K. V., Wu, W. T., Han, D. S., and Özçakar, L. (2017). Static and dynamic shoulder imaging to predict initial effectiveness and recurrence after ultrasound-guided subacromial corticosteroid injections. *Arch. Phys. Med. Rehabil.* 98, 1984–1994. doi: 10.1016/j.apmr.2017.01.022

Chang, K. V., Wu, W. T., Huang, K. C., Jan, W. H., and Han, D. S. (2018). Limb muscle quality and quantity in elderly adults with dynapenia but not sarcopenia: an ultrasound imaging study. *Exp. Gerontol.* 15, 54–61. doi: 10.1016/j.exger.2018.03.019

Guo, D., Guo, D., Guo, J., McCool, L. C., and Tonkin, B. (2017). A cadaveric study of the thread trigger finger release: the first annular pulley transection through thread transecting technique. *Hand (N Y)* 13, 170–175. doi: 10.1177/1558944717697433

Hoang, D., Lin, A. C., Essilfie, A., Minneti, M., Kuschner, S., Carey, J., et al. (2016). Evaluation of percutaneous first annular pulley release: efficacy and complications in a perfused cadaveric study. *J. Hand Surg. Am.* 41, 165–173. doi: 10.1016/j.jhsa.2016.04.009

Hopkins, J., and Sampson, M. (2014). Percutaneous tenotomy: development of a novel, percutaneous, ultrasound-guided needle-cutting technique for division of tendons and other connective tissue structures. *J. Med. Imaging Radiat. Oncol.* 58, 327–330. doi: 10.1111/1754-9485.12113

Lapègue, F., André, A., Meyrignac, O., Pasquier-Bernachot, E., Dupré, P., Brun, C., et al. (2016). US-guided percutaneous release of the trigger finger by using a 21-gauge needle: a prospective study of 60 cases. *Radiology* 280, 493–499. doi: 10.1148/radiol.2016151886

Lee, S. H., Choi, Y. C., and Kang, H. J. (2018). Comparative study of ultrasonography-guided percutaneous A1 pulley release versus blinded percutaneous A1 pulley release. *J. Orthop. Surg. (Hong Kong).* 26, 1–7. doi: 10.1177/2309499018772368

Ma, C., and Wu, S. (editor-in-chief). (2016). *Treatment and Rehabilitation of Soft Tissue Pain, 2nd Edn.* Guangzhou: Guangdong science and technology press. 1–350.

Nikolaou, V. S., Malahias, M. A., Kaseta, M. K., Sourlas, I., Babis. G. C. (2017). Comparative clinical study of ultrasound-guided A1 pulley release *versus* open surgical intervention in the treatment of trigger finger. *World J. Orthop.* 8, 163–169. doi: 10.5312/wjo.v8.i2.163

Paulius, K. L., and Maguina, P. (2009). Ultrasound-assisted percutaneous trigger finger release: is it safe? *Hand (N Y)* 4, 35–37. doi: 10.1007/s11552-008-9137-8

Rajeswaran, G., Healy, J. C., and Lee, J. C. (2016). Percutaneous Release Procedures: Trigger Finger and Carpal Tunnel. *Semin. Musculoskelet. Radiol.* 20, 432–440. doi: 10.1055/s-0036-1594283

Rajeswaran, G., Lee, J. C., Eckersley, R., Katsarma, E., and Healy, J. C. (2009). Ultrasound-guided percutaneous release of the annular pulley in trigger digit. *Eur. Radiol.* 19, 2232–2237. doi: 10.1007/s00330-009-1397-3

Rojo-Manaute, J. M., Capa-Grasa, A., Del Cerro-Gutiérrez, M., Martínez, M. V., Chana-Rodríguez, F., and Martín, J. V. (2012b). Sonographically

guided intrasheath percutaneous release of the first annular pulley for trigger digits, part 2: randomized comparative study of the economic impact of 3 surgical models. *J. Ultrasound Med.* 31, 427–438. doi: 10.7863/jum.2012.31.3.427

Rojo-Manaute, J. M., Rodríguez-Maruri, G., Capa-Grasa, A., Chana-Rodríguez, F., Del Valle Soto, M., and Martín, J. V. (2012a). Sonographically guided intrasheath percutaneous release of the first annular pulley for trigger digits, part 1: clinical efficacy and safety. *J. Ultrasound Med.* 31, 417–424. doi: 10.7863/jum.2012.31.3.417

Rojo-Manaute, J. M., Soto, V. L., De las Heras Sánchez-Heredero, J., Del Valle Soto, M., Del Cerro-Gutiérez, M., and Martín, J. V. (2010). Percutaneous intrasheath ultrasonographically guided first annular pulley release: anatomic study of a new technique. *J. Ultrasound Med.* 29, 1517–1529. doi: 10.7863/jum.2010.29.11.1517

Smith, J., Rizzo, M., and Lai, J. K. (2010). Sonographically guided percutaneous first annular pulley release: cadaveric safety study of needle and knife techniques. *J. Ultrasound Med.* 29, 1531–1542. doi: 10.7863/jum.2010.29.11.1531

Wu, W. T., Chang, K. V., Mezian, K., Nanka, O., Lin, C. P., and Özçakar, L. (2018). Basis of shoulder nerve entrapment syndrome: an ultrasonographic study exploring factors influencing cross-sectional area of the suprascapular nerve. *Front. Neurol.* 9:902. doi: 10.3389/fneur.2018.00902

Yin, L., and Guo, R. (2016). Application and progress of high frequency ultrasound in trigger finger. *Chin. J. Med. Ultrasound* 11, 875–880.

Conflict of Interest Statement: The authors declare that the research was conducted in the absence of any commercial or financial relationships that could be construed as a potential conflict of interest.

frontiers in Pharmacology

ORIGINAL RESEARCH
published: 04 April 2019
doi: 10.3389/fphar.2019.00312

Ultrasound on Erect Penis Improves Plaque Identification in Patients With Peyronie's Disease

*Yu Liu[1], Dequan Zheng[2], Xiaolin Liu[1], Xiaohong Shi[1], Shengchun Shu[1] and Jinbing Li[1]**

[1] Department of Ultrasonography, Second Clinical Medical College, Guangzhou University of Traditional Chinese Medicine, Guangzhou, China, [2] Andrology Center, Second Clinical Medical College, Guangzhou University of Traditional Chinese Medicine, Guangzhou, China

Objectives: To compare the sensitivity of identification of penile plaques in the erect and flaccid penises by ultrasound in patients with Peyronie's disease (PD).

Materials and Methods: A total of 75 PD patients were screened by palpation and ultrasonography for penile lesions in both flaccid and erect penises induced by prostaglandin E1 (PG-1) injection.

Results: A total of 138 lesions were identified by ultrasound in the erect penises induced by injection of PG-1. However, only 74.6% of the lesions (103) were detectable by the palpation of the flaccid penises, and 84.1% (116) by ultrasound of the flaccid penises. The ultrasound confirmed 99 of the palpated lesions in the flaccid penises. The detection rate of lesions in drug-induced erect penises by ultrasound was significantly higher than those in the flaccid penises by the ultrasound ($P < 0.01$) or palpation ($P < 0.0005$) The type of penile lesions identified by ultrasonography included tunical thickening, calcifications, septal fibrosis, and intracavernosal fibrosis. The ratios of these lesions confirmed by ultrasound were 52.6, 33.6, 6.0, and 7.8%, respectively, in the flaccid penises, and 55.8, 28.3, 8.7, and 7.2%, respectively, in the erect penises.

Conclusion: Drug-induced erection can be used in suspicious PD patients when penile lesion is not identified by palpation or ultrasound in the flaccid penis.

Keywords: Peyronie's disease, ultrasound, penis, palpation, lesion identification

OPEN ACCESS

Edited by:
Fei Yan,
Shenzhen Institutes of Advanced Technology (CAS), China

Reviewed by:
Jin-Fang Xing,
Shanghai Pudong Hospital, China
Fajin Dong,
Shenzhen People's Hospital, China

****Correspondence:***
Jinbing Li
marcher126@126.com

Specialty section:
This article was submitted to Translational Pharmacology, a section of the journal Frontiers in Pharmacology

Received: *23 December 2018*
Accepted: *14 March 2019*
Published: *04 April 2019*

Citation:
Liu Y, Zheng D, Liu X, Shi X, Shu S and Li J (2019) Ultrasound on Erect Penis Improves Plaque Identification in Patients With Peyronie's Disease. Front. Pharmacol. 10:312. doi: 10.3389/fphar.2019.00312

INTRODUCTION

Peyronie's disease (PD) is a common penile disorder with a prevalence between 3.2–8.9% (Schwarzer et al., 2001; Rhoden et al., 2001; Mulhall et al., 2004). PD is caused by the abnormalities in the tunica albuginea and the adjacent tissue of corpora cavernosa of the penis. PD can cause pain, deformity, shorting, as well as bending of the penis during erection, and ultimately results in erectile dysfunction (ED) (Hauck and Weidner, 2001; Ralph et al., 2010). It has been reported that PD is related to the penile plaques formed by aberrant wound healing after minor trauma on the penis (Zargooshi, 2004; Gur et al., 2011). Some PD patients have a genetic predisposition to localized fibrosis formation in response to trauma on the penis (Hauck et al., 2004; Domes et al., 2007).

Peyronie's disease can be initially diagnosed based on patient's history and palpation of the penis (Weidner et al., 1997; Hauck et al., 2003), and is subsequently confirmed with evidence of lesions by ultrasound. Ultrasound is able to distinguish calcified tissue from soft tissue in the penis of PD patients. Furthermore, it is more sensitive to find

smaller and non-palpable tissue in the penis than palpation alone, and be able to further evaluate the extent of tissue fibrosis (Kalokairinou et al., 2012). The sensitivity to detect a lesion in the penis by ultrasound varies between 39 and 100% (Balconi et al., 1988; Princivalle et al., 1989; Lopez and Jarow, 1991; Vosshenrich et al., 1995; Nicolai et al., 1996; Muralidhar et al., 1996).

Ultrasound is typically conducted on the flaccid penis. However, ultrasound on flaccid penis fails to reveal the lesions which can be detected by palpation in some PD patients, and pharmaceutical induced erection is required (Prando, 2009). Erection stretches the tunica albuginea, and subsequently facilitates the detection of minor lesions by the ultrasound (Kalokairinou et al., 2012). Hypoechoic and isoechoic lesions can be detected with distension or retraction of the corpora cavernosa (Kalokairinou et al., 2012). Although ultrasound has such advantages in diagnosis of PD, it suffers from a systematic comparing the sensitivity in order to find a lesion in flaccid and drug-induced erect penises in PD patients. Therefore, the present study used ultrasound to find penile lesions in a group of Chinese patients with PD. The penis was first examined in the flaccid state followed by a drug-induced erect state.

MATERIALS AND METHODS

Study Patients

All patients with PD were recruited from the Andrology Center of our hospital between the period of March, 2015 to May, 2018. A patient was included in the study if a palpable nodule, focal hardening, or bending of the axis of the penis during erection was found in the flaccid or erect penis. Exclusion criteria were congenital penile curvature and previous PD surgery. A total of 75 patients with median age of 45 years, ranging from 29 to 70 years were eventually included in this study. All participants provided written informed content as well. The study was approved by the Ethics Committee of our institute.

Penile Examination on PD Patients

A veteran urologist examined the penis on all the PD patients. A palpable penile plaque identified in the flaccid state was further confirmed by stretching the penis with one hand while gently compressing the penile shaft between the fingers and thumb of the other hand. The number, size, and location of the plaques were recorded, and the symptoms of pain were thoroughly evaluated.

Ultrasound

A Doppler ultrasound was used to visualize penile plaques following palpation. The GE Logq E9 or Philips IU22 units with a 5.0–15.0 MHZ linear-array transducer was used.

Two ultrasound protocols were adopted to compare their sensitivities in diagnosing PD. In the first protocol, the penis was checked at the flaccid state. In the second protocol, 10 mg of prostaglandin E1 (PG-1) was injected into the corpus cavernosum to induce erection. A second dose of PG-1 was administered if the penis was not fully erect. All 6 patients obtained satisfactory erection after the second injection of PG-1. Then, patients were examined in a supine position in a warm and quiet private room. The flaccid and erect penises were longitudinally and transversely checked from the sulcus coronarius to the base. The location, size, number, and morphological characteristics of plaques were recorded. The plaques were further classified into 4 types according to their locations and calcification status; tunical thickening (tunica thickness is greater than 2 mm), septal fibrosis, intracavernous fibrosis, and penile calcifications (Smith et al., 2009; Breyer et al., 2010; Chung et al., 2011, 2012).

Statistical Analysis

All data were statistically analyzed with SPSS 12.0 software (SPSS Inc., Chicago, IL, United States). The number and types of plaques were analyzed with the Wilcoxon test. A P-value <0.05 was defined as statistically significant.

RESULTS

Patients' Demographic Information and Clinical Complaints

Patients had various symptoms or noticed penile abnormalities for a duration of 4 to 42 months (**Table 1**). Pain during intercourse was the predominant complain in PD patients (49.33%). The penile abnormalities found in PD patients included curvature in erect state (26.67%), decreased penile rigidity (38.67%), penis shortening (9.33%), and inability to sustain erection (8.00%). Approximately 11% of patients reported a history of penile bruising or significant penile pain after intercourse.

Sonographic Characteristics of Plaques in Erect Penis

A total of 138 penis plaques were identified by ultrasound in 75 PD patients after PG-1 induced erection. Approximately 52% of the plaques were less than 1.5 cm in length, 37% ranged from 1.5 to 3.0 cm, and 11% were larger than 3.0 cm. The thickness of the plaques varied from 0.2 to 1.6 cm.

Ultrasound was able to distinguish penile plaques with different characteristics. Approximately 28.3% of the plaques were calcified, in which 15.9% were fibrosis, and 55.8% were

TABLE 1 | Patients' demographic information.

	Number (n = 75)
Age (years)	45 (29 – 70)
Duration of symptoms (months)	11 (4 – 41)
Penile trauma (%)	8(10.66)
Penile pain (%)	37 (49.33)
Penile curvature (%)	20 (26.67)
Penile shortening (%)	7 (9.33)
Decreased penile rigidity (%)	29 (38.67)

TABLE 2 | Types and percentages of penile plaques identified by ultrasound in PD patients (n = 75).

Group	US_F	US_E
Tunical thickening	61 (52.6%)	77 (55.8%)
Calcification	39 (33.6%)	39 (28.3%)
Septal fibrosis	7 (6.0%)	12 (8.7%)
Intracavernosal fibrosis	9 (7.8%)	10 (7.2%)
Total	116	138*

*US_F, ultrasound of the flaccid penis; US_E, ultrasound of the erect penis. *Number of lesions found by US_E was significantly higher than US_F, $p < 0.005$.*

tunical thickening (**Table 2**). Among the 99 non-calcified plaques, 10(10.1%) showed hypoechoic lesions, 21(21.2%) showed isoechoic lesions and 68(68.7%) showed hyperechoic lesions.

Plaque Was Easily Identified in Erected Penis

Compared with the number of penis plaques (138) found in the erect state, palpation in the flaccid state alone was able to identify 74.6% of them (103/138) in 71 out of 75 patients (**Figure 1**). The other 4 patients failed to display any focal or diffuse alteration in the penis by palpation, though they felt vague pain in the ventral base of the erect penis. All of the plaques were painless when the penis was in the flaccid state. The majority of plaques (90.29%) were palpable on the dorsal surface of the penis, followed by the ventral surface (7.77%), and the lateral surface (1.94%).

Ultrasound detected 84.1% (116/138) of the plaques in 71 out of 75 patients when the penis was examined in the flaccid state. The frequencies of tunical thickening, calcifications (**Figure 2**), septal fibrosis (**Figure 3**), and intracavernosal fibrosis were 52.6, 33.6, 6.0, and 7.8%, respectively. The sonographic examination did not reveal any type of focal or diffuse alteration of penile tissue in 4 patients in the flaccid state, though they had a small dorsal nodule palpable.

Numbers of Identified Plaques Were Significantly Different Among Three Examination Techniques

Palpation of the flaccid penis alone found one single plaque in each of 45 patients, 2 isolated plaques in 20 patients, and 3 plaques in the other 6 patients (**Figure 4**). Ultrasound of flaccid penis identified 36 patients with solitary plaque, 26 patients with 2 isolated plaques, 8 patients with 3 lesions, and 1 patient with 4 lesions. These findings were significant different ($P < 0.05$) in comparison with palpation. Application of ultrasound on drug-induced erection revealed that 28 patients had solitary lesion, 34 had 2 separate lesions, 10 had 3 lesions, and 3 had 4 lesions, which was significantly different from those with palpation ($P < 0.0005$) or ultrasound in the flaccid penis ($P < 0.01$).

Sonography Identified Plagues More Efficiently in Erect Penis in PD Patients

Ultrasound detected 99 of the 103 palpable lesions (96%) in flaccid penis. However, 17 additional lesions were found by ultrasound imaging. In addition, 8 out of the 17 additional lesions were located at the intracavernosum, 6 at the septum, and 3 at the ventral tunica albuginea of corpora cavernosa behind the corpus spongiosum. Therefore, a total of 116 plaques were identified in the flaccid penis with ultrasound.

All 120 lesions detected with palpation or sonography in the flaccid penis were identified in the erect penis by ultrasound (**Figure 5**). The plaques undetectable in the 4 patients by ultrasound in the flaccid penis were confirmed to be tunica albuginea thickening at the root of penis by the ultrasound in erect penis (**Figure 6**). One of four patients who complained

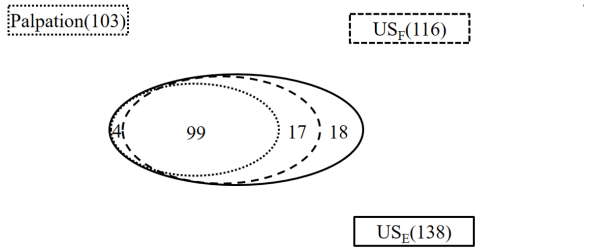

FIGURE 1 | The number of plaques found by palpation and ultrasound in the flaccid and erect penis. US_F, ultrasound of the flaccid penis; US_E, ultrasound of the erect penis.

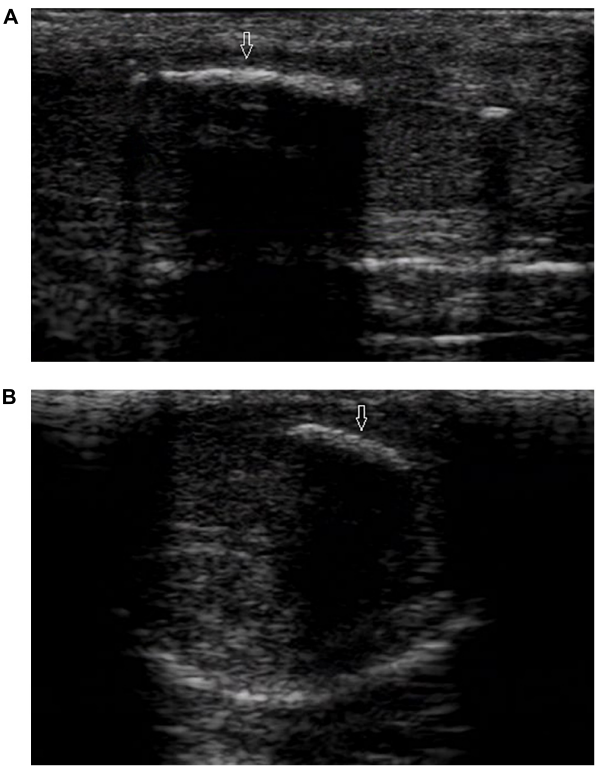

FIGURE 2 | A large calcified lesion in the tunica albuginea of the flaccid penis. **(A)** Longitudinal sonogram, dorsal access. Large calcified plaques (arrow) in the dorsal side with strong shadow caused dorsal curvature of the penis. **(B)** Axial sonogram, dorsal access. Plaque located in the tunica albuginea of left corpora cavernosa.

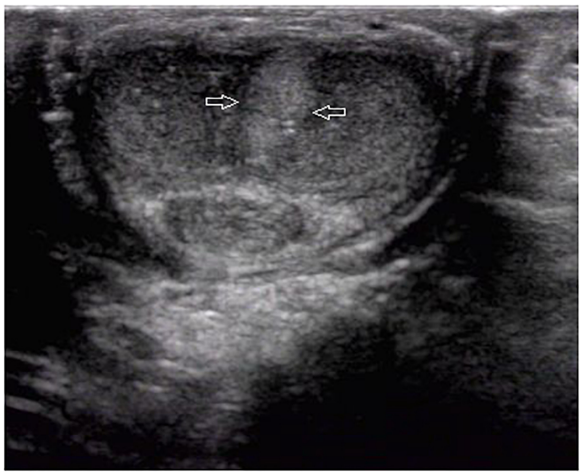

FIGURE 3 | A septal fibrosis in the flaccid penis. Axial sonogram, ventral access, the hyperechoic fibrosis (arrows) in the septum.

of vague pain in the ventral side of the base of erect penis failed to palpate any focal lesion, however, a large ventral tunica thickening was found by ultrasound with strong acoustic attenuation at the root of erect penis. No focal thickening of tunica albuginea was detected in the flaccid penis by ultrasound in this patient (**Figure 7**). In addition, 17 additional lesions were detected by ultrasound during erection including 11 tunical thickenings, 5 fibrosis at the septum, and 1 fibrosis in the intracavernosum. In comparison with ultrasound in the flaccid penis, the number of plaques found by the ultrasound in the erect penis was significantly higher than those in the former ($P < 0.01$).

DISCUSSION

The present study, to the best of knowledge, for the first time investigated the sensitivity of ultrasound in identifying penile plaques in Chinese PD patients. More penile plaques were identified when ultrasound was performed on a prostaglandin-induced erect penis compared with a flaccid one. The findings provide evidence that drug-induced erection modality can be used in patients with suspicious PD history and palpation but negative ultrasound findings in the flaccid penis.

PD may be diagnosed by palpation of penile plaques (Hauck and Weidner, 2001). However, palpation alone is difficult to find lesions in the septum, the intracavernosum, and the ventral tunica albuginea of the corpora cavernosa behind the corpus spongiosum due to their anatomic locations. Therefore, penile ultrasound is commonly used to confirm the diagnosis, and some penile lesions can only be identified by the ultrasound, e.g., the septal fibrosis, intracavernosal fibrosis, or sub-tunical calcifications (Brant et al., 2007). The present study confirmed the ability of ultrasonography to identify more penile plaques than palpation in PD patients. Similar findings were reported by Prando et al. that the ultrasound screening found penile plaques in 28 of 78 PD patients (35.8%) who had not reported any penile lesion by palpation alone (Prando, 2009). Therefore, penile ultrasound screening is a valuable tool to find lesions in patients with PD, especially lesions in the intracavernosum and septum.

In the present study, the ultrasound was able to detect 96 and 100% of palpated penile plaques in the flaccid and erection penis, respectively. Our results are similar to some studies (Balconi et al., 1988; Princivalle et al., 1989; Prando, 2009), however, they showed a higher detection rate than other

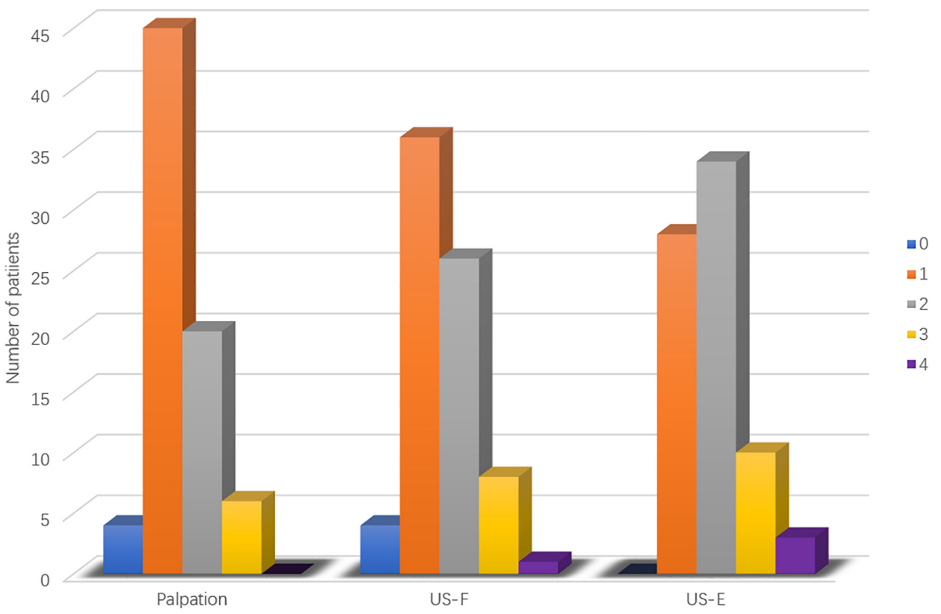

FIGURE 4 | Frequency of penile plaques in PD patients. Comparisons of palpation, ultrasound in the flaccid penis (US-F), and ultrasound in the erect penis (US-E). 0 to 4, number of lesions.

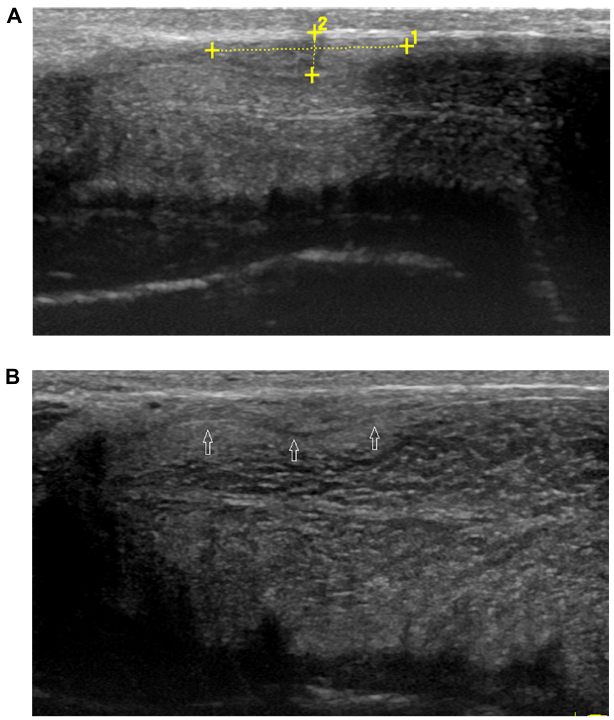

FIGURE 5 | Palpable ventral plaque of left corpus cavernosum. **(A)** Longitudinal sonogram, oblique ventral access (from the midline to the left lateral face of the penis). Fuzzy ventral tunica thickening of left corpus cavernosum in the flaccid penis. **(B)** Longitudinal sonogram, oblique ventral access (from the midline to the left lateral face of the penis). With the corpora cavernosa expansion, the local tunica albuginea thickening becomes obvious (arrows) in the erect penis.

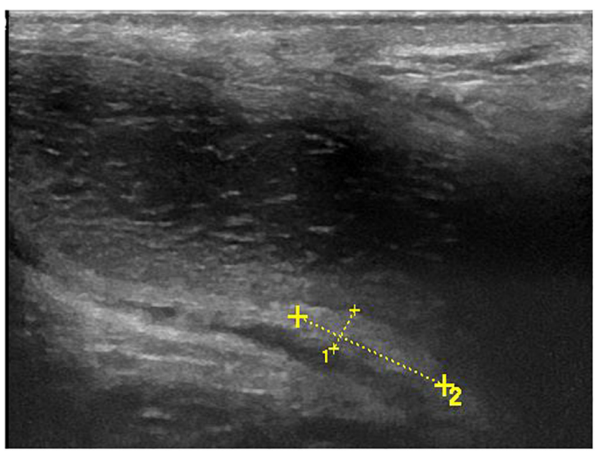

FIGURE 6 | Longitudinal sonogram (ventral access) of a palpable dorsal nodule. This nodule was not detected by the sonography in the flaccid penis. The sonography in erect penis shows obvious dorsal tunica albuginea thickening at the root of penis.

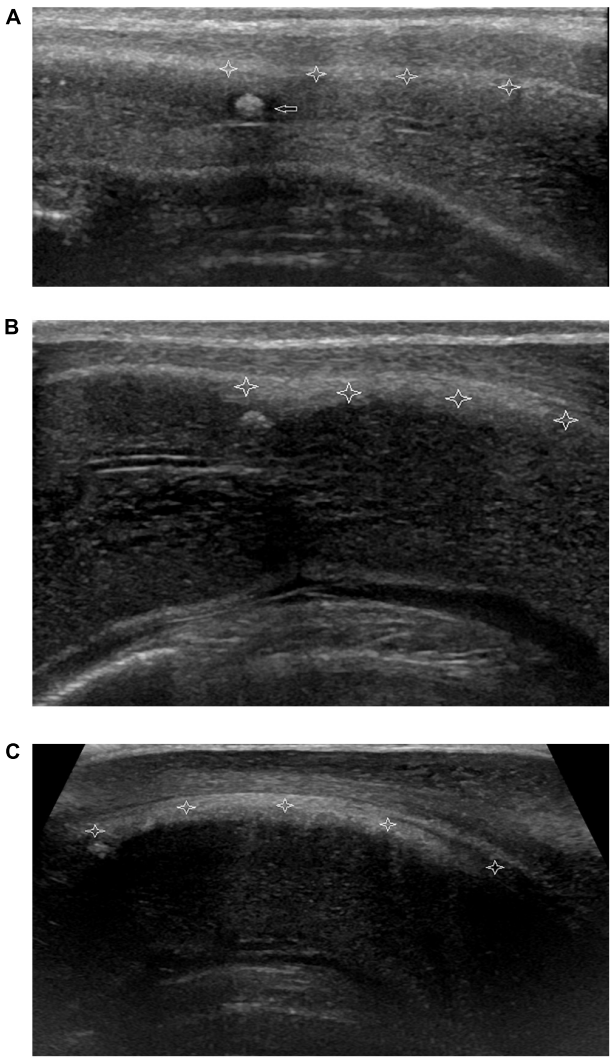

FIGURE 7 | Non-palpable nodule of focal thickening of the ventral tunica albuginea of corpora cavernosum behind corpora spongiosum at the root of penis. **(A)** Longitudinal sonogram, ventral access. No focal thickening of tunica albuginea of corpora cavernosum (stars) is shown and a hyperechoic fibrous plaque (arrow) in the corpora cavernosum in flaccid penis. **(B)** Longitudinal sonogram, ventral access. With the corpora cavernosa expansion, the local tunica albuginea shows thickening (stars) with the weak acoustic attenuation in the erect penis. **(C)** Longitudinal sonogram, ventral access. The acoustic attenuation behind the thickening tunica albuginea becomes strong when the penis reaches complete erection.

studies, which ranged from 39 to 72% (Lopez and Jarow, 1991; Vosshenrich et al., 1995; Nicolai et al., 1996; Hauck et al., 2003). The discrepancy between the present study and the others may be due to different ultrasound equipment used, different frequencies of the probes, different ethnic group of PD patients, and different experience of sonographers.

The present study demonstrated that the ultrasound performed better in identifying penile lesions when the penis was in the erect state. Dorsal palpable penile nodules in 4 PD patients were not detected by the ultrasound in the flaccid penis; however, they were well characterized by ultrasound in the erect penis. Furthermore, 18 new lesions were discovered by the ultrasound in the erect penis. The tunica

albuginea in the flaccid penis is thick, which can attenuate signal from the lesions within the corpora cavernosa. However, the tunica albuginea is stretched and becomes thinner due to the expansion of the corpora cavernosa in the erect penis. A penile lesion, which is usually not stretchable, can then be visualized by ultrasound due to the increased contrast enhancement between the lesion and peripheral normal tissue. Therefore, ultrasound in an erect penis can increase the chance of identifying a lesion which is not well contrast with the surrounding tissues, especially in the tunica albuginea and septum. However, the ultrasound was able to identify calcified lesions efficiently regardless of the penis state, which may be due to the distinctive shadow generated by the calcified lesions.

The present study had some limitations. Given the size of our patient population, and not all types of PD plaques were represented. In addition, ultrasound images were provided by one sonographer in both the flaccid and erect penis, which may cause bias in the data collection. Therefore, a second independent sonographer should be included in the future study.

CONCLUSION

The ultrasound screening of penile plaques in the erect penis was more sensitive than in the flaccid state for Chinese PD patients. Ultrasound of the erect penis can improve identification of lesions which are not obvious, especially lesions in the tunica albuginea and septum. Our results also suggest that ultrasound in erect penis should be considered in all suspicious PD patients in the clinical routine.

DATA AVAILABILITY

All datasets generated for this study are included in the manuscript and/or the supplementary files.

AUTHOR CONTRIBUTIONS

JL, YL, and DZ conceived of the study, participated in its design and drafted the manuscript. JL performed the examination of ultrasonography. XL and XS helped in data acquisition, analysis and interpretation. XL and SS helped in literature review and statistical analysis.

ACKNOWLEDGMENTS

We would like to thank *Medjaden* Bioscience Limited and MedSci for editing and proofreading the manuscript.

REFERENCES

Balconi, G., Angeli, E., Nessi, R., and Flaviis, L. (1988). Ultrasonographic evaluation of Peyronie's disease. *Urol. Radiol.* 10, 85–88. doi: 10.1007/bf02926543

Brant, W. O., Bella, A. J., Garcia, M. M., Tantiwongse, K., Dean, R. C., Lue, T. F., et al. (2007). Isolated septal fibrosis or hematoma–atypical Peyronie's disease? *J. Urol.* 177, 179–182. doi: 10.1016/j.juro.2006.08.065

Breyer, B. N., Shindel, A. W., Huang, Y. C., Eisenberg, M. L., Weiss, D. A., Lue, T. F., et al. (2010). Are sonographic characteristics associated with progression to surgery in men with Peyronie's disease? *J. Urol.* 183, 1484–1488. doi: 10.1016/j.juro.2009.12.026

Chung, E., De Young, L., and Brock, G. B. (2011). Penile duplex ultrasonography in men with Peyronie's disease: is it veno-occlusive dysfunction or poor cavernosal arterial inflow that contributes to erectile dysfunction? *J. Sex. Med.* 8, 3446–3451. doi: 10.1111/j.1743-6109.2011.02501.x

Chung, E., Yan, H., De Young, L., and Brock, G. B. (2012). Penile doppler sonographic and clinical characteristics in Peyronie's disease and/or erectile dysfunction: an analysis of 1500 men with male sexual dysfunction. *BJU. Int.* 110, 1201–1205. doi: 10.1111/j.1464-410X.2011.10851.x

Domes, T., De Young, L., O'Gorman, D. B., Gan, B. S., Bella, A. J., Brock, G., et al. (2007). Is there a role for proteomics in Peyronie's disease? *J. Sex. Med.* 4, 867–877. doi: 10.1111/j.1743-6109.2007.00470.x

Gur, S., Limin, M., and Hellstrom, W. J. (2011). Current status and new developments in Peyronie's disease: medical, minimally invasive and surgical treatment options. *Expert. Opin. Pharmacother.* 12, 931–944. doi: 10.1517/14656566.2011.544252

Hauck, E. W., Hackstein, N., Vosshenrich, R., Diemer, T., Schmelz, H. U., Bschleipfer, T., et al. (2003). Diagnostic value of magnetic resonance imaging in Peyronie's disease-a comparison both with palpation and ultrasound in the evaluation of plaque formation. *Eur. Urol.* 43, 293–300. doi: 10.1016/S0302-2838(03)00003-4

Hauck, E. W., Hauptmann, A., Haag, S. M., Bohnert, A., Weidner, W., Bein, G., et al. (2004). Alpha-1-antitrypsin levels and genetic variation of the alpha-1-antitrypsin gene in Peyronie's disease. *Eur. Urol.* 46, 623–628. doi: 10.1016/j.eururo.2004.04.028

Hauck, E. W., and Weidner, W. (2001). Francois de la Peyronie and the disease named after him. *Lancet* 357, 2049–2051. doi: 10.1016/S0140-6736(00)05119-9

Kalokairinou, K., Konstantinidis, C., Domazou, M., Kalogeropoulos, T., Kosmidis, P., Gekas, A., et al. (2012). US imaging in Peyronie's disease. *Clin. Imaging Sci.* 2, 63–72. doi: 10.4103/2156-7514.103053

Lopez, J. A., and Jarow, J. P. (1991). Duplex ultrasound findings in men with Peyronie's disease. *Urol. Radiol.* 12, 199–202. doi: 10.1007/bf02924008

Mulhall, J. P., Creech, S. D., Boorjian, S. A., Ghaly, S., Kim, E. D., Moty, A., et al. (2004). Subjective and objective analysis of the prevalence of Peyronie's disease in a population of men presenting for prostate cancer screening. *J. Urol.* 171, 2350–2353. doi: 10.1097/01.ju.0000127744.18878.f1

Muralidhar, S., Gulati, M., Kumar, B., Sharma, S. K., Suman, K., Roy, P. B., et al. (1996). An ultrasonographic study of Peyronie's disease. *Australas Radiol.* 40, 106–108. doi: 10.1111/j.1440-1673.1996.tb0036.x

Nicolai, M., Carriero, A., De Thomasis, R., Lantorno, R., Longeri, D., Tenaglia, R., et al. (1996). Dynamic magnetic resonance imaging versus dynamic echography in the staging of Peyronie's disease. *Arch. Ital. Urol. Androl.* 68, 97–100.

Prando, D. (2009). New sonographic aspects of peyronie disease. *J. Ultrasound Med.* 28, 217–232. doi: 10.7863/jum.2009.28.2.217

Princivalle, M., Simone, M., De Luca, C., Scutellair, P. N., Giqanti, M., Reqqiani, A., et al. (1989). Echographic diagnosis of Peyronie's disease. *Radiol. Med.* 78, 74–78.

Ralph, D., Gonzalez-Cadavid, N., Mirone, V., Perovic, S., Sohn, M., Usta, M., et al. (2010). The management of Peyronie's disease: evidence-based 2010 guidelines. *J. Sex. Med.* 7, 2359–2374. doi: 10.1111/j.1743-6109.2010.01850.x

Rhoden, E. L., Teloken, C., Ting, H. Y., Lucas, M. L., Teo-dosio da Ros, C., Ary Vargas, et al. (2001). Prevalence of Peyronie's disease in men over 50-y-old from Southern Brazil. *Int. J. Impot. Res.* 13, 291–293. doi: 10.1038/sj.ijir.3900727

Schwarzer, U., Sommer, F., Klotz, T., Braun, M., Reif-enrath, B., Engelmann, U., et al. (2001). The prevalence of Peyronie's disease: results of a large survey. *BJU. Int.* 88, 727–730. doi: 10.1046/j.1464-4096.2001.02436.x

Smith, J. F., Brant, W. O., Fradet, V., Shindel, A. W., Vittinghoff, E., Chi, T., et al. (2009). Penile sonographic and clinical characteristics in men with Peyronie's disease. *J. Sex. Med.* 6, 2858–2867. doi: 10.1111/j.1743-6109.2009.01438.x

Vosshenrich, R., Schroeder-Printzen, I., Weidner, W., Fischer, U., Funke, M., Ringert, R. H., et al. (1995). Value of magnetic resonance imaging in patients with penile induration (Peyronie's disease). *J. Urol.* 153, 1122–1125. doi: 10.1097/00005392-199504000-00016

Weidner, W., Schroder-Printzen, I., Weiske, W. H., and Vosshenrich, R. (1997). Sexual dysfunction in Peyronie's disease: an analysis of 222 patients without previous local plaque therapy. *J. Urol.* 157, 325–328. doi: 10.1097/00005392-199701000-00107

Zargooshi, J. (2004). Trauma as the cause of Peyronie's disease: penile fracture as a model of trauma. *J. Urol.* 172, 186–188. doi: 10.1097/01.ju.0000132144.71458.86

Conflict of Interest Statement: The authors declare that the research was conducted in the absence of any commercial or financial relationships that could be construed as a potential conflict of interest.

frontiers in Pharmacology

ORIGINAL RESEARCH
published: 11 April 2019
doi: 10.3389/fphar.2019.00374

Evaluation of Uterosacral Ligament Involvement in Deep Endometriosis by Transvaginal Ultrasonography

Yujuan Zhang[1,2], Xiaojun Xiao[1,2], Fanhua Xu[1,2], Qi Lin[1,2], Jinfeng Xu[1,2]* and Bo Du[3]**

[1] Department of Ultrasound, Shenzhen People's Hospital, The Second Clinical Medical College of Jinan University, The First Affiliated Hospital of Southern University of Science and Technology, Shenzhen, China, [2] Shenzhen Medical Ultrasound Engineering Center, Shenzhen, China, [3] Department of Emergency, Shenzhen People's Hospital, The Second Clinical Medical College of Jinan University, The First Affiliated Hospital of Southern University of Science and Technology, Shenzhen, China

This study was designed to conclude the ultrasonic characteristics of uterosacral ligament (USL) lesions involved by endometriosis and evaluated the value of transvaginal sonography (TVS) in diagnosing USL involvement in deep infiltrating endometriosis (DIE). A total of one hundred and eighteen patients with DIE were included in the study and underwent surgery. All these patients were evaluated by transvaginal ultrasound examination by one trained examiner. The gold standard for diagnosis was surgery and histopathology. 85 patients with USL endometriosis were confirmed by surgical pathology. 84 patients were diagnosed USL endometriosis by TVS and 81 of which were confirmed by the gold standard. The sensitivity, specificity, positive predictive value (PPV), negative predictive value (NPV), and accuracy of TVS for diagnosing USL endometriosis were 95.3, 90.9, 96.4, 88.2, and 94.1%, respectively. According to the ultrasound characteristics of USL endometriosis, we summarized four types: Type I. thickened and stiff lesions, Type II. local nodules, Type III. irregular striped lesions, and Type IV. mixed lesions. The conclusion of the study was that TVS was a convenient, accurate and first-line diagnostic technique for USL endometriosis and the USL lesions could be summarized into four types according to the ultrasound morphological changes.

Keywords: uterosacral ligament, transvaginal sonography, endometriosis, deep infiltrating endometriosis (DIE), diagnosis

OPEN ACCESS

Edited by:
Xiaobing Wang,
Shaanxi Normal University, China

Reviewed by:
Ning Shang,
Guangdong Women and Children Hospital, China
Zhiyi Chen,
The Third Affiliated Hospital of Guangzhou Medical University, China

***Correspondence:**
Qi Lin
linqik@sina.com
Jinfeng Xu
xujinfeng@yahoo.com
Bo Du
zyj_db@163.com

Specialty section:
This article was submitted to Translational Pharmacology, a section of the journal Frontiers in Pharmacology

Received: *12 October 2018*
Accepted: *26 March 2019*
Published: *11 April 2019*

Citation:
Zhang Y, Xiao X, Xu F, Lin Q, Xu J and Du B (2019) Evaluation of Uterosacral Ligament Involvement in Deep Endometriosis by Transvaginal Ultrasonography. Front. Pharmacol. 10:374. doi: 10.3389/fphar.2019.00374

INTRODUCTION

Deep infiltrating endometriosis (DIE) was defined as an endometriotic lesion that infiltrates the peritoneum and penetrates into the retroperitoneal space or the wall of the pelvic organs to a depth of at least 5 mm (Koninckx and Martin, 1992). It occurs in 15–30% of patients with endometriosis (Yantiss et al., 2001). The most common involved location was uterosacral ligament (USL) (Chapron et al., 2003; Bazot et al., 2007). The involvement of USL may cause many clinical symptoms, such as chronic pelvic pain and deep dyspareunia (Hummelshoj et al., 2014). However, there was always a delay between the onset of the first symptoms and the clinical diagnosis of endometriosis and usually the interval was approximately 7–10 years (Matsuzaki et al., 2006; Hudelist et al., 2012) because of the low sensitivity of TVS for USL endometriosis (Bazot et al., 2004; Vimercati et al., 2012; Holland et al., 2013). The latest meta-analysis (Guerriero et al., 2015)

for detection of USL endometriosis demonstrated that the overall pooled sensitivity of transvaginal sonography (TVS) was only 53% (95% confidence interval (CI), 35–70%). There were many reasons for the low diagnostic rate, such as the small space of posterior pelvic compartment and its complex structure, the diversity of ultrasound morphological characteristics and the differences of examiners' experiences. The aims of this study were to assess the value of TVS for diagnosing USL endometriosis performed by an experienced examiner and summarize the ultrasound morphological features of USL endometriosis, so that the examiners could quickly identify the lesion of the USL and improve the diagnostic rate.

MATERIALS AND METHODS

Ethics Statement

The Medical Science Ethics Committee of Shenzhen People's Hospital approved this study (NO. 2018100). Each patient or an appropriate family member provided informed written consent to obtain clinical materials.

Study Population

From October 2013 to October 2017, a total of 118 patients met the inclusion and exclusion criteria for the study. All patients were enrolled from the Shenzhen People's Hospital.

Inclusion and Exclusion Criteria

Inclusion Criteria

(1) Patients were diagnosed as DIE according to their clinical data. (2) Patients needed surgery treatment.

Exclusion Criteria

(1) Patients withdrawed from the study for personal reasons. (2) Patients who were pregnant while waiting for surgery. (3) Patients have not undergone surgery for any reasons.

Imaging Techniques

All TVS scans were performed by one examiner who had received professional training. The examiner was blinded to physical examination and previous imaging examination results but was aware that the women were being evaluated for chronic pelvic pain and that endometriosis was suspected. All the TVS examinations were performed within 2 weeks of surgery.

All patients were examined in the lithotomy position using either a GE E8 (GE Healthcare Ultrasound, United States) or Philips IU22 (Philips IU22, United States) scanner equipped with 5–9-MHz or C10-3 transducer for transvaginal visualization.

TVS Techniques

Transvaginal sonography examinations were performed with ultrasound transmission gel in the probe cover to create a stand-off to visualize the near-field area. In all patients, the uterus and ovaries were detected first to rule out adenomyosis and ovarian cysts, which are frequently associated with DIE (Somigliana et al., 2004; Chapron et al., 2009). Then, the transducer was withdrawn to the perineum and inserted into the vagina slowly to evaluate the vagina, rectovaginal septum, pouch of Douglas, USLs, bowel walls, etc., All of involved targets, especially painful sites, were evaluated in multiple scanning planes by rotating the transducer. The lesion size was measured in three orthogonal planes.

Uterosacral ligament involvement in DIE was best evaluated by placing the transvaginal probe in the posterior vaginal fornix at the midline in a sagittal plane and then sweeping the probe inferolaterally to the cervix.

The echogenicity, changes in shape, thickness, and size of the USLs were observed, described and recorded for analysis. The thickness of a "thickened" USL was measured in the transverse plane at the insertion of the ligament at the cervix.

Statistical Analysis

The ultrasound characteristics of USL lesions were summerized and divided into four types according to morphological changes. The sensitivity, specificity, positive predictive value (PPV), negative predictive value (NPV), and accuracy of TVS for diagnosing USL endometriosis were also analyzed. Patients who were confirmed to have bilateral involvement while TVS diagnosis was unilaterally affected were classified as false negative cases.

RESULTS

Surgical Findings

All 118 Patients were confirmed DIE by surgery and histopathology and their average age were 35.2 ± 6.2 years. In all cases, 85 had USL involvement, with 62 cases bilateral and 23 cases unilateral as shown in **Table 1**. For the cases with USL unilateral involvement, 15 were left-side and 8 were right-side. The other involved locations were intestines (60), pouch of Douglas (36), rectovaginal septum (28), bladder (14), vagina (9) and ureters (8), in descending order.

TVS Findings

In all the 118 DIE patients, TVS found 84 patients with USL endometriosis and 81 of which were confirmed by surgery and histopathology. Of the 81 patients, 60 had bilateral involvement and 21 had unilaterally involvement (13 left, 8 right).

We analyzed the ultrasound features of 81 confirmed cases and summerized 4 types of USL lesions: type I. thickened and stiff lesions (**Figure 1A**), in this type the root segment (the insertion of the ligament on the cervix) of USL was stiff, thickened and hypoechogenic and the middle and posterior portions were not

TABLE 1 | Distribution of 85 cases of USL confirmed by surgery.

	Bilateral	Unilateral	
		Left	Right
N	62	15	8
%	73.0	17.6	9.4

USL, uterosacral ligament involvement; N, number of patients; %, percentage.

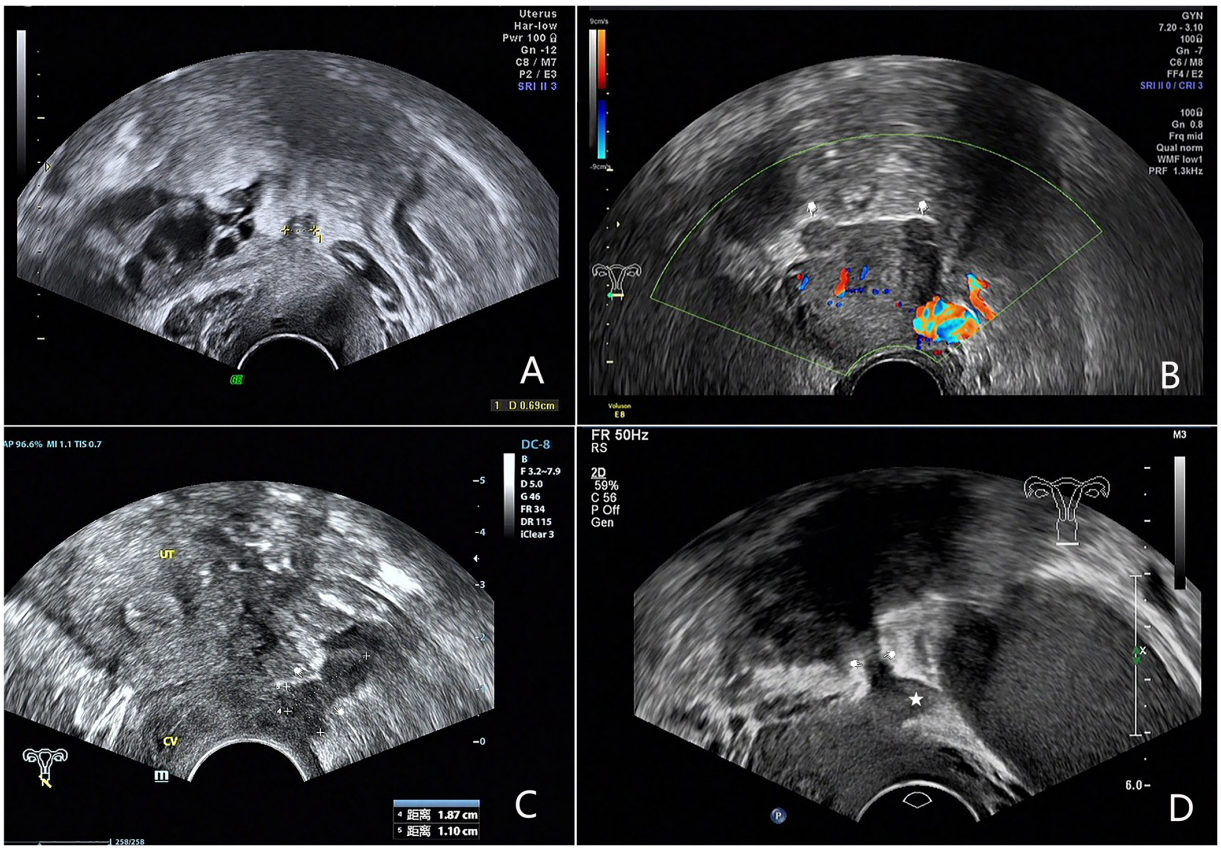

FIGURE 1 | Images showing four types of USL lesions according to ultrasound characteristics of USL endometriosis. **(A)** Type I: the root segament of USL is thickened and stiff. **(B)** Type II: the arrows show endometriosis nodules on both sides of the USL. **(C)** Type III: the arrows show hypoechogenic irregular striped endometriosis lesion. **(D)** Type IV: the arrows show irregular striped endometriosis lesion of the right USL, the Pentagram shows a nodule of the left USL.

visible; type II. local nodules (**Figure 1B**), which were visualized as local round or stellate hypoechogenic lesions with regular or irregular margins; type III. irregular striped lesions (**Figure 1C**), the lesions distribute along USL or adhered into other organs and they were generally larger than type I and II, the root and middle part or even posterior part of USL were usually involved; type IV. mixed lesions (**Figure 1D**), the lesions involved both sides and have two types of the above.

Table 2 shows there were 10 type I, 6 type II, and 5 type III lesions in patients with unilateral involvement and 21 type I, 19 type II, 15 type III, and 5 type IV lesions in patients with bilateral involvement.

Value of TVS for the Diagnosis of USL Endometriosis

The Sensitivity, Specificity, PPV, NPV, and accuracy of TVS for the diagnosis of USL endometriosis were 95.3, 90.9, 96.4, 88.2, and 94.1%, respectively, as shown in **Table 3**.

There were 4 false negative and 3 false positive cases. Of the 4 false negative patients, 2 were found to be unilaterally involved by TVS, but actually they were bilaterally affected. The other 2 patients were missed diagnosis because they had multiple lesions adhered together in the retrocervical region. Of the 3 false positive cases, one patient was diagnosed as USL tumor by histological examination and 2 patients were confirmed as inflammatory lesions.

DISCUSSION

Diagnosing USL endometriosis with TVS has always been a difficult point in clinical research. Diagnostic rates varied

TABLE 2 | Distribution and type of USL involvement in 81 confirmed cases.

	Bilateral	Unilateral	
		Left	Right
N	60	13	8
%	74.1	16.0	9.9
I	21	6	4
II	19	4	2
III	15	3	2
IV	5		

USL, uterosacral ligament; TVS, transvaginal sonography; %, percentage.

TABLE 3 | The value of TVS in diagnosis of USL involvement in deep endometriosis.

Location	Sensitivity (%)	Specificity (%)	PPV (%)	NPV (%)	Accuracy (%)
USL	95.3 (81/85)	90.9 (30/33)	96.4 (81/84)	88.2 (30/34)	94.1 (111/118)

TVS, transvaginal sonography; USL, uterosacral ligament; NPV, negative predictive value; PPV, positive predictive value.

greatly due to differences in diagnostic methods and diagnostic experience. A recent meta-analysis (Guerriero et al., 2015) demonstrated that the overall pooled sensitivity of TVS diagnosis USL endometriosis was 53%. A series of two studies by Bazot et al. (2003, 2004) showed that the sensitivity and accuracy of TVS to diagnose USL endometriosis were around 70.6–75% and 77–83.8%, respectively. However, in this study, the sensitivity and accuracy of TVS for the diagnosis of USL endometriosis were 95.3 and 94.1%, respectively, which were higher than those reported in most similar studies.

We obtained such good results due to increased awareness of the disease and improved diagnostic methods. In clinical research we have found many factors could lead to low diagnostic rates. Firstly, the retrocervical area was a small and complex anatomical region, the borders of involved organs become indistinguishable in DIE, especially in patients with severe adhesions. Secondly, many examiners were not familiar with the normal ultrasound imaging of USL, which was crucial to improve the diagnostic rate. Some studies (Bazot et al., 2004; Exacoustos et al., 2017) mentioned that the USL was invisible using TVS. However, as early as Ohba et al. (1996) reported that transrectal ultrasonography can be used to observe the USL in non-endometriosis patients and in patients with endometriosis and that the thickness of the USL was associated with clinical symptoms. In our experience, the normal USL can be easily observed in patients with fossa effusion, and the root portion can be seen in a few patients in the absence of fossa effusion. Our experienced examiners can image normal USL using 2D and 3D ultrasound in patients with fossa effusion (**Figure 2**). Normal USL is visible as a nearly isoechoic arc from the upper cervix extending to the rectum. Lesions can be identified easily if sonographers can master the anatomy of the USL. Thirdly, the examiner's experience was also an important factor affecting the accuracy. Researchers generally believed (Exacoustos et al., 2017) that the diagnosis of DIE required far more experience, and TVS was highly accurate for the noninvasive diagnosis of DIE in well-trained staff (Guerriero et al., 2015; Tammaa et al., 2015). The examiner of this study was experienced and professionally trained. At last, supplementary methods such as "tenderness-guided" methods and the use of a stand-off to visualize the near-field area (Guerriero et al., 2007) were also important to improve the detection rate. In our experience, the diagnostic accuracy will be lower if examiners do not pay attention to these factors.

In terms of classification of USL lesions, we summerized four types according to ultrasound characteristics. The purpose of our classification was to improve the examiner's understanding of the disease and to quickly and accurately identify USL lesions. The results demonstrated that types I and II were very common, but type IV was rare among the four types. This study also concluded the detailed distribution of USL involvement according to surgical findings. The most commonly involved locations were bilateral, the left side and the right side in descending order. Similarly, Charles Chapron discovered that DIE was more likely to affect the left USL than the right side (Chapro et al., 2001). However, several previous studies (Jenkins et al., 1986; Fabio and Ginecologica, 1994) failed to find any significant asymmetry in the location of endometriosis involving the USLs. The reasons for the high incidence of bilateral involvement in this study may be that most of the patients had severe endometriosis, and pelvic involvement was more serious. Of course, our conclusions also need support from a larger sample of clinical statistics.

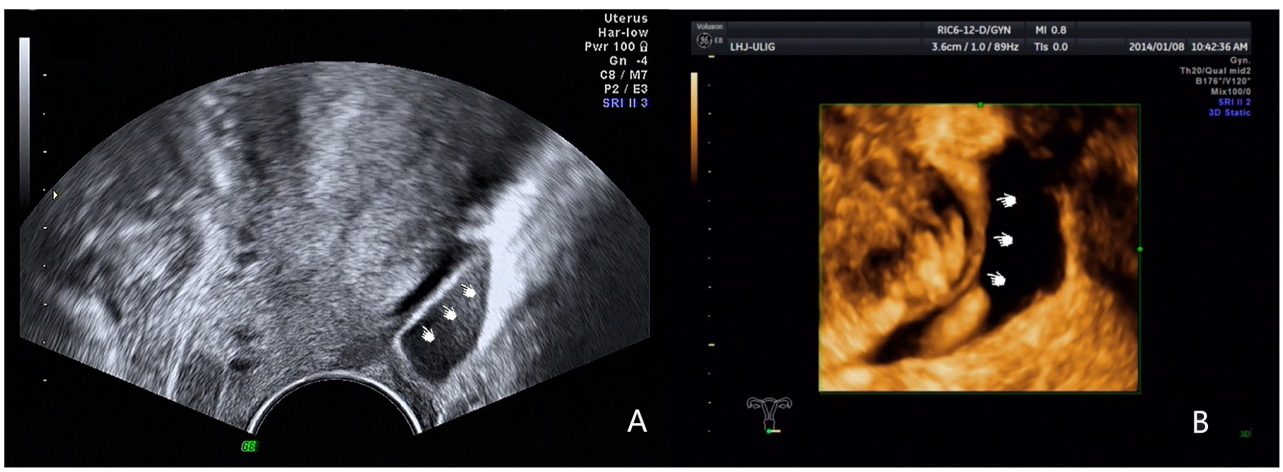

FIGURE 2 | Images showing the normal USL imaged by 2D and 3D ultrasound in patients with fossa effusion. **(A)** Normal USL imaged by 2D ultrasound. **(B)** Normal USL imaged by 3D ultrasound.

In addition, we noted that the specificity (90.9%) of TVS in diagnosis of USL endometriosis was relatively lower in our study. Bazot et al. (2004) and Guerriero et al. (2015) reported the specificity of 95.9 and 93%, respectively. There may be two reasons for this difference. Firstly, in our statistical analysis, we classified two patients (who were diagnosed unilateral lesion by TVS, but diagnosed as bilateral involvement during surgery) as false negative cases. However, this situation was not elaborated in other studies. Secondly, the other two cases had multiple lesions and severe adhesion in the posterior of the cervix which lead to difficulty in analysis. In this study, there were also three false positive cases. One patient was confirmed as a tumor by histology and another two patients were confirmed as inflammatory lesions. Therefore, it is also important to note that not all USL lesions are endometriosis, and a differential diagnosis should be made to rule out tumors and inflammatory changes (Nascu et al., 2006).

Some studies (Abrao et al., 2007; Bazot et al., 2009) reported that TVS has a lower sensitivity and accuracy for diagnosing USL involvement than MRI. However, our study showed that TVS has great value in the preoperative diagnosis of USL involvement with a sensitivity and accuracy of 95.3 and 94.1%, respectively. In addition, TVS is cost-effective, well accepted and widely available compared with MRI, so TVS should be used as the first line diagnostic technique (Saccardi et al., 2012).

Limitation

The present study does have some limitations. Firstly, only patients with severe pelvic endometriosis and surgical evidence of DIE were included which may increase the diagnostic rate. Secondly, we summarized the ultrasound characteristics of USL involvement in the study into four types and whether there are other types should be further studied.

CONCLUSION

Four types of USL endometriosis were summarized according to the ultrasound characteristics and the distribution of USL involvement was also concluded according to the results of surgery. TVS has significant value in diagnosis of USL endometriosis and can be used as a first-line tool for diagnosis.

ETHICS STATEMENT

The Medical Science Ethics Committee of Shenzhen People's Hospital approved this study (No. 2018100). Each patient or an appropriate family member provided informed written consent to obtain clinical materials.

AUTHOR CONTRIBUTIONS

YZ and BD conceived and designed the whole experiments and drafted the manuscript. JX performed the statistical analysis and interpreted the data. QL contributed to the clinical examination. XX contributed to the literature research. FX acquired the data. All authors read and approved the final manuscript.

FUNDING

This study was funded by Clinical Research Project of Shenzhen Health and Family Planning Commission in China (No. SZLY2018007), Shenzhen People's Hospital Young and Middle-aged Research Funds Cultivation Fund (No. SYKYPY201923), and Guangdong Medical Science and Technology Research Fund Project (No. A2016545).

REFERENCES

Abrao, M. S., Gonçalves, M. O., Dias, J. A. Jr., Podgaec, S., Chamie, L. P., and Blasbalg, R. (2007). Comparison between clinical examination, transvaginal sonography and magnetic resonanceimaging for the diagnosis of deep endometriosis. *Hum. Reprod.* 22, 3092–3097. doi: 10.1093/humrep/dem187

Bazot, M., Detchev, R., Cortez, A., Amouyal, P., Uzan, S., and Daraï, E. (2003). Transvaginalsonography and rectal endoscopic sonography for the assessment of pelvic endometriosis: apreliminary comparison. *Hum. Reprod.* 18, 1686–1692. doi: 10.1093/humrep/deg314

Bazot, M., Lafont, C., Rouzier, R., Roseau, G., Thomassin-Naggara, I., and Daraï, E. (2009). Diagnostic accuracy of physical examination, transvaginal sonography, rectal endoscopicsonography, and magnetic resonance imaging to diagnose deep infiltrating endometriosis. *Fertil. Steril.* 92, 1825–1833. doi: 10.1016/j.fertnstert.2008.09.005

Bazot, M., Malzy, P., Cortez, A., Roseau, G., Amouyal, P., and Daraï, E. (2007). Accuracy of transvaginalsonography and rectal endoscopic sonography in the diagnosis of deep infiltratingendometriosis. *Ultrasound Obstet. Gynecol.* 30, 994–1001. doi: 10.1002/uog.4070

Bazot, M., Thomassin, I., Hourani, R., Cortez, A., and Darai, E. (2004). Diagnostic accuracy of transvaginalsonography for deep pelvic endometriosis. *Ultrasound Obstet. Gynecol.* 24, 180–185. doi: 10.1002/uog.1108

Chapro, C., Fauconnier, A., Dubuisson, J. B., Vieira, M., Bonte, H., and Vacher-Lavenu, M. C. (2001). Does deep endometriosis infiltrating the uterosacral ligaments present an asymmetric lateral distribution? *BJOG* 108, 1021–1024.

Chapron, C., Fauconnier, A., Vieira, M., Barakat, H., Dousset, B., Pansini, V., et al. (2003). Anatomicaldistribution of deeply infiltrating endometriosis: surgical implications and proposition for aclassification. *Hum. Reprod.* 18, 157–161. doi: 10.1093/humrep/deg009

Chapron, C., Pietin-Vialle, C., Borghese, B., Davy, C., Foulot, H., and Chopin, N. (2009). Associatedovarian endometrioma is a marker for greater severity of deeply infiltrating endometriosis. *Fertil. Steril.* 92, 453–457. doi: 10.1016/j.fertnstert.2008.06.003

Exacoustos, C., Zupi, E., and Piccione, E. (2017). Ultrasound Imaging for ovarian and deep infiltratingendometriosis. *Semin. Reprod. Med.* 35, 5–24. doi: 10.1055/s-0036-1597127

Fabio, P., and Ginecologica (1994). Prevalence and anatomical distribution of endometriosis in women with selected gynaecological conditions: results from a multicentric Italian study. Gruppo italiano per lo studio dell'endometriosi. *Hum. Reprod.* 9, 1158–1162. doi: 10.1093/oxfordjournals.humrep.a138650

Guerriero, S., Ajossa, S., Gerada, M., D'Aquila, M., Piras, B., and Melis, G. B. (2007). Tenderness-guided" transvaginal ultrasonography: a new method for the detection of deependometriosis in patients with chronic pelvic pain. *Fertil. Steril.* 88, 1293–1297. doi: 10.1016/j.fertnstert.2006.12.060

Guerriero, S., Ajossa, S., Minguez, J. A., Jurado, M., Mais, V., Melis, G. B., et al. (2015). Accuracyof transvaginal ultrasound for diagnosis of deep endometriosis in uterosacral ligaments,rectovaginal septum, vagina and bladder: systematic review and meta-analysis. *Ultrasound Obstet. Gynecol.* 46, 534–545. doi: 10.1002/uog.15667

Holland, T. K., Cutner, A., Saridogan, E., Mavrelos, D., Pateman, K., and Jurkovic, D. (2013). Ultrasoundmapping of pelvic endometriosis: does the location and number of lesions affect the diagnosticaccuracy? A multicentre diagnostic accuracy study. *BMC Womens Health* 13:43. doi: 10.1186/1472-6874-13-43

Hudelist, G., Fritzer, N., Thomas, A., Niehues, C., Oppelt, P., Haas, D., et al. (2012). Diagnostic delay forendometriosis in Austria and Germany: causes and possible consequences. *Hum. Reprod.* 27, 3412–3416. doi: 10.1093/humrep/des316

Hummelshoj, L., DeGraaff, A., Dunselman, G., and Vercellini, P. (2014). Let's talk about sex andendometriosis. *J. Fam. Plann. Reprod. Health Care* 40, 8–10. doi: 10.1136/jfprhc-2012-100530

Jenkins, S., Olive, D. L., and Haney, A. F. (1986). Endometriosis: pathogenetic implications of theanatomic distribution. *Obstet. Gynecol.* 67, 335–338.

Koninckx, P. R., and Martin, D. C. (1992). Deep endometriosis: a consequence of infiltration or retractionor possibly adenomyosis externa? *Fertil. Steril.* 58, 924–928. doi: 10.1016/S0015-0282(16)55436-3

Matsuzaki, S., Canis, M., Pouly, J. L., Rabischong, B., Botchorishvili, R., and Mage, G. (2006). Relationshipbetween delay of surgical diagnosis and severity of disease in patients with symptomatic deepinfiltrating endometriosis. *Fertil. Steril.* 86, 1314–1316. doi: 10.1016/j.fertnstert.2006.03.048

Nascu, P. C., Vilos, G. A., Ettler, H. C., Abu-Rafea, B., Hollet-Caines, J., and Ahmad, R. (2006). Histopathologic findings on uterosacral ligaments in women with chronic pelvic pain andvisually normal pelvis at laparoscopy. *J. Minim. Invasive Gynecol.* 13, 201–204. doi: 10.1016/j.jmig.2006.02.002

Ohba, T., Mizutani, H., Maeda, T., Matsuura, K., and Okamura, H. (1996). Evaluation of endometriosisin uterosacral ligaments by transrectal ultrasonography. *Hum. Reprod.* 11, 2014–2017. doi: 10.1093/oxfordjournals.humrep.a019535

Saccardi, C., Cosmi, E., Borghero, A., Tregnaghi, A., Dessole, S., and Litta, P. (2012). Comparisonbetween transvaginal sonography, saline contrast sonovaginography and magneticresonance imaging in the diagnosis of posterior deep infiltrating endometriosis. *Ultrasound Obstet. Gynecol.* 40, 464–469. doi: 10.1002/uog.11102

Somigliana, E., Infantino, M., Candiani, M., Vignali, M., Chiodini, A., Busacca, M., et al. (2004). Association rate between deep peritoneal endometriosis and other forms of the disease: pathogenetic implications. *Hum. Reprod.* 19, 168–171. doi: 10.1093/humrep/deg513

Tammaa, A., Fritzer, N., Lozano, P., Krell, A., Salzer, H., Salama, M., et al. (2015). Interobserveragreement and accuracy of non-invasive diagnosis of endometriosis by transvaginalsonography. *Ultrasound Obstet. Gynecol.* 46, 737–740. doi: 10.1002/uog.14843

Vimercati, A., Achilarre, M. T., Scardapane, A., Lorusso, F., Ceci, O., Mangiatordi, G., et al. (2012). Accuracy of transvaginal sonography and contrast-enhanced magnetic resonance-colonographyfor the presurgical staging of deep infiltrating endometriosis. *Ultrasound Obstet. Gynecol.* 40, 592–603. doi: 10.1002/uog.11179

Yantiss, R. K., Clement, P. B., and Young, R. H. (2001). Endometriosis of the intestinal tract: a study of44 cases of a disease that may cause diverse challenges in clinical and pathologicevaluation. *Am. J. Surg. Pathol.* 25, 445–454. doi: 10.1097/00000478-200104000-00003

Conflict of Interest Statement: The authors declare that the research was conducted in the absence of any commercial or financial relationships that could be construed as a potential conflict of interest.

frontiers in Pharmacology

ORIGINAL RESEARCH
published: 24 April 2019
doi: 10.3389/fphar.2019.00413

Controlled *in vivo* Bone Formation and Vascularization Using Ultrasound-Triggered Release of Recombinant Vascular Endothelial Growth Factor From Poly(D,L-lactic-co-glycolicacid) Microbubbles

Yong Gong[1†], Songjian Li[1†], Wei Zeng[2], Jianing Yu[3], Yan Chen[2] and Bo Yu[1*]*

[1]Department of Orthopedics, Zhujiang Hospital, Southern Medical University, Guangzhou, China, [2]Ultrasound Medical Center, Zhujiang Hospital, Southern Medical University, Guangzhou, China, [3]The First School of Clinical Medicine, Southern Medical University, Guangzhou, China

Bone defects are challenging to treat in musculoskeletal system due to the lack of vascularization. Biomaterials with internal vascularization ability and osteoinduction bioactivity are promising strategies for orthopedic applications. Vascular endothelial growth factor (VEGF) has been widely used for angiogenesis and osteogenesis. Here, we developed VEGF-loaded PLGA microbubbles (MBs) for improvement of angiogenesis and osteogenesis in bone defect repair in combination with ultrasound-targeted microbubble destruction (UTMD). Release profile showed UTMD promoted the burst release of VEGF from PLGA MBs. We subsequently investigated the combination of ultrasound application with VEGF MBs for *in vitro* osteogenesis. The results demonstrated that the expression of osteogenesis-related genes and calcium deposits were increased by VEGF MBs in combination of UTMD. Micro-computed tomography (micro-CT) and histological analysis were conducted 4 and 8 weeks post-surgery. *In vivo* results show that VEGF MBs in combination of UTMD could significantly enhance new bone formation and vascular ingrowth at the defect site in a rat calvarial defect model. In summary, VEGF MBs in combination of UTMD could augment bone regeneration and vascularization at calvarial bone defects and hold huge potential for clinical translation.

Keywords: bone defect, vascular endothelial growth factor, angiogenesis, ultrasound, osteogenesis

OPEN ACCESS

Edited by:
Fei Yan,
Shenzhen Institutes of Advanced Technology (CAS), China

Reviewed by:
Fupo He,
Guangdong University of Technology, China
Ai-Ho Liao,
National Taiwan University of Science and Technology, Taiwan
Changsheng Chen,
Research Institute of Tsinghua University in Shenzhen, China

***Correspondence:**
Yan Chen
smu_chen@163.com
Bo Yu
gzyubo@163.com

[†]These authors have contributed equally to this work

Specialty section:
This article was submitted to Translational Pharmacology, a section of the journal Frontiers in Pharmacology

Received: *26 January 2019*
Accepted: *01 April 2019*
Published: *24 April 2019*

Citation:
Gong Y, Li S, Zeng W, Yu J, Chen Y and Yu B (2019) Controlled in vivo Bone Formation and Vascularization Using Ultrasound-Triggered Release of Recombinant Vascular Endothelial Growth Factor From Poly(D,L-lactic-co-glycolicacid) Microbubbles. Front. Pharmacol. 10:413. doi: 10.3389/fphar.2019.00413

INTRODUCTION

The clinical treatment of large bone defects is still a great challenge (Tang et al., 2016; Dang et al., 2017). Early vascularization at the defect area is essential for bone formation (Spiller et al., 2015). Since angiogenesis is closely related to bone regeneration, various growth factors including fibroblast growth factor 2 (FGF2), transforming growth factor (TGF-β), and vascular endothelial growth factor (VEGF) play an important role in neovascularization and endochondral

ossification (Florencio-Silva et al., 2015; Filipowska et al., 2017). Currently, treatments for angiogenesis aim to localized concentration and continuous usage of growth factors. The release of the drug system allows concentrated, low-dose angiogenic factors to act for a long time to promote tissue regeneration. Various natural, synthetic, and complex materials have been used as release carriers for angiogenic growth factors (Freudenberg et al., 2015). VEGF is a key regulator of angiogenesis and also plays an important role in osteogenesis (Gerber et al., 1999; Hu and Olsen, 2016). Localized VEGF delivery has proven effective for osteogenesis in many studies (Kempen et al., 2009; García et al., 2016).

Microbubbles (MBs) are widely used as ultrasound contrast agents, which also have potential therapeutic applications (Lawrie et al., 2000; Prentice et al., 2005). Drugs and genes can be incorporated in the bubble construct. Recently, poly(D,L-lactic-co-glycolicacid) (PLGA) MBs have been reported as drug and gene carriers in different medical and biological applications (Sirsi and Borden, 2009; Formiga et al., 2010). However, there are some limitations in the conventional drug-loaded MBs for controlled release, such as low local concentration and unable to target release (Hernot and Klibanov, 2008). Ultrasound targeted microbubble destruction (UTMD) has been demonstrated as a new promising strategy for non-invasive, targeted drug and gene delivery (Bekeredjian et al., 2006; Tinkov et al., 2009; Chen and Hwang, 2013). Various studies have developed MBs loaded with antitumor genes and drugs successfully in combination with ultrasound for treatment of tumors in animal models (Kiessling et al., 2012; Zhao et al., 2016). However, using VEGF-loaded microbubbles with UTMD for the treatment of bone defects have not been reported yet.

Therefore, in this study, we prepared PLGA MBs containing the angiogenic cytokine VEGF that burst release VEGF in response to ultrasound exposure. We fabricated MBs loaded with or without VEGF using the PLGA 50/50 and PLGA 75/25 copolymers and investigated the release profile, *in vitro* and *in vivo* osteogenesis and angiogenesis capacity.

MATERIALS AND METHODS

Materials

Recombinant human VEGF (rhVEGF165, Sf21-derived) and Quantikine VEGF Elisa kit were purchased from R&D Systems (Minneapolis, MN, USA). Poly(dl-lactide-co-glycolide) (PLGA; *L*/*G* = 50/50, *MW*: 40,000–75,000; *L*/*G* = 75/25, *MW*: 90,000–120,000) was provided by Jinan Daigang Biomaterials (Jinan, China). Polyethylene glycol (PEG; *MW*: 400), bovine serum albumin (BSA), and sodium azide were purchased from Sigma-Aldrich (USA). Poly(vinyl alcohol) (PVA) (*MW*: 125,000) was obtained from Polysciences, Inc. (Warrington, USA). Rabbit polyclonal to CD31 (ab28364)) was supplied by Abcam (Cambridge, MA, USA).

Preparation of PLGA MBs

PLGA MBs were fabricated by the emulsion solvent evaporation method. Briefly, 1.0 g PLGA (50/50, 75/25) was dissolved in 10 ml dichloromethane. A 100-μg VEGF and 5-μl PEG 400 dissolved in 200 μl of water were injected into PLGA solution. For preparation of BSA-loaded MBs, 5 mg of BSA and 5 μl of PEG 400 dissolved in 200 μl of water were injected into PLGA solution. Subsequently, mixed solution was injected into 100 ml of 1% PVA solution, resulting in a multiple emulsion. The multiple emulsion was stirred at 1,000 rpm for 10 h, then collected, and lyophilized. Finally, the MBs were resuspended in 1 ml of ultrapure water, frozen at −80°C, lyophilized, and stored at 4°C. MBs were sterilized by cobalt 60 (^{60}Co) irradiation.

Characterization of MBs

PLGA MBs were observed by scanning electron microscope (SEM, JSM-7001F, Japan). To evaluate the release profile, 3 mg of VEGF-loaded or BSA-loaded 75/25 and 50/50 microbubbles (n = 3) were suspended in 2.0 ml of 0.1 M phosphate buffer (pH 7.4), containing 0.1% BSA and microbiologically preserved with sodium azide. The samples were maintained in rotating vials at 37°C. At 2 and 7 days, sample tubes were exposed to ultrasound radiation. The parameters of US exposure were as follows: frequency, 1 MHz; intensity, 2 W/cm^2; duty cycle, 50%; pulse recurrent frequency, 100 Hz; and duration, 5 min. At scheduled time intervals, sample tubes were centrifuged (25,000 × *g*, 15 min) and the supernatants of 100 μl were harvested and frozen at −80°C. The amounts of released VEGF were quantified using ELISA kits, and released BSA was quantified using a BCA Protein Assay Kit. The *in vitro* ultrasound imaging of MBs was conducted using Visual Sonic 2100 with a MS-250 transducer (VisualSonics, Canada). Blank MBs and VEGF-MBs were dispersed in PBS at 1 × 10^6/ml, and PBS was used as a control.

Alizarin Red S Staining

Alizarin red S staining was determined as described previously (Chen et al., 2017). Briefly, bone marrow stromal cells (BMSCs) at different groups were relatively cultured in osteogenic induction medium at a density of 1.0 × 10^5 cells/well. After 21 days, cells were fixed with 4% (w/v) paraformaldehyde and then stained with 1% alizarin red S (Biochem, Shanghai, China) for 30 min at 25°C with gentle agitation. The cells were gently rinsed with ultrapure water for three times and observed under microscope (Olympus, Tokyo, Japan).

Real-Time Quantitative PCR (RT-qPCR)

After 10 days of co-culture, total RNA was isolated by lysis in TRIzol (Invitrogen Inc., Carlsbad, CA, USA). Total RNA was reverse-transcribed into cDNA from 1.0 μg of the RNA using ReadyScript cDNA Synthesis Mix (Sigma). The mRNA levels of osteogenic-specific genes including osteocalcin (OCN), alkaline phosphatase (ALP), and Runx2 were assessed by RT-qPCR using SYBR Green Master (Roche). β-actin was amplified as an internal control.

Animal Experiments

Ethical approval was obtained from Southern Medical University Institutional Animal Care and Use Committee.

Twenty-four male SD rats (190–240 g) were used for this experiment. The animals were housed under standard conditions with free access to food and water. The experimental groups included blank defect (control, $n = 6$), blank MB (MB, $n = 6$), VEGF-loaded MB (VEGF-MB, $n = 6$), and VEGF-loaded MB in combination with UTMD (VEGF-MB + US, $n = 6$). Under the general anesthesia of ketamine (100 mg/kg bodyweight) and xylazine (10 mg/kg bodyweight), the scalps were exposed. A 5-mm diameter bilateral calvarial defect was created in each rat using a dental bur. 75/25 and 50/50 blank MBs, and VEGF-loaded PLGA MBs were mixed with thiolated chitosan/hydroxyapatite thermo-sensitive hydrogel as we previously described (Liu et al., 2014). Hydrogels were implanted into the defects. After surgery, skin was sutured with a 4–0 silk suture. At 2 and 10 days post-surgery, skulls were exposed to ultrasound for 20 min at the same parameter with *in vitro* study.

Micro-CT Analysis

After harvesting, the skulls at 4 and 8 weeks post-operatively, the specimens were immediately fixed in 10% (v/v) neutral buffered formalin for 48 h. Specimens were scanned at 9 μm resolution for undecalcified samples using an advanced micro-CT instrument (ZKKS-MC-Sharp-IV, Zhongke Kaisheng Bio, Inc.) with scanning parameters of 50 kV, 200 mA and a 0.5-mm aluminum filter. Bone density measurement was performed based on the ROI determined in each sample slice. Trabecular number (Tb.N) was evaluated.

Immunohistochemistry and Histomorphometry

Specimens were decalcified in neutral 10% EDTA solution for 2 weeks at room temperature. After decalcification, 5-μm thick serial slices were sectioned and further stained with anti-CD31 (1:600 dilution; Abcam, Cambridge, MA, USA), respectively, at 4°C overnight. Samples were subsequently incubated with goat anti-rabbit second antibody conjugated with HRP (Boster Company of Biotechnology, China). The imagines of stained specimens were visualized with microscopy. The sections were also stained with hematoxylin and eosin (HE) staining.

Statistics

Descriptive statistics were used to determine group means and standard deviations. Quantitative data were statistically analyzed using the student's *t*-test analysis. Statistically, significance was set at $p < 0.05$.

RESULTS

Characterization of PLGA MBs

SEM analysis showed morphologically intact and smooth surface in blank MBs (**Figure 1A**). Blank MBs showed a fairly uniform distribution and good shelf stability. After loaded with VEGF, the surfaces of MBs were coarser (**Figure 1B**). The average diameter of MBs was about 50 μm. The concentration of MBs was 1×10^7/ml. For *in vitro* release investigation, 50/50 and 75/25 BSA-loaded PLGA MBs showed different release behaviors. The release of BSA from 50/50 PLGA MBs was maintained over 60 days, while 72/25 PLGA MBs exhibited a release period of 20 days (**Figures 1C,D**). **Figure 1E** shows the release profile of VEGF from MBs in PBS (pH 7.4) at 37°C. VEGF was incessantly released from the MBs without US radiation. After US exposure, the burst release was observed in the MBs. US exposure promoted the burst release of VEGF. **Figure 1F** shows the signal of blank MBs and VEGF-MBs can be visualized by ultrasound imaging.

In vitro Osteogenesis

The *in vitro* osteogenesis was investigated through alizarin red S staining 21 days after the BMSCs were cultured with these MBs. 75/25 and 50/50 blank MB cultured alone showed almost no positive staining, 75/25 and 50/50 VEGF-MB showed positive staining, while 75/25 VEGF-MB combined with US group presented the most significantly positive staining (**Figure 2A**). RT-qPCR analysis revealed that the expression of osteogenesis-associated genes OCN and ALP was highest in 75/25 VEGF-MB with ultrasound exposure (**Figure 2B**, $p < 0.05$).

UTMD Delivery of VEGF Promoted Bone Defect Repair

MB and VEGF-MB were mixed with thiolated chitosan/hydroxyapatite thermo-sensitive hydrogel. MBs were distributed in the hydrogel. The hydrogel was free flowing liquid at room temperature, but formed solid-like gel when heated to 37°C. We next investigated the effect of VEGF-MB and UTMD on rat calvarial defect repair at 4 and 8 weeks (**Figure 3B**). The micro-CT imaging performed at 4 and 8 weeks revealed no bone repair in the control group and blank MB (**Figure 3A**). Appreciable new bone formation and ingrowth occurred in the repaired area in the VEGF-MB group at 4 and 8 weeks. The VEGF-MB + US group showed most significant new bone formation among these groups at 4 and 8 weeks. According to micro-CT analysis, the trabecular number (Tb.N) was significantly higher in VEGF-MB + US group (**Figure 3C**) ($p < 0.05$). HE staining was performed after 8 weeks to further verify the repair effect. No new bone formation was observed in control or blank-MB group, but fibrous tissues appeared. The VEGF-MB group showed a small number of new bone formation. Massive bone formation was found in the repaired area in the VEGF-MB + US group (**Figure 4**). Immunohistochemical staining was also conducted to assess CD31 expression after 4 and 8 weeks. CD31 staining revealed slight positive staining in the control and blank-MB groups, while VEGF-MB group resulted in the modern density of new blood vessels (**Figure 5**). The VEGF-MB + US group showed most significant positive staining, suggesting that this group exhibits the best osteogenesis capacity and bone repair ability.

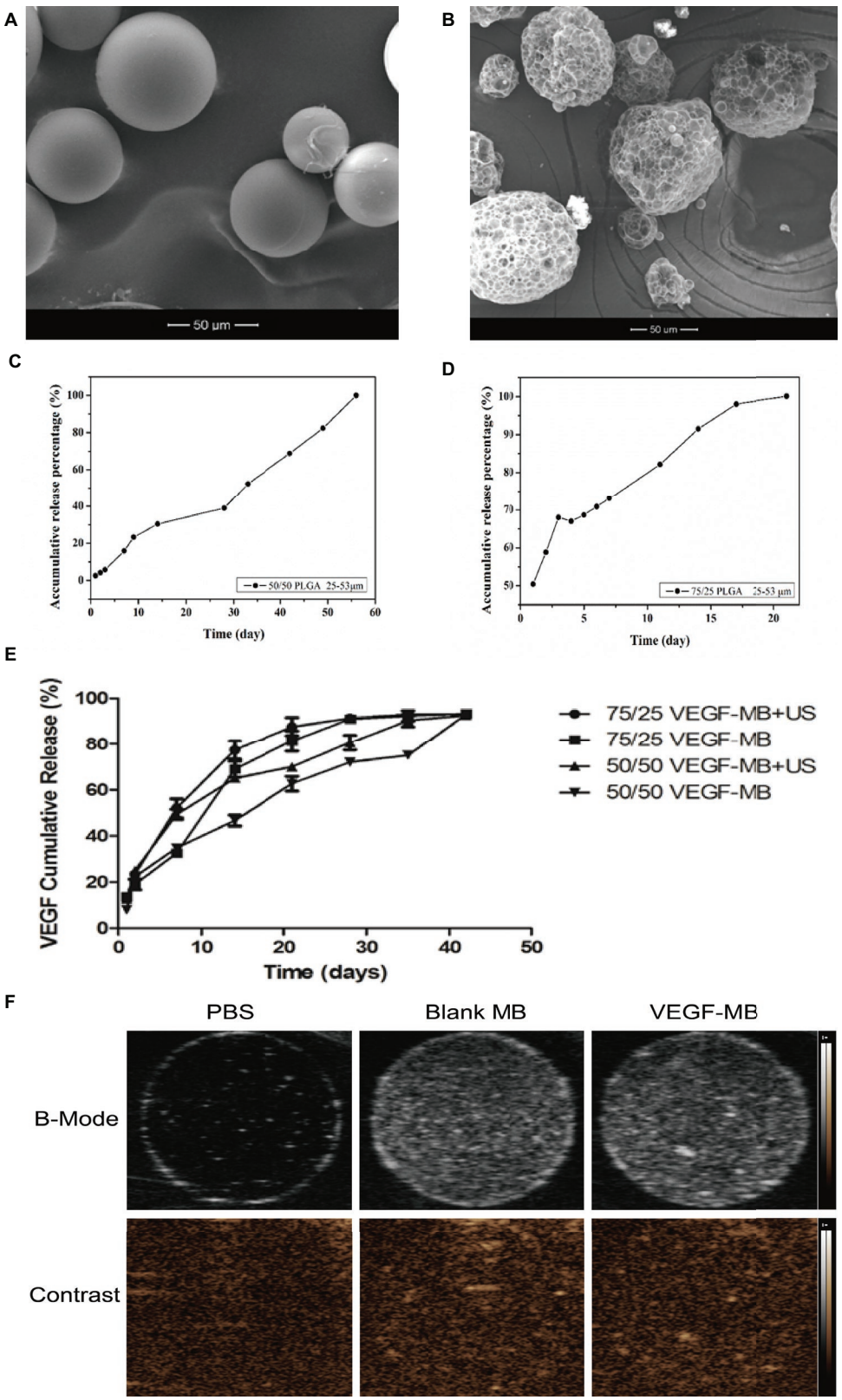

FIGURE 1 | Characterization of PLGA MBs. **(A)** SEM of blank PLGA MBs. **(B)** SEM of VEGF-loaded PLGA MBs. (Scale bar = 50 μm). **(C,D)** Release profile of BSA from 50/50 and 75/25 PLGA MBs. **(E)** Release profile of VEGF from 50/50 and 75/25 PLGA MBs with or without UTMD. **(F)** Ultrasound images of blank PLGA MBs and VEGF-loaded PLGA MBs dispersed in PBS. Upper panel, B-mode images; bottom panel, contrast-mode images.

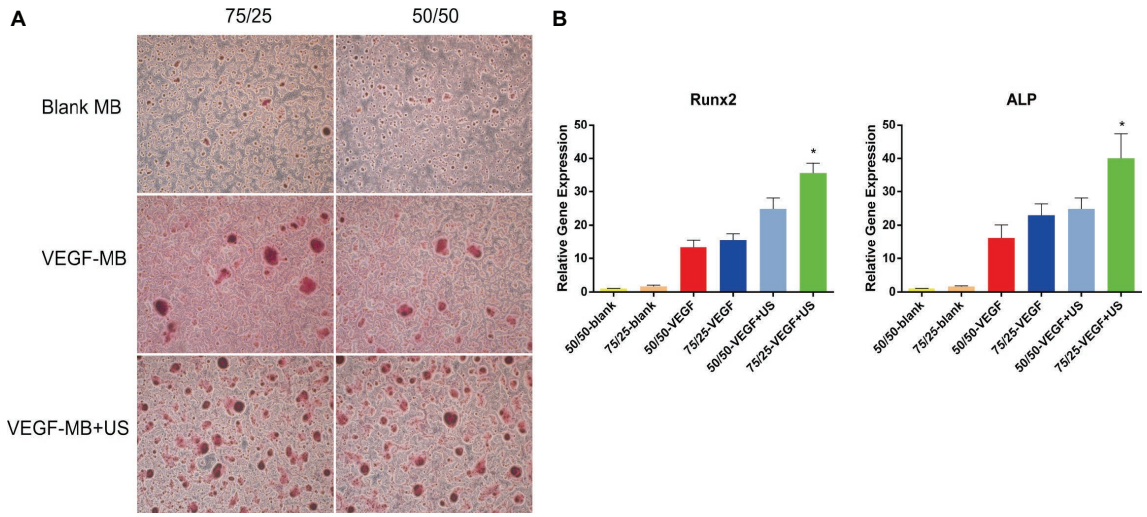

FIGURE 2 | *In vitro* osteogenesis of PLGA MBs. **(A)** Alizarin red S staining of BMSCs cultured with blank MB, VEGF-MB with or without UTMD for 21 days. **(B)** RT-qPCR analysis of osteogenesis-associated genes Runx2 and ALP expression. *$p < 0.05$.

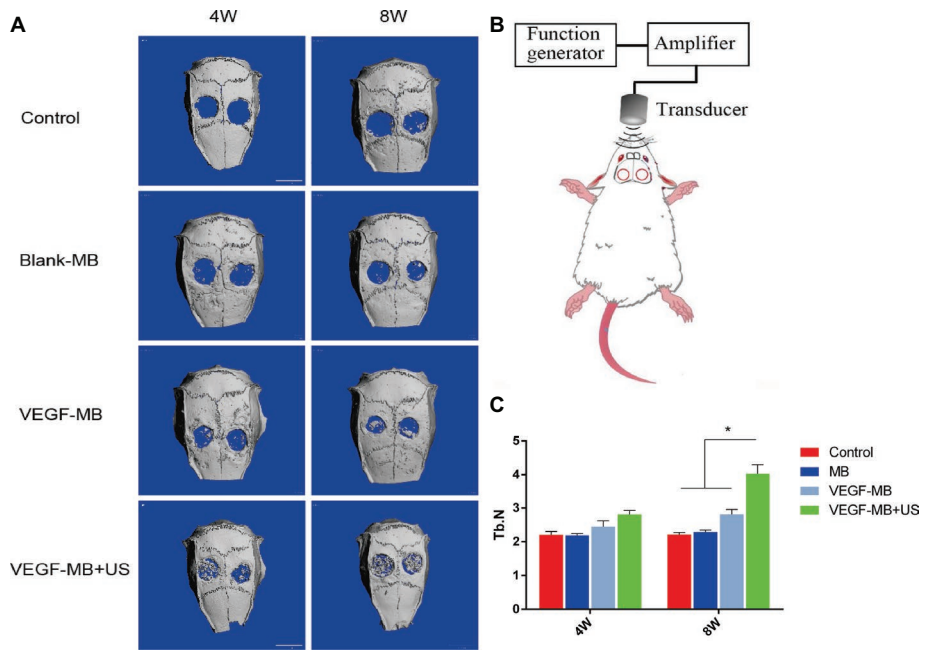

FIGURE 3 | Evaluation of calvarial bone defect repair *in vivo*. **(A)** Micro-CT analysis of skulls 4 and 8 weeks post-surgery. **(B)** Schematic representation of UTMD for *in vivo* investigation. **(C)** Quantitive analysis of trabecular number 4 and 8 weeks post-surgery. *$p < 0.05$.

DISCUSSION

Large or segmental bone defects caused by trauma, tumor, and inflammation have always been a difficult problem in clinical treatment (El-Rashidy et al., 2017). Injectable bone tissue engineering materials can be injected into the bone defect by minimally invasive methods. It can also carry and release growth factors and drugs. In this study, we designed VEGF-loaded microbubbles so that microbubbles could carry VEGF protein and locally burst release when conducting UTMD, leading to drug accumulation in bone defect area and enhanced repair effect. The repair and treatment of bone defects has always been one of the important problems in the clinical. The rate of autologous blood vessel growth is about tens of micrometers per day, especially for large-area bone defects, which is not enough to vascularize the entire implanted tissue (Padilla et al., 2017). It is the key factor to solve the problem of insufficient blood supply in the defect site and promote

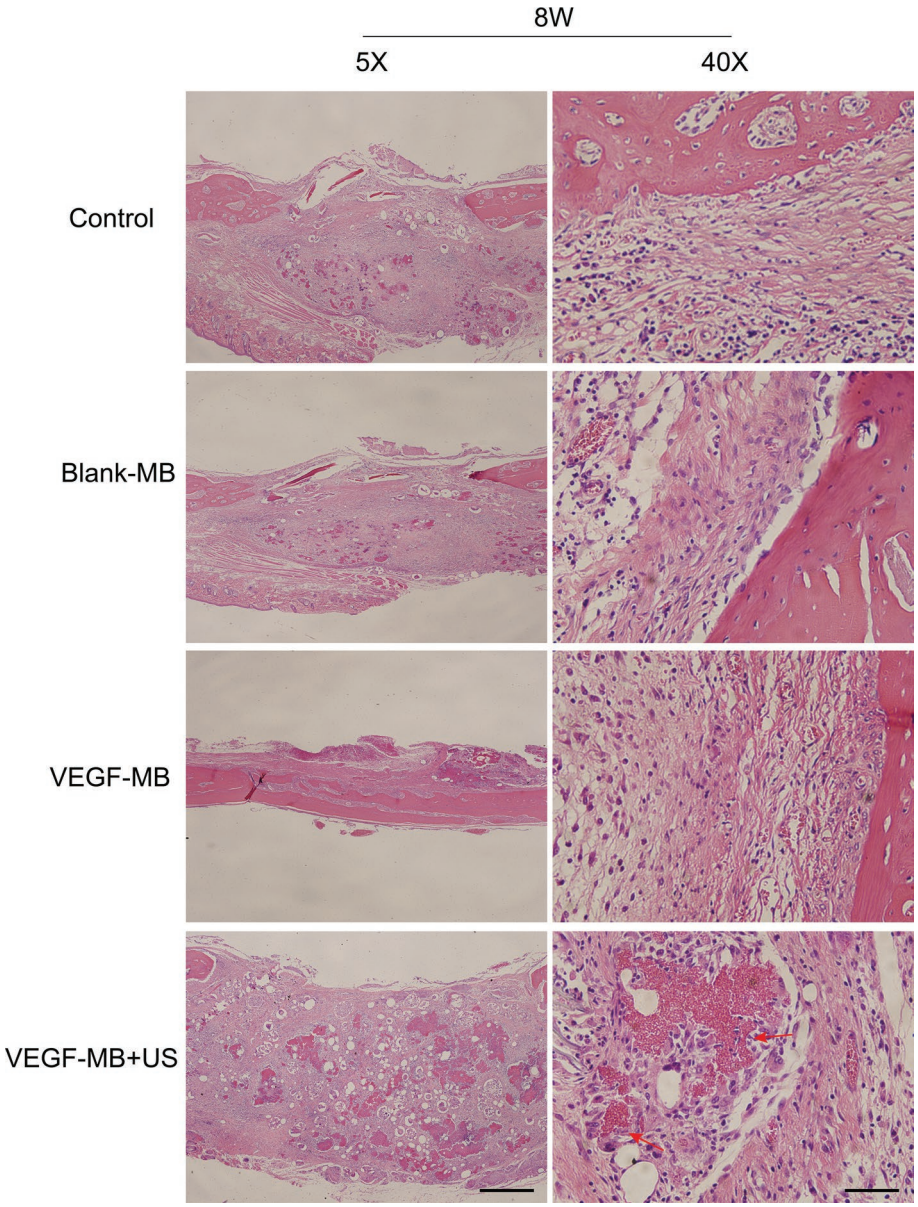

FIGURE 4 | Histological assessment of bone regeneration at 8 weeks after surgery by H&E staining. Red arrow represents new vessels formation (Scale bar = 400 and 50 μm).

the bone repair. Early vascularization is currently the most direct and effective method for vascularizing bone substitutes (Zhang et al., 2017). However, due to the deficiencies of multiple operations, this method is limited to the repair of small-area bone defects and soft tissue injuries.

VEGF is recognized as one of the most potent cytokines in inducing angiogenesis, also directly related to bone formation (Duan et al., 2016; Simons et al., 2016). In the inflammation phase during bone repair, VEGF is accumulated in the hematoma after bone injury (Loi et al., 2016). In endochondral bone formation during bone repair, VEGF improves the migration of osteoblastic cells and induces cartilage formation (Dai and Rabie, 2007). Various reports have investigated that VEGF affects bone repair and regeneration and developed systems for local delivery of VEGF (Martino et al., 2015; Schumacher et al., 2017; Sharmin et al., 2017). PLGA-coated β-TCP scaffolds containing VEGF were developed to deliver VEGF for bone repair (Khojasteh et al., 2016). The data showed the scaffolds with VEGF, presenting most significant bone regeneration *in vitro*. VEGF-loaded hydrogels exhibited significantly increased vascularization and bone formation in segmental bone defect animal models (García et al., 2016). In this study, we found that VEGF-loaded MB could increase osteogenesis both *in vitro* and *in vivo*, which was consistent with these studies.

Ultrasound-targeted microbubble destruction (UTMD) is a novel method for drug and gene transfection based on acoustic

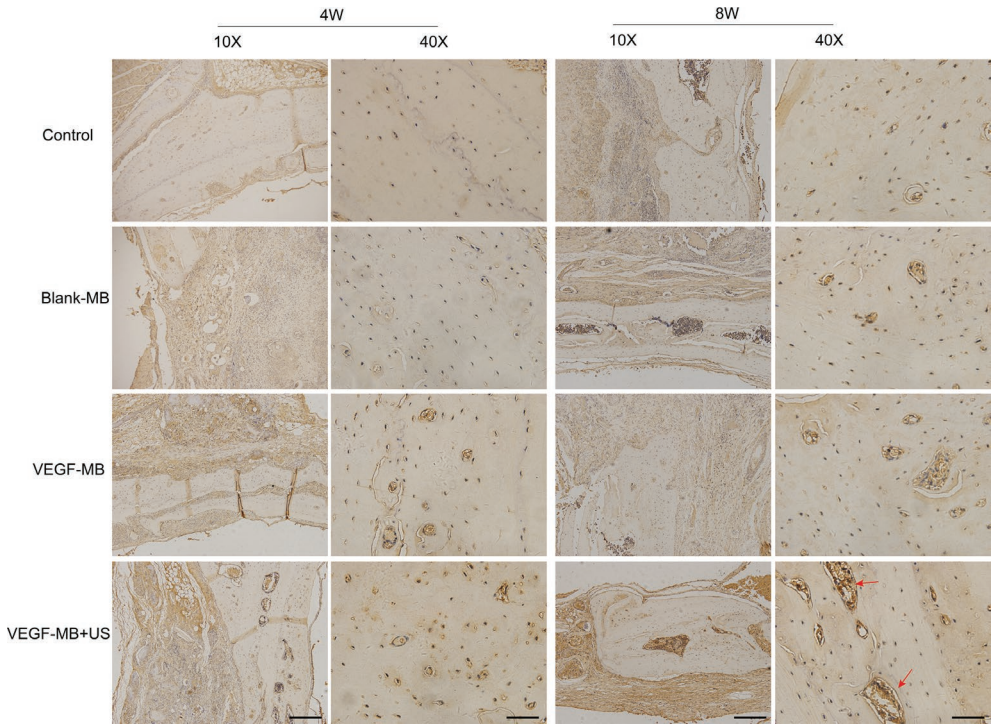

FIGURE 5 | Histological assessment of bone regeneration at 4 and 8 weeks after surgery by anti-CD31 immunohistochemistry staining. Red arrow represents new vessels formation. (Scale bar = 200 and 50 μm).

cavitation. UTMD can release the drug locally and achieve the goal of targeted therapy in animal models (Chen et al., 2006; Kopechek et al., 2015; Zhao et al., 2016). UTMD allows the spatiotemporal target release of encapsulated VEGF in the local bone defect area. In this study, we conducted UTMD after VEGF-loaded MB implanted into rat calvarial defects. We found that UTMD promoted the burst release of VEGF and presented most significant bone regeneration *in vivo*.

In conclusion, we demonstrated the use of VEGF-loaded MB for enhancing calvarial defects by UTMD burst release. Results showed that VEGF-loaded MB combined with UTMD promoted osteogenesis *in vitro* and enhanced bone repair *in vivo* compared with those groups without UTMD treatment.

ETHICS STATEMENT

This study was carried out in accordance with the recommendations of Guide for the Care and Use of Laboratory Animals, the Southern Medical University Institutional Animal Care and Use Committee. The protocol was approved by the Southern Medical University Institutional Animal Care and Use Committee.

AUTHOR CONTRIBUTIONS

YG, YC, and BY designed the experiment. YG, JY, WZ, and SL performed the experiment. YG investigated the study and wrote the manuscript. BY acquired funding, contributed to resources, and supervised the study.

FUNDING

This work was supported by the National Natural Science Foundation of China (grant number: 81871355, 81371931, and 81301240).

REFERENCES

Bekeredjian, R., Katus, H., and Kuecherer, H. (2006). Therapeutic use of ultrasound targeted microbubble destruction: a review of non-cardiac applications. *Ultraschall. Med.* 28, 134–140. doi: 10.1055/s-2005-858993

Chen, S., Ding, J.-H., Bekeredjian, R., Yang, B.-Z., Shohet, R. V., Johnston, S. A., et al. (2006). Efficient gene delivery to pancreatic islets with ultrasonic microbubble destruction technology. *Proc. Natl. Acad. Sci. U.S.A.* 103, 8469–8474. doi: 10.1073/pnas.0602921103

Chen, H., and Hwang, J. H. (2013). Ultrasound-targeted microbubble destruction for chemotherapeutic drug delivery to solid tumors. *J. Ther. Ultrasound* 1:10. doi: 10.1186/2050-5736-1-10

Chen, Y., Liu, X., Liu, R., Gong, Y., Wang, M., Huang, Q., et al. (2017). Zero-order controlled release of BMP2-derived peptide P24 from the chitosan scaffold by chemical grafting modification technique for promotion of osteogenesis in vitro and enhancement of bone repair in vivo. *Theranostics* 7, 1072–1087. doi: 10.7150/thno.18193

Dai, J., and Rabie, A. (2007). VEGF: an essential mediator of both angiogenesis and endochondral ossification. *J. Dent. Res.* 86, 937–950. doi: 10.1177/154405910708601006

Dang, M., Koh, A. J., Jin, X., McCauley, L. K., and Ma, P. X. (2017). Local pulsatile PTH delivery regenerates bone defects via enhanced bone remodeling in a cell-free scaffold. *Biomaterials* 114, 1–9. doi: 10.1016/j.biomaterials.2016.10.049

Duan, X., Bradbury, S. R., Olsen, B. R., and Berendsen, A. D. (2016). VEGF stimulates intramembranous bone formation during craniofacial skeletal development. *Matrix Biol.* 52, 127–140. doi: 10.1016/j.matbio.2016.02.005

El-Rashidy, A. A., Roether, J. A., Harhaus, L., Kneser, U., and Boccaccini, A. R. (2017). Regenerating bone with bioactive glass scaffolds: a review of in vivo studies in bone defect models. *Acta Biomater.* 62, 1–28. doi: 10.1016/j.actbio.2017.08.030

Filipowska, J., Tomaszewski, K. A., Niedźwiedzki, Ł., Walocha, J. A., and Niedźwiedzki, T. (2017). The role of vasculature in bone development, regeneration and proper systemic functioning. *Angiogenesis* 20, 291–302. doi: 10.1007/s10456-017-9541-1

Florencio-Silva, R., Sasso, G. R., Sasso-Cerri, E., Simões, M. J., and Cerri, P. S. (2015). Biology of bone tissue: structure, function, and factors that influence bone cells. *BioMed Res. Int.* 2015. doi: 10.1155/2015/421746

Formiga, F. R., Pelacho, B., Garbayo, E., Abizanda, G., Gavira, J. J., Simon-Yarza, T., et al. (2010). Sustained release of VEGF through PLGA microparticles improves vasculogenesis and tissue remodeling in an acute myocardial ischemia–reperfusion model. *J. Controlled Release* 147, 30–37. doi: 10.1016/j.jconrel.2010.07.097

Freudenberg, U., Zieris, A., Chwalek, K., Tsurkan, M. V., Maitz, M. F., Atallah, P., et al. (2015). Heparin desulfation modulates VEGF release and angiogenesis in diabetic wounds. *J. Controlled Release* 220, 79–88. doi: 10.1016/j.jconrel.2015.10.028

García, J. R., Clark, A. Y., and García, A. J. (2016). Integrin-specific hydrogels functionalized with VEGF for vascularization and bone regeneration of critical-size bone defects. *J. Biomed. Mater. Res. A* 104, 889–900. doi: 10.1002/jbm.a.35626

Gerber, H.-P., Vu, T. H., Ryan, A. M., Kowalski, J., Werb, Z., and Ferrara, N. (1999). VEGF couples hypertrophic cartilage remodeling, ossification and angiogenesis during endochondral bone formation. *Nat. Med.* 5, 623–628. doi: 10.1038/9467

Hernot, S., and Klibanov, A. L. (2008). Microbubbles in ultrasound-triggered drug and gene delivery. *Adv. Drug Delivery Rev.* 60, 1153–1166. doi: 10.1016/j.addr.2008.03.005

Hu, K., and Olsen, B. R. (2016). Osteoblast-derived VEGF regulates osteoblast differentiation and bone formation during bone repair. *J. Clin. Invest.* 126, 509–526. doi: 10.1172/JCI82585

Kempen, D. H., Lu, L., Heijink, A., Hefferan, T. E., Creemers, L. B., Maran, A., et al. (2009). Effect of local sequential VEGF and BMP-2 delivery on ectopic and orthotopic bone regeneration. *Biomaterials* 30, 2816–2825. doi: 10.1016/j.biomaterials.2009.01.031

Khojasteh, A., Fahimipour, F., Eslaminejad, M. B., Jafarian, M., Jahangir, S., Bastami, F., et al. (2016). Development of PLGA-coated β-TCP scaffolds containing VEGF for bone tissue engineering. *Mater. Sci. Eng. C Mater. Biol. Appl.* 69, 780–788. doi: 10.1016/j.msec.2016.07.011

Kiessling, F., Fokong, S., Koczera, P., Lederle, W., and Lammers, T. (2012). Ultrasound microbubbles for molecular diagnosis, therapy, and theranostics. *J. Nucl. Med.* 53, 345–348. doi: 10.2967/jnumed.111.099754

Kopechek, J. A., Carson, A. R., McTiernan, C. F., Chen, X., Hasjim, B., Lavery, L., et al. (2015). Ultrasound targeted microbubble destruction-mediated delivery of a transcription factor decoy inhibits STAT3 signaling and tumor growth. *Theranostics* 5, 1378–1387. doi: 10.7150/thno.12822

Lawrie, A., Brisken, A. F., Francis, S. E., Cumberland, D. C., Crossman, D. C., and Newman, C. M. (2000). Microbubble-enhanced ultrasound for vascular gene delivery. *Gene Ther.* 7, 2023–2027. doi: 10.1038/sj.gt.3301339

Liu, X., Chen, Y., Huang, Q., He, W., Feng, Q., and Yu, B. (2014). A novel thermo-sensitive hydrogel based on thiolated chitosan/hydroxyapatite/beta-glycerophosphate. *Carbohydr. Polym.* 110, 62–69. doi: 10.1016/j.carbpol.2014.03.065

Loi, F., Córdova, L. A., Pajarinen, J., Lin, T.-H., Yao, Z., and Goodman, S. B. (2016). Inflammation, fracture and bone repair. *Bone* 86, 119–130. doi: 10.1016/j.bone.2016.02.020

Martino, M. M., Briquez, P. S., Maruyama, K., and Hubbell, J. A. (2015). Extracellular matrix-inspired growth factor delivery systems for bone regeneration. *Adv. Drug Delivery Rev.* 94, 41–52. doi: 10.1016/j.addr.2015.04.007

Padilla, S., Sánchez, M., Orive, G., and Anitua, E. (2017). Human-based biological and biomimetic autologous therapies for musculoskeletal tissue regeneration. *Trends Biotechnol.* 35, 192–202. doi: 10.1016/j.tibtech.2016.09.008

Prentice, P., Cuschieri, A., Dholakia, K., Prausnitz, M., and Campbell, P. (2005). Membrane disruption by optically controlled microbubble cavitation. *Nat. Phys.* 1, 107–110. doi: 10.1038/nphys148

Schumacher, M., Reither, L., Thomas, J., Kampschulte, M., Gbureck, U., Lode, A., et al. (2017). Calcium phosphate bone cement/mesoporous bioactive glass composites for controlled growth factor delivery. *Biomater. Sci.* 5, 578–588. doi: 10.1039/C6BM00903D

Sharmin, F., McDermott, C., Lieberman, J., Sanjay, A., and Khan, Y. (2017). Dual growth factor delivery from biofunctionalized allografts: Sequential VEGF and BMP-2 release to stimulate allograft remodeling. *J. Orthop. Res.* 35, 1086–1095. doi: 10.1002/jor.23287

Simons, M., Gordon, E., and Claesson-Welsh, L. (2016). Mechanisms and regulation of endothelial VEGF receptor signalling. *Nat. Rev. Mol. Cell Biol.* 17, 611–625. doi: 10.1038/nrm.2016.87

Sirsi, S., and Borden, M. (2009). Microbubble compositions, properties and biomedical applications. *Bubble Sci. Eng. Technol.* 1, 3–17.

Spiller, K. L., Nassiri, S., Witherel, C. E., Anfang, R. R., Ng, J., Nakazawa, K. R., et al. (2015). Sequential delivery of immunomodulatory cytokines to facilitate the M1-to-M2 transition of macrophages and enhance vascularization of bone scaffolds. *Biomaterials* 37, 194–207. doi: 10.1016/j.biomaterials.2014.10.017

Tang, D., Tare, R. S., Yang, L.-Y., Williams, D. F., Ou, K.-L., and Oreffo, R. O. (2016). Biofabrication of bone tissue: approaches, challenges and translation for bone regeneration. *Biomaterials* 83, 363–382. doi: 10.1016/j.biomaterials.2016.01.024

Tinkov, S., Bekeredjian, R., Winter, G., and Coester, C. (2009). Microbubbles as ultrasound triggered drug carriers. *J. Pharm. Sci.* 98, 1935–1961. doi: 10.1002/jps.21571

Zhang, W., Feng, C., Yang, G., Li, G., Ding, X., Wang, S., et al. (2017). 3D-printed scaffolds with synergistic effect of hollow-pipe structure and bioactive ions for vascularized bone regeneration. *Biomaterials* 135, 85–95. doi: 10.1016/j.biomaterials.2017.05.005

Zhao, Y.-Z., Lin, Q., Wong, H. L., Shen, X.-T., Yang, W., Xu, H.-L., et al. (2016). Glioma-targeted therapy using Cilengitide nanoparticles combined with UTMD enhanced delivery. *J. Controlled Release* 224, 112–125. doi: 10.1016/j.jconrel.2016.01.015

Conflict of Interest Statement: The authors declare that the research was conducted in the absence of any commercial or financial relationships that could be construed as a potential conflict of interest.

The reviewer CC declared a past co-authorship with one of the authors with the author BY to the handling editor.

frontiers in Pharmacology

ORIGINAL RESEARCH
published: 08 May 2019
doi: 10.3389/fphar.2019.00478

Efficacy Assessment of Ultrasound Guided Lauromacrogol Injection for Ablation of Benign Cystic and Predominantly Cystic Thyroid Nodules

Yijie Dong, Jianqiao Zhou, Zhenhua Liu, Ting Luo and Weiwei Zhan*

Ruijin Hospital, School of Medicine, Shanghai Jiao Tong University, Shanghai, China

Background: To assess the efficacy and safeness of ultrasound guided lauromacrogol injection for ablation of benign cystic and predominantly cystic thyroid nodules.

Methods: From July 2016 to July 2018, 102 patients with 107 nodules were treated with ultrasound guided lauromacrogol injections for ablation and 43 nodules completed at least 12 months follow-up. Nodules sonographic characteristics, volume changes before and after USG-LIA, and complications were evaluated.

Results: Mean nodule volume decreased from 17.27 ± 20.51 ml to 5.35 ± 14.68ml ($P < 0.05$), and the overall resolution rate (volume reduction rate > 50%) was 91.67% in purely cysts and 75.90% in predominantly cystic nodules at the last follow-up. Within 6 months after treatment, the volume of the target nodule at each follow-up was smaller than the previous one ($P < 0.001$ for all). However, there was no significant difference of volume change between the 6th month and the 12th month. No severe complications occurred in this study.

Conclusion: Ultrasound guided lauromacrogol injection for ablation is an effective and safe treatment modality in both purely cystic and predominantly cystic thyroid nodules.

Keywords: ultrasound, lauromacrogol, ablation, thyroid, nodules

OPEN ACCESS

Edited by:
Fei Yan,
Shenzhen Institutes of Advanced Technology (CAS), China

Reviewed by:
Fajin Dong,
Shenzhen People's Hospital, China
Qiyu Zhao,
Zhejiang University, China

****Correspondence:***
Jianqiao Zhou
zhousu30@126.com

Specialty section:
This article was submitted to Translational Pharmacology, a section of the journal Frontiers in Pharmacology

Received: *25 January 2019*
Accepted: *16 April 2019*
Published: *08 May 2019*

Citation:
Dong Y, Zhou J, Liu Z, Luo T and Zhan W (2019) Efficacy Assessment of Ultrasound Guided Lauromacrogol Injection for Ablation of Benign Cystic and Predominantly Cystic Thyroid Nodules. Front. Pharmacol. 10:478. doi: 10.3389/fphar.2019.00478

INTRODUCTION

Cystic nodules are very common in benign thyroid nodules, which could cause symptomatic and cosmetic problems in 60–90% patients (Bennedbaek and Hegedus, 2003; Valcavi and Frasoldati, 2004). Surgery is the ultimate treatment for intractable benign cystic nodules. In addition to surgery, simple fine-needle aspiration, saline injection and ultrasound guided percutaneous ethanol injection (USG-PEI) are other alternative treatment options. It was reported that simple aspiration and saline injection had only 7–38% success rate. As a comparison, mainly USG-PEI had 75–86.3%

success rate (Valcavi and Frasoldati, 2004; Sung et al., 2013; Reverter et al., 2015). However, USG-PEI had a high recurrence rate in predominantly cystic nodules and complications included flushing, dizziness, and dysphonia, and even several ethyl toxic necrosis caused by ethanol leakage to surrounding tissues (Mauz et al., 2005; Jang et al., 2012; Suh et al., 2015). Lauromacrogol, another type of chemical sclerosants different from alcohol, has been widely used in esophageal variceal bleeding, varicose vein. Literature has also reported lauromacrogol treatments in cystic lesion of viscera such as hepatic cysts, renal cysts and pancreatic cystic neoplasms (Moser et al., 2013; Xue and Geng, 2015; Yonguc et al., 2015; Linghu et al., 2017; Star et al., 2018). However, lauromacrogol was rarely reported in the treatment of thyroid nodules.

Therefore, the aim of this study was to evaluate the efficacy and safeness of ultrasound guided lauromacrogol injection for ablation (USG-LIA) of cystic and predominantly cystic thyroid nodules.

MATERIALS AND METHODS

Patients

This prospective study was approved by our Institutional Review Board. From July 2016 to July 2018, 117 patients with symptomatic or aesthetical nodules which ultrasound confirmed purely cystic and predominantly cystic thyroid nodules were recommended for USG-LIA. Nodules with solid components less than 10% were defined as purely cyst. Nodules with solid components 10–50% were defined as predominantly cyst (Gharib et al., 2016). Patients were chosen according to the following criteria: (1) cystic nodules or predominantly cystic nodules (>50% fluid components on ultrasound); (2) cytology confirmed benign thyroid nodules with maximum diameter larger than 10 mm in ultrasound; (3) cosmetic problems or pressure symptoms but no dyspnea (vital signs were stable); (4) normal serum thyroid hormones and TSH level. The following exclusion criteria were also used: (1) reluctance to receive USG-LIA; (2) pregnancy; (3) coagulopathy (international normalized ratio > 1.5, platelets < 50,000); (4) lost follow-up. Finally, a total of 107 nodules in 102 patients were enrolled in this study. Thirty of them were male and 72 were female, aged 18–72 years (mean age, 50 ± 13 years).

Ultrasound Examination

All patients were fully informed of the advantages and disadvantages of surgery, ultrasound guided radiofrequency ablation (USG-RA) and USG-LIA in the treatment of thyroid nodules. Written informed consent was provided by each patient before procedure. Thyroid ultrasound examination and ultrasound-guided fine-needle aspiration cytology were performed before USG-LIA. Both procedures were performed by one of the two radiologists with more than 10, 20 years of ultrasound experiences and more than 5, 10 years of intervention experiences, respectively. Thyroid ultrasound examination was performed by using the Resona 7 ultrasound system (Mindray Medical International, Shenzhen, China) equipped with the L14-5 and L11-3 high frequency linear array probes. Gray-scale ultrasound images of the target thyroid nodule in transversal and longitudinal section were obtained. Ultrasound features of target nodule including size, location, shape, margin, and components were assessed. Volume of nodules was calculated using the following equation: $V = \pi$ abc / 6, where V is the volume, a is the largest diameter in longitudinal axis, and b and c are the other two diameters in transversal axis.

USG-LIA Procedure

Patients were placed in a supine position with mild neck extension. Ultrasound- guided fine-needle aspiration was performed by one radiologist using a 25-gaged needle. The samples from aspirated fluid in purely cystic nodules or solid components in predominantly cystic nodules were sent for cytology. USG-LIA was performed after the benign cytological result was reported. In general, USG-LIA was performed by two radiologists. One radiologist handled the probe with one hand, and a 18–22 gauge needle fitted to a T-junction with another hand. After regional skin sterilization but no anesthesia, the radiologist chose the best puncture path and inserted the needle tip into the target nodule under ultrasound guidance via the trans-isthmic approach. Then, the other radiologist connected a 20-ml plastic syringe with the T-junction and sucked the cystic fluid from the nodule. After the maximum volume of internal fluid was aspirated, lauromacrogol (Lauromacrogol Injection, 10 mL: 100 mg; Tianyu Pharmaceutical Co Ltd., Shanxi, China) was injected into the nodule. For nodules that were difficult to aspirate due to viscous cystic fluid, normal saline was used to lavage the cavity for 2–3 times before lauromacrogol injection. The volume of injected lauromacrogol usually corresponded to about 30–50% of the volume of aspirated fluid. Then, the needle was withdrawn slowly with minimal negative pressure of the syringe, thus preventing lauromacrogol leakage outside the thyroid gland. Volumes of aspirated fluid and injected lauromacrogol were recorded for each nodule. Patients were asked to stay for observation at least 30 min after the procedure. Images of the nodules and the procedures of USG-LIA were stored on both local hard disk and DICOM system.

Follow-up

Follow-up ultrasound examinations were performed 1st, 3rd, 6th, 12th month and a 6 months interval from 2nd year after the initial procedure. Any complications during follow-up were evaluated. Volume and ultrasound feature of treated nodule were assessed and recorded. Volume reduction rate (VRR) was defined as (initial volume − last volume)/ initial volume. If the volume reduction rate was less than 20% at the 3-month follow-up, repeated USG-LIA was performed again and the corresponding follow-up was also performed. If the reduction rate was less than 50%, and the solid part of the nodule is rich in blood supply, USG-RA or surgery was recommended, and the last volume of these nodules was set as the volume before USG-RA or surgery treatment. The resolution rate was defined as VRR > 50%. VRR < 50% was defined as

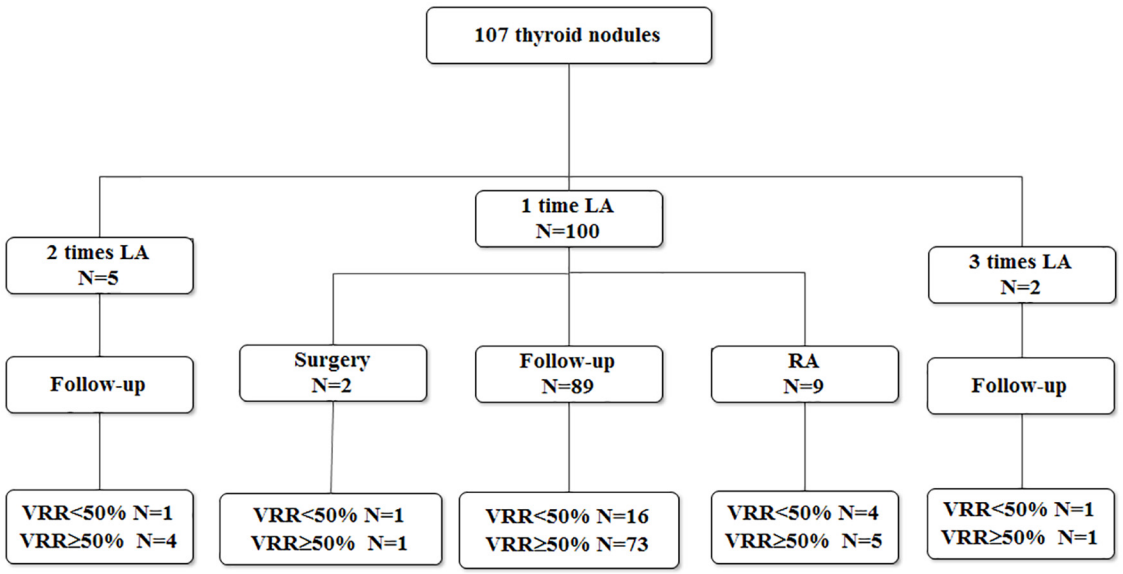

FIGURE 1 | Results of 107 thyroid nodules treated with USG-LIA.

ineffective, 50–90% was defined as effective, and > 90% was defined as cured.

Statistical Analysis

Statistical analyses were performed using SPSS version 17.0 (SPSS Inc., Chicago, IL, United States). Wilcoxon signed ranks test was used to compare initial and last volume and maximum diameter of the treated nodule before and after USG-LIA. This test was also used to compare volume changes during follow-up (initial volume vs. 1st month, 1st vs. 3rd month, 3rd vs. 6th month, 6th vs. 12th month, and 12th month vs. last volume). Mann-Whitney U test was used to assess the efficacy between purely cysts and predominantly cystic nodules. The predetermined level of significance was set at a *P* value of 0.05.

TABLE 1 | Baseline characteristics of 107 nodules treated with USG-LIA.

Characteristics	Results
Mean age, y (SD)	50 (13)
Sex, *n*	
Male	30
Female	72
Component, *n*	
Purely cysts	24
Predominantly cystic	83
Watery/Viscous, *n*	89/18
Volume of aspiration, mean (range)	15.6, (0.4–160)ml
Volume of remained lauromacrogol, mean (range)	6.37, (0.2–40)ml
Follow-up period, mean (range)	10.2, (1–24)month

TABLE 2 | Results of 107 nodules treated with USG-LIA.

Characteristics	Mean ± SD	Range	*P* value
Initial volume	17.27 ± 20.51	0.38–146 ml	0.000
Last volume	5.35 ± 14.68	0–139.95 ml	
Initial diameter (maximum)	37.92 ± 12.44	10.5–88.0 m m	0.000
Last diameter(maximum)	21.63 ± 12.39	0–77.2 mm	

RESULTS

There were 24 purely cystic (22.22%) and 83 predominantly cystic nodules (77.78%). The cytology results of these 107 nodules included 101 thyroid cysts, 5 goiters with cystic change, 1 adenoma with cystic change. One hundred of 107 (93.46%) nodules treated by one session of USG-LIA, 5 (4.67%) underwent 2 sessions of USG-LIA, 2 (1.87%) underwent 3 sessions of USG-LIA (**Figure 1**). The average volume of aspiration was 15.6 ml, range from 0.4 to160 ml, and mean volume of injected lauromacrogol was 6.37 ml, range from 0.2 to 40 ml. The medium of follow-up period was 10.2 months, range from 1 to 24 months (**Table 1**).

The effectiveness of USG-LIA according to initial volume of 107 nodules was listed in **Table 2**. The average initial volume and maximum diameter of nodules was 17.27 ± 20.51 ml and

TABLE 3 | Volume changes of 43 nodules with more than 12 months follow-up period.

Characteristics	Mean ± SD(ml)	Range
Initial volume	13.24 ± 15.46	0.38–88.26 ml
1 month volume	3.68 ± 6.47	0.19–37.38 ml
3 month volume	2.33 ± 4.84	0.1–27.23 ml
6 month volume	1.46 ± 2.84	0.03–14.14 ml
12 month volume	1.40 ± 2.84	0.04–14.14 ml

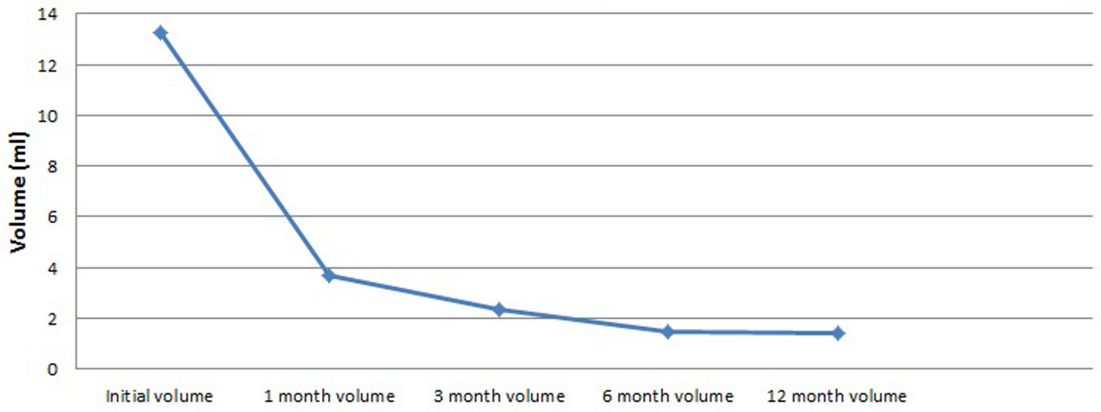

FIGURE 2 | Volume changes of 43 thyroid nodules after USG-LIA with more than 12 months follow-up.

37.92 ± 12.44 mm. The average last volume and maximum diameter of nodules was 5.35 ± 14.68 ml and 21.63 ± 12.39 mm. There was significance of volume and diameter reduction before and after treatment ($P = 0.000$ for both).

We analyzed volume changes of 43 nodules that follow-up at least 12 months and listed them in **Table 3** and **Figure 2**. After USG-LIA, the average volume reduced from 13.24 ± 15.46 ml (initial volume) to 3.68 ± 6.47 ml (1st month), 2.33 ± 4.84 (3rd month) and 1.46 ± 2.84 (6th month). By the time of terminal follow-up, the average volume reduced to 1.39 ± 2.84 ml. Within 6 months after treatment, the volume of the target nodule at each follow-up was smaller than the previous one ($P < 0.001$ for all). However, there was no significant difference of volume change between 6th month and 12th month.

Among 107 nodules treated by USG-LIA, 85 nodules (79.44%) had volume reduced rate > 50% and no recurrence by the end of the study. The overall resolution rate (VRR > 50%) was 91.67% in purely cysts and 75.90% in predominantly cystic nodules. The ineffective rate (VRR < 50%), effective rate (VRR 50–90%) and cured rate (VRR > 90%) were 8.33, 37.5, 54.17% in purely cysts and 24.10, 40.96, and 34.94% in predominantly cystic nodules, respectively (**Table 4** and **Figures 3**, **4**). There was significant difference in efficacy rate between purely cystic nodules and predominantly cystic nodules ($P = 0.047$).

TABLE 4 | Efficacy of USG-LIA treatment in purely cysts and Predominantly cystic nodules.

Nodule Characteristics	Volume reduction			Total
	<50%	50–90%	>90%	
Purely cysts	2 (8.33%)	9 (37.5%)	13 (54.17%)	24 (100%)
Predominantly cysts	20 (24.10%)	34 (40.96%)	29 (34.94%)	83 (100%)
Total	22 (20.56%)	43 (40.19%)	42 (39.25%)	107 (100%)

Twenty-two out of 107 nodules had a VRR < 50%. Among them, 20 were predominantly cystic nodules and only 2 of them were purely cysts. Of the 100 nodules that performed 1 session of USG-LIA, 20 of them had a VRR < 50%. Of the 5 that performed 2 sessions, 1 had a VRR < 50%. Of the 2 that performed 3 sessions, 1 had a VRR < 50%. The overall resolution rate (VRR > 50%) after 1 session, 2 sessions and 3 sessions of USG-LIA was 74.77% (80/107), 78.50% (84/107), 79.44% (85/107). Of the 7 nodules that performed 2–3 sessions of USG-LIA, 5 were predominantly cystic nodules.

Complications

Mild or moderate fever (37.5–39°C) with mild neck pain occurred in 5.9% patients (6/102) after treatment of USG-LIA within 3 days. All symptoms disappeared and patients recovered within 1 week after symptomatic treatment. No severe complications occurred in this study.

DISCUSSION

Cystic nodules are almost impossible to be malignant, and partially cystic nodules without any suspicious ultrasound features have a malignancy rate of < 3% (Haugen et al., 2016). It is generally considered that USG-PEI is a safe and effective therapy for benign purely cystic and predominantly cystic thyroid nodules (Gharib et al., 2016; Haugen et al., 2016). Lauromacrogol, a new sclerosing agent different from absolute alcohol was used in this study. Lauromacrogol injection is an effective sclerosing agent consisting of polyoxyethylene lauryl ether [molecular formula:C12H25(OCH2CH2)nOH (n = 9), formula weight:582.8], with accessories of alcohol and water. Lauromacrogol injection has been used in hemorrage of esophago gastric varices and varix of lower limb for a decade. It was believed that this sclerosing agent was safe and effective in treating heptatic cysts and renal cysts (Dell'Atti, 2015; Xue and Geng, 2015; Wijnands et al., 2018). Animal model experiments showed that lauromacrogol may destroy thyroid endothelial cells

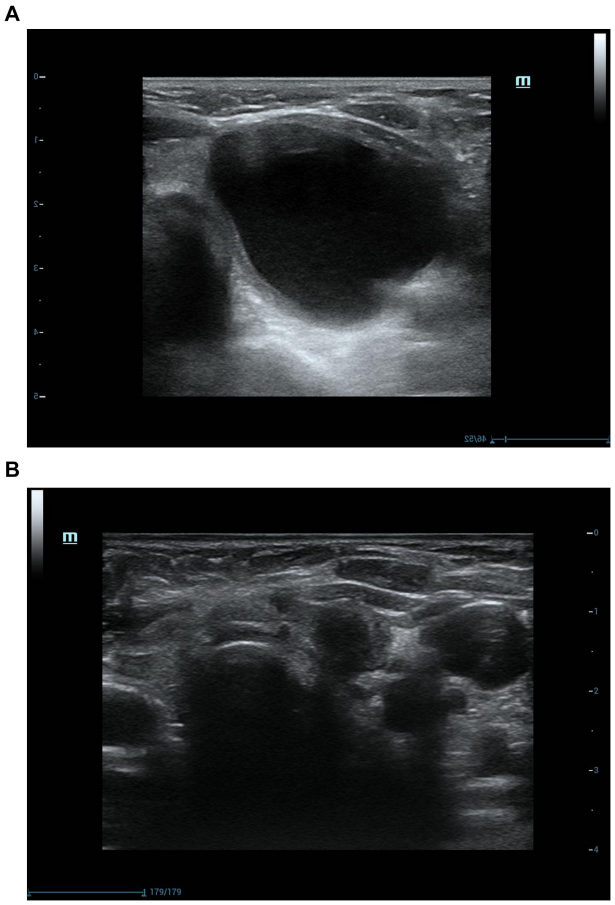

FIGURE 3 | Ultrasonograpic image of a 70 years old female before and after treatment.**(A)** A purely cystic nodule of sonography before USG-LIA.**(B)** 18 months after USG-LIA.

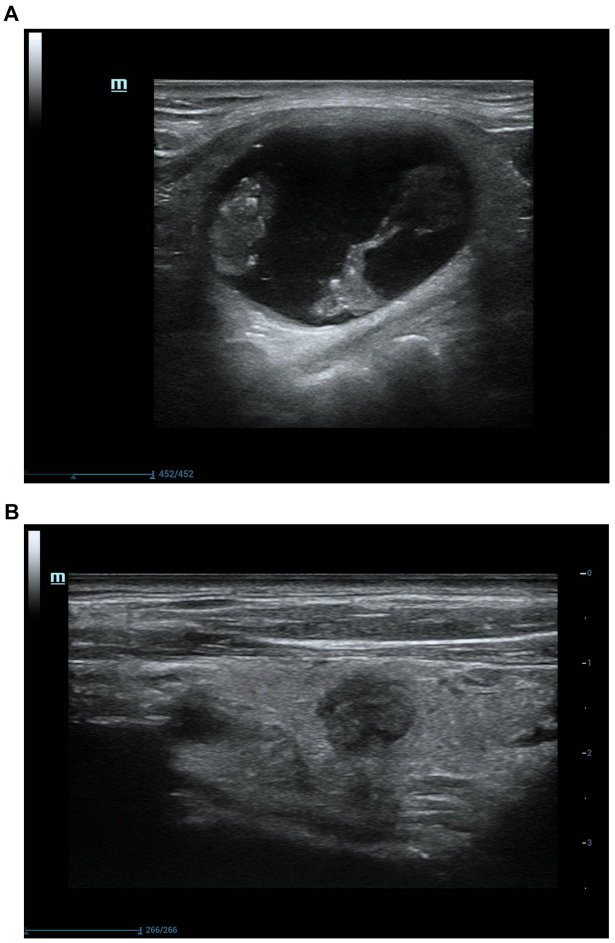

FIGURE 4 | Ultrasonograpic image of a 62 years old male before and after treatment.**(A)** A predominantly cystic nodule before USG-LIA.**(B)** 12 months after USG-LIA.

on the capsule wall of the cysts, leading to aseptic inflammation and increasing fibrosis (Idiz et al., 2016).

Our study found that there was a significant difference in efficacy rate of USG-LIA between purely cystic nodules and predominantly cystic nodules ($P = 0.047$). Results revealed that USG-LIA had excellent performance in the treatment of purely cysts, of which over 90% had an effective volume shrinkage (VRR > 50%), and more than half had been cured (VRR > 90%). As a contrast, in predominantly cystic nodules, 75.9% of the nodules had an effective volume shrinkage, and 34.9% had been cured. Kim reported that USG-PEI had superior effect in the treatment of purely cysts than predominantly cystic nodules (therapeutic success rate: 90.3 vs. 82.2%) (Kim et al., 2012). In this study, we obtained similar results (91.67 vs. 75.90%).

It was reported that USG-PEI had a 75–85% success rate in treating cystic nodules and 17.9–21% of USG-PEI patients had side effect such as mild pain, fever, blush, and dizziness (Bennedbaek and Hegedus, 2003; Valcavi and Frasoldati, 2004; Mauz et al., 2005; Suh et al., 2015). Comparing these with USG-PEI, our results demonstrated that USG-LIA had equivalent effects but fewer complications. Only 5.9% (6/102) of patients complained of mild-to-moderate fever with mild neck pain.

We found that the volume of the treated nodules gradually shrank within 6 months ($P < 0.001$ for all). However, 6 months after USG-LIA, the average volume of treated nodules reduced less obviously. Therefore, it seems reasonable that the next management plan of each nodule be decided in the 6th month follow-up. In this study, seven patients had more than two sessions of USG-LIA treatment and finally five of them had VRR > 50%. Therefore, repeated USG-LIA procedures should be performed in some intractable nodules.

This study was characterized by some limitations. First, our work was a single-center prospective study. Second, part of the patients (20/102) had a short follow-up period (1 months), which might cause under-estimation of effectiveness. Therefore, further studies are needed to verify our results.

In conclusion, our study demonstrates that USG-LIA is an effective and safe treatment modality in both purely cystic and predominantly cystic thyroid nodules, and can be used as an alternative to surgery.

AUTHOR CONTRIBUTIONS

JZ, WZ designed the study. ZL, TL acquired the data. YD contributed manuscript and analysis. JZ revised the manuscript.

ACKNOWLEDGMENTS

The authors would like to thank all the staff working in Ultrasound Department of Ruijin Hospital.

REFERENCES

Bennedbaek, F. N., and Hegedus, L. (2003). Treatment of recurrent thyroid cysts with ethanol: a randomized double-blind controlled trial. *J. Clin. Endocrinol. Metab.* 88, 5773–5777. doi: 10.1210/jc.2003-031000

Dell'Atti, L. (2015). Comparison between the use of 99% ethanol and 3% polidocanol in percutaneous echoguided sclerotherapy treatment of simple renal cysts. *Urol. Ann.* 7, 310–314. doi: 10.4103/0974-7796.152026

Gharib, H., Papini, E., Garber, J. R., Duick, D. S., Harrell, R. M., Hegedus, L., et al. (2016). American association of clinical endocrinologists, american college of endocrinology, and associazione medici endocrinologi medical guidelines for clinical practice for the diagnosis and management of thyroid nodules–2016 update. *Endocr. Pract.* 22, 622–639. doi: 10.4158/EP161208.GL

Haugen, B. R., Alexander, E. K., Bible, K. C., Doherty, G. M., Mandel, S. J., and Nikiforov, Y. E. (2016). 2015 american thyroid association management guidelines for adult patients with thyroid nodules and differentiated thyroid cancer: the american thyroid association guidelines task force on thyroid nodules and differentiated thyroid cancer. *Thyroid* 26, 1–133. doi: 10.1089/thy.2015.0020

Idiz, U. O., Aysan, E., Can, I., Buyukpinarbasili, N., Yardimci, E. Y., and Bektasoglu, H. (2016). The effects of lauromacrogol on thyroid tissue in rabbits. Is this a safe option for the treatment of nodular thyroid disease?. *Ann. Ital. Chir.* 87, 192–197.

Jang, S. W., Baek, J. H., Kim, J. K., Sung, J. Y., Choi, H., Lim, H. K., et al. (2012). How to manage the patients with unsatisfactory results after ethanol ablation for thyroid nodules: role of radiofrequency ablation. *Eur. J. Radiol.* 81, 905–910. doi: 10.1016/j.ejrad.2011.02.039

Kim, Y. J., Baek, J. H., Ha, E. J., Lim, H. K., Lee, J. H., Sung, J. Y., et al. (2012). Cystic versus predominantly cystic thyroid nodules: efficacy of ethanol ablation and analysis of related factors. *Eur. Radiol.* 22, 1573–1578. doi: 10.1007/s00330-012-2406-5

Linghu, E., Du, C., Chai, N., Li, H., Wang, Z., Sun, Y., et al. (2017). A prospective study on the safety and effectiveness of using lauromacrogol for ablation of pancreatic cystic neoplasms with the aid of EU. *Gastrointest. Endosc.* 86, 872–880. doi: 10.1016/j.gie.2017.03.1525

Mauz, P. S., Stiegler, M., Holderried, M., and Brosch, S. (2005). Complications of ultrasound guided percutaneous ethanol injection therapy of the thyroid and parathyroid glands. *Ultraschall Med.* 26, 142–145. doi: 10.1055/s-2005-857867

Moser, K. H., Mosch, C., Walgenbach, M., Bussen, D. G., Kirsch, J., Joos, A. K., et al. (2013). Efficacy and safety of sclerotherapy with polidocanol foam in comparison with fluid sclerosant in the treatment of first-grade haemorrhoidal disease: a randomised, controlled, single-blind, multicentre trial. *Int. J. Colorectal Dis.* 28, 1439–1447. doi: 10.1007/s00384-013-1729-2

Reverter, J. L., Alonso, N., Avila, M., Lucas, A., Mauricio, D., and Puig-Domingo, M. (2015). Evaluation of efficacy, safety, pain perception and health-related quality of life of percutaneous ethanol injection as first-line treatment in symptomatic thyroid cysts. *BMC Endocr. Disord.* 15:73. doi: 10.1186/s12902-015-0069-3

Star, P., Connor, D. E., and Parsi, K. (2018). Novel developments in foam sclerotherapy: focus on Varithena(R) (polidocanol endovenous microfoam) in the management of varicose veins. *Phlebology* 33, 150–162. doi: 10.1177/0268355516687864

Suh, C. H., Baek, J. H., Ha, E. J., Choi, Y. J., Lee, J. H., Kim, J. K., et al. (2015). Ethanol ablation of predominantly cystic thyroid nodules: evaluation of recurrence rate and factors related to recurrence. *Clin. Radiol.* 70, 42–47. doi: 10.1016/j.crad.2014.09.008

Sung, J. Y., Baek, J. H., Kim, K. S., Lee, D., Ha, E. J., and Lee, J. H. (2013). Symptomatic nonfunctioning parathyroid cysts: role of simple aspiration and ethanol ablation. *Eur. J. Radiol.* 82, 316–320. doi: 10.1016/j.ejrad.2012.10.009

Valcavi, R., and Frasoldati, A. (2004). Ultrasound-guided percutaneous ethanol injection therapy in thyroid cystic nodules. *Endocr. Pract.* 10, 269–275. doi: 10.4158/EP.10.3.269

Wijnands, T. F., Schoenemeier, B., Potthoff, A., Gevers, T. J., Groenewoud, H., Gebel, M. J., et al. (2018). Ethanol sclerotherapy or polidocanol sclerotherapy for symptomatic hepatic cysts. *United European Gastroenterol. J.* 6, 919–925. doi: 10.1177/2050640618764940

Xue, J., and Geng, X. (2015). Curative effect of lauromacrogol and absolute ethyl alcohol injection guided by ultrasound on simplex hepatic cyst. *Pak. J. Pharm. Sci.* 28(2 Suppl.), 697–700.

Yonguc, T., Sen, V., Aydogdu, O., Bozkurt, I. H., Yarimoglu, S., and Polat, S. (2015). The comparison of percutaneous ethanol and polidocanol sclerotherapy in the management of simple renal cysts. *Int. Urol. Nephrol.* 47, 603–607. doi: 10.1007/s11255-015-0953-9

Conflict of Interest Statement: The authors declare that the research was conducted in the absence of any commercial or financial relationships that could be construed as a potential conflict of interest.

frontiers in Pharmacology

ORIGINAL RESEARCH
published: 22 May 2019
doi: 10.3389/fphar.2019.00544

Ultrasound Stimulation Modulates Voltage-Gated Potassium Currents Associated With Action Potential Shape in Hippocampal CA1 Pyramidal Neurons

Zhengrong Lin[1†], Xiaowei Huang[1†], Wei Zhou[1], Wenjun Zhang[1,2], Yingzhe Liu[1,3], Tianyuan Bian[1,3], Lili Niu[1], Long Meng[1]* and Yanwu Guo[4]**

[1] Paul C. Lauterbur Research Center for Biomedical Imaging, Institute of Biomedical and Health Engineering – Shenzhen Institutes of Advanced Technology, Chinese Academy of Sciences, Shenzhen, China, [2] Key Laboratory of E&M, Ministry of Education and Zhejiang Province, Zhejiang University of Technology, Hangzhou, China, [3] Sino-Dutch Biomedical and Information Engineering School, Northeastern University, Shenyang, China, [4] The National Key Clinic Specialty, The Engineering Technology Research Center of Education Ministry of China, Guangdong Provincial Key Laboratory on Brain Function Repair and Regeneration, Department of Neurosurgery, Zhujiang Hospital, Southern Medical University, Guangzhou, China

Potassium channels (K^+) play an important role in the regulation of cellular signaling. Dysfunction of potassium channels is associated with several severe ion channels diseases, such as long QT syndrome, episodic ataxia and epilepsy. Ultrasound stimulation has proven to be an effective non-invasive tool for the modulation of ion channels and neural activity. In this study, we demonstrate that ultrasound stimulation enables to modulate the potassium currents and has an impact on the shape modulation of action potentials (AP) in the hippocampal pyramidal neurons using whole-cell patch-clamp recordings *in vitro*. The results show that outward potassium currents in neurons increase significantly, approximately 13%, in response to 30 s ultrasound stimulation. Simultaneously, the increasing outward potassium currents directly decrease the resting membrane potential (RMP) from −64.67 ± 1.10 mV to −67.51 ± 1.35 mV. Moreover, the threshold current and AP fall rate increase while the reduction of AP half-width and after-hyperpolarization peak time is detected. During ultrasound stimulation, reduction of the membrane input resistance of pyramidal neurons can be found and shorter membrane time constant is achieved. Additionally, we verify that the regulation of potassium currents and shape of action potential is mainly due to the mechanical effects induced by ultrasound. Therefore, ultrasound stimulation may offer an alternative tool to treat some ion channels diseases related to potassium channels.

Keywords: ultrasound stimulation, potassium currents, action potential, hippocampal neurons, neuro-modulation

OPEN ACCESS

Edited by:
Xiaobing Wang,
Shaanxi Normal University, China

Reviewed by:
Jie Tang,
Southern Medical University, China
Yi Yuan,
Yanshan University, China

***Correspondence:**
Lili Niu
ll.niu@siat.ac.cn
Long Meng
long.meng@siat.ac.cn
Yanwu Guo
eguoyanwu@163.com

[†]These authors have contributed equally to this work

Specialty section:
This article was submitted to Translational Pharmacology, a section of the journal Frontiers in Pharmacology

Received: *08 January 2019*
Accepted: *30 April 2019*
Published: *22 May 2019*

Citation:
Lin Z, Huang X, Zhou W, Zhang W, Liu Y, Bian T, Niu L, Meng L and Guo Y (2019) Ultrasound Stimulation Modulates Voltage-Gated Potassium Currents Associated With Action Potential Shape in Hippocampal CA1 Pyramidal Neurons. Front. Pharmacol. 10:544. doi: 10.3389/fphar.2019.00544

INTRODUCTION

Potassium channels (K^+), a high degree of diversity and ubiquity embedded within cellular membranes of neurons, are one of the most fundamental and important component in the function of ion channels (Mackinnon, 2003; Mckeown et al., 2008; Coetzee et al., 2010). Potassium channels-mediated trans-membrane ion currents play a critical role in neuronal resting membrane potential (RMP) and action potential repolarization (Schwindt et al., 1988; Kolb, 1990; Pongs, 1999; Vacher et al., 2008; Johnston et al., 2010). Dysfunction of K^+ channels has been found to associate with many diseases, such as long QT syndrome, episodic ataxia and epilepsy (Adelman et al., 1995; Shieh et al., 2000; Giudicessi and Ackerman, 2012; Maljevic and Lerche, 2014). A common feature of these diseases is associated to a reduction of potassium currents or loss of membrane potential repolarization (Lawson, 2000a; Sandhiya and Dkhar, 2009). Functional modulation of potassium channels is of great significance for clinical treatment of these relevant diseases (Lawson, 2000b; Maljevic and Lerche, 2013).

Ultrasound stimulation has emerged as a promising approach to modulate the nervous system that is capable of transmitting through the intact skull non-invasively and focusing acoustic energy in the deep brain nuclei precisely (Tufail et al., 2010, 2011; Bystritsky and Korb, 2015; Leinenga et al., 2016). It has been proven that neural activity could be evoked by ultrasound stimulation from model organism to human beings (Tufail et al., 2010; Legon et al., 2014; Li et al., 2016; Zhou et al., 2017; Lin et al., 2018). More importantly, various studies have demonstrated that regulation of neuronal activity induced by ultrasound stimulation resulted from activating ion channels with different types (Bystritsky et al., 2011). Tyler et al. (2008) illustrated that ultrasound could induce electrical activity in neurons by activating voltage-gated sodium channels and voltage-gated calcium channels. Chapman et al. (1980) demonstrated that ultrasound stimulation could modulate rates of influx and efflux of potassium ions in rat thymocytes *in vitro*. Kubanek et al. (2016) showed that ultrasound stimulation could directly modulate the trans-membrane currents flowing through the mechano-sensitive ion channels (sodium channels and potassium channels) expressed in *Xenopus oocytes*. Rencently, we reported that ultrasound stimulation enables to increase neuronal excitability by increasing the total sodium currents and modulating the sodium channels kinetics (Lin et al., 2018).

Although growing interest and research in ultrasound-induced modulation of different ion channels, little is known about the effect of ultrasound stimulation on potassium channels of neurons. In this paper, we first investigate the modulation of ultrasound stimulation on potassium channels in hippocampal pyramidal neurons using *in vitro* patch-clamp recording in brain slices. In neurons, action potentials play a central role in cell-to-cell communication and finely tuned by the diverse populations of ion channels expressed in cellular membranes which act as a molecular switch for controlling the activity of targeted neurons (Llinás, 1988; Hille, 2001; Bean, 2007). Small change in different types of ion channels conductance can lead to dramatic changes in action potential shape and even overall excitability (Swensen and Bean, 2005; Amendola et al., 2012; Goldman et al., 2013). We further quantify how the increased potassium currents induced by ultrasound stimulation impact AP properties and neural excitability. Moreover, the underlying mechanisms remains unknown and it is necessary to further investigate the candidate mechanisms including thermal effect, mechanical effect and cavitation effect on single neuron.

MATERIALS AND METHODS

Ultrasound Application

In this study, we developed an ultrasound neuro-modulation chip by the standard MEMS (Microelectromechanical systems) processes. This chip was a kind of surface acoustic wave device as described before (Lin et al., 2018) and generate a uniform acoustic field with a clear acoustic boundary which can precisely modulate neuronal activity in the region-specific slices. **Figure 1A** shows the ultrasound neuro-modulation chip which was compatible with the patch-clamp recording system. The response of the hippocampal CA1 slices to the ultrasound stimulation also could be recorded in a real time manner. Briefly, a pair of interdigital transducers (IDTs) at the resonant frequency of 27.38 MHz was excited to generate standing surface acoustic waves (SSAWs) to stimulate the neurons. The acoustic energy was localized to the substrate surface, facilitating the stimulation of the neurons located at a polydimethylsiloxane ring-shaped (PDMS, Sylgard 184, Dow Corning, United States) recording chamber with a relatively small input power (Klemic et al., 2002). Continuous radio frequency (RF) signals were generated by an arbitrary waveform generator (AFG 3102, Tektronix, Beaverton, OR, United States), amplified by a power amplifier (ZHL-1-2W+, Mini-Circuits, Brooklyn, NY, United States) and then applied to both IDTs. The spatial-peak-pulse-average intensity (I_{SPPA}) generated by IDTs in the experiments was approximately 465 mW/cm^2, measured by a Laser Doppler Velocimetry (UHF-120 Ultra High-Frequency Vibrometer, Polytec, Germany).

Slices Preparation

All animal experiments were performed according to the guidelines approved by the Use Committee and the Ethics Committee of Shenzhen Institutes of Advanced Technology, Chinese Academy of Sciences. Postnatal day 13–15 (P13–15) Sprague-Dawley (SD) rats were used in this study. Animals were sacrificed using a rodent guillotine under deep anesthesia with 20% urethane (10 ml/kg). The brain was rapidly removed from the skull and immersed in ice-cold, oxygenated high-sucrose cutting solution (0–2°C) containing (in mM): 60 NaCl, 3 KCl, 7 $MgCl_2$, 1.25 NaH_2PO_4, 25 $NaHCO_3$, 10 D-glucose, 115 sucrose, and 0.5 $CaCl_2$. Coronal slices (300 μm thick) containing the hippocampus CA1 area were prepared with a Vibratome (VT-1200 Series, Leica). The hippocampal slices were equilibrated and incubated in the artificial cerebrospinal fluid (ACSF) containing (in mM): 126 NaCl, 2.5 KCl, 1 $MgCl_2$, 1.25 NaH_2PO_4, 26 $NaHCO_3$, 10 D-glucose, 2 sodium pyruvate, 0.5 L-Ascorbic acid, and 2 $CaCl_2$, saturated continuously with 95% O_2−5% CO_2 and

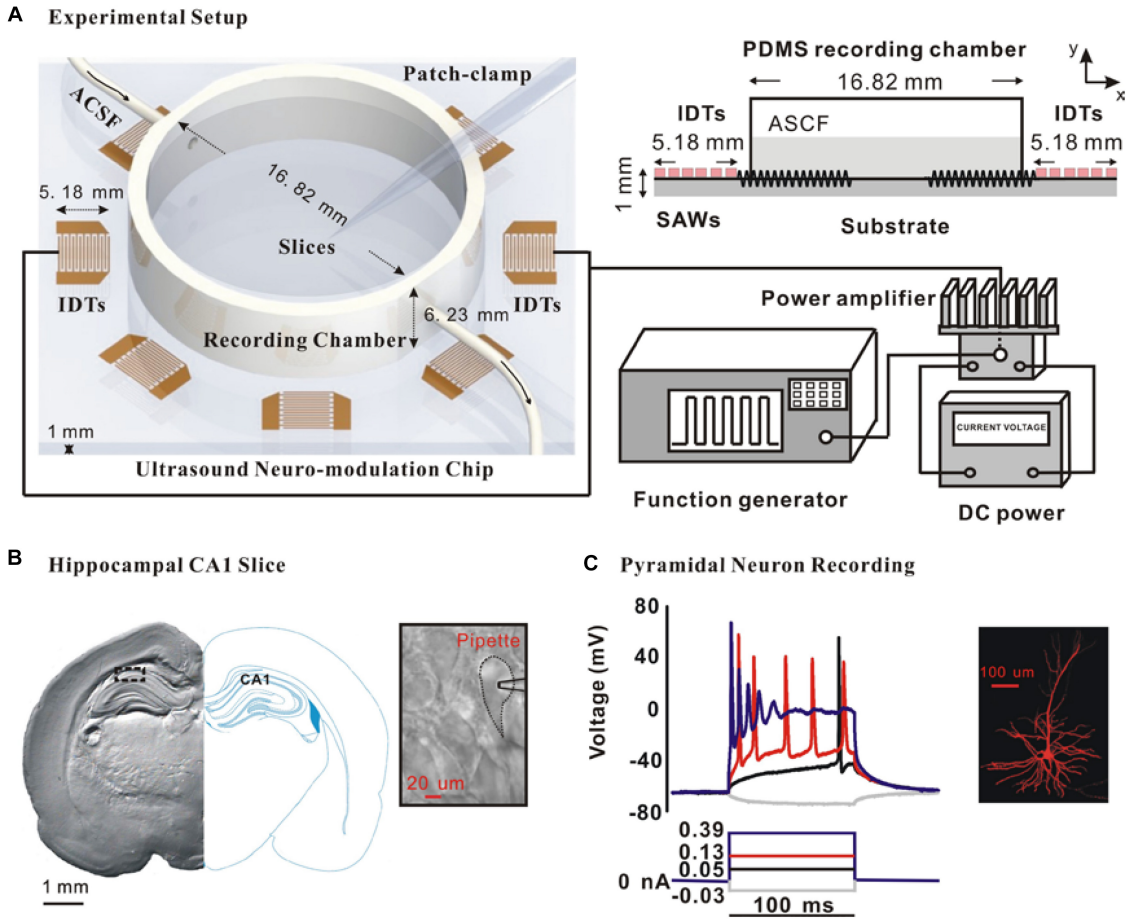

FIGURE 1 | Schematic of the experimental system and the whole-cell recording of pyramidal neurons in the hippocampal CA1 slices. **(A)** Schematic of the entire experimental system and a cross-sectional diagram of the exposure setting with the actual dimensions. **(B)** Photomicrograph of a coronal section of hippocampal CA1 slice and a typical pyramidal neuron for the whole-cell recording. **(C)** Action potential in response to prolonged depolarizing current injection is one important feature to identify pyramidal neuron. Moreover, intracellular injection with 0.25% biocytin shows the morphology of a typical CA1 pyramidal neuron.

maintaining the temperate at 35°C. The osmolality of ACSF was 300–310 Osm/kg.

Electrophysiological Recording

After incubation, brain slices were transferred to the recording chamber. The slices were per-fused with ACSF flowing at a rate of 2–3 ml/min which was maintained at 30°C by an automatic temperature controller (TC-344B, WARNER) in the experiments. As shown in **Figure 1B**, the CA1 pyramidal neurons in the hippocampus were visualized by the morphology using an infrared DIC microscope (FN-S2N, Nikon, Japan). Further identification was carried out by the intra-cellular injection of 0.25% biocytin (**Figure 1C**).

Traditional whole-cell voltage-clamp and current-clamp recording were performed to record the isolated K^+ currents and evoked action potentials of pyramidal neurons using a patch-clamp amplifier EPC 10 (HEKA, Germany). In whole-cell recording, series resistance (Rs) compensation was used to correct membrane voltage errors under conditions of high access resistance between pipette and cell interior. 70–90% compensation was applied to stabilize the final Rs value to 1–3 MOhm. Membrane potentials were corrected for junction potentials by applying the appropriate offset potential before recording. Leakage and capacitive currents were subtracted on-line. Patch glass microelectrodes were pulled by a micropipette puller (P-97, Sutter Instrument Co., Novato, CA, United States) and the resistance ranged from 5 to 10 MΩ after filling with the internal solution. To measure the isolated outward potassium currents in voltage-clamp mode, neurons were held at −70 mV, current-voltage (I-V) curve was obtained by applying depolarizing from −60 to +60 mV for 200 ms in 10 mV increment (Schwindt et al., 1988; Kolb, 1990; Pongs, 1999; Vacher et al., 2008; Johnston et al., 2010). The experiments were performed at room temperate (22–25°C). TTX (1 μM) and $CdCl_2$ (0.3 mM) were added to block sodium channels, Ca^{2+} current and Ca^{2+}-dependent K^+ currents. Furthermore, recording currents were further identified by a pharmacological blocker, and the recording currents could be fully blocked by the application of 1 mM 4-AP and 30 mM TEA-Cl. The outward potassium currents recording internal solution contained the

following (in mM): 120 KCl, 1 $MgCl_2$-$6H_2O$, 1 $CaCl_2$, 10 HEPE, 10 EGTA, 2 Mg-ATP, pH 7.2 adjusted with KOH and HCl, the osmolality was 300 Osm/kg. To investigate the influence of ultrasound stimulation on membrane properties of individual pyramidal neuron, action potentials were elicited by different injected current pulses (ranging between −100 to 400 pA, 100 ms timescale, 10 pA increment and 0.2 Hz frequency) using a whole-cell current clamp. Active membrane properties and the passive intrinsic properties were characterized as a function of neuronal activity (Franzen et al., 2015; Hong et al., 2016). F-I slope was defined as the slope of relation curve between the firing frequency and injected currents). Threshold current, also called rheobase, was defined as the minimum amount of current required for neurons to generate an action potential more than 50% of the time across 20 repetitive. RMP was defined as the actual measured value without considering the pipette offset potential. The current-clamp internal solution contained the following (in mM): 140 K-gluconate, 4.5 MgCl2, 5 EGTA, 4 Mg-ATP, 0.3 GTP, 4.4 phosphocreatine disodium salt hydrate, and 9 HEPEs.

Statistical Analysis

All electrophysiological data were analyzed offline using Patchmaster acquired software (HEKA, Germany), Clampfit analysis software (version 10.3; Molecular Devices, Silicon Valley, CA, United States); MiniAnalysis, MATLAB (version R2014b; The Math Works, Natick, MA, United States) and Origin 8.0. All numerical results are presented as mean ± standard error of the

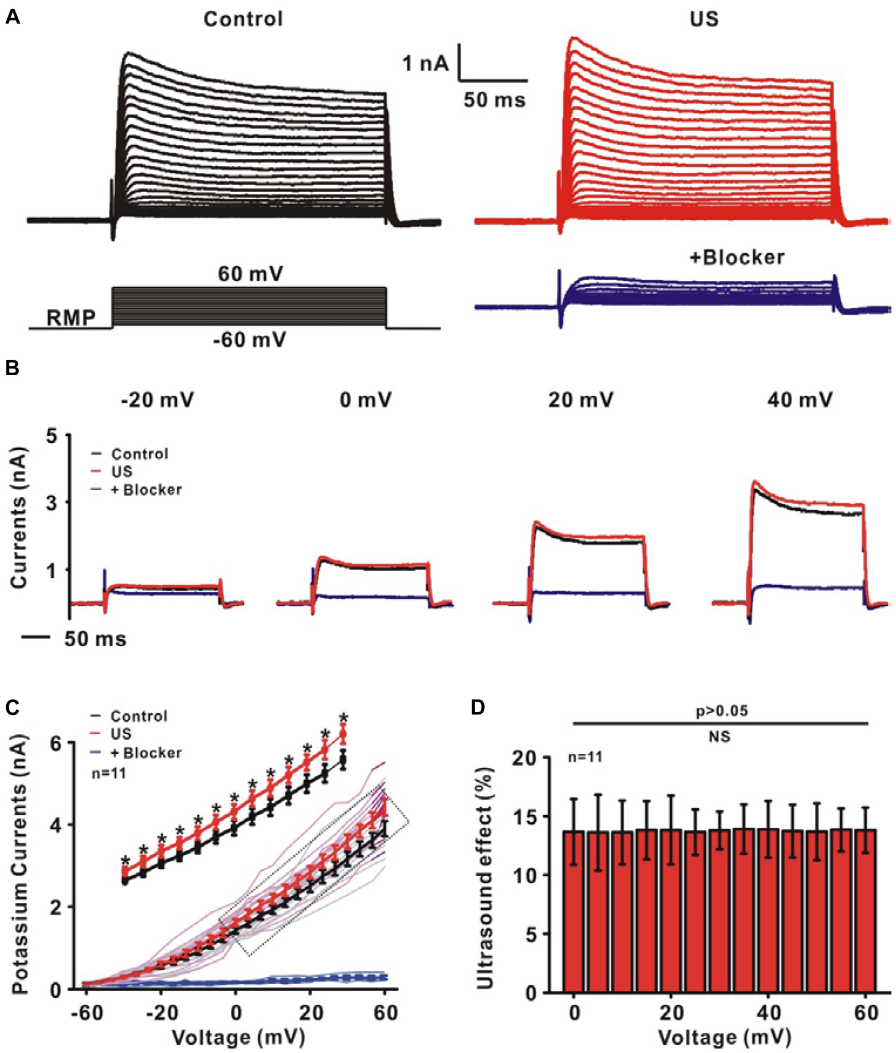

FIGURE 2 | The effect of ultrasound stimulation on voltage-gated potassium currents of pyramidal neurons in CA1 hippocampus slices. **(A)** Representative outward potassium currents recorded in the control (black) and ultrasound stimulation (red). The currents were elicited by a protocol in which cells were depolarized to a variety of potentials (–60 to +60 mV) from a holding potential of –70 mV and the currents could be blocked by 30 mM TEA-Cl and 1 mM 4-AP (blue). **(B)** The individual current traces correspond to the currents measured at voltage steps of –20, 0, 20, and 40 mV in control (black), US (red) and blocker (blue) group. **(C)** I–V curves of outward potassium currents showed that ultrasound stimulation increased the outward potassium currents (*$p < 0.05$). **(D)** The same relative changes of the outward potassium currents at different voltage steps were observed.

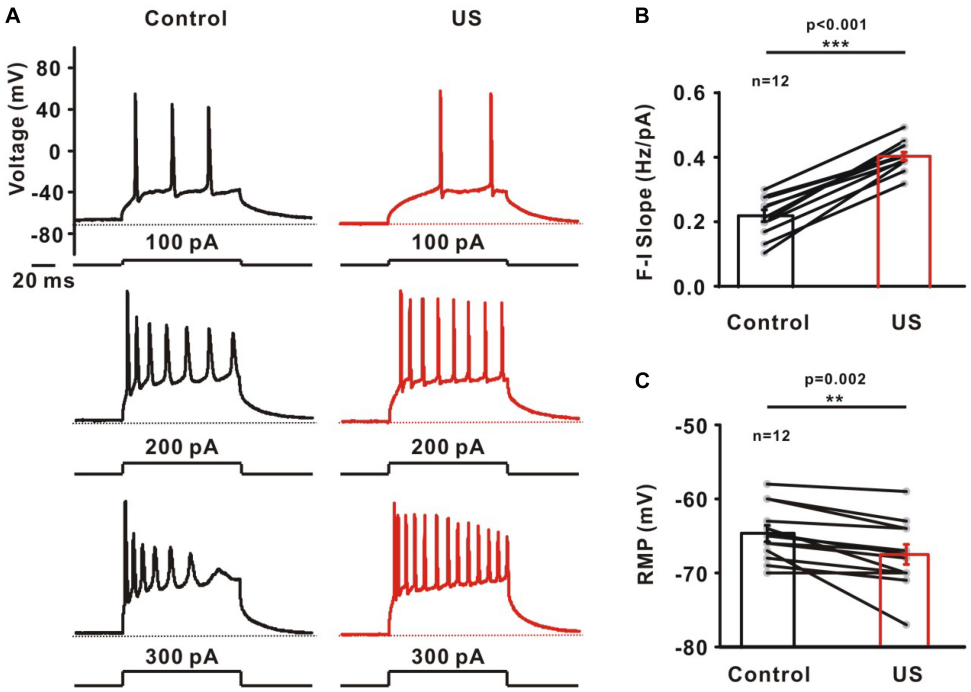

FIGURE 3 | The effect of ultrasound stimulation on evoked firing of pyramidal neurons in CA1 hippocampus slices. **(A)** Representative voltage traces of evoked action potentials in response to current injections (100, 200, and 300 pA) in control (balck) and ultrasound stimulation (red). Dashed lines located at resting membrane potential (RMP) of neurons. **(B)** Collected data on the slope of firing frequency-currents relationship (F-I slope) showed that ultrasound stimulation significantly increased the firing frequency of pyramidal neurons (***$p < 0.001$). Slope was determined by linear fit from 0 to 300 pA. **(C)** The effect of ultrasound stimulation on RMP was significantly decreased (**$p < 0.01$).

mean (SEM). Student's paired *t*-test and one-way ANOVA were used for all statistical analyses using the statistics software, SPSS ver.13.0. Statistical significance was defined as a value of $p < 0.05$.

RESULTS

Ultrasound Stimulation Directly Increased the Outward Potassium Currents of CA1 Pyramidal Neurons

To test whether ultrasound stimulation could modulate ion channels and neuronal activity in rat slices, an ultrasound stimulation system consisting of an ultrasound neuro-modulation chip and patch-clamp recording system was established to stimulate hippocampal CA1 slices *in vitro* and to record the electrophysiological activity of neurons synchronously, as shown in **Figure 1A**. The pyramidal neurons, located at the stratum pyramidal of hippocampus (**Figure 1B**), were identified by both firing pattern in response to current injections and typical morphology (**Figure 1C**). The ultrasound-induced modulatory response of ion channels was recorded using whole-cell voltage-clamp. Compared to the control group, ultrasound stimulation for 30 s duration on pyramidal neurons caused a significant increment in the peak amplitude of outward potassium currents, approximately 13% (**Figures 2A–C**). Moreover, **Figure 2D** shows that the relative change of outward potassium currents induced by ultrasound stimulation at different voltage steps did not show significant difference, indicating that the increment of potassium currents was caused by ultrasound stimulation, rather than electronic stimulation by holding voltage. Therefore, the results demonstrated that ultrasound stimulation was capable of modulating the potassium channels directly.

Ultrasound Modulated the Evoked Firing in CA1 Pyramidal Neurons

Potassium channels play a prominent role in determining intrinsic neuronal excitability, firing threshold and RMP, etc. Further experiments were carried out to investigate the effects of increased potassium currents induced by ultrasound stimulation on firing properties using whole-cell current-clamp recording (**Figure 3A**). The action potentials in pyramidal neurons were evoked by different current injections. **Figure 3B** shows the slope of the relationship between frequency and injected currents (F-I slope). The results indicated that ultrasound stimulation leads to the increased firing frequency of neurons (Control: 0.22 ± 0.02 Hz/pA; US: 0.41 ± 0.01 pA, ***$p < 0.001$, $n = 12$). In collected data, the RMP also decreased from −64.67 ± 1.10 mV to −67.51 ± 1.35 mV after ultrasound stimulation (**$p < 0.01$, **Figure 3C**, $n = 12$).

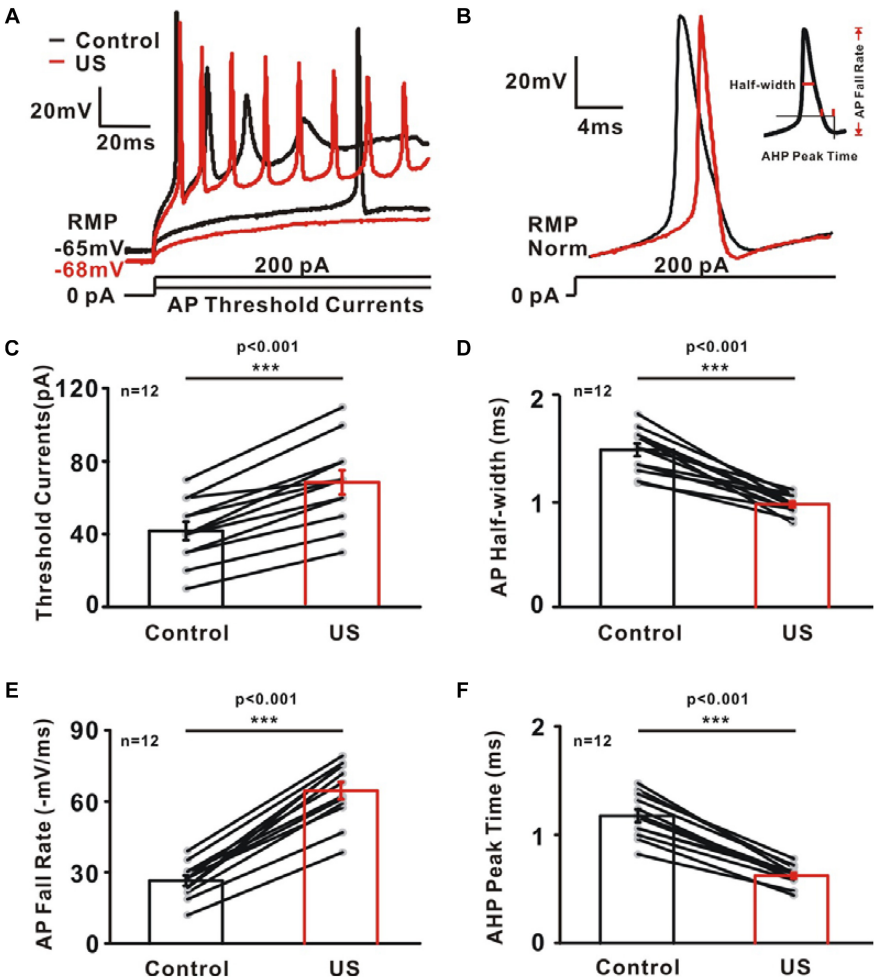

FIGURE 4 | The effect of ultrasound stimulation on action potential (AP) properties of pyramidal neurons in CA1 hippocampus slices. **(A)** Superimposed voltage traces in response to sustained threshold current (50 pA) and above threshold current (200 pA). Threshold current is defined as the minimum amount of current injection required for neuron to generate action potential. In contrast to the voltage traces of control (black), ultrasound stimulation (red) failed to generate action potential in the threshold current injection and generate more action potential in 200 Pa current injection. **(B)** Representative voltage trace of single AP in control (black) and US (red) group evoked by sustained above threshold current injections (200 pA). AP properties were further calculated and plotted as a function of potassium currents. **(C–F)** A population of 12 neurons showing the increment of threshold current **(C)** and AP fall rate **(E)** while the reduction of AP half-width **(D)** and AHP peak time **(F)** by ultrasound stimulation (***$p < 0.001$, paired *t*-test).

Regulation of AP Properties Associated With Potassium Channels by Ultrasound in CA1 Pyramidal Neurons

The increased potassium currents observed in pyramidal neurons may also alter the shape of single action potential. To test this hypothesis, further experiments were carried to investigate AP properties consisting of threshold current, AP half-width, AP fall rate and AHP peak time (**Figures 4A,B**). Ultrasound stimulation caused a significantly increment in the threshold current (Control: 41.67 ± 5.05 pA; US: 68.33 ± 6.61 pA, ***$p < 0.001$, **Figure 4C**, $n = 12$), AP fall rate (Control: 26.44 ± 2.1 mV/ms; US: 64.21 ± 3.63 mV/ms, ***$p < 0.001$, **Figure 4E**, $n = 12$) as well as a reduction in the AP half-width (Control: 1.49 ± 0.06 ms; US: 0.97 ± 0.03 ms, ***$p < 0.001$, **Figure 4D**, $n = 12$) and AHP peak time (Control: 1.17 ± 0.06 ms; US: 0.62 ± 0.03 ms, ***$p < 0.001$, **Figure 4F**, $n = 12$) of neurons in hippocampal CA1 slices.

Regulation of Passive Properties by Ultrasound Stimulation in CA1 Pyramidal Neurons

The passive intrinsic properties, including the membrane capacitance (CM), membrane input resistance (RM) and membrane time constant (TM), were highly relevant to the generation of APs. These properties were characterized by injecting a small hyperpolarizing current into the soma of neurons (−20 pA, **Figure 5A**). The results shows there was no significant change in CM (Control: 31.58 ± 2.22 pF; US: 29.82 ± 3.13 pF, NS $p = 0.297$, **Figure 5B**, $n = 12$). However, compared to the control, the RM (Control: 259.75 ± 17.24 MΩ;

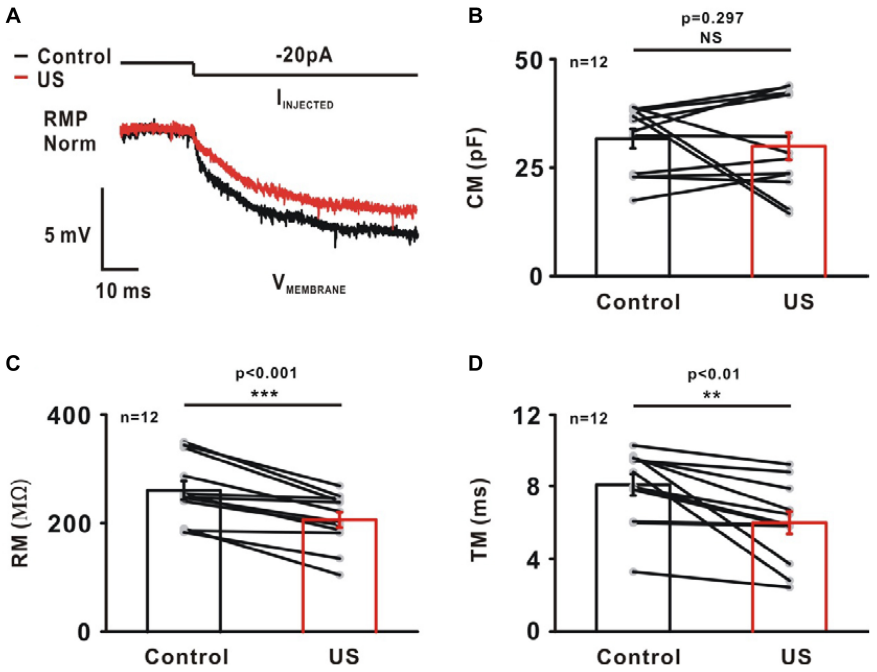

FIGURE 5 | The effect of ultrasound stimulation on passive properties of pyramidal neurons in CA1 hippocampus slices. **(A)** An example of representative voltage trace of pyramidal neuron in response to a small hyperpolarizing current (−20 pA). A single exponential was fitted to a 10 ms time window of voltage trace to calculate passive membrane properties, membrane capacitance (CM), membrane input-resistance (RM) and membrane time constant (TM). Ultrasound stimulation had little effect on CM (**B**, Control: 31.58 ± 2.22 pF; US: 29.82 ± 3.13 pF, $p = 0.297$, paired *t*-test). However, ultrasound stimulation caused a reduction in RM (**C**, Control: 259.75 ± 17.24 MΩ; US: 205.89 ± 14.11 MΩ, $^{***}p < 0.001$, paired *t*-test) and TM (**D**, Control: 8.07 ± 0.59 ms; US: 5.98 ± 0.62 ms, $^{**}p < 0.01$, paired *t*-test).

US: 205.89 ± 14.11 MΩ, $^{***}p < 0.001$, **Figure 5C**, $n = 12$) and the TM (Control: 8.07 ± 0.59 ms; US: 5.98 ± 0.62 ms, $^{**}p < 0.01$, **Figure 5D**, $n = 12$) decreased significantly in the presence of ultrasound.

Underlying Mechanisms of Ultrasound Stimulation in CA1 Pyramidal Neurons

Ultrasound has been reported to have a wide range of physical effects on the nervous system, such as thermal effect, mechanical effect or cavitation effect. The underlying mechanisms of ultrasound stimulation on the modulation of ion channels and neural activity remain unknown. Further experiments were carried out to investigate the biophysical effects of ultrasound. Substrate vibration-induced piezoelectric effects of the ultrasound neuro-modulation chip may have an effects on the potassium currents and neuronal activity (Yuchao et al., 2013). Air chamber was established to eliminate the ultrasound stimulation (**Figure 6A**) since ultrasound wave at high frequency could not propagate through the air medium. The result shows that no change in neural activity was detected, indicating the modulation of neurons was directly dependent on ultrasound stimulation, rather than electrical stimulation induced by the piezoelectric effects (**Figure 6B**). Thermal effect induced by ultrasound stimulation was another candidate responded for neuro-modulation. The experiment was further carried out to monitor the temperature elevation during the process of ultrasound stimulation (**Figure 6C**). As shown in the **Figure 6D**, small temperature elevation (less than 0.74 ± 0.09°C) was detected. Additionally, acoustic cavitation was highly dependent on the acoustic intensity and acoustic frequency. For 27.38 MHz, it is difficult to generate acoustic cavitation at such a high frequency in the absence of microbubbles, especially for such a small input power. These results indicated that the mechanical effects induced by ultrasound were the main reason for the modulation of potassium currents and the shape of action potential.

DISCUSSION

This study demonstrated the feasibility of ultrasound neuro-modulation on outward potassium currents and the regulation of AP properties in pyramidal neurons of hippocampal slices. The results show that ultrasound stimulation could directly increase outward potassium current, approximately 13%. Further data indicates that ultrasound enables to decrease the RMP as well as regulate AP properties, leading to the increment of threshold current, AP fall rate and the reduction of AP half-width, AHP peak time. Moreover, the regulation of potassium currents and the shape of action potential were mainly induced by the mechanical effect of ultrasound.

The ultrasound wave in the experiments is generated by an ultrasound neuro-modulation chip made of IDTs on a

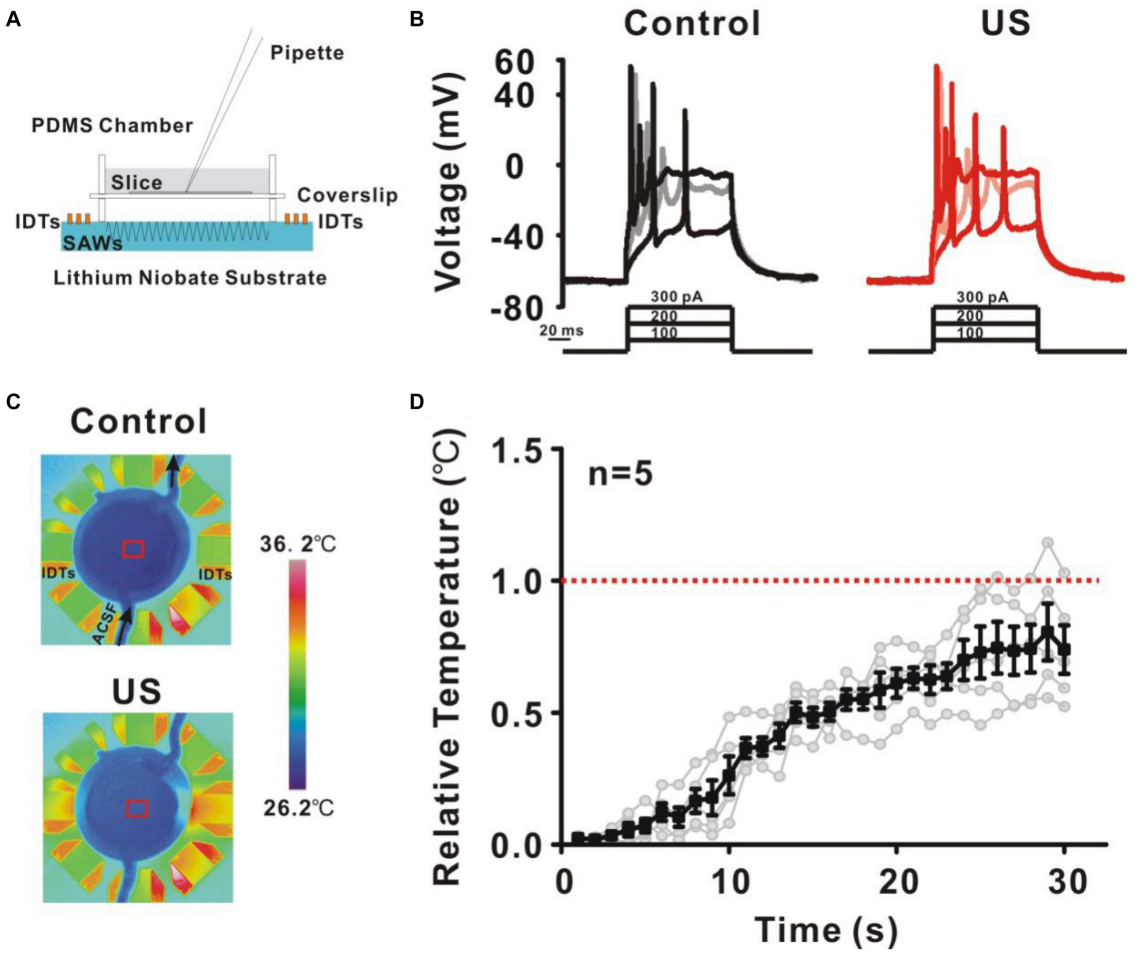

FIGURE 6 | The underlying mechanisms of ultrasound stimulation on modulation of potassium channels in pyramidal neurons. **(A)** A new recording chamber was developed to isolate ultrasound waves which consisting of a cavity and sputtered to a lithium niobate substrate. **(B)** Representative voltage traces recorded from pyramidal neurons in response to a sequence of sustained currents injection (100, 200, and 300 pA). The result showed that the isolated ultrasound has no effect on the activity of neurons. **(C)** Temperature elevation was monitored during ultrasound stimulation in recording chamber using a thermal infrared imager. **(D)** The temperature profile showed that the temperature elevation was relatively small (less than 0.74 ± 0.09°C) during 30 s ultrasound stimulation.

$LiNbO_3$ substrate using a standard MEMS technology (Sritharan et al., 2006; Friend and Yeo, 2011; Meng et al., 2011). The ultrasound generated by IDTs has a clear acoustic boundary and the neurons in the region-specific slices can be stimulated precisely. Compared to the clinical ultrasound, the frequency used in the experiment (27.38 MHz) is relatively high. It is an anticipated that neural activity is highly dependent on the acoustic intensity (acoustic pressure, pulse duration and pulse repetition frequency) (Tufail et al., 2010; Menz et al., 2013; Li et al., 2016). Furthermore, we fabricated the similar neuro-modulation chip with a lower resonant frequency of 8.7 MHz to investigate the influence of the acoustic frequency on the potassium currents and neural activity. The results demonstrate that the ultrasound at 8.7 MHz also enable to increase the potassium currents and modulate the action potential properties in hippocampal CA1 pyramidal neurons using the same parameters. Thus, the similar results were acquired indicating that the ultrasound frequency has little influence on neuronal activity and potassium channels. Furthermore, the energy of surface acoustic waves is confined to the substrate surface, facilitating the stimulation of the neurons with a relatively small input power. As ultrasound neuro-modulation chip is compatible with patch clamp and standard calcium imaging, this chip is readily to study the effects of ultrasound on modulation of neuronal activity and ion channels.

As a mechanical pressure waves, the interaction between ultrasound and neurons is relatively complex. Ultrasound induced thermal effect, mechanical effect and cavitation is considered to be related to the neuronal activity (Bystritsky et al., 2011; Tyler, 2011; Plaksin et al., 2014). Previous studies have demonstrated that the small temperature elevation could not affect the neuronal activity in brain slice (Rinaldi et al., 1991; Bachtold et al., 1998; Tufail et al., 2010; Yoo et al., 2011). Our previous experiment based on the *C. elegans* shows that the AFD neurons, a thermal sensitive neurons, cannot be activated

by the ultrasound stimulation, indicating that the response of the worms was not due to the temperature elevation (Zhou et al., 2017). We also stimulated the neuron in hippocampal slice using the heated ACSF (5°C temperature elevation) by water bath. The result shows 5°C elevation of ACSF perfusion has no significant effect on the spontaneous activity and could not evoke the firing of recording neurons, indicating that a small temperature elevation could not activate the neurons (Zhou et al., 2017). Furthermore, we carried out the experiment to monitor the temperature change during ultrasound stimulation using a thermal infrared imager. The result shows that ultrasound stimulation caused a relatively small temperature elevation in the recording chamber with ultrasound stimulation for 30 s (less than 0.74 ± 0.09°C, **Figure 6D**). Additionally, acoustic cavitation may be another reason for the ultrasound-induced modulation of neuronal activity (Wall et al., 1951; Menz et al., 2013). It was difficult to generate acoustic cavitation at 27.38 MHz with a small acoustic intensity, in the absence of microbubbles. Therefore, the mechanical effect of ultrasound was primary reason leading to the modulation of potassium currents and shape of action potential in hippocampus neurons.

The results demonstrated that ultrasound-induced mechanical effect was capable of modulating the potassium channels and regulating the AP properties of neurons directly. In mammalian neurons, there is a particularly large diversity of mechano-sensitive channels (Kuang et al., 2015). Numerous potassium channels (i.e., Shaker (Kv1.1); Ca^{2+}-activated K^+; TREK1; TRAAK; HCN2) have been found to be sensitive to mechanical stimulus (Maingret et al., 1999; Lin et al., 2007; Zhao and Sokabe, 2008; Brohawn et al., 2012; Hao et al., 2013; Gu and Gu, 2014). Recent studies have indicated that ultrasound stimulation can modulate the *trans*-membrane currents flowing TREK-1, TREK-2, TRAAK channels expressed in *Xenopus oocytes* (Kubanek et al., 2016). Ultrasound could induce behavioral responses by activation mechano-sensitive TRP-4 channel, a ion channel required for touch sensation in *C. elegans* (Ibsen et al., 2015; Kubanek et al., 2018). Our previous works indicated that the cultured neurons expressed with MscL, a mechano-sensitive channel from *Escherichia coli*, could be activated by low-pressure ultrasound (Ye et al., 2018). Transcriptional activities induced by ultrasound also have been investigated in mechano-sensitive Piezo1 channel expressed mammalian cells (Pan et al., 2018). Therefore, the underlying mechanism of ultrasound neuromodulation on neuronal activity may contribute to the activation of ion channels, especially mechano-sensitive channels.

Continuous ultrasound waves generated by ultrasound neuro-modulation chip were used in the experiments. The previous studies have shown that the modulatory effects were bimodal, whereby the neuronal activity could either be activated or suppressed, which was highly dependent on the acoustic parameters, such as acoustic pressure, pulse duration, pulse repetition frequency etc. (Pan et al., 2018). Further experiments are needed to be carried out to investigate the relationship between the modulatory effect of ion channels and acoustic parameters. The acoustic parameter also could be further optimized to modulate the neural activity more efficiently. By modulation of the potassium currents using ultrasound, some diseases related to potassium ion channels, such as long QT syndrome, epilepsy might be treated and ultrasound stimulation might pave a new way for clinical applications.

CONCLUSION

Using whole-cell patch-clamp recording *in vitro*, the results indicate that it is feasible to modulate potassium channels by ultrasound stimulation in hippocampal slices. During the ultrasound stimulation, the increment of outward potassium currents and a regulation of action potential shape could be achieved. Moreover, the opening of potassium channels is responded to the mechanical effect induced by ultrasound. These observations provide the support for its effectiveness of ultrasound neuro-modulation on ion channels and may offer an alternative tool to treat some diseases related to potassium channels.

ETHICS STATEMENT

All animal experiments were performed according to the guidelines approved by the Use Committee and the Ethics Committee of Shenzhen Institutes of Advanced Technology, Chinese Academy of Sciences.

AUTHOR CONTRIBUTIONS

ZL, XH, LN, and LM designed the experiments. ZL, XH, WZhou, and WZhang conducted the experiments. ZL, WZhou, YL, and TB managed the experimental animals and laboratory. ZL, LN, LM, and YG wrote the manuscript and revised manuscript.

FUNDING

The work was supported by National Key R&D Program of China (2016YFC0104700), National Natural Science Foundation of China (Grant Nos. 11774371, 11674347, 11874381, 11574341, 81527901, and 11534013), Natural Science Foundation of Guangdong Province (2017B030306011, 2016TQ03X716, and 2016TQ03R472), Youth Innovation Promotion Association CAS (2018393), Shenzhen Basic Science Research (JCYJ20160429184552717), Science and Technology Planning Project of Guangdong Province (2018B030031001), and Shenzhen Key Laboratory of Ultrasound Imaging and Therapy (ZDSYS201802061806314).

REFERENCES

Adelman, J. P., Bond, C. T., Pessia, M., and Maylie, J. (1995). Episodic ataxia results from voltage-dependent potassium channels with altered functions. *Neuron* 15:1449. doi: 10.1016/0896-6273(95)90022-5

Amendola, J., Woodhouse, A., Martineauclaire, M. F., and Goaillard, J. M. (2012). Ca2+/cAMP-sensitive covariation of IA, and IH voltage dependences tunes rebound firing in dopaminergic neurons. *J. Neurosci.* 32, 2166–2181. doi: 10.1523/jneurosci.5297-11.2012

Bachtold, M. R., Rinaldi, P. C., Jones, J. P., Reines, F., and Price, L. R. (1998). Focused ultrasound modifications of neural circuit activity in a mammalian brain. *Ultrasound Med. Biol.* 24, 557–565. doi: 10.1016/s0301-5629(98)00014-3

Bean, B. P. (2007). The action potential in mammalian central neurons. *Nat. Rev. Neurosci.* 8, 451–465. doi: 10.1038/nrn2148

Brohawn, S. G., Mármol, J. D., and Mackinnon, R. (2012). Crystal structure of the human K2P TRAAK, a lipid- and mechano-sensitive K+ ion channel. *Science* 335, 436–441. doi: 10.1126/science.1213808

Bystritsky, A., and Korb, A. S. (2015). A review of low-intensity transcranial focused ultrasound for clinical applications. *Curr. Behav. Neurosci. Rep.* 2, 60–66. doi: 10.1007/s40473-015-0039-0

Bystritsky, A., Korb, A. S., Douglas, P. K., Cohen, M. S., Melega, W. P., Mulgaonkar, A. P., et al. (2011). A review of low-intensity focused ultrasound pulsation. *Brain Stimul.* 4, 125–136. doi: 10.1016/j.brs.2011.03.007

Chapman, I. V., Macnally, N. A., and Tucker, S. (1980). Ultrasound-induced changes in rates of influx and efflux of potassium ions in rat thymocytes in vitro. *Ultrasound Med. Biol.* 6, 47–49. doi: 10.1016/0301-5629(80)90063-0

Coetzee, W. A., Amarillo, Y., Chiu, J., Chow, A., Lau, D., Mccormack, T., et al. (2010). Molecular diversity of K+ channels. *Ann. N.Y. Acad. Sci.* 868, 233–255.

Franzen, D. L., Gleiss, S. A., Berger, C., Kumpfbeck, F. S., Ammer, J. J., and Felmy, F. (2015). Development and modulation of intrinsic membrane properties control the temporal precision of auditory brain stem neurons. *J. Neurophysiol.* 113, 524–536. doi: 10.1152/jn.00601.2014

Friend, J., and Yeo, L. Y. (2011). Microscale acoustofluidics: microfluidics driven via acoustics and ultrasonics. *Rev. Modern Phys.* 83, 647–704. doi: 10.1103/revmodphys.83.647

Giudicessi, J. R., and Ackerman, M. J. (2012). Potassium-channel mutations and cardiac arrhythmias–diagnosis and therapy. *Nat. Rev. Cardiol.* 9, 319–332. doi: 10.1038/nrcardio.2012.3

Goldman, M. S., Golowasch, J., Marder, E., and Abbott, L. F. (2013). Global structure, robustness, and modulation of neuronal models. *J. Neurosci.* 21:5229. doi: 10.1523/jneurosci.21-14-05229.2001

Gu, Y., and Gu, C. (2014). Physiological and pathological functions of mechanosensitive ion channels. *Mol. Neurobiol.* 50, 339–347. doi: 10.1007/s12035-014-8654-4

Kolb, H. A. (1990). Potassium channels in excitable and non-excitable cells. *Rev. Physiol. Biochem. Pharmacol.* 115, 51–91. doi: 10.1007/978-3-662-41884-0_2

Hao, J., Padilla, F., Dandonneau, M., Lavebratt, C., Lesage, F., Noël, J., et al. (2013). Kv1.1 channels act as mechanical brake in the senses of touch and pain. *Neuron* 77, 899–914. doi: 10.1016/j.neuron.2012.12.035

Hille, B. (2001). *Ion Channels of Excitable Membranes*. Sunderland: Sinauer.

Hong, H., Rollman, L., Feinstein, B., and Sanchez, J. T. (2016). Developmental profile of ion channel specializations in the avian nucleus magnocellularis. *Front. Cell. Neurosci.* 10:80. doi: 10.3389/fncel.2016.00080

Ibsen, S., Tong, A., Schutt, C., Esener, S., and Chalasani, S. H. (2015). Sonogenetics is a non-invasive approach to activating neurons in *Caenorhabditis elegans*. *Nat. Commun.* 6:8264. doi: 10.1038/ncomms9264

Johnston, J., Forsythe, I. D., and Kopp Cheinpflug, C. (2010). SYMPOSIUM REVIEW: going native: voltage gated potassium channels controlling neuronal excitability. *J. Physiol.* 588(Pt 17), 3187–3200. doi: 10.1113/jphysiol.2010.191973

Klemic, K. G., Klemic, J. F., Reed, M. A., and Sigworth, F. J. (2002). Micromolded PDMS planar electrode allows patch clamp electrical recordings from cells. *Biosens. Bioelectron.* 17, 597–604. doi: 10.1016/s0956-5663(02)00015-5

Kuang, Q., Purhonen, P., and Hebert, H. (2015). Structure of potassium channels. *Cell. Mol. Life Sci.* 72, 3677–3693.

Kubanek, J., Shi, J., Marsh, J., Chen, D., Deng, C., and Cui, J. (2016). Ultrasound modulates ion channel currents. *Sci. Rep.* 6:24170. doi: 10.1038/srep24170

Kubanek, J., Shukla, P., Das, A., Baccus, S. A., and Goodman, M. B. (2018). Ultrasound elicits behavioral responses through mechanical effects on neurons and ion channels in a simple nervous system. *J. Neurosci.* 38, 3081–3091. doi: 10.1523/JNEUROSCI.1458-17.2018

Lawson, K. (2000a). Is there a role for potassium channel openers in neuronal ion channel disorders? *Exp. Opin. Invest. Drugs* 9, 2269–2280. doi: 10.1517/13543784.9.10.2269

Lawson, K. (2000b). Potassium channel openers as potential therapeutic weapons in ion channel disease. *Kidney Int.* 57, 838–845. doi: 10.1046/j.1523-1755.2000.00923.x

Legon, W., Sato, T. F., Opitz, A., Mueller, J., Barbour, A., Williams, A., et al. (2014). Transcranial focused ultrasound modulates the activity of primary somatosensory cortex in humans. *Nat. Neurosci.* 17, 322–329. doi: 10.1038/nn.3620

Leinenga, G., Langton, C., Nisbet, R., and Götz, J. (2016). Ultrasound treatment of neurological diseases [mdash] current and emerging applications. *Nat. Rev. Neurol.* 12, 161–174. doi: 10.1038/nrneurol.2016.13

Li, G. F., Zhao, H. X., Hui, Z., Fei, Y., Wang, J. Y., Xu, C. X., et al. (2016). Improved anatomical specificity of non-invasive neuro-stimulation by high frequency (5MHz) ultrasound. *Sci. Rep.* 6:24738.

Lin, W., Laitko, U., Juranka, P. F., and Morris, C. E. (2007). Dual Stretch responses of mHCN2 pacemaker channels: accelerated activation, accelerated deactivation. *Biophys. J.* 92, 1559–1572. doi: 10.1529/biophysj.106.092478

Lin, Z., Zhou, W., Huang, X., Wang, K., Tang, J., Niu, L., et al. (2018). On-chip ultrasound modulation of pyramidal neuronal activity in hippocampal slices. *Adv. Biosyst.* 2:1800041. doi: 10.1002/adbi.201800041

Llinás, R. R. (1988). The intrinsic electrophysiological properties of mammalian neurons: insights into central nervous system function. *Science* 242:1654. doi: 10.1126/science.3059497

Mackinnon, R. (2003). Potassium channels. *FEBS Lett.* 555, 62–65.

Maingret, F., Patel, A. J., Lesage, F., Lazdunski, M., and Honoré, E. (1999). Mechano- or acid stimulation, two interactive modes of activation of the TREK-1 potassium channel. *J. Biol. Chem.* 274, 26691–26696. doi: 10.1074/jbc.274.38.26691

Maljevic, S., and Lerche, H. (2013). Potassium channels: a review of broadening therapeutic possibilities for neurological diseases. *J. Neurol.* 260, 2201–2211. doi: 10.1007/s00415-012-6727-8

Maljevic, S., and Lerche, H. (2014). Chapter 2 – potassium channel genes and benign familial neonatal epilepsy. *Prog. Brain Res.* 213, 17–53. doi: 10.1016/B978-0-444-63326-2.00002-8

Mckeown, L., Swanton, L. P., and Jones, O. (2008). Surface expression and distribution of voltage-gated potassium channels in neurons. *Mol. Membr. Biol.* 25, 332–343. doi: 10.1080/09687680801992470

Meng, L., Cai, F., Jin, Q., Niu, L., Jiang, C., Wang, Z., et al. (2011). Acoustic aligning and trapping of microbubbles in an enclosed PDMS microfluidic device. *Sens. Actuat. B Chem.* 160, 1599–1605. doi: 10.1016/j.snb.2011.10.015

Menz, M. D., Oralkan, O., Khuriyakub, P. T., and Baccus, S. A. (2013). Precise neural stimulation in the retina using focused ultrasound. *J. Neurosci.* 33, 4550–4560. doi: 10.1523/JNEUROSCI.3521-12.2013

Pan, Y., Yoon, S., Sun, J., Huang, Z., Lee, C., Allen, M., et al. (2018). Mechanogenetics for the remote and noninvasive control of cancer immunotherapy. *Proc. Natl. Acad. Sci. U.S.A.* 115, 201714900. doi: 10.1073/pnas.1714900115

Plaksin, M., Shoham, S., and Kimmel, E. (2014). Intramembrane cavitation as a predictive bio-piezoelectric mechanism for ultrasonic brain stimulation. *Phys. Rev. X* 4, 331–344.

Pongs, O. (1999). Voltage-gated potassium channels: from hyperexcitability to excitement. *FEBS Lett.* 452, 31–35. doi: 10.1016/s0014-5793(99)00535-9

Rinaldi, P. C., Jones, J. P., Reines, F., and Price, L. R. (1991). Modification by focused ultrasound pulses of electrically evoked responses from an in vitro hippocampal preparation. *Brain Res.* 558:36. doi: 10.1016/0006-8993(91)90711-4

Sandhiya, S., and Dkhar, S. A. (2009). Potassium channels in health, disease & development of channel modulators. *Indian J. Med. Res.* 129, 223–232.

Schwindt, P. C., Spain, W. J., Foehring, R. C., Stafstrom, C. E., Chubb, M. C., and Crill, W. E. (1988). Multiple potassium conductances and their functions in

neurons from cat sensorimotor cortex in vitro. *J. Neurophysiol.* 59, 424–449. doi: 10.1152/jn.1988.59.2.424

Shieh, C. C., Coghlan, M., Sullivan, J. P., and Gopalakrishnan, M. (2000). Potassium channels: molecular defects, diseases, and therapeutic opportunities. *Pharmacol. Rev.* 52, 557–594.

Sritharan, K., Strobl, C. J., Schneider, M. F., Wixforth, A., and Guttenberg, Z. (2006). Acoustic mixing at low Reynold's numbers. *Appl. Phys. Lett.* 88:15.

Swensen, A. M., and Bean, B. P. (2005). Robustness of burst firing in dissociated purkinje neurons with acute or long-term reductions in sodium conductance. *J. Neurosci.* 25:3509. doi: 10.1523/jneurosci.3929-04.2005

Tufail, Y., Matyushov, A., Baldwin, N., Tauchmann, M. L., Georges, J., Yoshihiro, A., et al. (2010). Transcranial pulsed ultrasound stimulates intact brain circuits. *Neuron* 66, 681–694. doi: 10.1016/j.neuron.2010.05.008

Tufail, Y., Yoshihiro, A., Pati, S., Li, M. M., and Tyler, W. J. (2011). Ultrasonic neuromodulation by brain stimulation with transcranial ultrasound. *Nat. Protoc.* 6, 1453–1470. doi: 10.1038/nprot.2011.371

Tyler, W. J. (2011). Noninvasive neuromodulation with ultrasound? A continuum mechanics hypothesis. *Neuroscientist* 17, 25–36. doi: 10.1177/1073858409348066

Tyler, W. J., Tufail, Y., Finsterwald, M., Tauchmann, M. L., Olson, E. J., and Majestic, C. (2008). Remote excitation of neuronal circuits using low-intensity, low-frequency ultrasound. *PLoS One* 3:e3511. doi: 10.1371/journal.pone.0003511

Vacher, H., Mohapatra, D. P., and Trimmer, J. S. (2008). Localization and targeting of voltage-dependent ion channels in mammalian central neurons. *Physiol. Rev.* 88:1407. doi: 10.1152/physrev.00002.2008

Wall, P. D., Fry, W. J., Stephens, R., Tucker, D., and Lettvin, J. Y. (1951). Changes produced in the central nervous system by ultrasound. *Science* 114:686. doi: 10.1126/science.114.2974.686

Ye, J., Tang, S., Meng, L., Li, X., Wen, X., Chen, S., et al. (2018). Ultrasonic control of neural activity through activation of the mechanosensitive channel MscL. *Nano Lett.* 18, 4148–4155. doi: 10.1021/acs.nanolett.8b00935

Yoo, S. S., Bystritsky, A., Lee, J. H., Zhang, Y., Fischer, K., Min, B. K., et al. (2011). Focused ultrasound modulates region-specific brain activity. *Neuroimage* 56, 1267–1275. doi: 10.1016/j.neuroimage.2011.02.058

Yuchao, C., Xiaoyun, D., Sz-Chin, S. L., Shikuan, Y., Po-Hsun, H., Nitesh, N., et al. (2013). Tunable nanowire patterning using standing surface acoustic waves. *ACS Nano* 7, 3306–3314. doi: 10.1021/nn4000034

Zhao, H., and Sokabe, M. (2008). Tuning the mechanosensitivity of a BK channel by changing the linker length. *Cell Res.* 18, 871–878. doi: 10.1038/cr.2008.88

Zhou, W., Wang, J., Wang, K., Huang, B., Niu, L., Li, F., et al. (2017). Ultrasound neuro-modulation chip: activation of sensory neurons in *Caenorhabditis elegans* by surface acoustic waves. *Lab Chip* 17, 1725–1731. doi: 10.1039/c7lc00163k

Conflict of Interest Statement: The reviewer JT declared a shared affiliation, with no collaboration, with one of the authors, YG, to the handling Editor at time of review.

The remaining authors declare that the research was conducted in the absence of any commercial or financial relationships that could be construed as a potential conflict of interest.

frontiers in Pharmacology

ORIGINAL RESEARCH
published: 31 May 2019
doi: 10.3389/fphar.2019.00610

The Optimized Fabrication of a Novel Nanobubble for Tumor Imaging

Jiaqi Zhang[1,2†], Yihan Chen[1,2†], Cheng Deng[1,2], Li Zhang[1,2], Zhenxing Sun[1,2], Jing Wang[1,2], Yali Yang[1,2], Qing Lv[1,2], Wei Han[1,2] and Mingxing Xie[1,2*]*

[1] Department of Ultrasound, Union Hospital, Tongji Medical College, Huazhong University of Science and Technology, Wuhan, China, [2] Hubei Province Key Lab of Molecular Imaging, Wuhan, China

Nanobubbles with a size of less than 1 μm can be used as ultrasound contrast agents for diagnosis and as drug/gene carriers for therapy. However, the optimal method of preparing uniform-sized nanobubbles is considered controversial. In this study, we developed novel biocompatible nanobubbles by performing differential centrifugation to isolate the relevant subpopulation from the parent suspensions. Compared with the method of modulating the thickness of the phospholipid film without centrifugation, nanobubbles fabricated under optimal centrifugation conditions exhibited a uniform bubble size, good stability, and low toxicity. Using *in vitro* ultrasound imaging, nanobubbles displayed excellent enhancement ability, which was comparable to microbubbles. In an *in vivo* experiment, the video intensity of nanobubbles in tumors was stronger than that of microbubbles at different times (5 min, 163.5 ± 8.3 a.u. vs. 143.2 ± 7.5 a.u., $P < 0.01$; 15 min, 125.4 ± 5.2 a.u. vs. 97.3 ± 4.6 a.u., $P < 0.01$). Fluorescence imaging obtained by confocal laser scanning microscopy demonstrated that obviously more nanobubbles passed through the vessel wall into the extravascular and intercellular space of tumors, compared with microbubbles. In conclusion, this optimized preparation method will strongly promote the application of nanobubbles in imaging and therapy.

Keywords: nanobubbles, ultrasound, contrast imaging, tumor, fabrication

OPEN ACCESS

Edited by:
Fei Yan,
Shenzhen Institutes of Advanced Technology (CAS), China

Reviewed by:
Xiaobing Wang,
Shaanxi Normal University, China
Feng Wang,
Xinxiang Medical University, China
Yue Pan,
Sun Yat-Sen Memorial Hospital, China

***Correspondence:**
Wei Han
515875773@qq.com
Mingxing Xie
xiemx@hust.edu.cn

†These authors have contributed equally to this work.

Specialty section:
This article was submitted to Translational Pharmacology, a section of the journal Frontiers in Pharmacology

Received: *30 January 2019*
Accepted: *14 May 2019*
Published: *31 May 2019*

Citation:
Zhang J, Chen Y, Deng C, Zhang L, Sun Z, Wang J, Yang Y, Lv Q, Han W and Xie M (2019) The Optimized Fabrication of a Novel Nanobubble for Tumor Imaging. Front. Pharmacol. 10:610. doi: 10.3389/fphar.2019.00610

INTRODUCTION

Molecular imaging has undergone explosive growth since it emerged in the early 21st century. This technique is used not only to visualize the cellular functions in tissues and organs but also to monitor molecular processes in living organisms without disturbing these processes (Weissleder, 2006; Hussain and Nguyen, 2014; Keliher et al., 2017). As an important branch of molecular imaging, ultrasound-based molecular imaging has been extensively used in both experimental studies and clinical practices (Willmann et al., 2008b; Liu et al., 2015; Willmann et al., 2017).

Currently, the most used ultrasound contrast agents (UCAs) are microbubbles, with diameters ranging from 1 to 10 μm (Zhang et al., 2017). Microbubbles are widely used in molecular imaging of angiogenesis (Willmann et al., 2008a; Wu et al., 2011), inflammation (Machtaler et al., 2015; Liao et al., 2017), thrombi (Lu et al., 2016; Zhu et al., 2016), plaques (Zhang et al., 2016), and so on (Frauscher et al., 2001). But limited by the particle size, microbubbles cannot pass through the vessel wall and just served as blood pool agents (Ferrara et al., 2009; Moestue et al., 2012). To address this challenge, nanobubbles have attracted considerable attention.

Due to their nanoscale size, nanobubbles have great potential application in extravascular molecular imaging, especially in tumors (Maeda et al., 2009; Rapoport et al., 2009). In normal tissues, the vascular endothelial gap is less than 7 nm (Hobbs et al., 1998). Thus, the vast majority of particles cannot pass freely (**Figure 1A**). However, in tumors, the vascular endothelial gap is approximately 380–780 nm (Maeda et al., 2009). Nanobubbles could permeate through the vasculature and get into extravascular and intercellular space (**Figure 1B**). Furthermore, because of the EPR (enhanced permeability and retention) effect, nanobubbles exhibit exaggerated extravasation and retention in tumors. Therefore, nanobubbles have been applied in tumor-targeted imaging and therapy widely (Rosen et al., 2012; Gao et al., 2017; Song et al., 2017).

Many studies have reported the fabrication of nanobubbles (Zong et al., 2006; Krupka et al., 2010; Yin et al., 2012). Among these, nanobubbles composed of a phospholipid shell and a gas core are considered to have optimal contrast enhancement ability (**Figure 1C**). However, the preparation of uniform-sized nanobubbles has been controversial. Some studies showed that the centrifugal condition was the key factor that affects the diameter of nanobubbles (Yin et al., 2012), but others reported that phospholipid film thickness was critical in the determination of the diameter of nanobubbles (Liao et al., 2014; Cai et al., 2015). Until now, few studies have carefully analyzed the two types of methods.

In this study, we focused on the impact of centrifugal condition on the preparation of nanobubbles. The physical characteristics of nanobubbles produced by optimal centrifugal condition were investigated. At the same time, the morphology, particle size, and polydispersity index (PDI) of nanobubbles prepared by centrifugation and controlling phospholipid film thickness were compared.

MATERIALS AND METHODS

Materials

Phospholipids such as 1,2-distearoyl-sn-glycerol-3-phosphatidylcholine (DSPC) and 1,2-distearoyl-sn-glycerol-3-phosphoethanolamine *N*-[biotinyl(polyethyleneglycol) 2000] (DSPE–PEG 2000) were purchased in powder form (Avanti Polar Lipids Inc., Alabaster, AL). Octafluoropropane (C_3F_8) gas was purchased from the R&D Center for Specialty Gases at the Research Institute of Physical and Chemical Engineering of Nuclear Industry (Tianjin, China). The fluorescent dye DiI was purchased from Beyotime (Haimen, China). The Cell Counting Kit-8 (CCK-8) was purchased from Dojindo (Japan). BALB/c mice (8–10 weeks old) and Sprague–Dawley (SD) rats (weight, 200–220 g) were purchased from the Animal Breeding and Research Center of Tongji Medical College, Huazhong University of Science and Technology, China. All animals were treated according to the

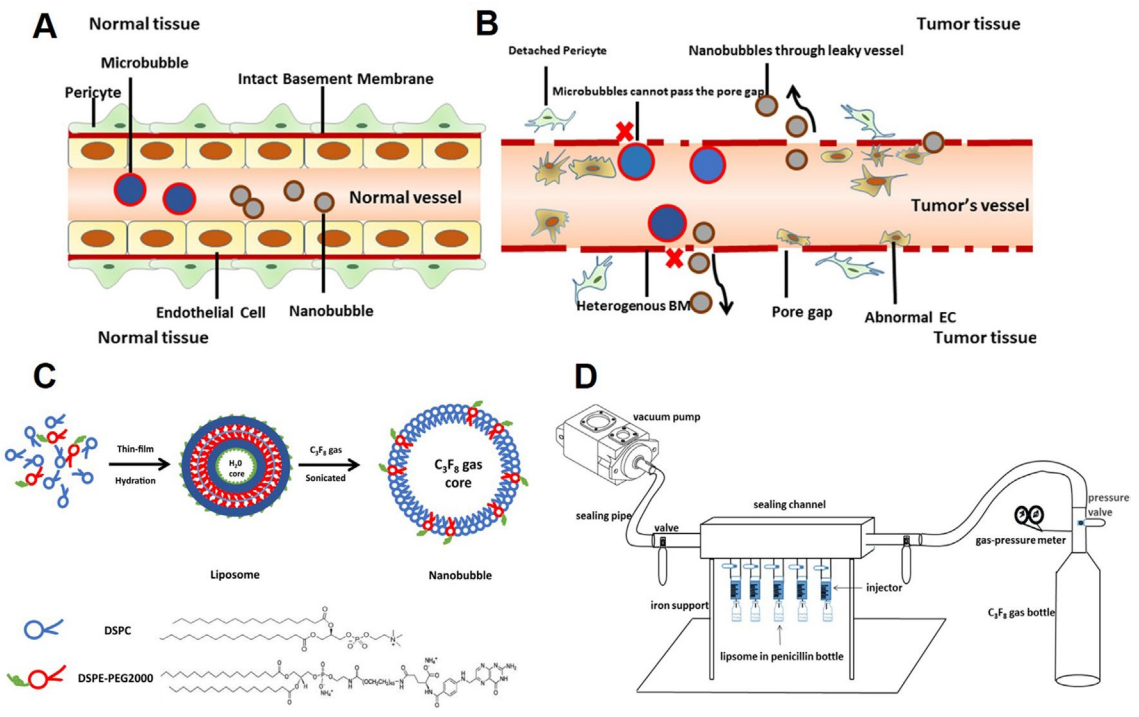

FIGURE 1 | Schematic illustration of this study. **(A)** Neither microbubbles nor nanobubbles can pass through the endothelial gap in normal tissues. **(B)** Microbubbles cannot pass the endothelial gap but nanobubbles can in tumor tissues. **(C)** The procedure for fabrication of nanobubbles. **(D)** The homemade setup for exchanging octafluoropropane (C_3F_8) gas.

policy and regulations approved by the Huazhong University of Science and Technology Animal Care and Use Committee.

Synthesis of Bubbles

We used two different methods to prepare nanobubbles. First, nanobubbles were prepared by controlling phospholipid film thickness, according to the previous study (Cai et al., 2015). In brief, fixed-ratio (molar ratios = 9:1) mixtures of DSPC and DSPE-PEG 2000 (5 mg, 10 mg, 15 mg, 20 mg, or 25 mg) were dissolved in chloroform. A small amount of red fluorescent membrane probe DiI was added. Then, the solvent was removed under nitrogen flow at room temperature, followed by vacuum treatment over 2 h. The dry lipid films were hydrated with a buffer solution consisting of 80% Tris (0.1 M, pH 7.4), 10% glycerol, and 10% propylene glycol (v/v) in a tube. Then, the tube was placed in a water bath at 55–60°C and treated by ultrasonic cleaner at 40 kHz for 10–15 min, until the films completely dissolved. The resulting solution was subpackaged into 4-mL vials (1 mL each vial) sealed by rubber caps. Finally, the air in the vial was exchanged with C_3F_8 using a homemade equipment (**Figure 1D**). Bubbles were formed by shaking the vial with a vibrator for 30 s.

Second, nanobubbles were prepared by centrifugation. A total of 15 mg of DSPC: DSPE-PEG 2000 in the molar ratio 9:1 was dissolved in chloroform. The following steps included thin-film formation, hydration, and sonication, just the same as the previous steps. After bubble mixtures were formed by the vibrator, different centrifugation speeds (20 g, 70 g, 140 g, and 400 g) were subsequently applied for 3 min. Small nanobubbles were collected after collecting the lower liquid layer. Finally, the nanobubbles were resuspended and stored at 4°C.

The concentration of nanobubbles was calculated using a hemacytometer. All measurements were carried out in triplicate and averaged.

Particle Sizing and Zeta Potential Measurements

The particle sizes were measured by dynamic light scattering (DLS) using a Delsa™ Nano (Beckman Instruments Corporation). In total, 10 μL of the sample and 90 μL of phosphate buffer saline (PBS) were mixed in sample wells before measuring the particle sizes at 25°C. The zeta potential of each sample was measured using a Zeta Analyzer (Beckman Instruments Corporation) to determine the electrophoretic light scattering at 25°C. All samples used for the zeta potential measurements were prepared at the same concentration as those used for particle sizing. The particle size of each sample was measured three times.

Morphology and Stability of Nanobubbles

The nanobubbles solution was diluted threefold and well mixed. Subsequently, a 5-mL suspension was dropped onto a transmission electron microscope (TEM) grid, negatively stained with 2% phosphotungstic acid, and allowed to rest for 6 h at room temperature. The morphologies and structures of the nanobubbles were then observed by TEM (Hitachi H-7500, Hitachi Limited, Tokyo, Japan). The particle size of the nanobubbles was calculated at 1, 3, 7, 10, and 14 days, and the concentration of the nanobubbles was examined after storage at 4°C for 1, 2, 3, 4, 5, and 6 h.

In Vitro Biocompatibility Tests and Cytotoxicity Assay

We have conducted an experimental study on the biocompatibility of nanobubbles (NBs). Briefly, bEnd3 (mouse brain endothelial) cells were chosen to evaluate the cytotoxicity of the NBs. The cells were seeded at a density of 5,000 cells/well in 96-well plates and then cultured in 100 μL of Roswell Park Memorial Institute-1640 (RPMI-1640) medium containing 10% fetal bovine serum (FBS, Biological Industries, Israel) in an incubator with 5% CO_2 for 24 h. The cells were subsequently incubated with gradient concentrations of nanobubbles (from 1×10^5 to 1×10^9 bubbles/mL) for 8 h. The medium was then replaced with 100 μL of fresh medium containing 10 μL of CCK-8 solution (Dojindo, Japan). Afterward, the cells were incubated for another 4 h. The absorbance of each well at 450 nm was recorded using an Infinite F200 multimode plate reader (Tecan, Männedorf, Switzerland). All experiments were carried out in triplicate.

In Vivo Safety and Toxicity Evaluations of Nanobubbles

To evaluate the potential toxicity and adverse effects of the nanobubbles, all rats were continuously observed for relevant indices such as appearance, independent activity, and mortality. Animal experiments were approved by the Animal Care and Use Committee of Huazhong University of Science and Technology. After the rats were sacrificed, the main organs (i.e., the heart, lung, liver, spleen, and kidney) were harvested and fixed in 4% paraformaldehyde. These tissues were sectioned and stained with hematoxylin and eosin (HE) for histopathological examination. A total of 25 healthy SD rats were randomly divided into five groups (n = 5 per group). The control group did not receive any injection, and the other four groups were injected intravenously with PBS, DSPC (dose, 1.2 mg/kg), DSPE-PEG 2000 (dose, 1.2 mg/kg), or NBs (10^9 NBs). These animals were sacrificed 24 h after the injections. Their heart, liver, spleen, lungs, and kidneys were then fixed, embedded in paraffin, and cut into 5-μm-thick sections for HE staining. Images were collected using an Olympus light microscope.

In Vitro Ultrasound Imaging

To compare the ultrasonic imaging ability of the nanobubbles and microbubbles, *in vitro* ultrasound imaging experiments were performed. Briefly, 1 mL of NB or MB suspension at various bubble concentrations (from 1.0×10^5 to 1.0×10^9 bubbles/mL) was added to the sample wells of a homemade 2% (w/v) agarose mold. A clinical ultrasound scanner (Philips IU Elite) system with an L12-5 high-frequency linear transducer was used. Mechanical index (MI) was 0.10. The focal zone was placed at a depth of 1.5 cm, which was at the center of the sample well. Three images of each sample were taken. ImageJ software was used to analyze the grayscale values of the samples. The quantitative grayscale ultrasonic intensity of the samples was normalized to that of

gas-free water. The intensity value was defined as the ratio of the grayscale value of the contrast agent to that of gas-free water.

In Vivo Contrast-Enhanced Ultrasound Imaging in Rats

The *in vivo* imaging capability of the nanobubble contrast agents was evaluated using SD rats. Each rat was anesthetized with 300 mg/kg of 10% chloral hydrate by intraperitoneal injection. The animals were placed on a warm blanket to maintain their body temperatures. In order to compare the performance of nanobubbles with microbubbles, 150 μL of nanobubble suspension (10^9 bubbles/mL) or microbubbles at the same amount were intravenously injected into the same mice in random order. A 1-h waiting time was allowed to clear contrast agents from previous injections. The left ventricular opacification (LVO) was conducted using a broadband L12-5 high-frequency linear transducer in contrast mode with an MI of 0.07.

In Vivo Passive Tumor-Targeting Ultrasound Imaging in Mice

CT26 cells were transplanted into BALB/c mice as a xenograft model. The cells had been previously cultured in RPMI-1640 medium supplemented with 10% FBS (GIBCO, Carlsbad, CA) at 37°C and 5% CO_2. A total of 10 BALB/c xenograft model mice (4–5 weeks old, 18–20 g) were examined. The cells (10^7) were suspended in phosphate-buffered saline and subcutaneously injected into the right flanks (at the level of the liver) for tumor xenografts. All *in vivo* experiments began when the tumors reached a diameter of 0.8–1.0 cm. Mice were anesthetized with 10% chloral hydrate and fixed on a plate before ultrasonic imaging. To decrease speckle variance, both the ultrasound probe and the animal were fixed and remained at the same position throughout the study. As described above, nanobubbles and microbubbles were used in the same mice to compare the performance. The interval between two injections was 2 h. Ultrasonic images were acquired by a PHILIPS IU22 ultrasound system with a 9–12 MHz linear probe. All digital clips and images were stored for offline examination. Grayscale images were analyzed using ImageJ (v1.37; National Institutes of Health, Bethesda, MA).

Confocal Laser Scanning Microscopy Examination

In order to confirm that nanobubbles were small enough to pass through the endothelial gaps in tumors, we used confocal laser scanning microscopy (CLSM) to determine the location of red fluorescently dyed nanobubbles *in vivo*. Tumor-bearing mice were randomly separated into two groups. One group was injected with DiI-labeled nanobubbles, and the other was injected with DiI-labeled microbubbles. After bubble injection, the heart of each mouse was perfused with 0.9% normal saline until the labeled bubbles were cleared from circulation. The tumors and muscles of the right thigh (used as negative controls because the endothelial cell connections are continuous in skeletal muscles) were immediately extracted and sectioned into 5-μm slices. To visualize the vessels in tumors, slices were incubated with rat anti-mouse CD31 antibody (eBioscience, San Diego, CA) at a dilution of 1:200 overnight at 4°C and then incubated with fluoresceine isothiocyanate (FITC)-conjugated anti-rat secondary antibodies (eBioscience, San Diego, CA). The nucleus was stained with 4′,6-diamidino-2-phenylindole (DAPI). Images were recorded using a laser scanning confocal microscope (TCS SP5, Leica, Germany).

Statistical Analysis

Statistical Product and Service Solutions (SPSS) 22.0 was used for the statistical analysis. The counting data are expressed as the mean ± standard deviation. The data sets were compared using analysis of variance. The significance level was set at $P < 0.05$.

RESULTS

Morphology and Size Distribution of Nanobubbles

The morphology of nanobubbles was observed under oil lens at ×1,000 magnifications. Nanobubbles produced by phospholipid film thicknesses controlling were presented with a dot or sphere with a bright center. DLS analysis shows that these nanobubbles were polydisperse, appearing in two different peaks on the size distribution curves: a higher peak and a lower peak. The higher peaks of nanobubbles fabricated by different film thicknesses appeared at 675.3 nm, 1,124.5 nm, 804.1 nm, 3,425.1 nm, and 976.4 nm, respectively. Meanwhile, the lower peaks appeared at 1,725.2 nm, 204.6 nm, 5,341.2 nm, 528.6 nm, and 7,281.3 nm, respectively (**Figure 2**).

Almost all nanobubbles produced by centrifugation were presented with dots. Particle sizing analysis shows that these nanobubbles were monodisperse with only one peak. When the centrifugal conditions were 20 g, 70 g, 140 g and 140 g, the peaks appeared at 972.2 nm, 476.4 nm, 397.0 nm, and 247.6 nm, respectively (**Figure 3**).

The Mean Diameters and Polydispersity Index of Nanobubbles

The mean diameters of nanobubbles were approximately increased with the increase of phospholipid film thicknesses. When the thickness was increased from 5 mg to 25 mg, the mean diameters were 723.9 ± 125.7 nm, 734.8 ± 117.6 nm, 977.2 ± 165.9 nm, 1027.5 ± 227.3 nm, and 1141.4 ± 131.8 nm, respectively (**Figure 4A**). However, the mean diameters of nanobubbles had a tendency to decrease as the centrifugal speed increased. When the centrifugal speed was increased from 20 g to 400 g, the mean diameters were 971.3 ± 11.5 nm, 475.2 ± 5.7 nm, 395.8 ± 5.5 nm, and 246.1 ± 8.7 nm, respectively (**Figure 4C**).

PDI is a specific index of particle size distribution. The PDI of nanobubbles produced by various phospholipid film thicknesses were 0.311, 0.211, 0.145, 0.193, and 0.284, respectively (**Figure 4B**). However, the PDIs of the nanobubbles that underwent the centrifugation process were 0.007, 0.005, 0.009, and 0.016, respectively (**Figure 4D**). The PDIs of nanobubbles fabricated by phospholipid film thicknesses controlling were all higher than that

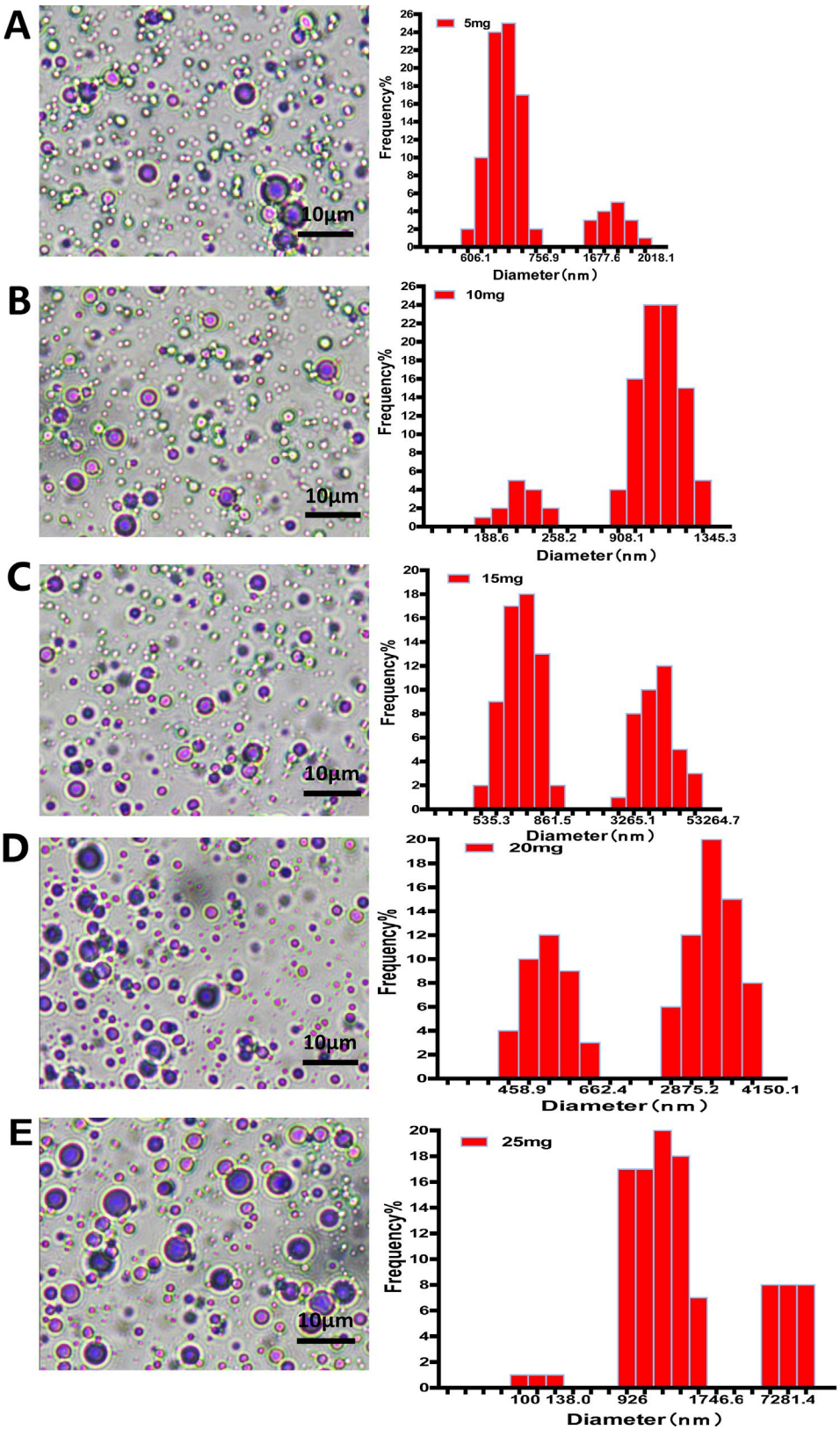

FIGURE 2 | The morphology and particle size distribution of nanobubbles prepared by controlling phospholipid film thickness at 5 mg **(A)**, 10 mg **(B)**, 15 mg **(C)**, 20 mg **(D)**, and 25 mg **(E)**.

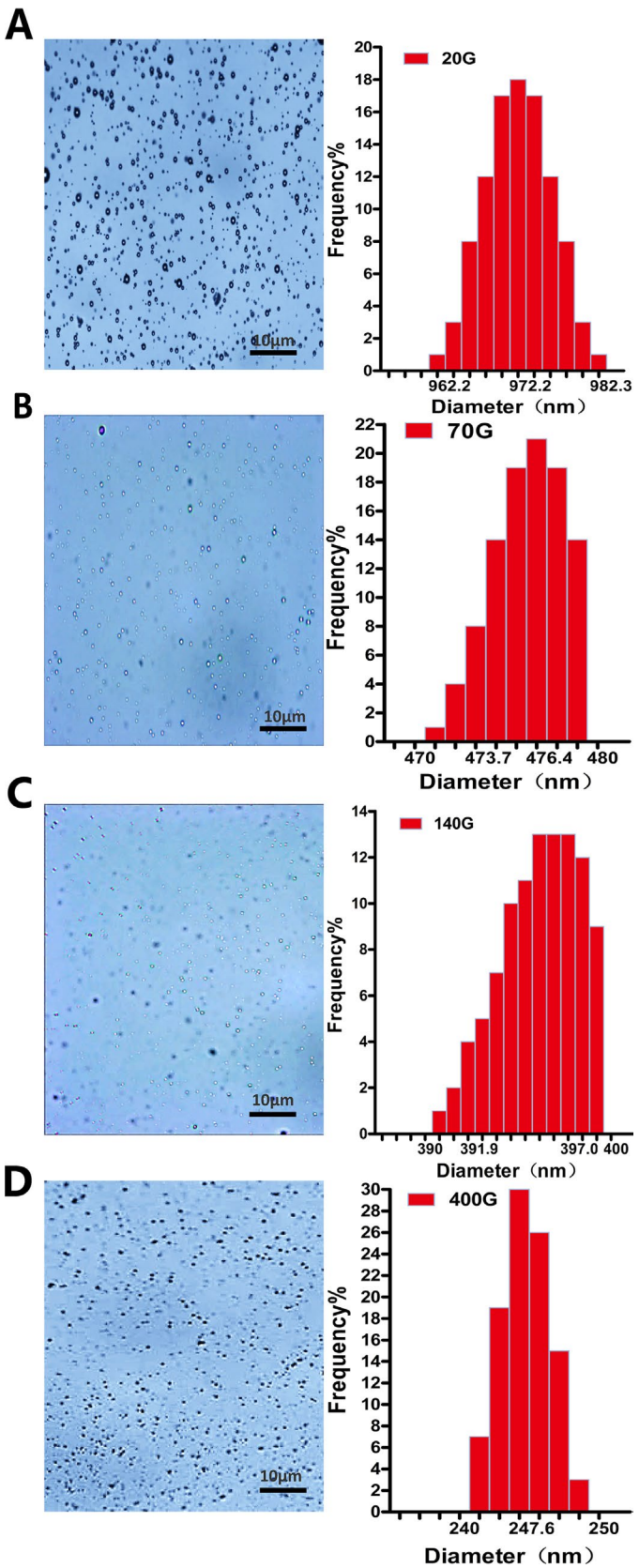

FIGURE 3 | The morphology and particle size distribution of nanobubbles prepared by different centrifugations at 20 g **(A)**, 70 g **(B)**, 140 g **(C)**, and 400 g **(D)**.

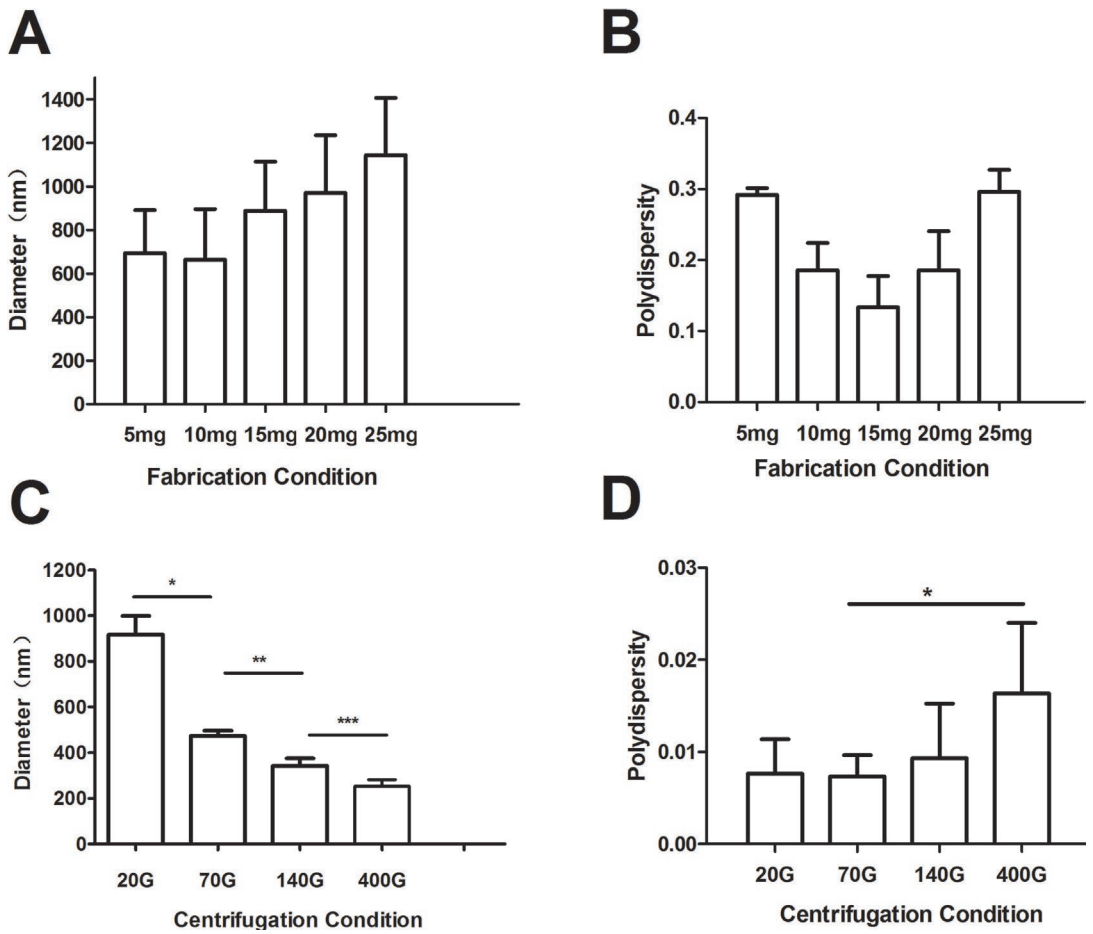

FIGURE 4 | The mean diameter and polydispersity of nanobubbles prepared by controlling phospholipid film thickness and different centrifugations. **(A)** Histogram of the average diameter of the bubbles produced with 5 mg, 10 mg, 15 mg, 20 mg, and 25 mg phospholipid. **(B)** Polydispersity of nanobubble produced with 5 mg, 10 mg, 15 mg, 20 mg, and 25 mg phospholipid. **(C)** Histogram of the average diameter of the bubbles prepared using centrifugation speeds of 20 g, 70 g, 140 g, and 400 g. **(D)** Polydispersity of nanobubbles prepared using centrifugation speeds of 20 g, 70 g, 140 g, and 400 g.

by centrifugation ($P < 0.01$), which indicated that the centrifugal process could improve the uniformity of nanobubbles.

Influence of Centrifugation on Concentration of Nanobubbles

When the centrifugal speeds were 20 g, 70 g, 140 g, and 400 g, the average concentration of nanobubbles were 6.4×10^9/mL, 5.1×10^9/mL, 1.1×10^9/mL, and 0.32×10^9/mL, respectively. Compared to 20 g, the concentration of nanobubbles at 70 g did not change obviously ($P > 0.05$). However, when the speed reached 140 g, the concentration began to decrease significantly ($P < 0.01$) (**Figure 5**).

As was clear from the above descriptions, 70 g might be the optimal centrifugal condition for nanobubble fabrication, under which the uniform size distribution, appropriate diameter, and relative high concentration of nanobubbles can meet the requirements of most experiments. Therefore, we used nanobubbles fabricated by 70 g in the following experiments.

Morphology of Nanobubbles Produced by the Optimal Concentration

The morphology of the nanobubbles prepared by the optimal centrifugal speed was observed under fluorescence microscope at ×400 magnifications and transmission electron microscope (TEM) at ×5,000 magnifications. The DiI-labeled nanobubbles were presented as uniform red dots under a fluorescence microscope and as bright dots in the corresponding bright field (**Figure 6A** and **B**). Under TEM, the phospholipid (negative control) appeared as a solid sphere (**Figure 6C** and **D**).

Stability of Nanobubbles

To study the stability of nanobubbles, the changes in concentration and size of nanobubbles were monitored at 25°C. The overall trend of nanobubble concentration was downward with the increasing storage time. The initial concentration (0 h) was about $5.4 \pm 1.2 \times 10^9$/mL. After storage for 1, 2, 3, 4, 5, and 6 h, the concentration changed to $4.3 \pm 0.9 \times 10^9$/mL, $3.7 \pm 0.7 \times 10^9$/mL, $3.5 \pm 0.2 \times 10^9$/mL, $3.3 \pm 0.4 \times 10^9$/mL, $2.6 \pm 0.4 \times 10^9$/mL,

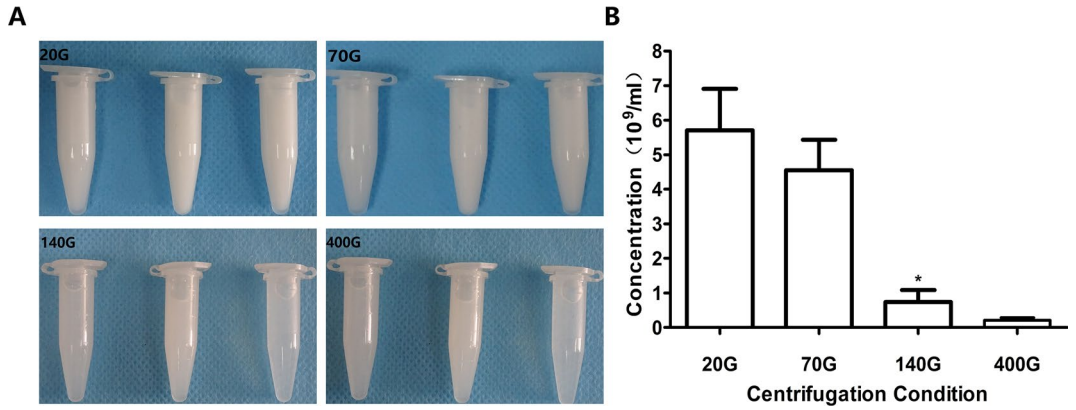

FIGURE 5 | Concentration of nanobubbles at different centrifugation speeds of 20 g, 70 g, 140 g, and 400 g. **(A)** Photos of nanobubbles produced by different centrifugal speed. **(B)** Quantitative analysis of centrifugation of different nanobubbles. *$P < 0.05$ compared with 20 g.

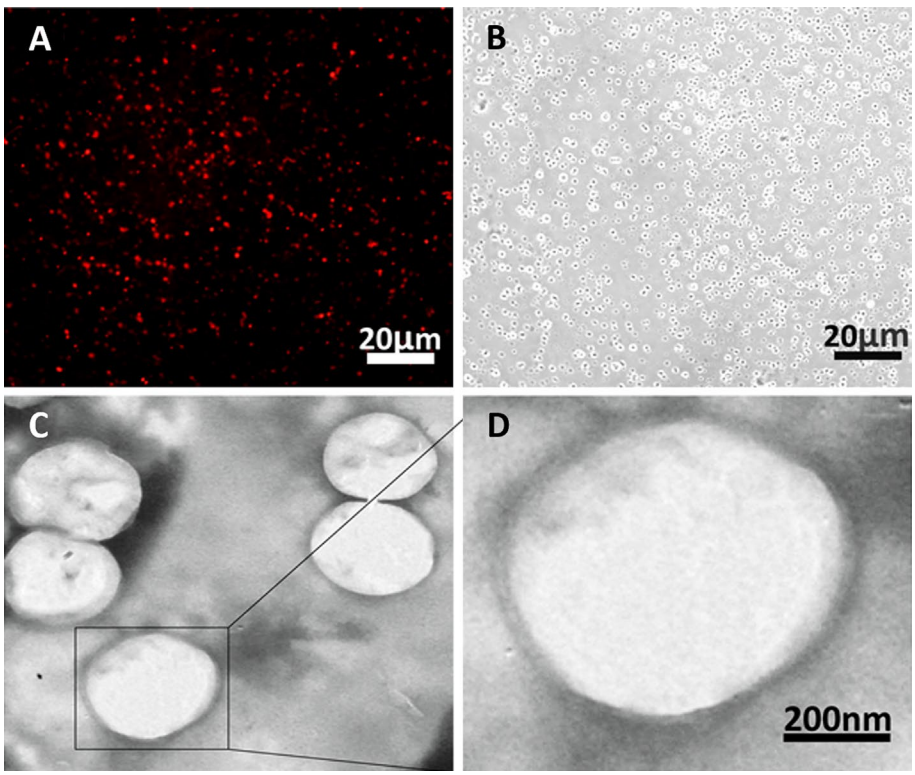

FIGURE 6 | Morphology of nanobubbles produced by optimal centrifugation. **(A)** Fluorescence field of nanobubbles at ×400 magnifications. **(B)** Corresponding bright field of nanobubbles was observed. **(C and D)** The micrograph of nanobubbles obtained by TEM.

and 1.5 ± 0.3 × 10^9/mL, respectively (**Figure 7A**). However, only the concentration at 6 h was statistically different compared with that at 0 h ($P < 0.01$), which indicated that the concentration of nanobubbles could remain unchanged for up to 6 h.

Moreover, the size of nanobubbles tended to be on the rise generally with the increasing storage time. The initial mean diameter of nanobubbles (0 day) was about 475.2 ± 5.7 nm. After storage for 1 day, 3 days, 7 days, 10 days, and 14 days, the diameters changed to 483.3 ± 29.0 nm, 495 ± 19.1 nm, 528.6 ± 35.8 nm, 544.9 ± 37.6 nm, and 859.3 ± 55.9 nm, respectively (**Figure 7B**). However, there was a significant change in nanobubble diameter until 14 days ($P < 0.05$), which indicated that the diameter of nanobubbles could be kept unchanged for up to 14 days.

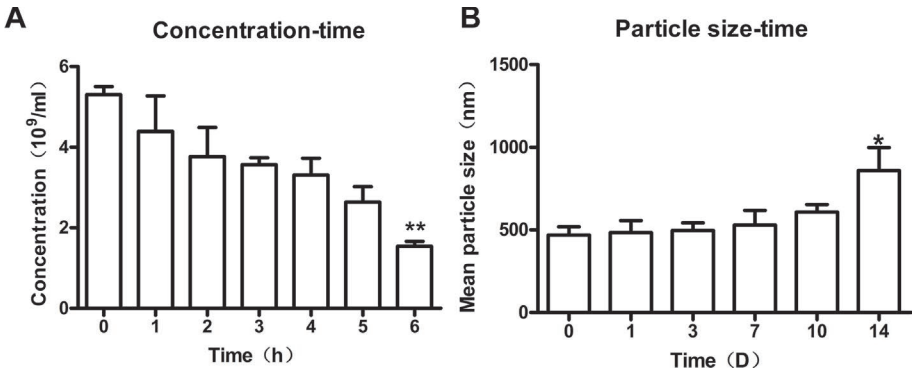

FIGURE 7 | Stability of nanobubbles produced by optimal concentration. **(A)** The concentration of nanobubbles after storage for 1 h, 2 h, 3 h, 4 h, 5 h, and 6h. **(B)** The particle size of nanobubbles after storage for 1 day, 3 days, 7 days, 10 days, and 14 days. 0 h, initial concentration; 0 D, initial size; D, day. $^{**}P < 0.01$ compared to 0 h; $^{*}P < 0.05$ compared to 0 D.

In Vitro and *In Vivo* Contrast Enhancement Abilities of Nanobubbles

In vitro, ultrasound images were acquired at various bubble concentrations using diagnostic high-frequency ultrasound (7 MHz). The contrast intensity of nanobubbles became stronger with the increase of nanobubble concentration. When the concentration reached 10^9/mL, because of the posterior attenuation generated by the strong reflex of the anterior nanobubbles close to the transducer, the ultrasonogram of contrast imaging was presented as a crescent. The performance of nanobubbles was similar to that of microbubbles *in vitro* (**Figure 8A**). Quantitative analysis shows that no significant difference was observed between the signal enhancements of the nanobubbles and microbubbles at each concentration ($P > 0.05$) (**Figure 8B**). After high-power ultrasound exposure, the grayscale intensity of nanobubbles decreased sharply because the nanobubbles were destroyed (**Figure 8C**).

In the LVO in rats, the contrast intensity of nanobubbles gradually became stronger with time at the beginning. It reached the peak at about 1 min after intravenous injection and subsequently decreased. The *in vivo* imaging performance of nanobubbles was similar to that of microbubbles (**Figure 9**).

Passive Targeting Ultrasound Imaging in Tumors

Contrast imaging was carried out on 10 tumor-carrying BALB/c mice. No animals died during the experiment. After injecting nanobubbles *via* the tail vein, the signal of nanobubbles became stronger with time and reached the peak at about 1 min, and then declined gradually (**Figure 10A**). At 10 s, 30 s, and 1 min after injection, the signal intensity of nanobubbles was comparable to that of microbubbles ($P > 0.05$). However, at 5 min and 15 min, the grayscale intensity of nanobubbles was significantly higher than that of microbubbles (5 min: 163.5 ± 8.3 a.u. vs. 143.2 ± 7.5 a.u., $P < 0.01$; 15 min: 125.4 ± 5.2 a.u. vs. 97.3 ± 4.6 a.u., $P < 0.01$) (**Figure 10B**). It demonstrated that the duration of contrast enhancement of nanobubbles was significantly longer than that of microbubbles.

Location of Nanobubbles in Tumors

The location of DiI-labeled nanobubbles or microbubbles in tumors was observed by CLSM, and skeletal muscle was used as control. Several DiI-labeled nanobubbles (red) were present in the extravascular and intercellular space of the tumor tissues. However, DiI-labeled microbubbles were hardly detected in tumors. In the skeletal muscle sections, however, DiI-labeled nanobubbles and microbubbles were both rare (**Figure 11**).

Biocompatibility Tests and Cytotoxicity Assay

After incubation with 10^5–10^9/mL (nine groups) nanobubbles for 8 h, the viability of bEnd.3 cells was calculated by CCK-8. When the concentration of nanobubbles ranged from 10^5 to 10^8/mL, the cell viability had no significant differences compared with the control group ($P > 0.05$). When the concentration went up to 10^9/mL, the cell viability declined ($P < 0.05$), but remained greater than 85% (**Figure 12**). The *in vivo* cytotoxicity assay showed that after injection of DSPC, DSPE-PEG 2000, or nanobubbles, no structural abnormality was observed in the major organs (heart, liver, spleen, lung, and kidney) in HE-stained slices (**Figure 13**).

DISCUSSION

Gas-filled bubbles are commonly used as echo-enhancers in ultrasonic diagnosis and as drug-loading vehicles in therapy (McEwan et al., 2015; Huang et al., 2017; Snipstad et al., 2017). Compared to microbubbles that were trapped in the blood pool, nanoscale bubbles (nanobubbles) are promising contrast agents for extravascular ultrasonic imaging and drug delivery (Guvener et al., 2017; Liu et al., 2017). However, research on the preparation condition of nanobubbles with uniform distribution is still in the initial stages (Perera et al., 2017). Thus, we investigated the influence of centrifugation on the character of nanobubbles and compared it with controlling phospholipid film thickness in this study.

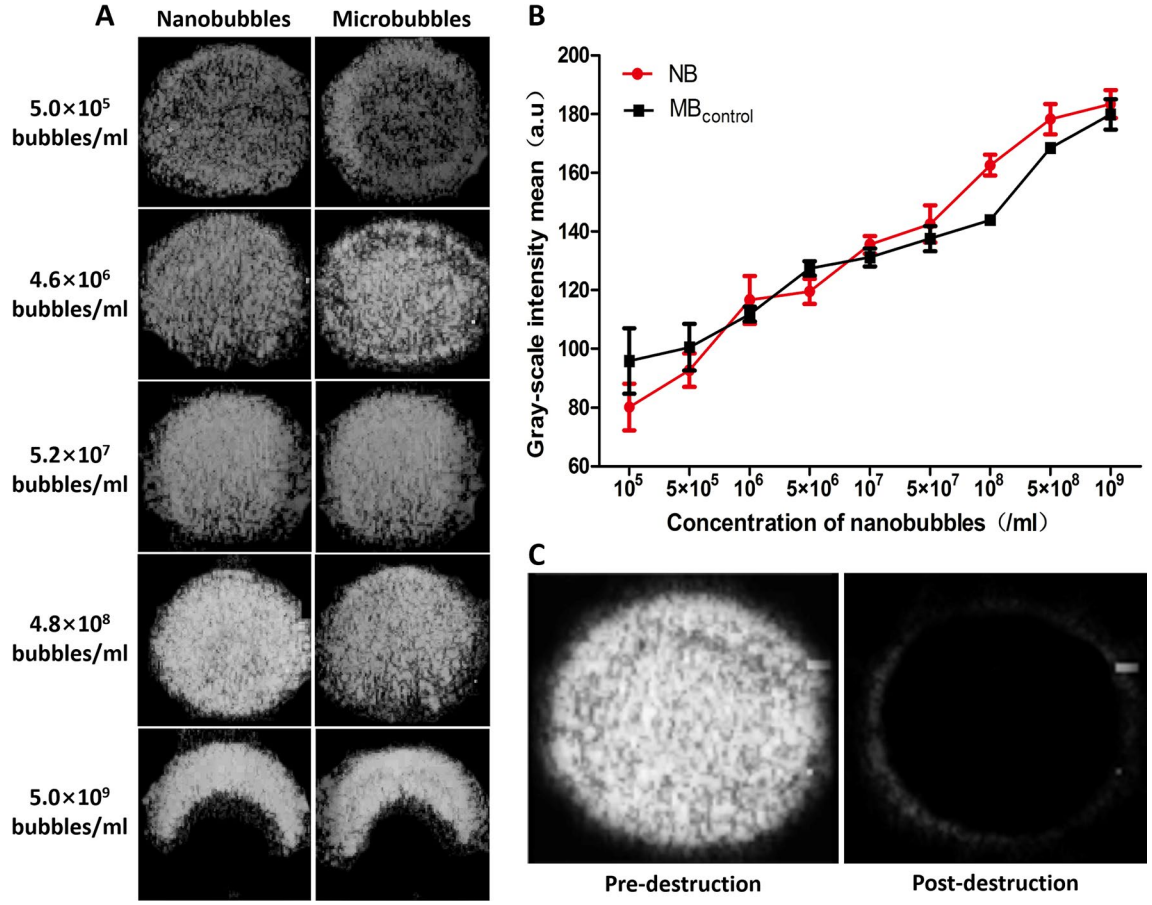

FIGURE 8 | *In vitro* ultrasound image enhancement. **(A)** Representative ultrasound images of nanobubbles and microbubbles *in vitro*. **(B)** Comparison of contrast intensity between nanobubbles and microbubbles at different concentrations. **(C)** Pre- and postdestruction of NBs at low-frequency ultrasound exposure.

The thickness of phospholipid was regarded as a critical factor for nanobubble diameters (Cai et al., 2015). We indeed found that the nanobubble diameter was obviously influenced by phospholipid film thickness. And the diameters seemingly increased with the rise of phospholipid film thickness. However, the uniformity of particle size was relatively poor. DLS analysis shows that the PDI values were high, and there were two peaks on the size distribution curve of different phospholipid film thicknesses. One peak was located at the nanoscale field, and one was located at the microscale field, which means that the bubble suspension acquired by controlling phospholipid film thickness was actually the mixture of nanobubbles and microbubbles. It was also confirmed using a microscope. Under the ×1,000 oil lens, some bubbles presented punctiform and some appeared as a sphere with a bright center. Moreover, the mean diameters were all higher than 700 nm at 5–25 mg of phospholipid, which means that the chance of passing through the tumor pore was poor. Therefore, an additional purification process was needed to separate nanobubbles from the mixture bubble suspension.

Centrifugation was an ideal method of purification. During centrifugation, larger-sized bubbles were separated from mixtures faster. Thus, in theory, if the conditions are set properly, we could obtain desired nanobubbles at any size we wanted. In our study, we found that the nanobubble diameters seemingly decreased with the rise of centrifugal speed. When the speed reaches 400 g, nanobubbles with a mean diameter at 246.1 ± 8.7 nm were obtained. Size uniformity was significantly improved after centrifugation. Compared to controlling phospholipid film thickness, the PDIs of nanobubbles after centrifugation were obviously smaller. The size distribution of nanobubbles were unimodal under different centrifugal conditions. However, the nanobubble concentration was negatively correlated with centrifugal speed. When the centrifugal speed was greater than 70 g, the concentration declined sharply. At a centrifugation of 70 g, the optimal nanobubbles were acquired, with an excellent PDI of 0.005, a mean diameter of 475.2 ± 5.7 nm, and a concentration of 5.4 ± 1.2 × 10^9/mL. Taking into account the bubble size, PDI, and concentration of all centrifugation conditions, we considered that nanobubbles acquired by 70 g would be most suitable for tumor imaging and drug delivery.

Next, we further studied the characteristics of nanobubbles produced by 70 g centrifugal speed. Fluorescence imaging and TEM further confirmed their morphology and particle size. The size of nanobubbles could remain unchanged

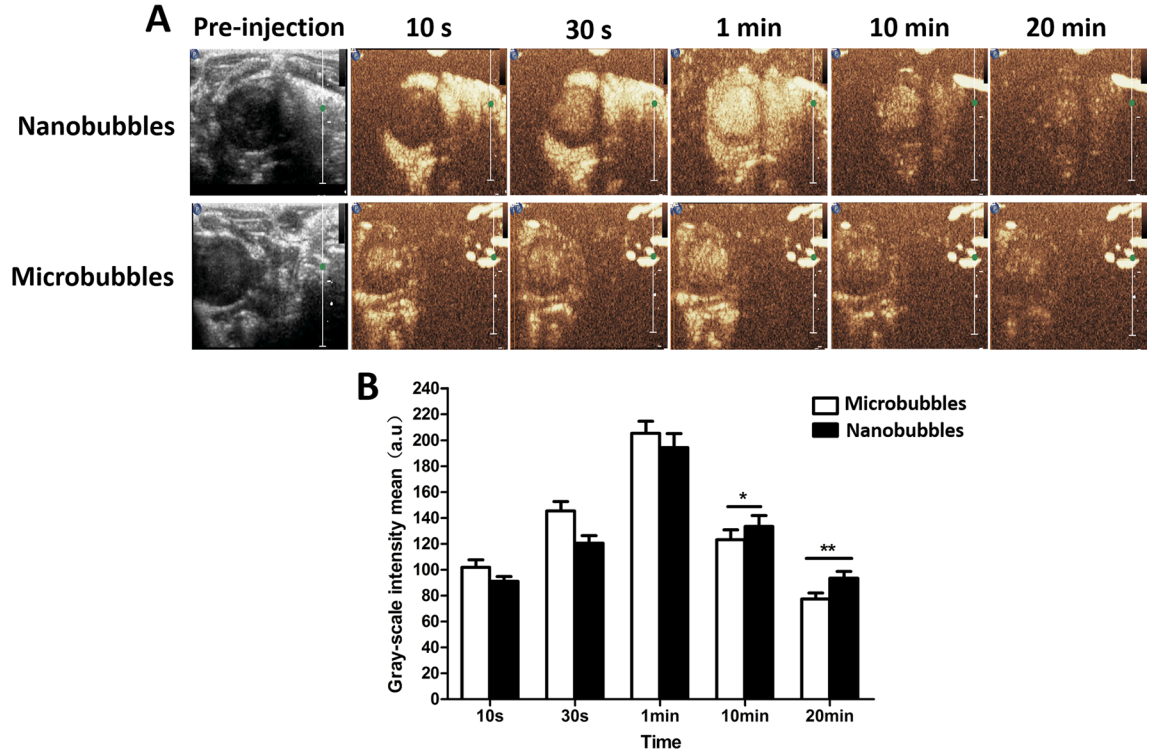

FIGURE 9 | The left ventricular opacification (LVO) in rats. **(A)** The representative LVO images of nanobubbles and microbubbles. **(B)** Grayscale intensity comparison between nanobubbles and microbubbles at the same time point.

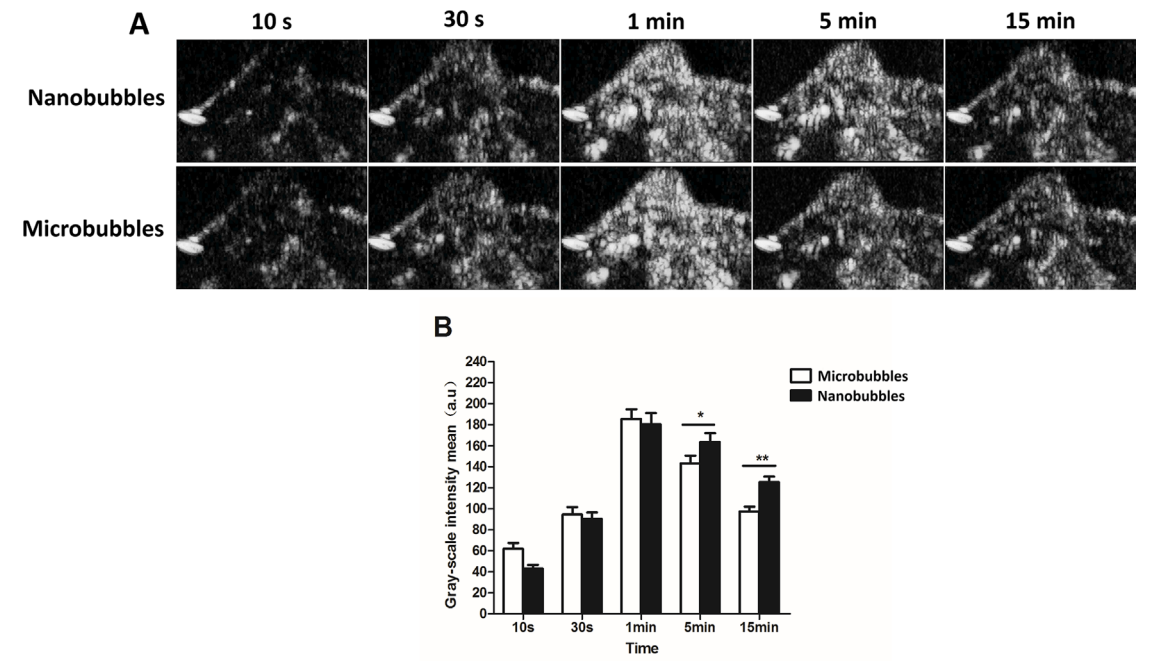

FIGURE 10 | Passive targeting ultrasound imaging of nanobubbles in tumors. **(A)** Representative ultrasound images of nanobubbles and microbubbles. **(B)** The quantitative comparison of imaging capability between nanobubbles and microbubbles at different time points.

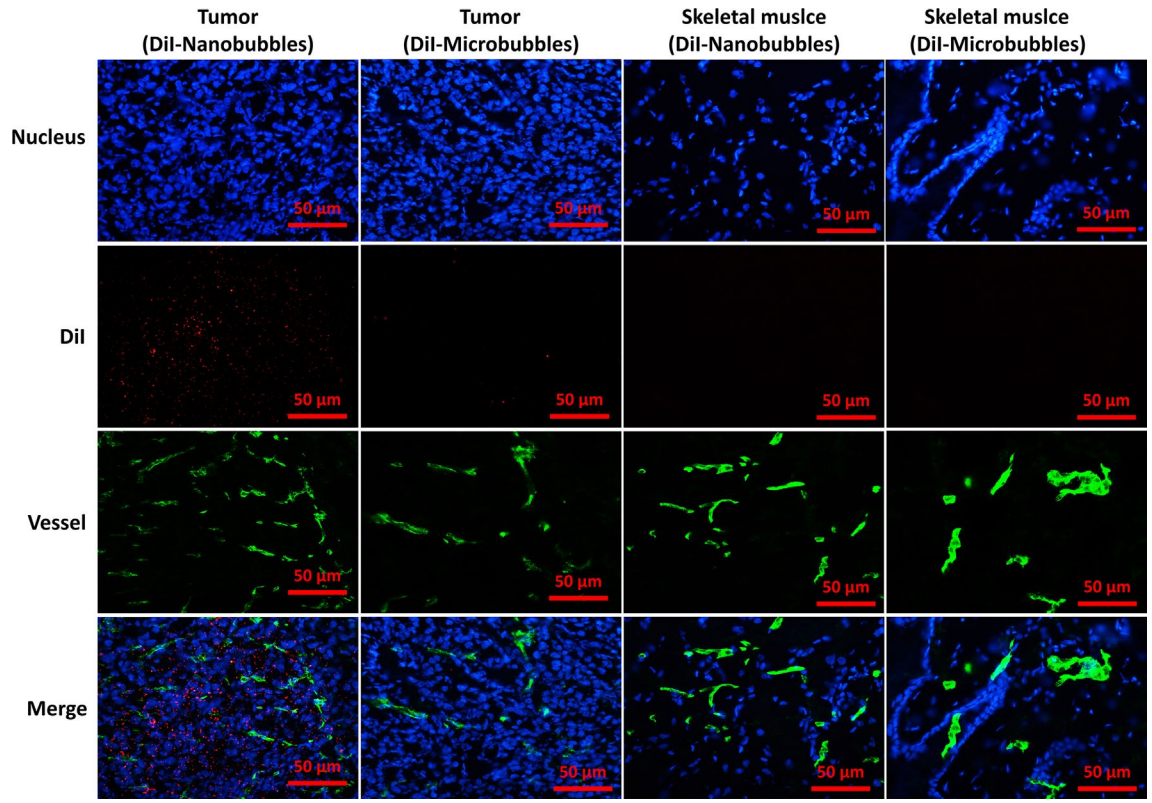

FIGURE 11 | Confocal laser-scanning microscopy images of frozen sections after vessels and nuclear labeling. A considerable number of Dil-labeled nanobubbles were observed in the intercellular space, whereas Dil-labeled microbubbles were hardly visible in tumors. Both Dil-labeled nanobubbles and microbubbles were difficult to detect in skeletal muscle.

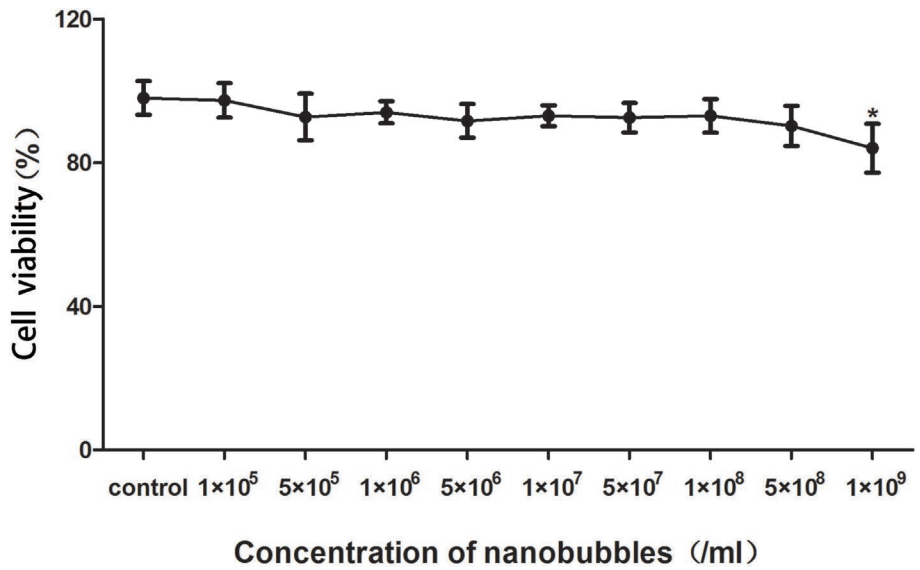

FIGURE 12 | *In vitro* biocompatibility evaluation of nanobubbles using Cell Counting Kit-8 (CCK-8) assay. Control, cells incubated with phosphate buffer saline (PBS) at the same volume.

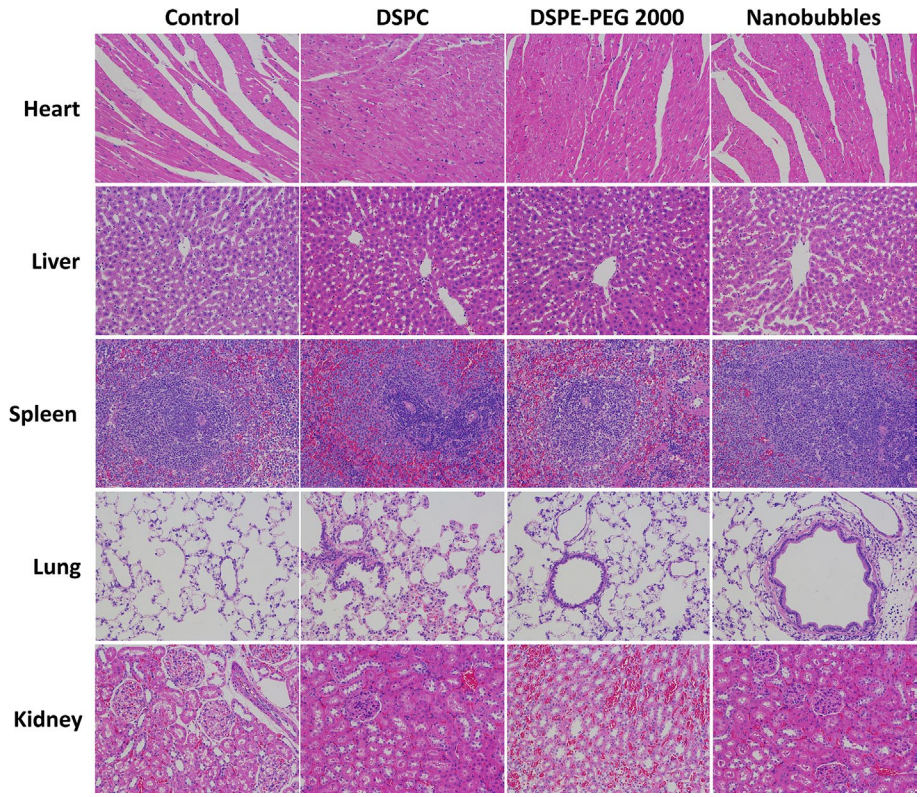

FIGURE 13 | *In vivo* toxicity evaluation of nanobubbles by HE staining of heart, liver, spleen, lung, and kidney (×200 magnification). Control, rats were treated by PBS injection at the same volume.

for 10 days. However, the concentration was markedly decreased after 6 h. Even so, this stability could still meet the requirements of most experiments. Under *in vitro* and *in vivo* ultrasound imaging, nanobubbles have shown optimal contrast enhancement abilities, which were similar to those of microbubbles. After high-power ultrasound exposure, the attenuation of grayscale intensity indicated that nanobubbles were destroyed, which illustrated that nanobubbles have a good acoustic response and could be used for drug delivery, just like microbubbles did.

Then, the passive targeting ability of nanobubbles was verified by ultrasound contrast imaging in tumor tissues. The contrast duration of the nanobubbles was significantly longer than that of microbubbles. CLSM imaging revealed that DiI-labeled nanobubbles penetrated through endothelial gaps and accumulated in the tumor, and red fluorescence was observed outside vessels. However, limited by their particle size, few microbubbles were present in tumor tissues. These phenomena could explain the ultrasound imaging performance. Because the endothelial gaps of normal tissue are less than 7 nm, neither nanobubbles nor microbubbles were observed in skeletal muscles. As a result, there was passive targeting of the nanobubbles to tumors.

Finally, the biosecurity of nanobubble was confirmed by the CCK-8 assay and histopathology. Phospholipids that made up nanobubbles are known to be low-toxicity materials. C_3F_8 is also nontoxic, which can be expelled through the lungs freely. Therefore, the nanobubbles were safe to use in cell studies and *in vivo* ultrasound imaging.

Nanobubbles have been widely used in ultrasound molecular imaging and drug/gene targeting delivery. When conjugated with specific ligands, nanobubbles can be used as a probe in ultrasound molecular imaging of various diseases, such as tumor (Lv et al., 2018), allograft rejection (Liu et al., 2018), and so on. Compared with microbubbles, nanobubbles can migrate from vasculature to the extravascular target site, which greatly expanded the application range of ultrasound molecular imaging. Similar to microbubbles, nanobubbles can also load drugs or genes for therapy. Because of their smaller size, nanobubbles can evade clearance by the reticuloendothelial system to a certain extent and have a longer retention time than microbubbles. As a result, nanobubbles can promote more drug/gene aggregation, especially in tumors because of the EPR effect (Wu et al., 2018). Therefore, this study provided a reference method for the preparation of stabilized nanobubbles with uniform particle size.

CONCLUSION

Nanobubbles show promise in tumor imaging and therapy. However, preparing uniform nanobubbles with a desirable size distribution remains a challenge. Lipid nanobubbles prepared by the thin-film

hydration method are commonly used currently. But there is still confusion about centrifugation and controlling phospholipid film thickness. In this study, we proved that, for the particle size and homogeneity of nanobubbles, centrifugation was better than controlling phospholipid film thickness. In addition, 70 g may be a relatively suitable centrifugal speed for pure nanobubbles preparation, which exhibited uniform size distribution, excellent passive targeting ability in tumors, and potential for therapy. In addition, it should be noted that centrifugation may generate a certain amount of material waste. However, we believe that this waste can be minimized by optimizing the formulation of lipid materials and centrifugation conditions, which is one of our further research projects in the future.

ETHICS STATEMENT

This study was carried out in accordance with the recommendations of the Animal Care and Use Committee of Huazhong University of Science and Technology. The protocol was approved by the Animal Care and Use Committee of Huazhong University of Science and Technology.

AUTHOR CONTRIBUTIONS

JZ and YC completed the main experiment and wrote the first draft of the paper together. CD prepared Figures 2 and 3. LZ and ZS prepared Figures 4 and 5. JW analyzed the data. YY, WH, and QL copyedited the manuscript. MX designed the research. All authors have reviewed the final version of the manuscript and approved it for publication.

FUNDING

This work was supported by the National Natural Science Foundation of China (grant nos. 81530056, 81727805, 81801715, 81501494, 81771851, and 81701716) and the HUST Interdisciplinary Innovation Team (0118530300).

REFERENCES

Cai, W. B., Yang, H. L., Zhang, J., Yin, J. K., Yang, Y. L., Yuan, L. J., et al. (2015). The optimized fabrication of nanobubbles as ultrasound contrast agents for tumor imaging. *Sci. Rep.* 5, 13725. doi: 10.1038/srep13725

Ferrara, K. W., Borden, M. A., and Zhang, H. (2009). Lipid-shelled vehicles: engineering for ultrasound molecular imaging and drug delivery. *Acc. Chem. Res.* 42 (7), 881–892. doi: 10.1021/ar8002442

Frauscher, F., Klauser, A., Halpern, E. J., Horninger, W., and Bartsch, G. (2001). Detection of prostate cancer with a microbubble ultrasound contrast agent. *Lancet* 357 (9271), 1849–1850. doi: 10.1016/S0140-6736(00)04970-9

Gao, Y., Hernandez, C., Yuan, H. X., Lilly, J., Kota, P., Zhou, H., et al. (2017). Ultrasound molecular imaging of ovarian cancer with CA-125 targeted nanobubble contrast agents. *Nanomedicine* 13 (7), 2159–2168. doi: 10.1016/j.nano.2017.06.001

Guvener, N., Appold, L., de Lorenzi, F., Golombek, S. K., Rizzo, L. Y., Lammers, T., et al. (2017). Recent advances in ultrasound-based diagnosis and therapy with micro- and nanometer-sized formulations. *Methods* 130, 4–13. doi: 10.1016/j.ymeth.2017.05.018

Hobbs, S. K., Monsky, W. L., Yuan, F., Roberts, W. G., Griffith, L., Torchilin, V. P., et al. (1998). Regulation of transport pathways in tumor vessels: role of tumor type and microenvironment. *Proc. Natl. Acad. Sci. U. S. A.* 95 (8), 4607–4612. doi: 10.1073/pnas.95.8.4607

Huang, C., Zhang, H., and Bai, R. (2017). Advances in ultrasound-targeted microbubble-mediated gene therapy for liver fibrosis. *Acta Pharm. Sin. B* 7 (4), 447–452. doi: 10.1016/j.apsb.2017.02.004

Hussain, T., and Nguyen, Q. T. (2014). Molecular imaging for cancer diagnosis and surgery. *Adv. Drug Deliv. Rev.* 66, 90–100. doi: 10.1016/j.addr.2013.09.007

Keliher, E. J., Ye, Y. X., Wojtkiewicz, G. R., Aguirre, A. D., Tricot, B., Senders, M. L., et al. (2017). Polyglucose nanoparticles with renal elimination and macrophage avidity facilitate PET imaging in ischaemic heart disease. *Nat. Commun.* 8, 14064. doi: 10.1038/ncomms14064

Krupka, T. M., Solorio, L., Wilson, R. E., Wu, H., Azar, N., and Exner, A. A. (2010). Formulation and characterization of echogenic lipid–pluronic nanobubbles. *Mol. Pharm.* 7 (1), 49–59. doi: 10.1021/mp9001816

Liao, A. H., Hsieh, Y. L., Ho, H. C., Chen, H. K., Lin, Y. C., Shih, C. P., et al. (2014). Effects of microbubble size on ultrasound-mediated gene transfection in auditory cells. *Biomed. Res. Int.* 2014, 840852. doi: 10.1155/2014/840852

Liao, A. H., Hung, C. R., Lin, C. F., Lin, Y. C., and Chen, H. K. (2017). Treatment effects of lysozyme-shelled microbubbles and ultrasound in inflammatory skin disease. *Sci. Rep.* 7, 41325. doi: 10.1038/srep41325

Liu, H., Chen, Y., Yan, F., Han, X., Wu, J., Liu, X., et al. (2015). Ultrasound molecular imaging of vascular endothelial growth factor receptor 2 expression for endometrial receptivity evaluation. *Theranostics* 5 (2), 206–217. doi: 10.7150/thno.9847

Liu, J., Chen, Y., Wang, G., Lv, Q., Yang, Y., Wang, J., et al. (2018). Ultrasound molecular imaging of acute cardiac transplantation rejection using nanobubbles targeted to T lymphocytes. *Biomaterials* 162, 200–207. doi: 10.1016/j.biomaterials.2018.02.017

Liu, J., Zhang, B., Li, M., Zhou, M., Li, F., Huang, X., et al. (2017). Preparation and characterization of a novel silicon-modified nanobubble. *PLoS One* 12 (5), e0178031. doi: 10.1371/journal.pone.0178031

Lu, Y., Wang, J., Huang, R., Chen, G., Zhong, L., Shen, S., et al. (2016). Microbubble-mediated sonothrombolysis improves outcome after thrombotic microembolism-induced acute ischemic stroke. *Stroke* 47 (5), 1344–1353. doi: 10.1161/STROKEAHA.115.012056

Lv, W., Shen, Y., Yang, H., Yang, R., Cai, W., Zhang, J., et al. (2018). A novel bimodal imaging agent targeting HER2 molecule of breast cancer. *J. Immunol. Res.* 2018, 6202876. doi: 10.1155/2018/6202876

Machtaler, S., Knieling, F., Luong, R., Tian, L., and Willmann, J. K. (2015). Assessment of inflammation in an acute on chronic model of inflammatory bowel disease with ultrasound molecular imaging. *Theranostics* 5 (11), 1175–1186. doi: 10.7150/thno.13048

Maeda, H., Bharate, G. Y., and Daruwalla, J. (2009). Polymeric drugs for efficient tumor-targeted drug delivery based on EPR-effect. *Eur. J. Pharm. Biopharm.* 71 (3), 409–19. doi: 10.1016/j.ejpb.2008.11.010

McEwan, C., Owen, J., Stride, E., Fowley, C., Nesbitt, H., Cochrane, D., et al. (2015). Oxygen carrying microbubbles for enhanced sonodynamic therapy of hypoxic tumours. *J. Control Release* 203, 51–6. doi: 10.1016/j.jconrel.2015.02.004

Moestue, S. A., Gribbestad, I. S., and Hansen, R. (2012). Intravascular targets for molecular contrast-enhanced ultrasound imaging. *Int. J. Mol. Sci.* 13 (6), 6679–6697. doi: 10.3390/ijms13066679

Perera, R. H., Wu, H., Peiris, P., Hernandez, C., Burke, A., Zhang, H., et al. (2017). Improving performance of nanoscale ultrasound contrast agents using *N*,*N*-diethylacrylamide stabilization. *Nanomedicine* 13 (1), 59–67. doi: 10.1016/j.nano.2016.08.020

Rapoport, N. Y., Nam, K. H., Gao, Z., and Kennedy, A. (2009). Application of ultrasound for targeted nanotherapy of malignant tumors. *Acoust. Phys.* 55 (4-5), 594–601. doi: 10.1134/S1063771009040162

Rosen, J. E., Chan, L., Shieh, D. B., and Gu, F. X. (2012). Iron oxide nanoparticles for targeted cancer imaging and diagnostics. *Nanomedicine* 8 (3), 275–290. doi: 10.1016/j.nano.2011.08.017

Snipstad, S., Berg, S., Morch, Y., Bjorkoy, A., Sulheim, E., Hansen, R., et al. (2017). Ultrasound improves the delivery and therapeutic effect of nanoparticle-stabilized microbubbles in breast cancer xenografts. *Ultrasound Med. Biol.* 43 (11), 2651–2669. doi: 10.1016/j.ultrasmedbio.2017.06.029

Song, W., Luo, Y., Zhao, Y., Liu, X., Zhao, J., Luo, J., et al. (2017). Magnetic nanobubbles with potential for targeted drug delivery and trimodal imaging in breast cancer: an *in vitro* study. *Nanomedicine (Lond)* 12 (9), 991–1009. doi: 10.2217/nnm-2017-0027

Weissleder, R. (2006). Molecular imaging in cancer. *Science* 312 (5777), 1168–1171. doi: 10.1126/science.1125949

Willmann, J. K., Bonomo, L., Carla Testa, A., Rinaldi, P., Rindi, G., Valluru, K. S., et al. (2017). Ultrasound molecular imaging with BR55 in patients with breast and ovarian lesions: first-in-human results. *J. Clin. Oncol.* 35 (19), 2133–2140. doi: 10.1200/JCO.2016.70.8594

Willmann, J. K., Lutz, A. M., Paulmurugan, R., Patel, M. R., Chu, P., Rosenberg, J., et al. (2008a). Dual-targeted contrast agent for US assessment of tumor angiogenesis *in vivo*. *Radiology* 248 (3), 936–944. doi: 10.1148/radiol.2483072231

Willmann, J. K., Paulmurugan, R., Chen, K., Gheysens, O., Rodriguez-Porcel, M., Lutz, A. M., et al. (2008b). US imaging of tumor angiogenesis with microbubbles targeted to vascular endothelial growth factor receptor type 2 in mice. *Radiology* 246 (2), 508–518. doi: 10.1148/radiol.2462070536

Wu, J., Leong-Poi, H., Bin, J., Yang, L., Liao, Y., Liu, Y., et al. (2011). Efficacy of contrast-enhanced US and magnetic microbubbles targeted to vascular cell adhesion molecule-1 for molecular imaging of atherosclerosis. *Radiology* 260 (2), 463–471. doi: 10.1148/radiol.11102251

Wu, M., Zhao, H., Guo, L., Wang, Y., Song, J., Zhao, X., et al. (2018). Ultrasound-mediated nanobubble destruction (UMND) facilitates the delivery of A10-3.2 aptamer targeted and siRNA-loaded cationic nanobubbles for therapy of prostate cancer. *Drug. Deliv.* 25 (1), 226–240. doi: 10.1080/10717544.2017.1422300

Yin, T., Wang, P., Zheng, R., Zheng, B., Cheng, D., Zhang, X., et al. (2012). Nanobubbles for enhanced ultrasound imaging of tumors. *Int. J. Nanomedicine* 7, 895–904. doi: 10.2147/IJN.S28830

Zhang, L., Sun, Z., Ren, P., You, M., Zhang, J., Fang, L., et al. (2017). Localized delivery of shRNA against PHD2 protects the heart from acute myocardial infarction through ultrasound-targeted cationic microbubble destruction. *Theranostics* 7 (1), 51–66. doi: 10.7150/thno.16074

Zhang, Y. J., Bai, D. N., Du, J. X., Jin, L., Ma, J., Yang, J. L., et al. (2016). Ultrasound-guided imaging of junctional adhesion molecule-A-targeted microbubbles identifies vulnerable plaque in rabbits. *Biomaterials* 94, 20–30. doi: 10.1016/j.biomaterials.2016.03.049

Zhu, Y., Guan, L., and Mu, Y. (2016). Combined low-frequency ultrasound and urokinase-containing microbubbles in treatment of femoral artery thrombosis in a rabbit model. *PLoS One* 11 (12), e0168909. doi: 10.1371/journal.pone.0168909

Zong, Y., Wan, M., Wang, S., and Zhang, G. (2006). Optimal design and experimental investigation of surfactant encapsulated microbubbles. *Ultrasonics* 44 Suppl 1, e119–122. doi: 10.1016/j.ultras.2006.06.005

Conflict of Interest Statement: The authors declare that the research was conducted in the absence of any commercial or financial relationships that could be construed as a potential conflict of interest.

The handling editor and reviewer XW declared their involvement as co-editors in the Research Topic, and confirm the absence of any other collaboration.

frontiers in Pharmacology

ORIGINAL RESEARCH
published: 19 June 2019
doi: 10.3389/fphar.2019.00655

Evaluation of the Expression of Matrix Metalloproteinase-1 of Laryngeal Squamous Cell Carcinoma by Ultrasound Molecular Imaging

Yi Zhou[1,5†], Zhuqing Song[2†], Qiao Hu[3], Xiaojuan Ji[4], Hongyu Zheng[3], Xiaoyan Wang[3] and Zhenzhou Li[5]**

[1] GuangZhou University School of Medicine, GuangZhou, China, [2] Department of Breast Surgery, Peking University Shenzhen Hospital, Shenzhen, China, [3] Department of Ultrasound, The People's Hospital of Guangxi Zhuang Autonomous Region, Nanning, China, [4] Department of Cardiology, Children's Hospital of Chongqing Medical University, Chongqing, China, [5] Department of Ultrasound, The Second People's Hospital of Shenzhen, The First Affiliated Hospital of Shenzhen University, Shenzhen, China

OPEN ACCESS

Edited by:
Fei Yan,
Shenzhen Institutes of Advanced Technology (CAS), China

Reviewed by:
Yihan Chen,
Huazhong University of Science and Technology, China
Feng Wang,
Xinxiang Medical University, China

***Correspondence:**
Qiao Hu
xyyxyhq@163.com
Zhenzhou Li
lizhenzhou2004@126.com

†These authors have contributed equally to this work.

Specialty section:
This article was submitted to Translational Pharmacology, a section of the journal Frontiers in Pharmacology

Received: 30 January 2019
Accepted: 20 May 2019
Published: 19 June 2019

Citation:
Zhou Y, Song Z, Hu Q, Ji X, Zheng H, Wang X and Li Z (2019) Evaluation of the Expression of Matrix Metalloproteinases-1 of Laryngeal Squamous Cell Carcinoma by Ultrasound Molecular Imaging. Front. Pharmacol. 10:655. doi: 10.3389/fphar.2019.00655

Purpose: The aims of this study were to evaluate the expression of matrix metalloproteinase-1 (MMP-1) on laryngeal squamous cell carcinoma (LSCC) and improve the early diagnosis rate *via* ultrasound molecular imaging (USMI).

Methods: The microsized MMP-1-targeted microbubbles (MB_{MMP-1}) and the control MBs (MB_{IgG}) based on perfluorocarbon-filled lipid-shelled MBs were constructed and characterized. The *in vitro* binding experiment was performed with human epidermoid laryngeal cancer cells (HEp-2) and tested the binding efficiency of MB_{MMP-1} and MB_{IgG}. In the *in vivo* study, the LSCC model was established in 10 mice. The MB_{MMP-1} and MB_{IgG} were randomly injected into tumor-bearing mice *via* the tail vein at Day 7, Day 12, and Day 17 to dynamically evaluate the differential targeted enhancement (dTE) signals *via* USMI. Subsequent immunofluorescence analysis was used for confirmation of MMP-1 expression.

Result: The effective adhesion rate of MB_{MMP-1} and MB_{IgG} to HEp-2 was 298.42 ± 16.57 versus 12.38 ± 3.26 bubbles/per field *in vitro* experiment, which shows a significant difference ($P < 0.01$). The *in vivo* ultrasound molecular imaging (USMI) results demonstrated that dTE signal intensity from MB_{MMP-1} was significantly higher than that from the MB_{IgG} at Day 7, Day 12, and Day 17 (Day 7, 41.21 ± 15.00 versus 2.25 ± 0.6 a.u., $P < 0.05$; Day 12, 124.64 ± 5.19 versus 11.13 ± 1.13 a.u., $P < 0.05$; Day 17, 332.01 ± 64.88 versus 42.99 ± 11.9 a.u., $P < 0.01$). Moreover, immunofluorescence analysis further confirmed the expression of MMP-1 in LSCC with a gradual increase with the tumor growth.

Conclusion: MB_{MMP-1} could be a potential probe that can be used in the early diagnosis of LSCC by USMI.

Keywords: ultrasound molecular imaging, matrix metalloproteinase-1, laryngeal squamous cell carcinoma, targeted microbubbles, vasculogenic mimicry

INTRODUCTION

Laryngeal squamous cell carcinoma (LSCC) is one of the common malignant tumors of the head and neck. Recent data from global epidemiology of head and neck cancers show that more than 245,000 new cases of laryngeal cancer will be expected by 2030 (Gupta et al., 2016). Although great significant progress has made in the diagnosis, its early diagnosis rate of LSCC still remains to be raised. Microbubble-based ultrasound molecular imaging (USMI) shows significant potential in the early diagnosis of tumors. Ultrasound contrast agents (UCAs) such as microbubbles (MBs) can emit significantly stronger acoustic signals under an appropriate sonic energy excitation, making them several thousand times more reflective than normal body tissues. Through designing ultrasonic contrast agents with specific molecular markers, USMI probes can be obtained and used to visualize molecular and genetic alterations of diseased cells, and to monitor the genesis and development of certain diseases. Previously, researchers have demonstrated that the MBs combined with antibodies or peptides, which can bind to vascular endothelial growth factor (VEGR) or αvβ3 integrin, and enhanced the contrast ultrasonography quality in LSCC *via* USMI (Paolo et al., 2006; Hu et al., 2016). However, in malignant LSCC tumors, the expression of EGFR or αvβ3 integrin was commonly not at a high level (Kumar, 2003; Gino et al., 2010).

Matrix metalloproteinase-1 (MMP-1), a member of the family of MMPs, plays crucial roles in vascular formation and remodeling *via* degrading vascular membrana basilaris and extracellular matrix (ECM) proteins (Raffetto and Khalil, 2008). In addition, several studies have confirmed that the MMP-1 is specially associated with LSCC growth, local invasion, and metastasis (Tsukifuji et al., 1999). Upile et al., (2011) had claimed that the angiogenesis of LSCC was not only a unique means to nourish tumor tissues. Specially, it generated "micro-vascular" channels without the composition of endothelial cells at the early stage. This event was known as vascular mimicry (VM) in which endothelial-like cells are transdifferentiated by their own stem cells. More importantly, both angiogenesis and VM as a part of tumor microenvironment are coordinately providing tumor initiation and progression, and the latter one even seriously contributed to the invasion of LSCC (Upile et al., 2011; Balkwill et al., 2012). In view of above-mentioned reasons, we believed that the biomarker of MMP-1 would provide a potential evaluation of its progress in LSCC biology, thus allowing for the design of new diagnostics and therapeutics for early cancer diagnosis and treatment.

To date, the positive rate of conventional medical imaging examination, such as computed tomography (CT) and magnetic resonance imaging (MRI), in detecting LSCC is still low in detection of LSCC (Castelijns and Mw, 1993; Yamazaki et al., 2008; Norling et al., 2014; Righi et al., 2015). USMI is a multifunctional and famous medical imaging tool for the detection and visualization of cancer-related biomarkers in early disease diagnosis (Pysz et al., 2010; Yan et al., 2011; Feng et al., 2013; Wood and Sehgal, 2015). In the past decades, MBs with different types of shells composed of phospholipids or polymers and gas cores (perfluorocarbon, nitrogen, sulfur hexafluoride, or air) had been applied in USMI and performed good contrast enhancement (Kiessling et al., 2009; Abou-Elkacem et al., 2016). Some special biomarkers of ligands such as integrin and Vascular cell adhesion molecule-1 (VCAM-1) or EGFR can be tightly bound on the surface of MBs for a better specificity diagnosis (Fabian et al., 2012). Recently, it has been successfully applied to various diseases such as vascular plaque and tissue inflammation, but its potential use in the diagnosis of LSCC has not been reported. In our study, we preliminarily developed the MB_{MMP-1} and dynamically evaluated the expression of MMP-1 separately at Day 7, Day 12, and Day 17 of LSCC progression *in vivo* by USMI.

MATERIALS AND METHODS

Preparation of MB_{MMP-1}

MB_{MMP-1} and control MB_{IgG} were prepared according to a previous report (Stieger et al., 2010). In brief, DSPC: DSPE-PEG2000:DSPE-PEG2000-biotin (Avanti Polar Lipids, Alabaster, AL, USA) (molar ratios = 9:0.5:0.5) was blended in chloroform, and the solvent was removed under nitrogen flow at room temperature, followed by vacuum treatment over 2 h. The dried blends were hydrated at 60°C with phosphate-buffered saline (PBS) and sub-packaged into vials (1 mL each vial). After that, perfluoropropane (C_3F_8; Flura, Newport, TN, USA) was added, and the admixture was mechanically vibrated for 45 s. After that, MB_{MMP-1} contrast group was prepared by incubating these biotinylated MBs with excess avidin, followed by adding a given proportion (50 μg × 10^8 MBs) of biotinylated anti-mouse MMP-1 monoclonal antibody (Novus Biologicals, Colorado, USA). Incubation at room temperature for 15–30 min and washing three to four times by centrifugation (400*g*) were necessary for avidin or antibody linkage. The biotinylated IgG antibody (Novus Biologicals, Colorado, USA) was used instead of MMP-1 to connect with biotinylated MBs in the same way to obtain MB_{IgG} in the control group.

Characterization of MB_{MMP-1}

The surface morphology of MB_{MMP-1} was investigated using a microscope (Leica DMI3000 B). Fluorescent microscopic examination was performed to verify the anti-mouse MMP-1 monoclonal primary antibody conjugation efficiency of MB_{MMP-1} according to fluorescent intensity of fluorescein isothiocyanate (FITC)-conjugated goat anti-mouse second antibody (St. Louis, MO, USA) under a fluorescent microscope (Olympus, Tokyo, Japan). MB_{MMP-1} average size, distribution, and differential intensity were evaluated three times for each sample using a diameter limit of 0.5 μm (AccuSizer 780; Particle Sizing Systems, Santa Barbara, CA, USA).

Cell Culture

Human epidermoid laryngeal cancer cells (Procell Life, Wuhan, China) (HEp-2) were cultured in Dulbecco's modified Eagle medium (DMEM) supplemented with 10% fetal bovine serum (FBS), 1% L-glutamine, and 1% penicillin–streptomycin. The cell cultures were maintained in a humidified atmosphere of 5% CO_2 at 37°C with the medium changed every other day.

Tumor Model

All animal studies were approved by the Institute's Animal Care and Use Committee of Shenzhen Second People's Hospital, Guangzhou University School of Medicine, China. The methods were carried out in accordance with the approved guidelines. Nude male Balb/c mice (6- to 8-week-old, body weight 20 ± 1.5 g) were supplied by Beijing Vital River Laboratory Animal Technology Co. Ltd. All mice were housed on a 12:12 light:dark cycle with free access to food and water. HEp-2 cells (1×10^6/each mouse) dissolved in 100 μL of PBS were injected into the left oxter of nude male Balb/c mice. Tumor-bearing mice were used for USMI when they had developed at Day 7, Day 12, and Day 17 after inoculation.

In Vitro Imaging Performance of MB_{MMP-1}

MB_{MMP-1} with concentrations of 1×10^5, 1×10^6, and 1×10^7 MBs/mL was placed in agar gel holes. The US imaging performance of MBs was detected from the side of the agar gel with VisualSonics Vevo2100 (VisualSonics, Inc., Toronto, Canada) to determine the intensity of the ultrasound signal of the MBs with concentrations of 1×10^5, 1×10^6, and 1×10^7 MBs/mL.

Binding Specificity of MB_{MMP-1} to Human Epidermoid Laryngeal Cancer Cells

In a 6-well plate (1×10^5 cells per well), 1×10^5 HEp-2 cells were cultured overnight. The next day, the culture medium was discarded, and the cells were washed three times with PBS, and then 1×10^8 MBs/mL of MB_{MMP-1} or MB_{IgG} was added to the cells and incubated to the plate for 5–6 min. After being washed three to five times with PBS, the binding efficiency of MB_{MMP-1} and control MB_{IgG} to cells was examined under an inverted microscope (Olympus, Tokyo, Japan). At the same time, the competitive binding inhibition experimental group (pre-blocking MMP-1 receptors by adding an excess of free MMP-1 monoclonal antibody) was also set up to study the binding specificity of MB_{MMP-1} to HEp-2.

In Vivo Ultrasound Molecular Imaging

USMI was conducted as described previously (Stieger et al., 2010). Briefly, the mice were kept anesthetized by continuous inhalation of 2% isoflurane in oxygen at 2 L/min on a heated stage during scanning. US imaging was performed using a dedicated small-animal high-resolution USMI system (Vevo2100, VisualSonics) equipped with an 18-MHz high-frequency nonlinear transducer. All imaging parameters (grain, 30 dB; focal depth, 2–4 mm; transmit power, 10%; MI, 0.1) were kept constant during all imaging sessions. MB_{MMP-1} or MB_{IgG} (5×10^8 MBs in 200 μL of PBS) was administered *via* the tail vein of the mice in random order to minimize bias, and injections were separated by at least 30 min to allow clearance of MBs from the blood circulation. To distinguish the acoustic signal from MBs that had adhered to MMP-1 receptors from the signal from freely circulating MBs, a destruction/replenishment approach was used in this study. In brief, after injection of MBs and waiting for 7 min, approximately 200 ultrasonographic frames of the tumor were acquired at a temporal resolution of 12 s. Then a high-power ultrasound destruction sequence was applied for 1 s to destroy the MBs. After the destruction pulse, another set of movie (≈200 frames) was acquired. Movie processing and quantification were performed using Vevo2100 built-in software of CQ and relying on two sets of movie: a pre-destruction set and a post-destruction (background) data set. The post-destruction movie signals were subtracted from the pre-destruction signals. The difference in movie signal intensity between pre-destruction and post-destruction ultrasonographic frames was calculated and expressed as movie intensity amplitude.

Imaging Data Analysis

The imaging data sets of all mice were analyzed by Vevo2100 built-in software CQ. Regions of interest were drawn covering the entire area of the tumor. The movie signal intensity from attached MBs was assessed by calculating an average for pre-destruction and post-destruction imaging signals and subtracting the average post-destruction signal from the average pre-destruction signal. The subtracted signal, so-called differential targeted enhancement (dTE), was colored red and then displayed as a colored overlay on the contrast-mode images.

Immunofluorescence

Tumor-bearing mice were euthanized after USMI, and the subcutaneous tumors were excised, embedded in optimal cutting temperature compound, and frozen in dry ice. Frozen blocks were sectioned at 5 μm (CM1950, Leica, Heidelberg, Germany) and mounted on glass slides for immunofluorescence staining. A double-staining procedure was employed to visualize MMP-1 expression on tumor cells. The following method was used for mouse MMP-1 staining. First, paraffin sections were successively dewaxed with xylene I for 15 min and xylene II for 15 min; hydrated with absolute ethanol I for 5 min, absolute ethanol II for 5 min, 85% ethanol for 5 min, and 75% ethanol for 5 min; and afterwards washed with distilled water. Second, these were subsequently blocked with 5% goat serum for 30 min at room temperature. And then the slides were co-incubated with rabbit anti-mouse MMP-1 primary antibody with dilution 1:1,500 ratio (Google Biotechnology Co., Ltd, Wuhan, China) overnight at 4°C and visualized by using Cy3-conjugated goat anti-rabbit second antibody (Servicebio, Wuhan, China) in a 1:300 ratio (Google Biotechnology Co., Ltd, Wuhan, China). Next, the slides were placed in PBS (pH 7.4) on as decolorization shaking table for 5 min. After the drying process, dihydrochloride (DAPI) dye was added to the slides, and samples were protected from light and incubated for 10 min. Finally, fluorescent images were acquired at ×400 magnifications with a laser scanning confocal microscope (TCS SP5, Leica, Germany). And then the correlation analysis between the signal intensity of USMI and mean optical density (/pixel) of MMP-1 expression was performed separately at Day 7, Day 12, and Day 17.

Statistical Analysis

Quantitative data were expressed as the means and standard deviation (mean ± SD). Data from two independent samples were

analyzed with Student's *t* test. Analysis of variance (ANOVA) was used to determine the significance of differences in multiple comparisons. A *P* value of less than 0.05 was considered statistically significant. Statistical analyses were performed using Statistical Product and Service Solutions (SPSS) software version 13.0 (SPSS Inc, Chicago, IL, USA).

RESULTS

Characterization of MB_{MMP-1}

Figure 1 shows a schematic illustration of MB_{MMP-1}. Microscopic image analysis at high magnification revealed that the resulting MB_{MMP-1} has regular spherical morphology, transparent center, and good dispersion with no adherence to each other (**Figure 2A**). The FITC-conjugated MB_{MMP-1} shows bright green fluorescence under fluorescence microscope (**Figure 2B**), indicating the successful conjugation of anti-MMP-1 antibodies onto the surface of MBs. Mean size distributions of the MB_{MMP-1} are shown in **Figure 2C** by AccuSizer 780, revealing that the mean diameter of the MB_{MMP-1} was centered at 1.11 ± 0.10 μm.

In Vitro Imaging Performance of MB_{MMP-1}

To confirm the imaging performance of MB_{MMP-1} as a contrast agent for USMI, three different concentrations of MB_{MMP-1} were assessed *in vitro via* contrast imaging mode (**Figure 3A, B, C**). We found the three samples' echoes are relatively well distributed. In addition, with the increase of the concentration of MB_{MMP-1}, the signal intensity of contrast imaging increases. In particular, we found that the best performance of contrast imaging was at 1×10^7 MBs/mL. Then, we quantified the average signal intensity of different concentrations of MB_{MMP-1}, revealing 4.11 ± 1.37, 24.03 ± 2.06, and 90.72 ± 4.92 a.u. at 1×10^5, 1×10^6, and 1×10^7 MBs/mL, respectively (**Figure 3D**).

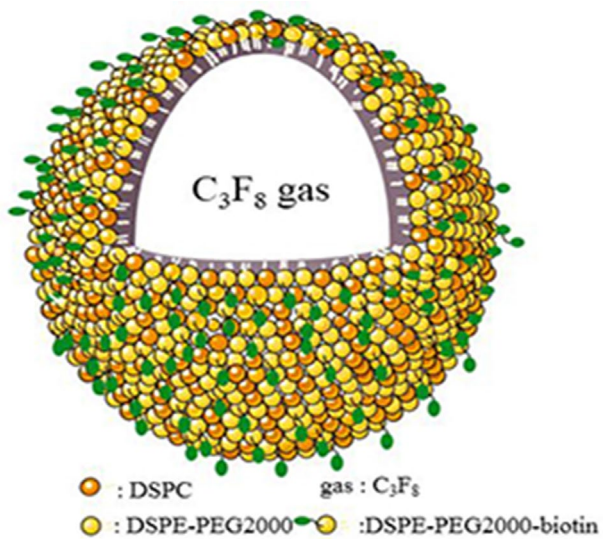

FIGURE 1 | Schematic illustration of MB_{MMP-1}. DSPC = distearoylphosphatidylcholine; DSPE = distearoylphosphatidylethanolamine; PEG2000 = polyethylene glycol 2000.

Binding Specificity of MB_{MMP-1} to Human Epidermoid Laryngeal Cancer Cells

To ensure the binding specificity of the MB_{MMP-1}, we further conducted the binding specificity of MB_{MMP-1} or MB_{IgG} with the HEp-2 by comparing with the group that was pre-incubated with free anti-MMP-1 antibodies for 5–6 min. In bright field, our results (**Figure 4A**) showed that the control MB_{IgG} only had a small number of non-targeted binding specificity on the HEp-2 surface with 12.38 ± 3.26 MBs/per field, while the MB_{MMP-1} could specifically bind to the HEp-2 with 298.42 ± 16.57 MBs/per field (**Figure 4B**) (298.42 ± 16.57 versus 12.38 ± 3.26 MBs/per field, $P < 0.01$). And as for the pre-blocking group by an excess of free anti-MMP-1 monoclonal antibody, it was found that the number of MB_{MMP-1} attached to HEp-2 was significantly decreased with 37.3 ± 6.94 MBs/per field (**Figure 4C**) (298.42 ± 16.57 versus 37.3 ± 6.94 MBs/per field, $P < 0.01$). Quantitative analysis indicated that the binding specificity of MB_{MMP-1} was significantly about 20 times higher than that of control MB_{IgG} (298.42 ± 16.57 versus 12.38 ± 3.26, $^{**}P < 0.01$) (**Figure 4D**).

USMI *In Vivo*

MB_{MMP-1} and MB_{IgG} were further evaluated in tumor-bearing mice at Day 7, Day 12, and Day 17 by USMI. The injections of MB_{MMP-1} or MB_{IgG} were separated by at least 30 min. From **Figure 5A**, we could clearly observe that the MB_{MMP-1} of color red had more retention rate in tumors and significantly enhanced the US imaging signal intensity, while the control MB_{IgG} showed a significantly lower enhancement than did MB_{MMP-1}. In addition, with the growth of LSCC, the dTE signal intensity was much higher in MB_{MMP-1}. From **Figure 5B**, we plotted the US dTE signal intensity from the LSCC versus growth time of the Day 7, Day 12, and Day 17. There were 20-, 10- and 8-folds higher dTE signal intensity from MB_{MMP-1} than control MB_{IgG}. Then we quantify the dTE signal intensity with Vevo2100 inner software CQ. Quantification revealed 41.21 ± 15.00 a.u. for MB_{MMP-1} versus 2.25 ± 0. 6 a.u. for MB_{IgG} at Day 7 ($^{*}P < 0.05$), 124.64 ± 5.19 a.u. MB_{MMP-1} versus 11.13 ± 1.13 a.u. MB_{IgG} at Day 12 ($^{*}P < 0.05$), and 332.01 ± 64.88 a.u. MB_{MMP-1} versus 42.99 ± 11. 9 a.u. MB_{IgG} at Day 17 ($^{**}P < 0.01$).

Tumor Immunofluorescence Staining

To confirm the results of USMI using the MB_{MMP-1}, the tumor slices at Day 7, Day 12, and Day 17 were executed and subsequently analyzed for MMP-1 expression by immunofluorescence. Immunofluorescence results are shown in **Figure 6**; we could clearly see that the MMP-1 (red) was highly expressed in LSCC, confirming the presence of mouse MMP-1 on plasma membrane within LSCC in our study. In addition, we did the correlation analysis between the dTE signal intensity of USMI and mean optical density (/pixel) of MMP-1 expression in **Figure 7**; it was obvious that the dTE signal intensity of USMI was linearly enhanced as the mean optical density under the growth of the tumor. On the whole, the results of immunofluorescent evaluation at Day 7, Day 12, and Day 17 are relevant to the dTE signal intensity acquired with the MB_{MMP-1} by USMI.

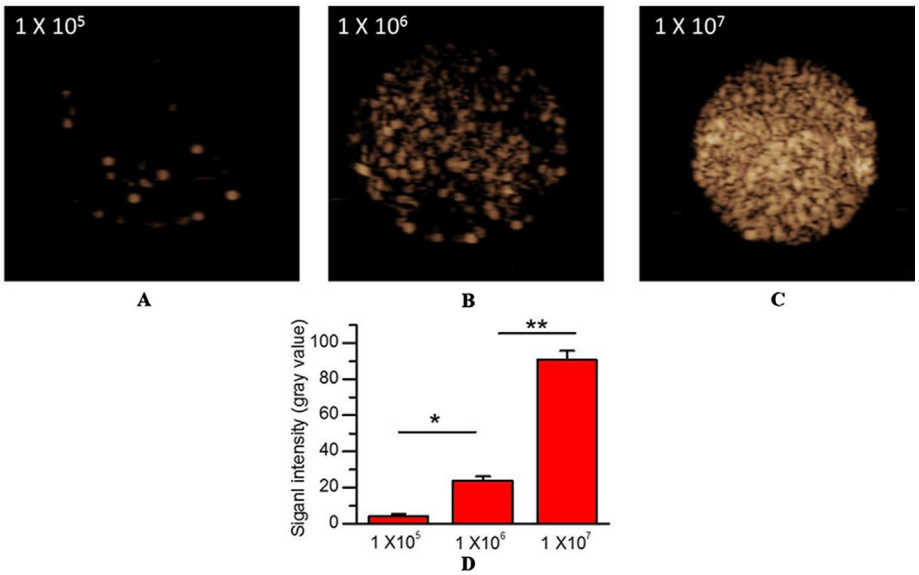

FIGURE 2 | In vitro US imaging performance. **(A)** 1×105 MBs/mL. **(B)** 1×106 MBs/mL. **(C)** 1×107 MBs/mL. **(D)** Quantitative analysis of US signal intensity of MBMMP-1 with three different concentrations.

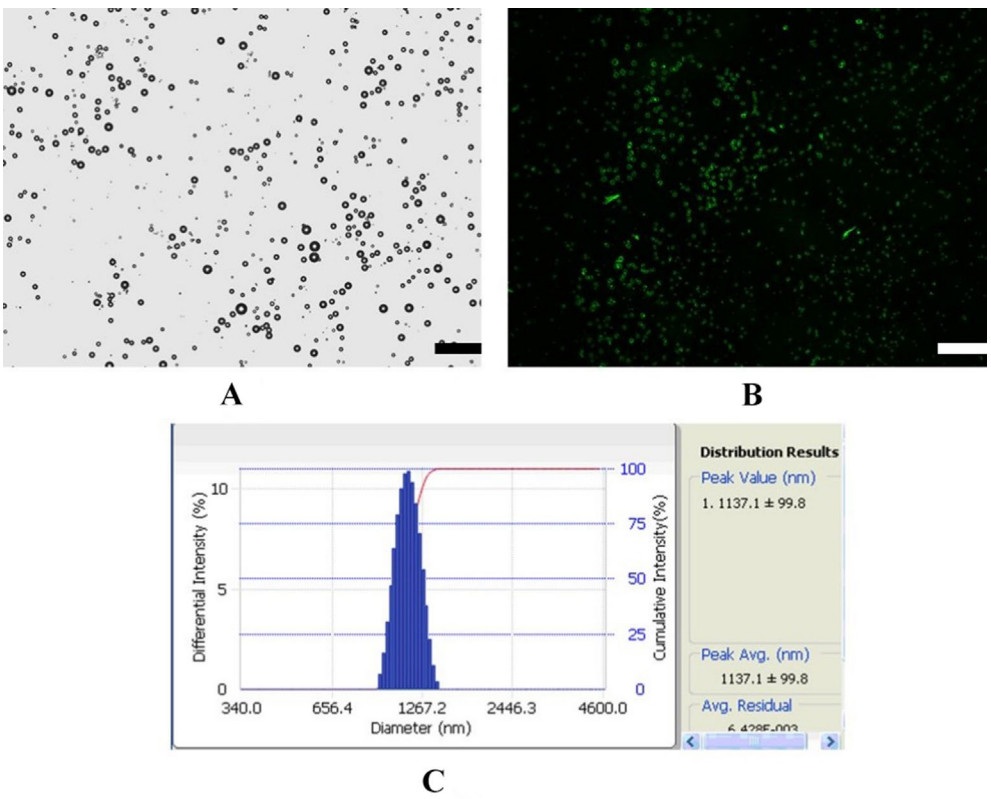

FIGURE 3 | Characterization of MB_{MMP-1}. **(A)** Bright-filed photograph of MB_{MMP-1}. **(B)** Fluorescent micrograph of FITC-labeled MB_{MMP-1}. **(C)** Average size and distribution of the MB_{MMP-1} (scale bar = 10 μm).

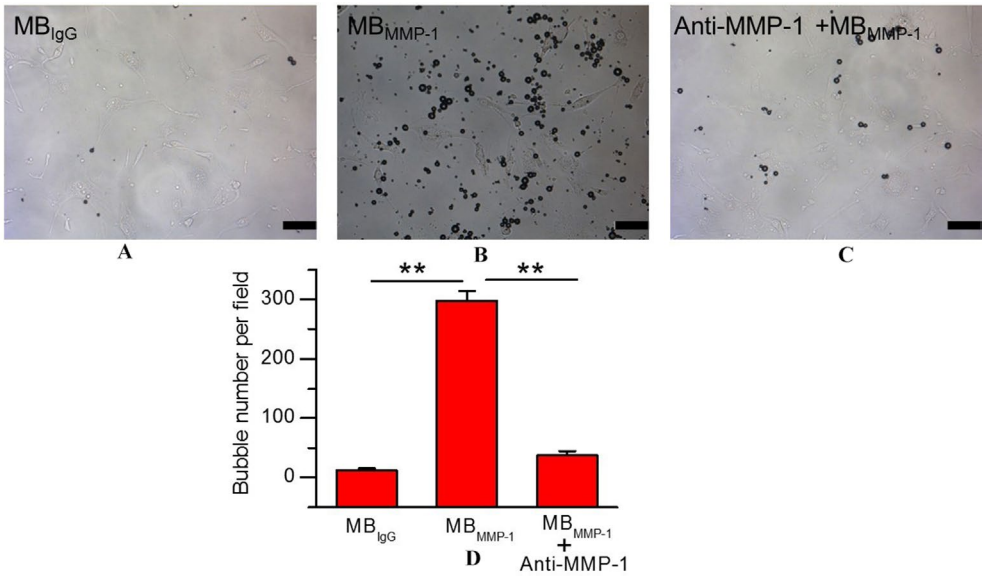

FIGURE 4 | *In vitro* binding specificity experiment of MB_{MMP-1} to human epidermoid laryngeal cancer cells (HEp-2). **(A)** White light micrograph after incubating control group MB_{IgG} with HEp-2 cells. **(B)** White light micrograph after incubating MB_{MMP-1} with HEp-2 cells. **(C)** White light micrograph after incubating pre-blocked with free anti- matrix metalloproteinase-1 (MMP-1) antibody. **(D)** Quantitative analysis of the number of MB_{MMP-1} and control group MB_{IgG} that adhered onto HEp-2 from five random view fields (**$P < 0.01$, $n = 5$). Scale bar = 10 μm.

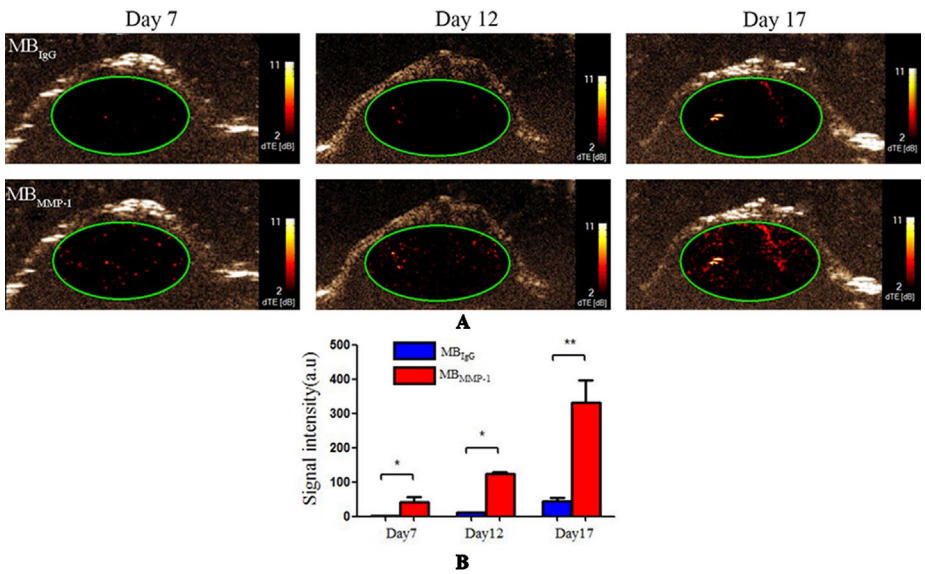

FIGURE 5 | Ultrasound molecular imaging (USMI) *in vivo.* **(A)** Color-coded differential targeted enhancement (dTE) signal sonograms separately at Day 7, Day 12, and Day 17. **(B)** Quantitative analysis of dTE for the MB_{MMP-1} and control group MB_{IgG} (*$P < 0.05$, **$P < 0.01$).

DISCUSSION AND CONCLUSION

Previous research had developed and tested arginine-glycine-aspartate (RGD)-MBs using αvβ3 integrin for a biomarker of the neovasculature in HEp-2 mouse tumor model (Hu et al., 2016). It had been proven that αvβ3 integrin-targeted RGD-MBs could effectively assess the expression of neovasculature and enhance the contrast imaging signal. However, the specificity of αvβ3-targeted MBs for LSCC detection was still not high enough because of its universality of expression in various types of malignant tumors (Sarmishtha et al., 2003; Brown et al., 2004; Hall and Jeffrey, 2004). Despite the growing number of published studies on USMI, a main obstacle for a clinical early diagnosis still exists.

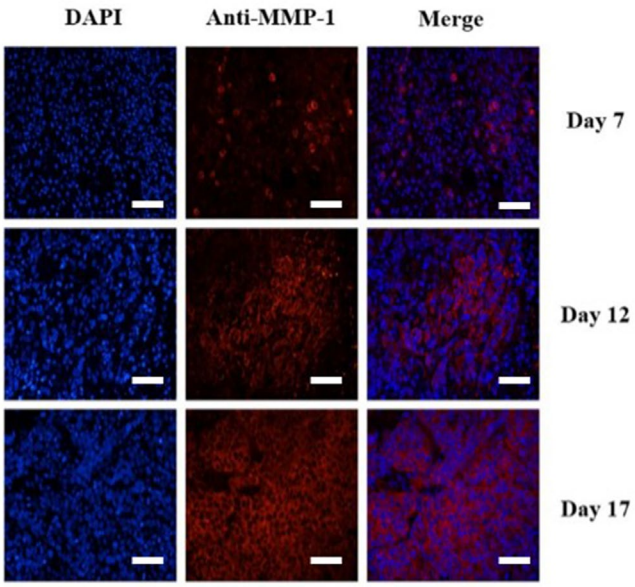

FIGURE 6 | Immunofluorescence staining of HEp-2 tumors for MMP-1 receptor. Immunofluorescence images of cell nucleus blue (first column), mouse MMP-1 red (second column), and merged (third column) MMP-1 and cell nucleus-stained image (the overlap of blue and red fluorescence confirms the co-localization of MMP-1) proved the expression of MMP-1 on plasma membrane in HEp-2 cells. MMP-1 was visualized with Cy3 dye (red). Cell nuclei were stained with DAPI (St. Louis, MO, USA) (blue). Scale bar = 200 μm.

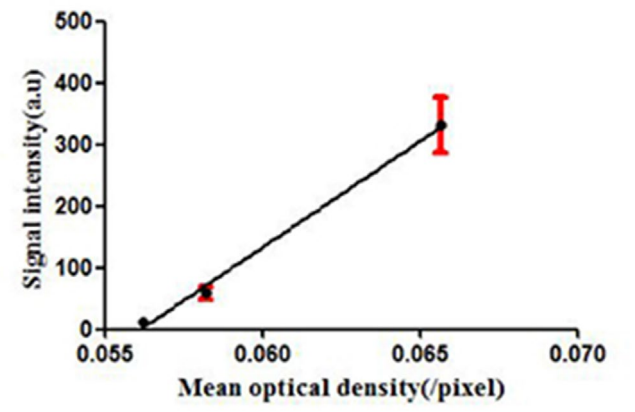

FIGURE 7 | dTE signal intensity of USMI and mean optical intensity (/pixel) images of tumor immunofluorescence staining separately at Day 7, Day 12, and Day 17.

In 1999, Maniotis and colleagues found the existence of VM in human melanoma cells (Maniotis et al., 1999). Subsequently, more and more studies had confirmed that VM is the new generation of tumor microcirculation without the participation of endothelial cells (Maniotis et al., 1999; Wang et al., 2010). And in tumor environment, it also was of importance to LSCC aggression and facilitates distant metastasis (Maniotis et al., 1999; Quail and Joyce, 2013). On the basis of these events, we assume that the lipid-shelled MBs loaded with mouse anti-MMP-1 monoclonal antibodies could tightly gather around VM to evaluate the expression of MMP-1 in LSCC.

In our current study, a novel MB_{MMP-1} USMI agent with C_3F_8-filled lipid-shelled MBs were prepared to dynamically evaluate the expression of MMP-1 in LSCC separately at Day 7, Day 12, and Day 17. First, we found that the MB_{MMP-1} had the ideal particle size range and that 1×10^8 MBs/mL concentration enhanced the US imaging signal *in vitro*. Then, we further confirmed the specific binding ability of MB_{MMP-1} to HEp-2. It revealed that MB_{MMP-1} not only exhibited significantly greater adhesion to HEp-2 than did control MB_{IgG} but also significantly provided a prospecting result for the next animal experiment. *In vivo*, we clearly found that the signal intensity of dTE of MB_{MMP-1} group had significantly higher retention than did control MB_{IgG} between each group. In addition, it is also noticeable that the signal intensity of dTE showed an upward trend with the time increasing of tumor. This result could be because a much more universal VM was newborn in the later period of LSCC than in the early period (Wang et al., 2010). A further study also confirmed that more and more newborn VM were increasing the participates in cancer progression and metastasis to supply tumor with sufficient nutrition (Hong and Hui, 2018). As expected, these *in vivo* dynamical evaluation results are further confirmed by immunofluorescence. From **Figure 6**, the red-stained MMP-1 receptors were much more expressed with the growth of tumors. This immunofluorescence analysis was well correlated with the results from signal intensity of dTE by USMI *in vivo* (**Figure 7**).

The following limitations of the study need to be solved. First, the size of MBs we chose is of microsize level, which can only indirectly draw support from no endothelial cells' VM by USMI. Second, although there was a strong significance in evaluating the expression of MMP-1 in LSCC, contrast agents adhering to more than one molecular biomarker may be advantageous over single-targeted contrast agents (Du et al., 2018) by increasing the number of MBs attached at sites of tumor neovascular and tumor tissue.

In conclusion, a novel MB_{MMP-1} US contrast agent will lay the foundation for the application of target biomarker of LSCC for USMI and will be a promising method to improve the early diagnosis.

ETHICS STATEMENT

All animal studies were approved by the Institute's Animal Care and Use Committee of Shenzhen Second People's Hospital, Guangzhou University School of Medicine, China.

AUTHOR CONTRIBUTIONS

QH and ZL proposed the project. YZ and ZS conducted the study, XJ, HZ, and XW analyzed the data. YZ wrote the manuscript. QH revised the manuscript. All authors reached an agreement with the final version of the manuscript.

FUNDING

The present study received financial support from The National Natural Science Foundation of China (81660292) and Shenzhen Science and Technology Project (project numbers JCYJ20170817171836611 and JCYJ20170306092258717). The National Natural Science Foundation of China (81260223 and 81301300) and GuangXi medical high-level backbone personnel training "139" project also supported this study.

REFERENCES

Abou-Elkacem, L., Wilson, K. E., Johnson, S. M., Chowdhury, S. M., Bachawal, S., Hackel, B. J., et al. (2016). Ultrasound molecular imaging of the breast cancer neovasculature using engineered fibronectin scaffold ligands: a novel class of targeted contrast ultrasound agent. *Theranostics* 6 (11), 1740–1752. doi: 10.7150/thno.15169

Balkwill, F. R., Capasso, M., and Hagemann, T. (2012). The tumor microenvironment at a glance. *J. Cell Sci.* 125 (23), 5591–5596. doi: 10.1242/jcs.116392

Brown, C. K., Khodarev, N. N., Yu, J., Moo-Young, T., Labay, E., Darga, T. E., et al. (2004). Libationary cells block radiation-induced programmed cell death of endothelial cells. *FEBS Lett.* 565 (1), 167–170. doi: 10.1016/j.febslet.2004.03.099

Castelijns, J. A., and Mw, V. D. B. (1993). Magnetic resonance imaging evaluation of extracranial head and neck tumors. *Magn. Reson. Q.* 9 (2), 113–128. doi: 10.1002/mrm.1910290620

Du, J., Li, X. Y., Hu, H., Xu, L., Yang, S. P., and Li, F. H. (2018). Preparation and imaging investigation of dual-targeted C_3F_8-filled PLGA nanobubbles as a novel ultrasound contrast agent for breast cancer. *Sci. Rep.* 8 (1), 3887. doi: 10.1038/s41598-018-21502-x

Fabian, K., Stanley, F., Patrick, K., Wiltrud, L., and Twan, L. (2012). Ultrasound microbubbles for molecular diagnosis, therapy, and theranostics. *J. Nucl. Med.* 53 (3), 345–348. doi: 10.2967/jnumed.111.099754

Feng, Y., Zhi-Yi, C., and Yan, L. (2013). Advancement of targeted ultrasound contrast agents and their applications in molecular imaging and targeted therapy. *Curr. Pharm. Des.* 19 (8), 1516–1527. doi: 10.2174/138161213804805469

Gino, M., Filippo, M., Stella, B., Emiliano, D. A., Luciano, G., Vincenza, G., et al. (2010). Neoangiogenesis in laryngeal carcinoma: angiogenin and CD105 expression is related to carcinoma recurrence rate and disease-free survival. *Histopathology* 57 (4), 535–543. doi: 10.1111/j.1365-2559.2010.03664.x

Gupta, B., Johnson, N. W., and Kumar, N. (2016). Global epidemiology of head and neck cancers: a continuing challenge. *Oncology* 91 (1), 13–23. doi: 10.1159/000446117

Hall, H., and Jeffrey, A. H. (2004). Matrix-bound sixth Ig-like domain of cell adhesion molecule L1 acts as an angiogenic factor by ligating αvβ33-integrin and activating VEGF-R2. *Microvasc. Res.* 68 (3), 169–178. doi: 10.1016/j.mvr.2004.07.001

Hong, G., and Hui, L. (2018). Overview of advances in vasculogenic mimicry—a potential target for tumor therapy. *Cancer Manag. Res.* 10, 2429–2437. doi: 10.2147/CMAR.S164675

Hu, Q., Wang, X. Y., Kang, L. K., Wei, H. M., Xu, C. M., Wang, T., et al. (2016). RGD-targeted ultrasound contrast agent for longitudinal assessment of Hep-2 tumor angiogenesis *in vivo*. *PLoS One* 11 (2), e0149075. doi: 10.1371/journal.pone.0149075

Kiessling, F., Huppert, J., and Palmowski, M. (2009). Functional and molecular ultrasound imaging: concepts and contrast agents. *Curr. Med. Chem.* 16 (5), 627–642. doi: 10.2174/092986709787458470

Kumar, C. C. (2003). Integrin alpha v beta 3 as a therapeutic target for blocking tumor-induced angiogenesis. *Curr. Drug Targets* 4 (2), 123–131. doi: 10.2174/1389450033346830

Maniotis, A. J., Folberg, R., Hess, A., Seftor, E. A., Gardner, L. M., Pe'Er, J., et al. (1999). Vascular channel formation by human melanoma cells *in vivo* and *in vitro*: vasculogenic mimicry. *Am. J. Pathol.* 155 (3), 739–752. doi: 10.1016/S0002-9440(10)65173-5

Norling, R., Buron, B. M., Therkildsen, M. H., Henriksen, B. M., Von, B. C., and Nielsen, M. B. (2014). Staging of cervical lymph nodes in oral squamous cell carcinoma: adding ultrasound in clinically lymph node negative patients may improve diagnostic work-up. *PLoS One* 9 (3), e90360. doi: 10.1371/journal.pone.0090360

Paolo, B., Locati, L. D., and Lisa, L. (2006). Biological agents in head and neck cancer. *Ann. Oncol.* 7 (11), 1643–1650. doi: 10.1586/14737140.7.11.1643

Pysz, M. A., Gambhir, S. S., and Willmann, J. K. (2010). Molecular imaging: current status and emerging strategies. *Clin. Radiol.* 65 (7), 500–516. doi: 10.1016/j.crad.2010.03.011

Quail, D. F., and Joyce, J. A. (2013). Microenvironmental regulation of tumor progression and metastasis. *Nat. Med.* 19 (11), 1423–1437. doi: 10.1038/nm.3394

Raffetto, J. D., and Khalil, R. A. (2008). Matrix metalloproteinases and their inhibitors in vascular remodeling and vascular disease. *Biochem. Pharmacol.* 75 (2), 346–359. doi: 10.1016/j.bcp.2007.07.004

Righi, P. D., Kopecky, K. K., Caldemeyer, K. S., Ball, V. A., Weisberger, E. C., and Radpour, S. (2015). Comparison of ultrasound-fine needle aspiration and computed tomography in patients undergoing elective neck dissection. *Head Neck* 19 (7), 604–610. doi: 10.1002/(SICI)1097-0347(199710)19:7<604::AID-HED7>3.3.CO;2-K

Sarmishtha, D., Juhua, C., Narizhneva, N. V., Warren, H., Jennifer, B., E Helene, S., et al. (2003). Molecular pathway for cancer metastasis to bone. *J. Biol. Chem.* 278 (40), 39044–39050. doi: 10.1074/jbc.M304494200

Stieger, S. M., Dayton, P. A., Borden, M. A., Caskey, C. F., Griffey, S. M., Wisner, E. R., et al. (2010). Imaging of angiogenesis using Cadence contrast pulse sequencing and targeted contrast agents. *Contrast Media Mol. Imaging* 3 (1), 9–18. doi: 10.1002/cmmi.224

Tsukifuji, R., Tagawa, K., Hatamochi, A., and Shinkai, H. (1999). Expression of matrix metalloproteinase-1, -2 and -3 in squamous cell carcinoma and actinic keratosis. *Br. J. Cancer* 80 (7), 1087–1091. doi: 10.1038/sj.bjc.6690468

Upile, T., Jerjes, W., Radhi, H., Al-Khawalde, M., Kafas, P., Nouraei, S., et al. (2011). Vascular mimicry in cultured head and neck tumour cell lines. *Head Neck Oncol.* 3 (1), 55. doi: 10.1186/1758-3284-3-55

Wang, W., Lin, P., Han, C., Cai, W., Zhao, X., and Sun, B. (2010). Vasculogenic mimicry contributes to lymph node metastasis of laryngeal squamous cell carcinoma. *J. Exp. Clin. Cancer Res.* 29 (1), 60. doi: 10.1186/1756-9966-29-60

Wood, A. K. W., and Sehgal, C. M. (2015). A review of low-intensity ultrasound for cancer therapy. *Ultrasound Med. Biol.* 41 (4), 905–928. doi: 10.1016/j.ultrasmedbio.2014.11.019

Yamazaki, Y., Saitoh, M., Notani, K. I., Tei, K., Totsuka, Y., Takinami, S. I., et al. (2008). Assessment of cervical lymph node metastases using FDG-PET in patients with head and neck cancer. *Ann. Nucl. Med.* 22 (3), 177–184. doi: 10.1007/s12149-007-0097-9

Yan, F., Li, X., Jin, Q., Jiang, C., Zhang, Z., Ling, T., et al. (2011). Therapeutic ultrasonic microbubbles carrying paclitaxel and LyP-1 peptide: preparation, characterization and application to ultrasound-assisted chemotherapy in breast cancer cells. *Ultrasound Med. Biol.* 37 (5), 768–779. doi: 10.1016/j.ultrasmedbio.2011.02.006

Conflict of Interest Statement: The authors declare that the research was conducted in the absence of any commercial or financial relationships that could be construed as a potential conflict of interest.

frontiers in Pharmacology

ORIGINAL RESEARCH
published: 21 June 2019
doi: 10.3389/fphar.2019.00672

Prospective Study About the Relationship Between CEUS of Carotid Intraplaque Neovascularization and Ischemic Stroke in TIA Patients

Zhenzhou Li[1†], Xianfeng Xu[2†], Lijie Ren[3], Yufeng Shao[3], Shuyu Luo[1], Shenghua Chen[1] and Xiaoyun Guan[1]*

[1] Department of Ultrasound, The Second People's Hospital of Shenzhen, The First Affiliated Hospital of Shenzhen University, Shenzhen, China, [2] Department of Obstetrics and Gynecology, The Second People's Hospital of Shenzhen, The First Affiliated Hospital of Shenzhen University, Shenzhen, China, [3] Department of Internal Neurology, The Second People's Hospital of Shenzhen, The First Affiliated Hospital of Shenzhen University, Shenzhen, China

OPEN ACCESS

Edited by:
Fei Yan,
Shenzhen Institutes of Advanced Technology (CAS), China

Reviewed by:
Kazem Zibara,
Lebanese University, Lebanon
Minhua Lu,
Shenzhen University, China

***Correspondence:**
Zhenzhou Li
lizhenzhou2004@126.com

†These authors have contributed equally to this work.

Specialty section:
This article was submitted to Translational Pharmacology, a section of the journal Frontiers in Pharmacology

Received: *31 January 2019*
Accepted: *23 May 2019*
Published: *21 June 2019*

Citation:
Li Z, Xu X, Ren L, Shao Y, Luo S, Chen S and Guan X (2019) Prospective Study About the Relationship Between CEUS of Carotid Intraplaque Neovascularization and Ischemic Stroke in TIA Patients. Front. Pharmacol. 10:672. doi: 10.3389/fphar.2019.00672

Objective: To evaluate the relationship between contrast-enhanced ultrasonography (CEUS) of carotid intraplaque neovascularization and ischemic stroke in transient ischemic attack (TIA) patients.

Methods: A total of 112 TIA patients were selected for the study. Routine carotid ultrasonic examination was performed for all the patients. CEUS was carried out for consecutive patients with plaque thicker than 2.5 mm in carotid bifurcation and follow-up for at least 24 months. The number of patients with incurrence of ischemic stroke or recurrence of TIA was obtained during the follow-up period. To detect the risk factors for incurrence of ischemic stroke or recurrence of TIA in 24 months, multivariate logistic regression analyses were performed for all the risk factors in all the selected patients.

Results: Ninety-one patients underwent CEUS and were followed up at least 24 months. There were statistical differences between recurrent and non-recurrent groups about hypertension, diabetes, hyperlipemia, smoking history, family history of stroke, medication compliance, two-dimensional ultrasound, and CEUS ($P < 0.05$). The higher CEUS intensity in the carotid plaque was, the higher was the possibility of ischemic stroke or recurrent TIA. Multivariate logistic regression analysis showed that the CEUS characteristics of carotid plaque such as linear enhancement or diffuse enhancement were independent risk factors for ischemic stroke or recurrent TIA in TIA patients ($P < 0.05$).

Conclusion: For carotid plaques, CEUS could evaluate the infusion mode, which could reflect the neovascularization in plaques. CEUS could predict the incurrence of ischemic stroke or recurrence of TIA in TIA patients, which is useful information when making a clinical decision.

Keywords: contrast-enhanced ultrasonography, carotid plaque, neovascularization, transient ischemic attack, ischemic stroke

BACKGROUND

Transient ischemic attack (TIA) is a brief and reversible episode of neurological dysfunction disorders. It is an important risk factor for cerebral infarction. Studies (Wu et al., 2007; Uehara et al., 2017) showed that the incidence of cerebral infarction after TIA ranged from 8.0% to 10.5%. Carotid arteries are essential arteries that supply the brain. Plaques building up inside the arteries are one of the leading causes of TIA and cerebral infarctions (Parmar et al., 2010; Sun et al., 2018). Some features of carotid plaque were mostly associated with the instability of plaque, including intraplaque hemorrhage, lipid-rich necrotic core, and surface disruption, and the instability of plaque is believed to be the main reason for the occurrence of ischemic strokes. Assessing plaque stability is one of the major objectives in the etiological study of ischemic stroke (Ott et al., 2008). With conventional ultrasound, stability can be estimated from the size, morphology, and echogenicity of the plaques, and it has a relatively high specificity in predicting the risk of ischemic stroke (Reiter et al., 2008). It is found that intraplaque neovascularization contributes to the instability of plaques (van Hoof et al., 2017).

A high signal intensity on T1-weighted magnetic resonance imaging (MRI) is a definitive finding indicating the vulnerability of carotid plaques (Hosseini et al., 2013). The addition of MRI to the pathological findings can confirm the vulnerability of carotid-artery plaques (Yuan et al., 2001). Contrast-enhanced carotid ultrasound (CEUS) has been shown to correlate with the MRI and pathological findings of carotid plaque, which can be used to evaluate intraplaque vessels and the vasa vasorum (Shimada et al., 2018) and which correlates significantly with the frequency of cardiovascular risk factors and the development of cardiovascular disease (Staub et al., 2010).

Thus, there is a need to further understand whether perfusion of intraplaque neovascularization is an independent risk factor for ischemic stroke or recurrent TIA. The aim of this study was to evaluate the perfusion mode of the intraplaque neovascularization by CEUS for TIA patients and investigate the correlation between the perfusion mode of carotid plaques and the risk of ischemic stroke or recurrent TIA.

METHODS

Study Population

A total of 112 TIA patients with carotid plaques were prospectively recruited at the Stroke Unit, Shenzhen No. 2 People Hospital between January 2014 and February 2016. The inclusion criteria were as follows: 1) Patients had a past history of TIA. According to the guidelines of the American Stroke Association (ASA) in 2009, TIA was defined as a brief episode of neurological dysfunction resulting from focal cerebral or retinal ischemia, with clinical symptoms typically lasting less than 1 h, and without evidence of acute infarction on imaging. 2) Carotid plaques were determined by conventional ultrasound with plaque thickness ≥2.5 mm. 3) Age >45 years. The exclusion criteria were as follows: 1) Patients had a history of cerebral vascular diseases such as ischemic and hemorrhagic infarctions. 2) Patients were disoriented and confused, or they could not follow the doctor's commands. 3) Patients had severe infections, malignant tumors, cardiopulmonary dysfunction, hepatorenal failure, or respiratory failure. 4) Plaques were mainly hyperechoic or uniformly hyperechoic. 5) Patients refused to undergo CEUS examination. 6) Patients were lost to follow-up.

One hundred and twelve patients were enrolled in this study; 17 patients did not undergo CEUS and follow-up return visits, owing to their plaques being mainly hyperechoic or uniformly hyperechoic, which means that the majority of or the whole plaque is calcification, which is difficult for CEUS. Four patients were lost follow-up. Ninety-one patients underwent CEUS and were followed up at least 24 months, of whom 41 were men and 50 were women. Age ranged from 48 to 88 years (median age, 67.8 ± 10.3 years). Subjects included 49 patients with hypertension, 59 patients with diabetes mellitus, 37 patients with hyperlipidemia, 39 patients with a history of smoking, 30 patients with a family history of stroke, and 33 patients with poor medication adherence. During at least 24 months of follow-up, 13 patients suffered an ischemic stroke and 24 patients had a recurrent TIA. All of the patients gave their written informed consent. Approval for this study was obtained from the institutional ethics committee of Shenzhen No. 2 People's Hospital.

Imaging Protocol

Subjects were imaged using a Siemens Acuson S2000 ultrasound platform equipped with contrast pulse sequence (CPS) software. A 9L4 linear probe (7–14 MHz) was used for ultrasound examinations. Subjects were asked to lie supine with head rotated away from the side being examined. After the longitudinal and transverse scanning of the common carotid arteries was done, the size, location, and intraplaque echogenicity of the plaques were intensively recorded. Common carotid or carotid bifurcation plaques thicker than 2.5 mm were selected for CEUS examination. For subjects with multiple plaques, only the largest plaque was selected. With reference to the echogenicity of adjacent sternocleidomastoid muscles, carotid plaques were defined as relatively hyperechoic, isoechoic, or hypoechoic. Features of instability including an ulcerated or irregular surface contour, discontinuous intima echo, eccentric index >2, and intraplaque liquefaction were marked.

After obtaining a satisfying image of the selected plaques, CEUS was turned on. The examination mode was then switched to cadence-CPS and the imaging was performed with a mechanical index of 0.2. A bolus of 2.5 ml of Sonovue suspension was injected into the median cubital vein of the left arm. Once the contrast agent had been injected, and the Intravenous access was flushed with 5 ml of 0.9% sodium chloride. The recording of the image was started as the contrast was injected. The filling process of contrast agents within the vessel lumen and the plaques were illustrated. In order to evaluate the intraplaque contrast enhancement, the ultrasonologists only took into account the dynamic spot hyperechoic lesions within the plaques or the border of the plaques (Coli et al., 2008). Grading of the intraplaque contrast agent enhancement followed the classification of Lee (Li et al., 2013): Grade 0: no enhancement; Grade 1: adventitia of arterial wall enhancement, no intraplaque enhancement; Grade 2: intraplaque spot enhancement; Grade

3: linear enhancement that extends into the plaque; Grade 4: intraplaque diffuse enhancement (**Figure 1**). Grading of the enhancement was completed by two trained and experienced doctors. When there was difference in grading between the two doctors, they discussed and determine the final result together.

Follow-Up

After ultrasound examination, subjects obtained routine treatments to reduce risk factors for cardiovascular diseases such as hypertension, diabetes mellitus, and hyperlipidemia. A follow-up evaluation should be conducted every 3 months for at least 24 months. During the follow-up, patients were asked if they had an ischemic stroke or recurrent TIA, and if they took medication as prescribed. Medication adherence was measured by the proportion of days when medications were taken as prescribed over the follow-up. A threshold of 80% was used to classify patients as adherent or nonadherent (Cramer et al., 2008). If a patient in the study could follow the doctor's orders to take medication greater than or equal to 80% days in the study period (24 months), we think that the patient is adherent; otherwise, the patient will be classified as nonadherent. Ischemic stroke was defined as a persistent neurological deterioration that occurred after TIA was resolved, accompanied by neuroimaging evidence. TIA was defined as a new onset neurological functional deficit with symptoms resolved within 1 h (Fang et al., 2013). After follow-up, subjects who had ischemic stroke or recurrent TIA were regarded as the "recurrent" group and those who did not have ischemic stroke or recurrent TIA were regarded as the "non-recurrent" group.

Statistical Analysis

Statistical analysis was performed using SPSS Statistics 17.0 software. Frequency and percentages (%) were used for categorical variables, whereas mean ± SD were employed for continuous variables. Continuous variables were compared between two groups using the independent *t* test. Proportions were compared using the chi-square test. To determine the association between variables and ischemic stroke or recurrent TIA after TIA, a

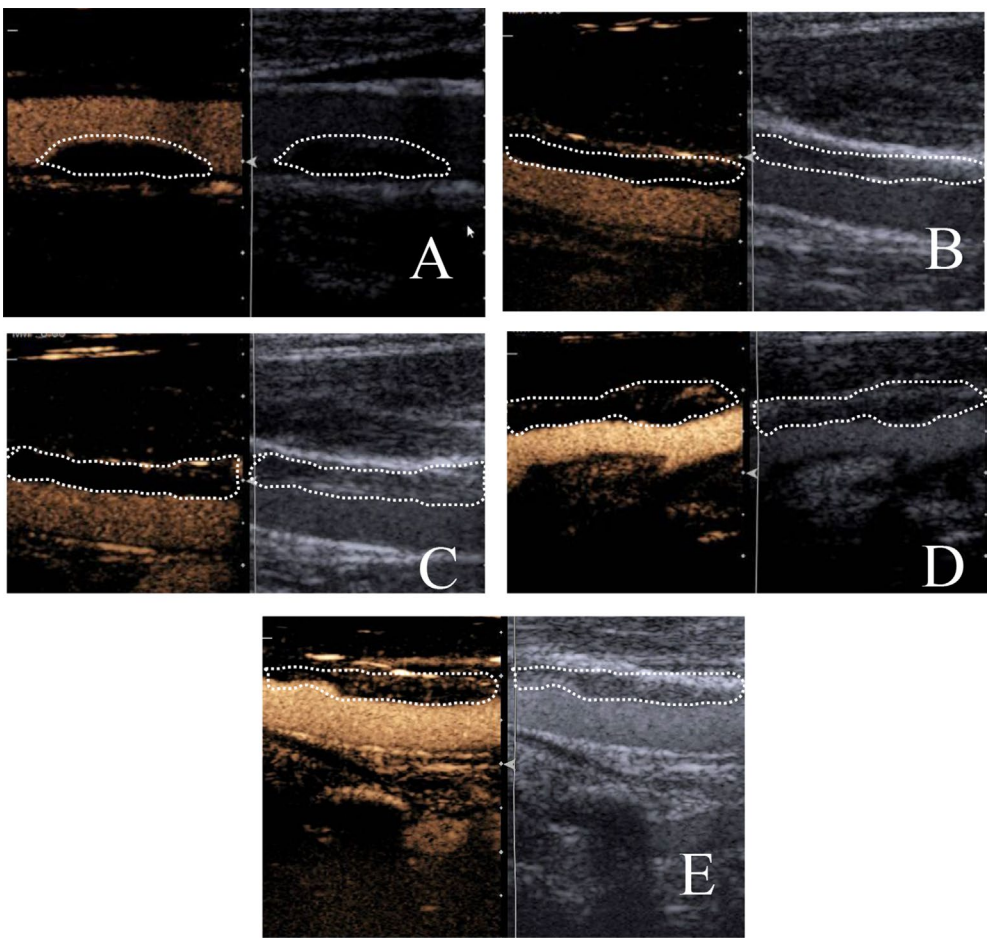

FIGURE 1 | Grading of the intraplaque contrast enhancement. **(A)** Grade 0: no enhancement; **(B)** Grade 1: adventitia of arterial wall enhancement, no intraplaque enhancement; **(C)** Grade 2: intraplaque spot enhancement; **(D)** Grade 3: linear enhancement that extends into the plaque; **(E)** Grade 4: intraplaque diffuse enhancement (left: plaques before contrast enhancement; right: plaques after contrast enhancement).

multivariate logistic regression analysis was performed. Receiver operation curve (ROC) was generated to examine the efficacy of the resulting model. The level of significance was set at $P < 0.05$.

Inter-Observer Variability

A total of 20 plaques with CEUS were selected, and the CEUS grade of the intraplaque contrast agent enhancement was judged by two blinded, experienced doctors. If the CEUS grade judgments of the two doctors were the same, we recorded it as uniformity; otherwise, we recorded it as nonuniformity. The inter-observer variability was expressed as percentile differences: the number of plaques recorded as nonuniformity/20 × 100%.

RESULTS

Of 91 patients who were included in this study, 37 were in the "recurrent" group, while 54 were in the "non-recurrent" group. There was no statistical difference in terms of age and sex ($P > 0.05$). **Table 1** shows the intergroup difference in history of hypertension ($P = 0.001$), diabetes ($P = 0.025$) or hyperlipidemia ($P = 0.001$), history of smoking ($P = 0.027$), the family history of cerebral stroke ($P = 0.029$), and medication adherence ($P = 0.001$).

Of 91 carotid plaques selected, 33 were isoechoic, 27 were hypoechoic, and 31 were mix-echoic. The maximal thickness of plaques was 3.2 ± 0.7 mm. Twenty-seven plaques were with signs of instability such as irregular or ulcerated surface contour, intraplaque liquefaction, and eccentric index >2. For contrast-enhanced plaques, 27 plaques were Grade 0, 10 were Grade 1, 23 were Grade 2, 20 were Grade 3, and 11 were Grade 4. **Table 2** illustrated the statistical difference between two groups in conventional ultrasonic features of instability and the grades of CEUS contrast enhancement ($P < 0.05$).

The data set consisted of one dichotomous dependent variable: prognosis coded 1 for the presence of ischemic stroke or the recurrence of TIA and 0 for no ischemic stroke or recurrent TIA. A multivariate logistic regression analysis was conducted. In the regression analysis, the presence of ischemic stroke and the recurrence of TIA were taken as dependent variables, and the eight independent variables whose intergroup differences were statistically significant (hypertension, diabetes mellitus, hyperlipidemia, smoking, family history of cerebral stroke, medication adherence, conventional ultrasonic features of instability, and grades of CEUS contrast enhancement) were taken as independent variables. **Table 3** shows the results from the multivariate regression analysis. Variables including family history of cerebral stroke, grade of CEUS in plaque, medication adherence, hypertension, conventional ultrasonic features of instability, and hyperlipidemia were independent risk factors of ischemic stroke and recurrent TIA. After adjusting for confounding effects, Grades 3–4 of CEUS contrast enhancement was found to be an independent risk factor to ischemic stroke or recurrent TIA ($P < 0.05$). These independent

TABLE 1 | Intergroup comparisons of patient characteristics.

Group	Age (years)	Sex (M/F, *n*)	Hypertension (Y/N, *n*)	Diabetes mellitus (Y/N, *n*)
Recurrent (*n* = 37)	70.1 ± 10.9	16/21	28/9	29/8
Non-recurrent (*n* = 54)	66.3 ± 9.6	25/29	21/33	30/24
t or χ^2	1.735	0.083	11.956	5.016
P	0.086	0.774	0.001	0.025
Group	**Hyperlipidemia (Y/N, *n*)**	**Smoking (Y/N, *n*)**	**FHx of cerebral stroke (Y/N, *n*)**	**Medication adherence (Y/N, *n*)**
Recurrent (*n* = 37)	23/14	21/16	17/20	16/21
Non-recurrent (*n* = 54)	14/40	18/36	13/41	42/12
t or χ^2	11.949	4.919	4.753	11.329
P	0.001	0.027	0.029	0.001

TABLE 2 | Intergroup comparison of conventional ultrasonic features of instability and grade of CEUS (number of cases).

Group	Mode of ultrasound (stable/unstable, *n*)	CEUS (Grades 0–2/Grades 3–4, *n*)	Mode of ultrasound + CEUS (stable/unstable, *n*)
Recurrent (*n* = 37)	20/17	18/19	13/24
Non-recurrent (*n* = 54)	44/10	42/12	34/20
t or χ^2	7.915	8.294	6.808
P	0.005	0.004	0.009

TABLE 3 | Multivariate logistic regression analysis for ischemic stroke and recurrent TIA.

Variables	*R*	SE	Wald	*P*	OR	95% CI	
						Lower	Upper
Family history of cerebral stroke	2.592	0.801	10.483	0.001	13.354	2.781	64.127
Grade of CEUS contrast enhancement	1.919	0.747	6.600	0.010	6.817	1.576	29.484
Medication adherence	1.864	0.654	8.126	0.004	6.448	1.790	23.224
Hypertension	1.678	0.622	7.266	0.007	5.353	1.581	18.131
Conventional ultrasonic features of instability	1.557	0.696	5.010	0.025	4.747	1.214	18.565
Hyperlipidemia	1.234	0.604	4.176	0.041	3.434	1.052	11.208

OR, odds ratio.

variables were further ranked according to the odds ratios, from highest to lowest: family history of cerebral stroke, grade of CEUS contrast enhancement, medication adherence, hypertension, conventional ultrasonic features of instability, and hyperlipidemia.

ROC was generated to examine the efficacy of the resulting model in predicting ischemic stroke or TIA recurrence (**Figure 2**). The area under the curve (AUC) was 0.888 (95% CI: 0.820–0.956, $P < 0.05$).

The inter-observer variability was 5% (1/20 × 100%). Thus, we can see that the uniformity between different doctors in judging the grade of plaque enhancement in CEUS is desirable.

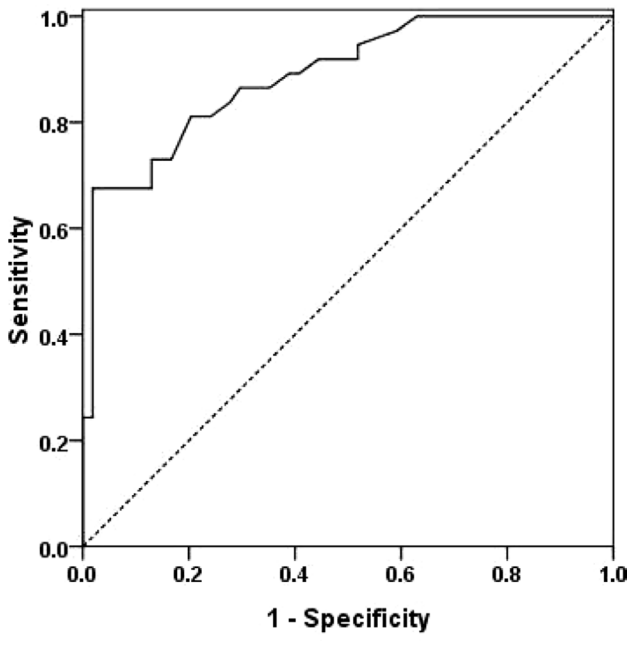

FIGURE 2 | Receiver operation curve (ROC) of the multivariate logistic regression analysis model.

DISCUSSION

High permeability of the neovessels plays an essential role in plaque growth. Furthermore, long-term presence of the neo-vessels can result in intraplaque hemorrhage and plaque progression, which increases the risk of ischemic stroke (Sun et al., 2016; Cheung et al., 2017).

TIA is considered to be an independent risk factor of ischemic stroke (Amarenco, 2018). Our study has demonstrated that with B-mode ultrasound, the proportion of unstable plaques detected was significantly higher in the recurrent group (17/37, 45.95%) compared to the non-recurrent group (10/54, 18.52%). This may suggest that the conventional ultrasonic features of instability were correlated with the occurrence of ischemic stroke. However, it is difficult to detect intraplaque neo-capillaries with conventional B-mode, color Doppler, or even power Doppler. Several studies (Huang et al., 2016; Amamoto et al., 2019) showed that CEUS had a high sensitivity in detecting neo-capillaries in carotid plaques. Based on a meta-analysis, the measurement of the degree of neovascularization was a promising tool in plaque evaluation (Huang et al., 2016). Unlike the contrast medium used in CT or angiography, the metabolic products of the contrast medium used in CEUS are exhaled from the lungs, such that the contrast medium is relatively safe. Based on the CEUS perfusion mode of neo-capillaries, the contrast enhancement of plaques was graded (Ott et al., 2008). Comparisons were made between post-endarterectomy carotid specimen and carotid arteries with different grades of contrast enhancement. Results showed a good correlation between the density of intraplaque microvessels and the grade of CEUS contrast enhancement. In addition, as for plaques with intraplaque hemorrhage, it has been proven that intraplaque liquefactive areas could be clearly shown and easily visible with CEUS, which may help in detecting unstable plaques (Varetto et al., 2015; Li et al., 2018).

The grading of intraplaque CEUS enhancement is based on the extent of ultrasonic contrast perfusion, which was strongly consistent with the density, course, and distribution of intraplaque capillaries. Results revealed that the proportion of Grade 3–4 contrast enhancement was apparently higher in

the recurrent group (19/37, 51.35%) than in the non-recurrent group (12/54, 22.22%). This may suggest that the extent of intraplaque neoangiogenesis was strongly correlated with the risk of ischemic stroke. Moreover, multivariate logistic regression analysis has revealed that the grade of CEUS contrast enhancement was an independent risk factor for ischemic stroke or recurrent TIA. Hence, plaques with Grade 3–4 contrast enhancement would be more unstable than those with Grade 0–2 enhancement. Therefore, grade of CEUS contrast enhancement could become one of the predictive indices of ischemic stroke. For patients with a CEUS enhancement of Grade 3–4, immediate and effective treatment should be given for the secondary prevention. Besides, in this study, risk factors including diabetes mellitus and smoking history were not included in the logistic regression model. This may be due to the fact that our study was only restricted to individuals with TIA and the sample size was relatively small.

There are a number of limitations associated with our study. Firstly, as for patients with multiple plaques, only the largest of the plaques was selected in consideration of the image quality and dosage limitation of contrast media. This may introduce some potential sources of bias into the study. Secondly, the assessment of carotid plaques in this study was based on a semi-quantitative grading system rather than accurate quantitative measurement. The follow-up period was only 24 months; hence, a long-term follow-up is required in the following studies. Thirdly, this study was only restricted to individuals with TIA, and the sample size was relatively small; therefore, large, prospective multicenter studies are needed.

To summarize, our study provided evidence that CEUS could be a useful tool in detecting unstable plaques that were hard to assess by B-mode ultrasound. Perfusion mode of carotid plaques was an independent risk factor of ischemic stroke and recurrent TIA, which could be useful in guiding the prevention and treatment of the diseases in clinics.

ETHICS STATEMENT

This study was carried out in accordance with the recommendations of institutional ethics committee of Shenzhen No.2 People's Hospital, with written informed consent from all subjects. All subjects gave written informed consent in accordance with the Declaration of Helsinki. The protocol was approved by the institutional ethics committee of Shenzhen No.2 People's Hospital.

AUTHOR CONTRIBUTIONS

ZL and XX contributed equally to this work. Other authors contributed equally to this work.

FUNDING

This study received financial support from Shenzhen Science and Technology Project (project number JCYJ20170817171836611, JCYJ20170306092258717, and KJYY20180703165202011).

REFERENCES

Amamoto, T., Sakata, N., Ogata, T., Shimada, H., Inoue, T. (2019). Intra-plaque vessels on contrast-enhanced ultrasound sonography predict carotid plaque histology. *Cerebrovasc. Dis.* 46 (5–6), 265–269. doi: 10.1159/000495299

Amarenco, P. (2018). Five-year risk of stroke after TIA or minor ischemic stroke. *N. Engl. J. Med.* 79 (16), 1580–1581. doi: 10.1056/NEJMoa1802712

Cheung, W. K., Shah, B.N., Stanziola, A., Gujral, D. M., Chahal, N. S., Cosgrove, D. O. (2017). Differential intensity projection for visualisation and quantification of plaque neovascularisation in contrast-enhanced ultrasound images of carotid arteries. *Ultrasound Med. Biol.* 43 (4), 831–837. doi: 10.1016/j.ultrasmedbio.2016.11.018

Coli, S., Magnoni, M., Sangiorgi, G., Marrocco-Trischitta, M. M., Melisurgo, G., Mauriello, A. (2008). Contrast-enhanced ultrasound imaging of intraplaque neovascularization in carotid arteries. *J. Am. Coll. Cardiol.* 52, 223–230. doi: 10.1016/j.jacc.2008.02.082

Cramer, J. A., Roy, A., Burrell, A., Fairchild, C. J., Fuldeore, M. J., Ollendorf, D. A. (2008). Medication compliance and persistence: terminology and definitions. *Value Health* 11 (1), 44–47. doi: 10.1111/j.1524-4733.2007.00213.x

Fang, M., Li, Q., Zhong, S., Liu, X. (2013). ABCD2 scores predicts risk of early recurrent events after transient ischemic attack: a hospital-based case series study. *J. Tongji Univ. (Med. Sci.)* 34, 72–77. doi: 10.3969/j.issn1008-0392.2013.02.018

Hosseini, A. A., Kandiyil, N., Macsweeney, S. T., Altaf, N., Auer, D. P. (2013). Carotid plaque hemorrhage on magnetic resonance imaging strongly predicts recurrent ischemia and stroke. *Ann. Neurol.* 73, 774–784. doi: 10.1002/ana.23876

Huang, R., Abdelmoneim, S. S., Ball, C. A., Nhola, L. F., Farrell, A. M., Feinstein, S. (2016). Detection of carotid atherosclerotic plaque neovascularization using contrast enhanced ultrasound: a systematic review and meta-analysis of diagnostic accuracy studies. *J. Am. Soc. Echocardiogr.* 29 (6), 491–502. doi: 10.1016/j.echo.2016.02.012

Li, C., He, W., Guo, D., Jin, X., Fan, P., Wang, W. (2013). Correlation of severity of carotid artery stenosis and intraplaque neovascularization detected by contrast-enhanced ultrasound. *Chin. J. Ultrasound Med.* 29 (2), 106–109. doi: 10.3969/j.issn.1002-0101.2013.02.005

Li, D., Zhao, H., Chen, X., Chen, S., Qiao, H., He, L. (2018). Identification of intraplaque haemorrhage in carotid artery by simultaneous non-contrast angiography and intraplaque haemorrhage (SNAP) imaging: a magnetic resonance vessel wall imaging study. *Eur. Radiol.* 28 (4), 1681–1686. doi: 10.1007/s00330-017-5096-1

Ott, C., Heller, G., Odermatt, M., Furrer, M. (2008). Intraoperative duplex ultrasonographyin carotid endarectomy: the impact on indication for immediate revision and intermediate-term outcome. *Vasa* 37 (2), 151–156. doi: 10.1024/0301-1526.37.2.151

Parmar, J. P., Rogers, W. J., Mugler, J. P., Baskurt, E., Altes, T. A., Nandalur, K. R. (2010). Magnetic resonance imaging of carotid atherosclerotic plaque in clinically suspected acute transient ischemic attack and acute ischemic stroke. *Circulation* 122 (20), 2031–2038. doi: 10.1161/CIRCULATIONAHA.109.866053

Reiter, M., Effenberger, I., Sabeti, S., Mlekusch, W., Schlager, O., Dick P. (2008). Increasing carotid plaque echolucency is predictive of cardiovascular events in high-risk patients. *Radiology* 248 (3), 1050–1055. doi: 10.1148/radiol.2483071817

Shimada, H., Ogata, T., Takano, K., Abe, H., Higashi, T., Yamashita, T., et al. (2018). Evaluation of the time-dependent changes and the vulnerability of carotid plaques using contrast-enhanced carotid ultrasonography. *J. Stroke Cerebrovasc. Dis.* 2 (27), 321–325

Staub, D., Patel, M. B., Tibrewala, A., Ludden, D., Johnson, M., Espinosa, P. (2010). Vasa vasorum and plaque neovascularization on contrast-enhanced carotid ultrasound imaging correlates with cardiovascular disease and past cardiovascular events. *Stroke* 41, 41–47. doi: 10.1161/STROKEAHA.109.560342

Sun, X. F., Wang, J., Wu, X. L., Xu, H. Y., Xing, Y. Q., Yang, F. (2016). Evaluation of the stability of carotid atherosclerotic plaque with contrast-enhanced ultrasound. *J. Med. Ultrason. (2001)* 43 (1), 71–76. doi: 10.1007/s10396-015-0647-z

Sun, R., Wang, L., Guan, C., Cao, W., Tian, B. (2018). Carotid atherosclerotic plaque features in patients with acute ischemic stroke. *World Neurosurg.* 112, e223–e228. doi: 10.1016/j.wneu.2018.01.026

Uehara, T., Minematsu, K., Ohara, T., Kimura, K., Okada, Y., Hasegawa, Y. (2017). Incidence, predictors, and etiology of subsequent ischemic stroke within one year after transient ischemic attack. *Int. J. Stroke* 12 (1), 84–89. doi: 10.1177/1747493016669884

van Hoof, R. H. M., Schreuder, F. H. B. M., Nelemans, P., Truijman, M. T. B., van Orshoven, N. P., Schreuder, T. H. (2017). Ischemic stroke patients demonstrate increased carotid plaque microvasculature compared to (ocular) transient ischemic attack patients. *Cerebrovasc. Dis.* 44 (5–6), 297–303. doi: 10.1159/000481146

Varetto, G., Gibello, L., Castagno, C., Quaglino, S., Ripepi, M., Benintende, E. (2015). Use of contrast-enhanced ultrasound in carotid atherosclerotic disease: limits and perspectives. *Biomed. Res. Int*. 2015, 1–7. doi: 10.1155/2015/293163

Wu, C. M., McLaughlin, K., Lorenzetti, D. L., Hill, M. D., Manns, B. J., Ghali, W. A. (2007). Early risk of stroke after transient ischemic attack: a systematic review and meta-analysis. *Arch. Intern. Med.* 167, 2417–2422. doi: 10.1001/archinte.167.22.2417

Yuan, C., Mitsumori, L. M., Ferguson, M. S., Polissar, N. L., Echelard, D., Ortiz, G. (2001). In vivo accuracy of multispectral magnetic resonance imaging for identifying lipid-rich necrotic cores and intraplaque hemorrhage in advanced human carotid plaques. *Circulation* 104, 2051–2056. doi: 10.1161/hc4201.097839

Conflict of Interest Statement: The authors declare that the research was conducted in the absence of any commercial or financial relationships that could be construed as a potential conflict of interest.

The reviewer ML declared a shared affiliation, with no collaboration, with all of the authors to the handling editor at time of review.

frontiers in Pharmacology

ORIGINAL RESEARCH
published: 26 June 2019
doi: 10.3389/fphar.2019.00716

Effect of Ultrasound Combined With Microbubble Therapy on Interstitial Fluid Pressure and VX2 Tumor Structure in Rabbit

Qianyun Zhang[1,2,3†], Hai Jin[1,2†], Liping Chen[1,2], Qiaoli Chen[1,2], Yan He[1,2], Yuwen Yang[1,2], Suihong Ma[1,2], Shuyi Xiao[1,2], Fen Xi[1,2], Qiong Luo[1,2] and Jianhua Liu[1,2]*

[1] Department of Medical Ultrasound, Guangzhou First People's Hospital, Guangzhou, China, [2] School of Medicine, South China University of Technology, Guangzhou, China, [3] Department of Medical Ultrasound, Guangzhou Women and Children's Medical Center, Guangzhou, China

OPEN ACCESS

Edited by:
Fei Yan,
Shenzhen Institutes of Advanced Technology (CAS), China

Reviewed by:
Hui-Xiong Xu,
Tongji University, China
Li Yingjia,
Southern Medical University, China

***Correspondence:**
Jianhua Liu
liujianhua266@163.com

† These authors have contributed equally to this work.

Specialty section:
This article was submitted to Translational Pharmacology, a section of the journal Frontiers in Pharmacology

Received: 30 January 2019
Accepted: 05 June 2019
Published: 26 June 2019

Citation:
Zhang Q, Jin H, Chen L, Chen Q, He Y, Yang Y, Ma S, Xiao S, Xi F, Luo Q and Liu J (2019) Effect of Ultrasound Combined With Microbubble Therapy on Interstitial Fluid Pressure and VX2 Tumor Structure in Rabbit. Front. Pharmacol. 10:716. doi: 10.3389/fphar.2019.00716

Interstitial fluid pressure (IFP) in tumor tissue is significantly higher than that in normal tissue, which reduces the effectiveness of therapeutic drugs. There are several methods to decrease the IFP, such as normalizing blood vessel, decreasing hyaluronic acid and collagen fiber content in the extracellular matrix (ECM), and recovering lymphatic function. Reducing tumor IFP might be developed as a novel approach in cancer therapy. In this study, we aimed to elucidate the relationship between ultrasound combined with microbubble therapy and IFP, and the associated mechanism. VX2 tumor in rabbit was treated with ultrasound combined with microbubbles at different intensities. The IFP was measured using the wick-in-needle (WIN) method. The collagen and reticular fibers were stained by Masson and Gordon–Sweets, respectively. The results showed that low-frequency non-focus ultrasound combined with microbubbles therapy influences the IFP in tumor tissues; low-frequency non-focus ultrasound with low pressure increased the IFP, whereas middle–high pressure decreased the IFP. The results showed that the structure and content of collagen and reticular fibers in tumor tissue were rarely influenced by the treatment. Our study provides a novel approach of reduced IFP antitumor therapy.

Keywords: blood vessel, collagen fiber, extracellular matrix, interstitial fluid pressure, reticular fiber

INTRODUCTION

Increasing incidence of cancer and associated mortality have forced innovations in tumor therapy. It has been reported that higher interstitial fluid pressure (IFP) in solid tumors leads to lower penetration efficiency of chemotherapy drugs from the capillary to tumor tissues, consequently limiting their antitumor effect (Heldin et al., 2004).

IFP is determined by hydrostatic pressure and oncotic pressure in the capillary and interstitial space, and it is also influenced by hydraulic conductivity and plasma protein reflectance. The pressure in normal tissues is slightly negative, ensuring easy material penetration from the blood vessels to the interstitial space. On the contrary, the pressure in many solid tumors is positive.

Abbreviations: BC, blank control; CEUS, contrast-enhanced ultrasound; MB, microbubble; MVD, micro vessel density; PI, perfusion index; US-MB, ultrasound combined with microbubble; VDA, vascular disrupting agent.

The tumor IFP is increased by several factors, such as abnormal blood vessels (Chen and Shi, 2002), dense extracellular matrix (ECM), abnormal fibrosis (Dufort et al., 2016), and abnormal lymphatic vessel (DiResta et al., 2000; Padera et al., 2004; Alitalo et al., 2006; Hagendoorn et al., 2006). Reducing tumor IFP might be developed as a novel approach in antitumor therapy. There are several methods to decrease the IFP, such as normalizing blood vessel (Lee et al., 2000; Tong et al., 2004; Willett et al., 2004; Goel et al., 2011), decreasing hyaluronic acid and collagen fiber content in the ECM (Brekken and de Lange Davies, 1998; Brekken et al., 2000a; Brekken et al., 2000b), and recovering lymphatic function (Starling; Young et al., 1950; Jain, 1987a; Jain, 1987b).

The ECM in animals, including the interstitial matrix, basement membrane, polysaccharide gel, and fibrin, consists of the interstitial matrix that fills the intercellular space to buffer various external stresses. Tumor ECM, including mesenchymal cells (fibroblasts, astrocytes, and inflammatory cells), collagen fibrils, glycosaminoglycans, and proteoglycans, which act as scaffolds to support growing tumor cells, separate tumor cells from blood vessels to increase the IFP and to compress tumor blood vessels and lymphatic vessels, resulting in lower blood flow and even collapse blood vessels (Jain, 1987a; Jain, 1987b; Less et al., 1992; Nathanson and Nelson, 1994). However, systematic studies on the ECM are limited owing to the complexity of its components.

Applying microbubbles in ultrasonic therapy is a hot spot. High-intensity ultrasound combined with microbubble (US-MB) therapy blocked blood flow to transplanted tumor in mice for 24 h and low-intensity US-MB therapy increased tumor perfusion temporarily (Matsumura and Maeda, 1986). However, there is no systematic research to clarify the relationship between non-focused US-MB therapy and tumor IFP. The aim of this study was to identify a novel approach in antitumor therapy by clarifying the relationship between US-MB therapy and tumor IFP, and the associated mechanism. Therefore, we established a rabbit model with VX2 tumor. The tumors were treated with different intensities of US-MB.

MATERIALS AND METHODS

Animal Model

Healthy New Zealand white rabbits weighing approximately 2.5 kg were obtained from an experiment center in Guangdong, China. Before inoculation, all rabbits were reared for at least 7 days at 24°C–26°C under 45–55% humidity. This study was carried out in accordance with the principles of the Basel Declaration and recommendations of *Guide for the Care and Use of Laboratory Animals* published by the United States National Institutes of Health (NIH publication no. 85-23, revised 1996). The protocol was approved by the Laboratory Animal Committee (LAC) of South China University of Technology, Guangdong, China.

VX2 tumor tissue specimens were obtained from the cell bank of Sun Yat-sen University (Guangzhou, China). The tumor tissues were chopped into small pieces (1 mm^3) and placed in a culture dish with physiological saline solution, and then injected subcutaneously to the superficial muscles of the left hind limb of rabbits. The experiment was performed for almost 10 days after tumor implantation, until the tumor reached a size of approximately L (length) 10 ± 0.7 mm and W (width) 5 ± 0.8 mm.

Experimental Procedure

All 48 tumor-bearing rabbits were divided into six groups randomly (n = 8 per group). These six groups included the low-intensity ultrasound combined with microbubble (1MPa-USMB), medium-intensity ultrasound combined with microbubble (3MPa-USMB), high-intensity ultrasound combined with microbubble (5MPa-USMB), medium-intensity ultrasound without microbubble (US), microbubble (MB), and blank control (BC) groups. Tumor tissues were examined by contrast-enhanced ultrasound (CEUS) before and after treatment (GE E9, Probe: ML6-15), and the peak intensity (PI) was recorded. The tumor IFP and surrounding tissue IFP were measured using the wick-in-needle (WIN) method. The tumor surrounding tissue IFP was measured before treatment, and the tumor IFP was measured before, during, and after the treatment (**Figure 1A**). After CEUS and measurement of IFP in tumor tissues and surrounding tissues, each group was treated according to the corresponding conditions. In the USMB group, the tumor-bearing rabbits were intravenously injected with 0.1 ml/kg of diluted lipid microbubbles (ZHIFUXIAN, Department of Ultrasound, Xinqiao Hospital Affiliated to Third Military Medical University, Chongqing, China), and the tumor was disposed by low-frequency, non-focused ultrasound of different intensities (acoustic pressure of 1, 3, and 5 MPa) for 5 min, pulse repetition frequency of 10 Hz, and duty ratio of 0.2%. The pulse emission/gap time was 9 s/3 s (**Figure 1B**). In the US group, the rabbits were intravenously injected with the same volume of sterile saline solution, and the tumor was disposed by 3 MPa ultrasound for 5 min. In the MB group, the rabbits were intravenously injected with the same volume of diluted lipid microbubbles, and the tumor was disposed by sham ultrasound exposure for 5 min. In the BC group, the rabbits were intravenously injected with the same volume of sterile saline solution, and the tumor was disposed by sham ultrasound exposure for 5 min. After measuring the tumor IFP, the rabbits were sacrificed. The tumor tissue was removed and fixed with 4% paraformaldehyde solution for 24 h, and then hematoxylin and eosin (H&E) staining, Masson staining, and Gordon–Sweets reticular fiber staining were performed.

Ultrasound Treatment

Ultrasound treatment was performed using a pulsed therapeutic ultrasound device equipped with a KHT-017 transducer (DCT-700; Shenzhen Well.D Medical Electronic, Shenzhen, China). To maintain a gap of 2 cm between the transducer and the skin, the transducer was fixed to a steel stand with a scale. Subsequently, ultrasound coupling gel was applied to the skin. Treatment was implemented for approximately 5 min. The US-MB treatment was applied to the tumor after intravenous injection of microbubbles at a dose of 0.1 mL/kg. The transducer was operated at a frequency of 1 MHz; an acoustic pressure of 1, 3, and 5 MPa; a

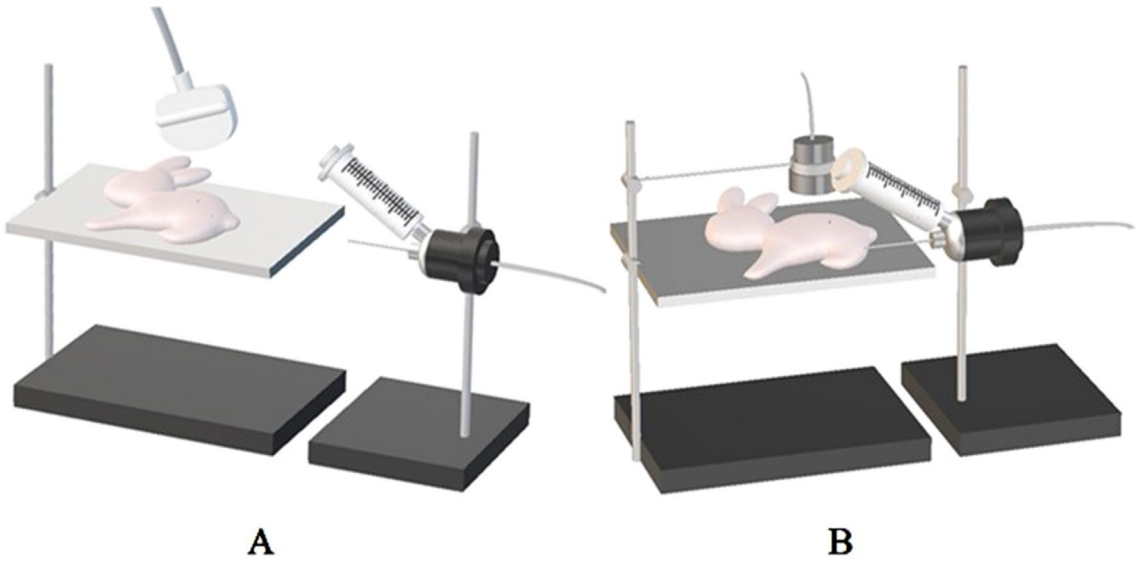

FIGURE 1 | (A) The puncture needle is connected to the bio-signal acquisition and analysis system and placed horizontally at the same level as the tumor. The needle was inserted horizontally into the center of the tumor under ultrasound guidance, and the stable reading as the corresponding interstitial fluid pressure (IFP) value. **(B)** The therapeutic probe of ultrasonic cavitation therapeutic instrument is fixed on the iron frame, and the therapeutic probe is placed on the corresponding body surface of the tumor with sufficient coupling, and the tumor is irradiated with energy of 1 MPa, 3 MPa, and 5 MPa according to the set treatment parameters in each group, respectively.

pulse repetition frequency of 10 Hz; and a duty cycle of 0.2%. The treatment was performed under an intermittent mode of 9 s on and 3 s off for 5 min.

Tumor IFP

The IFP of the tumor center was measured by the WIN method using a 25-G needle (**Figure 2**).

H&E Staining

To assess the therapeutic effect of treatments on tumor in each group, the tumor tissue was fixed in formalin, embedded in paraffin, sectioned serially, and stained using H&E. Ten fields of vision were selected randomly and observed using an optical microscope (Axio Scope A1; Zeiss, Oberkochen, Germany). The tumor cells, tumor micro-vessels, and the changes around them were observed by high-power optical microscopy.

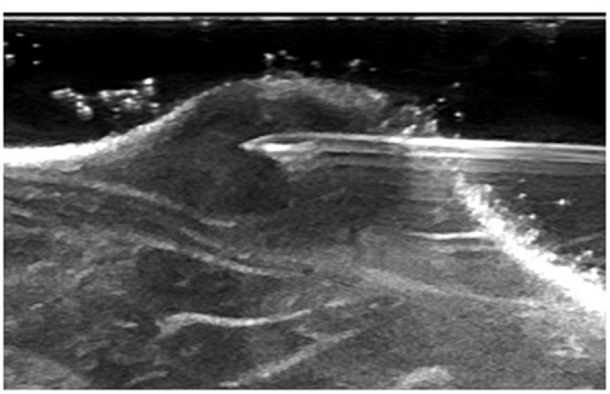

FIGURE 2 | The needle was inserted horizontally into the center of the tumor under ultrasound guidance.

Masson Staining and Gordon–Sweets Reticular Fiber Staining

To assess the effect of treatments on collagen and reticular fibers in each group, the tumor sections were subjected to Masson staining and Gordon–Sweets reticular fiber staining. Ten fields of vision were selected randomly and observed using an optical microscope (Axio Scope A1). Image-pro Plus 6.0 software was used to calculate the content of collagen and reticular fibers in each pathological section.

Statistical Analyses

Multiple comparisons were performed using the analysis of variance. Paired-sample *t* test was used to compare the differences before and after treatment in each group. The data are expressed as mean ± SD, and the results with P value < 0.05 were considered statistically significant. Statistical analyses were performed using SAS 9.4 (SAS Institute Inc. Cary, NC).

RESULTS

Contrast-Enhanced Ultrasound

Contrast-enhanced ultrasound (CEUS) was performed before and immediately after treatment in all the groups. Microbubbles filled into the tumor rapidly and evenly, and no filling defect was observed in all the groups before treatment. After treatment,

enhancement of the tumor was marginally stronger than that before treatment in the 1MPa-USMB group, but in the 3MPa-USMB group, the CEUS showed filling defect in the center of the tumor with a ring-shaped enhancement around the tumor. Furthermore, the filling defect was larger in the 5MPa-USMB group than in the 3MPa-USMB group. Blood perfusion after treatment in the US, MB, and BC groups was similar, and the microbubbles filled the tumor quickly and completely (**Figure 3**).

The PI, which indicates blood perfusion in tumor tissues, was recorded and analyzed. The pretreatment PI was not significantly different among the groups. The post-treatment PI was not significantly different in the US, MB, BC, and 1MPa-USMB groups. The PI in the 3MPa-USMB and 5MPa-USMB groups decreased by 66.3% and 86.7% ($p < 0.05$), respectively, after treatment compared with that before treatment. The results are shown in **Figure 4**.

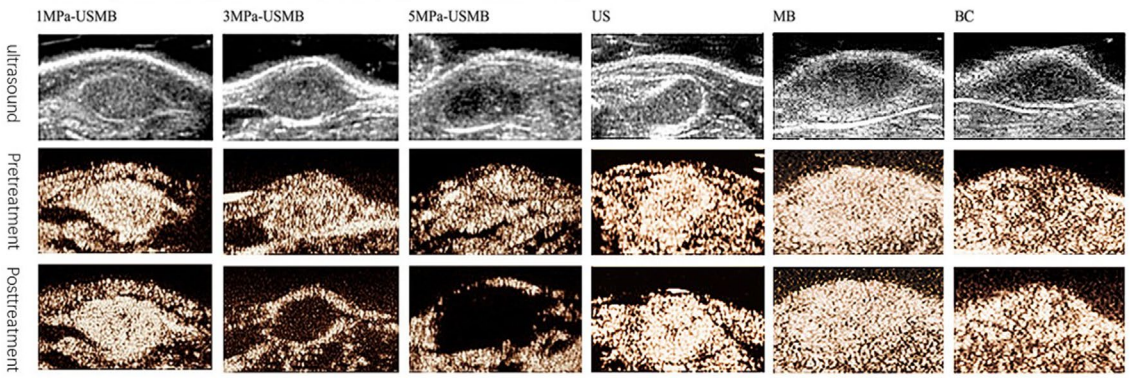

FIGURE 3 | Microbubbles were filled into the tumor rapidly and evenly, and no filling defect was found in all groups before treatment. After treatment, enhancement of the tumor was marginally stronger than pretreatment in low-intensity ultrasound combined with microbubble (1MPa-USMB) group, but in medium-intensity ultrasound combined with microbubble (3MPa-USMB) group, the contrast-enhanced ultrasound (CEUS) showed a filling defect in the center of the tumor with a ring-shaped enhancement around the tumor, and the filling defect was larger in high-intensity ultrasound combined with microbubble (5MPa-USMB) group than in 3MPa-USMB group. The blood perfusion after treatment in US group, MB group, and BC group were similar, and the microbubbles were filled into the tumor quickly and completely.

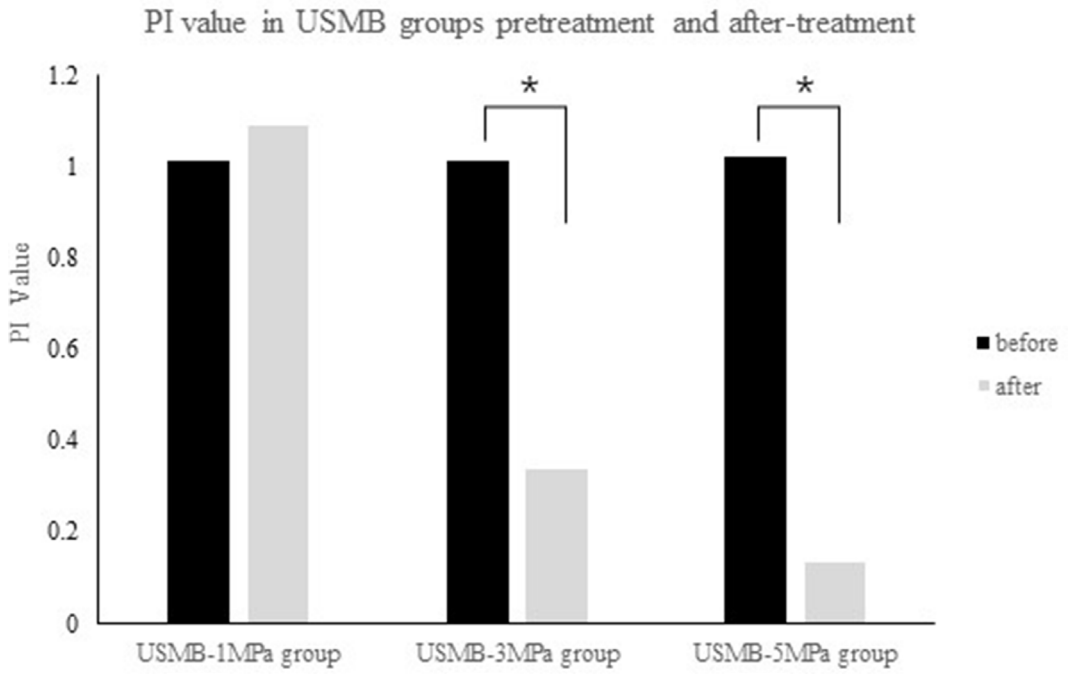

FIGURE 4 | The not significantly different in peak intensity (PI) was not significantly different in 1MPa-USMB group pre- and posttreatment. The PI value in 3MPa-USMB group and 5MPa-USMB group decreased 66.3% and 86.7% ($p < 0.05$), respectively, after treatment.

Interstitial-Fluid Pressure

Table 1 summarizes the IFP in each group before and after treatment. The overall mean IFP was 14.5 ± 6.8 mmHg in the tumor tissues and −6.7 ± 3.2 mmHg in the peripheral tissues. **Figure 5** shows the curve of IFP in the USMB groups post treatment. In the 3MPa-USMB and 5MPa-USMB groups, the curve decreased steadily during treatment, but it increased steadily in the 1MPa-USMB group. The IFP showed no significant change in the BC, US, and MB groups during the treatment. After treatment, the tumor IFP in the 1MPa-USMB group was slightly higher than that before treatment ($p < 0.0001$), but lower than that in the 3MPa-USMB and 5MPa-USMB groups ($p < 0.0001$). However, there was no significant difference in the IFP change between the 3MPa-USMB and 5MPa-USMB groups ($p > 0.05$).

H&E Staining

The pathological results were similar among the US, MB, and BC groups; the tumor cells were disordered, varied in size, and densely arranged, with large and dimorphic nuclei. The tumor blood vessels were branched and their structure was clear. Furthermore, the vessel wall was intact and continuous, with no obvious damage. Red blood cells were not observed at the periphery of the vessels. H&E staining revealed that the tumor from the 1MPa-USMB group was similar to that from the US, MB, and BC groups, but there were some red blood cells at

TABLE 1 | The interstitial fluid pressure (IFP) level in each group preprocedural and postprocedural (mmHg).

	BC	US	MB	1MPa-USMB	3MPa-USMB	5MPa-USMB
Preprocedural	13.2 ± 9.7	11.8 ± 6.1	18.0 ± 6.9	11.0 ± 3.3	17.7 ± 4.9	15.3 ± 7.3
Postprocedural	13.2 ± 9.5	11.7 ± 6.5	18.1 ± 7.0	13.0 ± 3.4	12.9 ± 5.5	9.8 ± 7.6
p				*	*	*

*$p < 0.0001$, preprocedural versus postprocedural.
The range of IFP level in tumors: 10–40 mmHg.

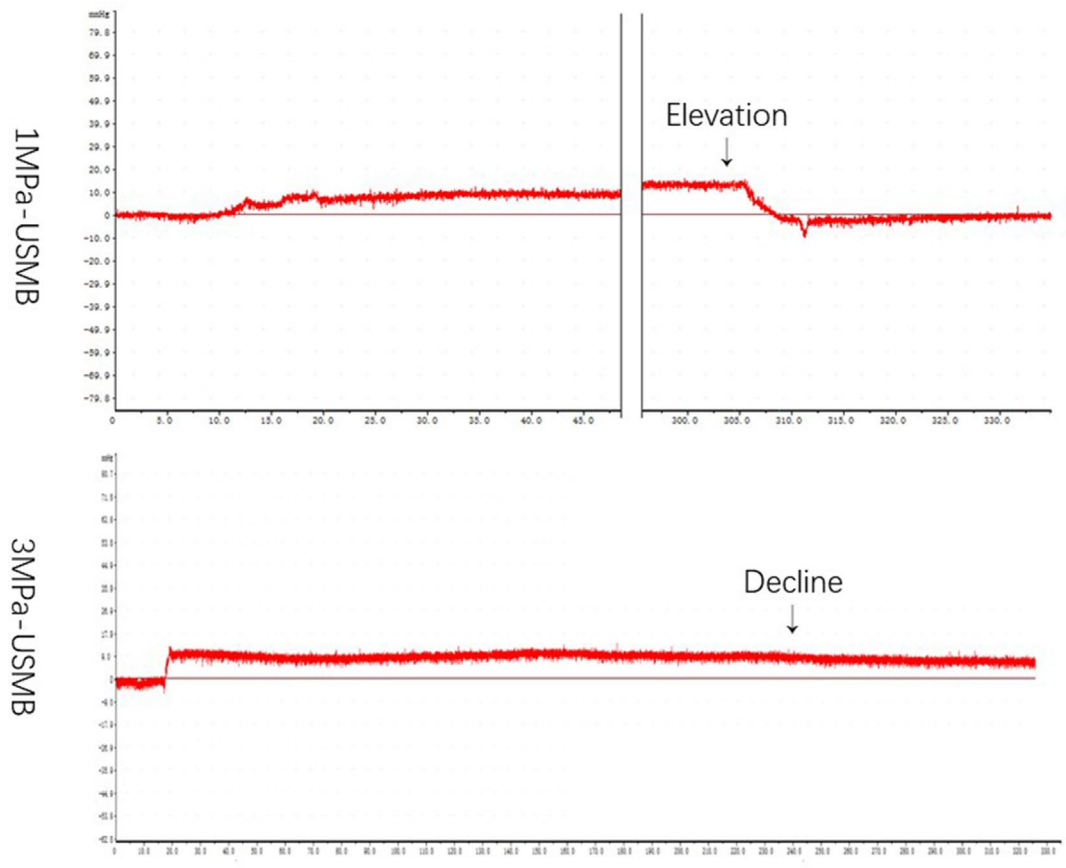

FIGURE 5 | The curve of IFP level in USMB group post-treatment: in 3MPa-USMB group and 5MPa-USMB group, the curve decreased steadily during the treatment, while it increased steadily in 1MPa-USMB group.

the periphery of the blood vessels. Focal necrosis of tumor cells was found in the 3MPa-USMB and 5MPa-USMB groups. Microvascular congestion and expansion were observed in the injured area, and the vessel wall was incomplete and red blood cells were observed around the vessels, which was more obvious in the 5MPa-USMB group than in the 3MPa-USMB group (**Figure 6**).

Masson Staining and Gordon–Sweets Staining

Figure 7 shows the tissue sections subjected to Masson staining and Gordon–Sweets staining. In the Masson-stained sections, the collagen fibers appeared blue, cytoplasm appeared red, and nucleus appeared blue. In Gordon–Sweets-stained sections, the reticular fibers appeared brownish black. The BC group represented the pretreatment state of the tumor tissues. **Figure 8** shows that the content of collagen fibers and reticular fibers in the BC group correlated with the pretreatment tumor IFP; the higher the content of collagen fiber and reticular fiber, the higher the IFP. **Table 2** summarizes the ratio of collagen and reticular fibers in each group. The results showed that there was no significant difference between each group ($p = 0.27$ and $p = 0.14$). This indicated that our treatment has little or no effect on the content of collagen and reticular fibers in tumor tissues.

DISCUSSION

CEUS can be used to evaluate blood perfusion into tumor tissues. Blood perfusion indicated the IFP in tumor tissues. In the present study, we adopted three different acoustic pressure (1, 3, and 5 MPa) low-frequency ultrasound treatments to represent low-intensity, medium-intensity, and high-intensity ultrasound treatments combined with microbubbles to determine the changes in tumor IFP. There was no significant difference in the CEUS before and after treatment in the 1MPa-USMB group. Studies have shown that above 1MPa-USMB treatment can improve vascular permeability; however, it is based on normal tissues. Vessels in tumor are abnormal and easily influenced by cavitation effect (Heldin et al., 2004; Li et al., 2011). The pathological results showed that the tumor vessels were still clear and intact, and that there was no obvious defect in the vessel wall; leakage of red blood cells was observed around the vessels. We suggest that 1MPa-USMB treatment can improve tumor vascular permeability, allowing more vascular contents to penetrate through the vessel wall into the interstitial space; thus, increasing colloidal osmotic pressure. Therefore, it is reasonable to consider that this mechanism increases the tumor IFP. The post-treatment CEUS in the 3MPa-USMB and 5MPa-USMB groups showed filling defect in the central region of tumor, and the PI decreased significantly. Filling defect indicates blockage in tumor blood perfusion, which is thought to be caused by microvascular destruction in the injured area of tumor tissue. Vessel wall damage, endothelial cell injury, and micro thrombosis are the factors that affect blood perfusion to tumor tissue (Heldin et al., 2004; Li et al., 2011). Studies have shown that vascular disrupting agents (VDAs) decrease the IFP in tumor tissues effectively (Gaya and Rustin, 2005). Based on this finding, it is reasonable to conclude that 3MPa-USMB and 5MPa-USMB treatments decrease the IFP by blocking blood perfusion like VDAs do.

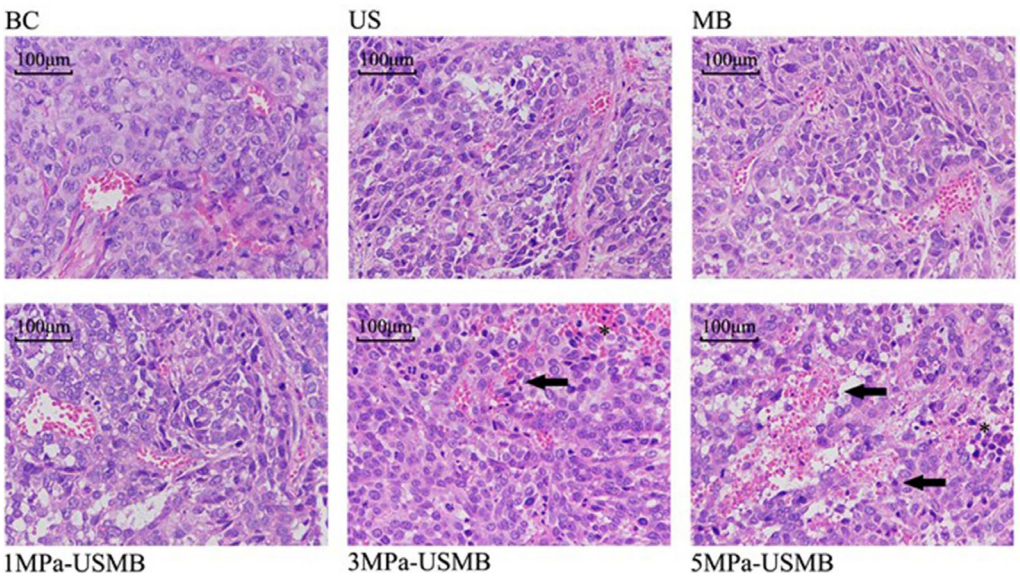

FIGURE 6 | The tumor cells are disordered, different in size, densely arranged, large nuclei stain and nuclei dimorphism. The tumor blood vessels were branched and their structure was clear. Furthermore, the vessel wall was intact and continuous, with no obvious damage. There are no red blood cells observed at the periphery of the vessels in US group, MB group, and BC group. There are some red blood cells observed at the periphery of the vessels in 1MPa-USMB group. The microvascular congestion and expansion can be seen in the injured area, the vessel-wall is incomplete (solid arrow), and red blood cells can be seen around the vessels (asterisk) in 3MPa-USMB group and 5MPa-USMB group.

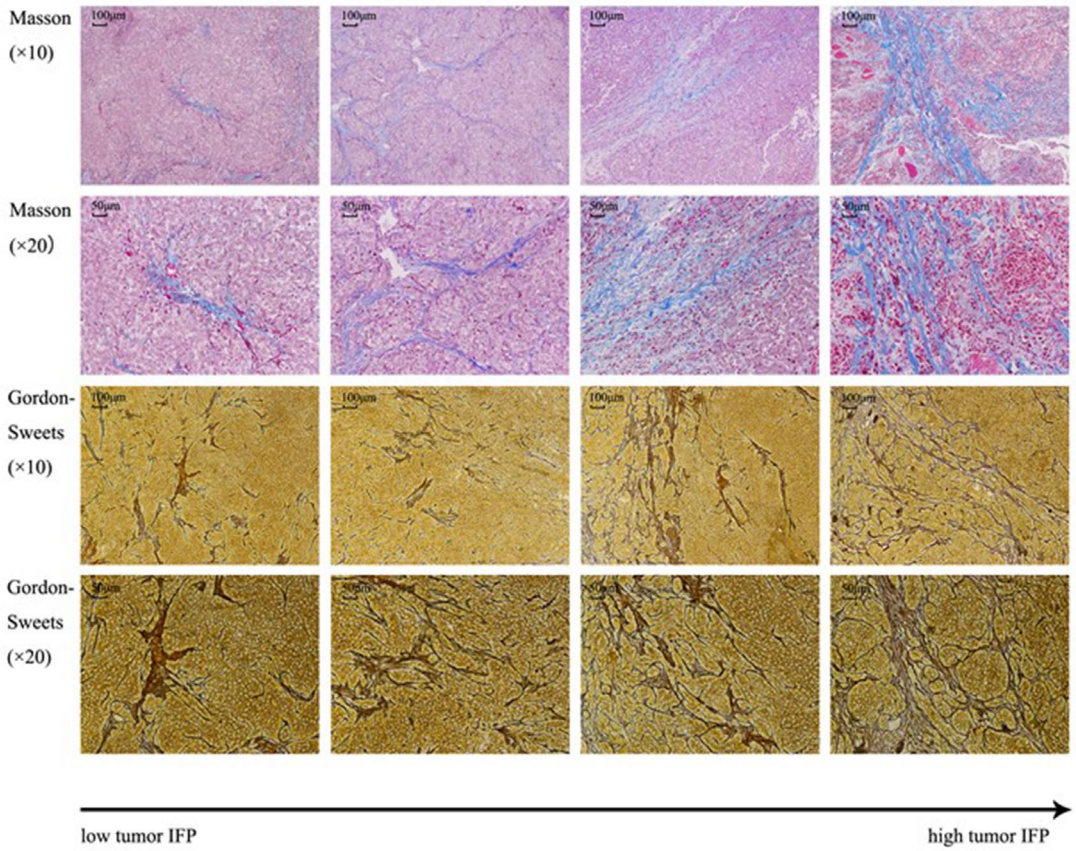

FIGURE 7 | Masson staining and Gordon–Sweets staining. In Masson staining, collagen fibers were indicated in blue, cytoplasm was indicated in red, and nucleus was indicated in blue. In Gordon–Sweets staining, reticular fibers were indicated in brownish black.

In our previous study, the micro vessel density in tumor tissues was significantly reduced after 3MPa-USMB and 5MPa-USMB treatments, but there was no significant difference between these two treatments. This explains why there was no significant difference in the IFP change between the 3MPa-USMB and 5MPa-USMB groups. The IFP change in the US, MB, and BC groups was not significantly different compared with that before treatment.

Abnormal interstitial structure in tumor tissues increases the IFP, and the collagen and reticular fibers are the scaffold for growing tumor cells in a suitable microenvironment. In the present study, the collagen fibers were stained by Masson staining and the reticular fibers were stained by Gordon–Sweets staining (Lee et al., 2017). The distribution of collagen and reticular fibers in tumor tissue was observed post treatment in each group. As there is no chance to observe these fibers pre treatment, we considered the BC group as the pre-treatment state. Analysis using image analysis software showed that there was no significant difference in the ratio and morphology of collagen and reticular fibers pre and post treatment in each group. That is, the content and structure of collagen and reticular fibers in each group did not change significantly pre and post treatment. The decrease in tumor IFP without changes in the collagen and reticular fibers indicate that the tumor IFP decrease was not due to a reduction in content of these fibers. Previous studies have shown that High-Intensity Focused Ultrasound (HIFU) reduces the tumor IFP by destroying the fibers, especially collagen fibers, due to the thermal and mechanical effects of HIFU (Matsumura and Maeda, 1986; Gaya and Rustin, 2005; Watson et al., 2012; Lee et al., 2017). In our study, we proved that the low-frequency non-focus US-MB has negligible effect on the ECM. Some studies have shown that the degradation of collagen fibers and hyaluronic acid in the matrix reduced the IFP effectively (Ross et al., 2002; Gaya and Rustin, 2005; Okada et al., 2005; Fukumura and Jain, 2007; Qiao et al., 2013; Lee et al., 2017). However, both collagen fibers and hyaluronic acid inhibit tumor growth and metastasis (Itano et al., 2002; Jojovic et al., 2002; Kovar et al., 2006); hence, whether the destruction of collagen fibers and hyaluronic acid in the ECM is beneficial in inhibiting tumor growth by decreasing tumor IFP should be evaluated further. Moreover, studies should be conducted on how to reduce the tumor IFP without breaking this barrier.

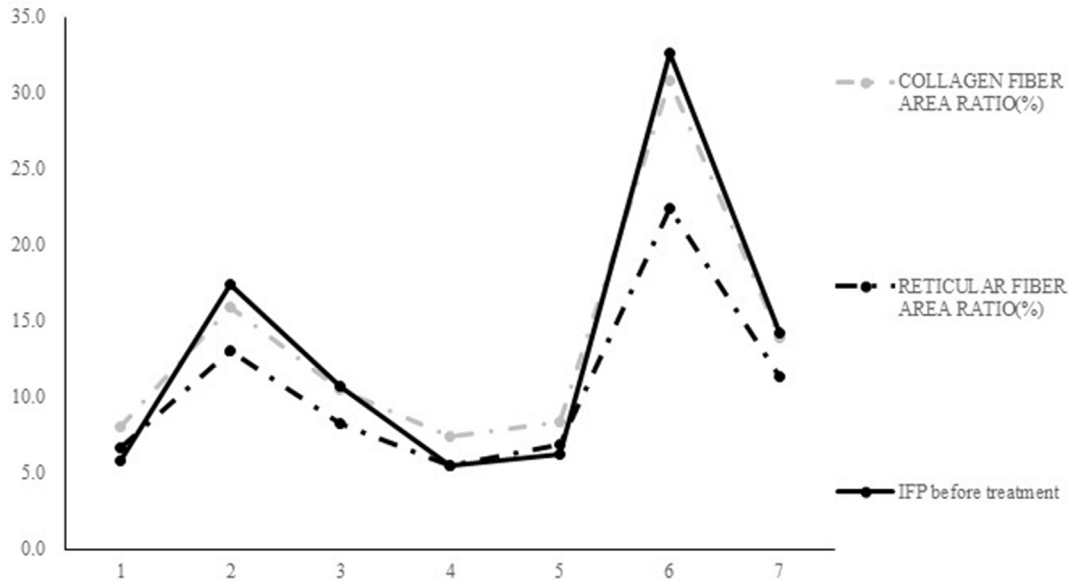

FIGURE 8 | The contents of collagen fibers and reticular fibers in BC group correlation with the level of pretreatment tumor IFP: the higher the contents of collagen fiber and reticular fiber, the higher the IFP level.

TABLE 2 | The ratio of collagen and reticular fibers in each group.

	BC	US	MB	1MPa-USMB	3MPa-USMB	5MPa-USMB
Collagen fibers (%)	13.6 ± 8.2	11.8 ± 4.0	16.8 ± 5.9	11.4 ± 2.6	16.8 ± 5.1	14.7 ± 7.0
Reticular fibers (%)	10.6 ± 5.9	8.9 ± 3.6	13.6 ± 5.0	9.2 ± 2.3	14.0 ± 4.4	11.4 ± 5.3

In conclusion, our study results revealed that there is a correlation between the IFP and the fibers in the BC group; the higher the IFP level, the more the collagen and reticular fiber content. This result is consistent with that of previous studies (Starling; Montesano and Orci, 1988; Clark et al., 1989; Boucher et al., 1990; Gullberg et al., 1990; Kitadai et al., 2001; Padera et al., 2004; Fukumura and Jain, 2007). The mechanism involved in the increase in IFP is the fibers restrict tumor deformation, and the mechanical pressure can destroy the lymphatic function (Sheikov et al., 2004; Thakkar et al., 2013; De Cock et al., 2015).

CONCLUSIONS

Low-frequency non-focus US-MB therapy can change the IFP of tumor tissue and cause no significant changes in the structure and content of collagen and reticular fibers in the tumor ECM. Low-frequency non-focus ultrasound with low acoustic pressure (1 MPa) increased the tumor IFP, whereas low-frequency non-focus ultrasound with medium-high acoustic pressure decreased the tumor IFP. There was no significant difference between the medium and high acoustic pressure groups in terms of decrease in the tumor IFP. Our study presents a novel approach of reduced IFP antitumor therapy.

AUTHOR CONTRIBUTIONS

QZ, HJ, and JL conceived and designed the experiments and wrote the paper; QZ and HJ performed the experiments and analyzed the data; PC, QC, FX, SX, SM, YY, HY, and QL contributed reagents/materials/analysis tools. All authors provided their approval for publication.

FUNDING

This study was supported by the Natural Science Foundation of Guangdong Province (grant no. 2016A030313461).

REFERENCES

Alitalo, K., Tammela, T., Petrova, T. V., Alitalo, K., and Tammela, T. (2006). Lymphangiogenesis in development and human disease. *Nature* 438 (7070), 946–953. doi: 10.1038/nature04480

Boucher, Y., Baxter, L. T., and Jain, R. K. (1990). Interstitial pressure gradients in tissue-isolated and subcutaneous tumors: implications for therapy. *Cancer Res.* 50 (15), 4478–4484.

Brekken, C., and de Lange Davies, C. (1998). Hyaluronidase reduces the interstitial fluid pressure in solid tumours in a non-linear concentration-dependent manner. *Cancer Lett.* 131 (1), 65–70. doi: 10.1016/S0304-3835(98)00202-X

Brekken, C., Bruland, Ø S., and de Lange Davies, C. (2000a). Interstitial fluid pressure in human osteosarcoma xenografts: significance of implantation site and the response to intratumoral injection of hyaluronidase. *Anticancer Res.* 20 (5B), 3503–3512.

Brekken, C., Hjelstuen, M. H., Bruland, Ø S., et al. (2000b). Hyaluronidase-induced periodic modulation of the interstitial fluid pressure increases selective antibody uptake in human osteosarcoma xenografts. *Anticancer Res.* 20 (5B), 3513–3519.

Chen, Y., and Shi, J., (2002). *Zhong liu fen zi xi bao sheng wu xue*. Beijing, China: People's Military Medical Press.

Clark, R. A., Folkvord, J. M., Hart, C. E., Murray, M. J., and McPherson, J. M. (1989). Platelet isoforms of platelet-derived growth factor stimulate fibroblasts to contract collagen matrices. *J. Clin. Invest.* 84 (3), 1036–1040. doi: 10.1172/JCI114227

De Cock, I., Zagato, E., Braeckmans, K., Luan, Y., de Jong, N., De Smedt, S. C., et al. (2015). Ultrasound and microbubble mediated drug delivery: acoustic pressure as determinant for uptake via membrane pores or endocytosis. *J. Control Release.* 197 (0), 20–28. doi: 10.1016/j.jconrel.2014.10.031

DiResta, G. R., Lee, J., Healey, J. H., Levchenko, A., Larson, S. M., and Arbit, E. (2000). "Artificial lymphatic system": a new approach to reduce interstitial hypertension and increase blood flow, pH and pO2 in solid tumors. *Ann. Biomed. Eng.* 28 (5), 543. doi: 10.1114/1.295

Dufort, C. C., Delgiorno, K. E., Carlson, M. A., Osgood, R. J., Zhao, C., Huang, Z., et al. (2016). Interstitial pressure in pancreatic ductal adenocarcinoma is dominated by a gel-fluid phase. *Biophys. J.* 110 (9), 2106. doi: 10.1016/j.bpj.2016.03.040

Fukumura, D., and Jain, R. K. (2007). Tumor microenvironment abnormalities: causes, consequences, and strategies to normalize. *J. Cell. Biochem.* 101 (4), 937–949. doi: 10.1002/jcb.21187

Gaya, A. M., and Rustin, G. J. (2005). Vascular disrupting agents: a new class of drug in cancer therapy. *Clin. Oncol.* 17 (4), 277. doi: 10.1016/j.clon.2004.11.011

Goel, S., Duda, D. G., Xu, L., Munn, L. L., Boucher, Y., Fukumura, D., et al. (2011). Normalization of the vasculature for treatment of cancer and other diseases. *Physiol. Rev.* 91 (3), 1071. doi: 10.1152/physrev.00038.2010

Gullberg, D., Tingström, A., Thuresson, A. C., Olsson, L., Terracio, L., Borg, T. K., et al. (1990). Beta 1 integrin-mediated collagen gel contraction is stimulated by PDGF. *Exp. Cell Res.* 186 (2), 264–272. doi: 10.1016/0014-4827(90)90305-T

Hagendoorn, J., Tong, R., Fukumura, D., Lin, Q., Lobo, J., Padera, T. P., et al. (2006). Onset of abnormal blood and lymphatic vessel function and interstitial hypertension in early stages of carcinogenesis. *Cancer Res.* 66 (7), 3360. doi: 10.1158/0008-5472.CAN-05-2655

Heldin, C. H., Rubin, K., Pietras, K., and Ostman, A. (2004). High interstitial fluid pressure—an obstacle in cancer therapy. *Nat. Rev. Cancer* 4 (10), 806–813. doi: 10.1038/nrc1456

Itano, N., Atsumi, F., Sawai, T., Yamada, Y., Miyaishi, O., Senga, T., et al. (2002). Abnormal accumulation of hyaluronan matrix diminishes contact inhibition of cell growth and promotes cell migration. *Proc. Natl. Acad. Sci. U. S. A.* 99 (6), 3609. doi: 10.1073/pnas.052026799

Jain, R. K. (1987a). Transport of molecules across tumor vasculature. *Cancer Metastasis. Rev.* 6 (4), 559. doi: 10.1007/BF00047468

Jain, R. K. (1987b). Transport of molecules in the tumor interstitium: a review. *Cancer Res.* 47 (12), 3039–3051.

Jojovic, M., Delpech, B., Prehm, P., and Schumacher, U. (2002). Expression of hyaluronate and hyaluronate synthase in human primary tumours and their metastases in scid mice. *Cancer Lett.* 188 (1–2), 181. doi: 10.1016/S0304-3835(02)00037-X

Kitadai, Y., Amioka, T., Haruma, K., Tanaka, S., Yoshihara, M., Sumii, K., et al. (2001). Clinicopathological significance of vascular endothelial growth factor (VEGF)-C in human esophageal squamous cell carcinomas. *Int. J. Cancer* 93 (5), 662. doi: 10.1002/ijc.1379

Kovar, J. L., Johnson, M. A., Volcheck, W. M., Chen J., and Simpson, M. A. (2006). Hyaluronidase expression induces prostate tumor metastasis in an orthotopic mouse model. *Am J. Pathol* 169 (4), 1415–1426. doi: 10.2353/ajpath.2006.060324

Lee, C. G., Heijn, M., di Tomaso, E., Griffon-Etienne, G., Ancukiewicz, M. Z., Koike, C., et al. (2000). Anti-vascular endothelial growth factor treatment augments tumor radiation response under normoxic or hypoxic conditions. *Cancer Res.* 60 (19), 5565.

Lee, S., Han, H., Koo, H., Na, J. H., Yoon, H. Y., Lee, K. E., et al. (2017). Extracellular matrix remodeling in vivo, for enhancing tumor-targeting efficiency of nanoparticle drug carriers using the pulsed high intensity focused ultrasound. *J. Control Release*. 263, 68–78. doi: 10.1016/j.jconrel.2017.02.035

Less, J. R., Posner, M. C., Boucher, Y., Borochovitz, D., Wolmark, N., and Jain, R. K. (1992). Interstitial hypertension in human breast and colorectal tumors. *Cancer Res.* 52 (22), 6371–6374.

Li, Y., Wang, J., Wientjes, M. G., and Au, J. L. (2011). Delivery of nanomedicines to extracellular and intracellular compartments of a solid tumor. *Adv. Drug Deliver Rev.* 64 (1), 29–39. doi: 10.1016/j.addr.2011.04.006

Marquet, F., Teichert, T., Wu, S. Y., Tung, Y. S., Downs, M., Wang, S., et al. (2014). Real-time, transcranial monitoring of safe blood–brain barrier opening in non-human primates. *PloS One* 9 (2), e84310. doi: 10.1371/journal.pone.0084310

Matsumura, Y., and Maeda, H. (1986). A new concept for macromolecular therapeutics in cancer chemotherapy: mechanism of tumoritropic accumulation of proteins and the antitumor agent smancs. *Cancer Res.* 46 (1), 6387–6392. doi: 10.1016/0304-3835(86)90075-3

Montesano, R., and Orci, L. (1988). Transforming growth factor beta stimulates collagen-matrix contraction by fibroblasts: implications for wound healing. *Proc Natl Acad Sci U S A.* 85 (13), 4894–4897. doi: 10.1073/pnas.85.13.4894

Nathanson, S. D., and Nelson, L. (1994). Interstitial fluid pressure in breast cancer, benign breast conditions, and breast parenchyma. *Ann. Surg. Oncol.* 1(4), 333–338. doi: 10.1007/BF03187139

Okada, K., Kudo, N., Niwa, K., and Yamamoto, K. (2005). A basic study on sonoporation with microbubbles exposed to pulsed ultrasound. *J. Med. Ultrason.* 32 (1), 3. doi: 10.1007/s10396-005-0031-5

Padera, T. P., Stoll, B. R., Tooredman, J. B., Capen, D., di Tomaso, E., and Jain, R. K. (2004). Pathology: cancer cells compress intratumour vessels. *Nature* 427 (6976), 695. doi: 10.1038/427695a

Qiao, Y., Yin, H., Li, Z., and Wan, M. (2013). Cavitation distribution within large phantom vessel and mechanical damage formed on surrounding vessel wall. *Ultrason. Sonochem.* 20 (6), 1376–1383. doi: 10.1016/j.ultsonch.2013.03.007

Ross, J. P., Cai, X., Chiu, J. F., Yang, J., and Wu, J. (2002). Optical and atomic force microscopic studies on sonoporation. *J. Acoust. Soc. Am.* 111 (3), 1161. doi: 10.1121/1.1448340

Sheikov, N., McDannold, N., Vykhodtseva, N., Jolesz, F., and Hynenen, K. (2004). Cellular mechanisms of the blood–brain barrier opening induced by ultrasound in presence of microbubbles. *Ultrasound. Med. Biol.* 30 (7), 979–989. doi: 10.1016/j.ultrasmedbio.2004.04.010

Starling, E. H. On the absorption of fluids from the connective tissue spaces. *J. Physiol* 19 (4), 312–316. doi: 10.1113/jphysiol.1896.sp000596

Thakkar, D., Gupta, R., Monson, K., and Rapoport, N. (2013). Effect of ultrasound on the permeability of vascular wall to nanoemulsion droplets. *Ultrasound. Med. Biol.* 39 (10), 1804–1811. doi: 10.1016/j.ultrasmedbio.2013.04.008

Tong, R. T., Boucher, Y., Kozin, S. V., Winkler, F., Hicklin, D. J., and Jain, R. K. (2004). Vascular normalization by vascular endothelial growth factor receptor 2 blockade induces a pressure gradient across the vasculature and improves drug penetration in tumors. *Cancer Res.* 64 (11), 3731–3736. doi: 10.1158/0008-5472.CAN-04-0074

Watson, K. D., Lai, C. Y., Qin, S., Kruse, D. E., Lin, Y. C., Seo, J. W., et al. (2012). Ultrasound increases nanoparticle delivery by reducing intratumoral pressure

and increasing transport in epithelial and epithelial–mesenchymal transition tumors. *Cancer Res.* 72 (6), 1485–1493. doi: 10.1158/0008-5472.CAN-11-3232

Willett, C. G., Boucher, Y., di Tomaso, E., Duda, D. G., Munn, L. L., Tong, R. T., et al. (2004). Direct evidence that the VEGF-specific antibody bevacizumab has antivascular effects in human rectal cancer. *Nat. Med.* 10 (2), 145. doi: 10.1038/nm988

Young, J. S., Lumsden, C. E., and Stalker, A. L. (1950). The significance of the tissue pressure of normal testicular and of neoplastic (Brown–Pearce carcinoma) tissue in the rabbit. *J. PatholBacteriol.* 62 (3), 313–333. doi: 10.1002/path.1700620303

Conflict of Interest of Statement: The authors declare that the research was conducted in the absence of any commercial or financial relationships that could be construed as a potential conflict of interest.

frontiers in Pharmacology

ORIGINAL RESEARCH
published: 09 July 2019
doi: 10.3389/fphar.2019.00767

The Role of Blood Flow in Corpus Luteum Measured by Transvaginal Two-Dimensional and Three-Dimensional Ultrasound in the Prediction of Early Intrauterine Pregnancy Outcomes

Huijuan Han[1†], Xinhai Mo[2†], Yuqin Ma[2], Yuqing Zhou[1] and Bo Zhang[2*]*

[1] Department of Ultrasound, Shanghai Changning Maternity and Infant Health Hospital, Shanghai, China, [2] Department of Ultrasound in Medicine, Shanghai East Hospital, Tongji University School of Medicine, Shanghai, China

OPEN ACCESS

Edited by:
Xiaobing Wang,
Shaanxi Normal University, China

Reviewed by:
Livia Stocco Sanches Valentin,
University of São Paulo, Brazil
Tao Ying,
Shanghai Sixth People's Hospital Affiliated to Shanghai Jiao Tong University, China

****Correspondence:***
Yuqing Zhou
doczhou@qq.com
Bo Zhang
zhangbo2016@tongji.edu.cn

†These authors have contributed equally to this work.

Specialty section:
This article was submitted to Translational Pharmacology, a section of the journal Frontiers in Pharmacology

Received: *07 January 2019*
Accepted: *13 June 2019*
Published: *09 July 2019*

Citation:
Han H, Mo X, Ma Y, Zhou Y and Zhang B (2019) The Role of Blood Flow in Corpus Luteum Measured by Transvaginal Two-Dimensional and Three-Dimensional Ultrasound in the Prediction of Early Intrauterine Pregnancy Outcomes. Front. Pharmacol. 10:767. doi: 10.3389/fphar.2019.00767

Objective: The purpose of this study was to explore the application of transvaginal two-dimensional and three-dimensional power Doppler ultrasound in pregnancy corpus luteum to predict the final outcome of early intrauterine pregnancy.

Methods: This is a prospective observational cohort study. Six hundred early intrauterine pregnant women in Shanghai Changning Maternity and Infant Health Hospital were selected as the research objects from January 2015 to December 2015. According to the follow-up of 12 weeks, these pregnant women were divided into the normal pregnancy group (group A, $n = 512$) and the terminational pregnancy group (group B, $n = 88$). They all underwent both transvaginal two-dimensional ultrasound and three-dimensional power Doppler ultrasound to obtain relevant parameters of corpus luteum, namely, the average diameter of the corpus luteum (D), resistance index (RI), pulsatility index (PI), corpus luteum volume (V), vascularization index (VI), blood flow index (FI), and vascularized blood flow index (VFI). Among them, V, VI, FI, and VFI were calculated with the virtual organ computer-aided analysis method. Receiver operator characteristic (ROC) curves were drawn. The corresponding diagnostic cut-off, sensitivity, and specificity were calculated and compared.

Results: Compared with group A, the D, V, VI, FI, and VFI of corpus luteum in group B were statistically significant lower while RI and PI were statistically significant higher ($P < 0.05$). The diagnostic cut-off values in the prediction of early intrauterine pregnancy outcomes were D: 14.48, RI: 0.56, PI: 0.81, V: 3.89, VI: 21.48, FI: 38.99, and VFI: 10.21 respectively, and the sensitivity and specificity were D (99.2%, 67.0%), RI (98.9%, 65.0%), PI (78.4%, 89.1%), V (95.1%, 78.4%), VI (74.%, 90.9%), FI (91.8%, 90.9%), and VFI (93.9%, 87.5%) respectively. The area under the ROC curve of the combined index (RI + FI) was 0.963, which was not significantly higher compared with any single index, and both the sensitivity and specificity were 94.3%.

Conclusion: Both transvaginal two-dimensional and three-dimensional ultrasonography are of high diagnostic value in predicting the early intrauterine pregnancy outcomes.

Keywords: transvaginal two-dimensional ultrasound, transvaginal three-dimensional ultrasound, receiver operator characteristic curve, early intrauterine pregnancy, corpus luteum

INTRODUCTION

Early spontaneous abortion is one of the common complications during pregnancy, which may be attributed to embryonic factors, maternal factors, immune dysfunction, and environmental factors (Hassold et al., 2012). The corpus luteum (CL) is the primary organ producing progesterone during early first trimester, after which the placenta is capable of producing enough progesterone (Niswender et al., 2000). Continuing rescue of the CL by human chorionic gonadotropin (hCG) is essential, otherwise declining progesterone secretion is detrimental to maintaining pregnancy (Jarvela et al., 2008). Therefore, the normal function of CL is vital for pregnancy. However, its function may be affected by the abnormal oosperm, embryo implantation dysfunction, or other systemic disease (Wathes et al., 2003). Based on the researches at home and abroad, the capacity of the CL to produce progesterone is highly related to the extent of its vascular network (Tamanini and De, 2010). That is to say the more blood flow exists in CL, the more progesterone can be produced. The amount of vasculature accounts for more than 20% of the total volume of the CL, exceeding that of any other tissue, which enables to obtain oxygen, nutrients, and hormone precursors necessary to synthesize and release large amounts of progesterone (Henriquez et al., 2016). Therefore, it is crucial to detect the functional status of the CL in clinical work. Clinical symptoms of vaginal bleeding or abdominal pain and low level of hCG or progesterone are usually considered as a sign of the CL insufficiency (Wang et al., 2015). But the above performance is lack of specificity and accuracy to assist diagnosis and therapy. Hence, some accurate, objective, convenient and non-invasive parameters of the CL function are currently needed for early prediction of pregnancy outcome. It is commonly recognized that transvaginal two-dimensional ultrasound with color Doppler flow imaging (CDFI) is the optimum non-invasive imaging method for evaluating the sonographic features and vascularization of CL (Durfee and Frates, 2015). Doppler flow study with its indices such as pulsatility index (PI) and resistance index (RI) provides important information about perfusion and angiogenesis in the ovarian follicles (Guiot et al., 2008). Transvaginal three-dimensional ultrasound with power Doppler is a new emerging method of studying vascularization recently (Jokubkiene et al., 2012). It might better reflect vascular changes than two-dimensional color or power Doppler, because vascular changes in a whole organ can be assessed through blood flow velocity in one or a few vessels, and the results of quantitative analysis can be acquired by using the virtual organ computer-aid analysis (VOCAL) software (Jarvela et al., 2003). The histogram facility of the Vocal software automatically obtains three vascularity indices, namely vascularization index (VI), flow index (FI), and vascularization flow index (VFI), which potentially can reflect the vascular density, blood flow, and tissue perfusion respectively. So the quantification of complete blood flow of the region of interest from the analysis of power Doppler signals can be fully studied (Martins et al., 2011). To the best of our knowledge, there are few published studies where transvaginal two-dimensional and three-dimensional ultrasound have been used simultaneously to study the CL vascularity and its relationship with the pregnancy outcome in early first trimester. The aim of this study was to explore the prognostic value of transvaginal two-dimensional and three-dimensional ultrasound in predicting early intrauterine pregnancy outcome by measuring the blood flowing parameters related to the CL.

MATERIALS AND METHODS

Subjects

This is a prospective observational cohort study. Six hundred patients with early pregnancy and fertility requirements from January 2015 to December 2015 in Shanghai Changning Maternity and Infant Health Hospital were selected as the research objects with average age (27.1 ± 10.5) years old and average menstrual time (47.61 ± 6.18) days. Inclusion criteria: 1) Plain menstrual rules; 2) Exclusion of gynecological diseases such as uterine fibroids, adenomyosis, and ovarian cysts; 3) Exclusion of congenital uterine malformations. 4) Exclusion of repeated pregnancy loss, adverse pregnancy outcome, polycystic ovary syndrome (PCOS), and other systemic disease. According to the follow-up of 12 weeks, these pregnant women were divided into the normal pregnancy group (group A, $n = 512$) and the terminational pregnancy group (group B, $n = 88$). Informed consent was obtained from all women after a full explanation of the objectives of the study. The research protocol was approved by the Ethics Committee of Shanghai Changning Maternity and Infant Health Hospital (protocol number: CNFBLLYR-20150102).

Equipment and Sonographer

All data were acquired using a US GE Volusion E8 ultrasound system equipped with a 4–9 MHz transvaginal transducer. The Vocal software was provided for automatically measurement of relevant vascular parameters. Identical fixed pre-installed power Doppler ultrasound settings were used in all selected women: 1) High quality imaging (Qual high); 2) Frequency (Frq mid); 3) Color gain without overflow (gain 0); 4) Pulse repetition frequency (PRF) 0.3 kHz; 5) Mixing ratio (mix 20%/80%); 6) The wall motion filter to "low 1". All ultrasound examinations were performed by the same dedicated sonographers with more than 5 years of working experience.

Ultrasound Examination

All pregnant women were examined in the lithotomy position with an empty bladder. The ultrasound probe was introduced slowly into the vagina, and care was taken to avoid exerting undue pressure. First, in the grayscale mode, routine transvaginal two-dimensional ultrasound was first conducted to identify normal intrauterine pregnancy and seek for the pregnancy CL, scan, and record the average diameter of the corpus luteum (D). Next, observe the blood flow signal of CL with CDFI, adjust the color scale to the best mode, and place the sampling line at the most vivid color of the blood flow signal to start. Pulse Doppler detection measures the resistance index (RI) and the pulsatility index (PI) after acquiring more than three consecutive spectra. Then, based on the satisfactory view, the 3D ultrasound mode was switched on, then adjust the position and size of the sampling frame and start the VOCAL program, for A, B, and C as shown in **Figure 1**. The A plane (vertical axis) in the plane was manually outlined, and the rotation angle of the adjacent section was set to 30°. Once six contours had been drawn, the volume of the CL (V) was calculated automatically. Using the histogram facility of Vocal software, three vascular indices were generated: vascularization index (VI) means the proportion of the volume showing a flow signal in the fetal brain; blood flow index (FI) is the average flow signal intensity inside the fetal brain and vascularized blood flow index (VFI) is a combination of the information concerning vessel presence and the amount of flow obtained by multiplying VI and FI.

Statistical Analysis

All WSS data were analyzed by Microsoft Excel and SPSS 22.0 software (SPSS Inc., Chicago, IL, USA). Shapiro–Wilk test was used to assess the distribution of continuous variables. Results were expressed as frequencies and percentages for categorical variables, mean ± standard deviation (SD) for normally distributed variables, and median (interquartile range) for non-normally distributed variables. Continuous variables were compared by one-way analysis of variance with Bonferroni *post hoc* test or Kruskal–Wallis tests. Mann–Whitney *U* test for nonparametric variables. Receiver operating characteristic (ROC) curves was used to evaluate the individual ability of the parameters to predict the pregnant outcomes. Areas under the curve (AUC) for each ROC curve were calculated and compared by *Z* test. $P < 0.05$ difference was statistically significant.

RESULTS

Overall, 600 pregnant women were detected in our study. The 512 pregnant women were enrolled in group A and the median (interquartile range) age was 29(5) years in group A, whereas in group B of 88 pregnant women, the median age was 29(6) years.

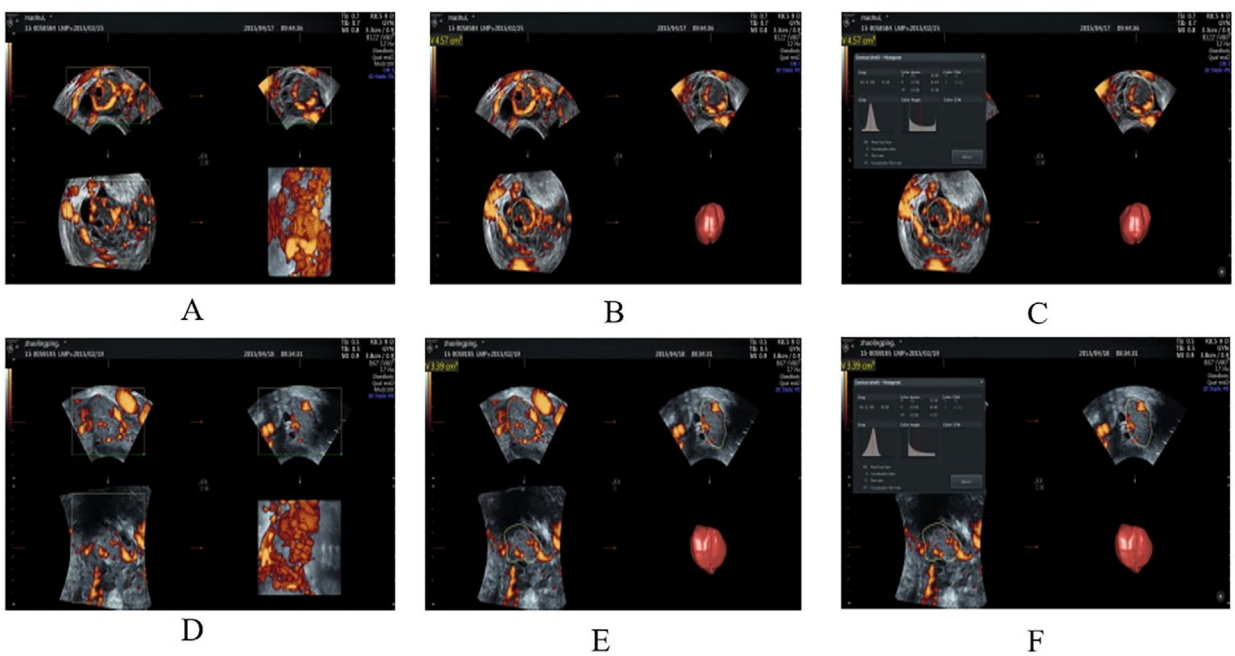

FIGURE 1 | Three-dimensional ultrasound images of corpus luteum in group A and group B. **(A, B)** The 3D-PD ultrasound images of the corpus luteum in group A (27 y, G1P0, menolipsis 69 days, no symptoms of abdominal pain or vaginal bleeding, intrauterine pregnancy, having yolk sac, germ, and fetal heart beating). **(C)** The histogram of gestational corpus luteum in the same patient. **(D, E)** The 3D-PD ultrasound images of the corpus luteum in group B (34 y, G1P0, menolipsis 59 days, with the symptoms of abdominal pain and vaginal bleeding, intrauterine pregnancy, having yolk sac and germ, no fetal heart beating). **(F)** The histogram of gestational corpus luteum in the same patient. 3D-PD indicates the three-dimensional power Doppler.

There was no significant difference ($P < 0.05$) when comparing group A with group B.

Transvaginal Two-Dimensional Parameters of Corpus Luteum

The transvaginal two-dimensional parameters of the two groups were compared in **Table 1**. The mean D value was significantly higher in group A (21.06 ± 3.08 mm), compared to the value in group B (13.92 ± 2.86 mm; $P < 0.05$). While the RI and PI were significantly lower in group A (0.54 ± 0.22 and 0.72 ± 0.21, respectively) than those values of group B (0.61 ± 0.32 and 0.86 ± 0.14, respectively; $P < 0.05$).

Transvaginal Three-Dimensional Parameters of Corpus Luteum

The transvaginal three-dimensional parameters of the two groups were compared in **Table 2**. The V, VI, FI, and VFI were significantly higher in group A (6.64 ± 1.98 mm^3, 26.16 ± 11.51, 49.58 ± 21.71 and 14.60 ± 3.62, respectively), compared to group B (3.58 ± 1.58 mm^3, 15.61 ± 6.55, 31.268 ± 6.31 and 6.92 ± 3.12, respectively; $P < 0.05$).

ROC Curves for Both Transvaginal Two-Dimensional and Transvaginal Three-Dimensional Parameters

As shown in **Figure 2**, ROC curves were drawn according to the parameters of group A and group B. The diagnostic cut-off value, sensitivity, and specificity of all parameters were described in **Table 3**.

Binary Logistic Regression Analysis

From the above analysis, we found that the AUC for ROC curve of RI among the two-dimensional parameters and FI among three-dimensional parameters were significantly higher. The ROC curve analysis of the joint indicator of RI and FI was performed by the binary logistic regression analysis as shown in **Figure 3**. The joint indicator of RI and FI was not superior to individual RI or FI in the prediction of early intrauterine pregnancy outcomes, with an AUC not significantly higher (**Table 4**).

TABLE 1 | Transvaginal two-dimensional parameters of corpus luteum in two groups.

Variable	Group A	Group B	*P* value
D (mm)	21.06 ± 3.08	13.92 ± 2.86	0.000*
RI	0.54 ± 0.22	0.61 ± 0.32	0.000*
PI	0.72 ± 0.21	0.86 ± 0.14	0.000*

**means P < 0.05; D indicates the average diameter of the corpus luteum; RI, the resistance index; and PI, the pulsatility index.*

TABLE 2 | Transvaginal three-dimensional parameters of corpus luteum in two groups.

Variable	Group A	Group B	*P* value
V (mm^3)	6.64 ± 1.98	3.58 ± 1.58	0.000*
VI	26.16 ± 11.51	15.61 ± 6.55	0.000*
FI	49.58 ± 21.78	31.26 ± 6.31	0.000*
VFI	14.60 ± 3.62	6.92 ± 3.12	0.000*

**means P < 0.05; V indicates corpus luteum volume; VI, vascularization index; FI, blood flow index; VFI, vascularized blood flow index.*

DISCUSSION

Spontaneous abortions are serious life events for both family and society. The frequency of early spontaneous abortions is estimated to be 10–15% of clinically recognized pregnancies and as many as 30% of clinically unrecognized pregnancies (Baba et al., 2011). Although chromosomal abnormalities of the fetus or increasing maternal age are the major risk factors of early spontaneous abortions, it is not uncommon to attribute such adverse event to the CL insufficiency in clinic (Duru and Nagadeepti, 2013). At present, the prognosis of intrauterine pregnancy mostly depends on the clinical symptoms such as vaginal bleeding and abdominal pain and low level of hCG or progesterone, which have poor specificity and sensitivity (Dinelli et al., 2014). It is well-known that the CL continues to grow under the stimulation of hCG after fertilization and is the only source to produce progesterone to maintain pregnancy before the formation of placenta (Sgs et al., 2017). An abnormal endometrial lymphocyte pattern occurs in infertile women affected by PCOS, together with profound impairment of the endometrial cytokine balance, even after normal ovulation (Matteo et al., 2010). The cut-off value for serum progesterone (35 nmol/L) demonstrated clinical relevance and allow clinicians to stratify patients into high and low risk groups for spontaneous miscarriage (Lek et al., 2017). Therefore, the normal function of CL is vital for pregnancy. In early pregnancy, the ovary can be induced to sprout new blood vessels which emitting collateral circulation into the CL, so the blood perfusion around the CL is significantly abundant (Tamura et al., 2008).

Transvaginal sonography has unique advantages in detecting the CL function by measuring its morphology, echo, size, volume, as well as evaluating the vascularity with color Doppler velocimetry. Previous researches did not reach an agreement about the morphology and echo of CL, which may attribute to individual difference (Pareja et al., 2010; Durfee and Frates, 2015). Therefore, we did not research the morphology and echo of CL in our study. Three-dimensional ultrasound scanning and power Doppler angiography have been introduced in clinical practice recently. This technique overcomes some limitations of conventional B-mode and color/power Doppler ultrasound scanning. It was relatively independent with high sensitivity and reproducibility, which can detect small and slow blood vessels in three-dimensional space of the CL (Martins, 2010). With the three-dimensional power Doppler ultrasound, ultrasound parameters VI, VFI, and FI can be measured and statistically analyzed in the histogram facility of the Vocal software so as to reduce the error caused by subjective judgment (Pellaers et al., 2017).

The major findings of our study were: a) the RI and PI were significantly lower in normal pregnancy group, while the D, V, VI, FI, and VFI were significantly higher; b) the AUC for ROC curve

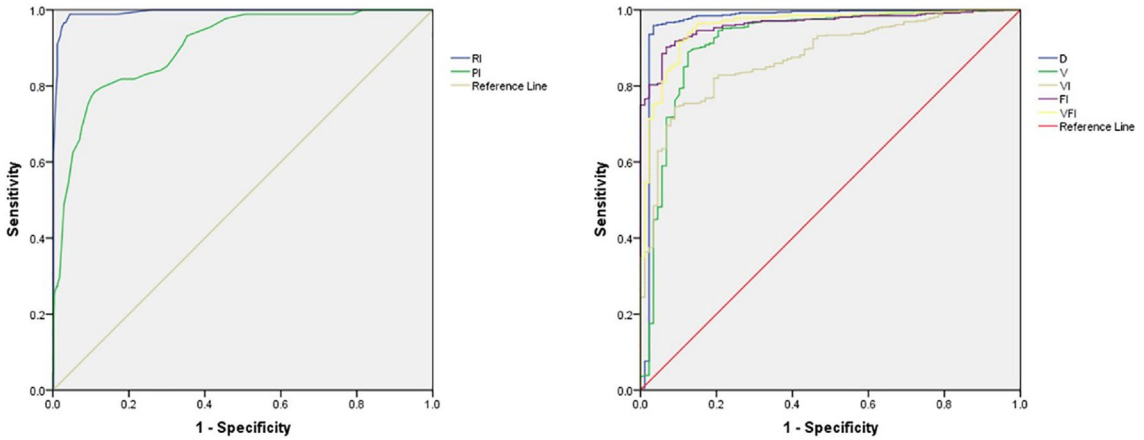

FIGURE 2 | Receiver operator characteristic (ROC) curves for RI, PI, D, V, VI, FI, and VFI. RI indicates the resistance index; PI, the pulsatility index; D, the average diameter of the corpus luteum; V, corpus luteum volume; VI, Vascularization index; FI, blood flow index; and VFI, vascularized blood flow index.

TABLE 3 | AUC for ROC curves for D, RI, PI, V, VI, FI, and VFI.

Variable	AUC	95% CI
D (mm)	0.970	0.940–1.000
RI	0.992	0.985–0.999
PI	0.903	0.870–0.936
V (mm^3)	0.917	0.877–0.985
VI	0.875	0.840–0.910
FI	0.962	0.948–0.977
VFI	0.957	0.935–0.979

AUC indicates areas under the curve; ROC, receiver operator characteristic; CI, confidence interval; D, the average diameter of the corpus luteum; RI, the resistance index; PI, the pulsatility index; V, corpus luteum volume; VI, vascularization index; FI, blood flow index; and VFI, vascularized blood flow index.

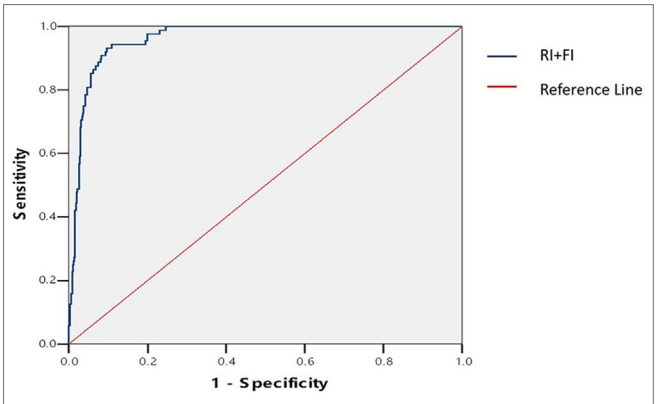

FIGURE 3 | ROC curve for joint parameter (RI+FI). RI indicates the resistance index; and FI, blood flow index.

of RI among the two-dimensional parameters and FI among three-dimensional parameters were significantly higher; c) the joint indicator of RI and FI was not superior to individual RI or FI in the prediction of early intrauterine pregnancy outcomes. Our results were in accordance with the previous study (Pareja et al., 2010),

TABLE 4 | AUC for ROC curve for RI, FI, and RI+FI.

Variable	AUC	95% CI	*P* value
RI	0.992	0.985–0.999	<0.05*
FI	0.962	0.948–0.977	<0.05†
RI+FI	0.963	0.948–0.978	–

**P < 0.05 versus RI+FI; †P > 0.05 versus RI+FI; AUC indicates areas under the curve; CI, confidence interval; RI, the resistance index; and FI, blood flow index.*

when comparing the diameter and volume of the CL of normal pregnant women with those who aborted, found lower diameter and volume in cases of abortion. Many studies had demonstrated that RI and PI were significantly higher in patients of abortion (Applebaum, 1995; Durfee and Frates, 2015). RI is an indicator of blood circulation resistance. The smaller the RI value, the more abundant the blood flow. In the study by Zhang et al. (2016), VI, FI, and VFI were significantly higher in normal pregnancy group, which was consistent with our study. On contrary, Ahmad et al. (2015) found there was no significant difference by comparing the VI between those who aborted and those with good outcome. As the reflection of the degree of vascular blood supply, the higher VI, FI, and VFI are, the richer newborn blood vessels are within the CL (Alcãzar, 2008). This is consistent with our findings. The joint indicator of RI and FI was not superior in the prediction of early intrauterine pregnancy outcomes, with an AUC not significantly higher. It is probably because either RI or FI has higher specificity and sensitivity. From the results of the study, among all the parameters, the RI and FI can better reflect the blood perfusion of the CL and have a high guiding value for prognosis estimation of pregnant outcomes. The findings in our study may be helpful for obstetricians and gynecologists in early diagnosis, timely prevention, and effective therapy of spontaneous abortions.

There are certain limitations in our study. Firstly, the fetus of group B did not undergo karyotype analysis, although the incidence of aneuploid pregnancy is relatively low. Secondly, it is prone to bring errors in the identification of the contour edge of

CL by manual tracing which will affect the software's calculation of the volume and blood perfusion. Therefore, we should improve the above operations as much as possible to get more accurate statistical results in the future research.

CONCLUSION

Both transvaginal two-dimensional and three-dimensional ultrasonography are of high diagnostic value in predicting the early intrauterine pregnancy outcomes. Therefore, they provide a useful tool for early and accurate diagnosis and guiding for treatment timely in clinic.

ETHICS STATEMENT

This study was carried out in accordance with the recommendations of World Health Organization guidelines with written informed consent from all subjects. All subjects gave written informed consent in accordance with the Declaration of Helsinki. The protocol was approved by the Ethical Committee of Shanghai Changning Maternity and Infant Health Hospital.

AUTHOR CONTRIBUTIONS

HH and XM performed the literature review. HH and YZ carried out echocardiography measurements. YZ and BZ checked the validity of data. HH and YM analyzed the data. BZ supported the experiments financially. HH, XM and YM wrote the manuscript. XM and YM revised the manuscript. All authors read and approved the final manuscript.

FUNDING

The study was funded by the Pudong Health Bureau of Shanghai (Grant No. PWZbr2017-09), and the National Natural Science Foundation of China (Grant No. 81401428, 81571693, and 81871361).

ACKNOWLEDGMENTS

The authors thank the staff at the Department of Ultrasound of Shanghai Changning Maternity and Infant Health Hospital for their sincere help.

REFERENCES

Ahmad, R. A., Sadek, S. M., and Abdelghany, A. M. (2015). 3D power Doppler ultrasound characteristics of the corpus luteum and early pregnancy outcome. *Middle East Fertil. Soc. J.* 20 (4), 280–283. doi: 10.1016/j.mefs.2015.04.004

Alcāzar, J. L. (2008). Three-dimensional power Doppler derived vascular indices: what are we measuring and how are we doing it? *Ultrasound Obstet. Gynecol.* 32 (4), 485–487. doi: 10.1002/uog.6144

Applebaum, M. (1995). Corpus luteum blood flow in normal and abnormal early pregnancy: evaluation with transvaginal color and pulsed Doppler sonography. *J. Ultrasound Med.* 14 (10), 756. doi: 10.7863/jum.1995.14.10.756

Baba, S., Noda, H., Nakayama, M., Waguri, M., Mitsuda, N., and Iso, H. (2011). Risk factors of early spontaneous abortions among Japanese: a matched case–control study. *Hum. Reprod.* 26 (2), 466–472. doi: 10.1093/humrep/deq343

Dinelli, L., Courbiere, B., Achard, V., Jouve, E., Deveze, C., Gnisci, A., et al. (2014). Prognosis factors of pregnancy after intrauterine insemination with the husband's sperm: conclusions of an analysis of 2,019 cycles. *Fertil. Steril.* 101 (4), 994–1000. doi: 10.1016/j.fertnstert.2014.01.009

Durfee, S. M., and Frates, M. C. (2015). Sonographic spectrum of the corpus luteum in early pregnancy: gray-scale, color, and pulsed Doppler appearance. *J. Clin. Ultrasound* 27 (2), 55–59. doi: 10.1002/(SICI)1097-0096(199902)27:2<55::AID-JCU1>3.3.CO;2-K

Duru, S., and Nagadeepti, N. (2013). Luteal insufficiency in first trimester. *Indian J. Endocrinol. Metab.* 17 (1), 44–49. doi: 10.4103/2230-8210.107834

Guiot, C., Gaglioti, P., Oberto, M., Piccoli, E., Rosato, R., and Todros, T. (2008). Is three-dimensional power Doppler ultrasound useful in the assessment of placental perfusion in normal and growth-restricted pregnancies? *Ultrasound Obstet. Gynecol.* 31 (2), 171–176. doi: 10.1002/uog.5212

Hassold, T., Chen, N., Funkhouser, J., Jooss, T., Manuel, B., Matsuura, J., et al. (2012). A cytogenetic study of 1000 spontaneous abortions. *Ann. Hum. Genet.* 44 (2), 151–164. doi: 10.1111/j.1469-1809.1980.tb00955.x

Henriquez, S., Kohen, P., Xu, X., Veenstra, T. D., Munoz, A., Palomino, W. A., et al. (2016). Estrogen metabolites in human corpus luteum physiology: differential effects on angiogenic activity. *Fertil. Steril.* 106 (1), 230–+. doi: 10.1016/j.fertnstert.2016.03.003

Jarvela, I. Y., Ruokonen, A., and Tekay, A. (2008). Effect of rising hCG levels on the human corpus luteum during early pregnancy. *Hum. Reprod.* 23 (12), 2775–2781. doi: 10.1093/humrep/den299

Jarvela, I. Y., Sladkevicius, P., Tekay, A. H., Campbell, S., and Nargund, G. (2003). Intraobserver and interobserver variability of ovarian volume, gray-scale and color flow indices obtained using transvaginal three-dimensional power Doppler ultrasonography. *Ultrasound Obstet. Gynecol.* 21 (3), 277–282. doi: 10.1002/uog.62

Jokubkiene, L., Sladkevicius, P., and Valentin, L. (2012). Ovarian size and vascularization as assessed by three-dimensional grayscale and power Doppler ultrasound in asymptomatic women 20-39 years old using combined oral contraceptives. *Contraception* 86 (3), 257–267. doi: 10.1016/j.contraception.2011.12.013

Lek, S. M., Ku, C. W., Allen, J. C., Jr., Malhotra, R., Tan, N. S., Østbye, T., et al. (2017). Validation of serum progesterone <35nmol/L as a predictor of miscarriage among women with threatened miscarriage. *Bmc Pregnancy Childbirth* 17 (1), 78–84. doi: 10.1186/s12884-017-1261-4

Matteo, M., Serviddio, G., Massenzio, F., Scillitani, G., Castellana, L., Picca, G., et al. (2010). Reduced percentage of natural killer cells associated with impaired cytokine network in the secretory endometrium of infertile women with polycystic ovary syndrome. *Fertil. Steril.* 94 (6), 2222–2227, 2227.e2221–2223. doi: 10.1016/j.fertnstert.2010.01.049

Martins, W. P. (2010). Three-dimensional power Doppler: validity and reliability. *Ultrasound Obstet. Gynecol.* 36 (5), 530–533. doi: 10.1002/uog.8836

Martins, W. P., Raine-Fenning, N. J., Leite, S. P., Ferriani, R. A., and Nastri, C. O. (2011). A standardized measurement technique may improve the reliability of measurements of endometrial thickness and volume. *Ultrasound Obstet. Gynecol.* 38 (1), 107–115. doi: 10.1002/uog.9016

Niswender, G. D., Juengel, J. L., Silva, P. J., Rollyson, M. K., and McIntush, E. W. (2000). Mechanisms controlling the function and life span of the corpus luteum. *Physiol. Rev.* 80 (1), 1–29. doi: 10.1152/physrev.2000.80.1.1

Pareja, O. S., Urbanetz, A. A., Urbanetz, L. A., de Carvalho, N. S., and Piazza, M. J. (2010). Echographic characteristics of the corpus luteum in early pregnancy: morphology and vascularization. *Braz. J. Gynecol Obstet.* 32 (11), 549–555. doi: 10.1590/S0100-72032010001100006

Pellaers, D., Schiffer, V., Gruiskens, G., Van Kuijk, S., Ghossein, C., Spaanderman, M., et al. (2017). P17.09: Assessment and validation of a novel three-dimensional power Doppler VOCAL sonobiopsy technique. *Ultrasound Obstet. Gynecol.* 50 (S1), 210–210. doi: 10.1002/uog.18173

Sgs, D. T., Gda, G., Bashir, S. T., Gastal, M. O., Apgar, G. A., and Gastal, E. L. (2017). Follicle vascularity coordinates corpus luteum blood flow and progesterone production. *Reprod. Fertil. Dev.* 29 (3), 448. doi: 10.1071/RD15223

Tamanini, C., and De, A. M. (2010). Angiogenesis in developing follicle and corpus luteum. *Reprod. Domest. Anim.* 39 (4), 206–216. doi: 10.1111/j.1439-0531.2004.00505.x

Tamura, H., Takasaki, A., Taniguchi, K., Matsuoka, A., Shimamura, K., and Sugino, N. (2008). Changes in blood-flow impedance of the human corpus luteum throughout the luteal phase and during early pregnancy. *Fertil. Steril.* 90 (6), 2334–2339. doi: 10.1016/j.fertnstert.2007.10.056

Wang, L., Hu, C., and Wu, J. (2015). Analysis of the treatment of threatened abortion caused by corpus luteum insufficiency and the correlation between serum progesterone levels and pregnancy outcomes. *Prog. Obstet. Gynecol.* 24 (1), 40–43. doi: 10.13283/j.cnki.xdfcjz.2015.01.011

Wathes, D. C., Taylor, V. J., Cheng, Z., and Mann, G. E. (2003). Follicle growth, corpus luteum function and their effects on embryo development in postpartum dairy cows. *Reproduction* 61 (1), 219–237. doi: 10.1530/rep.0.1230067

Zhang, T., Lin, X. Y., Zhong, W. M., Wang, Z. X., Bin, N. I., and Xiao-Hong, H. E. (2016). Clinical analysis of transvaginal three-dimensional power Doppler ultrasound on early intrauterine pregnancy of corpus luteum. *Hainan Med. J.* 27 (16), 2661–2664. doi: 10.3969/j.issn.1003-6350.2016.16.028

Conflict of Interest Statement: The authors declare that the research was conducted in the absence of any commercial or financial relationships that could be construed as a potential conflict of interest.

frontiers in Pharmacology

ORIGINAL RESEARCH
published: 18 April 2019
doi: 10.3389/fphar.2019.00326

Focused Ultrasound Improves NK-92MI Cells Infiltration Into Tumors

Chaopin Yang[1,2], Meng Du[1,2], Fei Yan[3] and Zhiyi Chen[1,2]**

[1] Department of Ultrasound Medicine, Laboratory of Ultrasound Molecular Imaging, The Third Affiliated Hospital of Guangzhou Medical University, Guangzhou, China, [2] Experimental Center, The Liwan Hospital of the Third Affiliated Hospital of Guangzhou Medical University, Guangzhou, China, [3] Paul C. Lauterbur Research Center for Biomedical Imaging, Institute of Biomedical and Health Engineering, Shenzhen Institutes of Advanced Technology, Chinese Academy of Sciences, Shenzhen, China

The efficiency of natural killer (NK) cells, adoptively transferred, for treatment against solid tumors is hindered by their difficulty to enter tumors from the blood circulation as well as their inability to prolong viability in the absence of IL-2. Among different sources of NK cells, we used genetically modified NK-92MI cells, a suitable candidate which can release IL-2 to maintain their viability and overcome undesirable side effects caused by systemic administration of exogenous IL-2. In this study, we evaluated whether the combination of focused ultrasound (FUS) and microbubbles can improve adoptively NK-92MI cell infiltration into ovarian tumors through biodistribution, immunofluorescence, and flow cytometry. The treatment effects of using this strategy twice a week were explored. The potential molecular mechanism of FUS assisting NK cell therapy was also initially explored through evaluating the expression of ICAM1 and CX3CL1 by qRT-PCR. Our results indicated that FUS and microbubbles can improve NK-92MI cells' infiltration into tumors, and the combination of FUS and NK-92MI cells had a better treatment effect compared to the PBS group, but not compared to the NK-92MI group. The qRT-PCR results also showed that CX3CL1 may be involved in the process of FUS-assisted NK cell infiltration. These results indicate that further optimization of the FUS-assisted strategy is still needed to achieve therapeutic benefit.

Keywords: natural killer cells, IL-2, focused ultrasound, microbubbles, ovarian cancer

OPEN ACCESS

Edited by:
Ali H. Eid,
American University of Beirut, Lebanon

Reviewed by:
Hao-Li Liu,
Chang Gung University, Taiwan
Virginie Papadopoulou,
University of North Carolina at Chapel Hill, United States
Jean-Michel Escoffre,
INSERM U1253Imagerie et Cerveau (iBrain), France

****Correspondence:***
Zhiyi Chen
winchen@vip.126.com
Fei Yan
fei.yan@siat.ac.cn

Specialty section:
This article was submitted to Translational Pharmacology, a section of the journal Frontiers in Pharmacology

Received: *04 January 2019*
Accepted: *19 March 2019*
Published: *18 April 2019*

Citation:
Yang C, Du M, Yan F and Chen Z (2019) Focused Ultrasound Improves NK-92MI Cells Infiltration Into Tumors. Front. Pharmacol. 10:326. doi: 10.3389/fphar.2019.00326

INTRODUCTION

Natural killer (NK) cells are the first line of the body's defense against tumors and play critical roles in tumor cell immunotherapy (Cheng et al., 2013; Davis et al., 2015). Specifically for tumor therapy, there are various sources of NK cells that can be used for NK cell therapy, such as iPSC-derived NK cells, peripheral blood mononuclear cells, cord blood-derived NK cells and NK cell lines (NK-92 and NK-92MI). Among them, NK-92MI is a preferable choice because it is "off-the-shelf," homogenous and easy to expand to satisfy the clinical demands. NK-92MI cells can secrete sufficient quantities of bioactive IL-2, a pivotal cytokine which has proved to be able to activate NK-lymphocytes and enhance immunity against cancer as well as to proliferate and mediate the antitumor effects in the absence of exogenous IL-2. Normal NK cell adoptive therapy often needs

intravenous IL-2 to maintain vitality, but administration of high dose IL-2 intravenously will cause serious side effects including fever, chills, hypotension, or tachycardia (Ardizzoni et al., 1994; Kilbourn et al., 2015; Mao et al., 2015), while low-dose IL-2 efficacy is limited by the short half-life (less than 10 min) *in vivo* (Donohue and Rosenberg, 1983). Therefore, stable expression of the IL-2 transgene in NK cells can improve their therapeutic potential in tumor-bearing hosts and avoid the above side effects.

Natural killer cell immunotherapies have proved to be effective for some hematologic malignancies such as acute myeloid leukemia, but the anti-tumor effect of NK cell therapy against solid tumors remains poor. One main reason is the inadequate homing of infused NK cells to the tumor site. It has been demonstrated that increasing the number of NK cells in tumors yields a better prognosis for certain cancers (Ishigami et al., 2000; Murray and Lundqvist, 2016). Patients with a high level of NK cell infiltration were often also found to have a better prognosis than those with a low level of NK cell infiltration (Ishigami et al., 2000; Mamessier et al., 2011; Rusakiewicz et al., 2013; Gras et al., 2015). Therefore, it is important to boost the homing potential of adoptively transferred NK cells.

Ultrasound-mediated microbubble destruction (UTMD) is a promising method that could enhance the release of drugs, genes, nanoparticles, and even cells from vasculature to tumor tissues. The interaction of ultrasound with the microbubbles in vessels can affect the integrity of the tight junctional-complexes through opened intercellular clefts or can stimulate the tumor vasculature for transcytosis, being particularly useful for drug and gene delivery into target tissue (Sheikov et al., 2004, 2008; Deng et al., 2012; Lammertink et al., 2015). The UTMD technique was the most applied technique in drug delivery; for example, Yan et al. (2013) used PTX-liposome loaded microbubbles to increase PTX fourfold in 4T1 tumors. Burke et al. (2014) used 5FU-NP-loaded microbubbles to have twofold decrease in tumor volumes and improve survival compared to 5FU alone. UTMD was also widely used to open the blood-brain barrier and promote

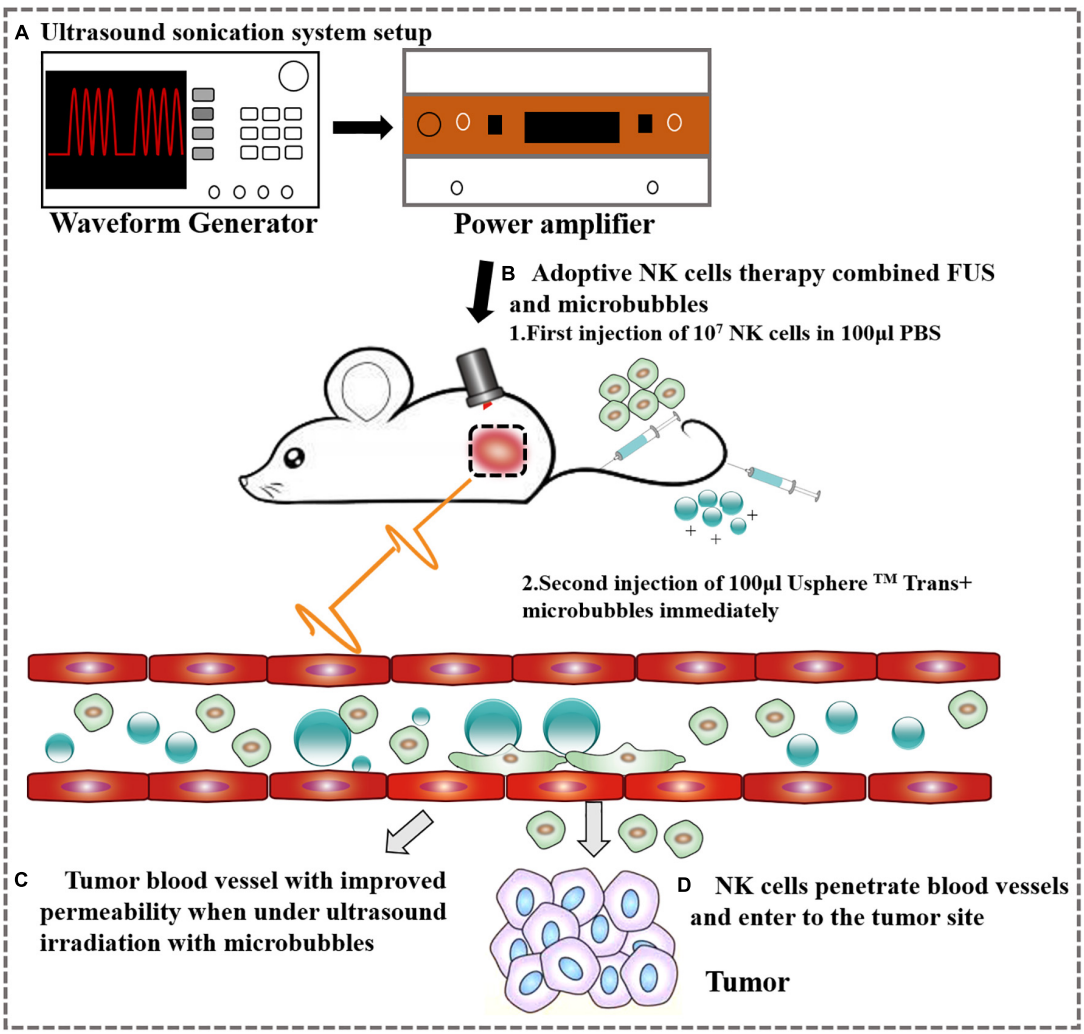

FIGURE 1 | A schematic representation of the ovarian cancer treatment with FUS and NK cells. **(A)** Ultrasound sonication system setup. **(B)** Adoptive therapy of NK cells. **(C)** Tumor blood vessel with improved permeability after ultrasound irradiation. **(D)** NK cells extravasate from the tumor vessel following FUS.

drug and gene delivery to the brain (Burgess and Hynynen, 2016). Lin used UTMD to open the blood-brain tumor barrier and successfully deliver liposome consisted of luciferase and glial cell line-derived neurotrophic factor (GDNF) genes to the brain (Lin et al., 2016). Fan et al. (2016) also used cationic microbubbles to load GDNF genes combined with focused ultrasound (FUS) to gain a neuroprotection effect in a Parkinson's disease xenograft. Arvanitis et al. explored the delivery of two anticancer drugs (doxorubicin and ado-trastuzumab emtansine) into an orthotopic xenograft model of breast cancer brain metastasis using UTMD. Sevenfold and twofold increases for these two drugs in tumor growth were observed compared to the non-FUS group (Arvanitis et al., 2018).

Besides drug and gene delivery, a few reports have also shown the potential of UTMD in favoring immune cell delivery. Alkins et al. (2013a,b) demonstrated that using MRI-guided FUS and microbubbles can deliver targeted NK-92 cells to the desired regions of the brain. Early intensive treatment (daily treatments in the first 5 days) with targeted NK-92 cells and ultrasound could improve long-term survival in 50% of subjects compared with either treatment alone. Sta et al. (2015) also used low dose FUS with microbubbles (ldbFUS with 0.50 MPa peak acoustic pressure) to facilitate the targeting and accumulation of NK cells in a mouse xenograft of human colorectal adenocarcinoma NSG mice in the presence of an anti-CEA immunocytokine (ICK), hT84.66/M5A-IL-2 (M5A-IL-2).

To improve the anti-tumor effect of NK cells for ovarian tumors through enhancing the numbers of NK cells into tumors and to prolong viability of NK cells without administration of exogenous IL-2, in this study, we investigated whether UTMD can assist adoptive NK-92MI cells to accumulate into ovarian tumors from blood vessels, and further explored the treatment effects of the combination of UTMD and NK-92MI cells in ovarian tumor xenograft.

MATERIALS AND METHODS

Mice

The Institutional Animal Care and Use Committee (IACUC) of Guangzhou Medical University approved this research study. All procedures were approved by the IACUC. NOD-Prkdc^{em26}Il2rg^{em26}/Nju (NCG) female mice (4–6 weeks old from Nanjing Biomedical Research Institute of Nanjing University, NBRI) were subcutaneously injected with SKOV3 tumor cells combined with matrigel matrix (Corning, United States) in a ratio of 1:1 (5×10^6 cells in 0.2 ml) at the right flank site. Animals were treated approximately 14 days post-implantation, when the tumors reached 50–100 mm^3.

Twenty animals with SKOV3 tumors (5 animals for each group) were grouped as follows: (group 1) PBS, (group 2) FUS, (group 3) NK-92MI, and (group 4) FUS and NK-92MI cells. On the day of treatment, animals were assigned to receive PBS,

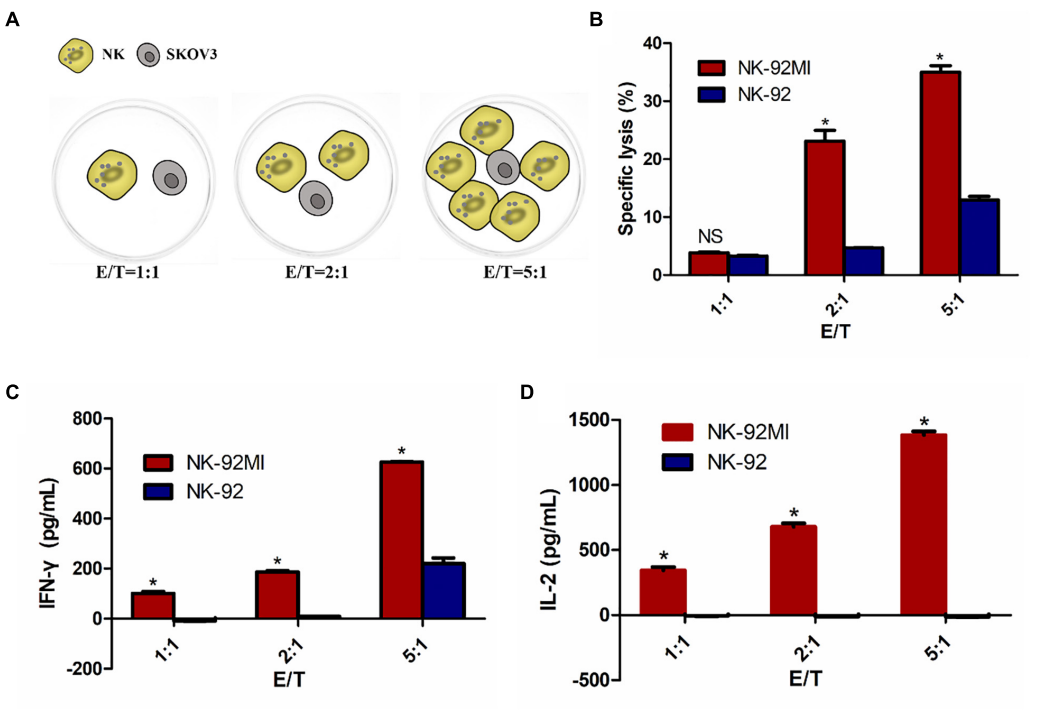

FIGURE 2 | NK-92 and NK-92MI cytotoxicity assay on ovarian cancer cells SKOV3. **(A)** Schematic representation of NK cells against SKOV3 cells. E/T, effector (NK cells) to target (SKOV3 cells) ratio. **(B)** Cell killing by NK-92 and NK-92MI were investigated after co-incubation with SKOV3 cells as targets for 6 h at different effector to target ratios. **(C)** IFN-γ release by NK-92 and NK-92MI in the presence of SKOV3 using a standard ELISA assay. **(D)** IL-2 release by NK-92 and NK-92MI in the presence of SKOV3 using a standard ELISA assay. Statistical analysis by Student's *t*-test.*$P < 0.05$ was considered statistically significant.

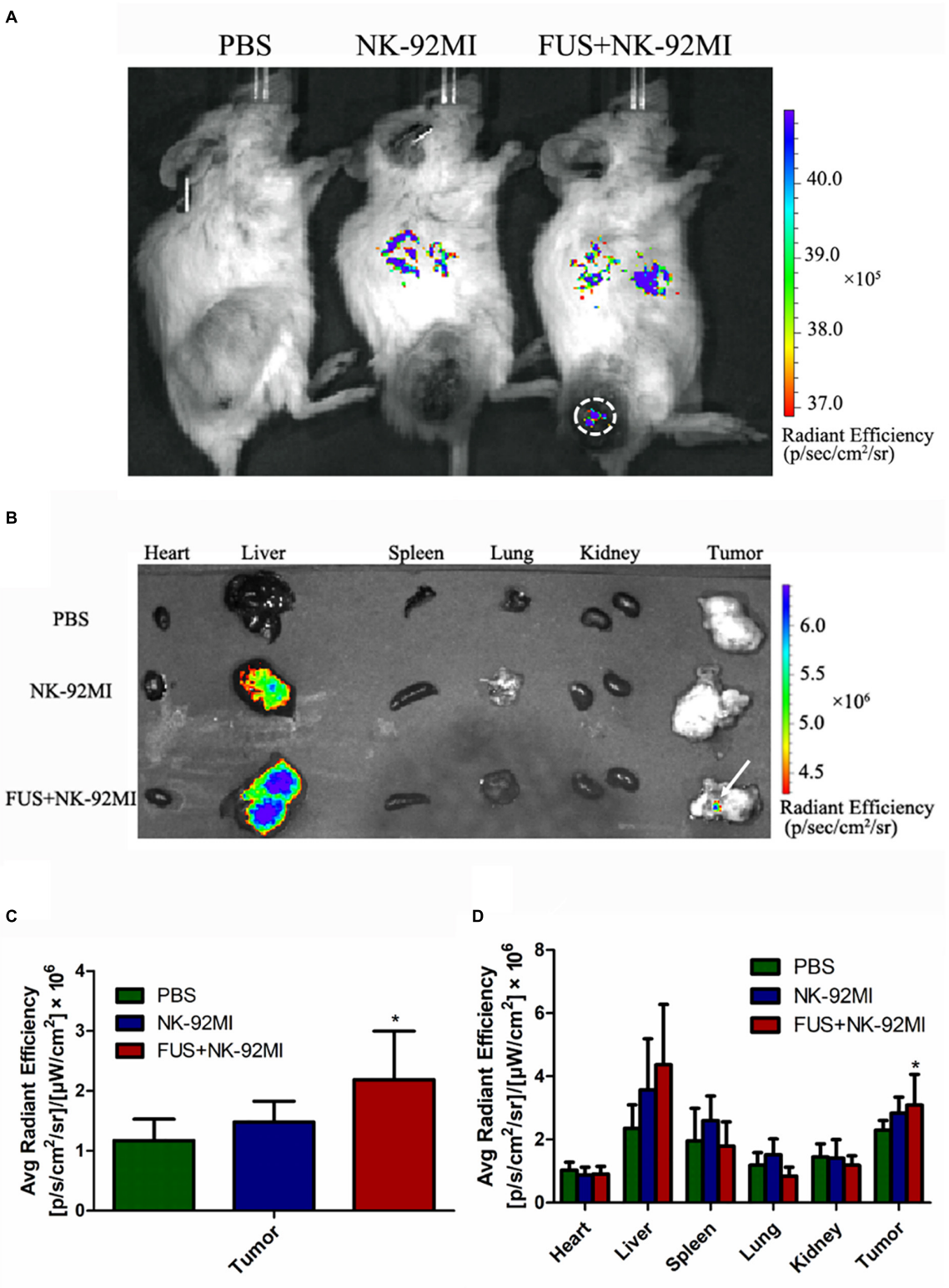

FIGURE 3 | Biodistribution of NK-92MI in xenograft ovarian tumor model. **(A)** NCG female mice were subcutaneously injected with SKOV3 cells. On day –14, the tumors were allowed to grow to 70–100 mm^3. Mice were randomly divided into three groups (PBS, NK-92MI, and FUS+NK-92MI). Then, animals were treated by intravenous injection of 10^7 NK-92MI stained with DiR dye. The biodistribution of NK-92MI was assessed with Caliper Spectrum IVIS system. **(B)** Special DiR tissue fluorescence for each organ was quantified using the Caliper Spectrum IVIS system. **(C)** Quantification analysis of fluorescent intensity in the PBS, NK-92MI

(Continued)

FIGURE 3 | Continued
and FUS+NK-92MI groups from panel **(A)**. The tumor site of the FUS+NK-92MI group has stronger fluorescent intensity compared with the PBS and NK-92MI groups. **(D)** Quantification analysis of fluorescent intensity from different organs in panel **(B)**. The tumor site of the FUS+NK-92MI group has stronger fluorescent intensity compared with the PBS and NK-92MI groups. $^{*}P < 0.05$ was considered statistically significant.

FUS, NK-92MI and a combination of FUS and NK-92MI cells. For (group 2), the mice received intravenous injection of 100 μl Usphere^{TM} Trans+ microbubbles (Trust Bio Sonics, Taiwan). For (group 4), NCG mice had NK-92MI cells injected immediately prior to FUS interacted with microbubbles. The mice were treated twice a week. Tumor volume and the mice weight were measured every time before treatment. The tumor volume was calculated using the formula V = (1/2 × length × width × width) before each treatment.

Cells Lines

NK-92 and NK-92MI (which was virally transduced to stably express IL-2) cells were purchased from ATCC. NK-92MI cells were maintained in MEMα (Invitrogen, Carlsbad, CA, United States) supplemented with 12.5% horse serum (gibco, United States), 12.5% fetal bovine serum (gibco, United States), 0.2 mM inositol, 0.1 mM β-mercaptoethanol, 0.02 mM folic acid and penicillin/streptomycin. NK-92 was cultured based on the NK-92MI culture medium, and 100–200 U/ml recombinant IL-2 was added. Human ovarian cancer cell lines SKOV3 were maintained in DMEM basic supplemented with 10% fetal bovine serum and penicillin/streptomycin.

Cellular Cytotoxicity Assay

Natural killer cell-mediated cellular cytotoxicity was determined using a non-radioactive cellular cytotoxicity assay kit (Promega, United States). In a round bottom 96-well plate (Corning Inc.) 100 μl of NK-92MI cells at effector-to-target ratios (means ratios of NK-92MI cells to SKOV3 cells) of 1:1, 2:1, and 5:1 were incubated at 37°C with 5% CO_2 for 6 h. The target spontaneous release (SKOV3), culture medium background, target maximum release (add lysis solution to SKOV3 before 45 min from the end of the incubation) and volume correction control (10 μl lysis solution and 100 μl culture medium) were operated according to the manufacturer's instructions. After the incubation, the 96-well plate was centrifuged at 250 *g* for 2 min, the supernatants (100 μl each) were removed to a new flat bottom 96-well plate for detection. The absorbance was read in microplate at 490 nm after the end of the reactions. All experiments were performed in triplicate. Specific lysis (%) was calculated as % Cytotoxicity = (Experimental spontaneous-Effector spontaneous-Target spontaneous)/(Target maximum-Target spontaneous) × 100%.

IFN-γ and IL-2 Release Assay

The total of 1×10^6 of NK cells per well were co-incubated with SKOV3 cells in 96-well plates at ratios of 1:1, 2:1, and 5:1 for 6 h at 37°C. The culture supernatants were assayed for IFN-γ or IL-2 secretion by enzyme-linked immunosorbent assay (ELISA) using a kit from R&D Systems according to the manufacturer's protocol. Data depicted in figures represent mean values of

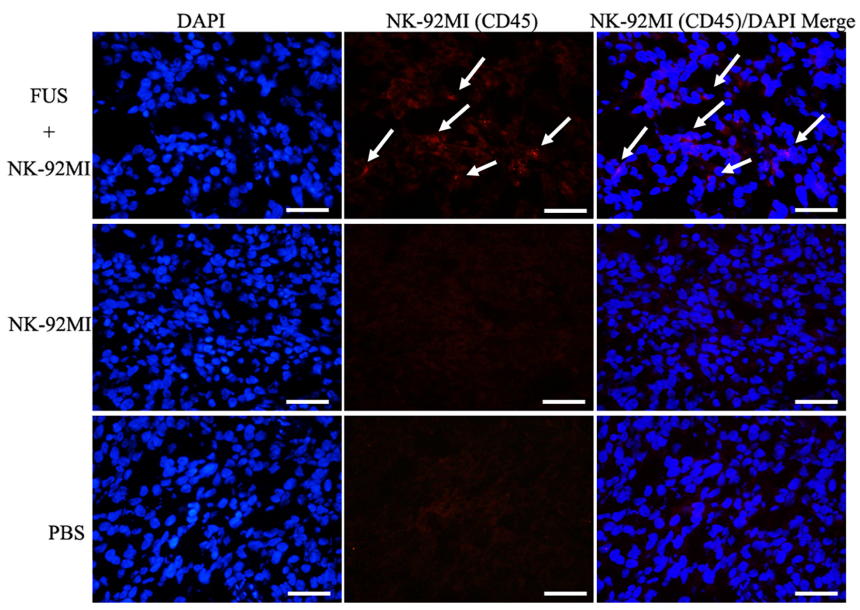

FIGURE 4 | Immunofluorescence evaluation of NK-92MI cells in tumor. Anti-CD45-Cy3 (Red) staining of tumor regions show accumulation of NK-92MI cells (white arrows) in the FUS+NK-92MI group. Nuclei were stained with DAPI (Blue). Scale bar: 50 μm.

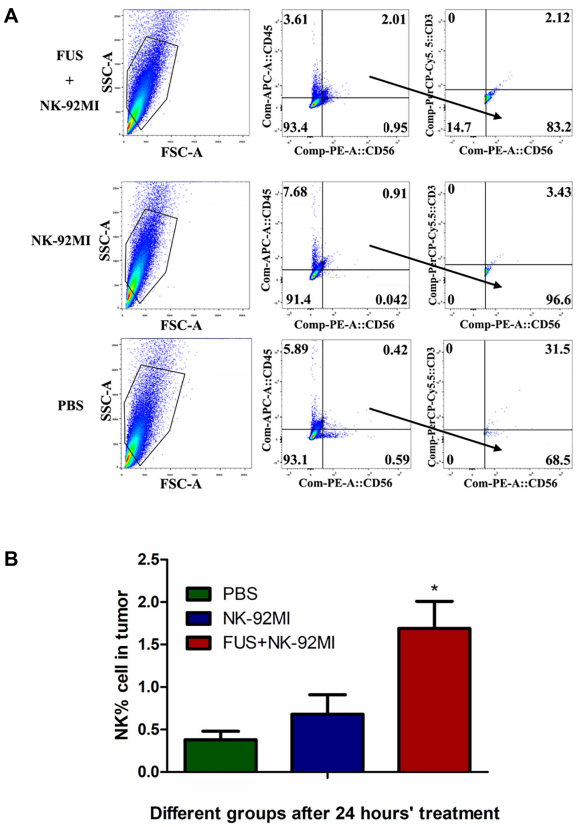

FIGURE 5 | Flow cytometry evaluation of NK-92MI cell numbers from single tumor cell suspension in different treatment groups. **(A)** Single tumor cell suspension of different groups was assessed through flow cytometry. The CD56+CD45+CD3- cells were recognized as NK cells. **(B)** The number of NK-92MI cells in the FUS+NK-92MI group was significantly higher than those in the PBS and NK-92MI groups. $^*P < 0.05$ was considered statistically significant ($n = 3$ for each group).

triplicate wells from one of three representative experiments with similar results.

Flow Cytometry to Detect NK Cells Number in Peripheral Blood and Tumor

The following antibodies were used: CD56-PE, CD45-APC, CD3-PercpCy5.5, all from Becton Dickson. Flow cytometry was done on a BD FACS Aria^{TM} III and data were analyzed using FlowJo software (BD).

Briefly, venous whole blood was collected into vacutainer tubes containing heparin. Then 100 μl whole blood was transferred into epoxy epoxide tube and incubated with CD56-PE, CD45-APC, CD3-PercpCy5.5 for 30 min in dark. Then 100 μl whole blood was added to 2 ml BD Lysing Buffer to lyse red blood cells for 15–30 min until solution clarification. The whole blood was further centrifuged in 500 g for 5 min. Then, the cell precipitation was washed. The solution was replaced with 350 μl PBS. Samples were collected on BD FACS Aria III cytometer, and the data were analyzed using FlowJo software.

Tumors were minced with a razor blade as much as possible, then incubated in collagenase IV (Sigma: #C5138), 0.1 mg hyaluronidase (Diamond:A005477), and 200 U DNase I (Sigma:#D5025) DPBS with Mg^{2+}/Ca^{2+} at 37°C for 1–2 h to make single cells. Then the mixture was stained with antibodies against human CD56-PE, CD45-APC, and CD3-PercpCy5.5. Samples were collected on BD FACS Aria^{TM} III cytometer, and data were analyzed using BD FACS Aria^{TM} III Cytometer software and FlowJo software.

RT-qPCR

Total RNA was extracted from tumor tissues using the RNeasy Kit (Servicebio, China). The primers for the analysis were synthesized by Servicebio. The primer sets used are the following: GAPDH: F, 5′-ACTTTGGTATCGTGG AAGGACTCAT-3′, R, 5′-GTTTTTCTAGACGGCAGGTCAGG-3′; CX3CL1: F, 5′-GGGAATGGACGAGTCTGTGG-3′, R, 3′-ACGGGAGGCACTCGGAAAA-5′; ICAM1: F, 5′-CCGTTG CCTAAAAAGGAGTTGC-3′, R, 3′-TGGCAGCGTAGGGTAA GGTTC-5′. Quantitative real-time PCR was performed using fluorescent dye SYBR green Supermix according to the manufacturer's instructions. Amplification was performed on a Bio-Rad FFX96 Real-time System. GAPDH was used as an internal control and the ΔΔCT method was used to calculate changes in fold expression as fold increase ($2^{-\Delta CT}$), where ΔCT = CT (Target gene)-CT (GAPDH).

Histological Analysis

Animals were sacrificed by excessive anesthesia. Tumors were removed and fixed in 10% paraformaldehyde. Prior to cutting sections, the block was allowed to equilibrate to 20°C. Tissue blocks were sectioned at 18 μm thickness. Sections from the same blocks were also stained for anti-CD45 fluorescence markers (546 nm) and DAPI. Images from sections were captured using Zeiss upright widefield microscope and ZEN software. Mice that received Dir-NK cells underwent the same procedure for tissue preparation and sectioning. Immunohistochemistry results are observed using the confocal microscopy. The Cy3 fluorescence of CD45 expression (mouse anti-human, 1:200, BD, United States) represents the NK-92MI cells.

Cardiotoxicity

The heart tissues were harvested after the last injection over 1 week and fixed in 4% paraformaldehyde. The tissues were frozen and then cut into sections and mounted onto glass slides, then stained with H&E. Finally, the H&E-stained sections of heart tissue were imaged with light microscopy (Nikon Ti, Japan) and examined for safety problems by FUS and NK-92MI cells. Cardiotoxicity was defined as myofibrillar loss and disarray, as well as cytoplasmic vacuolization.

FUS Therapy System and *in vivo* FUS Therapy

A focused transducer (1.0 MHz, IBG0112, ndtXducer, United States; SF = 1.75″, Diameter 38 mm) was used for all ultrasound exposures. The system consists of a function

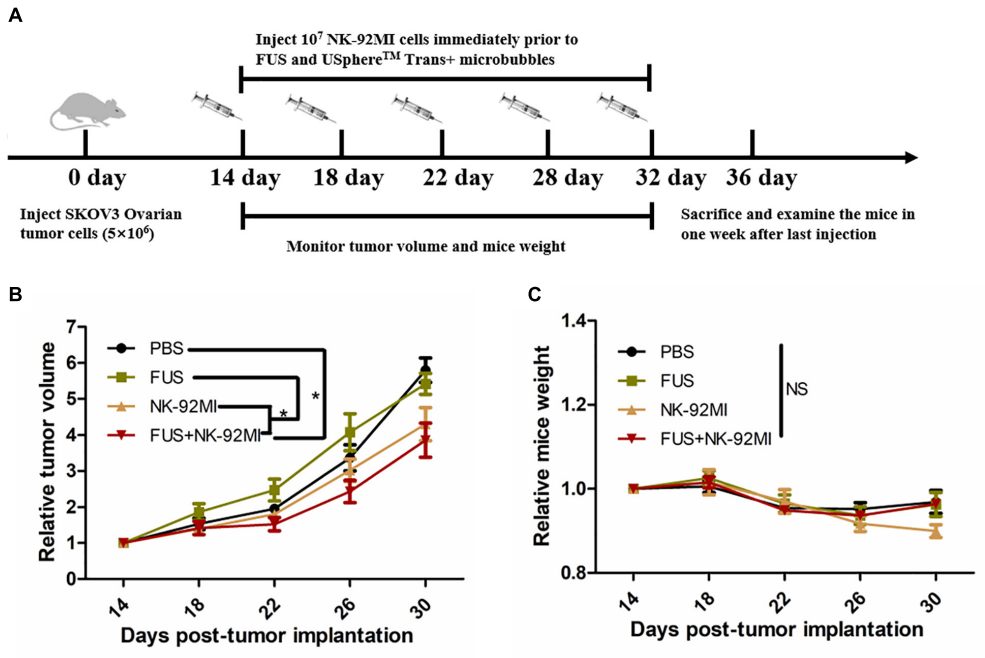

FIGURE 6 | FUS delivery of NK-92MI cells inhibits SKOV3 tumor growth. **(A)** Schematic of *in vivo* studies using FUS interacted with microbubbles assisted adoptive NK cells to treat SKOV3 tumors in a mouse xenograft NCG mice. **(B)** Relative tumor volumes in NK-92MI cell-based treatment. **(C)** Relative mice weight in NK-92MI cells-based treatment, respectively. Statistical analysis by repeated measure ANOVA. $^*P < 0.05$ was considered statistically significant ($n = 5$ for each group).

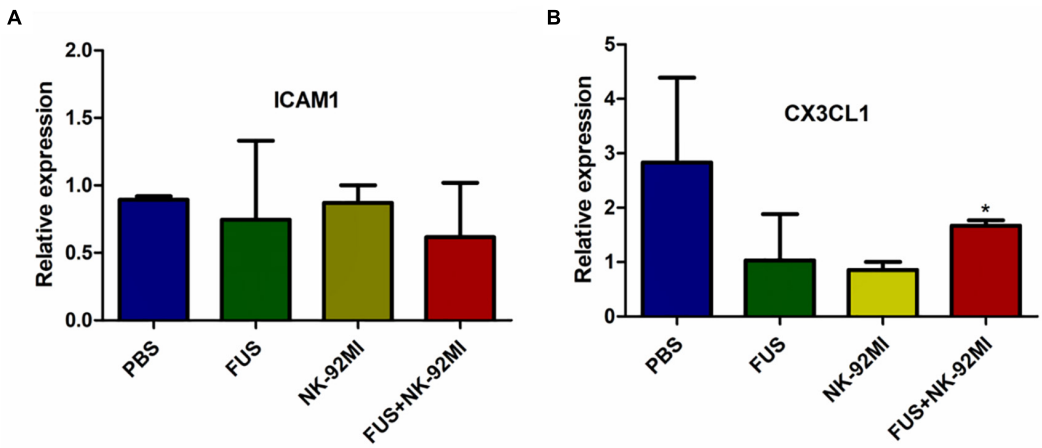

FIGURE 7 | qRT-PCR analysis of ICAM1 and CX3CL1 expression 24 h after treatment. **(A,B)** ICAM1 and CX3CL1 expression 24 h after treatment, respectively. No relative expression of ICAM1 was observed. CX3CL1 expression in the FUS+NK-92MI group was higher than in the NK-92MI group, but not different from PBS and FUS group. $^*P < 0.05$ was considered statistically significant.

generator Tektronix AFG3102C drove 120 mV (cycles 100, interval 1 ms) and an Amplifier Research (AR) RF amplifier 200A400A is the model of amplifier 60%–a transducer is capable of delivering focused and spatiotemporally controlled ultrasound energy. An ultrasound test tank system (Precision Acoustics Ltd., United Kingdom) equipped with a hydrophone (2010, Precision Acoustics Ltd., Dorchester, United Kingdom) in degassed water was used to calibrate the negative peak rarefication pressure of the focused transducer. It was found that the focused transducer could deliver 0.5 MPa in 10% duty cycle if set up according to the parameters above.

The mouse was placed on the table and the coupling cone was positioned on the tumor with ultrasound transmission gel. The transducer was used to scan the tumor manually at its frequency (1 MHz) for 10 ms every second for 1 min. During the 1 min of ultrasound, 100 μl USphere^{TM} Trans^{+} microbubbles (0.8–1.5 μm, 1–4 × 10^{10} particles/ml) and 100 μl of 10^7 NK cells were delivered via a tail vein catheter (**Figure 1**). The USphere^{TM}

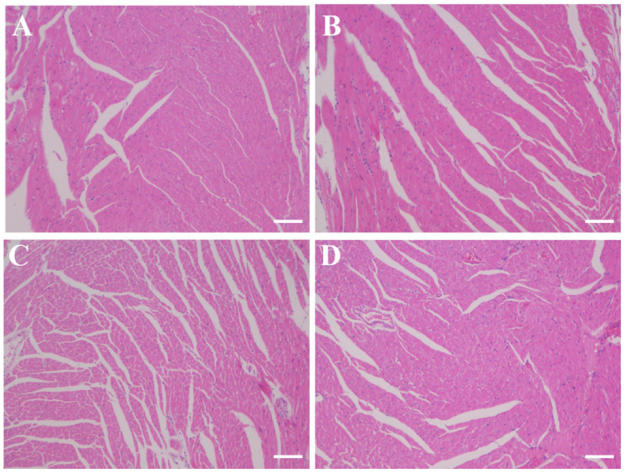

FIGURE 8 | Histology slides for cardiac toxicity in different treatment groups **(A)** PBS group; **(B)** FUS group; **(C)** NK-92MI group; **(D)** FUS+NK-92MI group). Cardiac tissues were fixed and frozen, and sections were mounted on glass slides. The frozen sections were stained with H&E and examined by light microscopy for morphological analysis. Only one representative image from each group was shown. Scale bar: 100 μm.

Trans^{+} microbubbles were bought from Trust Bio Sonics, with a diameter of 0.8–1.5 μm and a concentration of 2–6 × 10^{10} particles/ml–the potential was +40∼+50 mV. The microbubbles were diluted 1.5 times with PBS before used.

Statistical Analysis

All graphs were created using GraphPad Prism 6 (GraphPad Software Inc.), and the statistical analyses were carried out using SPSS software (version 22.0, SPSS, Chicago, IL, United States). The cellular cytotoxicity assays of NK cells against SKOV3 were repeated three times. The IFN-γ and IL-2 release assays were also repeated at least three times for at least three independent samples. The standard deviations were indicated as error bars in each graph, and the data were analyzed by Student's *t*-test. The results of tumor volumes and mice weight were analyzed with one-way repeated measures ANOVA to compare different treatment effects in different groups. *P*-values less than 0.05 (with asterisk) were considered statistically significant, and no asterisk meant the result was not significant. The continuous data were presented as mean ± SEM. Data from all experiments were representative of at least three experiments unless otherwise indicated.

RESULTS

NK-92MI Cells Have Stronger Cytotoxic Effects Against SKOV3 Cells *in vitro*

To determine whether IL-2 expression could confer NK-92 with enhanced IFN-γ production and cytolytic activity, we assessed cytotoxicity of NK-92MI and NK-92 cells against SKOV3 cells using an LDH assay at varying ratios of effector cells to target cells (1:1, 2:1, and 5:1). Cell lysis was proportional to the ratios of effector-to-target cells, consistent with both previously published reports (Li et al., 2017; Zhang et al., 2017). The results showed significantly enhanced cytotoxicity of NK-92MI cells against SKOV3 cells compared with NK-92 cells (**Figure 2**).

There was 34.51% specific lysis at an E/T ratio of 5:1 for NK-92MI cells (**Figure 2B**). A corresponding increase in the expression of IFN-γ and IL-2 at an E/T ratio of 5:1 for NK-92MI cells was observed–648.40 and 1383.37 pg/ml, respectively (**Figures 2C,D**). In contrast, there was no IL-2 secretion for NK-92 cells (**Figure 2D**).

FUS Can Enhance Accumulation of NK Cells in Ovarian Cancer Xenograft

We performed a biodistribution study to determine whether FUS can enhance NK cells homing to the tumor site. The fluorescent dye lipophilic carbocyanine $DiOC_{18}$ (Murray and Lundqvist, 2016) (DiR) was used to label NK-92MI cells and to track their presence *in vivo*. Mice were intravenously injected with PBS, and NK-92MI cells were stained with DiR or the combination of FUS, and NK-92MI cells were stained with DiR. The DiR-labeled NK cells *in vivo* were imaged at 24 h after the injection by IVIS Spectrum. The *in vivo* imaging results showed that the FUS + NK-92MI cell group had more NK-92MI cells compared to the NK-92MI and PBS groups in the tumor sites ($P < 0.05$) (**Figures 3A,C**). The DiR fluorescence for each organ was also quantified using the IVIS Spectrum imaging system, and the majority of NK-92MI cells accumulated in the liver. Nevertheless, the bioluminescence signals of NK cells in the tumor were detectable in the FUS+NK-92MI group and had much stronger signals compared to the NK-92MI and PBS groups ($P < 0.05$) (**Figures 3B,D**). These results could be further verified by immunofluorescence with anti-CD45-Cy3 (red) and DAPI (blue) (**Figure 4**).

The NK cells in tumor tissue after 24 h were also quantified with CD45+CD56+CD3- through flow cytometry, and about 1.69 ± 0.32% NK-92MI in all cells were detected in tumor tissue (**Figure 5**). The number of NK-92MI cells into the tumor was increased 2.5-fold compared to the NK-92MI cell group with the combination of FUS (**Figure 5B**). No NK cells in the blood were detected.

Tumor Progression

Totally, only tumor volumes in the FUS+NK-92MI group were statistically smaller than the PBS group ($P < 0.05$) (**Figure 6**). However, the tumor volumes in the FUS+NK-92MI group were not significantly smaller than the NK-92MI group. More NK-92MI cells did enter into the tumor with the assistance of FUS compared to the NK-92 MI group, which was proved previously by immunofluorescence and flow cytometry results in this study. These conflicting results may be explained by the fact that the NK cells that entered into tumor still had not reached a high enough number to work effectively in the FUS+NK-92MI group. Another possibility could be that the NK cells that entered the tumor were suppressed by the tumor microenvironment. It

was not expected that the tumor volumes in the NK-92MI or FUS+NK-92MI groups were statistically smaller than the FUS group. It was intriguing that tumor volumes in the FUS group appeared to have a faster growth rate than the PBS group initially.

There were no significant differences in mice weight in different groups ($P > 0.05$) (**Figure 6C**). However, the mice weight in the FUS+NK-92MI group appeared to have a weight loss compared with other groups (although without significant differences), which indicated that the FUS+NK-92MI group may undertake the anti-tumor effect.

The Relationships Between FUS Treatment and ICAM1 and CX3CL1 Expression

In this study, we used RT-qPCR to evaluate the expression of intercellular adhesion molecule 1 (ICAM1) and chemokine (C-X3-C motif) ligand 1 (CX3CL1). We investigated whether the effect of FUS-combined microbubbles could induce ICAM1 expression. ICAM1 plays an important role for tissue homing and residency within ICAM-rich endothelial vessels. Our results showed that ICAM1 expression in the PBS, NK-92MI and FUS+NK-92MI groups 24 h after treatment had no differences between each other (**Figure 7A**). Interestingly, we found that the CX3CL1 expression of the FUS+NK-92MI group was significantly higher than the NK-92MI group 24 h after treatment ($P < 0.05$) (**Figure 7B**), which meant that the combination therapy can stimulate CX3CL1 expression.

Cardiotoxicity Results

No damage of the cardiac tissues in any of the treatment groups was observed (**Figure 8**).

DISCUSSION

In this study, we demonstrated that FUS interacting with microbubbles could promote intravenous NK-92MI cells to enter a tumor. The results of flow cytometry using $CD56^{+}CD45^{+}CD3^{-}$ revealed that the ratio of NK-92MI to tumor cells in the tumor was $1.69 \pm 0.32\%$, which was similar to two other studies the NK cell to brain tumor cell ratio in the blood-brain barrier (BBB) opening with UTMD is 1:100 (Alkins et al., 2013a) whereas the NK cell to human colorectal adenocarcinoma cell ratio in blood tumor barriers opening with UTMD is $1.21 \pm 0.32\%$ (Sta et al., 2015).

The mechanism of how FUS and microbubbles facilitated cells to accumulate into the tumor is still not clear. Most studies focusing on the BBB opening believed that it was the sterile inflammatory response (SIR) caused by stable oscillations or possibly inertial cavitation, which increases the cytokines, chemokines, trophic factors (CCTF) and cell adhesion molecules (CAM) expression in the parenchymal microenvironment (Gadani et al., 2015; Kovacs et al., 2015). These cytokines can attract immune cells to the inflammatory sites (Maghazachi, 2010; Czaja, 2014; Kondo et al., 2015). In these studies, we used qRT-PCR to assess ICAM1 and CX3CL1 expression. There were no significant differences for the ICAM1 expression after 24 h. CX3CL1 is chemokines that can induce NK cell migration (El-Shazly et al., 2013; Ponzetta et al., 2013). It was interesting that FUS could enhance the CX3CL1 expression when combined with NK-92MI cells. The combined method could improve the CX3CL1 expression and further attract NK cells into tumor. However, the molecular mechanism of FUS and microbubbles were explored only initially in this study. Different time points after FUS treatment and transcriptome analysis need to be further explored to reveal the related mechanism in a much more comprehensive manner (Kovacs et al., 2017; Yang et al., 2017). It is important to figure out the key molecular basis for NK cells' homing being assisted by FUS and to further improve the UTMD's efficiency.

Other studies reported that SIR following increased BBB relied on microbubble doses, only pFUS+Definity at 100 μl/kg resulted in a clear activation of the NFκB signaling pathways, which is associated with inflammatory pathways, while 10 μl/kg did not elevate the NFκB pathways (El-Shazly et al., 2013). Thus, the microbubble doses may be another important factor that should be considered in improving the efficiency of UTMD (McMahon and Hynynen, 2017). Additionally, chemokine's receptors modifying NK cells is also a novel strategy to improve the NK cells' homing to tumors (Somanchi et al., 2012; Kremer et al., 2017).

It was consistent with our hypothesis that the FUS+NK-92MI group had a much better effect compared to the PBS group, which indicated that IL-2 played an important role in the function of NK cells *in vivo*. However, the FUS+NK-92MI group showed no significant differences compared to the NK-92MI group alone. When compared with Alkins' research, the treatment therapy only succeeded when the tumor volume was small and treated in an intensive way early on (daily treatment in first 5 days) (Alkins et al., 2013b). Failures were observed when treatment was twice per week. These results indicated that adopting intensive early treatment may also be necessary for NK-92MI cells, even for NK cells with IL-2 genetic modification. When treating a small tumor burden, the ultrasound irradiation can irradiate most part of the tumor. However, when the tumor grew bigger, FUS could not irradiate the whole tumor, and necrosis without blood vessels in bigger tumors will also influence the NK cells' delivery efficiency. Some studies developed a method to irradiate the whole tumor by irradiating every 1-mm grid extending over the entire tumor volume and improving the irradiation time to 5 min (Bandyopadhyay et al., 2016). The *in vitro* cellular cytotoxicity assay in this study showed that when the ratio of E/T was 2:1, the cytotoxicity of NK-92MI cells will work. Thus, further study should focus on the optimization of microbubble dosage, ultrasound irradiation time or treatment intensity to have therapeutic benefit.

CONCLUSION

In conclusion, we demonstrated that the combination of FUS and microbubbles could increase the NK-92MI cells' infiltration into tumors in this study. The combination of FUS and NK-92MI

had a much better therapeutic effect when compared with the PBS group, but no superior therapeutic effect when compared with the NK-92MI group. In total, FUS and microbubbles can improve NK cells' infiltration into tumors, but future work is still needed to improve NK-92MI cells' delivery efficiency for solid tumor treatment.

ETHICS STATEMENT

This study was carried out in accordance with the recommendations of Institutional Animal Care and Use Committee (IACUC) of Guangzhou Medical University.

AUTHOR CONTRIBUTIONS

CY, FY, and ZC designed the study. CY and MD performed the experimental work. CY were dealt the manuscript and data analysis, and drafted the manuscript. FY and ZC revised the manuscript.

FUNDING

This work was supported by the National Natural Science Foundation of China (No. 81671707), the Natural Science Foundation of Guangdong Province (Nos. 2016A030311054 and 2018A030313678), Research Projects of Guangzhou Science Technology and Innovation Commission (No. 201607010201), and Research Fund for Lin He's Academician Workstation of New Medicine and Clinical Translation.

ACKNOWLEDGMENTS

We thank Dr. Hong Pan from Shenzhen Institutes of Advanced Technology, Chinese Academy of Sciences, particularly for samples and data analysis for FACs data acquisition.

REFERENCES

Alkins, R., Burgess, A., Ganguly, M., Francia, G., Kerbel, R., Wels, W. S., et al. (2013a). Focused ultrasound delivers targeted immune cells to metastatic brain tumors. *Cancer Res.* 73, 1892–1899. doi: 10.1158/0008-5472.CAN-12-2609

Alkins, R., Burgess, A., Kerbel, R., Wels, W. S., and Hynynen, K. (2013b). Early treatment of HER2-amplified brain tumors with targeted NK-92 cells and focused ultrasound improves survival. *Neuro. Oncol.* 18, 974–981. doi: 10.1158/0008-5472

Ardizzoni, A., Bonavia, M., Viale, M., Baldini, E., Mereu, C., Verna, A., et al. (1994). Biologic and clinical effects of continuous infusion interleukin-2 in patients with non-small cell lung cancer. *Cancer* 73, 1353–1360. doi: 10.1002/1097-0142(19940301)73:5<1353::AID-CNCR2820730508>3.0.CO;2-H

Arvanitis, C. D., Askoxylakis, V., Guo, Y., Datta, M., Kloepper, J., Ferraro, G. B., et al. (2018). Mechanisms of enhanced drug delivery in brain metastases with focused ultrasound-induced blood-tumor barrier disruption. *Proc. Natl. Acad. Sci. U.S.A.* 115, E8717–E8726. doi: 10.1073/pnas.1807105115

Bandyopadhyay, S., Quinn, T. J., Scandiuzzi, L., Basu, L., Partanen, A., Tomé, W. A., et al. (2016). Low-intensity focused ultrasound induces reversal of tumor-induced T Cell tolerance and prevents immune escape. *J. Immunol.* 196, 1964–1976. doi: 10.4049/jimmunol.1500541

Burgess, A., and Hynynen, K. (2016). Microbubble-assisted ultrasound for drug delivery in the brain and central nervous system. *Adv. Exp. Med. Biol.* 880, 293–308. doi: 10.1007/978-3-319-22536-4_16

Burke, C. W., Alexander, E. T., Timbie, K., Kilbanov, A. L., and Price, R. J. (2014). Ultrasound-activated agents comprised of 5FU-bearing nanoparticles bonded to microbubbles inhibit solid tumor growth and improve survival. *Mol. Ther.* 22, 321–328. doi: 10.1038/mt.2013.259

Cheng, M., Chen, Y., Xiao, W., Sun, R., and Tian, Z. (2013). NK cell-based immunotherapy for malignant diseases. *Cell. Mol. Immunol.* 10, 230–252. doi: 10.1038/cmi.2013.10

Czaja, A. J. (2014). Review article: chemokines as orchestrators of autoimmune hepatitis and potential therapeutic targets. *Aliment. Pharmacol. Ther.* 40, 261–279. doi: 10.1111/apt.12825

Davis, Z. B., Felices, M., Verneris, M. R., and Miller, J. S. (2015). Natural killer cell adoptive transfer therapy: exploiting the first line of defense against cancer. *Cancer J.* 21, 486–491. doi: 10.1097/PPO.0000000000000156

Deng, J., Huang, Q., Wang, F., Liu, Y., Wang, Z., Zhang, Q., et al. (2012). The role of caveolin-1 in blood-brain barrier disruption induced by focused ultrasound combined with microbubbles. *J. Mol. Neurosci.* 46, 677–687. doi: 10.1007/s12031-011-9629-9

Donohue, J. H., and Rosenberg, S. A. (1983). The fate of interleukin-2 after in vivo administration. *J. Immunol.* 130, 2203–2208.

El-Shazly, A. E., Doloriert, H. C., Bisig, B., Lefebvre, P. P., Delvenne, P., and Jacobs, N. (2013). Novel cooperation between CX3CL1 and CCL26 inducing NK cell chemotaxis via CX3CR1: a possible mechanism for NK cell infiltration of the allergic nasal tissue. *Clin. Exp. Allergy* 43, 322–331. doi: 10.1111/cea.12022

Fan, C. H., Ting, C. Y., Lin, C. Y., Chan, H. L., Chang, Y. C., Chen, Y. Y., et al. (2016). Noninvasive, targeted, and non-viral ultrasound-mediated GDNF-plasmid delivery for treatment of parkinson's disease. *Sci. Rep.* 6:19579. doi: 10.1038/srep19579

Gadani, S. P., Walsh, J. T., Lukens, J. R., and Kipnis, J. (2015). Dealing with danger in the CNS: the response of the immune system to injury. *Neuron* 87, 47–62. doi: 10.1016/j.neuron.2015.05.019

Gras, N. A., Bjorklund, A. T., and Chekenya, M. (2015). Therapeutic potential and challenges of natural killer cells in treatment of solid tumors. *Front. Immunol.* 6:202. doi: 10.3389/fimmu.2015.00202

Ishigami, S., Natsugoe, S., Tokuda, K., Nakajo, A., Che, X., Iwashige, H., et al. (2000). Prognostic value of intratumoral natural killer cells in gastric carcinoma. *Cancer* 88, 577–583. doi: 10.1002/(SICI)1097-0142(20000201)88:3<577::AID-CNCR13>3.0.CO;2-V

Kilbourn, R. G., Fonseca, G. A., Trissel, L. A., and Griffith, O. W. (2015). Strategies to reduce side effects of interleukin-2: evaluation of the antihypotensive agent NG-monomethyl-L-arginine. *Cancer J. Sci. Am.* 6(Suppl. 1), S21–S30.

Kondo, Y., Kimura, O., Tanaka, Y., Ninomiya, M., Iwata, T., Kogure, T., et al. (2015). Differential expression of CX3CL1 in Hepatitis B virus-replicating hepatoma cells can affect the migration activity of CX3CR1+ immune cells. *J. Virol.* 89, 7016–7027. doi: 10.1128/JVI.00716-15

Kovacs, Z. I., Burks, S. R., and Frank, J. A. (2015). Focused ultrasound with microbubbles induces sterile inflammatory response proportional to the blood brain barrier opening: attention to experimental conditions. *Theranostics* 8, 2245–2248. doi: 10.7150/thno.24181

Kovacs, Z. I., Kim, S., Jikaria, N., Qureshi, F., Milo, B., Lewis, B. K., et al. (2017). Disrupting the blood-brain barrier by focused ultrasound induces sterile inflammation. *Proc. Natl. Acad. Sci. U.S.A.* 114, E75–E84. doi: 10.1073/pnas.1614777114

Kremer, V., Ligtenberg, M. A., Zendehdel, R., Seitz, C., Duivenvoorden, A., Wennerberg, E., et al. (2017). Genetic engineering of human NK cells to express CXCR2 improves migration to renal cell carcinoma. *J. Immunother. Cancer* 5:73. doi: 10.1186/s40425-017-0275-9

Lammertink, B. H., Bos, C., Deckers, R., Storm, G., Moonen, C. T., and Escoffre, J. M. (2015). Sonochemotherapy: from bench to bedside. *Front. Pharmacol.* 6:138. doi: 10.3389/fphar.2015.00138

Li, Y., Hermanson, D. L., Moriarity, B. S., and Kaufman, D. S. (2017). Human iPSC-derived natural killer cells engineered with chimeric antigen receptors enhance anti-tumor activity. *Cell Stem Cell* 23, 181–192. doi: 10.1016/j.stem.2018.06.002

Lin, C. Y., Hsieh, H. Y., Pitt, W. G., Huang, C. Y., Tseng, I. C., Yeh, C. K., et al. (2016). Focused ultrasound-induced blood-brain barrier opening for non-viral, non-invasive, and targeted gene delivery. *J. Control Release* 212, 1–9. doi: 10.1016/j.jconrel.2015.06.010

Maghazachi, A. A. (2010). Role of chemokines in the biology of natural killer cells. *Curr. Top. Microbiol. Immunol.* 341, 37–58. doi: 10.1007/82_2010_20

Mamessier, E., Sylvain, A., Thibult, M. L., Houvenaeghel, G., Jacquemier, J., Castellano, R., et al. (2011). Human breast cancer cells enhance self tolerance by promoting evasion from NK cell antitumor immunity. *J. Clin. Invest.* 121, 3609–3622. doi: 10.1172/JCI45816

Mao, Y., Sarhan, D., Steven, A., Seliger, B., Kiessling, R., and Lundqvist, A. (2015). Inhibition of tumor-derived prostaglandin-e2 blocks the induction of myeloid-derived suppressor cells and recovers natural killer cell activity. *Clin. Cancer Res.* 20, 4096–4106. doi: 10.1158/1078-0432.CCR-14-0635

McMahon, D., and Hynynen, K. (2017). Acute inflammatory response following increased blood-brain barrier permeability induced by focused ultrasound is dependent on microbubble dose. *Theranostics* 7, 3989–4000. doi: 10.7150/thno.21630

Murray, S., and Lundqvist, A. (2016). Targeting the tumor microenvironment to improve natural killer cell-based immunotherapies: on being in the right place at the right time, with resilience. *Hum. Vaccin. Immunother.* 12, 607–611. doi: 10.1080/21645515.2015.1096458

Ponzetta, A., Sciumè, G., Benigni, G., Antonangeli, F., Morrone, S., Santoni, A., et al. (2013). CX3CR1 regulates the maintenance of KLRG1^{+} NK cells into the bone marrow by promoting their entry into circulation. *J. Immunol.* 191, 5684–5694. doi: 10.4049/jimmunol.1300090

Rusakiewicz, S., Semeraro, M., Sarabi, M., Desbois, M., Locher, C., Mendez, R., et al. (2013). Immune infiltrates are prognostic factors in localized gastrointestinal stromal tumors. *Cancer Res.* 73, 3499–3510. doi: 10.1158/0008-5472.CAN-13-0371

Sheikov, N., McDannold, N., Sharma, S., and Hynynen, K. (2008). Effect of focused ultrasound applied with an ultrasound contrast agent on the tight junctional integrity of the brain microvascular endothelium. *Ultrasound Med. Biol.* 34, 1093–1104. doi: 10.1016/j.ultrasmedbio.2007.12.015

Sheikov, N., McDannold, N., Vykhodtseva, N., Jolesz, F., and Hynynen, K. (2004). Cellular mechanisms of the blood-brain barrier opening induced by ultrasound in presence of microbubbles. *Ultrasound Med. Biol.* 30, 979–989. doi: 10.1016/j.ultrasmedbio.2004.04.010

Somanchi, S. S., Somanchi, A., Cooper, L. J., and Lee, D. A. (2012). Engineering lymph node homing of ex vivo-expanded human natural killer cells via trogocytosis of the chemokine receptor CCR7. *Blood* 119, 5164–5172. doi: 10.1182/blood-2011-11-389924

Sta, M. N., Barnes, S. R., Weist, M. R., Colcher, D., Raubitschek, A. A., and Jacobs, R. E. (2015). Low dose focused ultrasound induces enhanced tumor accumulation of natural killer cells. *PLoS One* 10:e142767. doi: 10.1371/journal.pone.0142767

Yan, F., Li, L., Deng, Z., Jin, Q., Chen, J., Yang, W., et al. (2013). Paclitaxel-liposome-microbubble complexes as ultrasound-triggered therapeutic drug delivery carriers. *J. Control. Release* 166, 246–255. doi: 10.1016/j.jconrel.2012.12.025

Yang, Q., Nanayakkara, G. K., Drummer, C., Sun, Y., Johnson, C., Cueto, R., et al. (2017). Low-intensity ultrasound-induced anti-inflammatory effects are mediated by several new mechanisms including gene induction, immunosuppressor cell promotion, and enhancement of exosome biogenesis and docking. *Front. Physiol.* 8:818. doi: 10.3389/fphys.2017.00818

Zhang, Q., Tian, K., Xu, J., Zhang, H., Li, L., Fu, Q., et al. (2017). Synergistic effects of cabozantinib and EGFR-specific CAR-NK-92 cells in renal cell carcinoma. *J. Immunol. Res.* 2017:6915912. doi: 10.1155/2017/6915912

Conflict of Interest Statement: The authors declare that the research was conducted in the absence of any commercial or financial relationships that could be construed as a potential conflict of interest.

frontiers in Pharmacology

CORRECTION
published: 06 August 2019
doi: 10.3389/fphar.2019.00875

Corrigendum: Focused Ultrasound Improves NK-92MI Cells Infiltration Into Tumors

Chaopin Yang[1,2], Meng Du[1,2], Fei Yan[3] and Zhiyi Chen[1,2]**

[1] Department of Ultrasound Medicine, Laboratory of Ultrasound Molecular Imaging, The Third Affiliated Hospital of Guangzhou Medical University, Guangzhou, China, [2] Experimental Center, The Liwan Hospital of the Third Affiliated Hospital of Guangzhou Medical University, Guangzhou, China, [3] Paul C. Lauterbur Research Center for Biomedical Imaging, Institute of Biomedical and Health Engineering, Shenzhen Institutes of Advanced Technology, Chinese Academy of Sciences, Shenzhen, China

OPEN ACCESS

Approved by:
Frontiers Editorial Office, Frontiers Media SA, Switzerland

***Correspondence:**
Zhiyi Chen
winchen@vip.126.com
Fei Yan
fei.yan@siat.ac.cn

Specialty section:
This article was submitted to Translational Pharmacology, a section of the journal Frontiers in Pharmacology

Received: *24 June 2019*
Accepted: *10 July 2019*
Published: *06 August 2019*

Citation:
Yang C, Du M, Yan F and Chen Z (2019) Corrigendum: Focused Ultrasound Improves NK-92MI Cells Infiltration Into Tumors. Front. Pharmacol. 10:875. doi: 10.3389/fphar.2019.00875

Keywords: natural killer cells, IL-2, focused ultrasound, microbubbles, ovarian cancer

A Corrigendum on

Focused Ultrasound Improves NK-92MI Cells Infiltration Into Tumors.
Yang C, Du M, Yan F and Chen Z (2019) Front. Pharmacol. 10:326. doi: 10.3389/fphar.2019.00326

In the original article, the name of one author was missed in the reference for "Ponzetta, A., Sciume, G., Benigni, G., Antonangeli, F., Morrone, S., and Santoni, A. (2013). CX3CR1 regulates the maintenance of KLRG1+ NK cells into the bone marrow by promoting their entry into circulation. *J. Immunol.* 191, 5684–5694. doi: 10.4049/jimmunol.1300090." It should be "Ponzetta, A., Sciume, G., Benigni, G., Antonangeli, F., Morrone, S., Santoni, A., et al. (2013). CX3CR1 regulates the maintenance of KLRG1+ NK cells into the bone marrow by promoting their entry into circulation. *J. Immunol.* 191, 5684–5694. doi: 10.4049/jimmunol.1300090."

The authors apologize for this error and state that this does not change the scientific conclusions of the article in any way. The original article has been updated.

frontiers in Pharmacology

ORIGINAL RESEARCH
published: 03 September 2019
doi: 10.3389/fphar.2019.00960

Ultrasound-Guided Biopsy of Pleural-Based Pulmonary Lesions by Injection of Contrast-Enhancing Drugs

Ying Fu, Yuan-Yuan Zhang, Li-Gang Cui, Shi Tan and Yan Sun*

Department of Ultrasound, Peking University Third Hospital, Beijing, China

In this study, a total of 58 patients with single subpleural pulmonary lesions (males: 36, females: 22, mean age: 63 ± 16.2 years) who underwent contrast-enhanced ultrasonography (CEUS) and had a definite diagnosis (benign lesions:25, malignant lesions:33) were enrolled. The number of biopsies, diagnostic accuracy rate, and the incidence of complications were recorded. The nodules were divided into two size subgroups: ≥5 cm (group 1), and <5 cm (group 2). The display rate of internal necrosis and change of pre-scheduled puncture paths were compared between subgroups. Also, the arrival times, intensity and uniformity of enhancement after the contrast agent injection, as well as the display rate of internal necrosis were recorded and compared between malignant and benign lesions. Finally, the average number of punctures was 2.9 ± 0.7 times. The total diagnosis rate was 98.3%. Local pneumothorax occurred in 2 patients. Hemoptysis occurred in 1 patient. No serious complications occurred. Internal necrosis was demonstrated in 20 of 58 lesions (34.5%). Sixteen of them had changed the planned puncture path due to the large necrosis area (80%, 16/20). For lesions in group 1, necrosis was found in 15 lesions and there was a statistically significant difference in the necrosis rate between the two subgroups (15/26 vs 5/32, $p = 0.001$). The change in the pre-scheduled puncture path occurred in 12 patients in group 1 while 4 patients in group 2 exhibited a change in the planned puncture path ($p = 0.004$). There was a statistically significant difference in the arrival times and intensity of enhancement between benign and malignant lesions ($p < 0.05$). In conclusion, CEUS guided biopsy is an effective, sensitive, and safe method for the diagnosis of pleural-based pulmonary lesions by facilitating a distinction between necrosis and active tissue. The current findings indicated that CEUS before a biopsy may be especially vital in lesions ≥5 cm.

Keywords: contrast media, lung neoplasms, biopsy, diagnostic imaging, sonography

OPEN ACCESS

Edited by:
Fei Yan,
Shenzhen Institutes of Advanced Technology (CAS), China

Reviewed by:
Yuanyi Zheng,
Shanghai Sixth People's Hospital, China
Kun Yan,
Peking University Cancer Hospital, China

****Correspondence:***
Li-Gang Cui
cuijuegang@126.com

Specialty section:
This article was submitted to Translational Pharmacology, a section of the journal Frontiers in Pharmacology

Received: *10 November 2018*
Accepted: *29 July 2019*
Published: *03 September 2019*

Citation:
Fu Y, Zhang Y-Y, Cui L-G, Tan S and Sun Y (2019) Ultrasound-Guided Biopsy of Pleural-Based Pulmonary Lesions by Injection of Contrast-Enhancing Drugs. Front. Pharmacol. 10:960. doi: 10.3389/fphar.2019.00960

INTRODUCTION

Lung cancer is a primary cancer that has become a major public health concern. It is the most frequent cause of cancer-related mortality in men, and lung cancer-related morbidity and mortality are both increasing (Ferlay et al., 2015). The detection rate of peripheral pulmonary lesions has increased in the recent years with the application of computed tomography (CT),

especially multi-slice spiral CT, in the diagnosis of lung cancer (Swensen, 2002). Clinically, peripheral pulmonary lesions are primarily diagnosed on the basis of exfoliative sputum cytology, fiberoptic bronchoscopy, bronchoalveolar lavage, medical thoracoscopy, and needle biopsy results (Ofiara et al., 2012). Ultrasound-guided percutaneous lung biopsy has a success rate similar to that obtained with CT guidance, a lower complication rate, and a shorter operation time; also, it is more economical, does not involve radiation, and offers a more convenient puncture guidance method. This technique has gained wide acceptance in clinical conditions and shows satisfactory puncture results (Khosla et al., 2016). However, conventional ultrasonography cannot distinguish between atelectatic lung tissue and necrotic lesions, which often results in false-negative biopsy results that can confound clinical diagnosis and treatment and cause complications (Wang et al., 2015).

The new ultrasound contrast agents that have emerged in recent years have greatly increased visualization of the microcirculation on ultrasonography. SonoVue (Bracco SpA, Milan, Italy) is a second-generation ultrasound contrast agent that contains sulfur hexafluoride as a low-solubility inert gas phase surrounded by a layer of phospholipids. The microbubbles have an average diameter of 2.5 μm, and 90% of the microbubbles have a diameter of less than 6 μm. After intravenous injection, the contrast agent microbubbles enter the arterial system through the pulmonary circulation barrier and participate in systemic circulation, greatly enhancing the backscattering of sound waves. This, combined with low mechanical index ultrasound contrast imaging technology, permits a sensitive, real-time determination of tissue microcirculation and can distinguish between living areas and necrotic foci in tissues. Currently, this technique is widely used for guidance in needle biopsies of liver and thyroid nodules and has yielded satisfactory results (Wu et al., 2006; Li and Luo, 2013; Eso et al., 2016).

Lungs have a dual blood supply, which provides a pathophysiological basis for using ultrasonography to distinguish between benign and malignant lesions. The pulmonary artery blood supply phase is observed 2–6 s after the injection of a contrast agent and the bronchial artery blood supply phase is observed 7–20 s after injection (Görg et al., 2006a). Most malignant lesions are supplied by the bronchial artery, so the time phase can be used to distinguish lesions originating from lung tissue or the bronchial blood supply, thereby avoiding an unnecessary needle biopsy (Görg et al., 2006b). Contrast-enhanced ultrasonography (CEUS) can also effectively avoid necrotic tissue inside the lesion and atelectatic lung tissue at the periphery of the lesion, thereby accurately guiding the biopsy.

Previously published reports of CEUS guidance for peripheral pulmonary lesions have focused on the differences between contrast-enhanced guidance and conventional ultrasound guidance. However, they did not focus on the effects of lesion size. Thus, the purpose of our study is to examine the diagnostic efficacy of CEUS guidance for needle biopsies of peripheral pulmonary lesions, with an emphasis on the effects of nodule size on contrast-enhanced guidance.

MATERIALS AND METHODS

Patients

A total of 58 patients with peripheral pulmonary lesions diagnosed by chest CT and confirmed by pathological assessments between May 2016 and May 2018 were selected for the study. The study population consisted of 36 males and 22 females, the average age was 63 ± 16.2 years, and the average lesion size was 4.4 ± 2.7 cm. Written, informed consent was obtained from all patients prior to the CEUS and ultrasound-guided percutaneous lung biopsy. This retrospective study has been reviewed by the Institutional Review Board of Peking University Third Hospital.

Ultrasound Contrast Agent and Ultrasound Examination Procedure

All included patients were examined by CT to confirm the location of the lesions. Next, two-dimensional ultrasonography was performed to record its location and size, and conventional color Doppler ultrasonography was used to determine blood flow distribution. An ultrasound specialist with 10 years of experience marked possible intercostal puncture sites and planned needle paths. Next, a CEUS examination was performed, and the size of the lesion, the target puncture region, and the presence or absence of perfusion defects as well as their range were confirmed on the basis of lesion perfusion. This information was recorded and discussed by two physicians experienced in puncture biopsy based on the CEUS results. Once a consensus was reached, a new needle path was planned.

The ultrasound contrast agent SonoVue (Bracco, Italy), which contains sulfur hexafluoride (SF_6) enclosed in phospholipid microcapsules, was used. It was dissolved and mixed thoroughly with 5 mL normal saline, and 2.4 mL (5 mg/ml concentration, 12 mg SF_6/patient) was rapidly injected into the body through the superficial cephalic vein over 2–3 s each time. The GE Logiq 9 (GE Healthcare, Milwaukee, WI) ultrasound instrument was used with a C5-1 probe at a probe frequency of 3.0–5.0 MHz. The instrument was initialized with a low mechanical index (MI: 0.11–0.13). A timer was started at the same time the contrast agent was injected, and the changes in enhanced perfusion of the lesion were observed in real time. After imaging, the size and position of the lesions were carefully recorded based on video data. Contrast-enhanced and non-contrast-enhanced regions and their adjacencies were confirmed by observing contrast agent perfusions and the process of enhancement in the lesion. Solid enhancement regions were identified as targets for punch biopsies, and needle insertion points, needle paths, biopsy target regions, and sample lengths were confirmed. A needle biopsy was performed within 30–60 min after imaging.

Diagnosis using CEUS was performed by a physician with 5 years of experience in this technique. The main descriptive indicators included were the time of the contrast agent's arrival to the lesion on imaging, the time of its arrival to peripheral lung tissue or the intercostal artery, the uniformity of lesion enhancement, and the peak intensity. The time of arrival to the lesion on imaging refers to the time at which the lesion is filled with the contrast agent. The time of arrival to the lung

tissue is the first time when the contrast agent microbubbles fill the peripheral lung tissue. The time of arrival to the intercostal artery is the time at which the contrast agent fills the intercostal artery. The difference in arrival times between the lesion and the lung tissue was calculated. The enhancement time was close to the bronchial artery if it was greater than 3 s and close to the pulmonary artery if it was 3 s or less. The uniformity within the lesion was defined as the uniformity and consistency of the filling of the lesion with contrast agent; low uniformity indicated that the lesion was not uniformly enhanced. Peak intensity was divided into level-high enhancement and low enhancement. The reference was the degree of enhancement of the peripheral lung tissue. Enhancement equal to or higher than that of the lung tissue was deemed level-high enhancement, and enhancement lower than that of the lung tissue was deemed low enhancement.

Needle Biopsy Indications and Biopsy Method

Inclusion criteria for CEUS guidance were as follows: imaging confirms that the lesion is located at the periphery of the lungs and is visible on ultrasonography, a signed informed consent form is acquired, and no contraindications are suggested based on the instructions of the ultrasound contrast agent. Exclusion criteria were as follows: coagulopathy or bleeding diathesis, biopsy intolerance due to cardiopulmonary insufficiencies or a severe cough, the lesion is not clearly visible on ultrasonography, allergy to ultrasound contrast agents, and refusal of CEUS.

After confirming the needle path, a conventional aseptic drape was applied. Local anesthesia was achieved by injection of 1% lidocaine (Liduokayin; Yimin Pharmaceutical Co., Ltd, Beijing, China) from the upper edge of the rib between the predetermined intercostals. The patient was asked to hold his or her breath, and the biopsy needle was used to rapidly puncture the tumor margin under ultrasound guidance. The Bard automatic biopsy gun (Bard, USA) was equipped with an 18-gauge biopsy needle. The biopsy gun had a range of 15–22 mm. Areas in the lesion with significant enhancement based on imaging conditions were selected for biopsy. Collected tissues were fixed in a 10% formalin solution. Biopsies were collected 1–4 times as tolerated by the patient.

After the operation, the patient's vital signs and hemoptysis were closely observed. Follow-up complications such as hemothorax, pneumothorax, and chest pain were observed. Patient with uncomfortable symptoms underwent same-day X-ray examinations to promote the early detection of complications such as pneumothorax.

Pathological Diagnosis and Follow-Up

Two pathologists with 10 years of experience read images together and made a final determination. Benign lesions were followed up for more than 6 months to confirm shrinkage or that they did not enlarge before being diagnosed as benign. If tissue collection was insufficient, a pathological diagnosis could not be made, and the puncture biopsy was considered to have failed and needed to be re-performed. Some patients who had undergone surgical resection, such as patients whose diagnoses were not consistent with the diagnosis from surgical resection specimens, were subject to postoperative pathological diagnosis.

Observational Indices

Several indices were used in our analysis. First, the lesion time of arrival on imaging was recorded as close to the pulmonary artery or close to the bronchial artery. In addition, the uniformity of lesion enhancement, the peak intensity, presence of necrosis inside the lesion, and changes in the originally planned needle path a result of CEUS were recorded. Second, the success rate of ultrasound-guided percutaneous lung puncture biopsy and the incidence of post-biopsy complications were recorded. Third, based on their size, lesions were classified as either less than 5 cm or greater than or equal to 5 cm, and the necrosis rate and needle path change rate in the two groups were compared.

Statistical Analysis

SPSS 21.0 statistical software (IBM Corporation, Armonk, NY) was used. Continuous data are shown as the mean ± standard deviation (x ± s). The $\chi 2$ test was used for pairwise comparisons of discrete data. The independent or paired samples *t*-test was used for comparisons of differences in lesion size. Differences with $p < 0.05$ were considered statistically significant.

RESULTS

Number of Biopsy Puncture Attempts and Diagnostic Accuracy Rate

The average frequency of puncture attempts was 2.9 ± 0.7 times, and the average tissue length was 1.2 ± 0.4 cm. Pathological assessments indicated benign lesions in 25 cases and malignant lesions in 33 cases. The specific pathological types are shown in **Table 1**.

Internal necrotic foci were found in 20 cases on imaging (20/58, 34.5%). Of these, the originally planned needle path was changed in 16 cases (27.6%) due to the large extent of necrosis (**Figure 1**). Necrosis was found in 15 of 26 cases of nodules that were 5 cm or larger ($p = 0.001$), of which the original needle path was changed in 12 cases ($p = 0.004$). Necrosis was found in 5 of the 32 cases of nodules less than 5 cm in size, of which the original needle path was changed in cases (**Tables 2** and **3**). **Figure 2** showed

TABLE 1 | Pathological types of the cases.

Pathological type	Number of cases
Benign	25
Inflammation	12
Tuberculosis	5
Mycosis	2
Organizing pneumonia	6
Malignant	33
Adenocarcinoma	23
Squamous cell carcinoma	4
Small cell lung carcinoma	1
Lymphoma	1
Metastatic cancer	4

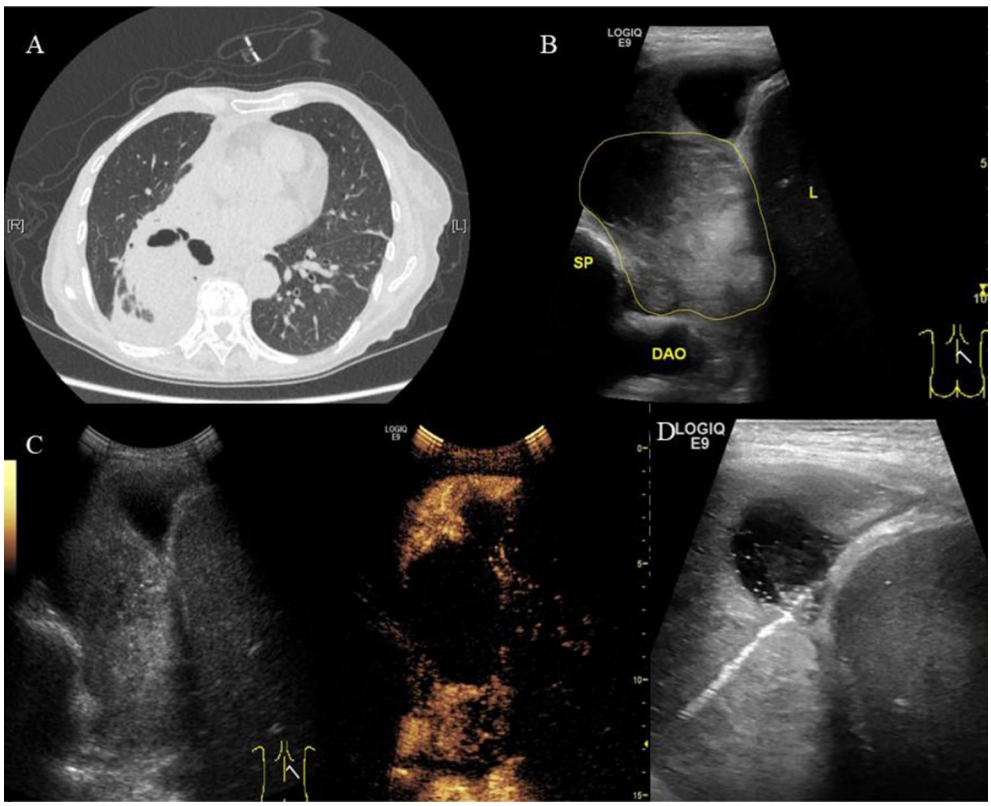

FIGURE 1 | A 70-year-old female patient was admitted to our hospital with cough, hemoptysis and fever. The representative CT image showed lung lesion in right lower lobe. **(A)** An elliptical mass with soft tissue density was presented in the basal segment of the right lower lobe, the boundary was unclear. Low density and the gas–liquid plane was observed in central region of the mass. Atelectasis was observed around the mass. **(B)** Two-dimensional ultrasound showed a hypoechoic solid mass with diameter of about 6 cm (the yellow line). The boundary of the mass was blurred. A small amount of pleural fluid was observed around the mass. DAO, descending aorta; SP, spine; L, liver. **(C)** Contrast-enhanced ultrasound showed a significantly inhomogeneous enhancement of mass. Uniform enhancement was observed in the superficial part of the mass at 9 s without enhancement in the deep part of the mass. However, the deep part of the mass was inhomogeneously enhanced at 13 s, showing a large non-enhanced necrotic area. **(D)** The superficial part of the mass may represent the atelectatic lung tissue. The necrotic tissue and alive tumor tissue respectively located in the middle and deep parts. Therefore, we targeted the deep part of the mass as puncture area for biopsy. The arrow indicated the puncture needle. The biopsy specimen was white. The pathological findings were adenocarcinoma of the lung.

TABLE 2 | Necrosis in lesions of different sizes.

Group	Necrosis found	No necrosis found	*p*-value
>5 cm	15	11	0.001
<5 cm	5	27	
Total	20	38	

TABLE 3 | Changes in the original puncture path in lesions of different sizes.

Group	Puncture path changed	No puncture path change	*p*-value
>5 cm	12	14	0.004
<5 cm	4	28	
Total	16	42	

necrosis in 58 patients with different lesion size. **Table 4** showed the patient demographics and lesion characteristics.

The success rate of biopsy procedures guided by CEUS was 98.3% (57/58 cases). In only one case, the necrotic area was too large, and the pathological results of the puncture biopsy did not yield a clear conclusion. That patient underwent surgical resection and was found to have lung adenocarcinoma.

Ultrasound Imaging Results

The average lesion size from imaging was 4.2 ± 2.8 cm, which was not significantly different from the size measured using 2-dimensional ultrasonography (p = 0.886). **Table 5** showed the imaging presentation of the lesions. The difference in enhancement time between benign and malignant cases was statistically significant (p = 0.003). The enhancement time was near the pulmonary artery in 88% of the benign cases, and only 3 of the 25 benign cases showed enhancement time near the bronchial artery. There was no statistically significant difference in the degree of uniformity and peak intensity between the two groups.

Complications

Local pneumothorax occurred in two cases and improved after conservative treatment. One patient developed hemoptysis after

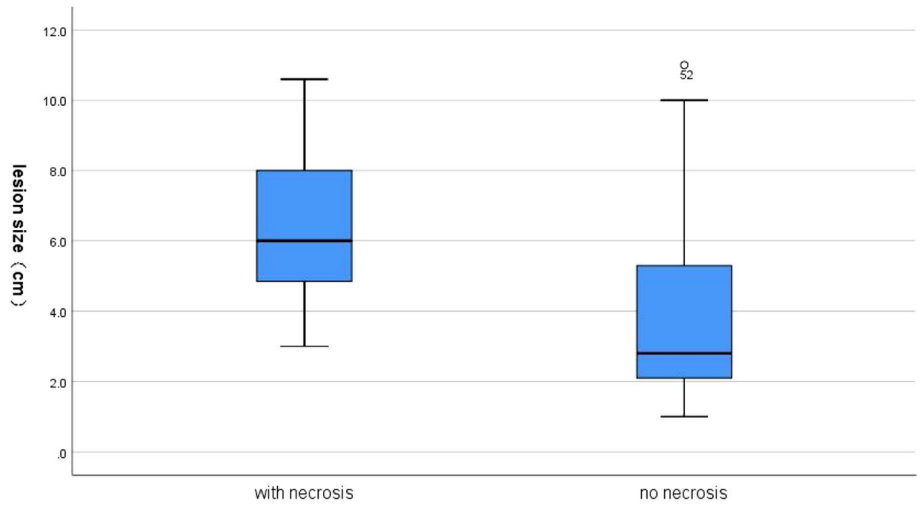

FIGURE 2 | A box-plot between necrosis and lesion size.

TABLE 4 | Patient demographics and lesion characteristics.

Characteristics	Malignant	Benign	*p*-value
Sex			0.175
Male	18	18	
Female	15	7	
Median age(years)	60.0 ± 20.0	66 ± 12.0	0.46
Median size (cm)	5.0 ± 2.9	3.5 ± 2.4	0.59
Necrosis present	12	8	0.729
the originally planned needle path changed	9	7	0.951

TABLE 5 | Lesion enhancement of cases.

Enhancement	Number of cases			*p*-value
Time to enhancement	Total	Benign	Malignant	0.003
Near pulmonary artery	39	22	17	
Near bronchial artery	19	3	16	
Uniformity				0.512
Uniform	25	12	13	
Not uniform	33	13	20	
Peak intensity				
Level-high	42	18	24	0.004
Low	16	7	9	

one needle puncture. The puncture was discontinued, and the pathology after puncture was confirmed. The complication rate was 5.17% (3/58), and no inflammatory complications occurred.

DISCUSSION

The aim of this study was to evaluate ultrasound-guided biopsies of pleural-based pulmonary lesions by injecting contrast-enhanced drugs. There were significant differences in the necrosis rate between different lesion sizes visible *via* CEUS. Therefore, a change in the pre-scheduled puncture path occurred more often in patients with lesions ≥5 cm, with statistical significance. The overall diagnosis rate was 98.3% with no serious complications. We can conclude that CEUS can distinguish necrosis and active tissue sensitively, which is helpful and crucial in improving the biopsy success rate. Furthermore, CEUS before a biopsy may be more important in lesions ≥5 cm.

Diagnostic techniques for lung cancer include chest radiography, exfoliative sputum cytology, fiberoptic bronchoscopy, and CT examination. However, the positive rates with these techniques are insufficient, and serum cancer marker measurements have not shown acceptable outcomes with respect to early diagnosis. Final diagnosis of many intrathoracic masses can only be made by a chest biopsy to collect lung tissue for pathological examination, but this is often rejected by patients and their families (Ofiara et al., 2012).

Ultrasound-guided peripheral lung puncture has recently gained gradual acceptance in clinical conditions. In comparison with traditional CT guidance, ultrasound guidance shows similar accuracy, but it does not involve radiation, is safe, can monitor the position of the needle tip at all times, can be performed at the bedside, and has a low cost. It is now widely employed in clinical practice and has been extended to the diagnosis of pleural lesions. The diagnostic rate achieved by this minimally invasive procedure is 66.6–78% (Sagar et al., 2000; Cao et al., 2011), with more false-negative findings that may be closely related to tumor size (Sartori et al., 2004). In a study of CT-guided biopsies, Yeow et al. (Yeow et al., 2003) analyzed 631 biopsy results and found that lesion sizes smaller than 1.5 cm and larger than 5 cm were closely associated with low diagnostic accuracy. The low diagnostic accuracy for lesions smaller than 1.5 cm can be easily explained by unsatisfactory sample collection through biopsy needles due to the small lesion size. In contrast, the increased necrotic regions in lesions larger than 5 cm are the main cause of false-negative findings in larger lesions. Although ultrasonography can distinguish obviously necrotic regions, not all necrotic regions are characterized as anechoic and are easily distinguished, and some necrotic regions are also hypoechoic or isoechoic (Sartori et al., 2004). Thus, 9–26% of the cases of nodules with large necrotic regions will yield insufficient data (Trevisani et al., 1994; Sagar et al., 2000). In addition,

conventional ultrasonography has a limited ability to distinguish between tumor tissue and atelectatic lung tissue.

The recent emergence of a new generation of ultrasound contrast agents has greatly improved the ability of ultrasound technology to visualize the microcirculation in lesions. The new type of ultrasound contrast agent represented by SonoVue is a pure blood pool contrast agent. It has an average diameter of 2.5 μm, which is smaller than the diameter of red blood cells, so it remains in the circulation for a long time, does not enter the interstitial space, and has good stability in blood vessels. The microscopic distribution of microbubbles in small blood vessels in tissues can be more clearly observed, which is more conducive to studies of microvascular perfusion. Finally, these microbubbles are excreted from the body by respiration, so they offer the advantages of being harmless to the human body and being extremely safe, while providing good image development efficacy. Because the components contained in the microbubbles are non-toxic, they have no effect on the liver and kidneys. Ultrasound contrast can improve the effects of imaging, primarily in low mechanical index ultrasonic scanning. Vibration does not rupture the contrast agent microbubbles, and such situations can produce nonlinear effects. This technology can receive signals from the contrast agent microbubbles, filtering out harmonic signal interference from the tissue. The technique allows for the separation of signals from the contrast agent microbubbles and tissue, overcoming the limitation of traditional color Doppler ultrasonography, which shows insensitivity to low-velocity small blood vessels. Thus, this method can provide better information for a qualitative diagnosis of tumors on the basis of the blood supply characteristics of different tumors (Lim et al., 2004).

Currently, ultrasound contrast agents have been used in the differential diagnosis of lung lesions (Sperandeo et al., 2006; Dong et al., 2015; Bai et al., 2016). The natural blood supply to the lungs is a dual blood supply. The difference in tissue vascular anatomical structure and hemodynamics between benign and malignant lesions provides a pathophysiological basis for CEUS (Görg et al., 2006b) and can help distinguish atelectatic lung tissue and lung lesions through the time phase. Most researchers believe that the pulmonary artery blood supply is mainly responsible for gas exchange in the lungs, whereas neovascularization of malignant tumors is supplied by the bronchial artery (Görg et al., 2006a; Dong et al., 2015). Görg et al. found that the time to arrival of contrast agents in malignant lesions was significantly longer than that in benign lesions (Görg et al., 2006a). Caremani et al. proposed an arrival time of 10 s as the boundary for distinguishing between benign and malignant lesions but did not provide a statistical basis for this finding (Caremani et al., 2008). Wen et al. used 8 s as the boundary between benign and malignant lesions and considered a time of arrival of more than 8 s as an indication of bronchial artery blood supply, thus defined as a malignant lesion, but the diagnostic specificity was only 73.3% (Wen et al., 2013).

Due to the complexity underlying the physiological conditions in the human body, such as the physiological anastomosis between the pulmonary arterial and the bronchial arterial circulation, the intrapleural pressure gradient, cardiac function, examination position, and other factors will affect circulatory status. In addition, some artificial factors, such as the injection rate of contrast agents by different operators, also affect the time of arrival of the contrast agent to the lesion (Sperandeo et al., 2017). Therefore, relying solely on the time of arrival to the lesion cannot completely distinguish between benign and malignant lesions.

In the present study, the method of finding the difference in the times of arrival to the lesion and to the peripheral pulmonary tissue proposed by Bai et al. (2016) was used. This eliminates the differences in the time of arrival due to differences in the circulation of different individuals, thus effectively distinguishing between benign and malignant lesions. Because the study by Bai et al. used software to distinguish the time of arrival, the boundary value was 2.5 s. This observation was made visually in the present study, and thus the boundary value was set to 3 s, which also yielded informative results. It is worth noting that there were 17 cases of malignant lesions in this study with blood supply from the pulmonary artery (**Table 4**), which may be related to factors such as lesions being mixed with atelectasis. Therefore, relying solely on CEUS findings to distinguish between benign and malignant lesions is likely to produce false-negative findings, which has also been criticized in a recently published large-scale clinical study (Sperandeo et al., 2017). This is not the primary research purpose of this paper; instead, the study aimed to determine whether puncture biopsy can be effectively guided by enhancement after increased micro-perfusion.

In addition, although there were only two cases with a pulmonary lesion and atelectatic lung tissue in our group, the time to enhancement of atelectasis was shown to be significantly earlier than that of lung cancer (**Figure 1**). Also, the extent of enhancement was higher than lung cancer. This is consistent with the literature reports. Lei et al explored the clinical value of CEUS for biopsy in patients with central lung cancer with obstructive atelectasis (Lei et al., 2018). Enhancement of the central lung cancer mass began at 10–15 s, while that of 100 cases with atelectatic lung tissue began at 6–10 s and 12 cases at 10–15 s. The peak intensity was also higher in atelectasis for the contrast media may trapped in the lung tissue after having washed out of the blood pool. By analyzing the time to enhancement and extent of enhancement, CEUS can be used for differentiating atelectasis and lung cancer. CEUS can also distinguish atelectasis of different causes, mainly obstructive atelectasis and compression atelectasis. Görg et al studied 30 patients with atelectasis using CEUS. They found CEUS showed different patterns of enhancement in compression atelectasis and obstructive atelectasis. Compression atelectasis is characterized by a high specific CEUS pattern with a short time to enhancement and a marked extent of enhancement, indicating predominant pulmonary vascularization. In patients with obstructive atelectasis, a variable CEUS pattern was found (Görg et al, 2006b). Despite the small number of cases, CEUS shows a certain ability to identify and it deserves further study.

CEUS-guided tumor biopsy has been widely used in liver, mediastinal, and thyroid tumors. Fu et al. (2016) studied the value of CEUS in puncture biopsy of anterior mediastinal tumors. They concluded that CEUS guided technique could reliably differentiate the viable regions from necrotic tissues in a lesion and identify large superficial blood vessels in anterior

medial mediastinal lesions before biopsy. Therefore, the safety and accuracy of puncture biopsy are improved.

Cao et al. (2011) conducted a comparative study of puncture biopsies of peripheral pulmonary lesions and mediastinal lesions. A diagnostic accuracy of 93.6% was achieved in 62 cases with ultrasound-guided biopsy, whereas a diagnostic accuracy of only 78% was achieved in 59 cases with conventional ultrasound guidance. The lesion necrosis rate in the CEUS group was 41.9%. The importance of CEUS in puncture biopsies of peripheral lung lesions is to distinguish between necrotic and active tissue; this was also verified in our study (necrosis rate: 34.5%). It is well known that necrotic tissue often develops in malignant lesions, and as tumor volume increases, the likelihood that necrotic tissue appears in the tumor increases. In the present study, a subgroup analysis was performed, which found that the necrosis rate in lesions 5 cm and larger was significantly higher than that in lesions smaller than 5 cm. In addition, the planned needle path was changed in most cases, indicating the necessity of preoperative CEUS for larger nodules.

In lung lesions, necrosis in benign tubercle lesions is common in addition to necrosis in malignant lesions. In the present study, four of the five patients with tuberculosis had necrosis confirmed by CEUS. Therefore, it is especially important to perform CEUS on peripheral pulmonary lesions before a puncture biopsy because it can clearly show necrotic regions without blood supply, and can also clearly depict active lesions with low-velocity blood supply. After CEUS, the position and adjacencies of the non-enhanced and enhanced regions within the lesion can be judged. During a puncture biopsy, the necrotic tissue can be avoided, and the enhanced regions with blood supply can be selected for a puncture biopsy, significantly improving the positive rate.

The advantage of CT-guided puncture biopsy is that it can puncture masses in various parts of the lung and is less restricted by location. Its disadvantages include the higher cost and the effects of radiation. The literature reports that the incidence of pneumothorax with CT guidance can reach 27–54% (Klein et al., 1996; Collings et al., 1999). The advantages of ultrasonography and CEUS guidance are that the whole puncture biopsy process is performed under direct vision. It allows for the observation of lung movements in real time, and instantly allows the patient to hold the needle after holding his or her breath, thereby facilitating the avoidance of structures such as gas-filled lungs, blood vessels, nerves, or necrotic tissue. It has low operational difficulty, can be completed in a short time, is safe and accurate, and has a low incidence of complications. Although the incidence of complications in the present study was 5.17%, they were all minor complications, and the patients improved after conservative treatment. In other studies, the incidence of complications of CEUS guidance in peripheral pulmonary disease was 3.3% or less (Cao et al., 2011; Dong et al., 2015; Wang et al., 2015). The reduced occurrence of complications may be related to the fact that the ultrasound techniques described above can monitor local conditions in real time. In addition, the low complication rate is related to the currently small number of cases of CEUS-guided pulmonary nodule puncture biopsies.

The present study has the following shortcomings: the number of cases is relatively small and the nature of the study was retrospective. However, the results of this study may greatly inspire interest, and participation, among clinicians regarding ultrasound-guided peripheral pulmonary nodule puncture techniques and provide the foundation for future large-scale prospective clinical studies.

CONCLUSION

CEUS-guided peripheral pulmonary lesion biopsy is a safe and effective technique with high patient and clinical acceptance. It can effectively distinguish between necrotic and active tissue, atelectatic lung tissue, tumor tissue, etc., thus improving the success rate of puncture biopsy. CEUS is particularly important for needle biopsies of lung lesions that are 5 cm or larger.

ETHICS STATEMENT

This study was carried out in accordance with the recommendations of the Institutional Review Board of Peking University Third Hospital, with written informed consent form all subjects. All subjects gave written informed consent in accordance with the Declaration of Helsinki. The protocol was approved by the Institutional Review Board of Peking University Third Hospital.

AUTHOR CONTRIBUTIONS

YF drafted the manuscript, coordinated data collection, analyzed the data, and reported the study results. L-GC developed the study protocol, revised the manuscript, supported in data collection, analyzed the data, and reported the study results. Y-YZ, ST, YS participated in the design of the study and revised the manuscript. All authors read and approved the final manuscript.

REFERENCES

Bai, J., Yang, W., Wang, S., Guan, R. H., Zhang, H., Fu, J. J., et al. (2016). Role of arrival time difference between lesions and lung tissue on contrast-enhanced sonography in the differential diagnosis of subpleural pulmonary lesions. *J. Ultrasound Med.* 35, 1523–1532. doi: 10.7863/ultra.15.08022

Cao, B. S., Wu, J. H., Li, X. L., Deng, J., and Liao, G. Q. (2011). Sonographically guided transthoracic biopsy of peripheral lung and mediastinal lesions: role of contrast-enhanced sonography. *J. Ultrasound Med.* 30, 1479–1490. doi: 10.7863/jum.2011.30.11.1479

Caremani, M., Benci, A., Lapini, L., Tacconi, D., Caremani, A., Ciccotosto, C., et al. (2008). Contrast enhanced ultrasonography (CEUS) in peripheral lung lesions: a study of 60 cases. *J. Ultrasound* 11, 89–96. doi: 10.1016/j.jus.2008.05.008

Collings, C. L., Westcott, J. L., Banson, N. L., and Lange, R. C. (1999). Pneumothorax and dependent versus nondependent patient position after needle biopsy of the lung. *Radiology* 210, 59–64. doi: 10.1148/radiology.210.1.r99ja1759

Dong, Y., Mao, F., Wang, W. P., Ji, Z. B., and Fan, P. L. (2015). Value of contrast-enhanced ultrasound in guidance of percutaneous biopsy in peripheral pulmonary lesions. *Biomed. Res. Int.* 2015, 531507. doi: 10.1155/2015/531507

Eso, Y., Takai, A., Takeda, H., Matsumoto, T., Lee, M., Inuzuka, T., et al. (2016). Sonazoid-enhanced ultrasonography guidance improves the quality of pathological diagnosis in the biopsy of focal hepatic lesions. *Eur. J. Gastroenterol. Hepatol.* 28, 1462–1467. doi: 10.1097/MEG.0000000000000745

Ferlay, J., Soerjomataram, I., Dikshit, R., Eser, S., Mathers, C., Rebelo, M., et al. (2015). Cancer incidence and mortality worldwide: sources, methods and major patterns in GLOBOCAN 2012. *Int. J. Cancer* 136, E359–E386. doi: 10.1002/ijc.29210

Fu, J., Yang, W., Wang, S., Bai, J., Wu, H., Wang, H., et al. (2016). Clinical value of contrast-enhanced ultrasound in improving diagnostic accuracy rate of transthoracic biopsy of anteriormedial mediastinal lesions. *Chin. J. Cancer Res.* 28, 617–625. doi: 10.21147/j.issn.1000-9604.2016.06.08

Görg, C., Bert, T., and Kring, R. (2006a). Contrast-enhanced sonography of the lung for differential diagnosis of atelectasis. *J. Ultrasound Med.* 25, 35–39. doi: 10.7863/jum.2006.25.1.35

Görg, C., Kring, R., and Bert, T. (2006b). Transcutaneous contrast-enhanced sonography of peripheral lung lesions. *AJR Am. J. Roentgenol.* 187, W420–W429. doi: 10.2214/AJR.05.0890

Khosla, R., McLean, A. W., and Smith, J. A. (2016). Ultrasound-guided versus computed tomography-scan-guided biopsy of pleural-based lung lesions. *Lung India* 33, 487–492. doi: 10.4103/0970-2113.188961

Klein, J. S., Salomon, G., and Stewart, E. A. (1996). Transthoracic needle biopsy with a coaxially placed 20-gauge automated cutting needle: results in 122 patients. *Radiology* 198, 715–720. doi: 10.1148/radiology.198.3.8628859

Lei, Z., Lou, J., Bao, L., and Lv, Z. (2018). Contrast-enhanced ultrasound for needle biopsy of central lung cancer with atelectasis. *J. Med. Ultrason.* 45, 461–467. doi: 10.1007/s10396-017-0851-0

Li, F., and Luo, H. (2013). Comparative study of thyroid puncture biopsy guided by contrast-enhanced ultrasonography and conventional ultrasound. *Exp. Ther. Med.* 5, 1381–1384. doi: 10.3892/etm.2013.1016

Lim, A. K., Patel, N., Eckersley, R. J., Taylor-Robinson, S. D., Cosgrove, D. O., and Blomley, M. J., (2004). Evidence for spleen-specific uptake of a microbubble contrast agent: a quantitative study in healthy volunteers. *Radiology* 231, 785–788. doi: 10.1148/radiol.2313030544

Ofiara, L. M., Navasakulpong, A., Ezer, N., and Gonzalez, A. V. (2012). The importance of a satisfactory biopsy for the diagnosis of lung cancer in the era of personalized treatment. *Curr. Oncol.* 19, S16–S23. doi: 10.3747/co.19.1062

Sagar, P., Gulati, M., Gupta, S. K., Gupta, S., Shankar, S., Joshi, K., et al. (2000). Ultrasound-guided transthoracic co-axial biopsy of thoracic mass lesions. *Acta Radiol.* 41, 529–532. doi: 10.1080/028418500127346117

Sartori, S., Nielsen, I., Trevisani, L., Tombesi, P., Ceccotti, P., and Abbasciano, V. (2004). Contrast-enhanced sonography as guidance for transthoracic biopsy of a peripheral lung lesion with large necrotic areas. *J. Ultrasound Med.* 23, 133–136. doi: 10.7863/jum.2004.23.1.133

Sperandeo, M., Rea, G., Grimaldi, M. A., Trovato, F., Dimitri, L. M., and Carnevale, V. (2017). Contrast-enhanced ultrasound does not discriminate between community acquired pneumonia and lung cancer. *Thorax* 72, 178–180. doi: 10.1136/thoraxjnl-2016-208913

Sperandeo, M., Sperandeo, G., Varriale, A., Filabozzi, P., Decuzzi, M., Dimitri, L., et al. (2006). Contrast-enhanced ultrasound (CEUS) for the study of peripheral lung lesions: a preliminary study. *Ultrasound Med. Biol.* 32, 1467–1472. doi: 10.1016/j.ultrasmedbio.2006.06.018

Swensen, S. J. (2002). CT screening for lung cancer. *AJR Am. J. Roentgenol.* 179 (4), 833–836. doi: 10.2214/ajr.179.4.1790833

Trevisani, L., Sartori, S., Putinati, S., and Abbasciano, V. (1994). Needle aspiration biopsy and ultrasonic guidance. *Chest* 106, 650. doi: 10.1378/chest.106.2.650

Wang, S., Yang, W., Zhang, H., Xu, Q., and Yan, K. (2015). The role of contrast-enhanced ultrasound in selection indication and improving diagnosis for transthoracic biopsy in peripheral pulmonary and mediastinal lesions. *Biomed. Res. Int.* 2015, 231782. doi: 10.1155/2015/231782

Wen, Q., Huang, P. T., Pan, M. Q., Guan, R. H., Zhang, H., Fu, J. J., et al. (2013). The value of arrival time in differential diagnosis of peripheral pulmonary lesions. *Chin. J. Ultrasonogr.* 22, 271–272. doi: 10.3760/cma.j.issn.1004-4477.2013.03.030.

Wu, W., Chen, M. H., Yin, S. S., Yan, K., Fan, Z. H., Yang, W., et al. (2006). The role of contrast-enhanced sonography of focal liver lesions before percutaneous biopsy. *AJR Am. J. Roentgenol.* 187, 752–761. doi: 10.2214/AJR.05.0535

Yeow, K. M., Tsay, P. K., Cheung, Y. C., Lui, K. W., Pan, K. T., and Chou, A. S. (2003). Factors affecting diagnostic accuracy of CT-guided coaxial cutting needle lung biopsy: retrospective analysis of 631 procedures. *J. Vasc. Interv. Radiol.* 14, 581–588. doi: 10.1097/01.RVI.0000071087.76348.C7

Conflict of Interest Statement: The authors declare that the research was conducted in the absence of any commercial or financial relationships that could be construed as a potential conflict of interest.

frontiers in Pharmacology

REVIEW
published: 07 February 2020
doi: 10.3389/fphar.2020.00019

The Application of DVDMS as a Sensitizing Agent for Sono-/Photo-Therapy

Bingjie Mai, Xiaobing Wang, Quanhong Liu, Kun Zhang and Pan Wang *

National Engineering Laboratory for Resource Development of Endangered Crude Drugs in Northwest China, The Key Laboratory of Medicinal Resources and Natural Pharmaceutical Chemistry, The Ministry of Education, College of Life Sciences, Shaanxi Normal University, Xi'an, China

Both photodynamic therapy (PDT) and sonodynamic therapy (SDT) are fast growing activated therapies by using light or ultrasound to initiate catalytic reaction of sensitizing agents, showing great potentials in clinics because of high safety and noninvasiveness. Sensitizers are critical components in PDT and SDT. Sinoporphyrin sodium (DVDMS) is an effective constituent derived from Photofrin that has been approved by FDA. This review is based on previous articles that explore the applications of DVDMS mediated photodynamic/sonodynamic cancer therapy and antimicrobial chemotherapy. Researchers utilize different cell lines, distinct treatment protocols to explore the enhanced therapeutic response of neoplastic lesion. Moreover, by designing a series of nanoparticles for loading DVDMS to improve the cellular uptake and antitumor efficacy of PDT/SDT, which integrates diagnostics into therapeutics for precision medical applications. During the sono-/photo-activated process, the balance between oxidation and antioxidation, numerous signal transduction and cell death pathways are also involved. In addition, DVDMS mediated photodynamic antimicrobial chemotherapy (PACT) can effectively suppress bacteria and multidrug resistant bacteria proliferation, promote the healing of wounds in burn infection. In brief, these efficient preclinical studies indicate a good promise for DVDMS application in the activated sono-/photo-therapy.

Keywords: sinoporphyrin sodium, sonodynamic therapy, photodynamic therapy, photodynamic antimicrobial therapy, nanomaterials

OPEN ACCESS

Edited by:
Fei Yan,
Shenzhen Institutes of Advanced Technology (CAS), China

Reviewed by:
Feng Wang,
Xinxiang Medical University, China
Wei Tang,
Shaanxi Normal University, China
Zhiguo Zhang,
Harbin Institute of Technology, China

****Correspondence:***
Pan Wang
wangpan@snnu.edu.cn

Specialty section:
This article was submitted to Translational Pharmacology, a section of the journal Frontiers in Pharmacology

Received: *07 February 2019*
Accepted: *08 January 2020*
Published: *07 February 2020*

Citation:
Mai B, Wang X, Liu Q, Zhang K and Wang P (2020) The Application of DVDMS as a Sensitizing Agent for Sono-/Photo-Therapy. Front. Pharmacol. 11:19. doi: 10.3389/fphar.2020.00019

INTRODUCTION

According to the World Health Organization's latest global cancer data, the cancer burden has risen to 18.1 million new cases and 9.6 million deaths by 2018. Global patterns show that nearly half of the new cases and more than half of the cancer deaths occur in Asia (Data, 2018). From the overall trend, the number of cancer patients and the number of deaths in the world will continue to grow, and the situation in China is becoming more and more serious.

Traditional cancer treatments, i.e., surgical resection, radiation therapy, and chemotherapy have distinct limitations. Due to the expansion of tumor tissue and the root-like infiltration, the lymphatic and blood distant organ metastasis has already occurred when the tumor is diagnosed, so the complete surgical removal would be impossible. Meanwhile, radiotherapy and traditional chemotherapy produce

severe side-effects, they cannot selectively kill tumor cells and result in serious damage to the immune system (Miller et al., 2016). Moreover, the current therapies are very expensive, which could be a fatal blow to the whole family and cause many patients give up treatment because they cannot afford the high treatment price. Many researchers are trying to develop new strategies to combat cancer. Among the newly emerged cancer therapies, the activated therapy using light or ultrasound as stimulus for stimulating sensitizers, and the derived photodynamic therapy (PDT) and sonodynamic therapy (SDT) will bring new hope to improve the life time and quality of cancer patients (Kenyon et al., 2009).

The first generation sensitizer Photofrin® belongs to one kind of porphyrin derivatives, it has efficient singlet oxygen production and been approved by FDA for treating cancers *via* PDT (AB and HS, 2013). Although Photofrin® has achieved positive therapeutic effects in clinic, there are still many shortcomings, such as complex components, unsatisfactory spectrums, and systemic dark toxicities (O'Connor et al., 2010). One of the important reasons is that Photofrin® is a mixture of unclear porphyrin components. Sinoporphyrin sodium (DVDMS) is an effective constituent based on Photofrin® (Hu et al., 2015). DVDMS has 98.7% chemical purity and is highly soluble in water, resulting in relatively short-term skin sensitivity and high potential of singlet oxygen yield. Studies indicate the photosensitivity of DVDMS is 10 times higher than that of Photofrin® (Wang et al., 2015). Besides, the sonoactivity of DVDMS is also much higher than that of Photofrin® and several other porphyrins (Xiong et al., 2015). SDT uses ultrasound to stimulate sonosensitizer that mostly derived from photosensitizers in PDT (Trendowski, 2014). Ultrasound has good biological tissue penetration, and can focus its energy into the specific depth to produce bioeffects in the targeting site (Rosenthal et al., 2004). To some extent, SDT overcomes the limitation of PDT superficial diseases treatment because of the short penetration of light. In addition to the singlet oxygen mechanism in PDT, more complex explanations referring to mechanical stress, cavitational effects, and multiple reactive oxygen species are involved in SDT (McHale et al., 2016). In addition to cancer disease, the spread of multidrug resistant bacteria are another threat to human health, and the excessive abuse of antibiotics has aroused great concerns in recent years (Roy et al., 2016). Photodynamic antimicrobial therapy (PACT) is a promising alternative for the treatment of drug-resistant infections (Wainwright, 1998). Therefore, in this work, we provide a state-of-the-art overview of the applications of DVDMS for sono-/photo-therapy, including DVDMS in antitumor and antibacteria research. In recent studies, researchers have worked closely with advanced nanobiotechnology to investigate the potential of nanoDVDMS in precison theranostics (**Table 1**).

DVDMS USED IN ACTIVATED CANCER THERAPY

Basic Features of DVDMS

The spectroscopic properties of sensitizers are critical for activated therapies (Dougherty, 1985). Wang et al. measured the characteristic absorption and fluorescence of DVDMS in various pH values and ionic strength (Wang et al., 2015b). The results suggest that DVDMS existed as a monomer in aqueous solution, which was similar to the porphyrin results reported in other literatures. Porphyrin dimers and trimers compounds were unstable as solid power or in solution by Pandey' study (Pandey and Dougherty, 1989). For comparison, Wang and Ni et al. evaluated the safety of DVDMS in the 4T1-bearing mice and beagle dogs, respectively. They did not find any significant signs of toxicity from physical examination, biochemical indicators, or histopathological observations (Ni et al., 2015; Wang et al., 2015b). According to the results, the unobserved negative effect levels is 2 mg/kg in mice and 1 mg/kg in dogs, and DVDMS administration is relatively safe. The photo-/sono-therapy triggered by DVDMS has broad prospects in future clinical transformation.

DVDMS Accumulation in Tumors

The principle of PDT/SDT is based on the preferential accumulation of sensitizing agent in tumors, and the enhanced cytotoxicity after activation by light or ultrasound (Kolarova et al., 2009; Sadanala et al., 2014). Therefore, PDT/SDT treatment can not only kill tumor cells to the maximum extent, but also minimize adverse effects (Shirasu et al., 2010). *In vitro* studies suggest DVDMS has a preferential uptake in tumor cells compared with normal healthy cell lines (Hu et al., 2014; Xiong et al., 2015). And DVDMS mainly localizes in the mitochondria of tumor cells, which shares the similarity with other porphyrins (Wu et al., 2016), suggesting mitochondria would be a potential target during photo-/sono-therapy. By using the inherent fluorescence of DVDMS, the *in vivo* findings indicate DVDMS distributes high level in tumor as well as in liver and kidney, the retention ratio of tumor to surrounding healthy tissues is above 3 (Wang et al., 2015b). This agrees well with others' investigations, which show that porphyrins may metabolize through liver and kidney and result in high enrichments (Liu et al., 2007; Wang et al., 2007; Li et al., 2014). The possible tumor accumulation could be explained as follows. First, such selective uptake is determined by the microenvironment surrounding the tumor. Many types of tumor cells express a large number of low-density lipoprotein receptors, and sensitizers combined with low-density protein-binding enter tumor cells *via* endocytosis (Jori and Reddi, 1993; Allison et al., 2010). In addition, the pH value in tumors is generally lower than that in most normal tissues, and cell uptake is reported to increase with decreasing pH (Moan et al., 1980). Second, studies have shown that tumor-associated macrophages take up large amounts of porphyrin derivative in tumors (Korbelik et al., 1991; M et al., 1991). Thus, tumor-associated macrophages may be one of the reasons for DVDMS selective absorption. Third, the abnormal structural characteristics of tumor matrix such as leaky vasculature, compromised lymphatic drainage, a high amount of newly generated collagen that bound porphyrins also contribute to the enhanced accumulation of DVDMS in tumors (Musser et al., 1980). Moreover, compared with Hp, PpIX, and photofrin, DVDMS showed much higher intrinsic red fluorescence, indicating that DVDMS has additional advantages in further clinical tumor tracing and imaging (Xiong et al., 2015).

TABLE 1 | The application of DVDMS as a sensitizing agent for activated cancer and bacteria therapy.

Treatment method	Targets	*In vitro/ In vivo*	Sensitizer	Reference
SDT	K562, U937, Eca109, NIH3T3, SW620, SPL, PBMC Cells	*In vitro*	DVDMS	Anti-Cancer Drugs 2014, 25, 174–182
PDT	Eca-109 Cells	*In vitro*	DVDMS	Photochemistry and Photobiology, 2014, 90 1404–1412
SDT	S180 Cells	*In vitro/In vivo*	DVDMS	Biopharm. Drug Dispos. 35 50–59 (2014)
SDT	Eca-109 Cells	*In vitro*	DVDMS	International Journal of Nanomedicine. 2014:9 3077–3090
PDT	Beagle dogs	*In vivo*	DVDMS	Photochem. Photobiol. Sci.,2015, 14, 815
PDT	4T1 Cells	*In vitro/In vivo*	DVDMS	Theranostics 2015; 5(7) 772-786
SDT	NIH3T3 cells, S180 cells	*In vitro/In vivo*	DVDMS	Scientic Reports. 2015 Dec 3;517485
SPDT	4T1 Cells	*In vitro/In vivo*	DVDMS	Ultrasonics Sonochemistry 31 (2016) 437–448
PDT	MDA-MB-231 Cells	*In vitro*	DVDMS	Photodiagnosis and Photodynamic Therapy 13 (2016) 58–65
PDT	4T1 Cells	*In vivo*	DVDMS	Journal of Photochemistry & Photobiology, B Biology 160 (2016) 299–305
SDT	U87 MG-Red-FLuc human glioblastoma	*In vitro/In vivo*	DVDMS	Ann Biomed Eng. 2018 Oct 12
PDT	Eca-109 Cells	*In vitro*	DVDMS	Photodiagnosis and Photodynamic Therapy 24 (2018) 198–205
SDT	CT26 Cells	*In vitro/In vivo*	DVDMS+MB	International Journal of Biological Sciences. 2015; 11(12) 1401-1409.
SDT + 2DG	MDA-MB-231, MCF-7, HUVEC, 4T1 Cells	*In vitro/In vivo*	DVDMS	Ultrasound Med Biol. 2018 Jun;44(6)1233-1243.
PDT, Fluorescence imaging	U87MG Cells	*In vitro/In vivo*	GO-PEG-DVDMS	Biomaterials. 2015 February; 42 94–102
PDT/PTT	PC9 Cells	*In vitro/In vivo*	GO-PEG-DVDMS	Nanoscale. 2015 February 14; 7(6): 2520–2526
PDT/PTT	MCF-7 Cells	*In vitro/In vivo*	Mn/DVDMS	Adv Mater. 2017 June; 29(23):
PTT/PDT	4T1 Cells	*In vitro/In vivo*	RGD-ferritins-DVDMS	Biomater. Sci., 2017, 5, 1512
SDT	MDA-MB-231, 4T1 Cells	*In vitro/In vivo*	DVDMS-liposome–microbubble complexes (DLMBs)	Nano Research-s12274-017-1719-8
PDT	MCF-7 Cells	*In vitro/In vivo*	DVDMS-PTX-liposome (PDL)	Biomaterials 141 (2017) 50e62
SDT, MR and fluorescence imaging	U87 human glioma Cells	*In vitro/In vivo*	DVDMS-manganese ions-nanoliposomes (DVDMS-Mn-LPs)	J Cell Mol Med. 2018 Nov;22(11)5394-5405
SDT	U87 MG-Red-FLuc human glioblastoma	*In vitro/In vivo*	DVDMS	Ann Biomed Eng. 2019 Feb; 47(2): 549-562
SDT	H446 Cells	*In vitro/In vivo*	DVDMS	Cell Physiol biochem. 2018; 51(6):2938-2954.
SDT	C6 gliomas Cells	*In vitro/In vivo*	iRGD-Lipo- DVDMS	Biomater Sci. 2019 Jan 2. Doi:10.1039/ c8bm01187g.
SDT	Hepatocellular carcinoma (HCC) Cells	*In vitro*	DVDMS	Int J Biochem Cell Biol. 2019 Jan 17.
PDT	Human colorectal cancer (CRC)	*In vitro/In vivo*	DVDMS	Int J Biol Sci. 2019 Jan 1; 15(1):12-23.
PACT	S. aureus	*In vitro*	DVDMS	Lasers in Surgery and Medicine 48400–408 (2016)
PACT	S. aureus, MDR-S. aureus	*In vitro/In vivo*	DVDMS	International Journal of Nanomedicine 201712 5915–5931

DVDMS-Based Photo-Therapy

Oxidative damage is the main mechanism of PDT, and the singlet oxygen production is proportional to the effectiveness of PDT (**Figure 1**) (Gorman et al., 2004). Wang et al. utilized the photo-oxidation of DPBF (1, 3-diphenylisobenzofuran) as a quantitative method to evaluate singlet oxygen yield, and the results suggest much higher singlet oxygen production of DVDMS compared with the other porphyrins (Hp, PpIX, and Photofrin) because of its double porphyrin rings (Wang et al., 2015a; Yan et al., 2015).

For direct cell killing, compared to the clinically approved Photofrin®, DVDMS at a dose of 1/10 concentration can achieve the same killing effect of Photofrin® (Jiang et al., 2013; Zang et al., 2017a). Intracellular ROS production is

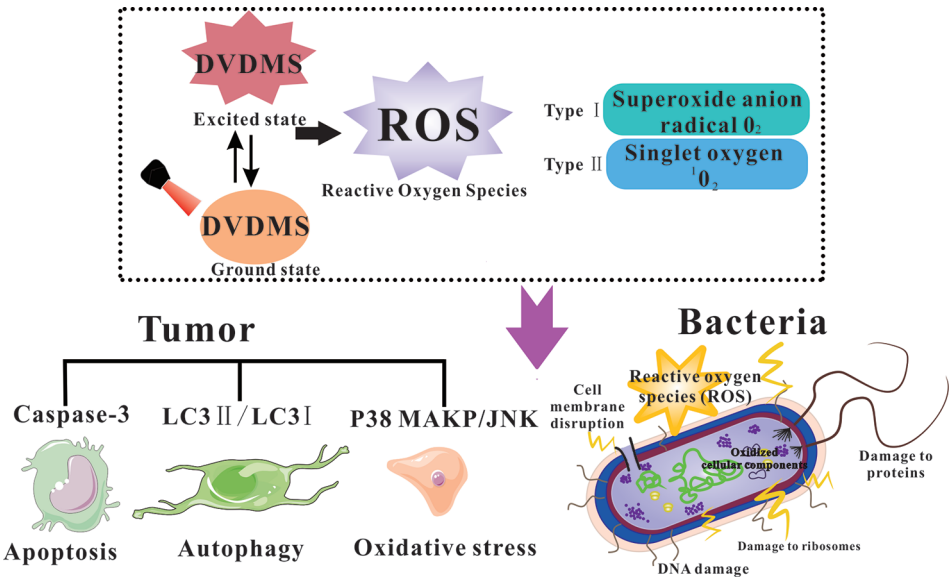

FIGURE 1 | Diagram of ROS generation for photodynamically killing cancer cells and pathogenic microorganisms.

considered as the main cause of PDT induced cell death (Allison and Moghissi, 2013). An oxidative stress accompanied with mitochondria dysfunction was involved in DVDMS-PDT (Hu et al., 2015). Apoptosis is a programmed cell death involving protease cascade reactions (Danon et al., 2004). The apoptosis executor Caspase-3 is observed with increasing activity during DVDMS-PDT (Shi et al., 2018). Meanwhile, autophagy plays different roles in different tumor stages and is a vital response to various therapeutic strategies (DJ and SD, 2000). It has been reported that ROS generated by PDT could induce both autophagy and apoptosis in cancer cells. Pretreatment with autophagy inhibitor decreased the ratio of LC3 II/LC3 I, a standard autophagy marker, suggesting DVDMS-PDT initiated autophagic response in tumor cells. MAPK pathways are also involved in ROS triggered cellular responses. Heme oxygenase-1 (HO-1) is a rate-limiting enzyme that has a special protective effect on cells (So and Oh, 2016). After photo-therapy, phosphorylation of p38 MAPK and JNK was upregulated, the expression of HO-1 was rapidly increased and gradually returned to normal levels; the ROS scavenger further decreased phosphorylation of p38MAPK and HO-1, suggesting increased ROS level post PDT would trigger multiple signals activation and some contribute to the ultimate cell death, while others protect cellular oxidative stress (Wang et al., 2014). Zhu et al. evaluated the role of autophagy in the antitumor process of DVDMS-PDT against human colorectal cancer (Zhu et al., 2019). DVDMS-PDT showed better antitumor efficiency than Photofrin®-PDT. Chloroquine (CQ) promoted apoptosis by inhibiting autophagy, suggesting that autophagy may play a protective role in DVDMS-PDT treated cells. Furthermore, no visible tumor cells were found in the CQ+DVDMS-PDT group, which confirmed the hypothesis that autophagy was protective under the experimental conditions.

Surgical removal of the primary tumor is highly effective in many cancer patients. However, survival is noneffective when there are metastatic lesions and no response to treatment (Jr et al., 2011). Therefore, inhibition of metastasis is crucial to the prognosis of tumor therapy. Wang et al. reported that DVDMS-PDT inhibited the invasion capacity and migration of 4T1 cells (Wang et al., 2015b). Many investigations have shown that microvilli on the surface of tumor cell are closely related with cell migration (Hrazdira et al., 1998). Microvilli mediate the exchanges of substances and nutrition and promote the malignant proliferation and attachment of tumor cells. Herein, the microvilli were observed to disappear after DVDMS-PDT treatment under scanning electron microscope. Moreover, the F-actin cytoskeleton is a critical structural network that affects cell contraction, movement, and vesicular transport (Furukawa et al., 2013). DVDMS-PDT interferes with the regular pattern of actin filaments in a light-dose dependent manner, suggesting that the collapse of actin network was involved in cell migration and invasion (Wu et al., 2016). This is consistent with previous report that PDT may cause damage to the cell surface or cytoskeleton, thus produce inhibitory effects on cell proliferation and motility (Pacheco-Soares et al., 2014). Hu et al. compared the metastasis suppression between DVDMS-PDT and Photofrin®-PDT in 4T1 xenograft model, showing better efficiency in the former than in the latter.

Moreover, PDT belongs to nonionizing irradiation and can be administered repeatedly without causing long-term complications. Clinical and experimental results have proved that repeated application of PDT has effectively improved the therapeutic effect (Togsverd-Bo et al., 2015). Xiong et al. designed different regimens to explore the optimal therapeutic effect of DVDMS-PDT, suggesting one injection of DVDMS followed by three time laser exposure within a special intervals exhibited superior

inhibition for tumor growth, angiogenesis and metastasis (Xiong et al., 2016).

DVDMS-Based Sono-Therapy

Sono-therapy based on the synergy of sensitizer and ultrasound, involves several mechanical, chemical, and cavitational activated mechanisms (**Figure 2**). Shen et al. explored the antitumor effect of DVDMS-SDT on the human small lung cancer (Shen et al., 2018). DVDMS-SDT increased cellular apoptosis, ROS levels as well as cleaved caspase-3, -8, -9, and -10, decreased the levels of MMP, RIP3, Bcl-2, VEGF, and TNF-α, suggesting DVDMS-SDT induced H446 cells apoptosis in part by mitochondria-dependent signaling pathway and the extrinsic apoptosis was also involved. This is the first study to provide evidence that RIP3 expression was inhibited by DVDMS-SDT in H446 cells. The antitumor effect of DVDMS-SDT is generally ROS-apoptosis dependent Li et al. studied the antitumor effect of DVDMS-SDT on hepatocellular carcinoma cell lines (Li et al., 2019). The results indicate that DVDMS-SDT was more effective than PpIX-SDT in inhibiting the growth of HepG2 cells, accompanied by the increased enrichment of DVDMS in cells and G2/M phase arrest with decrease of CDK1 and Cyclin B1. Furthermore, the increased of ROS level can up-regulate the expression of p53 and Bax, down-regulate the expression of Bcl-2, leading to the activation of caspase-3 and ultimate initiation of cell apoptosis. Besides, ultrasound is relatively repeatable, easily accessible, inexpensive, and nontoxic, the multiple exposure of DVDMS would be more efficient against tumors. Xiong et al. monitored a significant proliferating cell nuclear antigen (PCNA) drop after DVDMS plus multiple ultrasound treatments compared with either mono-treatment. Such multiple SDT also significantly reduced the microvessel density (MVD) and tumor growth of xenografts (Xiong et al., 2015).

Microbubbles (MBs) are widely used as contrast agents in medical diagnosis (Dijkmans et al., 2004). The shock waves generated by MBs during the sound pressure process improve the permeability of cell membranes by transient sonoporation (Rapoport et al., 2009). Based on this mechanism, MBs has been widely used in drug delivery in recent years (Yang et al., 2014). With the development of SDT, MBs are introduced to enhance its curative effect (Roberto et al., 2013). SonoVue® is a clinically-approved MB, and currently widely used in clinic application (Nicolau et al., 2004). Wang et al. investigated the associated effects of DVDMS-SDT and SonoVue®, and the findings suggest that the existence of MBs promoted the transient transportation and internalization of DVDMS, which further enhanced the cytotoxicity of ultrasound. Ultrasound-targeted microbubble destruction (UTMD) combines the advantages of ultrasound diagnosis, therapeutics, and spatiotemporal controllable-platform, gradually becoming a theranostic strategy in various diseases. The use of UTMD to promote the accumulation of sensitizers in the lesions, is considered to be one of the ways to improve the antitumor activity of SDT (Wang et al., 2015a). Pi et al. investigated the antitumor effect of DVDMS-SDT on intracranial human glioblastoma in nude mice (Pi et al., 2019). Longitudinal bioluminescence imaging showed that the growth of intracranial glioblastoma was slower in SDT group. The median survival time was prolonged to 30.25 days after SDT treatment, indicating that DVDMS-SDT with the help of MBs provides a new promising therapeutic strategy against glioblastoma. Pi's study also shows UTMD caused significantly enhanced delivery of DVDMS, including apoptosis increase as well as cell proliferation suppression. These indicate that MBs combined with DVDMS-SDT may be a promising treatment for human glioblastoma.

The Combined Strategy for Enhanced Sonoeffects

The Combination of SDT With PDT

Sono-PDT (SPDT) is a new combination of SDT and PDT for the treatment of cancer (Jin et al., 2000). Previous studies have shown that SPDT can significantly enhance the antitumor activities against of various malignants at preclinical and clinical levels. From the perspective of physical properties of ultrasound, enhanced therapeutic effects may involve ROS formation, thermal effect, mechanical stress, cavitational effect and other factors (Hirschberg and Madsen, 2017). Liu et al. examined the effects of DVDMS-SPDT, the findings show that: (1) compared with either monotherapy, combined therapy significantly enhanced tumor inhibition; (2) SPDT achieved a

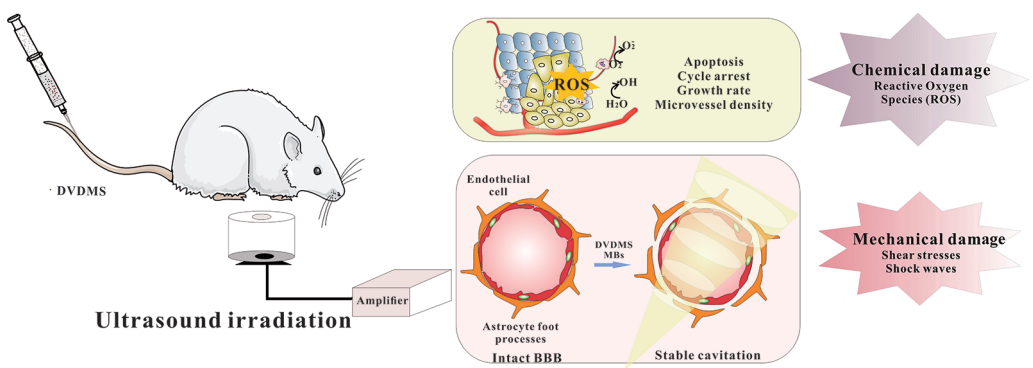

FIGURE 2 | The possible mechanisms of DVDMS-SDT.

more efficient outcome even utilizing a much lower PDT dose, which may be due to subsequent SDT could compensate for the inevitable attenuation of PDT upon reaching deep tissues; (3) excessive ROS contributes to the enhanced anticancer efficiency of the combination; (4) ultrasound increased permeability of cell membrane and thus induced improvement of cellular uptake of DVDMS. Based on the results, the combination of PDT with subsequent SDT would be a good treatment option. High ROS levels play a key role in cell death. And ultrasound-induced cavitation effects and changes in membrane permeability also contribute to the enhancement of combined therapy (Liu et al., 2016). Because of the complicated system of SPDT, its mechanisms have not been clearly revealed. Further preclinical studies and clinical trials are needed to verify and improve SPDT.

The Glycolysis Blockage Aggravated SDT Effects

Changes in the basic characteristics of cancer are interwoven with the intrinsic metabolism of cancer cells (Romero-Garcia et al., 2011). Different tumor cells have different metabolic phenotypes. Glycolysis and mitochondrial oxidative phosphorylation may coexist at the same time, and the mutual conversion also called energy reprogramming happens frequently and differently under distinct treatment conditions (Moreno-Sa´nchez et al., 2007).

Unlike most normal cells, tumor cells have an increased metabolic requirement for glycolysis, also known as the Warburg effect, which generally helps promote metastasis and inhibit apoptosis (Vander Heiden et al., 2009; Cairns et al., 2011). Therefore, the improvement of glycolysis level makes it possible to target tumor metabolism to combat cancer. 2-deoxyglucose (2DG) is the most commonly used antiglycolytic drug. When 2DG enters malignant tumor cells, it is phosphorylated by hexokinase II and inhibits the generation of ATP (Feng et al., 2015). Nevertheless, due to the systemic toxicity of 2DG, it has not been satisfactory in clinical trials for some cancer treatments (Maschek et al., 2004). Xie et al. reported that using SDT and 2DG to target mitochondria and aerobic glycolysis simultaneously was more effective than either alone against breast cancer both *in vitro* and *in vivo*. 2DG regulates cell viability through the metabolic enzymes that affected by ROS generation, and ROS is one of the determinants of SDT, so the synergistic action between 2DG and DVDMS-SDT may converge on ROS. Intracellular ROS levels in SDT+2DG groups was increased approximately 2-fold and 30-fold than that in SDT and 2DG groups, respectively. The cellular oxygen consumption rate (OCR) level and ATP generation decreased after 2DG treatment, especially in SDT. Therefore, it can be speculated that the combination of SDT and 2DG significantly suppressed oxidative phosphorylation and glycolysis, leading to ATP depletion. Besides, SDT increases the sensitivity of tumor cells to 2DG treatment by blocking the energy replenishment pathways. Ultimately, the tumor inhibition rate of the combined therapy was higher than the monotherapies (Xie et al., 2018). The findings indicate that SDT +2DG could provide a new noninvasive treatment for high mortality metastatic tumors.

DVDMS-LOADED NANOPARTICLES FOR PRECISION THERANOSTICS

We summarize the different nanoDVDMS used in photo-/sono-therapy and imaging-guided modality for cancer treatment, such as liposomes, micro-/nano-bubbles, graphene oxide, metal NPs (**Figure 3**).

NanoDVDMS for Imaging Guided Photo-Therapy

In order to improve the controllability of drug release, a variety of nanoscale drug delivery systems (DDS) have been developed. Light-responsive DDS attract great interest because of its easy application and spatiotemporal performance (Pashkovskaya et al., 2009). Wang et al. developed a dual-effect liposome with coencapsulation of DVDMS and an antimitotic agent (PTX). Both *in vivo* and *in vitro* studies have confirmed that the compound liposomes had excellent anticancer activity through the synergistic effect of PDT and PTX cytotoxicity, and the DVDMS fluorescence guided photo-therapy exhibited minimal side effects. As a ROS production promoter, DVDMS enhanced the release of embedded PTX and enhanced the efficiency of chemotherapy by reducing the core molecule McL-1, thereby activating apoptosis. DVDMS-PDT treatment reduced cellular glycolysis, thus preventing the possible energy conversion and struggling survival after PTX treatment. Therefore, apoptosis sensitivity is the main reason for laser-irradiated liposome nanoDVDMS to enhance PTX sensitivity of cells (Wang et al., 2017). Sun et al. used iRGD modified DVDMS liposome (iRGD-Lipo-DVDMS) combined with UTMD to open the BBB and targeted glioma therapy (Sun et al., 2019). The results show that iRGD-modified liposomes improved the targeting ability of tumors compared with the liposomes without iRGD. The iRGD-Lipo-DVDMS exhibited significantly improved drug accumulation in monolayer cells, 3D tumor spheroids and transplanted C6 tumors, and significant apoptosis in glioma cells after combined with SDT treatment. In addition, the developed nanosonosensitizers have good biocompatibility *in vivo* and have broad prospects in fluorescence image-guided sonodynamic tumor therapy. Taken together, iRGD-Lipo-DVDMS can provide targeting ultrasound actived DDS and would become an alternative strategy for glioma treatment.

As an inorganic nanocarrier, graphene oxide (GO) has many advantages, such as abundant functional groups and easy surface modification (Tang et al., 2012). Chen et al. designed a novel phototheranostic nanoplatform based on DVDMS-loaded PEGylated GO (GO-PEG-DVDMS). In this study, GO-PEG enhanced the tumor accumulation efficiency of DVDMS and fluorescence imaging-guided PDT, showing a strong antitumor effect (Yan et al., 2015). Further, they strategically designed another nanotheranostic platform based on GO-PEG-DVDMS for enhanced fluorescence/photoacoustic (PA) dual-modal imaging (Yan et al., 2014). The GO-PEG carrier greatly improved the fluorescence characteristics, PA imaging and PTT of DVDMS through intramolecular charge transfer and near infrared (NIR) absorption. The treatment effect of GO-PEG-DVDMS is significantly better than that of PDT or PTT alone. In another

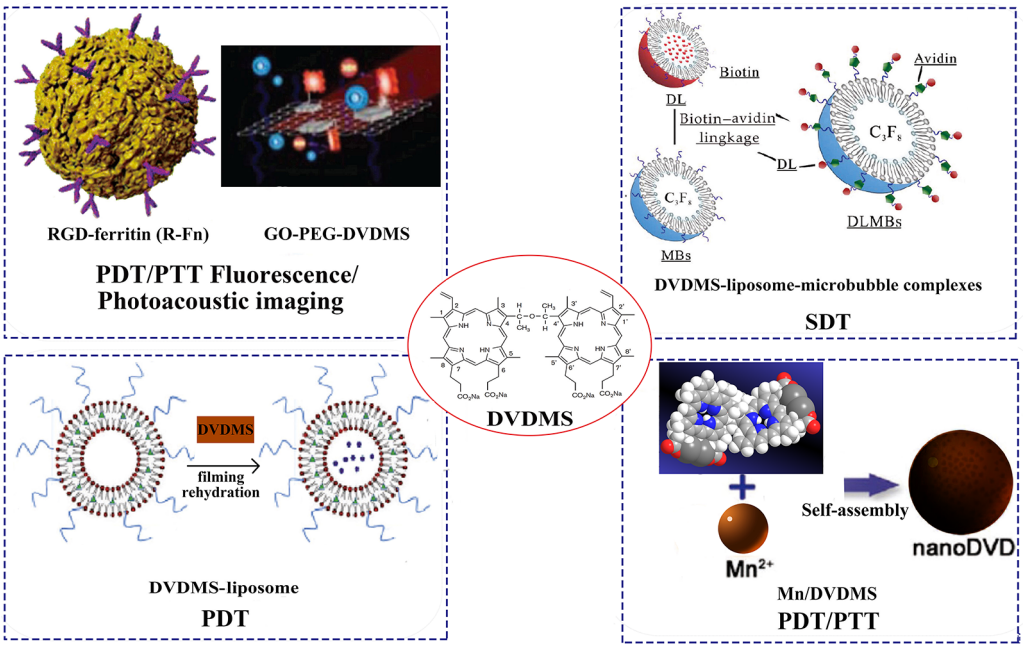

FIGURE 3 | Different DVDMS nanoparticles of photo-/sono-therapy and image-guided cancer treatment. Reprinted with permission of ref. (Yan et al., 2014), (Huang et al., 2017), Royal Society Of Chemistry. (Liu et al., 2018), WILEY.

report, DVDMS were loaded into RGD-modified ferritin nanoparticles for image-guided PDT/PTT combination therapy. The loading capacity of DVDMS in the prepared nanocomposites was up to 66.67 wt%, and the tumor treatment effect was significantly better than that of DVDMS (Huang et al., 2017).

In addition, photosensitizers in photo-therapy are often limited by photobleaching and tumor hypoxia. Through supramolecular assembly, the researchers further developed the coordinated assembly strategy of tumor environmental trigger to form Mn/DVDMS nanotheranostics for cancer photo-therapy (Chu et al., 2017). In MCF-7 cells and xenograft tumors, MnO_2/DVDMS was reduced by glutathione (GSH) and H_2O_2 and reassembled into nanoDVDMS, which can be monitored by activated magnetic resonance/fluorescence/photoacoustic signals. Interestingly, the reduction of GSH, the generation of O_2 and the formation of nanoDVDMS have synergistic effects with photo-therapy, which have improved the antitumor efficacy and provided a new approach for tumor treatment.

Zang et al. designed Gd-DVDMS as a water-soluble and multifunctional theranostic agent as it can serve as a PS in PDT, a phosphorescence-based oxygen indicator, and a magnetic resonance imaging contrast agents (Zang et al., 2017b).

DVDMS-Loaded Nanoparticles for Enhanced Sono-Therapy

MBs can be used as potential delivery carriers. The therapeutic agents can be coadministrated with MBs in a variety of ways: drugs that co-injected together with MBs; drugs that encased in MBs casings/cavities; drugs that covalently linked at the shell surface of MBs; drugs that encapsulated in nanoparticles and then linked with MBs (Heleen et al., 2015; Zhang et al., 2017). Based on the sonoactivated features of DVDMS, Li et al. designed the liposome-encapsulated DVDMS with microbubbles *via* biotin-avidin linkage, resulting in a complex called DLMBs. Compared with free or liposome DVDMS, DLMBs has better ultrasonic cytotoxicity to breast cancer. Both *in vivo* and *in vitro* studies have confirmed that DLMBs combined with ultrasonic therapy has significant antitumor activity. The active substance induced by ultrasound was the key mediator that triggers the increased release of DVDMS in DLMBs, promotes cellular uptake and intratumor diffusion, and enhances sonotoxicity of DVDMS (Li et al., 2018).

Liu et al. reported a multifunctional theranostic agent that integrate imaging and therapy into a single nanoplatform for MR and fluorescence image-guided SDT treatment. SDT reagents were prepared by encapsulating DVDMS chelating with manganese ions into nanoliposomes (DVDMS-Mn-LPs) (Liu et al., 2018). Both cell and animal studies demonstrated that SDT combined with DVDMS-Mn-LPs significantly improved the antitumor growth efficiency. In addition, DVDMS-Mn-LPs are good for MR and fluorescence imaging. Therefore, DVDMS-Mn-LPs may provide a promising strategy for imaging-guided modality for cancer treatment.

DVDMS USED IN ANTIBACTERIAL APPLICATION

In terms of nononcology disease research, the abuse of antibiotics has caused a growing problem of bacterial resistance (Costerton et al., 1999). Mai et al. investigated the

effect of DVDMS-PACT of *Staphylococcus aureus* (*S. aureus*) and Multidrug-resistant (MDR)-*S. aureus* (Mai et al., 2016; Mai et al., 2017). The results show that DVDMS-PACT decreased the survival of bacteria planktonic and biofilm culture. PACT treatment produces a large amount of reactive oxygen species. Furthermore, the DNA damage and membrane permeability after DVDMS-PACT were significantly increased, which might be crucial for PACT efficient outcome. Studies demonstrate that *S. aureus*/MDR- *S. aureus* could rapidly photoinactivate in wound infection when it is treatment with DVDMS-PACT. Moreover, the levels of inflammatory cytokines decreased and growth factors increased after PACT treatment at wound sites, suggesting that the treatment can inhibit wound deterioration, reduce inflammation and promote wound healing. There are no detectable side effects using DVDMS-PACT at the therapeutic dose according to the preliminary safety analysis.

CONCLUSION AND OUTLOOK

DVDMS has good physical and chemical properties, which would be a valuable reference for further investigation of DVDMS mediated activated cancer therapy. DVDMS-triggered sono-/photo-therapy produces significant efficiency both *in vitro* and *in vivo*, and numerous signal transduction and cell death pathways are also involved in the oxidization stress and antioxidant processes during SDT/PDT. Besides, DVDMS-PACT can greatly suppress bacteria and MDR-bacteria proliferation, and promote the healing of wounds in burn infection. Moreover, with the development of nanotechnology, various nanoDVDMS has been designed to provide better biocompatibility, physiological stability, excellent targeting, enhanced sono/phototoxicity, and integration of diagnostic and therapeutic features. These novel theranosic nanoplatforms hold great promise for precision recognition and treatment of malignant tumor as well as other diseases, which could be expected to be applied in future clinical translation.

AUTHOR CONTRIBUTIONS

PW and XW contributed design of this review. BM, QL, and KZ organized the literatures and wrote the draft of this manuscript. BM, XW, and PW contributed to manuscript revision. All authors read and approved the submitted version.

FUNDING

This research was supported by the National Natural Science Foundation of China (Grant No. 81872497 and No. 81972900) and the Fundamental Research Founds for the Central Universities (2017TS039).

REFERENCES

AB, O., and HS, F. (2013). Dye aensitizers for photodynamic therapy. *Materials* 6 (3), 817–840. doi: 10.3390/ma6030817

Allison, R. R., and Moghissi, K. (2013). Photodynamic therapy (PDT): PDT mechanisms. *Clin. Endoscopy* 46 (1), 24–29. doi: 10.5946/ce.2013.46.1.24

Allison, B. A., Waterfield, E., Richter, A. M., and Levy, J. G. (2010). The effects of plasma lipoproteins on *in vitro*tumor cell killing and *in vivo* tumor photosensitization with benzoporphyrin derivative. *Photochem. Photobiol.* 54 (5), 709–715. doi: 10.1111/j.1751-1097.1991.tb02079.x

Cairns, R. A., Harris, I. S., and Mak, T. W. (2011). Regulation of cancer cell metabolism. *Nat. Rev. Cancer* 11 (2), 85–95. doi: 10.1038/nrc2981

Chu, C., Lin, H., Liu, H., Wang, X., Wang, J., Zhang, P., et al. (2017). Tumor microenvironment-triggered supramolecular system as an insitu nanotheranostic generator for cancer phototherapy. *Adv. Mater.* 29 (23), 1605928. doi: 10.1002/adma.201605928

Costerton, J. W., Stewart, P. S., and Greenberg, E. P. (1999). Bacterial biofilms: a common cause of persistent infections. *science* 284 (5418), 1318–1322. doi: 10.1126/science.284.5418.1318

Danon, A., Rotari, V. I., Gordon, A., Mailhac, N., and Gallois, P. (2004). Ultraviolet-C overexposure induces programmed cell death in Arabidopsis, which is mediated by caspase-like activities and which can be suppressed by caspase inhibitors, p35 and defender against Apoptotic Death. *J. Biol. Chem.* 279 (1), 779–787. doi: 10.1074/jbc.M304468200

Data. (2018). International Agency for Research on Cancer (IARC), World Health Organization, Latest global cancer data: Cancer burden rises to 18.1 million new cases and 9.6 million cancer deaths in 2018.

Dijkmans, P. A., Juffermans, L. J. M., Musters, R. J. P., Van Wamel, A., Ten Cate, F. J., Van Gilst, W., et al.(2004). Microbubbles and ultrasound: from diagnosis to therapy. *Eur. J. Echocardiography J. Working Group Echocardiography Eur. Soc. Cardiol.* 5 (4), 245. doi: 10.1016/j.euje.2004.02.001

DJ, K., and SD, E. (2000). Autophagy as a regulated pathway of cellular degradation. *Science* 290 (5497), 1717–1721. doi: 10.1126/science.290.5497.1717

Dougherty, T. J. (1985). Photodynamic Therapy *Adv. Exp. Med. Biol.* 193, 313–328. (Springer US). doi: 10.1007/978-1-4613-2165-1_30

Feng, X., Pan, W., Liu, Q., Zhang, T., Mai, B., and Wang, X. (2015). Glycolytic inhibitors 2-deoxyglucose and 3-bromopyruvatesynergize with photodynamic therapy respectively to inhibit cell migration. *J. Bioenerg. Biomembr.* 47 (3), 189–197. doi: 10.1007/s10863-015-9604-1

Furukawa, S., Soeda, S., Kiko, Y., Suzuki, O., Hashimoto, Y., Watanabe, T., et al. (2013). MCP-1 promotes invasion and adhesion of human ovarian cancer cells. *Anticancer Res.* 33 (11), 4785–4790. doi: 10.1093/annonc/mdt460.34

Gorman, A., Killoran, J., O'Shea, C., Kenna, T., Gallagher, W. M., and O'Shea, D. F. (2004). In vitro demonstration of the heavy-atom effect for photodynamic therapy. *J. Am. Chem. Soc.* 126 (34), 10619–10631. doi: 10.1021/ja047649e

Heleen, D., Katrien, V., Hendrik, H., Emmelie, S., Luc, D., Myriam, H., et al. (2015). Theranostic mRNA-loaded microbubbles in the lymphatics of dogs: implications for drug delivery. *Theranostics* 5 (1), 97–109. doi: 10.7150/thno.10298

Hirschberg, H., and Madsen, S. J. (2017). Synergistic efficacy of ultrasound, sonosensitizers and chemotherapy: a review. *Ther. Delivery* 8 (5), 331–342. doi: 10.4155/tde-2016-0080

Hrazdira, I., Skorpíková, J., and Dolníková, M. (1998). Ultrasonically induced alterations of cultured tumour cells. *Eur. J. Ultrasound Off. J. Eur. Fed. Soc. Ultrasound Med. Biol.* 8 (1), 43–49. doi: 10.1016/S0929-8266(98)00049-4

Hu, J., Wang, X., Zhang, K., Wang, P., Su, X., Li, Y., et al. (2014). Sinoporphyrin sodium: a novel sensitizer in sonodynamic therapy. *Anticancer Drugs* 25 (2), 174–182. doi: 10.1097/CAD.0000000000000031

Hu, J., Wang, X., Liu, Q., Zhang, K., Xiong, W., Xu, C., et al.(2015). Antitumor effect of sinoporphyrin sodium-mediated photodynamictherapy on human esophageal cancer Eca-109 cells. *Photochem. Photobiol.* 90 (6), 1404–1412. doi: 10.1111/php.12333

Huang, C., Chu, C., Wang, X., Lin, H., Wang, J., Zeng, Y., et al. (2017). Ultra-high loading of sinoporphyrin sodium in ferritin for single-wave motivated photothermal and photodynamic co-therapy. *Biomater. Sci.* 5 (8), 1512–1516. doi: 10.1039/C7BM00302A

Jiang, Z., Shi, R., Li, C., and Wang, A. (2013). Inhibitory effects of DVDMS-2-based-photodynamic therapy on the growth of tumor and *in vitro in vivo*. *Carcinogenesis Teratogenesis Mutagenesis* 25, 163–167. doi: 10.3969/j.issn.1004-616x.2013.03.001

Jin, Z.h., Miyoshi, N., Ishiguro, K., Umemura, S.i., Kawabata, K.i., Yumita, N., et al. (2000). Combination effect of photodynamic and sonodynamic therapy on experimental skin squamous cell carcinoma in C3H/HeN mice. *J. Dermatol.* 27 (5), 294–306. doi: 10.1111/j.1346-8138.2000.tb02171.x

Jori, G., and Reddi, E. (1993). The role of lipoproteins in the delivery of tumour-targeting photosensitizers. *Int. J. Biochem.* 25 (10), 1369–1375. doi: 10.1016/0020-711X(93)90684-7

Jr, I. W., Muss, H. B., and Mayer, D. K. (2011). Symptom management in metastatic breast cancer. *Oncologist* 16 (9), 1203–1214. doi: 10.1634/theoncologist.2011-0159

Kenyon, J. N., Fulle, R. J., and Lewis, T. J. (2009). Activated cancer therapy using light and ultrasound - a case series of sonodynamic photodynamic therapy in 115 patients over a 4 year period. *Curr. Drug Ther.* 4 (3). doi: 10.2174/157488509789055036

Kolarova, H., Tomankova, K., Bajgar, R., Kolar, P., and Kubinek, R. (2009). Photodynamic and sonodynamic treatment by phthalocyanine on cancer cell lines. *Ultrasound In Med. Biol.* 35 (8), 1397–1404. doi: 10.1016/j.ultrasmedbio.2009.03.004

Korbelik, M., Krosl, G., Olive, P. L., and Chaplin, D. J. (1991). Distribution of Photofrin between tumour cells and tumour associated macrophages. *Br. J. Cancer* 64 (3), 508. doi: 10.1016/0304-3835(91)90213-2

Li, C., Zhang, K., Wang, P., Hu, J., Liu, Q., and Wang, X. (2014). Sonodynamic antitumor effect of a novel sonosensitizer on S180 solid tumor. *Biopharm. Drug Disposition* 35 (1), 50–59. doi: 10.1002/bdd.1868

Li, Y., An, H., Wang, X., Wang, P., Qu, F., Jiao, Y., et al. (2018). Ultrasound-triggered release of sinoporphyrin sodium from liposome-microbubble complexes and its enhanced sonodynamic toxicityin breast cancer. *Nano Res.* 11 (2), 1038–1056. doi: 10.1007/s12274-017-1719-8

Li, E., Sun, Y., Lv, G., Li, Y., Zhang, Z., Hu, Z., et al. (2019). Sinoporphyrin sodium based sonodynamic therapy induces anti-tumor effects in hepatocellular carcinoma and activates p53/caspase 3 axis. *Int. J. Biochem. Cell Biol.* 113, 104–114. doi: 10.1016/j.biocel.2019.01.009

Liu, Q., Wang, X., Wang, P., and Xiao, L. (2007). Sonodynamic antitumor effect of protoporphyrin IX disodium salt on S180 solid tumor. *Chemotherapy* 53 (6), 429–436. doi: 10.1159/000110008

Liu, Y., Pan, W., Liu, Q., and Wang, X. (2016). Sinoporphyrin sodium triggered sono-photodynamic effects on breast cancer both *in vitro* and *in vivo*. *Ultrasonics Sonochem.* 31, 437–448. doi: 10.1016/j.ultsonch.2016.01.038

Liu, H., Zhou, M., Sheng, Z., Chen, Y., Yeh, C. K., Chen, W., et al. (2018). Theranostic nanosensitizers for highly efficient MR/fluorescence imaging-guided sonodynamic therapy of gliomas. *J. Cell. Mol. Med.* 22 (11), 5394–5405. doi: 10.1111/jcmm.13811

M, K., G, K., and DJ, C. (1991). Photofrin uptake by murine macrophages. *Cancer Res.* 51 (9), 2251–2255.

Mai, B., Wang, X., Liu, Q., Leung, A. W., Wang, X., Xu, C., et al. (2016). The antibacterial effect of sinoporphyrin sodium photodynamic therapy on Staphylococcus aureus planktonic and biofilm cultures. *Lasers In Surg. Med.* 48 (4), 400–408. doi: 10.1002/lsm.22468

Mai, B., Gao, Y., Li, M., Wang, X., Zhang, K., Liu, Q., et al. (2017). Photodynamic antimicrobial chemotherapy forStaphylococcus aureusand multidrug-resistant bacterial burn infection *in vitro* and *in vivo*. *Int. J. Nanomed.* 12, 5915–5931. doi: 10.2147/IJN.S138185

Maschek, G., Savaraj, N., Priebe, W., Braunschweiger, P., Hamilton, K., Tidmarsh, G. F., et al. (2004). 2-deoxy-D-glucose increases the efficacy of adriamycin and paclitaxel in human osteosarcoma and non-small cell lung cancers *in vivo*. *Cancer Res.* 64 (1), 31. doi: 10.1158/0008-5472.CAN-03-3294

McHale, A. P., Callan, J. F., Nomikou, N., Fowley, C., and Callan, B. (2016). Sonodynamic therapy: concept, mechanism and application to cancer treatment. *Adv. Exp. Med. Biol.* 880, 429–450. doi: 10.1007/978-3-319-22536-4_22

Miller, K. D., Siegel, R. L., Lin, C. C., Mariotto, A. B., Kramer, J. L., Rowland, J. H., et al. (2016). Cancer treatment and survivorship statistics, 2016. *CA: A Cancer J. Clinicians* 66 (4), 271–289. doi: 10.3322/caac.21349

Moan, J., Smedshammer, L., and Christensen, T. (1980). Photodynamic effects on human cells exposed to light in the presence of hematoporphyrin. pH effects. *Cancer Lett.* 9 (4), 327–332. doi: 10.1016/0304-3835(80)90025-7

Moreno-Sańchez, R., Rodríguez-Enríquez, S., Marín-Hernańdez, A., and Saavedra, E. (2007). Energy metabolism in tumor cells. *FEBS J.* 274 (2007), 1393–1418. doi: 10.1111/j.1742-4658.2007.05686.x

Musser, D. A., Wagner, J. M., Weber, F. J., and Datta-Gupta, N. (1980). The binding of tumor localizing porphyrins to a fibrin matrix and their effects following photoirradiation. *Res. Commun. In Chem. Pathol. Pharmacol.* 28 (3), 505.

Ni, L., Chao, L., Zhonghua, W., Jingxuan, Z., Xiangfeng, Y., Wenjing, G., et al. (2015). A safety study of a novel photosensitizer, sinoporphyrin sodium,for photodynamic therapy in Beagle dogs. *Photochem. Photobiol. Sci.* 14 (4), 815–832. doi: 10.1039/C4PP00463A

Nicolau, C., Catalá, V., Vilana, R., Gilabert, R., Bianchi, L., Solé, M., et al. (2004). Evaluation of hepatocellular carcinoma using SonoVue, a second generation ultrasound contrast agent: correlation with cellular differentiation. *J. Hepatol.* 40 (6), 1092–1099. doi: 10.1007/s00330-004-2298-0

O'Connor, A. E., Gallagher, W. M., and Byrne, A. T. (2010). Porphyrin and nonporphyrin photosensitizers in oncology:preclinical and clinical advances in photodynamic therapy. *Photochem. Photobiol.* 85 (5), 1053–1074. doi: 10.1111/j.1751-1097.2009.00585.x

Pacheco-Soares, C., Maftou-Costa, M., Da, C. M. C. C., Ac, D. S. S., and Moraes, K. C. (2014). Evaluation of photodynamic therapy in adhesion protein expression. *Oncol. Lett.* 8 (2), 714. doi: 10.3892/ol.2014.2149

Pandey, R. K., and Dougherty, T. J. (1989). Syntheses and photosensitizing activity of porphyrins joined with ester linkages. *Cancer Res.* 49 (8), 2042–2047. doi: 10.1002/1097-0142(19890415)63:8<1645::AID-CNCR2820630835>3.0.CO;

Pashkovskaya, A., Kotova, E., Zorlu, Y., Dumoulin, F., Ahsen, V., Agapov, I., et al. (2009). Light-triggered liposomal release: membrane permeabilization by photodynamic action. *Langmuir* 26 (8), 5726–5733. doi: 10.1021/la903867a

Pi, Z., Huang, Y., Shen, Y., Zeng, X., Hu, Y., Chen, T., et al. (2019). Sonodynamic therapy on intracranial glioblastoma xenografts using sinoporphyrin sodium delivered by ultrasound with microbubbles. *Ann. Biomed. Eng.* 47 (2), 549–562. doi: 10.1007/s10439-018-02141-9

Rapoport, N. Y., Kennedy, A. M., Shea, J. E., Scaife, C. L., and Nam, K. (2009). Controlled and targeted tumor chemotherapy by ultrasound-activated nanoemulsions/microbubbles. *J. Controlled Release* 138 (3), 268–276. doi: 10.1016/j.jconrel.2009.05.026

Roberto, C., Greta, V., Marco, B., Federica, F., Giovanna, S., Andrea, G., et al. (2013). Polymeric nanoparticles enhance the sonodynamic activity of meso-tetrakis (4-sulfonatophenyl) porphyrin in an *in vitro* neuroblastoma model. *Int. J. Nanomed.* 2013 (Issue 1), 4247–4263. doi: 10.2147/IJN.S51070

Romero-Garcia, S., Lopez-Gonzalez, J. S., B´ ez-Viveros, J. L., Aguilar-Cazares, D., and Prado-Garcia, H. (2011). Tumor cell metabolism: an integral view. *Cancer Biol. Ther.* 12 (11), 939–948. doi: 10.4161/cbt.12.11.18140

Rosenthal, I., Sostaric, J. Z., and Riesz, P. (2004). Sonodynamic therapy—a review of the synergistic effectsof drugs and ultrasound. *Ultrasonics Sonochem.* 11 (6), 349–363. doi: 10.1016/j.ultsonch.2004.03.004

Roy, I., Shetty, D., Hota, R., Baek, K., Kim, J., Kim, C., et al. (2016). A Multifunctional subphthalocyanine nanosphere for targeting, labeling, and killing of antibiotic-resistant bacteria. *Angewandte Chemie* 127 (50), 15367–15370. doi: 10.1002/ange.201507140

Sadanala, K. C., Chaturvedi, P. K., Seo, Y. M., Kim, J. M., Jo, Y. S., Lee, Y. K., et al. (2014). Sono-photodynamic combination therapy: a review on sensitizers. *Anticancer Res.* 34 (9), 4657–4664. doi: 10.1245/s10434-014-3557-1

Shen, J., Cao, S., Sun, X., Pan, B., Cao, J., Che, D., et al. (2018). Sinoporphyrin Sodium-mediated sonodynamic therapy inhibits RIP3 expression and induces apoptosis in the H446 small cell lung cancer cell line. *Cell. Physiol. Biochem.* 51 (6), 2938–2954. doi: 10.1159/000496045

Shi, Y., Zhang, B., Feng, X., Qu, F., Wang, S., Wu, L., et al. (2018). Apoptosis and autophagy induced by DVDMs-PDT on human esophageal cancer Eca-109 cells. *Photodiagnosis Photodynamic Ther.* 24, 198–205. doi: 10.1016/j.pdpdt.2018.09.013

Shirasu, N., Nam, S. O., and Kuroki, M. (2010). Tumor-targeted photodynamic therapy. *Lasers In Surg. Med.* 38 (5), 522–531. doi: 10.1002/lsm.20345

So, K. Y., and Oh, S. H. (2016). Heme oxygenase-1-mediated apoptosis under cadmium-induced oxidative stress is regulated by autophagy, which is

sensitized by tumor suppressor p53. *Biochem. Biophys. Res. Commun.* 479 (1), 80–85. doi: 10.1016/j.bbrc.2016.09.037

Sun, Y., Wang, H., Wang, P., Zhang, K., Geng, X., Liu, Q., et al. (2019). Tumor targeting DVDMS-nanoliposomes for an enhanced sonodynamic therapy of gliomas. *Biomater. Sci.* 7 (3), 985–994. doi: 10.1039/C8BM01187G

Tang, L., Chang, H., Liu, Y., and Li, J. (2012). Duplex DNA/Graphene Oxide biointerface: from fundamental understanding to specificenzymatic effects. *Adv. Funct. Mater.* 22 (14), 3083–3088. doi: 10.1002/adfm.201102892

Togsverd-Bo, K., Omland, S., Wulf, H., Sørensen, S., and Haedersdal, M. (2015). Primary prevention of skin dysplasia in renal transplant recipients with photodynamic therapy: a randomized controlled trial. *Am. J. Transplant.* 15 (11), 2986–2990. doi: 10.1111/ajt.13358

Trendowski, M. (2014). The promise of sonodynamic therapy. *Cancer Metastasis Rev.* 33 (1), 143–160. doi: 10.1007/s10555-013-9461-5

Vander Heiden, M. G., Cantley, L. C., and Thompson, C. B. (2009). Understanding the Warburg effect: the metabolic requirements of cell proliferation. *Science* 324 (5930), 1029. doi: 10.1126/science.1160809

Wainwright, M. (1998). Photodynamic antimicrobial chemotherapy (PACT). *J. Antimicrob. Chemother.* 42 (1), 13–28. doi: 10.1093/jac/42.1.13

Wang, P., Wang, X. B., and Liu, Q. H. (2007). HpD Distribution in H-22 tumor-bearing mice.*Acta Laboratorium Anim. Sci. Sin.* 15 (6), 401–405.

Wang, J., Ma, D., Fang, Q., Wang, P., Gao, R., and Sun, J. (2014). Down-regulation of HO-1 promoted apoptosis induced by decitabine via increasing p15INK4B promoter demethylation in myelodysplastic syndrome. *Am. Soc. Hematol.* doi: 10.1182/blood.V124.21.5213.5213

Wang, H., Pan, W., Li, L., Zhang, K., Wang, X., and Liu, Q. (2015a). Microbubbles enhance the antitumor effects of sinoporphyrin sodium mediated sonodynamic therapy both in vitro and in vivo. *Int. J. Biol. Sci.* 11 (12), 1401–1409. doi: 10.7150/ijbs.12802

Wang, X., Hu, J., Wang, P., Zhang, S., Liu, Y., Xiong, W., et al. (2015b). Analysis of the *in vivo* and *in vitro* effects of photodynamic therapy on breast cancer by using a sensitizer, sinoporphyrin sodium. *Theranostics* 5 (7), 772–786. doi: 10.7150/thno.10853

Wang, X., Liu, X., Li, Y., Wang, P., Feng, X., Liu, Q., et al. (2017). Sensitivity to antitubulin chemotherapeutics is potentiated by a photoactivable nanoliposome. *Biomaterials* 141, 50–62. doi: 10.1016/j.biomaterials.2017.06.034

Wu, L., Wang, X., Liu, Q., Leung, A. W., Wang, P., and Xu, C. (2016). Sinoporphyrin sodium mediated photodynamic therapy inhibits the migration associated with collapse of F-actin filaments cytoskeleton in MDA-MB-231 cells. *Photodiagnosis Photodynamic Ther.* 13, 58–65. doi: 10.1016/j.pdpdt.2015.12.008

Xie, L., Feng, X., Shi, Y., He, M., Wang, P., Wang, X., et al. (2018). Blocking the glycolytic pathway sensitizes breast cancer to sonodynamic therapy. *Ultrasound In Med. Biol.* 44 (6), 1233. doi: 10.1016/j.ultrasmedbio.2018.01.020

Xiong, W., Wang, P., Hu, J., Jia, Y., Wu, L., Chen, X., et al. (2015). A new sensitizer DVDMS combined with multiple focused ultrasound treatments: an effective antitumor strategy. *Sci. Rep.* 5, 17485. doi: 10.1038/srep17485

Xiong, W., Wang, X., Hu, J., Liu, Y., Liu, Q., and Wang, P. (2016). Comparative study of two kinds of repeated photodynamic therapystrategies in breast cancer by using a sensitizer, sinoporphyrin sodium. *J.Photochem. Photobiol. B. Biol.* 160, 299–305. doi: 10.1016/j.jphotobiol.2016.04.024

Yan, X., Hu, H., Lin, J., Jin, A. J., Niu, G., Zhang, S., et al. (2014). Optical and photoacoustic dual-modality imaging guided synergistic photodynamic/photothermal therapies. *Nanoscale* 7 (6), 2520–2526. doi: 10.1039/C4NR06868H

Yan, X., Niu, G., Lin, J., Jin, A. J., Hu, H., Tang, Y., et al. (2015). Enhanced fluorescence imaging guided photodynamic therapy of sinoporphyrin sodium loaded graphene oxide. *Biomaterials* 42 (42), 94–102. doi: 10.1016/j.biomaterials.2014.11.040

Yang, S., Wang, P., Wang, X., Su, X., and Liu, Q. (2014). Activation of microbubbles by low-level therapeutic ultrasound enhances the antitumor effects of doxorubicin. *Eur. Radiol.* 24 (11), 2739–2753. doi: 10.1007/s00330-014-3334-3

Zang, L., Zhao, H., Hua, J., Qin, F., Zheng, Y., Zhang, Z., et al. (2017a). Water-soluble gadolinium porphyrin as a multifunctional theranostic agent: Phosphorescence-based oxygen sensing and photosensitivity. *Dyes Pigments* 142, 465–471. doi: 10.1016/j.dyepig.2017.03.056

Zang, L., Zhao, H., Fang, Q., Fan, M., Chen, T., Tian, Y., et al. (2017b). Photophysical properties of sinoporphyrin sodium and explanation of its high photo-activity. *J. Porphyrins Phthalocyanines* 21 (01), 59–66. doi: 10.1142/S1088424617500055

Zhang, L., Sun, Z., Ren, P., You, M., Zhang, J., Fang, L., et al. (2017). Localized delivery of shRNA against PHD2 Protects the heart from acute myocardial infarction through ultrasound-targeted cationic microbubble destruction. *Theranostics* 7 (1), 51–66. doi: 10.7150/thno.16074

Zhu, B., Li, S., Yu, L., Hu, W., Sheng, D., Hou, J., et al. (2019). Inhibition of autophagy with chloroquine enhanced sinoporphyrin sodium mediated photodynamic therapy-induced apoptosis in human colorectal cancer cells. *Int. J. Biol. Sci.* 15 (1), 12. doi: 10.7150/ijbs.27156

Conflict of Interest: The authors declare that the research was conducted in the absence of any commercial or financial relationships that could be construed as a potential conflict of interest.

The handling editor is currently organizing a Research Topic with one of the authors, XW, and confirms the absence of any other collaboration.

The reviewer WT declared a shared affiliation, with no collaboration, with the authors to the handling editor at time of review.

Advantages of publishing in Frontiers

OPEN ACCESS
Articles are free to read for greatest visibility and readership

FAST PUBLICATION
Around 90 days from submission to decision

HIGH QUALITY PEER-REVIEW
Rigorous, collaborative, and constructive peer-review

TRANSPARENT PEER-REVIEW
Editors and reviewers acknowledged by name on published articles

Frontiers
Avenue du Tribunal-Fédéral 34
1005 Lausanne | Switzerland

Visit us: www.frontiersin.org
Contact us: info@frontiersin.org | +41 21 510 17 00

REPRODUCIBILITY OF RESEARCH
Support open data and methods to enhance research reproducibility

DIGITAL PUBLISHING
Articles designed for optimal readership across devices

FOLLOW US
@frontiersin

IMPACT METRICS
Advanced article metrics track visibility across digital media

EXTENSIVE PROMOTION
Marketing and promotion of impactful research

LOOP RESEARCH NETWORK
Our network increases your article's readership